

Medical Radiology · Diagnostic Imaging

Series Editors: Hans-Ulrich Kauczor · Paul M. Parizel · Wilfred C.G. Peh

Hatem Alkadhi

André Euler

David Maintz

Dushyant Sahani *Editors*

Spectral Imaging

Dual-Energy, Multi-Energy and
Photon-Counting CT

 Springer

Medical Radiology

Diagnostic Imaging

Series Editors

Hans-Ulrich Kauczor

Paul M. Parizel

Wilfred C. G. Peh

The book series *Medical Radiology – Diagnostic Imaging* provides accurate and up-to-date overviews about the latest advances in the rapidly evolving field of diagnostic imaging and interventional radiology. Each volume is conceived as a practical and clinically useful reference book and is developed under the direction of an experienced editor, who is a world-renowned specialist in the field. Book chapters are written by expert authors in the field and are richly illustrated with high quality figures, tables and graphs. Editors and authors are committed to provide detailed and coherent information in a readily accessible and easy-to-understand format, directly applicable to daily practice.

Medical Radiology – Diagnostic Imaging covers all organ systems and addresses all modern imaging techniques and image-guided treatment modalities, as well as hot topics in management, workflow, and quality and safety issues in radiology and imaging. The judicious choice of relevant topics, the careful selection of expert editors and authors, and the emphasis on providing practically useful information, contribute to the wide appeal and ongoing success of the series. The series is indexed in Scopus.

More information about this series at <https://link.springer.com/bookseries/174>

Hatem Alkadhi • André Euler
David Maintz • Dushyant Sahani
Editors

Spectral Imaging

Dual-Energy, Multi-Energy
and Photon-Counting CT

Editors

Hatem Alkadhi
Institute of Diagnostic
and Interventional Radiology
University Hospital Zurich
Zurich
Switzerland

André Euler
Institute of Diagnostic
and Interventional Radiology
University Hospital Zurich
Zurich
Switzerland

David Maintz
Department of Radiology
Universitätsklinikum Köln
Köln, Nordrhein-Westfalen
Germany

Dushyant Sahani
Department of Radiology
University of Washington
Seattle, WA
USA

ISSN 0942-5373
Medical Radiology
ISSN 2731-4677
Diagnostic Imaging

ISSN 2197-4187 (electronic)

ISSN 2731-4685 (electronic)

ISBN 978-3-030-96284-5 ISBN 978-3-030-96285-2 (eBook)
<https://doi.org/10.1007/978-3-030-96285-2>

© The Editor(s) (if applicable) and The Author(s), under exclusive license to Springer Nature Switzerland AG 2022

This work is subject to copyright. All rights are solely and exclusively licensed by the Publisher, whether the whole or part of the material is concerned, specifically the rights of translation, reprinting, reuse of illustrations, recitation, broadcasting, reproduction on microfilms or in any other physical way, and transmission or information storage and retrieval, electronic adaptation, computer software, or by similar or dissimilar methodology now known or hereafter developed. The use of general descriptive names, registered names, trademarks, service marks, etc. in this publication does not imply, even in the absence of a specific statement, that such names are exempt from the relevant protective laws and regulations and therefore free for general use.

The publisher, the authors and the editors are safe to assume that the advice and information in this book are believed to be true and accurate at the date of publication. Neither the publisher nor the authors or the editors give a warranty, expressed or implied, with respect to the material contained herein or for any errors or omissions that may have been made. The publisher remains neutral with regard to jurisdictional claims in published maps and institutional affiliations.

This Springer imprint is published by the registered company Springer Nature Switzerland AG
The registered company address is: Gewerbestrasse 11, 6330 Cham, Switzerland

Foreword

CT was the first cross-sectional imaging technique to be widely introduced over 50 years ago, and it was enthusiastically received by the medical community. After the advent of magnetic resonance imaging, however, CT began to lose its appeal. Multiplanar slices, superior soft tissue contrast, and the absence of ionizing radiation were considered substantial advantages. Not to be forgotten, MRI was considered more intellectually demanding, because it was necessary to select from the multitude of pulse sequences the one best suited to the clinical problem at hand. Even new and specific contrast agents were developed. Therefore, it was not surprising that CT was considered a diligent and patient, but somewhat boring workhorse.

Tremendous developments have occurred since then: Spiral CT, multislice CT, iterative image reconstruction, and finally Spectral Imaging and Photon Counting CT. It is to the great credit of the editors of this book, *Spectral Imaging: Dual-Energy, Multi-Energy and Photon-Counting CT*, to provide a competent and easily understandable overview of these fascinating developments.

The international editorial team of Hatem Alkadhi, André Euler, David Maintz, and Dushyant Sahani, all distinguished and highly recognized imaging scientists, have recruited experienced and knowledgeable experts as authors.

In the first part, the methodological and technical fundamentals of spectral CT and photon counting CT as well as the application of contrast agents are presented. These chapters impress by the clarity of the presentation, so that they are understandable even for physicians without a more extensive background in science and engineering. The fundamentals of spectral CT and photon counting CT are covered, as are the emerging future developments. In spectral CT, the major manufacturers pursue different strategies, which are explained in individual chapters, so that the reader can make his or her own objective assessment.

The chapter on contrast media impressively demonstrates that spectral and photon counting CT also allow a differentiated and targeted use of contrast media, which contributes to an improvement in the diagnostic accuracy. With the new CT technologies, elements other than iodine, such as lanthanides, hafnium, tantalum, tungsten, or even gold, could also be used as a basis for new contrast media, which could result in fascinating and completely new indications.

The main focus of the book is taken by chapters on the clinical applications of spectral imaging in various organs and diseases. It becomes clear that spectral imaging has great potential for a variety of clinical problems and that extensive experience has been gained in this field in recent years. It becomes clear that these are often very important, even therapy-decisive questions, such as the detection or exclusion of an active hemorrhage or a fresh vertebral fracture.

In the last two contributions, the question is raised as to what will happen next with CT. What can the new CT techniques in radiomics and artificial intelligence contribute and what can be expected from photon counting CT. Due to new developments, the limitations of CT compared to MRI mentioned at the beginning of this preface no longer exist or exist only in part. Spectral CT can provide multiplanar imaging, accurate tissue characterization, and is associated with significantly lower radiation exposure. Needless to say, modern CT is anything but boring but an exciting and dynamically evolving technology that will keep us on our toes for a long time to come!

I would like to recommend this book to the readers, and I am sure that they will find it as exciting and informative as I do. I would like to congratulate the editors and the authors on their successful project and thank them for their effort and hard work.

Prof. em. Dr. Dr. h.c. Maximilian Reiser, FACR, FRCR, ML
Department of Radiology
Ludwig-Maximilians-University
Munich, Germany

Contents

Part I Technical Principles

Material Decomposition and Post-processing: History and Basic Principles	3
Jia Wang, Xinhui Duan, and Cynthia H. McCollough	
Dual-Energy: The Siemens Approach	15
Bernhard Schmidt and Thomas Flohr	
Dual-Energy: The Philips Approach	29
Ami Altman, Galit Kafri, and Sary Shenhav	
Dual-Energy: The GE Approach	45
Scott Slavic and Mats Danielsson	
Dual-Energy: The Canon Approach	63
Kirsten Boedeker, Jay Vaishnav, Ruoqiao Zhang, Zhou Yu, and Satoru Nakanishi	
Basic Principles and Clinical Applications of Photon-Counting CT	73
Thomas Flohr, Martin Petersilka, Stefan Ulzheimer, Bernhard Schmidt, Klaus Erhard, Bernhard Brendel, Marjorie Villien, Philippe Coulon, Salim Si-Mohamed, and Sara Boccacini	
Contrast Media for Modern Computed Tomography	93
Hubertus Pietsch and Gregor Jost	

Part II Clinical Applications

Neuroradiological Imaging	109
Sebastian Winklhofer, Dominik Nakhostin, and Mohammed Fahim Mohammed	
Head and Neck Imaging	127
David Zopfs	
Clinical Applications in Cardiac Imaging	143
Basel Yacoub, Josua Decker, U. Joseph Schoepf, Tilman Emrich, Jon F. Aldinger, and Akos Varga-Szemes	

Dual-Energy CT Angiography	163
Matthias Stefan May and Armin Muttko	
Thoracic Imaging: Ventilation/Perfusion	183
Hye Jeon Hwang, Sang Min Lee, and Joon Beom Seo	
Thoracic Oncology	201
Philip Konietzke	
Gastrointestinal Imaging: Oncology (Liver, Pancreas, Bowel Cancer, and Treatment Response)	219
Simon Lennartz and Nils Große Hokamp	
Gastrointestinal Imaging: Liver Fat and Iron Quantification	235
Malte Niklas Bongers	
Bowel Imaging	245
Markus M. Obmann	
Role of Dual-Energy Computed Tomography (DECT) in Acute Abdomen	255
Saira Hamid, Muhammad Umer Nasir, Aneta Keckler-Pietrzyk, Adnan Sheikh, Nicolas Murray, Faisal Khosa, and Savvas Nicolaou	
Spectral Computed Tomography Imaging of the Adrenal Glands	277
Matthias Benndorf, August Sigle, and Fabian Bamberg	
Urogenital Imaging: Kidneys (Lesion Characterization)	285
Ali Pourvaziri, Anushri Parakh, Avinash Kambadakone, and Dushyant Sahani	
Urogenital Imaging: Kidneys: Urinary Stones	295
Nils Große Hokamp	
Skeletal Imaging: Bones	301
Christian Booz, Julian L. Wichmann, and Tommaso D'Angelo	
Gout	315
Torsten Diekhoff	
Dual-Energy CT in Radiation Oncology	333
Christian Richter and Patrick Wohlfahrt	
The Future of Spectral CT: Radiomics and Beyond	347
Bettina Baessler and Davide Cester	
Photon-Counting CT: Initial Clinical Experience	363
Victor Mergen, André Euler, Kai Higashigaito, Matthias Eberhard, and Hatem Alkadhi	

Part I

Technical Principles



Material Decomposition and Post-processing: History and Basic Principles

Jia Wang, Xinhui Duan,
and Cynthia H. McCollough

Contents

1	Introduction and History	3
2	Methods of Material Decomposition	4
3	Synthetic Images from Material Decomposition and Post-Processing	6
3.1	Mixed CT Images	7
3.2	Material-Specific Images	7
3.3	Virtual Monoenergetic Images	8
3.4	Electron Density and Effective Atomic Number Images	9
4	Image Quality and Quantitative Accuracy of Synthetic DECT Images	10
5	Conclusion	11
	References	11

1 Introduction and History

The concept of using two-energy beams in CT imaging dates back to Hounsfield's early work (Hounsfield 1973), where he explained that by using two distinct tube potentials, one could enhance the contrast of and differentiate between specific materials. Several important papers pub-

lished in the 1970s and the 1980s established the theoretical foundation of dual-energy CT imaging (Alvarez and Macovski 1976; Macovski et al. 1976; Kelcz et al. 1979; Lehmann et al. 1981; Kalender et al. 1986). Due to the limitations of CT technology at that time, dual-energy CT could not be used routinely in clinical practice. A breakthrough happened in 2006, when a dual-source CT scanner was made commercially available, enabling dual-energy CT in routine patient exams (Flohr et al. 2006; Johnson et al. 2007).

Currently, CT manufacturers offer several solutions for dual-energy CT imaging. However, they all share the similar basic physics principle. The data acquisition for dual-energy CT requires (1) the minimal time interval between the two CT acquisitions, which ideally occur simultaneously, and (2) sufficient difference of photon energies

J. Wang
Department of Environmental Health and Safety,
Stanford University, Stanford, CA, USA
e-mail: wangjia@stanford.edu

X. Duan
UT Southwestern Medical Center, Dallas, TX, USA
e-mail: xinhui.duan@utsouthwestern.edu

C. H. McCollough (✉)
Department of Radiology, Mayo Clinic,
Rochester, MN, USA
e-mail: mccollough.cynthia@mayo.edu

between the two CT acquisitions. The time interval requirement ensures that the images from the two CT acquisitions have minimal registration errors, and the sufficient energy difference requirement controls noise level in the post-processed images to ensure acceptable image quality for diagnosis. After two CT acquisitions are obtained, the post-processing performed in all the dual-energy CT platforms perform the same basic physics task i.e., material decomposition.

2 Methods of Material Decomposition

X-ray attenuation characteristics depend on photon energy and the physical property of the incident material, i.e., mass density (ρ) and atomic number (Z). In the photon energy range of diagnostic imaging, there are three main mechanisms in X-ray photon interacting with matter: photoelectric effect, Compton scatter, and coherent scatter (Rayleigh scatter). The mass attenuation coefficient $\left(\frac{\mu}{\rho}\right)$ of a material is the summation of the mass attenuation coefficients of the three mechanisms,

$$\left(\frac{\mu}{\rho}\right) = \left(\frac{\mu}{\rho}\right)_{\text{Photoelectric}} + \left(\frac{\mu}{\rho}\right)_{\text{Compton}} + \left(\frac{\mu}{\rho}\right)_{\text{Coherent}} \quad (1)$$

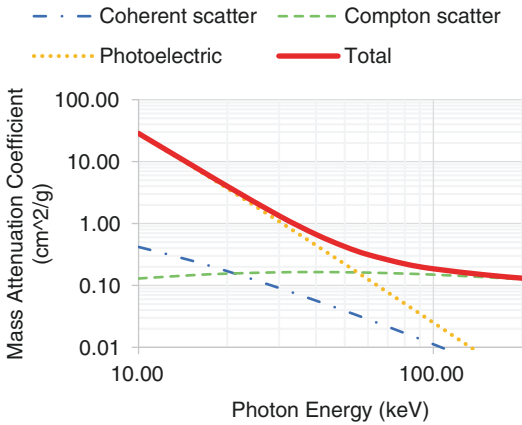


Fig. 1 Mass attenuation coefficients as a function of photon energy for cortical bone (ICRU 44) (left) and soft tissue (ICRU 44) (right). Photoelectric effect, Compton

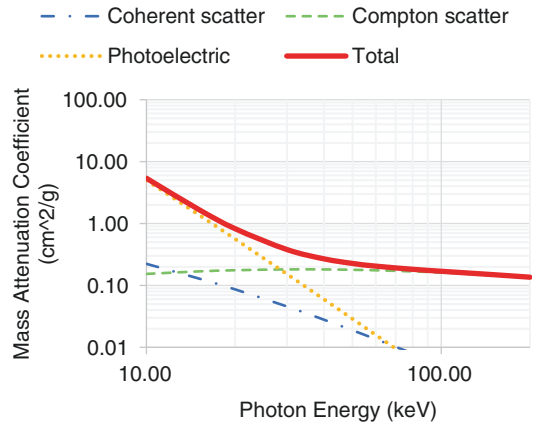
scatter, and coherent scatter have distinct dependencies with photon energy. These unique behaviors are the foundation for dual-energy CT imaging

$$\left(\frac{\mu}{\rho}\right) = \left(\frac{\mu}{\rho}\right)_{\text{Photoelectric}} + \left(\frac{\mu}{\rho}\right)_{\text{Compton}} \quad (2)$$

This mathematic formula for the mass attenuation due to the photoelectric effect and Compton scatter have been long established through theoretical physics and experimental measurements (Bushberg et al. 2012). The mass attenuation coefficient can be separated into a product of a material-dependent term and a photon-energy-dependent term, so that the mass attenuation coefficient can be written as

$$\left(\frac{\mu}{\rho}\right)(E) = \alpha_p f_p(E) + \alpha_c f_c(E) \quad (3)$$

where α_p and α_c are material-dependent factors for the photoelectric effect and Compton scatter, and f_p and f_c are energy-dependent factors, respectively. When ignoring the K-edge effect, the format of α and f are known through X-ray physics (Bushberg et al. 2012).



scatter, and coherent scatter have distinct dependencies with photon energy. These unique behaviors are the foundation for dual-energy CT imaging

To determine the α_p and α_c , we need attenuation measurements from two different energy levels, E_{Low} (low energy) and E_{High} (high energy),

$$\begin{aligned} \left(\frac{\mu}{\rho}\right)_{\text{Low}} &= \alpha_p f_p(E_{\text{Low}}) + \alpha_c f_c(E_{\text{Low}}) \\ \left(\frac{\mu}{\rho}\right)_{\text{High}} &= \alpha_p f_p(E_{\text{High}}) + \alpha_c f_c(E_{\text{High}}) \end{aligned} \quad (4)$$

This process of determining material composition through two measurements is often called material decomposition and Eq. (4) is a physical effect model since it is based on the photoelectric effect and Compton scatter. This model is straightforward, but has limitations because it only models two mechanisms for X-ray interactions with materials; other mechanisms which are ignored in the model will cause some error in the calculation (Williamson et al. 2006). Another commonly used model is the basis material model. Instead of using the photoelectric and Compton effects as the base functions, we use the attenuation coefficient of two selected materials, namely basis materials or base materials. Given two basis materials 1 and 2 (e.g., iodine and bone),

$$\begin{aligned} \left(\frac{\mu}{\rho}\right)_1(E) &= \alpha_{1,p} f_p(E) + \alpha_{1,c} f_c(E) \\ \left(\frac{\mu}{\rho}\right)_2(E) &= \alpha_{2,p} f_p(E) + \alpha_{2,c} f_c(E) \end{aligned} \quad (5)$$

a third material would have the same format,

$$\left(\frac{\mu}{\rho}\right)(E) = \alpha_{3,p} f_p(E) + \alpha_{3,c} f_c(E) \quad (6)$$

Substituting $f_p(E)$ and $f_c(E)$ from (5) in to (6), the third material can be represented as

$$\left(\frac{\mu}{\rho}\right)(E) = m_1 \left(\frac{\mu}{\rho}\right)_1(E) + m_2 \left(\frac{\mu}{\rho}\right)_2(E) \quad (7)$$

where $m_1 = \frac{\alpha_{3,p}\alpha_{2,c} - \alpha_{3,c}\alpha_{2,p}}{\alpha_{1,p}\alpha_{2,c} - \alpha_{2,p}\alpha_{1,c}}$ and

$$m_2 = \frac{\alpha_{3,c}\alpha_{1,p} - \alpha_{3,p}\alpha_{1,c}}{\alpha_{1,p}\alpha_{2,c} - \alpha_{2,p}\alpha_{1,c}}$$

Equation (7) shows the attenuation of any material can be represented by a linear combination of two basis materials. It is worth noting that although Eq. (5) is deduced from the two physical effects model, it does not have the limitation that only two physical mechanisms are modeled since the attenuation coefficients of the basis materials 1 and 2 contain all the attenuation information. Neither the two physical effects model nor the two-basis material model work well when the K-edge effect is a significant source of attenuation.

If a mixture contains three different materials and we would like to determine the concentration of each material, we will need another independent equation. Usually, we assume mass or volume conservation which means the mass fraction or volume fraction of the three materials must add up to 1,

$$f_1 + f_2 + f_3 = 1, f_1 \geq 0, f_2 \geq 0, f_3 \geq 0, \quad (8)$$

where f_1, f_2 , and f_3 are mass or volume fractions of the materials. This is often called three-material decomposition.

The K-edge is a unique attenuation feature (Fig. 2). The abrupt change in attenuation around the k-edge energy has a different behavior than the smooth attenuation curves of the photoelectric effect and Compton scatter. Thus, a K-edge term

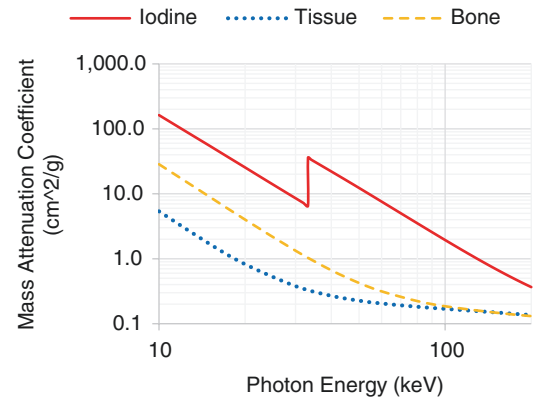


Fig. 2 Mass attenuation coefficient of iodine, soft tissue (ICRU 44), and cortical bone (ICRU 44). Iodine curve has an abrupt attenuation increase at 33.2 keV, which is called the absorption k-edge of iodine

needs to be added into the decomposition model when the K-edge contributes substantially to the total attenuation. The mass attenuation coefficient with the K-edge term can be expressed as

$$\left(\frac{\mu}{\rho}\right)(E) = \alpha_p f_p(E) + \alpha_c f_c(E) + \alpha_k f_k(E) \quad (9)$$

where a_K and f_K are the material- and energy-dependent terms representing the K-edge effect. If there are multiple K-edge materials in the measurements, each material needs to have a separate term in the attenuation formula. Similarly, basis material models can be updated to include K-edge materials,

$$\begin{aligned} \left(\frac{\mu}{\rho}\right)(E) = & m_1 \left(\frac{\mu}{\rho}\right)_1(E) + m_2 \left(\frac{\mu}{\rho}\right)_2(E) \\ & + m_k \left(\frac{\mu}{\rho}\right)_k(E) \end{aligned} \quad (10)$$

where m_k and $\left(\frac{\mu}{\rho}\right)_k(E)$ are the terms for the K-edge material.

When there are multiple K-edge materials in the model, two measurements from dual-energy CT imaging become insufficient to solve the problem, even with mass or volume conservation. That is, the number of unknowns is higher than the number of equations. Photon-counting CT can measure the energy of each X-ray photon and store the photon counts separately in multiple energy intervals, namely, energy bins. With the sufficient number of energy bins, this provides sufficient independent measurements for K-edge imaging. Furthermore, photon-counting CT can adjust the positions of its energy bins to be just before and just after the K-edge energy level to boost the signal from the K-edge attenuation (Roessl and Proksa 2007). This opens up the possibility for new CT contrast agents and imaging of multiple contrast agents simultaneously (Schlomka et al. 2008; Muenzel et al. 2017; Willemink et al. 2018).

The material decomposition we discussed so far is calculated using mass or linear attenuation coefficients, which means the decomposition is performed using the CT images. The decomposition process can also be performed using projec-

tion data. In dual-energy CT, the projection data can be modeled as,

$$\begin{cases} p_{\text{Low}} = \int_0^{E_{\text{lm}}} S_L(E) \exp(-A_p f_p(E) - A_c f_c(E)) dE \\ p_{\text{High}} = \int_0^{E_{\text{hm}}} S_H(E) \exp(-A_p f_p(E) - A_c f_c(E)) dE \end{cases} \quad (11)$$

where $A_p = \int \alpha_A(\bar{x}) ds$, $A_c = \int \alpha_c(\bar{x}) ds$ are the projections of the α_A and α_c , p_L and p_H are measured projection data, E_{Lm} and E_{Hm} are the maximum photon energy for the low- and high-energy X-ray beams, and $S_L(E)$ and $S_H(E)$ are the energy functions, which combine X-ray spectra and detector response functions. Solving Eq. (11), α_A and α_c are obtained by performing CT reconstruction using A_p and A_c . This is projection-space decomposition using the photoelectric and Compton effects and it works similarly as the two-basis material model. In principle, the projection-space decomposition provides more accurate results than image-space decomposition since it models the imaging chain more precisely. However, in practice, the performance difference of image-space and projection-space decomposition might not be as significant as expected (Jacobsen et al. 2018; Sellerer et al. 2018; Taylor et al. 2019).

3 Synthetic Images from Material Decomposition and Post-Processing

In this section, we will discuss the creation, application, and pitfalls of the common types of synthetic images from spectral CT. In conventional single-energy CT, although CT images acquired at the chosen tube potential can be created with multiple reconstruction kernels to serve different clinical tasks, the reconstruction kernels only impact the noise and spatial resolution of the CT images, and the tissue and material contrast of the CT images is approximately kept the same. On the other hand, spectral CT, including dual-energy CT (DECT), not only provides conventional image sets with the desired noise and

spatial resolution, but also provides images that feature different tissue contrasts and additional material-specific information. These synthetic images can be generated either from projection data (Alvarez and Macovski 1976; Lehmann et al. 1981; Kalender et al. 1986; Wang and Pelc 2011) or CT images of multiple energies (Yu et al. 2011; Liu et al. 2009; Niu et al. 2014; Li et al. 2015) after a spectral CT scan. For clarity we will focus our discussion on DECT in the following sections, because CT systems with multi-energy (more than two) capabilities have just been approved for clinical use. However, all essential features of synthetic images discussed below apply to both DECT and multi-energy CT systems.

3.1 Mixed CT Images

Mixed images are generated by blending the low- and high-energy CT images from a DECT scan. The primary use of mixed images is for routine diagnostic interpretation and they serve as a surrogate for the conventional single-energy CT images that the clinical users are familiar with, even though they may be new to DECT technology.

One common way to create the mixed images is to add the low- and high-energy images with user-adjustable weighting factors:

$$I_{\text{Mixed}} = w_{\text{Low}} I_{\text{Low}} + w_{\text{High}} I_{\text{High}} \quad (12)$$

where I_{Low} and I_{High} denote the low- and high-energy images respectively, and w_{Low} and w_{High} denote the corresponding weighting factor, and $w_{\text{Low}} + w_{\text{High}} = 1$. The optimal choice of weighting factors depends on the clinical task, patient size, and dose partition between low- and high-energy scans. Yu et al. showed that linearly mixed images from DECT provide similar or improved noise and iodine contrast-to-noise ratio (CNR) relative to 120 kV images using the same radiation dose over a wide range of phantom sizes (from 30 cm to 45 cm in lateral width), but inferior iodine CNR compared to 80 kV images for 30-cm small phantom (Yu et al. 2009). Behrendt et al. found weighting factor 0.5 provides the best subjective

image quality in a DECT angiography study (Behrendt et al. 2009). In clinical DECT applications, the linear mix weighting factor (w_{Low}) is commonly set between 0.5 and 0.7 to provide a balance between iodine contrast and image noise.

The mixed images can also be created in a non-linear fashion. Holmes et al. showed in a liver CT study that a non-linear blending method based on a modified sigmoid function provides higher iodine CNR and better subjective score compared to a linear mixed approach (Holmes 3rd et al. 2008).

3.2 Material-Specific Images

The foremost advantage of DECT over conventional single-energy CT is its ability to provide material specific information for the anatomy of interest. Through the material decomposition steps discussed before, the density maps of basis materials can be calculated to provide quantitative maps of their distribution.

Based on the two-basis material assumption, solving Eq. (7) using data acquired at low- and high energy yields the mass densities of two basis materials (Yu et al. 2011):

$$\rho_1 = \frac{\mu_{\text{Low}} \left(\frac{\mu}{\rho} \right)_{\text{High},2} - \mu_{\text{High}} \left(\frac{\mu}{\rho} \right)_{\text{Low},2}}{\left(\frac{\mu}{\rho} \right)_{\text{Low},1} \left(\frac{\mu}{\rho} \right)_{\text{High},2} - \left(\frac{\mu}{\rho} \right)_{\text{Low},2} \left(\frac{\mu}{\rho} \right)_{\text{High},1}} \quad (13)$$

$$\rho_2 = \frac{-\mu_{\text{Low}} \left(\frac{\mu}{\rho} \right)_{\text{High},1} + \mu_{\text{High}} \left(\frac{\mu}{\rho} \right)_{\text{Low},1}}{\left(\frac{\mu}{\rho} \right)_{\text{Low},1} \left(\frac{\mu}{\rho} \right)_{\text{High},2} - \left(\frac{\mu}{\rho} \right)_{\text{Low},2} \left(\frac{\mu}{\rho} \right)_{\text{High},1}}$$

where μ_{Low} and μ_{High} denote the linear coefficients measured at low- and high-energy scan, $\left(\frac{\mu}{\rho} \right)_{\text{Low},1}$ and $\left(\frac{\mu}{\rho} \right)_{\text{High},1}$ represent the mass attenuation coefficient of the basis material 1 at the low and high energy, respectively, and the similar denotation applies to basis material 2. If there is a third material in the mixture, either mass or volume

conservation can be assumed to add another independent condition to solve the three-material decomposition (Liu et al. 2009). In clinical applications, the commonly used unit of the mass density maps is mg/ml, which indicates the concentration of the material. However, some CT manufacturers convert the concentration unit into CT numbers in Hounsfield units. The advantages of using CT-like density maps is that they are more familiar to clinical users and more compatible with PACS systems. However, if the users are looking for the absolute concentration information of certain materials, the density maps with the unit of mg/ml are preferred.

DECT provides a variety of material specific images depending on the clinical tasks.

3.2.1 Material Differentiation Images

Material differentiation images, sometimes referred as material maps, display a material's distribution, typically in a color-coded fashion, but does not provide the concentration information. For example, in DECT scan of patient with kidney stones, color maps are generated for differentiation of uric acid from non-uric-acid kidney stones based on their difference in effective atomic numbers (Primak et al. 2007; Graser et al. 2008). Similarly, based on DECT differentiation of uric acid from calcium, diagnosis of gout was established by using DECT to identify monosodium urate crystals in synovial fluid or tissue aspirates (Bongartz et al. 2015). DECT has also been used to provide color-coded maps of silicon for evaluation of the integrity of silicone breast implants (Johnson et al. 2013).

3.2.2 Material Quantification Images

Material quantification images provide both the distribution and concentration information of target materials. Iodine quantification is the most common use of DECT and has been adopted in a variety of clinical applications for characterization of liver (Lee et al. 2011) and renal lesions (Mileto et al. 2014), hemorrhage in stroke patients (Gupta et al. 2010), thyroid nodules (Li et al. 2012), and bowel disease (Fulwadhva et al. 2016). Calcium quantification with DECT has been applied to differentiate between calcium

and hemorrhage in unenhanced head CT exams (Hu et al. 2016). Iron maps are used in DECT to evaluate the liver iron accumulation for hematological patients (Luo et al. 2015; Werner et al. 2019). Fat quantification in liver has been evaluated in DECT exams using a three-material decomposition including fat, liver tissues, and iron (Fischer et al. 2011). Xenon maps acquired from DECT can be used to evaluate the distribution of morphologic and functional changes in pulmonary diseases such as chronic obstructive pulmonary disease (COPD) and asthma (Kong et al. 2014).

3.2.3 Material Negative Images

With material density maps calculated from DECT material decomposition, certain material can be virtually removed from the CT images to improve diagnostic accuracy and confidence. In iodine contrast enhanced DECT exams, a set of virtual non-contrast (VNC) images are created to potentially eliminate the need to acquire the true non-contrast images, therefore reducing radiation dose to patients (Ferda et al. 2009; Graser et al. 2009). In DECT of bone marrow, calcium signal is removed from bone images to evaluate bone marrow edema (Wang et al. 2013).

3.3 Virtual Monoenergetic Images

In addition to mixed images and material-specific images, DECT datasets can be used to create virtual monoenergetic images (VMI) which are gray-scale images mimicking the appearance of CT images acquired with a true monochromatic X-ray source. In theory, monoenergetic images can be created at any individual X-ray energy, but in clinical practice, the typical range of selected energy is from 40 to 200 keV, depending on the diagnostic tasks.

In principle, the creation of VMIs can be considered as the by-product of the mass density maps from material decomposition in Sect. 3.2. Once the mass density images are generated from either projection-space or image-space material decomposition, the linear attenuation coefficient $\mu(E)$ can

be calculated based on basis material mass density maps and each material's mass attenuation coefficient at a chosen energy, as shown below:

$$\mu(E) = \left(\frac{\mu}{\rho}\right)_1(E) \bullet \rho_1 + \left(\frac{\mu}{\rho}\right)_2(E) \bullet \rho_2 \quad (14)$$

where $\left(\frac{\mu}{\rho}\right)_1(E)$ and $\left(\frac{\mu}{\rho}\right)_2(E)$ denote the mass attenuation coefficient of the two basis materials at the chosen energy E , and ρ_1 and ρ_2 are their mass density. The VMIs can then be obtained by scaling the $\mu(E)$ from Eq. (14) with $\mu(E)$ of water to create the CT-like images. Alternatively, Yu et al. showed that monoenergetic images can be calculated by the linear combination of CT images from the low and high energy (Yu et al. 2011):

$$CT(E) = w(E) \bullet CT_{Low} + (1 - w(E)) \bullet CT_{High} \quad (15)$$

where CT_{Low} and CT_{High} denote the low- and high-energy CT images, and $w(E)$ is the weighting factor. Two things are worth mentioning here. First, the $w(E)$ here should not be confused with the weighting factor w_{Low} and w_{High} used for creating mixed images in Eq. (12). Second, although not given explicitly in Eq. (15), the approach of linear combination of CT images is also based on the assumption that there are only two basis materials in the material decomposition process (Yu et al. 2011).

Because of the freedom to create VMIs at any energy, they play multiple roles in DECT clinical applications. First, on DECT scanners using fast kV switching technology, no mixed images from low- and high-energy scans are created. VMIs are used as a substitute for the conventional single-energy images for routine diagnosis purpose. The monoenergetic images can be created at an energy level that approximately matches the mean energy of either a 100 kV or 120 kV polychromatic energy beam, depending on user preference. Second, VMIs are often created to provide optimal iodine signal in contrast enhanced DECT exams. Because the X-ray attenuation of iodine increases faster than tissue with the decrease of X-ray beam energy, VMIs at low energy, typically below 60 keV, show higher iodine contrast signal

than conventional 100 kV or 120 kV CT images (Albrecht et al. 2019). However, the image noise of VMIs also increases at lower energies. Alvarez et al. showed that the noise of VMIs has a non-monotonic relationship with the monochromatic energy and a minimum noise exists (Alvarez and Seppi 1979). Yu et al. showed that a maximum CNR of iodine exists at certain monochromatic energy, but the optimal energy level depends on the phantom size and dose partition between the low- and high-energy scans. Third, when the monoenergetic images are created from projection-space material decomposition, the beam hardening artifacts can be more effectively reduced because the shape of the polychromatic X-ray spectrum and spectral response of CT detectors are properly considered in the material decomposition process. Fourth, because beam hardening is a significant cause of metal-induced artifacts in CT scan, monoenergetic images created at higher energy levels can potentially reduce artifacts caused by metal objects (Cha et al. 2017; Guggenberger et al. 2012). Fifth, with VMIs created over a range of monochromatic energies, spectral attenuation curves can be created to characterize tissue types, such as differentiation of contrast enhancing solid renal mass from hyperdense cyst (Silva et al. 2011).

3.4 Electron Density and Effective Atomic Number Images

Electron density ρ^e can be calculated from the mass density as following:

$$\rho^e = \frac{\rho}{A_m} Z N_A \quad (16)$$

where ρ^e is the electron density, ρ is mass density, Z is the atomic number, A_m is the atom mass, and N_A is Avogadro's number. The effective atomic number of a composite material is defined as,

$$Z_{eff} = \sum_i w_i^e Z_i^n, i = 1, \dots, N \quad (17)$$

where w_i^e is the function of the total number of electrons of the i^{th} material, Z_i is the atomic

number of the i th material, N is the total number of materials in the composite, and n is a constant in the range of 3–4 (Heismann et al. 2003). Effective atomic number of materials can be estimated with either material decomposition (Alvarez and Macovski 1976) or empirical calibration based methods (Liu et al. 2009; Heismann et al. 2003; Landry et al. 2013). Attention must be paid to the unit of the created images. For example, on one CT manufacturer's DECT platform, the electron density values are converted to the Hounsfield Unit scale, which means water has a value of 0 HU and air has a value of -1000 HU. The effective atom number is often presented in units of 1 and shown as colored overlay image. Using electronic density and effective atomic number information, DECT has been evaluated to improve the accuracy of stopping power ratio calculation over single-energy CT for proton therapy treatment (Yang et al. 2010). Atomic number Z_{eff} is converted to mean excitation potential, which was used with electron density to calculate stopping power ratio (Bourque et al. 2014). The DECT-based approach is found to be more accurate and less susceptible to small perturbations of human tissues compositions in SPR calculation than using single-energy CT images (Yang et al. 2010).

4 Image Quality and Quantitative Accuracy of Synthetic DECT Images

Material-specific and virtual monoenergetic images created from DECT are susceptible to noise because of the noise amplification in the material decomposition process (Alvarez and Seppi 1979). The increase of noise in virtual monoenergetic images with decreasing energy may diminish the advantage of enhanced iodine contrast at low monochromatic energy (Alvarez and Seppi 1979). On most DECT platforms, conventional iterative reconstruction, which is routinely used on single-energy CT images, can also be applied to synthetic DECT images.

A lot of effort has been dedicated to reducing image noise in DECT material decomposition by

taking advantage of the fact that when using all the radiation dose in the DECT acquisition, a minimum noise level can be reached either at certain monochromatic energy or by optimally mixing images from low- and high energies. Grant et al. used a frequency-split technique to reduce the image noise in VMIs (Grant et al. 2014). By decomposing the VMIs into low- and high-frequency image sets, they created composite low-energy (e.g., 40 keV) monoenergetic images that maintain the high iodine contrast but have the image noise reduced to the minimal level typically found at 70 keV. This approach is currently implemented on a commercial DECT platform (Mono+, syngo Dual-Energy, Siemens Healthcare). Leng et al. developed a method to reduce the image noise in multi-energy CT by exploiting information redundancies in the energy domain (Leng et al. 2011). Using this approach, they showed a noise reduction of up to 59% and CNR increase of up to 64% in VMIs in clinical DECT exams (Leng et al. 2015). Tao et al. used a prior-knowledge-aware iterative denoising approach to reduce noise and improve iodine CNR of VMIs from DECT (Tao et al. 2019). By introducing total-variation regularization of the difference image between the original VMIs and the low-noise mixed images of low and high energy, the spatial and spectral data redundancy are both exploited. With this approach, besides preserving the image resolution and noise texture of original VMIs, the denoised images showed a 1.8-fold increase in iodine CNR compared to the VMIs produced by the commercial dual-energy processing application (Mono+).

Recently, deep learning has been increasingly used in medical imaging reconstruction (Wang et al. 2020), image noise reduction in CT (Chen et al. 2017; Yang et al. 2018; Solomon et al. 2020; Missert et al. 2020), and CT dose optimization (McCollough and Leng 2020). In DECT applications, Zhang et al. developed a butterfly convolutional neural network (CNN) to perform image domain DECT material decomposition and showed superior noise reduction in deep learning generated material images over images from direct matrix inversion and iterative decomposition method (Zhang et al. 2019). Poirot et al.

incorporated the conventional VNC images as a function of the corresponding CT numbers at low and high energy into a CNN to reduce image noise of VNC images. The deep learning approach showed lower noise and higher similarity to true non-contrast images compared to the conventional VNC images (Poirot et al. 2019). Gong et al. proposed an Incept-net CNN architecture that utilizes multiresolution features of local image structure and improves the robustness against local noise and artifacts while preserving the structural details. They showed improved accuracy of material quantification and reduced image noise and artifact in comparison to conventional least-square-based, total-variation regularized, and U-net-based material decomposition methods (Gong et al. 2020).

When quantitative information is required from material-specific images, it is important to understand the impact of the assumption used in material decomposition (McCullough et al. 2020). For example, bone will appear in iodine maps from the iodine-water based material decomposition because the attenuation of bone is decomposed as a combination of iodine and water and the portion that is assigned to iodine will be shown as positive signal on the iodine map. Similarly, the pixel values of fat on a VNC image might be different from the fat on a true non-contrast image because the iodine-water pair is assumed in creation of the VNC images. Even with accurate models for material decomposition, material quantification accuracy and reproducibility in DECT is also impacted by other factors, such as radiation dose, patient size, and manufacturer-dependent DECT acquisition techniques (Jacobsen et al. 2018; Goodsitt et al. 2011; Foley et al. 2016; Pelgrim et al. 2017; Nute et al. 2018).

5 Conclusion

With the advancement in emerging detector technology and novel material decomposition methods, DECT and multi-energy CT are playing an increasing role in clinical CT imaging by adding functional information, providing diag-

nostic images with better image quality, and potentially reducing radiation dose to patients. A good understanding on the advantages and limitations of the synthetic images is essential for a successful adoption of DECT into clinical practice.

Compliance with Ethical Standards

Disclosure of Interests CHM is the principal investigator of a research grant to Mayo Clinic from Siemens Healthcare.

References

- Albrecht MH, Vogl TJ, Martin SS et al (2019) Review of clinical applications for virtual Monoenergetic dual-energy CT. *Radiology* 293(2):260–271. <https://doi.org/10.1148/radiol.2019182297>
- Alvarez RE, Macovski A (1976) Energy-selective reconstructions in X-ray computerized tomography. *Phys Med Biol* 21(5):733–744. <https://doi.org/10.1088/0031-9155/21/5/002>
- Alvarez R, Seppi E (1979) A comparison of noise and dose in conventional and energy selective computed tomography. *IEEE Trans Nucl Sci* 26(2):2853–2856. <https://doi.org/10.1109/TNS.1979.4330549>
- Behrendt FF, Schmidt B, Plumhans C et al (2009) Image fusion in dual energy computed tomography: effect on contrast enhancement, signal-to-noise ratio and image quality in computed tomography angiography. *Investig Radiol* 44(1):1–6. <https://doi.org/10.1097/RLI.0b013e31818c3d4b>
- Bongartz T, Glazebrook KN, Kavros SJ et al (2015) Dual-energy CT for the diagnosis of gout: an accuracy and diagnostic yield study. *Ann Rheum Dis* 74(6):1072–1077. <https://doi.org/10.1136/annrheumdis-2013-205095>
- Bourque AE, Carrier JF, Bouchard H (2014) A stoichiometric calibration method for dual energy computed tomography. *Phys Med Biol* 59(8):2059–2088. <https://doi.org/10.1088/0031-9155/59/8/2059>
- Bushberg JT, Seibert AJ, Leidholdt EM Jr, Boone JM (2012) *The essential physics of the medical imaging*. Lippincott Williams & Wilkins
- Cha J, Kim HJ, Kim ST, Kim YK, Kim HY, Park GM (2017) Dual-energy CT with virtual monochromatic images and metal artifact reduction software for reducing metallic dental artifacts. *Acta Radiol* 58(11):1312–1319. <https://doi.org/10.1177/0284185117692174>
- Chen H, Zhang Y, Kalra MK et al (2017) Low-dose CT with a residual encoder-decoder convolutional neural network. *IEEE Trans Med Imaging* 36(12):2524–2535. <https://doi.org/10.1109/TMI.2017.2715284>

- Ferda J, Novák M, Mírka H et al (2009) The assessment of intracranial bleeding with virtual unenhanced imaging by means of dual-energy CT angiography. *Eur Radiol* 19(10):2518–2522. <https://doi.org/10.1007/s00330-009-1495-2>
- Fischer MA, Gnannt R, Raptis D et al (2011) Quantification of liver fat in the presence of iron and iodine: an ex-vivo dual-energy CT study. *Investig Radiol* 46(6):351–358. <https://doi.org/10.1097/RLI.0b013e31820e1486>
- Flohr TG, McCollough CH, Bruder H et al (2006) First performance evaluation of a dual-source CT (DSCT) system. *Eur Radiol* 16(2):256–268. <https://doi.org/10.1007/s00330-005-2919-2>
- Foley WD, Shuman WP, Siegel MJ et al (2016) White paper of the society of computed body tomography and magnetic resonance on dual-energy CT, part 2: radiation dose and iodine sensitivity. *J Comput Assist Tomogr* 40(6):846–850. <https://doi.org/10.1097/rct.0000000000000539>
- Fulwadhva UP, Wortman JR, Sodickson AD (2016) Use of dual-energy CT and iodine maps in evaluation of bowel disease. *Radiographics* 36(2):393–406. <https://doi.org/10.1148/rg.2016150151>
- Gong H, Tao S, Rajendran K, Zhou W, McCollough CH, Leng S (2020) Deep-learning-based direct inversion for material decomposition. *Med Phys*. <https://doi.org/10.1002/mp.14523>
- Goodsitt MM, Christodoulou EG, Larson SC (2011) Accuracies of the synthesized monochromatic CT numbers and effective atomic numbers obtained with a rapid kVp switching dual energy CT scanner. *Med Phys* 38(4):2222–2232. <https://doi.org/10.1118/1.3567509>
- Grant KL, Flohr TG, Krauss B, Sedlmair M, Thomas C, Schmidt B (2014) Assessment of an advanced image-based technique to calculate virtual monoenergetic computed tomographic images from a dual-energy examination to improve contrast-to-noise ratio in examinations using iodinated contrast media. *Investig Radiol* 49(9):586–592. <https://doi.org/10.1097/rli.0000000000000060>
- Graser A, Johnson TR, Bader M et al (2008) Dual energy CT characterization of urinary calculi: initial in vitro and clinical experience. *Investig Radiol* 43(2):112–119. <https://doi.org/10.1097/RLI.0b013e318157a144>
- Graser A, Johnson TR, Hecht EM et al (2009) Dual-energy CT in patients suspected of having renal masses: can virtual nonenhanced images replace true nonenhanced images? *Radiology* 252(2):433–440. <https://doi.org/10.1148/radiol.2522080557>
- Guggenberger R, Winklhofer S, Osterhoff G et al (2012) Metallic artefact reduction with monoenergetic dual-energy CT: systematic ex vivo evaluation of posterior spinal fusion implants from various vendors and different spine levels. *Eur Radiol* 22(11):2357–2364. <https://doi.org/10.1007/s00330-012-2501-7>
- Gupta R, Phan CM, Leidecker C et al (2010) Evaluation of dual-energy CT for differentiating intracerebral hemorrhage from iodinated contrast material staining. *Radiology* 257(1):205–211. <https://doi.org/10.1148/radiol.10091806>
- Heismann BJ, Leppert J, Stierstorfer K (2003) Density and atomic number measurements with spectral x-ray attenuation method. *J Appl Phys* 94(3):2073–2079. <https://doi.org/10.1063/1.1586963>
- Holmes DR 3rd, Fletcher JG, Apel A et al (2008) Evaluation of non-linear blending in dual-energy computed tomography. *Eur J Radiol* 68(3):409–413. <https://doi.org/10.1016/j.ejrad.2008.09.017>
- Hounsfield GN (1973) Computerized transverse axial scanning (tomography). 1. Description of system. *Br J Radiol* 46(552):1016–1022. <https://doi.org/10.1259/0007-1285-46-552-1016>
- Hu R, Besheli LD, Young J et al (2016) Dual-energy head CT enables accurate distinction of Intraparenchymal hemorrhage from calcification in emergency department patients. *Radiology* 280(1):177–183. <https://doi.org/10.1148/radiol.2015150877>
- Jacobsen MC, Schellingerhout D, Wood CA et al (2018) Intermanufacturer comparison of dual-energy CT iodine quantification and monochromatic attenuation: a phantom study. *Radiology* 287(1):224–234. <https://doi.org/10.1148/radiol.2017170896>
- Johnson TR, Krauss B, Sedlmair M et al (2007) Material differentiation by dual energy CT: initial experience. *Eur Radiol* 17(6):1510–1517. <https://doi.org/10.1007/s00330-006-0517-6>
- Johnson TR, Himsi I, Hellerhoff K et al (2013) Dual-energy CT for the evaluation of silicone breast implants. *Eur Radiol* 23(4):991–996. <https://doi.org/10.1007/s00330-012-2667-z>
- Kalender WA, Perman WH, Vetter JR, Klotz E (1986) Evaluation of a prototype dual-energy computed tomographic apparatus. I. Phantom studies. *Med Phys* 13(3):334–339. <https://doi.org/10.1118/1.595958>
- Kelcz F, Joseph PM, Hilal SK (1979) Noise considerations in dual energy CT scanning. *Med Phys* 6(5):418–425. <https://doi.org/10.1118/1.594520>
- Kong X, Sheng HX, Lu GM et al (2014) Xenon-enhanced dual-energy CT lung ventilation imaging: techniques and clinical applications. *Am J Roentgenol* 202(2):309–317. <https://doi.org/10.2214/AJR.13.11191>
- Landry G, Seco J, Gaudreault M, Verhaegen F (2013) Deriving effective atomic numbers from DECT based on a parameterization of the ratio of high and low linear attenuation coefficients. *Phys Med Biol* 58(19):6851–6866. <https://doi.org/10.1088/0031-9155/58/19/6851>
- Lee SH, Lee JM, Kim KW et al (2011) Dual-energy computed tomography to assess tumor response to hepatic radiofrequency ablation: potential diagnostic value of virtual noncontrast images and iodine maps. *Investig Radiol* 46(2):77–84. <https://doi.org/10.1097/RLI.0b013e3181f23fcd>
- Lehmann LA, Alvarez RE, Macovski A et al (1981) Generalized image combinations in dual KVP digital radiography. *Med Phys* 8(5):659–667. <https://doi.org/10.1118/1.595025>

- Leng S, Yu L, Wang J, Fletcher JG, Mistretta CA, McCollough CH (2011) Noise reduction in spectral CT: reducing dose and breaking the trade-off between image noise and energy bin selection. *Med Phys* 38(9):4946–4957. <https://doi.org/10.1118/1.3609097>
- Leng S, Yu L, Fletcher JG, McCollough CH (2015) Maximizing iodine contrast-to-noise ratios in abdominal CT imaging through use of energy domain noise reduction and virtual Monoenergetic dual-energy CT. *Radiology* 276(2):562–570. <https://doi.org/10.1148/radiol.2015140857>
- Li M, Zheng X, Li J et al (2012) Dual-energy computed tomography imaging of thyroid nodule specimens: comparison with pathologic findings. *Investig Radiol* 47(1):58–64. <https://doi.org/10.1097/RLI.0b013e318229fef3>
- Li Z, Leng S, Yu L, Yu Z, McCollough CH (2015) Image-based material decomposition with a general volume constraint for photon-counting CT. *Proc SPIE Int Soc Opt Eng* 9412. <https://doi.org/10.1117/12.2082069>
- Liu X, Yu L, Primak AN, McCollough CH (2009) Quantitative imaging of element composition and mass fraction using dual-energy CT: three-material decomposition. *Med Phys* 36(5):1602–1609. <https://doi.org/10.1118/1.3097632>
- Luo XF, Xie XQ, Cheng S et al (2015) Dual-energy CT for patients suspected of having liver iron overload: can virtual iron content imaging accurately quantify liver iron content? *Radiology* 277(1):95–103. <https://doi.org/10.1148/radiol.2015141856>
- Macovski A, Alvarez RE, Chan JL, Stonestrom JP, Zatz LM (1976) Energy dependent reconstruction in X-ray computerized tomography. *Comput Biol Med* 6(4):325–336. [https://doi.org/10.1016/0010-4825\(76\)90069-x](https://doi.org/10.1016/0010-4825(76)90069-x)
- McCollough CH, Leng S (2020) Use of artificial intelligence in computed tomography dose optimisation. *Ann ICRP* 49(1_suppl):113–125. <https://doi.org/10.1177/0146645320940827>
- McCollough CH, Boedeker K, Cody D et al (2020) Principles and applications of multienergy CT: report of AAPM task group 291. *Med Phys* 47(7):e881–e912. <https://doi.org/10.1002/mp.14157>
- Mileto A, Marin D, Alfaro-Cordoba M et al (2014) Iodine quantification to distinguish clear cell from papillary renal cell carcinoma at dual-energy multidetector CT: a multireader diagnostic performance study. *Radiology* 273(3):813–820. <https://doi.org/10.1148/radiol.14140171>
- Missert AD, Yu L, Leng S, Fletcher JG, McCollough CH (2020) Synthesizing images from multiple kernels using a deep convolutional neural network. *Med Phys* 47(2):422–430. <https://doi.org/10.1002/mp.13918>
- Muenzel D, Bar-Ness D, Roessl E et al (2017) Spectral photon-counting CT: initial experience with dual-contrast agent K-edge colonography. *Radiology* 283(3):723–728. <https://doi.org/10.1148/radiol.2016160890>
- Niu T, Dong X, Petrongolo M, Zhu L (2014) Iterative image-domain decomposition for dual-energy CT. *Med Phys* 41(4):041901. <https://doi.org/10.1118/1.4866386>
- Nute JL, Jacobsen MC, Stefan W, Wei W, Cody DD (2018) Development of a dual-energy computed tomography quality control program: characterization of scanner response and definition of relevant parameters for a fast-kVp switching dual-energy computed tomography system. *Med Phys* 45(4):1444–1458. <https://doi.org/10.1002/mp.12812>
- Pelgrim GJ, van Hamersvelt RW, Willemsink MJ et al (2017) Accuracy of iodine quantification using dual energy CT in latest generation dual source and dual layer CT. *Eur Radiol* 27(9):3904–3912. <https://doi.org/10.1007/s00330-017-4752-9>
- Poirot MG, Bergmans RHJ, Thomson BR et al (2019) Physics-informed deep learning for dual-energy computed tomography image processing. *Sci Rep* 9(1):17709. <https://doi.org/10.1038/s41598-019-54176-0>
- Primak AN, Fletcher JG, Vrtiska TJ et al (2007) Noninvasive differentiation of uric acid versus non-uric acid kidney stones using dual-energy CT. *Acad Radiol* 14(12):1441–1447. <https://doi.org/10.1016/j.acra.2007.09.016>
- Roessl E, Proksa R (2007) K-edge imaging in x-ray computed tomography using multi-bin photon counting detectors. *Phys Med Biol* 52(15):4679–4696. <https://doi.org/10.1088/0031-9155/52/15/020>
- Schlomka JP, Roessl E, Dorscheid R et al (2008) Experimental feasibility of multi-energy photon-counting K-edge imaging in pre-clinical computed tomography. *Phys Med Biol* 53(15):4031–4047. <https://doi.org/10.1088/0031-9155/53/15/002>
- Sellerer T, Noël PB, Patino M et al (2018) Dual-energy CT: a phantom comparison of different platforms for abdominal imaging. *Eur Radiol* 28(7):2745–2755. <https://doi.org/10.1007/s00330-017-5238-5>
- Silva AC, Morse BG, Hara AK, Paden RG, Hongo N, Pavlicek W (2011) Dual-energy (spectral) CT: applications in abdominal imaging. *Radiographics* 31(4):1031–1046. <https://doi.org/10.1148/rg.314105159>. discussion 1047-50
- Solomon J, Lyu P, Marin D, Samei E (2020) Noise and spatial resolution properties of a commercially available deep learning-based CT reconstruction algorithm. *Med Phys* 47(9):3961–3971. <https://doi.org/10.1002/mp.14319>
- Tao S, Rajendran K, Zhou W, Fletcher JG, McCollough CH, Leng S (2019) Improving iodine contrast to noise ratio using virtual monoenergetic imaging and prior-knowledge-aware iterative denoising (mono-PKAID). *Phys Med Biol* 64(10):105014. <https://doi.org/10.1088/1361-6560/ab17fa>
- Taylor RE, Mager P, Yu NC, Katz DP, Brady JR, Gupta N (2019) Iodine quantification and detectability thresholds among major dual-energy CT platforms. *Br J Radiol* 92(1104):20190530. <https://doi.org/10.1259/bjr.20190530>

- Wang AS, Pelc NJ (2011) Synthetic CT: simulating low dose single and dual energy protocols from a dual energy scan. *Med Phys* 38(10):5551–5562. <https://doi.org/10.1118/1.3633895>
- Wang CK, Tsai JM, Chuang MT, Wang MT, Huang KY, Lin RM (2013) Bone marrow edema in vertebral compression fractures: detection with dual-energy CT. *Radiology* 269(2):525–533. <https://doi.org/10.1148/radiol.13122577>
- Wang G, Ye JC, De Man B (2020) Deep learning for tomographic image reconstruction. *Nat Mach Intell* 2(12):737–748. <https://doi.org/10.1038/s42256-020-00273-z>
- Werner S, Krauss B, Haberland U et al (2019) Dual-energy CT for liver iron quantification in patients with haematological disorders. *Eur Radiol* 29(6):2868–2877. <https://doi.org/10.1007/s00330-018-5785-4>
- Willeminck MJ, Persson M, Pourmorteza A, Pelc NJ, Fleischmann D (2018) Photon-counting CT: technical principles and clinical prospects. *Radiology* 289(2):293–312. <https://doi.org/10.1148/radiol.2018172656>
- Williamson JF, Li S, Devic S, Whiting BR, Lerma FA (2006) On two-parameter models of photon cross sections: application to dual-energy CT imaging. *Med Phys* 33(11):4115–4129. <https://doi.org/10.1118/1.2349688>
- Yang M, Virshup G, Clayton J, Zhu XR, Mohan R, Dong L (2010) Theoretical variance analysis of single- and dual-energy computed tomography methods for calculating proton stopping power ratios of biological tissues. *Phys Med Biol* 55(5):1343–1362. <https://doi.org/10.1088/0031-9155/55/5/006>
- Yang Q, Yan P, Zhang Y et al (2018) Low-dose CT image Denoising using a generative adversarial network with Wasserstein distance and perceptual loss. *IEEE Trans Med Imaging* 37(6):1348–1357. <https://doi.org/10.1109/TMI.2018.2827462>
- Yu L, Primak AN, Liu X, McCollough CH (2009) Image quality optimization and evaluation of linearly mixed images in dual-source, dual-energy CT. *Med Phys* 36(3):1019–1024. <https://doi.org/10.1118/1.3077921>
- Yu L, Christner JA, Leng S, Wang J, Fletcher JG, McCollough CH (2011) Virtual monochromatic imaging in dual-source dual-energy CT: radiation dose and image quality. *Med Phys* 38(12):6371–6379. <https://doi.org/10.1118/1.3658568>
- Zhang W, Zhang H, Wang L et al (2019) Image domain dual material decomposition for dual-energy CT using butterfly network. *Med Phys* 46(5):2037–2051. <https://doi.org/10.1002/mp.13489>



Dual-Energy: The Siemens Approach

Bernhard Schmidt and Thomas Flohr

Contents

1	General Aspects and Workflow	15
2	Dual Source-Based Dual-Energy	19
3	Twin Spiral Dual-Energy	22
4	TwinBeam Dual-Energy	23
5	Conclusions	26
	References	26

1 General Aspects and Workflow

The first medical CT scanner capable of DE scanning by means of fast kV-switching was the SOMATOM DRH introduced by Siemens in 1987 (Kalender 1987). It allowed for dual-energy acquisitions in topogram and axial scan mode; however,

the main clinical benefit of this new technical capability was a significant improvement in the accuracy of bone mineral density quantification. Although several clinical studies demonstrated the advantage of DE CT over single energy CT especially in the presence of fat—elimination of the so-called “fat error”—(Laval-Jeantet 1986; Genant 1977; Vetter 1986), the fast kV-switching technique to acquire DE data was abandoned in subsequent CT systems. Technical limitations led to compromised scan data acquisition, degradation in image quality, and increased radiation dose to the patient since attenuation-based tube current modulation and necessary adaptations of the tube current between the kV-switches was not feasible due to basic physical limitations of the technology. On top of this new technical opportunities such as DEXA (dual-emission X-ray absorptiometry) became available and limited the need for DE CT bone densitometry. Other clinically relevant applications, however, were not within reach at that time.

B. Schmidt (✉)
Siemens Healthcare GmbH, Computed Tomography,
Forchheim, Germany

Friedrich-Alexander-Universität Erlangen, Institute
for Medical Physics, Erlangen, Germany
e-mail: bernhard.schmidt@siemens-healthineers.com

T. Flohr
Siemens Healthcare GmbH, Computed Tomography,
Forchheim, Germany

Eberhard-Karls-Universität Tübingen, Institute of
Diagnostic and Interventional Radiology,
Tübingen, Germany
e-mail: thomas.flohr@siemens-healthineers.com

In 2006 DE CT was reintroduced with the advent of dual source CT systems (Flohr et al. 2006) which enabled the acquisition of DE CT data without the significant limitations of the previous technology, rather a much wider clinical application spectrum. Since then, the utilization of DE CT has been growing steadily, prompted in part by the introduction of newer generations of dual source CT systems with further improved dual-energy performance. A few years later, the portfolio for DE data acquisition techniques was extended to non-dual source CT systems with the introduction of subsequent spiral scanning at different X-ray tube voltages (Twin Spiral; Siemens Healthineers, Germany). This—in a second development step—was further improved upon by adding just to the high voltage spiral portion of the Twin Spiral acquisition an additional pre-filtration, already being well established for dual source CT systems. Hereby a dual-energy separation comparable to second and third generation of dual source CT was accomplished. To further substantially reduce the time delay between the high and low voltage data acquisition, a few years later TwinBeam (Siemens Healthineers, Germany) was introduced to single source CT systems. In this system a split filter is added to the X-ray tube collimator box, allowing examinations even in case of high contrast dynamics as in a contrast-enhanced scan in the arterial phase.

From a clinical perspective, DE CT imaging proves far more valuable than standard CT scans because, unlike them, it provides functional information on top of the mere anatomical visualization (Schneider et al. 2014). Kidney stones can be differentiated (Primak et al. 2007; Scheffel et al. 2007; Stolzmann et al. 2010), the differential diagnosis of gout is possible (Mallinson et al. 2016), and lesions can be characterized by quantifying their iodine uptake (Graser et al. 2010). In oncology, structures more responsive to treatment may potentially be identified early during treatment by reduced iodine uptake rather than by mere lesion size measurements (Apfalter et al. 2012; Uhrig et al. 2013; Agrawal et al. 2014; Knobloch et al. 2014). Perfusion defects in the lung parenchyma in patients with pulmonary embolism are visible in DE scans (Pontana et al.

2008; Remy-Jardin et al. 2014; Apfalter et al. 2014), as well as post-traumatic bone bruises or bone-marrow infiltration of the spine in patients with multiple myeloma (Pache et al. 2010; Thomas et al. 2015). DE CT has been applied in the characterization of perfusion defects in the myocardium (Ruzsics et al. 2009; Vliegenthart et al. 2012), as well as the iron uptake of the liver in patients with liver iron overload (Luo et al. 2015; Werner et al. 2019). Maps of effective atomic numbers obtained with DE CT may be used to improve radiation treatment planning, particularly in proton therapy. The applications listed above are an incomplete list of clinically relevant DE applications which are available on Siemens CT machines, and are either already being applied clinically or currently evaluated.

Besides dedicated clinical DE applications like the ones mentioned above, acquired data also can be used for calculation of virtual mono-energetic images. Similar to raw data-based approaches back in 1986 (Kalender et al. 1986), high- and low-energy images can be used for decomposition into materials differing in photoelectric and Compton characteristics, such as water and iodine (Yu et al. 2012). The concentrations of both materials in each image pixel are calculated by means of an image-based material decomposition algorithm that requires calibration measurements for the attenuation of iodine in phantoms of different diameter for the different X-ray spectra. The concentrations are subsequently multiplied with predicted CT numbers per concentration at the desired pseudo mono-chromatic energy (derived from NIST tables) and summed up to form the final mono-energetic images. Pseudo mono-energetic images derived from image-based material decomposition have similar applications as raw data-based images. Metal artifacts are reduced at higher energies/keV (Mangold et al. 2014), the contrast of iodine and bone increases at lower energies. Like in raw data-based techniques, image noise is amplified at energy levels far away from the mean energy of the mixed images (~ 70 keV). To avoid this undesirable increase in noise, which not only limits the ultimate clinical benefit of mono-energetic images but also limits the gains from

improved iodine contrast-to-noise ratio at lower keV, a novel algorithm for the computation of pseudo mono-energetic images was recently introduced (Mono+, Siemens Healthcare, Forchheim, Germany) that efficiently reduces image noise in pseudo mono-energetic images at low and high keV (Grant et al. 2014). Using this approach, images at the target keV and images at optimal keV from a noise perspective (typically, minimum image noise is obtained at approximately 70 keV) are computed. By means of a frequency-split technique, both the images at the target keV and the images with minimum image noise level are broken down into two sets of sub-images. The first set contains only lower spatial frequencies and thus most of the object information, the second one contains the remaining high spatial frequencies and subsequently mostly image noise. Finally, the lower spatial frequency stack at the target keV is combined with the high spatial frequency stack at optimal keV from a noise perspective to combine the benefits of both image stacks, see Fig. 1.

The Mono+ technique can be used to significantly increase the iodine CNR in CT angiographic studies by computing pseudo mono-energetic images at low keV (Albrecht et al. 2019). It has been shown (Grant et al. 2014) that it may be more efficient to perform DE scans and compute pseudo mono-energetic images at 40 keV using Mono+ to optimize iodine CNR

than to perform low kV-scans, which is today the recommended method to improve iodine CNR. The image-based Mono+ approach is available for all DE data from Siemens CT systems, and levels of the pseudo mono-energetic images can be selected between 40 keV and 190 keV in steps of 1 keV. Figure 2 shows a clinical example for illustration.

Although clinical DE applications and the possibility for improved image quality and better contrast-to-noise ratio are well perceived in the medical community, one of the remaining challenges of dual-energy imaging is workflow and workflow optimizations. In general, DE processing on Siemens CT systems is mainly based on the high and low voltage image stacks, which can be flexibly stored in PACS, or loaded and processed retrospectively by the various DE application classes provided in the Siemens syngo Dual-Energy application—irrespective of which scanner of the Siemens Healthineers CT scanner portfolio is used for data acquisition. In addition, automated dual-energy processing is offered to users who prefer PACS-focused reading over interactive processing and expert viewing in the syngo Dual-Energy application. User selected combinations of DE results are processed and transferred to the user-owned PACS fully automatically, thus being available whenever and wherever the user may need them, even for retrospective analysis. The most established mecha-

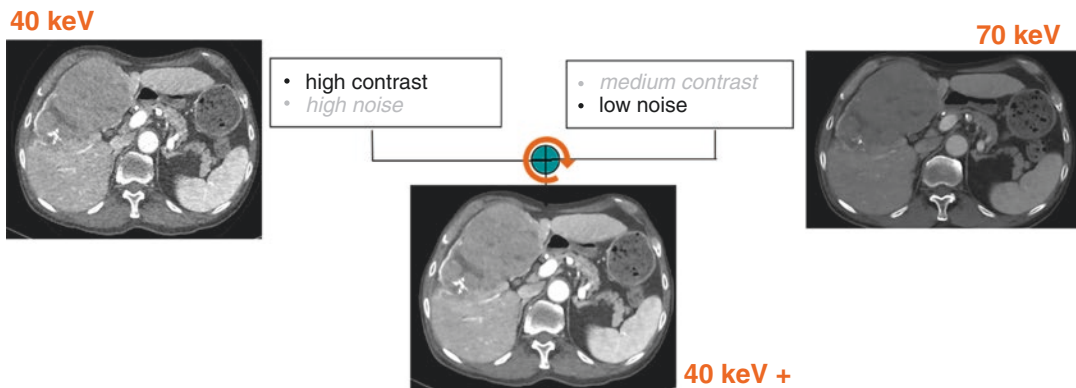


Fig. 1 Schematic illustration of the concept used to calculate Mono+ images. In this example, the CNR of iodine versus soft tissue is enhanced. Images with high iodine contrast and high image noise (40 keV) are mixed with

images showing lower iodine contrast and lower noise (70 keV) to obtain improved CNR at low keVs (Grant et al. 2014)

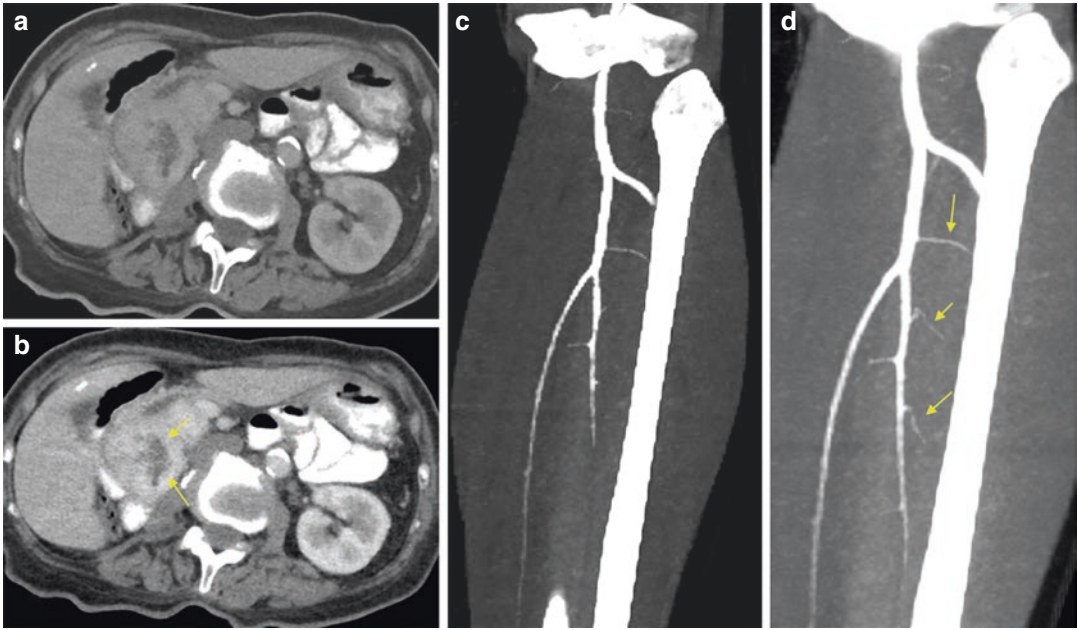


Fig. 2 Left: DE images acquired on a third-generation DSCT scanner through the upper abdomen using the kV-combination 80 kV/150 kV with tin filter, and only 30 cc IV contrast media. Improved contrast and better lesion discernability in case of Mono+ at low keVs (b) compared to a mixed image, corresponding to a standard 120 kV

acquisition (a). Right: Pseudo mono-energetic image using the Mono+ technique at 50 keV (d) compared to 80 keV (c). Note the significantly increased iodine CNR of vascular structures with Mono+. (Courtesy of NYU Medical Center, Department of Radiology, New York, USA)

nisms for this workflow are “Rapid Results Technology” or “Recon&Go Inline Results.” Here the user has the ability to define at the scanner which processing steps should happen automatically, such as the generation of oblique Mono+ images or classified VRT images from a DE renal calculi application. Respective data are then processed automatically, and the results sent to the PACS system for further reading allowing for an efficient and integrated DE workflow (see Fig. 3).

One basic assumption for image-based material decomposition—used in the Siemens approach—is the validity of the thin absorber model. If we use water and iodine, for example, as the basis materials for image-based dual-energy evaluation, the maximum X-ray attenuation coefficient $\mu_1(E)$ and the maximum thickness d_1 of the iodine along any measured ray path are expected to be so small that it is valid to assume a linear contribution of the additional non-water-like attenuation $\mu_1(E) \cdot d_1$ to the total attenuation.

It can be shown that the thin absorber model breaks down for iodine samples with more than 5000 HU cm in water based on 120 kV, which corresponds to the clinical situation of an object with 200 HU iodine enhancement and 25 cm thickness. In almost all clinically relevant situations, the thin absorber model remains valid. Exceptions are scan scenarios where extremely high iodine concentrations may be present, such as CT urographic scans.

In addition, the thin absorber model is based on the concept of an effective spectrum: the measured absorption with a polychromatic X-ray spectrum is assumed to be independent of the spatial distribution of the traversed materials along the beam. In practice, this means that neither the CT-value of water nor the CT-value of a small iodine sample depends on its position within the scanned object. The scanner must therefore be equipped with a bowtie filter of sufficient beam hardening and the approximately cylindrical patient cross-section has to be cen-

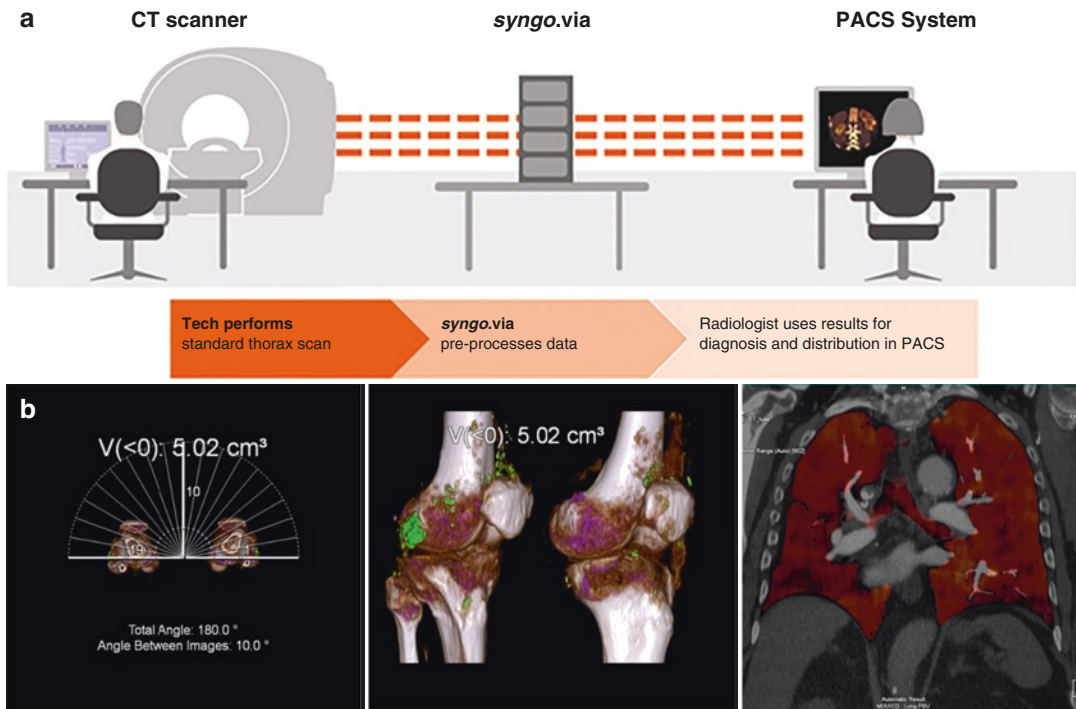


Fig. 3 Optimized workflow on Siemens CT systems: Acquired DE image data are automatically labeled, processed by syngo via in the background and sent to PACS using Rapid Results Technology without any additional user interactions (a). Alternatively, on selected CT models a similar automatic advanced processing is possible directly at the scanner, where yet again results are processed self-operationally and sent directly to PACS for

further reading. Examples for respective results are shown in (b), where in addition to the visualization of DE results the gout volume is automatically calculated (in this example 5.02 cm^3). Beside material and Mono+ images, anatomically oriented DE VRTs with classified results (left and middle) and fused images (right: overlay of mixed and iodine) can be generated

tered within the SFOV. In a real-world setting, electronics noise, scanner calibration, stability of emitted spectra, cone beam effects, and scattered radiation can have a larger impact on the obtained results than the analysis method.

As stated in the beginning of this article, Siemens is processing—irrespective of the CT system type used for acquisition—based on low and high voltage image stacks. This makes storing of images, transferring and retrospective application of various DE classes easy. On the data acquisition side Siemens offers various solutions—depending on the technical capabilities of the respective CT system. In the following paragraphs, the different concepts and technical realizations are introduced and discussed.

2 Dual Source-Based Dual-Energy

A dual source CT is a CT system with two measurements systems, such as two X-ray tubes and the corresponding detectors. Both measurement systems acquire scan data simultaneously at the same anatomical level of the patient (same z-position). In 2006, the first dual source CT (DSCT) was commercially introduced by Siemens, the SOMATOM Definition (Siemens Healthcare GmbH, Forchheim, Germany), see Fig. 4.

The two acquisition systems A and B are mounted onto the rotating gantry at an angular offset of 90° for the first-generation DSCT (Flohr

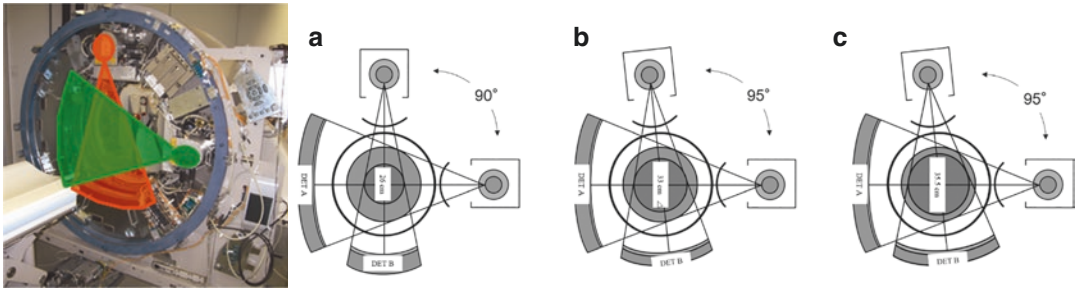


Fig. 4 DSCT with two independent measurement systems. Left: Open gantry of a dual source CT system—red and green fans indicate the beams of the two X-ray tubes. (a) First generation: The system angle between both mea-

surement systems is 90° . (b) Second generation: To increase the SFOV of detector B, a larger system angle of 95° was chosen. With the third-generation DSCT (c), the SFOV of detector B was further increased to 35.5 cm

et al. 2006), and at an angular offset of 95° for the second- and third-generation DSCT. Detector A covers the full SFOV of 50 cm diameter, while detector B is restricted to a smaller FOV of 26 cm (first generation), 33 cm (second generation), or 35.6 cm (third generation) as a consequence of space limitations on the gantry. The shortest gantry rotation times are 0.33 s (first generation), 0.28 s (second generation), and 0.25 s (third generation). DSCT systems provide significantly improved temporal resolution for cardio-thoracic imaging. The shortest data acquisition time for an image corresponds to a quarter of the gantry rotation time (Flohr et al. 2006). Meanwhile, several clinical studies have demonstrated the potential of DSCT to accurately assess coronary artery stenosis in patients with high and irregular heart rates (Achenbach et al. 2006, Johnson et al. 2006, Scheffel et al. 2006, Matt et al. 2007, Leber et al. 2007, Ropers et al. 2007).

Moreover, with a DSCT system, dual-energy data can be acquired by simultaneously operating both X-ray tubes at different kV settings, e.g., 80 kV and 140 kV (Flohr et al. 2006; Johnson et al. 2007). Scan parameters (e.g., tube current and potential) can be adjusted individually for both measurement systems, resulting in a balanced radiation dose distribution between the low- and the high-energy scans. A wide range of routine scan protocols is available, with no

restrictions in the choice of scan parameters such as gantry rotation time. Use of anatomical tube current modulation allows for adaptation of the radiation dose to the patient's anatomy. Mixed images (a weighted average of low- and high-energy images) and Mono+ are routinely available, allowing dual-energy CT scans to be performed in routine clinical practice similar to conventional imaging protocols, with dual-energy information available when needed. It should be noted that dual-energy imaging and the ability for Mono+ as well as iodine quantification being helpful, e.g., for the assessment of the perfusion of the myocardium is also possible for gated cardiac scans on dual source systems. An example is shown in Fig. 5.

Spectral separation, a key measure for DE performance, can be improved by introducing additional pre-filtration into the high kV beam, e.g., by means of a filter that can be moved into the beam when needed and moved out for standard applications. The quality of DE CT examinations generally relies on the separation of the energy spectra. High spectral overlap and bad energy separation result in increased image noise in the base-material decomposition which in turn requires compensation by increased radiation dose. The second-generation DSCT makes use of an additional tin filter (Sn) with a thickness of 0.4 mm to shift the mean energy of the 140 kV

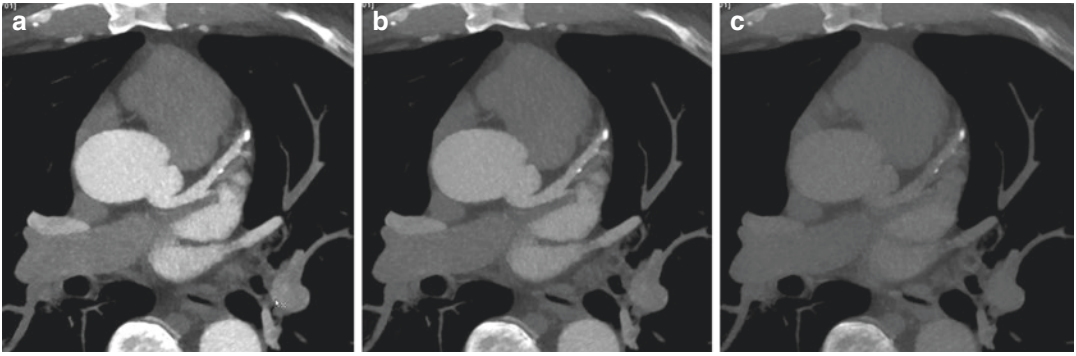


Fig. 5 ECG-triggered “step-and-shoot” DE cardiac CT acquisition using a third-generation DSCT at 90 kV/150 Sn kV, rotation time 0.25 s: Based on the acquired data, images with 66 ms temporal resolution can be reconstructed. In addition, since data from A and B are

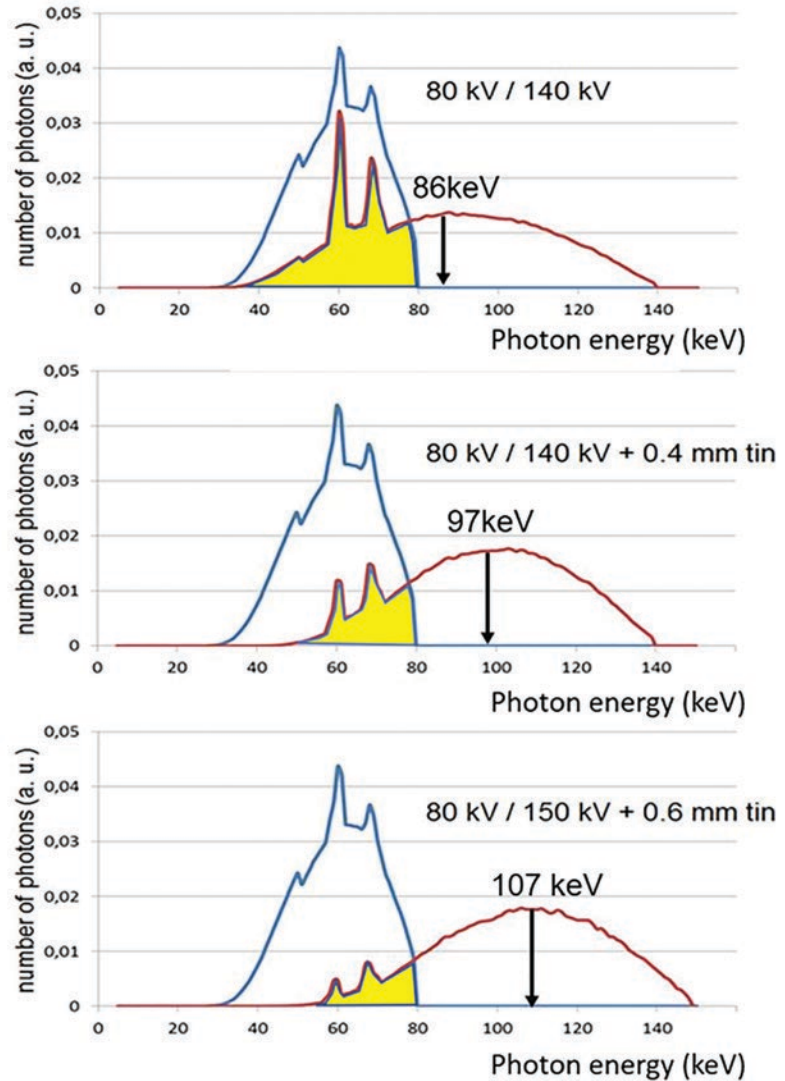
acquired simultaneously, DE information can be used to optimize iodine contrast in coronary vessels based on Mono+ imaging: 55 keV (a), 70 keV (b), and 110 keV (c). Courtesy of Medical University of South Carolina, Charleston, USA

spectrum from 86 keV to 97 keV (after 20 cm water), see Fig. 6. The mean energy of the 80 kV spectrum is 60 keV. The third-generation DSCT provides 150 kV X-ray tube voltage with more aggressive tin pre-filtration (0.6 mm), shifting the mean energy of the 150 kV spectrum to 107 keV, see also Fig. 6. The tin filter improves spectral separation between the low- and high-energy spectra, narrows the high kV spectrum (which results in better dose efficiency and less beam hardening artifacts), and reduces the influence of cross-scattering. A relevant parameter to quantify the performance of a DE CT acquisition technique with regard to energy separation and material differentiation capability is the Dual-Energy (DE) ratio. The DE ratio of a material is defined as its CT number (in HU) at low kV divided by its CT number (in HU) at high kV (Krauss et al. 2015). Water has a DE ratio of 1, meaning its CT number does not change in CT scans at different kV settings. The DE ratio for iodine, a commonly used base material for material decomposition in contrast-enhanced CT scans, increases from 1.9 to 2 at the standard 80 kV/140 kV X-ray tube voltage combination to about 3.4 for 80 kV/150 kV and 0.6 mm tin pre-filtration (measured in a 20 cm water phantom, Krauss et al.

2015). The larger DE ratio results in better conditioned equations for base-material differentiation into, for example, water and iodine as base materials, and leads to less image noise in the material-specific images. Consequently, this enables DE data acquisition at the radiation dose of typical medical CT examinations, without additional dose penalty, see, e.g., (Schenzle et al. 2010; Bauer et al. 2011; Henzler et al. 2012).

As a downside, DE evaluation with dual source CT is restricted to the smaller central SFOV of detector B. Raw data-based dual-energy algorithms cannot be realized because high-energy and low-energy projections are not simultaneously acquired at the same z-position. Dual-energy algorithms are therefore image-based. Another challenge of dual source DE CT is cross-scattered radiation, i.e., scattered radiation originating from tube A and detected by detector B, and vice versa, which has to be carefully corrected for to avoid distortions of CT numbers by cupping or streaking artifacts. This can be done either by measurement of cross-scattered radiation or by model-based approaches (Petersilka et al. 2010). Figure 7 shows a clinical example of a DE CT scan acquired with a third-generation DSCT system.

Fig. 6 Typical 80 kV and 140 kV spectra (after 20 cm water), normalized to equal areas under the curves (top). 80 kV spectrum and 140 kV spectrum with additional 0.4 mm tin pre-filtration (center), and 80 kV spectrum and 150 kV spectrum with additional 0.6 mm tin pre-filtration (bottom). Note the shift of the mean energy of the high-energy spectrum to higher values (arrow) and the reduced spectral overlap. The yellow marked areas indicate the portion of the spectra that measured redundant information



3 Twin Spiral Dual-Energy

For non-dual source CT systems, the most straightforward approach for acquiring dual-energy CT data are two subsequent CT scans of the same anatomical structure, one with low X-ray tube voltage (80 kV), the other with high X-ray tube voltage (140 kV). The spectral separation achieved with this approach is reasonably effective. DE CT is feasible with standard CT systems

with a 50 cm diameter full scan field of view (SFOV). However, the disadvantage is that the time delay between the two scans presents a challenge for the evaluation of fast moving organs. Furthermore, examinations with administration of contrast agent are challenging, at least in early arterial phases when the contrast density changes rapidly between the two scans. The resulting CT-number changes will be misinterpreted by DE material decomposition techniques.

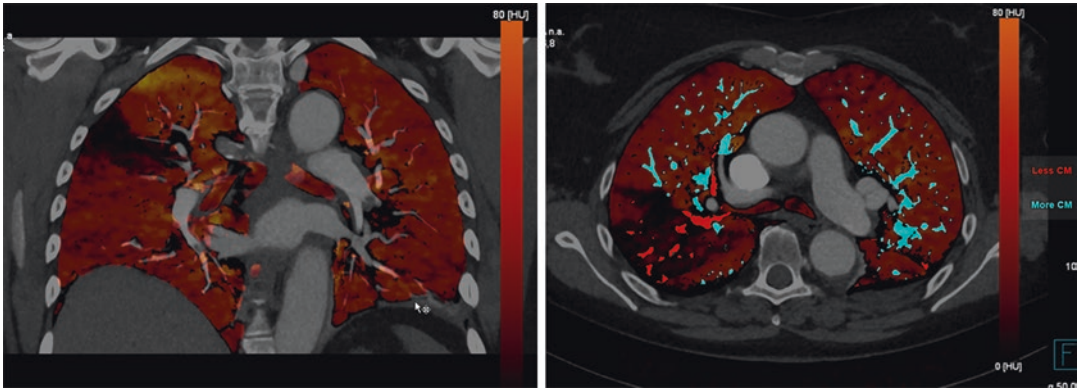


Fig. 7 Contrast-enhanced DE CT scan of a patient with acute pulmonary embolism acquired with a third-generation DSCT scanner at 90 kV/150 kV with 0.6 mm tin pre-filtration. Left: Mixed image overlaid by the quantitative perfusion information of the lung parenchyma, showing a v-like perfusion defect caused by an

occluding clot. Right: In addition to parenchymal information, DE-based color-coding of the vessel lumen. Non-iodinated vessels—matching with the perfusion defect—are highlighted in red. Courtesy of University Hospital of Frankfurt, Germany

A technical realization was first introduced with the SOMATOM Definition AS, SOMATOM Edge (Siemens Healthcare GmbH, Forchheim, Germany), where the DE acquisition relies on two automatically, workflow-wise completely coupled spiral (helical) scans of the same body region, the first performed at 80 kV and the second at 140 kV. The approach to go for volumetric acquisitions instead of a single axial scan is advantageous since mismatch due to motion can be corrected by a respective volumetric registration approach. As in standard CT examinations, radiation dose to the patient can be optimized by anatomical tube current modulation (Marin et al. 2014), and iterative reconstruction can be applied. Because of the small time delay between the two spiral scans, the use of this technique is indicated for non-dynamic examinations that do not require the administration of contrast agent, such as characterization of kidney stones, or the examination of tophaceous lesions in patients with gout, or for the calculation of pseudo mono-energetic images to reduce metal artifacts at a metal-specific high energy.

With the introduction of the SOMATOM X. Cite in 2019 and the SOMATOM X.ceed 2021, Siemens introduced tin filtration that had already been well established in Dual Source CT systems to Twin Spiral scanning, allowing for a substan-

tial improvement of spectral separation and better DE performance (see Fig. 8). A clinical example is shown in Fig. 9, where a voltage combination of 80 kV and 150 Sn kV had been used.

4 TwinBeam Dual-Energy

Recently, a new method was introduced to acquire DE CT data with a single source CT system without kV-switching, but with better temporal registration than by performing two separate consecutive axial or spiral scans of the examination volume of interest. Two different pre-filters in the tube collimator housing are used to split the X-ray beam in the scan direction, called “TwinBeam” (e.g., on SOMATOM Definition Edge, Siemens Healthcare GmbH, Forchheim, Germany), see Fig. 10.

The X-ray tube is operated at 120 kV tube voltage. One half of the multi-slice detector in the scan direction is illuminated by an X-ray beam pre-filtered with 0.6 mm tin; compared to the standard 120 kV spectrum, the mean energy of this pre-filtered spectrum is increased, see Fig. 10, right. The other half of the detector in the scan direction is pre-filtered with a thin gold filter; as a consequence of the K-edge of gold at 80.7 keV, the mean energy of this spectrum is decreased, see Fig. 10, right. The total attenuation of the pre-filters is adjusted to bal-

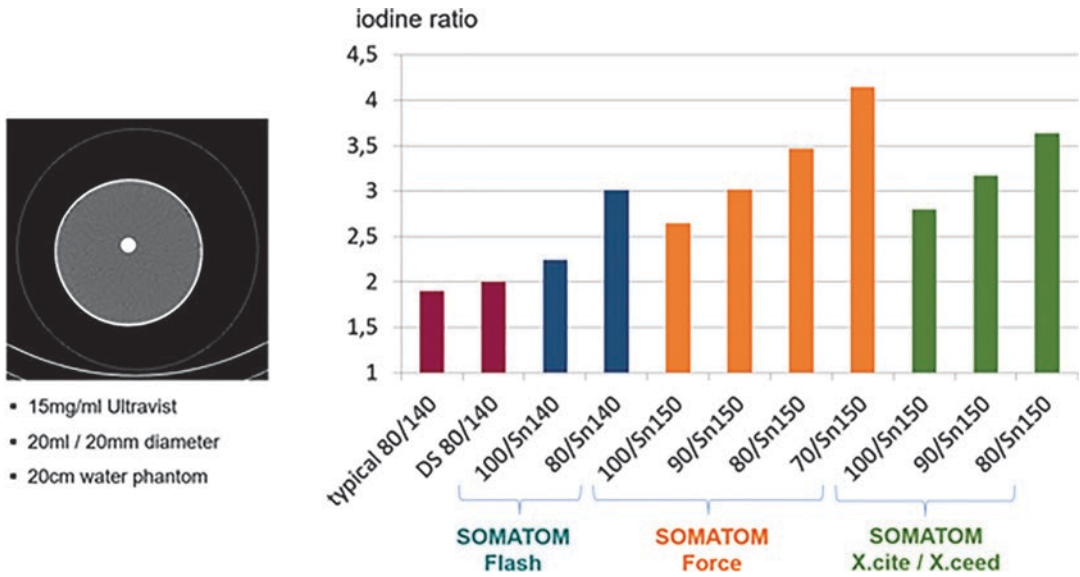


Fig. 8 DE performance can be measured quantitatively in terms of iodine ratio (HU at low energy divided by HU at high energy): For the high kV beam, additional tin filtration was introduced for dual systems to improve DE

performance. Additional tin filtration of 0.7 mm introduced with the SOMATOM X.cite and X.ceed, increases dual-energy separation for Twin Spiral into the range of second- and third-generation dual source CTs

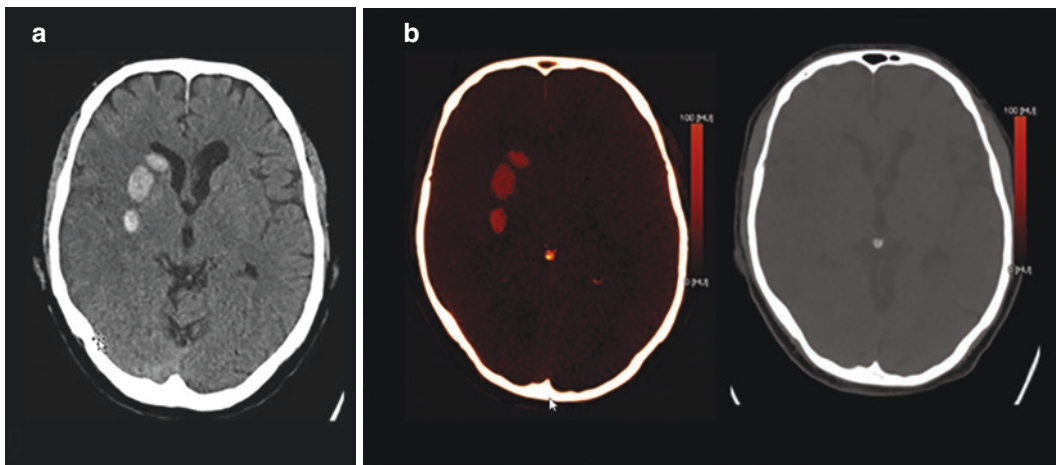


Fig. 9 Clinical example for dual-energy imaging technique relying on two consecutive spiral scans (Twin Spiral) at 80 kV and 150 Sn kV on SOMATOM X.cite. Post-thrombectomy follow-up CT: Hyperattenuating intraparenchymal area visible in the conventional mixed

image (a). Iodine overlay image (b) derived from spectral information reveals that area of hyper-attenuation corresponds to an area of diffused contrast material extravasation. Virtual non-contrast image excludes active bleeding. Courtesy of University Hospital Zurich, Switzerland

ance the radiation dose of the low-energy and the high-energy beam. The CT system is operated in a spiral (helical) scan mode at fast gantry rotation speed (0.28 s) with a maximum spiral pitch of 0.5 (referring to the full z-width of the detector). Moreover, recently introduced CT systems equipped with a split filter, the SOMATOM go.Top,

X.cite and X.ceed, even allow for adaptation of tube voltage. Depending on the clinical need and the size of the patient (attention information is derived from the topogram), either 120 kV or 140 kV is selected for the use with the split filter. The possibility for a higher voltage is of advantage for two reasons: First, spectral separation is increased. Secondly,

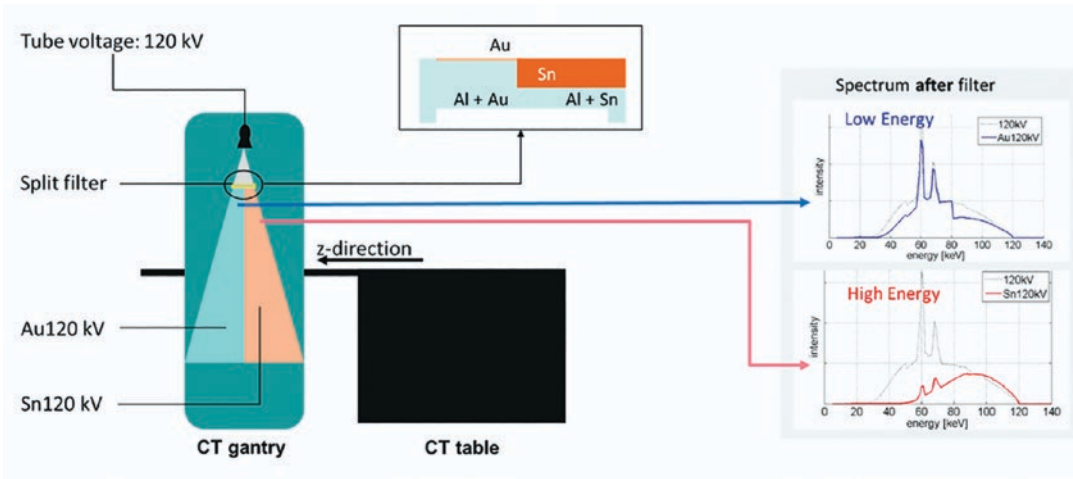


Fig. 10 Left: Principle of a DE acquisition technique that uses a split filter, called “TwinBeam” (Siemens Healthcare GmbH, Forchheim, Germany), in the tube collimator housing to split the X-ray beam in the scan direction.

Right: The standard 120 kV spectrum is split into a low-energy spectrum after filtering with gold (Au, top), and a high-energy spectrum after filtering with tin (Sn, bottom)

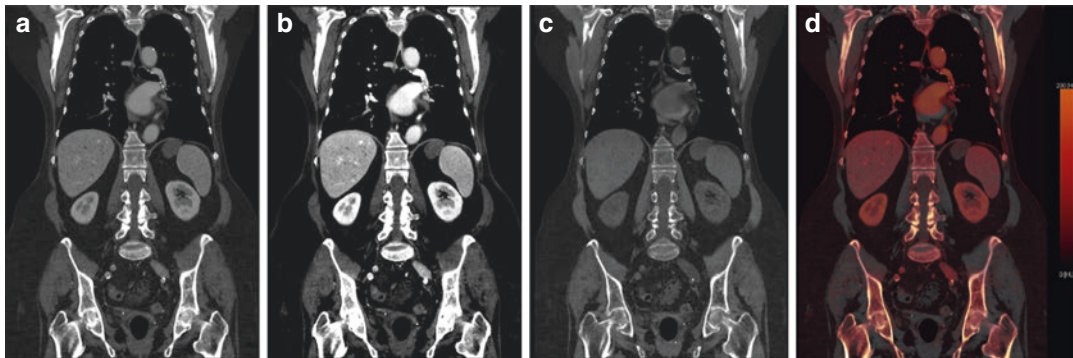


Fig. 11 Contrast-enhanced thorax-abdominal CT examination on a SOMATOM X.cite using Twin Spiral technique. From the acquired DE data, Mono+ images can be generated to increase iodine contrast. At lower energies of 45 keV (b), delineation of anatomical structures and con-

spicuity of lesions is improved compared to 70 keV images (a). In addition, virtual non-contrast images (c) and iodine—as overlay—images (d) can be extracted. The latter in particular allows for quantitative analysis of iodine distribution. Courtesy of Erlangen University, Germany

140 kV allows for a higher tube output and enables scanning of larger patients. Then, for the reconstruction of the TwinBeam data, each half of the detector acquires a complete spiral data set because of the lower spiral pitch, allowing for low- and high-energy images to be reconstructed at any z-position as an input into Mono+ and/ or image-based material decomposition techniques.

This technology provides DE data in the full SFOV of 50 cm diameter. The radiation dose to the patient can be optimized by means of anatomical tube current modulation or risk organ-dependent tube current modulation, in addition to iterative

reconstruction techniques. The data sets are temporally registered, enabling DE CT scans with contrast agent even in the arterial phase. The downside of this approach is that spectral separation is worse than with approaches using two different kV-settings of the X-ray tube. Furthermore, a powerful X-ray tube is required because the pre-filtration absorbs a considerable portion of the X-ray flux, in turn limiting the use of this technique to non-obese patients. Because of the maximum spiral pitch of 0.5, maximum volume coverage speed is limited. Figure 11 shows a clinical example acquired with the split filter technique.

5 Conclusions

Since 2006, with the introduction of DE on Dual Source CT systems, DE imaging has experienced a renaissance. Its clinical application spectrum is growing, and different technical solutions for data acquisition are available. With ongoing technological progress, such as improved spectral separation by means of dedicated pre-filtration of the high-energy beam, successful DE applications have been demonstrated without increased radiation dose to the patient compared to standard single energy CT scans. The dual source dual-energy CT solution provides technical and clinical advantages, such as flexible selection of the kVs of the low-energy beam allows for optimized scanning, adapted to clinical needs. The wide detector coverage combined with the high rotation time allows scanning of even challenging patients, for example those short of breath. Twin Spiral and TwinBeam are alternatives available for single source CTs. Despite the different technical realizations, the same image-based automatic processing techniques and processing applications are applied, allowing the use of DE in a routine clinical workflow.

Compliance with Ethical Standards

Disclosure of Interests Bernhard Schmidt and Thomas Flohr are employees of Siemens Healthineers.

References

- Achenbach S, Ropers D, Kuettner A, Flohr T, Ohnesorge B, Bruder H, Theessen H, Karakaya M, Daniel WG, Bautz W, Kalender WA, Anders K (2006) Contrast-enhanced coronary artery visualization by dual-source computed tomography – initial experience. *Eur J Radiol* 57(3):331–335
- Agarwal MD, Pinho DF, Kulkarni NM, Hahn PF, Guimaraes AR, Sahani DV (2014) Oncologic applications of dual-energy CT in the abdomen. *Radiographics* 34(3):589–612
- Albrecht MH, Vogl TJ, Martin SS, Nance JW, Duguay TM, Wichmann JL, De Cecco CN, Varga-Szemes A, van Assen M, Tesche C, Schoepf UJ (2019) Review of clinical applications for virtual monoenergetic dual-energy CT. *Radiology* 293(2):260–271
- Apfaltrer P, Meyer M, Meier C, Henzler T, Barraza JM Jr, Dinter DJ, Hohenberger P, Schoepf UJ, Schoenberg SO, Fink C (2012) Contrast-enhanced dual-energy CT of gastrointestinal stromal tumors: is iodine-related attenuation a potential indicator of tumor response? *Invest Radiol* 47(1):65–70
- Apfaltrer P, Sudarski S, Schneider D et al (2014) Value of monoenergetic low-kV dual energy CT datasets for improved image quality of CT pulmonary angiography. *Eur J Radiol* 83:322–328
- Bauer RW, Kramer S, Renker M et al (2011) Dose and image quality at CT pulmonary angiography: comparison of first and second generation dual energy CT and 64-slice CT. *Eur Radiol* 21:2139–2147
- Flohr TG, McCollough CH, Bruder H, Petersilka M, Gruber K, Süß C, Grasruck M, Stierstorfer K, Krauss B, Raupach R, Primak AN, Küttner A, Achenbach S, Becker C, Kopp A, Ohnesorge BM (2006) First performance evaluation of a dual-source CT (DSCT) system. *Eur Radiol* 16(2):256–268
- Genant HK, Boyd D (1977) Quantitative bone mineral analysis using dual energy computed tomography. *Invest Radiol* 12(6):545–551
- Grant KL, Flohr TG, Krauss B, Sedlmair M, Thomas C, Schmidt B (2014) Assessment of an advanced image-based technique to calculate virtual monoenergetic computed tomographic images from a dual-energy examination to improve contrast-to-noise ratio in examinations using iodinated contrast media. *Invest Radiol* 49(9):586–592
- Graser A, Becker CR, Staehler M et al (2010) Single-phase dual-energy CT allows for characterization of renal masses as benign or malignant. *Invest Radiol* 45(7):399–405
- Henzler T, Fink C, Schoenberg SO, Schoepf UJ (2012) Dual energy CT: radiation dose aspects. *Am J Roentgenol* 199:S16–S25
- Johnson TRC, Nikolaou K, Wintersperger BJ, Leber AW, von Ziegler F, Rist C, Buhmann S, Knez A, Reiser MF, Becker CR (2006) Dual source cardiac CT imaging: initial experience. *Eur Radiol* 16:1409–1415
- Johnson TRC, Krauß B, Sedlmair M, Grasruck M, Bruder H, Morhard D, Fink C, Weckbach S, Lenhard M, Schmidt B, Flohr T, Reiser MF, Becker CR (2007) Material differentiation by dual energy CT: initial experience. *Eur Radiol* 17(6):1510–1517
- Kalender W (1987) Vertebral bone mineral analysis. *Radiology* 164:419–423
- Kalender WA, Perman WH, Vetter JR, Klotz E (1986) Evaluation of a prototype dual-energy computed tomographic apparatus. I. Phantom studies. *Med Phys* 13(3):334–339
- Knobloch G, Jost G, Huppertz A, Hamm B, Pietsch H (2014) Dual-energy computed tomography for the assessment of early treatment effects of regorafenib in a preclinical tumor model: comparison with dynamic contrast-enhanced CT and conventional contrast-enhanced single-energy CT. *Eur Radiol* 24(8):1896–1905

- Krauss B, Grant KL, Schmidt BT, Flohr TG (2015) The importance of spectral separation: an assessment of dual-energy spectral separation for quantitative ability and dose efficiency. *Invest Radiol* 50(2):114–118
- Laval-Jeantet AM, Roger B, Bouysee S, Bergot C, Mazess RB (1986) *Radiology* 159(2):463–6. <https://doi.org/10.1148/radiology.159.2.3961178>.
- Leber AW, Johnson T, Becker A, von Ziegler F, Tittus J, Nikolaou K, Reiser M, Steinbeck G, Becker CR, Knez A (2007) Diagnostic accuracy of dual-source multislice CT-coronary angiography in patients with an intermediate pretest likelihood for coronary artery disease. *Eur Heart J* 28(19):2354–2360
- Luo XF, Xie XQ, Cheng S, Yang Y, Yan J, Zhang H, Chai WM, Schmidt B, Yan FH (2015) Dual-energy CT for patients suspected of having liver iron overload: can virtual iron content imaging accurately quantify liver iron content? *Radiology* 277(1):95–103
- Mallinson PI, Coupal TM, McLaughlin PD, Nicolaou S, Munk PL, Ouellette HA (2016) Dual-energy CT for the musculoskeletal system. *Radiology* 281(3):690–707
- Mangold S, Gatidis S, Luz O, König B, Schabel C, Bongers MN, Flohr TG, Claussen CD, Thomas C (2014) Single-source dual-energy computed tomography: use of monoenergetic extrapolation for a reduction of metal artifacts. *Invest Radiol* 49(12):788–793
- Marin D, Boll DT, Mileto A, Nelson RC (2014) State of the art: dual-energy CT of the abdomen. *Radiology* 271(2):327–342
- Matt D, Scheffel H, Leschka S, Flohr TG, Marincek B, Kaufmann PA, Alkadhi H (2007) Dual-source CT coronary angiography: image quality, mean heart rate, and heart rate variability. *Am J Roentgenol* 189(3):567–573
- Pache G, Krauss B, Strohm P, Saueressig U, Blanke P, Bulla S, Schäfer O, Helwig P, Kotter E, Langer M, Baumann T (2010) Dual-energy CT virtual noncalcium technique: detecting posttraumatic bone marrow lesions – feasibility study. *Radiology* 256(2):617–624
- Petersilka M, Stierstorfer K, Bruder H, Flohr T (2010) Strategies for scatter correction in dual source CT. *Med Phys* 37:5971–5992
- Pontana F, Faivre JB, Remy-Jardin M et al (2008) Lung perfusion with dual-energy multidetector-row CT (MDCT): feasibility for the evaluation of acute pulmonary embolism in 117 consecutive patients. *Acad Radiol* 15(12):1494–1504
- Primak AN, Fletcher JG, Vrtiska TJ, Dzyubak OP, Lieske JC, Jackson ME, Williams JC Jr, McCollough CH (2007) Noninvasive differentiation of uric acid versus non-uric acid kidney stones using dual-energy CT. *Acad Radiol* 14(12):1441–1447
- Remy-Jardin M, Faivre JB, Pontana F, Molinari F, Tacelli N, Remy J (2014) Thoracic applications of dual energy. *Semin Respir Crit Care Med* 35(1):64–73
- Ropers U, Ropers D, Pflederer T, Anders K, Kuettner A, Stilianakis NI, Komatsu S, Kalender W, Bautz W, Daniel WG, Achenbach S (2007) Influence of heart rate on the diagnostic accuracy of dual-source computed tomography coronary angiography. *J Am Coll Cardiol* 50(25):2393–2398
- Ruzsics B, Schwarz F, Schoepf UJ et al (2009) Comparison of dual-energy computed tomography of the heart with single photon emission computed tomography for assessment of coronary artery stenosis and of the myocardial blood supply. *Am J Cardiol* 104(3): 318–326
- Scheffel H, Alkadhi H, Plass A, Vachenaue R, Desbiolles L, Gaemperli O, Schepis T, Frauenfelder T, Schertler T, Husmann L, Grunenfelder J, Genoni M, Kaufmann PA, Marincek B, Leschka S (2006) Accuracy of dual-source CT coronary angiography: first experience in a high pre-test probability population without heart rate control. *Eur Radiol* 16(12):2739–2747
- Scheffel H, Stolzmann P, Frauenfelder T, Schertler T, Desbiolles L, Leschka S, Marincek B, Alkadhi H (2007) Dual-energy contrast-enhanced computed tomography for the detection of urinary stone disease. *Invest Radiol* 42(12):823–829
- Schenzle JC, Sommer WH, Neumaier K et al (2010) Dual energy CT of the chest: how about the dose? *Invest Radiol* 45:347–353
- Schneider D, Apfaltrer P, Sudarski S et al (2014) Optimization of kiloelectron volt settings in cerebral and cervical dual-energy CT angiography determined with virtual monoenergetic imaging. *Acad Radiol* 21:431–436
- Stolzmann P et al (2010) In vivo identification of uric acid stones with dual-energy CT: diagnostic performance evaluation in patients. *Abdom Imaging* 35(5):629–635
- Thomas C, Schabel C, Krauss B, Weisel K, Bongers M, Claussen CD, Horger M (2015) Dual-energy CT: virtual calcium subtraction for assessment of bone marrow involvement of the spine in multiple myeloma. *Am J Roentgenol* 204(3):W324–W331
- Uhrig M, Sedlmair M, Schlemmer HP, Hassel JC, Ganten M (2013) Monitoring targeted therapy using dual-energy CT: semi-automatic RECIST plus supplementary functional information by quantifying iodine uptake of melanoma metastases. *Cancer Imaging* 13(3):306–313
- Vetter JR, Perman WH, Kalender WA, Mazess RB, Holden JE (1986) Evaluation of a prototype dual-energy computed tomographic apparatus. II. Determination of vertebral bone mineral content. *Med Phys* 13(3):340–3. <https://doi.org/10.1118/1.595951>.
- Vliegenthart R, Pilgrim GJ, Ebersberger U, Rowe GW, Oudkerk M, Schoepf U (2012) Dual-energy CT of the heart. *Am J Roentgenol* 199:S54–S63
- Werner A, Krauss B, Haberland U, Bongers M, Starke U, Bakchoul T, Enkel S, Nikolaou K, Horger M (2019) Dual-energy CT for liver iron quantification in patients with haematological disorders. *Eur Radiol* 29(6):2868–2877
- Yu L, Leng S, McCollough C et al (2012) Dual-energy CT-based monochromatic imaging. *Am J Roentgenol* 199(5 Suppl):S9–S15



Dual-Energy: The Philips Approach

Ami Altman, Galit Kafri, and Sary Shenhav

Contents

1	Spectral Detection Through a Dual-Layer Detector	30
2	Spectral Material Decomposition and Reconstruction	31
3	Spectral Results	34
3.1	MonoE: Monoenergetic Images [HU].....	34
3.2	VNC: Virtual Non-Contrast.....	36
3.3	Iodine No Water [mg/ml].....	37
3.4	Calcium Suppression [HU].....	37
3.5	Iodine Density [mg/ml].....	38
3.6	Contrast-Enhanced Structures [HU].....	38
3.7	Iodine Removed [HU].....	39
3.8	Uric Acid and Uric Acid Removed Pair [HU].....	39
3.9	Z Effective.....	40
3.10	Electron Density [%EDW].....	40
	References	42

Abstract

The Philips dual-layer detector approach for spectral imaging was introduced as early as 2005 in a prototype installed in Hadassah University Medical Center, Israel. Since then both the detector design and the material decomposition and reconstruction techniques were further developed and improved to allow better SNR and CNR in spectral results. This

single-source approach to spectral imaging has some clear advantages: energies acquisition is perfectly aligned by design; it does not require a special dual-energy acquisition mode thus making all scans spectral and enables projection-based material decomposition. It also allows for advanced clinical application, such as cardiac and perfusion, to utilize spectral imaging. In addition, it allows to easily overcome limitations of the source-based techniques in the sense that it does not have dose penalties, field of view restriction, it does not require to slow rotation time, and it is not limited by patient habitus.

A. Altman · G. Kafri · S. Shenhav (✉)
Philips Medical Systems Technologies Ltd.,
Advanced Technologies Center, Haifa, Israel
e-mail: sary.shenhav@philips.com

In this chapter, we will discuss the dual-layer detector architecture, projection-based material decomposition and image reconstruction as well as the different spectral results and their clinical use.

1 Spectral Detection Through a Dual-Layer Detector

While material decomposition in energy-selective CT was proposed by Alvarez and Macovski in 1976, a dual-layer detector for a simultaneous acquisition of two energies in CT was first proposed by Brooks and Di Chiro in 1978. A Philips Healthcare team proposed a different configuration and implementation of that idea (Carmi et al. 2005; Altman et al. 2006) and in October 2005 Philips has installed the world first clinical prototype utilizing a single-source spectral detection technique at the Hadassah Medical Center in Jerusalem, Israel. This implementation included two attached scintillator layers, optically separated, and read by a side-looking, edge-on, silicon photodiode, thin

enough to maintain the same detector pitch and geometrical efficiency as a conventional CT detector (Figs. 1 and 2). The top scintillator layer's atomic number and thickness have been optimized to maximize energy separation at 120 and 140 kVp, while maintaining high enough signal statistics for the low-energy raw data even for a large patient. A low Z (atomic number) Garnet scintillator material, with a high light-output (~15%–20% better than GOS), has been developed to meet these requirements. This contributes to a high SNR in the top (low-energy) layer detector, enabling it to function at a very low dose without causing artifacts, typical to electronic-noise dominant signals.

The mean energy separation of the dual-layer detector, at 120 kVp, with and without a 30-cm water absorber, is shown in Fig. 3. The decrease in energy separation with increasing patient size is compensated due to the complete consistency in sampling of the two energies.

The Philips approach to spectral imaging is unique in the sense that it is based on a single source and spectral detection. Compared to source-based dual-energy techniques, the detector-based technique has some clear advan-

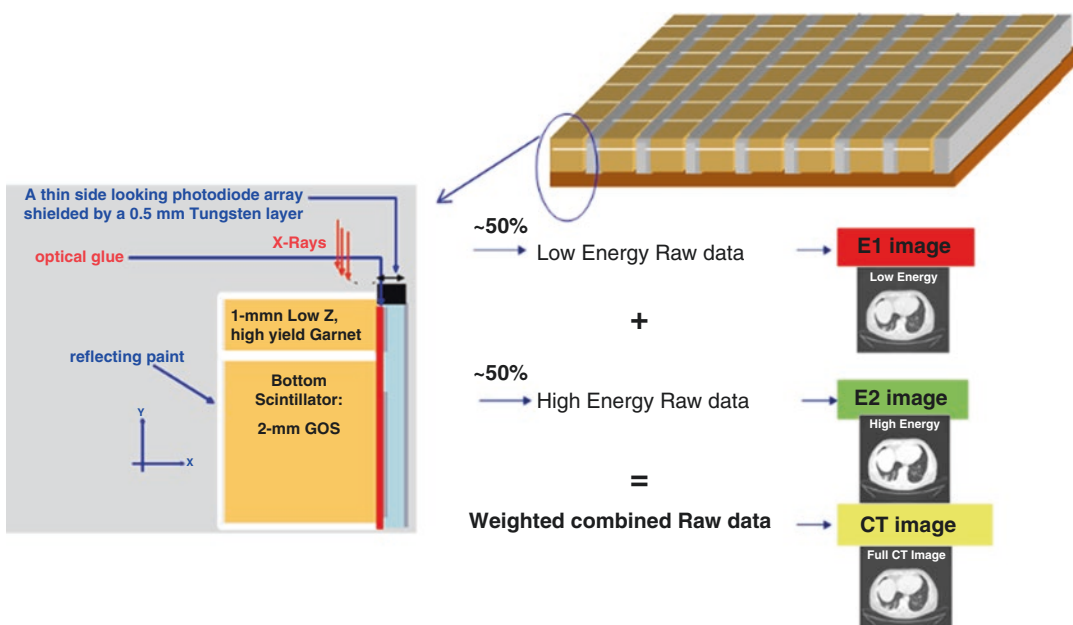


Fig. 1 A schematic view of the Philips Healthcare dual-layer detector

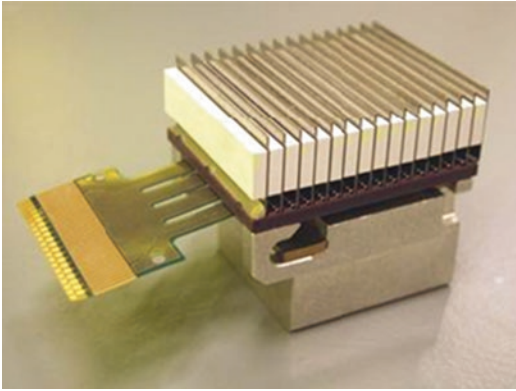


Fig. 2 A vertical implementation of a 16×16 pixels dual-layer detector

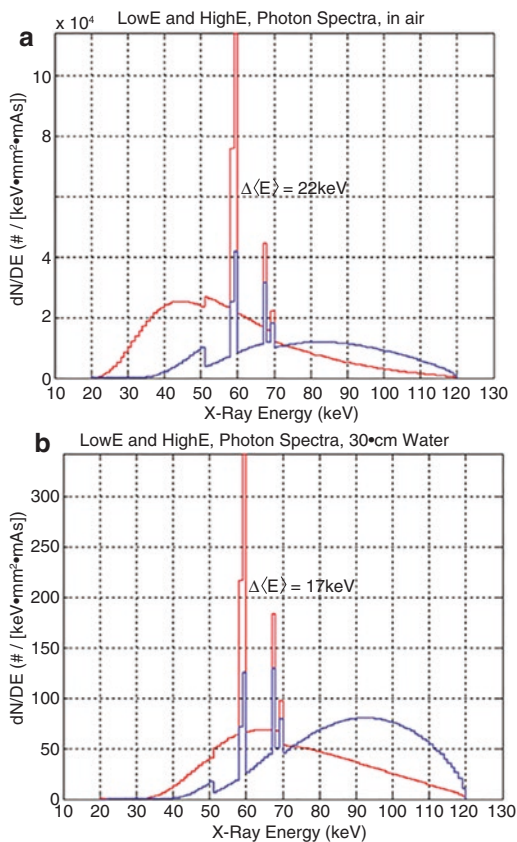


Fig. 3 Top and bottom layers' spectra and mean energy difference in air (a) and with 30-cm water absorber (b), for 120 kVp

tages: energies acquisition is perfectly aligned by design as they are not only simultaneously measured, but also sampled exactly at the same angle at the same pixel, unlike the other methods of dual-energy CT; it does not require a special dual-energy acquisition mode thus making all scans spectral and enables projection-based material decomposition (see next section) which in turns allows better SNR and CNR in spectral results, like iodine quantification, effective atomic number image, electron densities, and virtual MonoE images (Sellerer et al. 2018; Ehn et al. 2018). It also allows for advanced clinical application, such as cardiac and perfusion, to utilize spectral imaging. In addition, it allows to easily overcome limitations of the source-based techniques in the sense that it does not have dose penalties, field of view restriction, it does not require to slow rotation time and it is not limited by patient habitus.

2 Spectral Material Decomposition and Reconstruction

Dual-energy spectral decomposition in the projection domain, using a two-base model, was first proposed by Alvarez and Macovski (1976). In this approach, the two projections data sets of the low and high energies are transformed into a new pair of projections data sets, from which all the various spectral results can be derived. The resulting two spectral-projections data sets are independent of the incident spectrum, hence clear from beam hardening effect, while even metal beam hardening and artifacts can be suppressed quite easily. This is a very important result of the projection-domain spectral decomposition, unlike image-domain spectral decomposition, where the resulting spectral images (e.g., virtual monochromatic images) suffer from beam hardening effects, and require special beam hardening correction, which is, often, insufficient (see e.g., Carmi et al. 2005).

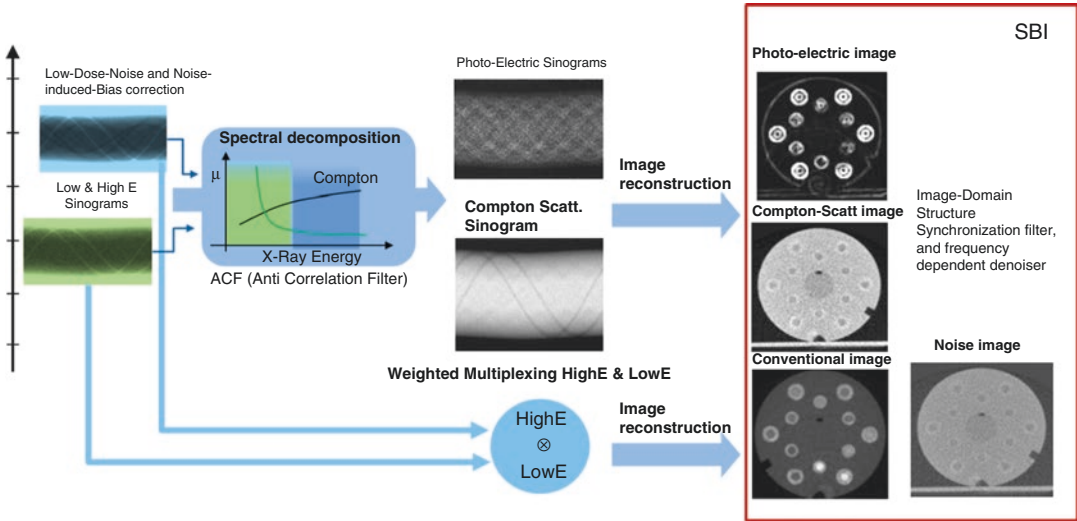


Fig. 4 A schematic description of the Philips spectral decomposition and image reconstruction

The Philips implementation of projection-domain spectral decomposition (Altman et al. 2015) assumes an accurate forward model of the projection’s formation, as an input. This includes the precise source X-ray spectrum, the beam filtration, its variations in the directions to all the detection pixels, and the resulting different spectrum incident on each detection pixel in air. This implementation is simpler than the empirical approach proposed in (Alvarez and Macovski 1976), or the maximum-likelihood method proposed by Alvarez (Alvarez et al. 2011).

The basic Philips approach to the transformation from the **low** and **high energies** projections data sets to the Photo-Electric and Compton-scattering projections data sets is described below in Fig. 4 and the following equations:

$$\begin{aligned} \left\{ P_{\text{high}} \right\}, \left\{ P_{\text{low}} \right\} &\Rightarrow \left\{ P_{\text{scatt.}}^M \right\}, \left\{ P_{\text{photo}}^M \right\} \\ \text{Spectrum dependent} &\quad \text{Spectrum independent} \\ &= \mu_0 \cdot \left\{ a_{\text{scatt.}}^M \right\}, \mu_0 \cdot \left\{ a_{\text{photo}}^M \right\} \end{aligned}$$

where μ_0 is an arbitrary quantity with a dimension of an attenuation coefficient, which the end results are divided by at the end of the process.

The above transformation utilizes a two-base model:

$$\begin{aligned} \mu^M(E) &= \mu_{sc}^M(E) + \mu_{ph}^M(E) \cong f_{sc}(E) \cdot \mu_{sc}^M(Z_\xi, \rho_\xi) \\ &\quad + f_{ph}(E) \cdot \mu_{ph}^M(Z_\xi, \rho_\xi) \end{aligned}$$

where M represents a material mix, optimized for energy-dependence “universality” (~71% soft tissue, ~28% bone, ~1% iodine), while assuming the following:

1. Variable separation between the energy dependence and the Z dependence of the attenuation coefficient components (cross sections) is possible within the X-rays energy range used in CT.
2. The energy dependence of Compton Scattering, and the Photo-Electric cross sections, can be considered to be the same for all patients and test phantoms, based on the above material mix (this excludes phantoms and objects with a very large content of heavy metals/elements).
3. Coherent scattering can be either neglected or included in the photo-electric component (Energy dependence is $\sim 1/E^2$).

Assuming the above, the line integrals can be expressed as:

$$\int \mu(\xi, E) d\xi \cong f_{scat}^M(E) \cdot \int \mu_{scat}^M(\xi) d\xi + f_{phot}^M(E) \cdot \int \mu_{phot}^M(\xi) d\xi$$

$$\boxed{= a_{scat}^M} \qquad \boxed{= a_{phot}^M}$$

$$P_{h,l} = -\log \left(\frac{\int_0^\infty \exp(-\int \mu(\xi, E) d\xi) \cdot F_{h,l}(E) \cdot EdE}{\int_0^\infty F_{h,l}(E) \cdot EdE} \right)$$

and the projections value for each line integral (detection pixel) can be obtained:

$$P_{h,l} = -\log \left(\frac{\int_0^\infty \exp(-f_{scat.}(E) \cdot a_{scat}^M - f_{phot}(E) \cdot a_{phot}^M) \cdot F_{h,l}(E) \cdot EdE}{\int_0^\infty F_{h,l}(E) \cdot EdE} \right)$$

From which, the values of a_{scat}^M and a_{phot}^M , the spectral line integrals are derived.

Where,

1. The functions $f_{phot}(E)$ and $f_{scat}(E)$ are derived from the E dependence of the chosen material mix M, calculated from NIST tables.
2. $F_l(E)$ and $F_h(E)$ are the energy distributions of the X-ray beam in air, incident on the top layer pixels and the bottom layer pixels, respectively (after all filtration and without any scanned object/body). Note that both $F_l(E)$ and $F_h(E)$ are matrices of distribution functions that must be pre-calculated and require full input/knowledge of the filtration along the rays to each detector pixel.
3. The material decomposition procedure described above has two important “side effects” that are addressed:
 - (a) Anti-correlated Noise: The transformation, mentioned above, determines the specific portions of LowE signal and HighE signal, assigned to the Scatter and to the Photo projection signals, respectively. As a result any portion of a radiation signal that is assigned to the Scatter projection signal, while it should have been assigned to the Photo signal, would cause a correlated error in the correspond-

ing Photo-Electric signal, and vice versa. This would result in a correlated noise between the two, hence would need a special consideration of how to reduce this noise through an Anti-Correlation Filter (ACF) in the projection domain.

- (b) Noise Induced Bias: It occurs in many cases, since the original radiation intensity per detection pixel is divided between two separate projection signals (Scatter and Photo projections sets in Philips approach). In this case, taking the logarithm of the raw signal, the statistical uncertainty of which is at the tail of the Poisson distribution, is causing a DC bias. This bias is corrected by a special filter at the input to the material decomposition process.
4. Following the reconstruction of the Photo-Electric and the Scatter images, special filters/algorithms are used, in the image domain, to conserve image structures, edges, and features, adapted from the conventional image, while reducing the image noise in a frequency-dependent form.

It is important to emphasize that projection-domain spectral decomposition can be used only if the signals from the two X-ray energies are

sampled both simultaneously (“Equi-time”) and at the same angle (“Equi-angle”). Only the spectral-detector and the fast-kVp-switching methods meet this condition.

3 Spectral Results

The Philips spectral CT system can provide a variety of spectral image types, on top of the conventional images, which are reconstructed through advanced spectral algorithms. Those spectral results can be generated either prospectively, on the scanner and sent to PACS, or retrospectively, directly on PACS utilizing Spectral Based Images known as SBI (as described above) and have the potential for additional clinical information to conventional CT imaging. Each spectral result is designed for a different clinical usage as will be explained in this chapter.

As described above, data from the low and high energy layers of the spectral detector undergo spectral decomposition in the projection space to generate optimal photo-electric absorption and Compton scattering images that are used as a two-base model. These optimal photo-electric absorption and Compton scattering images do not represent the pure Compton and photo-electric effects. They are slightly modified version of them. This is because different materials have slightly different energy dependencies, mainly at low energies, from the expected theoretical models of the two basic physical interactions. Moreover, coherent scattering which is the third component that contributes to the total attenuation of X-ray in matter need to be included, despite its relatively small contribution.

The optimal Photo and Scatter sets of images are stored together with the derived noise-images set in a special SBI (Spectral Based Images) format. All the relevant spectral results and images can be derived from the SBI series, using various algorithms. Hence, the spectral results can be created on demand and reviewed as needed on PACS and are not required to be sent to PACS prospectively.

The conventional images are analogous to the images obtained from a single-energy scanner

and are utilized for routine diagnostic purposes. For every scan, the pre reconstructed sum of the signals from the simultaneous acquisition of the high- and the low-energy data is combined to obtain the total amount of absorbed energy. Filtered back projection or iterative reconstruction algorithms are then used to reconstruct the combined raw data and create true conventional images. It has been shown that image quality of these conventional images from the Philips spectral CT system are comparable to images obtained from a single-energy scanner (Hojjati et al. 2017; Van Ommen et al. 2018).

Spectral results can have units of attenuation (HU) and other voxel values that represents physical quantities, for example, density in mg/ml. The clinical use of the different spectral results generated from the spectral-detector DECT have been demonstrated in several papers for several clinical applications in body, cardiac and neuro imaging (Brun Andersen et al. 2020; Fulton et al. 2017; Rajiah et al. 2017a; Neuhaus et al. 2017a) as well as for emergency imaging (Demirler Simsir et al. 2020). The high quantitative accuracy of the various spectral results was recently demonstrated in several studies (Ehn et al. 2017; Hua et al. 2018).

In the following, the algorithm and the potential clinical usage of the different spectral results will be discussed.

3.1 MonoE: Monoenergetic Images [HU]

MonoE images are virtual mono-energy images which simulate images as if they are obtained using a pure monochromatic X-ray beam at a specific keV value. Virtual monochromatic images are generated between 40 keV and 200 keV, in increment of 1 keV, and the voxels in these images represent Hounsfield values (HU). This is illustrated in Fig. 5. The MonoE images are created by a linear combination of the two-base model, namely the photo-electric effect (PE) and Compton scattering (Sc) components, where a different weight is used for each KeV. In the low energy range the proportion of the photo-

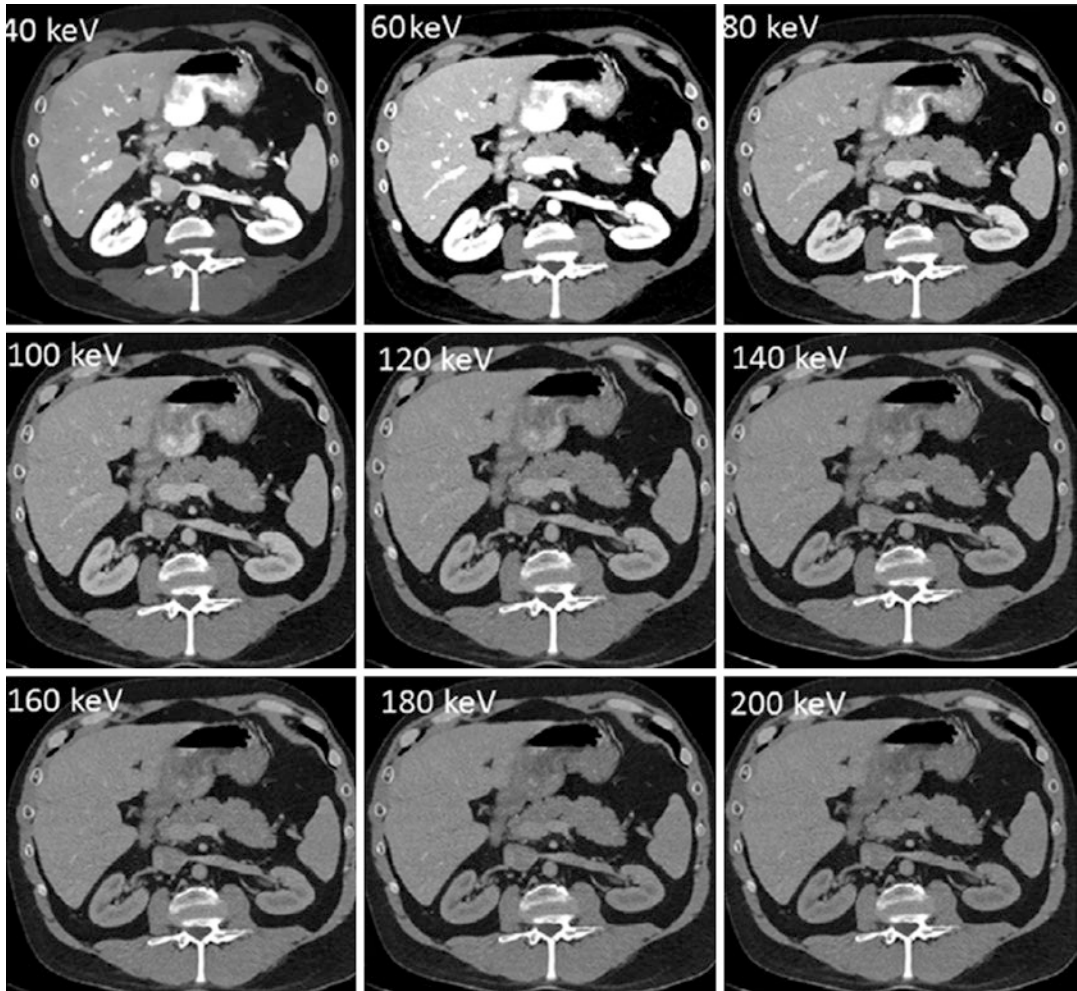


Fig. 5 Virtual mono-energetic images from 40 to 200 keV displaying tissue attenuation properties similar to those resulting from imaging with a mono-energetic beam at a single keV level (Fulton et al. 2017)

electric effect is high and the Compton scattering is low, whereas in the high energy range it is opposite. In the 70 keV the proportions of these two components are very similar.

It should be noted that it is possible to generate monoE results also for keV values higher than the used kVp value since the behavior of the universal energy dependent basis is known also for high energies. Also, in order to stay above the K-edge of Iodine (33.2 keV), the lowest monoE was selected to be 40 keV.

In the Philips spectral CT system, the noise in the spectral results is typically lower than in the

corresponding conventional images due to special noise reduction techniques that are used in the spectral reconstruction process to minimize the noise and to optimize the signal to noise ratio (Kaltsz et al. 2017). See also Spectral Material Decomposition and Reconstruction section above.

A specific result named mono E-equivalent to conventional CT can be generated as well. This result has almost the same HU value as a conventional image generated from 120 kVp voltage (regardless of the actual tube voltage used during the scan) but with lower artifacts and noise.

The equivalent monochromatic images are 70 keV, 66 keV, and 64 keV for body, head, and extremities, respectively.

Monochromatic images may overcome some of the limitations of a polychromatic X-ray beam. A conventional CT image is created from a poly-energetic X-ray tube with a certain voltage (e.g., 120 kVp, 140 kVp) and therefore it is reconstructed from multiple energies. Since the mono-energetic series (MonoE) represents a single energy, it minimizes some of the known limitations of a polychromatic X-ray beam. For example, beam-hardening, metallic, and calcium blooming artifacts.

The potential benefits of the high virtual mono-energetic images derived from dual-layer CT scans for reduction of artifacts caused by orthopedic metal implants, were demonstrated both in a phantom study (Wellenberg et al. 2017) and clinical studies for implants in the spine, pelvis, and extremities (Neuhaus et al. 2017b; Große Hokamp et al. 2017a) as well as dental implants (Große Hokamp et al. 2018).

Low-energy mono-energetic images are influenced by photo-electric data, resulted in increasing attenuation and signal to noise ratio (SNR) and are therefore useful for all vascular imaging. The increased attenuation at low keVs can be used for contrast reduction, which is especially important in patients with renal insufficiency (Oda et al. 2018; Tsang et al. 2017; Nagayama et al. 2017; Hickethier et al. 2020) and for improvement in image quality when the contrast enhancement is suboptimal, salvaging angiographic studies and reducing the need for additional contrast or radiation dose. Also, low MonoE reconstructions allow the user to create angiography studies from a routine contrast-enhanced exam, adding additional diagnostic information to the exam. In addition, low MonoE images are used for better lesion conspicuity (Liu et al. 2019; Yoon et al. 2020; Große Hokamp et al. 2017b).

The advantage of the monochromatic images was also demonstrated in neuroimaging by reducing beam hardening artifacts for optimized gray-white matter contrast (Neuhaus et al. 2017c) and for visualization improvement of intracranial

hemorrhage and brain lesions (Lennartz et al. 2018). In addition, it was demonstrated that improved gray-white matter differentiation in cranial CT by using virtual mono-energetic images enables a radiation dose reduction compared to conventional images (Reimer et al. 2019). The reduction of blooming artifacts for coronary stent assessment and calcium blooming reduction in cardiac imaging was recently demonstrated as well (Hickethier et al. 2017; Van Hedent et al. 2018).

The next spectral results that are described are the virtual non-contrast (VNC), iodine no water, and calcium suppressed. These three spectral types belong to the same category of two-material decomposition. A two-material decomposition algorithm assumes that each voxel consists of two types of materials only. In order to achieve this, a simple linear basis transformation from the basis of the photo-electric effect and Compton scattering components into a new basis representation of two selected materials is performed. By selecting the two materials to be iodine and water, it is possible to generate the virtual non-contrast (VNC) and the iodine no water results. By selecting the materials to be a calcium-based material and water, a calcium suppressed image can be created.

3.2 VNC: Virtual Non-Contrast

This is a spectral result that mimics the attenuations values of a non-contrast CT scan from a data that is acquired with a contrast injection. It thus has the potential of replacing a true non-contrast series. By applying the two-materials decomposition to a NIST-based iodine and water basis, the iodine attenuation contribution of each voxel is removed and only the water attenuation contribution of each voxel in HU is displayed according to the mono 70 keV image. Due to the nature of this algorithm, the HU of the bony structures and calcium pixels are decreased by about 50% of their value in the 70 keV image.

A recent study compared the VNC images derived from the dual-layer spectral detector to a true non-contrast (TNC), found a good agree-

ment of the attenuation measurements between the two images in most abdominal tissues with an overestimation in fatty tissues (Jamali et al. 2019). This is in agreement with prior studies (Ananthakrishnan et al. 2017; Sauter et al. 2018) where the quality of iodine removal in VNC images was not influenced by the original contrast enhancement and thus has a potential advantage in reducing the radiation dose delivered to the patient in biphasic and triphasic examinations.

It was also shown that with an appropriately chosen proportionality factor as a correction coefficient, spectral CT VNC can reliably estimate the calcium score from a contrast-enhanced coronary CTA and shows good agreement with the conventional technique (Nadjiri et al. 2018).

3.3 Iodine No Water [mg/ml]

This is a spectral result type in which the voxel values represent the iodine concentration of the displayed tissue in mg/ml as calculated from the iodine-water two-material decomposition algorithm. The quantification of the iodine density is calculated by scaling the iodine projection on the water basis. Non-enhanced soft tissues are set to approximately 0 mg/ml of iodine.

Iodine no water [mg/ml] images have the potential to allow for improved visualization of iodine-enhanced tissues. This result can also be used for iodine quantification, but only in areas where iodine is present.

The accuracy of the iodine concentrations was tested in a phantom study for a range of concentrations between 2 and 20 mg/ml and found to be within a 0.3 mg/ml accuracy (Hua et al. 2018).

In Fig. 6, we show an example where a conventional, VNC, and iodine no water images are compared for a renal lesion.

3.4 Calcium Suppression [HU]

In this image type, voxels containing calcium are suppressed and replaced by virtual HU values as similar as possible to the expected HU without calcium contribution to the attenuation. In a similar way to the VNC algorithm, the contribution of the calcium-based material attenuation of each voxel is removed and only the water attenuation contribution of each voxel is displayed in HU according to the mono 70 keV. In contrast to VNC algorithm, where the iodine material is represented by a specific slope, the bony structures cannot be represented by one slope but of a range of calcium-based materials slopes. According to

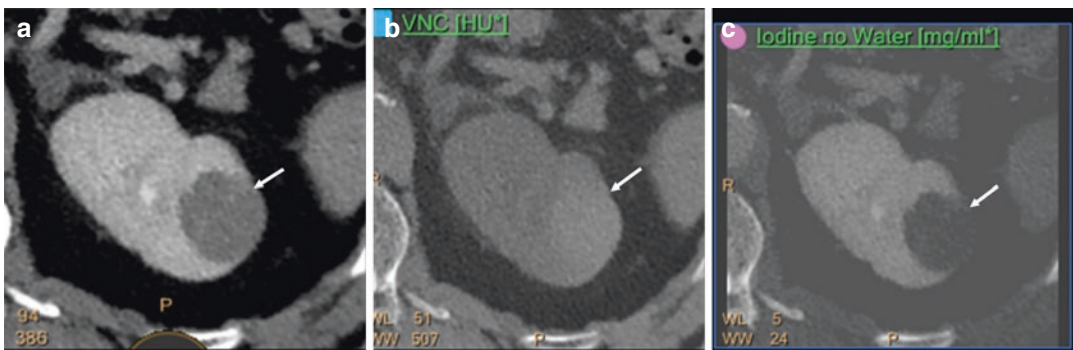


Fig. 6 (a) Axial CT scan at the level of left kidney shows a cystic lesion, which has attenuation higher than a simple cyst (arrow); (b) virtual non-contrast CT at the same level shows that there is higher attenuation in the VNC image indicating that this is a hemorrhage; and (c) iodine-only

image at the same level shows absence of significant iodine in the lesion thus confirming that there was no contrast uptake in the lesion, but the high attenuation is consistent with hemorrhage, thus a complicated cyst (Fulton et al. 2017)

the calcium composition weight in each bony structure, an appropriate index value can be selected. A low index value selection targets tissues with a low calcium composition weight; a high index value selection targets tissues with a high calcium composition weight.

In a recent study, the calcium suppressed images from dual-layer CT have been used to visualize the bone marrow edema in traumatic vertebral compression fractures (Neuhaus et al. 2018). In a different study (Abdullayev et al. 2019), it was found that calcium suppressed images are capable of improving differentiation between a metastatic and a normal bone. Also, it was demonstrated that calcium suppressed images could clearly present the temporomandibular joint displacement. This suggested that calcium suppressed images could be used to diagnose the displacement of the temporomandibular joint disc (Zhang et al. 2020).

In the above described spectral types, where the two-material decomposition is applied, the algorithm didn't attempt to separate between two selected materials. In the spectral results that are explained below, a classification method between two materials is performed. The spectral results that are included in this category are the iodine density, contrast-enhanced structures, iodine removed, and the pair uric acid and non-uric acid removed.

3.5 Iodine Density [mg/ml]

This is an image type in which, similarly to the iodine no water result, the voxels values represent the iodine concentration of the displayed tissue in mg/ml. In this image, the non-negative iodine quantification for all voxels which are classified as including Iodine is calculated by scaling the iodine projection on the water basis as explained for the iodine no water result. Voxels which are classified as not included iodine are set to 0 mg/ml and are visualized as black pixels.

Similar to the iodine no water result, iodine density images enable the identification of

iodine-containing structures as well as direct quantification of iodine.

The accuracy of the iodine concentrations for iodine density was tested in a phantom study for a range of concentrations between 2 and 20 mg/ml and found to be within a 0.3 mg/ml accuracy (Hua et al. 2018).

It was shown that iodine density allows one to detect occult bone lesions that cannot be detected with conventional CT due to the high contrast of the bone and the lack of bone destructions. Iodine density yields high sensitivity and adequate specificity for the differentiation of vertebral trabecular metastases and healthy trabecular bone (Borggreffe et al. 2019). In another study (Kikano et al. 2020), it was shown that iodine density images can help elucidate and differentiate between various cardiothoracic pulmonary perfusion anomalies and may enhance a radiologist's diagnostic confidence. Also, Lennartz et al. showed that iodine overlay images obtained with spectral-detector CT improve visual and quantitative diagnostic accuracy in assessing skeletal muscle metastases compared to conventional images (Lennartz et al. 2019). In a study case, iodine density images allowed for differentiation of benign and malignant pulmonary nodules (Große Hokamp et al. 2019).

In Fig. 7, we show hypodense lesion in the head of the pancreas using conventional CT, mono-energetic 40 KeV, iodine density, and Z effective. The Z effective result will be discussed shortly.

3.6 Contrast-Enhanced Structures [HU]

In this result all the voxels, which are classified as including iodine, remain identical to MonoE 70 keV. All bone classified voxels are displayed as black voxels. Contrast-enhanced structures images have the potential of providing bone-free images which can help in visualizing vascular structures without bone or calcifications.

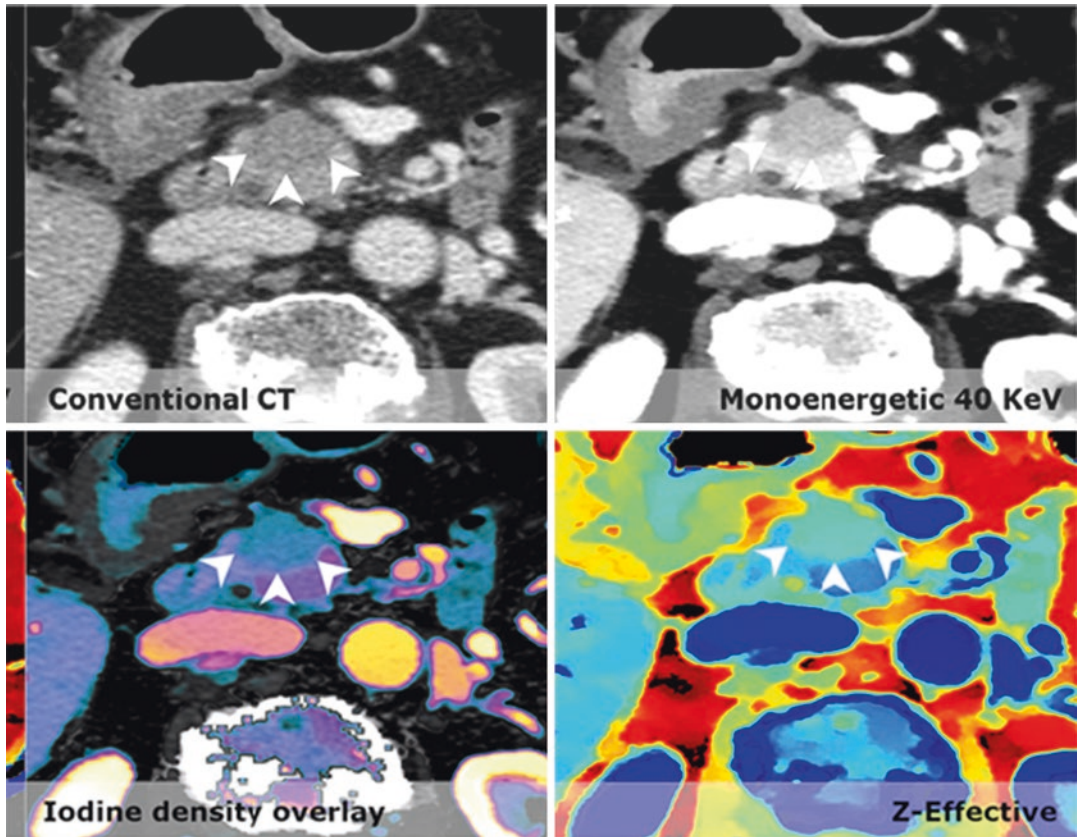


Fig. 7 Patient with a slight increase in volume in the head of the pancreas and stranding in the peripancreatic fat. In the pancreatic head, a slight hypodense lesion (arrowheads outline the lesion) is visible on the conventional image; however, it is easily missed. On iodine density as

well as mono 40 keV and Zeff images, the lesion stands out against the normal pancreatic parenchyma and the lesion was correctly diagnosed as a pancreatic adenocarcinoma (Brun Andersen et al. 2020)

3.7 Iodine Removed [HU]

An image type in which all the voxels which are classified as not including iodine above a certain threshold are displayed as black voxels. All other voxels remain identical to MonoE 70 keV.

3.8 Uric Acid and Uric Acid Removed Pair [HU]

In these two spectral results, the classification is done between uric acid and calcium voxels and the two results are complementary with each other.

3.8.1 Uric Acid [HU]

In the uric acid result, all the voxels which are classified as including uric acid remain identical to MonoE 70 keV. All other voxels classified as not including uric acid are displayed as black voxels.

3.8.2 Uric Acid Removed [HU]

In the uric acid removed result, all the voxels which are classified as not including uric acid remain identical to MonoE 70 keV. All other voxels classified as including uric acid are displayed as black voxels.

The uric acid and uric acid removed image pair are intended for uric acid and calcium classifica-

tion and therefore have a potential use in gout disease diagnosis and stone characterization.

In gout disease, the attenuation of low-atomic-weight monosodium urate (MSU) crystals differs from that of high-atomic-weight calcium such as calcium pyrophosphate dihydrate (CPPD) crystals, that exist in pseudogout and can have a clinical presentation like that of gout.

Uric acid-calcium pairs are also useful in characterizing urinary calculus composition as demonstrated by Rajiah et al. (2017b).

The last two spectral results that are described below, Z effective and electron density can be used for material characterization.

3.9 Z Effective

This is an image in which the voxel values represent the effective atomic number of the displayed tissue. While the atomic number is characteristic of an element, the effective atomic number is characteristic of materials consisting of more than one element such as water, soft tissue, and bone.

A Z effective calculation is based on the ratio of attenuations at two different energies and is therefore independent of the material density. The expected Zeff values for known different tissues from the literature were calculated and a conversion curve between the monoEs ratio and the calculated Z effective was created.

The Z effective images can be displayed in color or gray scales. The dynamic range is set to be between 5 and 30, where water is 7.4 and air is set to be zero. Non-enhanced soft tissues have Z effective value of approximately seven. Fatty tissues have lower Z effective than water, while bone and contrast-enhanced tissues have higher values compared with water Z effective. Metal implants have a high Z effective possibly higher than 30.

In a phantom study (Hua et al. 2018), different tissues with different Z effective values from approximately 6 (adipose tissue) to about 13 (cortical bone) were scanned in different configura-

tions. It was found that the accuracy of the Z effective is on the order of $\pm 2\%$ for both soft tissue and bone-equivalent materials, with somewhat larger percentage deviations for lung-mimicking materials. The accuracies were found to be similar in different scans and reconstruction parameters.

Z Effective images have the potential to differentiate tissues based on their atomic number values, for example, in stone characterization (Fulton et al. 2017). This is shown in Fig. 8 in a different study. In addition, it was shown that the use of contrast-enhanced spectral CT including Z effective images increases the confidence of the radiologists in correctly characterizing various lesions and minimizes the need for supplementary examinations (Brun Andersen et al. 2020). See Fig. 8.

The benefit of the dual-layer spectral CT was recently demonstrated in the emergency department (Demirler Simsir et al. 2020). It was shown that by using iodine density and Zeff maps, the detection of subtle filling defects and demonstration of the presence or lack of lung perfusion deficits in pulmonary embolism is better. This is shown in Fig. 9.

3.10 Electron Density [%EDW]

This is a spectral result that displays the electron density of each voxel relative to the electron density of water (3.34×10^{29} electrons \times m⁻³) in units of percent where the expected value for water in these units is 100 [%EDW].

The electron density (ED) estimation is based on a linear combination of the photo-electric effect and Compton scattering where the Compton scattering component dominates. The two parameters of the linear combination coefficients were determined by finding the best fit to the expected electron densities of known literature tissues. The normalization was chosen so that the relative ED of water is 100.

For several decades, in order to calculate the radiation dose distribution, HU were converted to

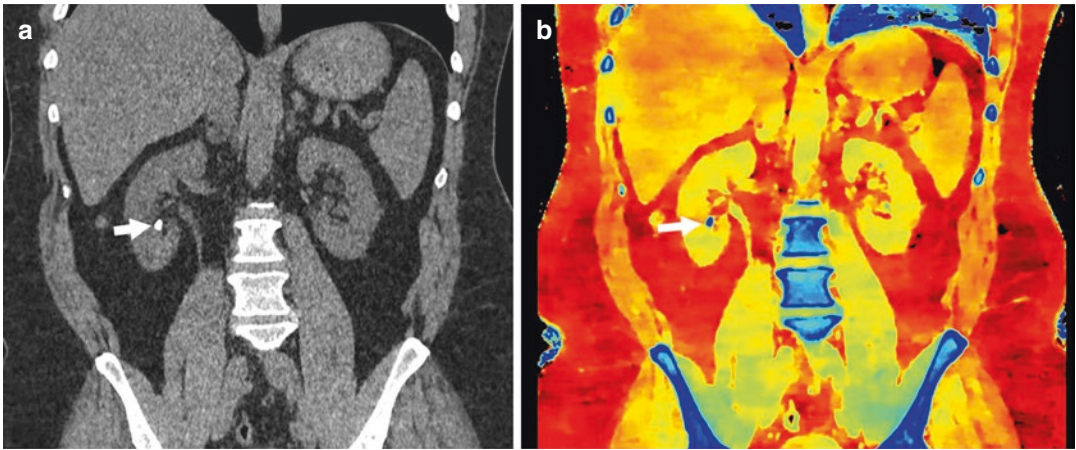


Fig. 8 Urinary calculus composition. (a) Coronal 120-kVp routine diagnostic image in a patient with acute abdominal pain shows a 7-mm calculus in the inferior pole of the right kidney (arrow). (b) Effective atomic

number-based reconstruction at the same level shows that the calculus has high atomic number (arrow) consistent with a calcium calculus (Rassouli et al. 2017)

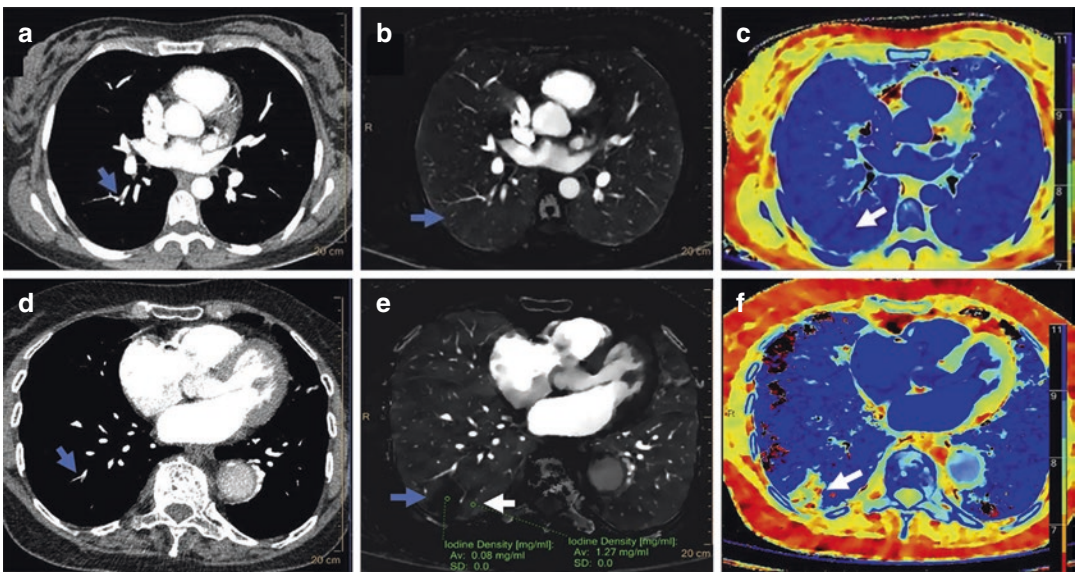


Fig. 9 A 36-year-old woman presented with right-sided acute chest pain (upper row). (a) On conventional CT, a small filling defect was present in right lower lobe sub-segmental pulmonary artery (arrow). (b) Iodine density and (c) Zeff maps showed no perfusion deficit distal to the filling defect (arrows). A 90-year-old woman presented with dyspnea, right-sided chest pain (lower row), (d) Conventional CT, small filling defect was present in right lower lobe sub-segmental pulmonary artery (arrow). (e)

Iodine density map demonstrated a wedge-shaped area of decreased perfusion (iodine density; 0.08 mg/ml; blue arrow) compared to the adjacent lung parenchyma (iodine density; 1.27 mg/ml; white arrow) indicating a sub-segmental pulmonary embolism with perfusion deficit. (f) The Zeff map demonstrated the wedge-shaped area with decreased perfusion color-coded in light blue, yellow, and red (arrow) (Demirler Simsir et al. 2020)

the electron or physical density via a calibration curve, in the case of photon therapy or to the proton stopping power, in the case of proton therapy.

Dual-layer CT allows a direct calculation of the electron density on a pixel-by-pixel basis. This approach can potentially enhance the workflow of radiation therapy planning by eliminating the need for a calibration curve mapping for photon therapy and improve the range accuracy for proton therapy.

The accuracy of the electron density was assessed recently in phantoms studies (Hua et al. 2018; Rassouli et al. 2017). Hua et al. concluded that the electron density accuracy is of the order of $\pm 1\%$ for both soft tissue and bone-equivalent materials and did not appear to be sensitive to different scans and reconstruction parameters. Ohira et al. (2019) found that percentage error of the electron density for each reference material varied from -2.0% to 1.2% and therefore the use of dual-layer spectral CT can enhance radiotherapy treatment planning. In another study, it was demonstrated that in homogeneous and heterogeneous phantoms, the use of electron density and Z effective can improve the accuracy of the stopping power ratio (SPR) predictions for particle therapy resulting in remaining discrepancies in the order of 1% . This can minimize the beam range uncertainty and allow for reduced safety margins in the patient (Faller et al. 2020).

Recently, it was demonstrated on few case reports that ED imaging improves GGO visualization compared with conventional CT. It was suggested that ED imaging may improve the detection of early-stage COVID-19, a stage for which conventional CT has shown limited sensitivity for detection (Daoud et al. 2020).

Compliance with Ethical Standards

Disclosure of Interests All authors are Philips employees.

Ethical Approval This article does not contain any studies with human participants performed by any of the authors.

Ethical Approval This article does not contain any studies with animals performed by any of the authors.

References

- Abdullayev N et al (2019) Improvements of diagnostic accuracy and visualization of vertebral metastasis using multi-level virtual non-calcium reconstructions from dual-layer spectral detector computed tomography. *Eur Radiol* 29(11):5941–5949
- Altman A, Shapiro O, Levene S, et al. (2006) Double decker detector for spectral CT. US States Patent US 7,968,853
- Altman A, Goshen L, Shechter G, Brown K, Yagil Y, Katchalski T, Carmi R, Proksa R, Thran A, Brendel B, Daerr H, Romman Z (2015) From a dual-energy spectral detector to photon-counting, and the benefit of multi energy-bins detectors. CERN SpecsXray Workshop April 2015
- Alvarez RE (2011) Estimator for photon counting energy selective x-ray imaging with multi-bin pulse height analysis. *Med Phys* 38(5):2324–2334
- Alvarez RE, Macovski A (1976) Energy-selective reconstruction in X-ray computerized tomography. *Phys Med Biol* 21(5):733–744
- Ananthakrishnan L et al (2017) Spectral detector CT-derived virtual noncontrast images: comparison of attenuation values with unenhanced CT. *Abdom Radiol* 42(3):702–709
- Borggreffe J et al (2019) Accuracy of iodine density thresholds for the separation of vertebral bone metastases from healthy-appearing trabecular bone in spectral detector computed tomography. *Eur Radiol* 29(6):3253–3261
- Brooks RA, Di Chiro G (1978) Split detector computed tomography: a preliminary report. *Radiology* 126(1):255–257
- Brun Andersen M et al (2020) Impact of spectral body imaging in patients suspected for occult cancer: a prospective study of 503 patients. *Eur Radiol* 30(10):5539–5550
- Carmi R, Naveh G, Altman A (2005) Material separation with dual-layer CT. Presented at the IEEE-MIC Conference. Puerto Rico: Wyndham El Conquistador; 23–29 Oct 2005. First, and original presentation of the 2D scatter-plot based dual-energy material decomposition method in image plane. See also US PATENT: US7,778,380 B2, 2010, by the same authors
- Daoud B et al (2020) Could spectral CT have a potential benefit in coronavirus disease (COVID-19)? *Am J Roentgenol* 216(2):349–354
- Demirler S, Sinsir B, Danse E, Coche E (2020) Benefit of dual-layer spectral CT in emergency imaging of different organ systems. *Clin Radiol*
- Ehn S et al (2017) Assessment of quantification accuracy and image quality of a full-body dual-layer spectral CT system. *J Appl Clin Med Phys* 19(1):204–217
- Faller FK et al (2020) Pre-clinical evaluation of dual-layer spectral computed tomography-based stopping power prediction for particle therapy planning at the Heidelberg Ion Beam Therapy Center. *Phys Med Biol* 65(9):095007

- Fulton N et al (2017) Abdominal applications of a novel detector-based spectral CT. *Curr Probl Diagn Radiol* 47(2):110–118
- Große Hokamp N et al (2017a) Reduction of artifacts caused by orthopedic hardware in the spine in spectral detector CT examinations using virtual monoenergetic image reconstructions and metal-artifact-reduction algorithms. *Skeletal Radiol* 47(2):195–201
- Große Hokamp N et al (2017b) Assessment of arterially hyper-enhancing liver lesions using virtual monoenergetic images from spectral detector CT: phantom and patient experience. *Abdom Radiol* 43(8):2066–2074
- Große Hokamp N et al (2018) Artifact reduction from dental implants using virtual monoenergetic reconstructions from novel spectral detector CT. *Eur J Radiol* 104:136–142
- Große Hokamp N et al (2019) Stratification of pulmonary nodules using quantitative iodine maps from dual-energy computed tomography. *Am J Respir Crit Care Med* 199(2):e3–e4
- Hickethier T et al (2017) Fourth update on CT angiography of coronary stents: in vitro evaluation of 24 novel stent types. *Acta Radiol* 59(9):1060–1065
- Hickethier T et al (2020) Venous-phase chest CT with reduced contrast medium dose: Utilization of spectral low keV monoenergetic images improves image quality. *Eur J Radiol* 122:108756
- Hojjati M et al (2017) Quality of routine diagnostic abdominal images generated from a novel detector-based spectral CT scanner: a technical report on a phantom and clinical study. *Abdom Radiol* 42(11):2752–2759
- Hua C-H et al (2018) Accuracy of electron density, effective atomic number, and iodine concentration determination with a dual-layer dual-energy computed tomography system. *Med Phys* 45(6):2486–2497
- Jamali S et al (2019) Virtual unenhanced phase with spectral dual-energy CT: is it an alternative to conventional true unenhanced phase for abdominal tissues? *Diagn Interv Imaging* 100(9):503–511
- Kaltsz K et al (2017) Noise characteristics of virtual monoenergetic images from a novel detector based spectral CT scanner. *Eur J Radiol* 98:118–125
- Kikano EG et al (2020) Utility of iodine density perfusion maps from dual-energy spectral detector CT in evaluating cardiothoracic conditions: a primer for the radiologist. *Am J Roentgenol* 214(4):775–785
- Lennartz S et al (2018) Dual-layer detector CT of the head: initial experience in visualization of intracranial hemorrhage and hypodense brain lesions using virtual monoenergetic images. *Eur J Radiol* 108:177–183
- Lennartz S et al (2019) Diagnostic value of spectral reconstructions in detecting incidental skeletal muscle metastases in CT staging examinations. *Cancer Imaging* 19(1):50
- Liu J-J et al (2019) Improved visualization of gastric cancer and increased diagnostic performance in lesion depiction and depth identification using monoenergetic reconstructions from a novel dual-layer spectral detector CT. *Acad Radiol* 27(6):e140–e147
- Nadjiri J et al (2018) Accuracy of calcium scoring calculated from contrast-enhanced coronary computed tomography angiography using a dual-layer spectral CT: a comparison of calcium scoring from real and virtual non-contrast data. *PLoS One* 13(12):e0208588
- Nagayama Y et al (2017) Dual-layer DECT for multiphase hepatic CT with 50 percent iodine load: a matched-pair comparison with a 120 kVp protocol. *Eur Radiol* 28(4):1719–1730
- Neuhaus V et al (2017a) Improvement of image quality in unenhanced dual-layer CT of the head using virtual monoenergetic images compared with polyenergetic single-energy CT. *Invest Radiol* 52(8):470–476
- Neuhaus V et al (2017b) Metal artifact reduction by dual-layer computed tomography using virtual monoenergetic images. *Eur J Radiol* 93:143–148
- Neuhaus V et al (2017c) Improvement of image quality in unenhanced dual-layer CT of the head using virtual monoenergetic images compared with polyenergetic single-energy CT. *Invest Radiol* 52(8):470–476
- Neuhaus V et al (2018) Bone marrow edema in traumatic vertebral compression fractures: Diagnostic accuracy of dual-layer detector CT using calcium suppressed images. *Eur J Radiol* 105:216–220
- Oda S et al (2018) Low contrast material dose coronary computed tomographic angiography using a dual-layer spectral detector system in patients at risk for contrast induced nephropathy. *Br J Radiol* 92(1094):20180215
- Ohira S et al (2019) Estimation of electron density, effective atomic number and stopping power ratio using dual-layer computed tomography for radiotherapy treatment planning. *Phys Med* 56:34–40
- Rajiah P et al (2017a) Spectral detector CT for cardiovascular applications. *Diagn Interv Radiol* 23(3):187–193
- Rajiah P et al (2017b) Benefit and clinical significance of retrospectively obtained spectral data with a novel detector-based spectral computed tomography – initial experiences and results. *Clin Imaging* 49:65–72
- Rassouli N et al (2017) Detector-based spectral CT with a novel dual-layer technology: principles and applications. *Insights Imaging* 8(6):589–598
- Reimer RP et al (2019) Virtual monoenergetic images from spectral detector CT enable radiation dose reduction in unenhanced cranial CT. *AJNR Am J Neuroradiol* 40(10):1617–1623
- Sauter AP et al (2018) Dual-layer spectral computed tomography: virtual non-contrast in comparison to true non-contrast images. *Eur J Radiol* 104:108–114
- Sellerer T et al (2018) Dual-energy CT: a phantom comparison of different platforms for abdominal imaging. *Euro Radiology* 28(7):2745–2755. <https://doi.org/10.1007/s00330-017-5238-5>
- Tsang DS et al (2017) Quantifying potential reduction in contrast dose with monoenergetic images synthesized from dual-layer detector spectral CT. *Br J Radiol* 90(1078):20170290

- Van Hedent S et al (2018) Effect of virtual monoenergetic images from spectral detector computed tomography on coronary calcium blooming. *J Comput Assist Tomogr* 42(6):912–918
- Van Ommen F et al (2018) Image quality of conventional images of dual-layer SPECTRAL CT: a phantom study. *Med Phys* 45(7):3031–3042
- Wellenberg RHH et al (2017) Quantifying metal artefact reduction using virtual monochromatic dual-layer detector spectral CT imaging in unilateral and bilateral total hip prostheses. *Eur J Radiol* 88:61–70
- Yoon JH et al (2020) Double low-dose dual-energy liver CT in patients at high-risk of HCC. *Invest Radiol* 55(6):340–348
- Zhang X et al (2020) Evaluating the temporomandibular joint disc using calcium-suppressed technique in dual-layer detector computed tomography. *J Int Med Res* 48(3):300060519891332



Dual-Energy: The GE Approach

Scott Slavic and Mats Danielsson

Contents

1	Background	46
2	Balanced System Design	46
3	Image Reconstruction	48
4	Projection-Based Material Decomposition	48
5	Image Generation and Post-processing	49
5.1	Image Types	49
5.2	Noise Suppression	52
6	Workflow and Clinical Processing	53
7	Spectral Applications and Future	55
8	Photon Counting: The Next Leap in Spectral Imaging	56
8.1	Photon Counting with Deep Silicon	57
8.2	X-Ray Detection Efficiency for Deep Silicon	58
8.3	X-Ray Scatter in the Detector	58
8.4	Count Rate Performance	59
8.5	Deep Silicon Summary	61
	References	61

Abstract

This chapter provides an overview of the GE Dual-Energy Approach to Spectral Imaging known as Gemstone Spectral Imaging (GSI). Since 2010 when GE launched GSI on Discovery™ CT750 HD, GE has provided continued improvements to the technology, capabilities, and workflow, as well as spectral clinical tools to support advances in diagnosis and solutions across the Discovery™ GSI,

S. Slavic (✉)
GE Healthcare, Waukesha, WI, USA
e-mail: Scott.Slavic@ge.com

M. Danielsson
Department of Physics, KTH Royal Institute of
Technology, AlbaNova University Center,
Stockholm, Sweden
e-mail: matsdan@kth.se

Revolution™ CT Frontier, and Revolution™ CT/Revolution™ Apex platforms.

The GSI acquisition method enables precise temporal registration of the dual-energy sinograms, projection-based material decomposition, and delivers a full 50 cm material decomposition scan field of view.

The technologies employed to achieve the dual-energy acquisitions are detailed in the discussion of balanced system design below. Calibration of fast kVp switching data, material decomposition, and visualization of the resulting images are covered in the image reconstruction, projection-based material decomposition, and post-processing/clinical applications sections. The chapter closes with GSI implementation in the context of workflow, imaging improvements, solutions to challenging diagnostic applications, and the path to the future of photon counting.

Academic research and clinical exploration of GSI have grown rapidly and resulted in rich scientific publications and extensive clinical adoption. GSI has shown benefits in:

- Better lesion characterization by providing information about the chemical composition and material characteristics
- Improving lesion detection with enhanced contrast-to-noise ratio
- Reducing beam hardening and metal artifacts
- Optimizing iodine load in contrast enhanced CT studies

1 Background

Dual-energy in CT has grown since vendors introduced it in the early 2010s. Relative to conventional single kVp imaging, dual-energy imaging has the capability to enhance material differentiation and reduce beam hardening artifacts. Fast kVp switching, where the kVp alternates between low and high kVp for every view has several benefits including fine temporal view registration (high temporal consistency between high and low energy views), helical and axial

acquisitions, and full 50 cm field of view. It also presents some implementation challenges.

A balanced system design must enable rapid kVp rise and fall¹ while achieving sufficient energy separation and angular view sampling within the constraints of medical diagnostic rotation speeds. Detector primary decay and afterglow performance are critical to avoiding spectral blurring between views. Concurrently, there needs to be a strategy for dose efficiency through balancing the flux between the two spectrums and noise reduction processing, and advanced reconstruction techniques to ensure image quality across resolution, spectral performance, noise, texture, and other image quality metrics.

Gemstone spectral imaging (GSI) is based on projection-based material decomposition. The mixed kVp sinogram is transformed into view-aligned low and high kVp sinograms. Material basis decomposition is performed on the paired kVp measurements accounting for the tube spectrum, bowtie filter, and beam hardening properties of the basis materials. The noise correlation of the resulting material density images is well understood and employed in noise reduction processing (Alvarez and Seppi 1979) and advanced deep learning techniques.

While the technology to enable dual-energy is important, image quality, clinical workflow, and clinical applications to provide the right images and clinical answers are equally critical to ensure adoption and clinical acceptance.

Future research and development into spectral imaging continues to expand and new technologies are in development in the dual-energy space and photon counting space (Chandra and Langan 2011).

2 Balanced System Design

The fundamental principle behind fast kVp switching is the acquisition of two different

¹Since the kVp rise and fall are incorporated into the view measurements, a fast switching generator is required, and any remaining low level nonidealities are accounted for in the spectral calibration of the data.

kVps, alternating on a view-by-view basis between low and high kVp in a single rotation. This enables precise temporal registration of views, thereby freezing motion as the alternating spectrums penetrate the patient. This significantly reduces image artifact. For decades, the barrier preventing successful clinical introduction has been the limitations in the acquisition and detection systems.

The advancements in system components comprising GE scanners make GSI possible. Both high and low energy data sets are acquired simultaneously for axial and helical acquisitions at the full 50 cm field of view.

The generator and tube are capable of reliably switching between 80 and 140 kVp settings within microseconds to achieve 0.25 ms cycle time (Fig. 1). This capability has been achieved by a patented high frequency generator and tube with novel generator control hardware and firmware, a low capacitance interface, and microsecond-level tube electrostatic focal spot size and position control.

The Gemstone detector is a key contributor to fast kVp switching acquisitions through its scintillator and data acquisition system (DAS). GE Healthcare's (GEHC) scintillator material, referred to as Gemstone, is a complex rare earth-based oxide, which has a chemically replicated garnet crystal structure. This lends itself to imaging that requires high light output, fast primary speed, very low afterglow,² and almost undetectable radiation damage.

Gemstone™ has a primary decay time of 30 ns, making it 100 times faster than GOS (Gd₂O₂S), while also having afterglow levels that are lower than 25% of GOS levels, making it ideal for fast sampling. The capabilities of the scintillator are matched with a fast-sampling DAS, enabling simultaneous acquisition of low and high kVp sinograms at customary rotation speeds.

²Afterglow refers to a secondary decay of light emitting from the scintillator for several milliseconds after the X-ray source is turned off. It carries a part of the signal from one view to the next during a scan, thereby smearing the information, and potentially causing unwanted spectral decomposition artifact.

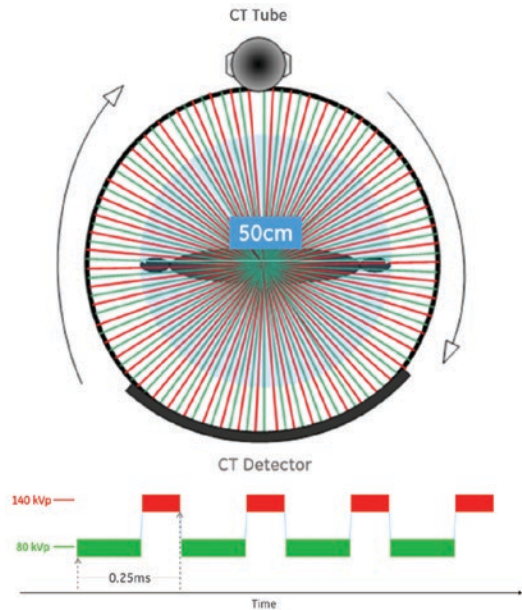


Fig. 1 Illustration of ultra-fast kV switching. The views objected at high and low kVp levels are indicated in red and green, respectively

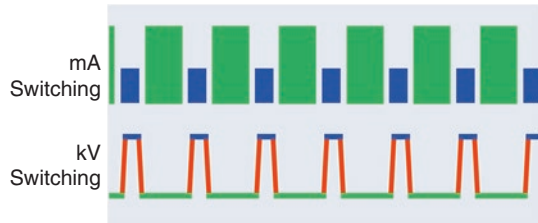


Fig. 2 Simultaneous kVp and mA switching. In this example, the mA value used for the high kVp views is lower than for the low kVp views

In order to combat the traditional flux issues that have challenged fast kVp switching, low kVp and high kVp acquisitions are flux balanced through advances in the DAS and generator via two methods: dynamically changing view integration times, and more recently, near instantaneous modulation of both kVp and mA (Fig. 2). Dynamic view integration times are accomplished by allocating additional time to the low kVp acquisition relative to the high kVp acquisition in order to reduce the possibility of photon starvation conditions. Coupled with the appropriate rotation speed, a more balanced flux condi-

tion between the two kVp scans is achieved and this serves to minimize patient dose. Near instantaneous kVp and mA switching is accomplished via advanced cathode technologies that allow for very fast control of both kVp and mA.

By means of flux balance methodologies and noise reduction techniques, GSI is designed to minimize additional dose relative to single-energy scans (Chandra and Langan 2011).

Studies performed between 2012 and 2014 demonstrated abdominal GSI doses of between 12.8 and 21.8 mGy. These values are below the ACR's 25 mGy reference dose level for a single-phase abdominal CT. The noise levels with GSI were comparable to those with SECT (Dubourg et al. 2014; Lin et al. 2012; Schuman et al. 2014).

3 Image Reconstruction

Following the acquisition, calibration corrections are applied to the data. Spectral calibration is complicated by the nonideal kVp rise and fall making it difficult to find a fixed kVp having precisely the same spectral response as an actual fast kVp switching energy spectrum. As a result, the spectrum is fitted to a linear combination of single kVp spectra. The overall spectrum (S_p) is decomposed into a superposition of several known kVp (p) spectra through the measurement of the detector response to the bowtie-attenuated beam:

$$S_p(E) = \sum_k^{N_k} \alpha_k S_k(E),$$

where $S_k(E)$ are the basis spectra of the fixed kVps, N_k is the total number of the basis spectra, and the α_k are the weights of the basis spectra.

The self-normalized detector response to this spectrum can be written as:

$$R(d) = \frac{\sum_k \alpha_k G_k(d)}{\sum_d \sum_k \alpha_k G_k(d)},$$

with

$$G_k(d) = \int_E S_k(E) E \left[1 - e^{-\mu_d(E)I_d} \right] e^{-\sum_b \mu_b(E,d)I_b(d)} dE$$

where $\mu_d(E)$ is the linear attenuation coefficient of the detectors, t_d is detector thickness, $\mu_b(E,d)$ and $I_b(d)$ are respectively the linear attenuation coefficient and the thickness of bowtie material b corresponding to detector channel d . $R(d)$ can be measured through a fast-switching air scan, and $G_k(d)$ can be calculated based on the system geometry. The problem now becomes one of solving for $R(d)$. This is an overdetermined problem and can be easily solved by least squares fitting. Once the calibration corrections have been applied to the low and high kVp data sets, they are aligned in projection space, transformed into a material basis pair projection (such as water and iodine), and then reconstructed. These material density images³ may be combined to create a monochromatic image at any specific keV level. A pictorial flow is presented in Fig. 3 (Chandra and Langan 2011).

4 Projection-Based Material Decomposition

Dual-energy material decomposition is based upon the mass attenuation coefficient across the medical diagnostic imaging spectrum being a function of two independent variables: attenuation due to the photoelectric effect and that due to Compton scatter (Alvarez and Macovski 1976). Through a mathematical change of basis one can express the energy-dependent attenuation observed in two kVp measurements in terms of two basis materials:

³Material density images represent the effective density for the material necessary to create the observed kVp measurements. For example, pure water appears as 1000 mg/mL in a water image, 20 mg/mL of dilute iodine is labeled as such an iodine image.

$$p_{\text{low}=-\ln\left(\frac{I}{I_o}\right)_{\text{low}}} = -\ln\left[\frac{\int S_{\text{low}}(E)\exp\{-[m_1\mu_1(E)+m_2\mu_2(E)]\}dE}{\int S_{\text{low}}(E)dE}\right]$$

$$p_{\text{high}=-\ln\left(\frac{I}{I_o}\right)_{\text{high}}} = -\ln\left[\frac{\int S_{\text{high}}(E)\exp\{-[m_1\mu_1(E)+m_2\mu_2(E)]\}dE}{\int S_{\text{high}}(E)dE}\right]$$

where I represents the attenuated X-ray spectrum, I_o represents the reference spectrum, $\mu_1(E)$ and $\mu_2(E)$ represent the mass attenuation coefficients of the basis materials, and m_1 and m_2 are their respective effective densities. $S_{\text{low}}(E)$ and $S_{\text{high}}(E)$ are defined by the source spectrum, source filtration, and detector performance. The solution for m_1 and m_2 accounts for spectral variation over the field of view due to the bowtie filter, and multi-material beam hardening. As a consequence, projection-based material decomposition provides the opportunity for more quantitative precision than may be achieved with single kVp imaging.

$$p = -\ln\left(\frac{I}{I_o}\right) = m_1\mu_1(E) + m_2\mu_2(E)$$

Given the material basis density images, one can compute attenuation data (p) that would be

measured with a monoenergetic X-ray source. For consistency with the Hounsfield unit, one can normalize the attenuation measurement with respect to water (Chandra and Langan 2011).

5 Image Generation and Post-processing

5.1 Image Types

5.1.1 Monochromatic

Monochromatic images, ranging from 40 to 140 keV, depict objects as if they were imaged with a theoretical monochromatic beam whose X-ray energy is measured in kiloelectron volts (keV) instead of peak kilovoltage (kVp).

Monochromatic images with lower energy levels generally improve the contrast-to-noise ratio (CNR) and can even achieve higher CNR

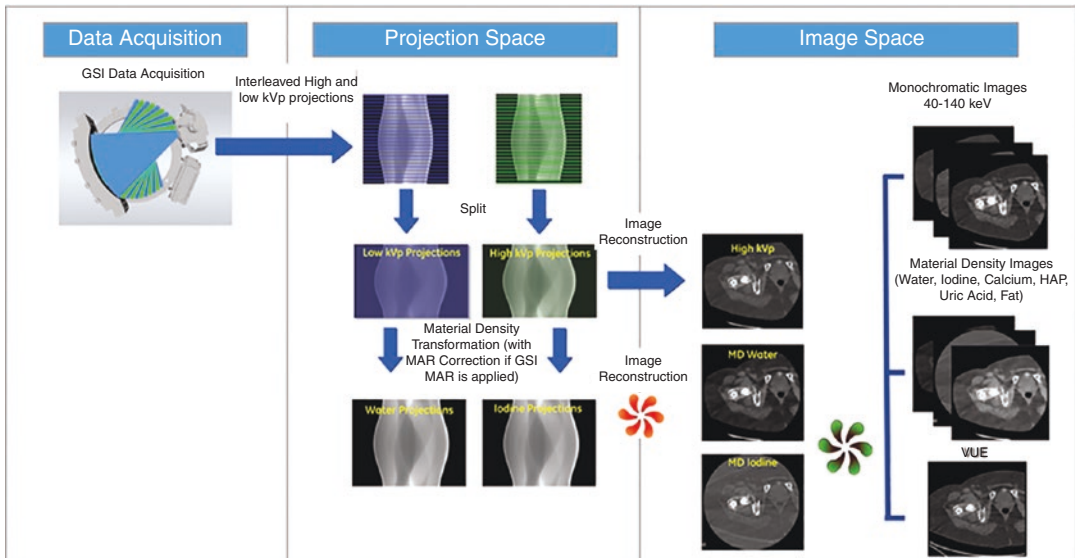


Fig. 3 Schematic illustration of the GSI Material Decomposition process

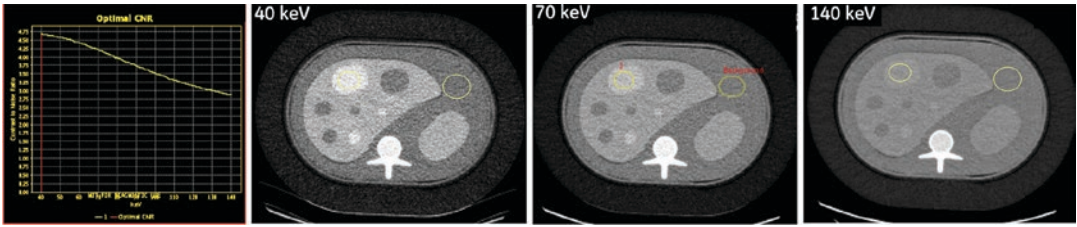


Fig. 4 A 30 cm × 40 cm QRM phantom, simulating a large patient, was scanned with 80 mm GSI helical at a CTDIvol of 24 mGy. The contrast-to-noise ratio (CNR) of

the liver ROI against the background was automatically computed using the GSI Viewer Optimal CNR tool

than single-energy imaging at the same dose. This is because monochromatic images at lower energy levels (40–70 keV) are closer to the K-edge of iodine (33.2 keV), at which iodine exhibits much higher attenuation as compared to conventional single-energy CT at 120 kVp. Figure 4 shows the increased CNR at lower keV. A big advantage over single-energy scanning is the availability of the range of keV images from a single exposure vs. single energy where the CNR is fixed based on the technique chosen.

Clinical studies confirm that low energy monochromatic images (40–70 keV) can depict more subtle contrast enhancement by improving the CNR between a lesion and background parenchyma¹³. Monochromatic images provide more reliable attenuation values than conventional polychromatic CT images.

5.1.2 Material Density

Material density (MD) images are generated natively or via post-processing from spectral data and provide qualitative and quantitative information regarding tissue composition and contrast media distribution (Patino et al. 2016)

MD images are generated as a material basis pair (e.g., water/iodine, uric acid/calcium). For example, when the water and iodine pair is generated, the iodine images visualize the density of the object with suppressed water information (written as “iodine (water)”) and water images visualize the density of the object with suppressed iodine information (written as “water (iodine)”). Note that the measured pixel intensity values in these

images are proportional to material density (concentration) and are expressed in mg/ml.

GSI can detect iodine contrast in concentrations as low as 0.5 mg/ml in density at a dose as low as 8 mGy.⁴ Iodine detectability is a performance metric that is key to the clinical value of dual-energy CT.

As Patino/Sahani et al. (Patino et al. 2016) summarized, material-specific images generated by spectral CT expand the current role of CT and overcome several limitations of single-energy CT.

The selection of the optimal material pairs for reconstruction is based on the specific clinical task.

The most common material pair used clinically is iodine and water, because the iodine (water) image can be used to assess iodine distribution, to increase tissue contrast, and to amplify subtle differences in attenuation between normal and abnormal tissues. This capability facilitates improved lesion detection and characterization, tumor viability quantification, and treatment response monitoring (Patino et al. 2016; Agrawal et al. 2014). Figure 5 illustrates how a color iodine overlay can aid in identifying cancer lesions.

In chest imaging, iodine (water) images that represent the iodine distribution in the lung parenchyma (an example of which appears in Fig. 6) can also help to identify pulmonary embolism-associated perfusion defects, espe-

⁴Detectability demonstrated on Revolution™ CT and Revolution™ Apex Products. Detection of 0.5 mg/mL at 8 mGy was demonstrated in head phantom testing

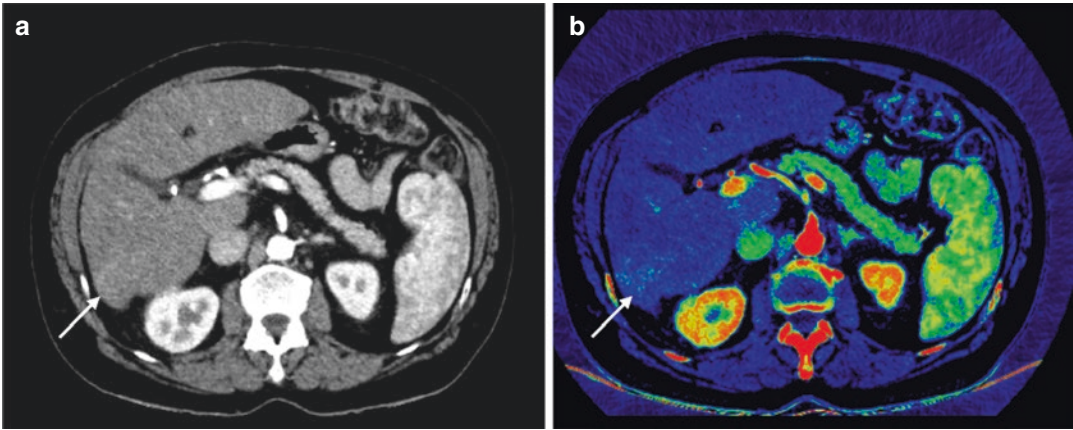


Fig. 5 A patient with recurrent liver carcinoma. **(b)** Iodine color overlay on 55 keV can better visualize recurrent cancer lesions (arrows) than **(a)** 55 keV image

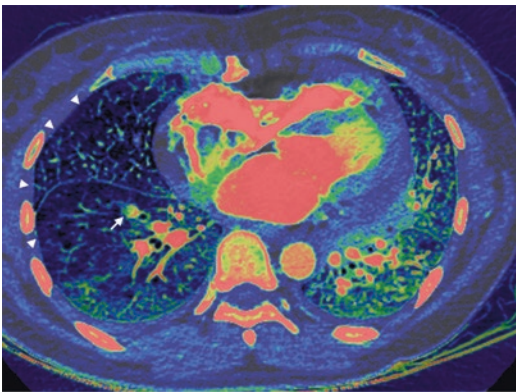


Fig. 6 A patient with pulmonary embolus. An iodine color overlay on this 70 keV image aids in the identification of embolus (arrow) and the area of lung perfusion abnormality (arrow heads)

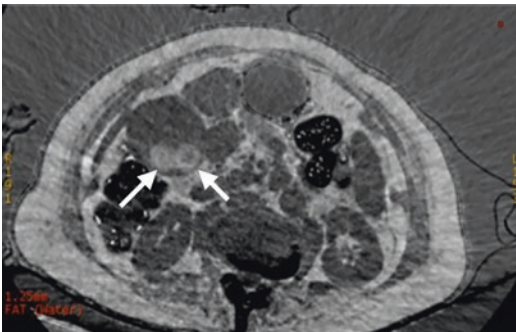


Fig. 7 A patient with gallbladder cholesterol stone. This fat (water) image characterizes the fat contents of the stone (arrows)

cially in patients with underlying perfusion abnormalities (Bauer et al. 2011; Pontana et al. 2008).

Fat (iodine) or fat (water) images can be used to characterize fat content in abdominal lesions, such as cholesterol stones in the gallbladder (Fig. 7) and fat-containing renal lesions. Morgan et al. demonstrated that fat (iodine) images permit differentiation between low- and high-fat-containing adrenal lesions with a high specificity of 94% (Morgan et al. 2013).

5.1.3 Material-Suppressed Iodine

Spectral information in GSI Images may be utilized to generate virtual unenhanced images (VUE) by subtracting iodine from the images. The VUE algorithm is based on multi-material decomposition (MMD), which replaces the volume fraction of contrast by the same volume fraction of blood, producing iodine-suppressed images. The VUE images provide attenuation information in Hounsfield units. Figure 8 shows an example of a non-contrast scan acquired at 120 kVp, and GSI contrast enhanced 70 keV and VUE images derived from a GSI contrast enhanced scan. The iodine filled vessels are removed in the VUE images.

VUE Imaging has shown promise in clinical use cases where a True unenhanced (TUE) image is typically used (Mileto et al. 2021).

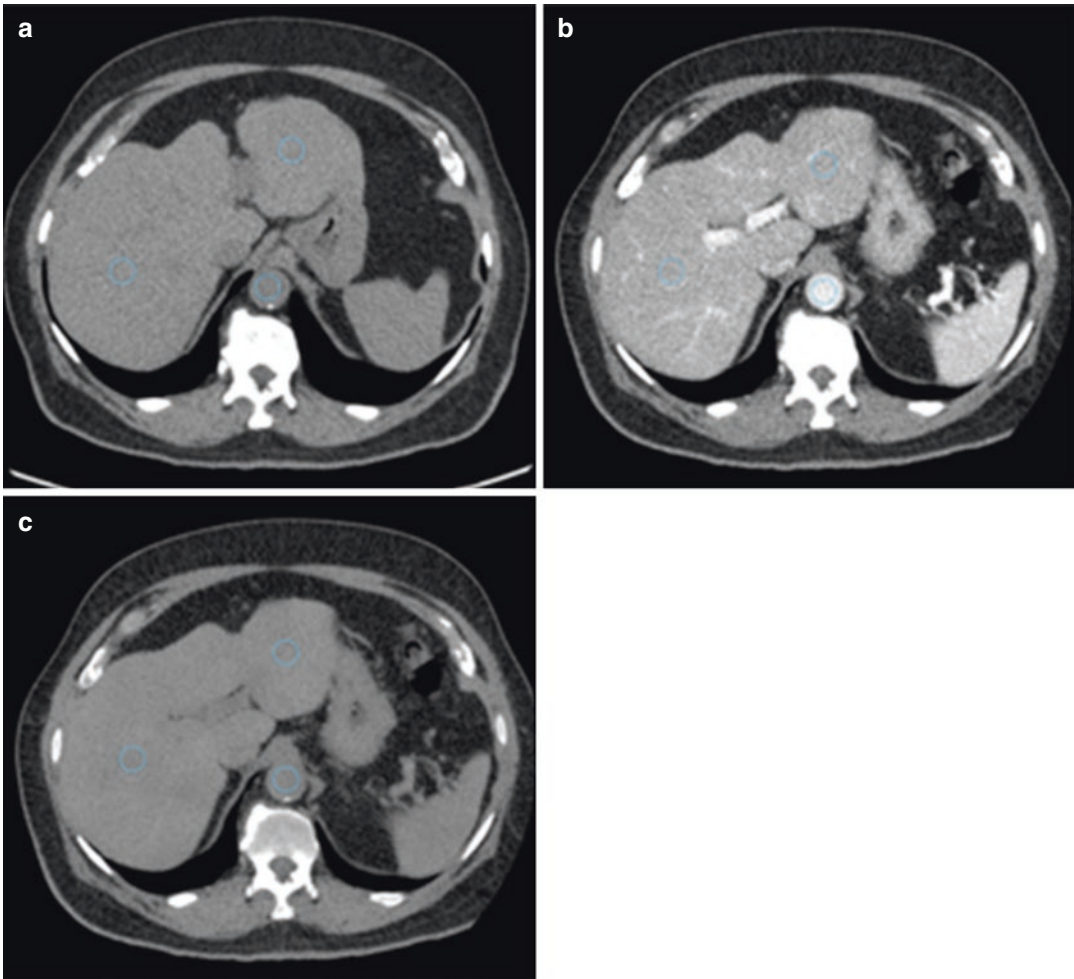


Fig. 8 Examples of (a) a non-contrast image acquired at 120 kVp, and (b) GSI contrast enhanced 70 keV image, (c) VUE image derived from GSI contrast enhanced scan

5.1.4 Metal Artifact Reduction

Patients imaged with CT routinely have metal implants which can cause artifacts due to photon starvation, beam hardening, and scatter. GSI Metal Artifact Reduction (GSI MAR) is a dual-energy metal artifact reduction algorithm designed to reveal anatomic details obscured by metal artifacts. GSI MAR can reduce metal artifacts using a three-stage correction to address all three factors. This approach generates metal-corrected images, while preserving spatial resolution and data integrity near the metal (Girijesh et al. 2014; Pal et al. 2013a, b; Hsieh et al. 2013). The output sinograms are used as input to the improved spectral imaging chain to generate the final GSI MAR images (Fig. 9). Metal artifact

reduction used in conjunction with higher keV settings (>100 keV) that also provide beam hardening reduction has allowed GSI and GSI MAR to realize enhanced metal artifact reduction that exceeds the performance of both of conventional MAR, and the metal artifact suppression achieved in high keV virtual monoenergetic images.

5.2 Noise Suppression

Noise suppression is very important due to flux challenges with the low kVp samples in any multi-energy technology. To address this issue, GE has used two methodologies to date in GSI

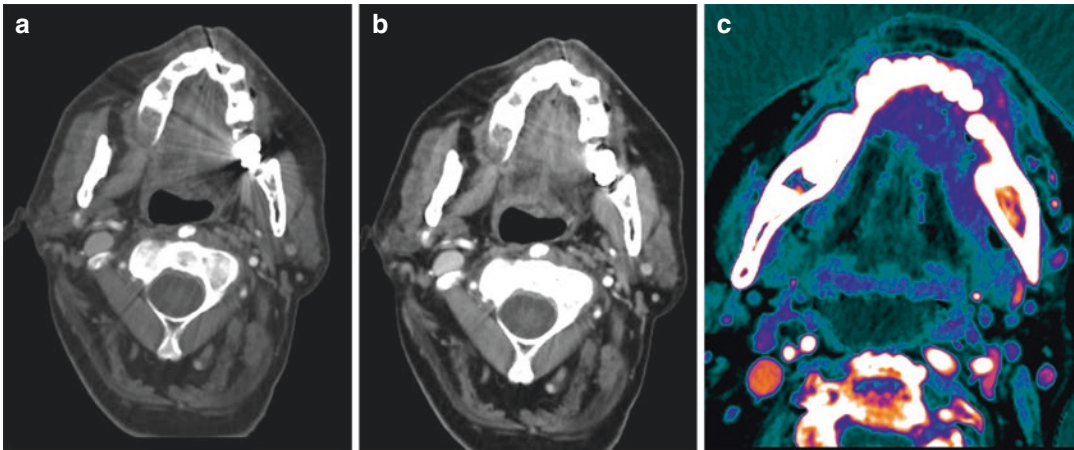


Fig. 9 A patient with metal denture and mouth floor carcinoma. **(a)** 60 keV image shows the artifacts caused by the metal denture. **(b)** 60 keV with GSI MAR and **(c)**

iodine color overlay with GSI MAR can reduce metal artifacts and reveal enhanced mouth floor carcinoma

imaging. Noise suppression in GSI by virtue of the projection-based material decomposition is applied in the material density space in order to enhance image quality without shifting mean values. This allows for noise suppression techniques to propagate to all image types: Virtual Monochromatic, Material Density, Metal Artifact-Reduced Images, and Post-Processed images such as Virtual Unenhanced images.

5.2.1 Iterative Reconstruction

The initial noise suppression method deployed with GSI leverages the statistical iterative reconstruction approach taken by ASIR⁵ (Fan et al. 2010) while simultaneously leveraging well-known noise correlation properties of the projection space material decomposition process (Alvarez and Seppi 1979).

5.2.2 TrueFidelity™ GSI

Recent advancements in deep learning have led to the application of deep learning techniques to

increase the noise reduction capability while maintaining and improving other imaging metrics such as texture and resolution. TrueFidelity™ was designed to produce image quality performance not easily achievable by conventional analytical and iterative techniques. Rather than manually optimizing the reconstruction over many parameters to balance image noise, spatial resolution, overall texture, and other quality metrics across a multitude of clinical imaging scenarios, the deep learning approach uses a neural network to learn the desired characteristics of the reconstructed images.

While both noise reduction techniques represent clinically relevant and robust performance, TrueFidelity™ GSI represents a step change in overall image quality. Examples of noise suppression and the improvements made from iterative reconstruction and deep learning are presented in Figs. 10, 11, 12 and 13.

6 Workflow and Clinical Processing

GE's GSI Workflow has evolved with the approach to assist the technologist through the workflow to ensure dose and image quality are optimized, organize the output images based on

⁵ASIR focuses on the statistical modeling of the noise properties of the system in conjunction with the properties of the scanned object. As a result, it provides significant benefit for those examinations that may experience limitations due to noise in the reconstructed images. In the case of spectral imaging, this is applied to reduce the noise in the material density images to enhance image quality.

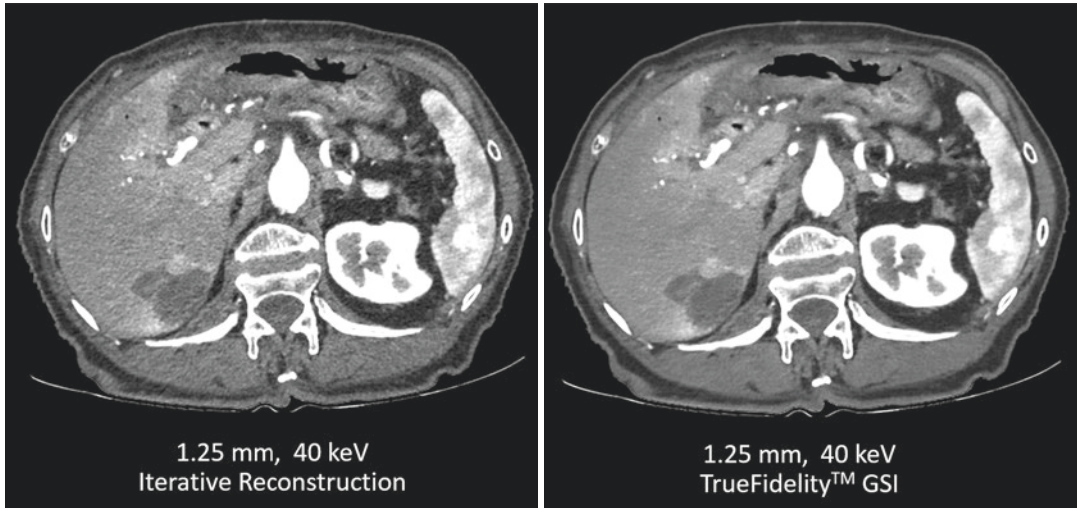


Fig. 10 Iterative reconstruction and deep learning noise suppression—monochromatic images. (Image courtesy of Houston Methodist)

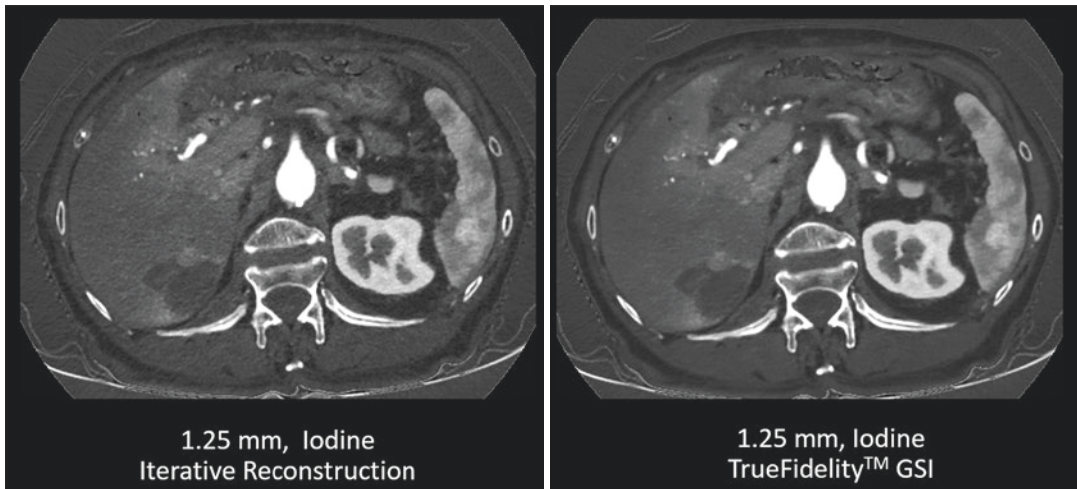


Fig. 11 Iterative reconstruction and deep learning noise suppression—material density images. (Image courtesy of Houston Methodist)

clinical function, and transfer the relevant images to PACS for the initial read. The images still contain spectral information for later analysis and post-processing as needed on advanced workstations (Slavic et al. 2017).

Key features that allow this workflow include:

- *GSI Profiles*: available at a higher level in protocol management to standardize, automate, and personalize GSI scan and recon parameters based on clinical needs.
- *GSI Assist*: personalizes GSI scan parameters to clinical indications and the anatomy of the patient.
- *Xtream Recon*: reconstructs GSI specific images natively on the console with real-time reconstruction speed, using parallel processing of the spectral information to greatly speed up the overall recon process.
- *Direct transfer to PACS*: offers the direct transfer of all natively reconstructed GSI images to PACS.

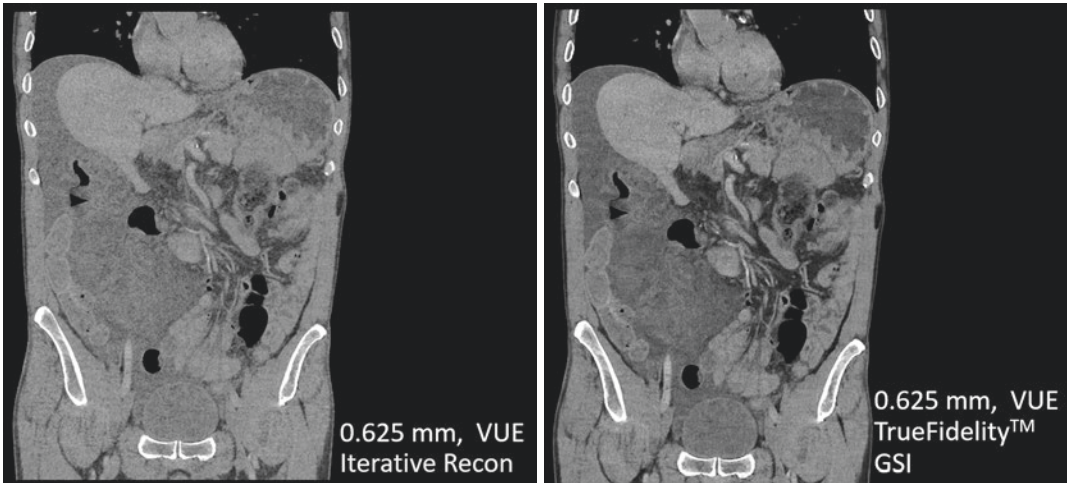


Fig. 12 Iterative reconstruction and deep learning noise suppression—virtual unenhanced images. (Image courtesy of UZ Brussels)

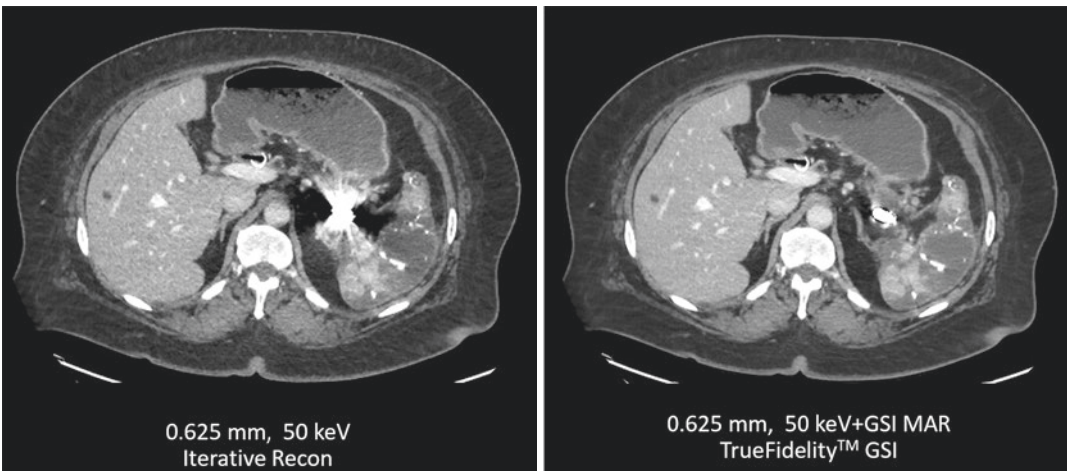


Fig. 13 Iterative reconstruction and deep learning noise suppression—monochromatic images with metal artifact reduction. (Image courtesy of Froedtert Hospital)

These workflow features allow the user to automate scanning, dose, and reconstructions to allow seamless usage in clinical workflow. The customization capability allows users to customize the strategy per their clinical needs (Gauntt 2019)

Figure 14 shows how GSI Profiles and GSI Assist automate and assist in the GSI workflow. Figure 15 represents the Xstream Recon flow parallelizing the reconstruction process and allowing the fast direct-to-PACS methodology.

7 Spectral Applications and Future

Workflow, PACS clinical tools continue to advance, facilitating spectral imaging solutions and leading to widespread adoption. With GE, this spans the Advantage Workstation (AW) and the Edison Platform to provide viewing, analysis, and analytics platforms to support clinical workflows.

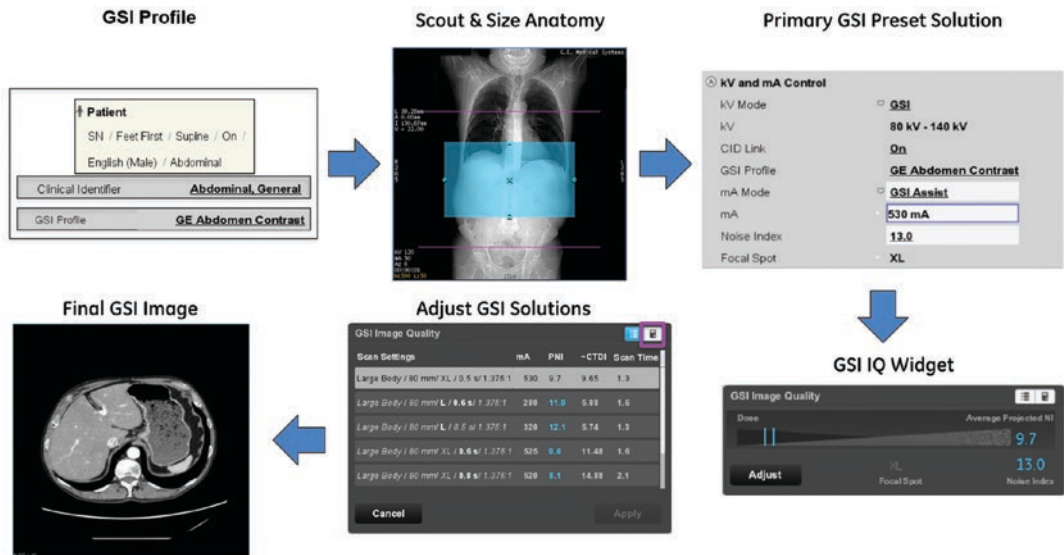


Fig. 14 GSI Assist/Profiles workflow

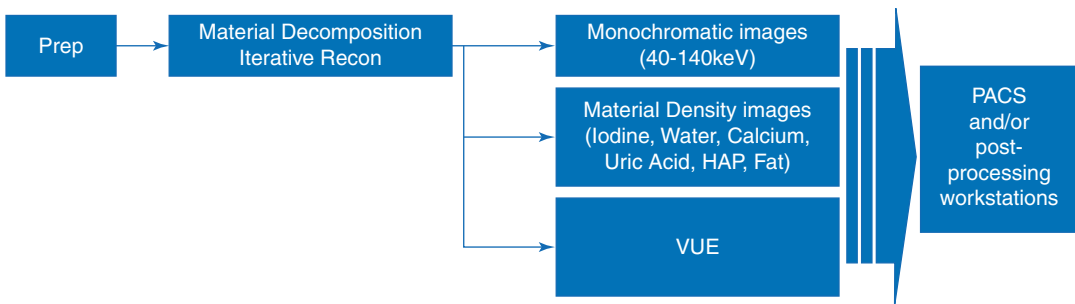


Fig. 15 Illustration of Xstream Recon technology and direct transfer to PACS. An intermediate stage is created after projection data preparation and material decomposi-

tion iterative recon process. From this juncture multiple GSI DICOM images can be natively reconstructed

With spectral imaging, in addition to the image types, viewers and applications are able to utilize spectral data for quantitative analysis spanning, material assessment, effective Z imaging and histograms, spectral response curves, contrast-to-noise (CNR) curves, overlays of spectral data, and post-processed imaging. This tool suite continues to develop, provide more automated solutions, and incorporate advanced imaging (AI) techniques.

Figures 16, 17 and 18 represent examples of clinical outputs from GE clinical tools. These advanced tools incorporate a combination of

spectral analysis, multi-material decomposition, advanced segmentation, and colorization of images to help automate clinical outputs and clinical findings.

8 Photon Counting: The Next Leap in Spectral Imaging

The next revolutionary step in spectral imaging is photon counting. GE is pursuing a novel approach in this area.

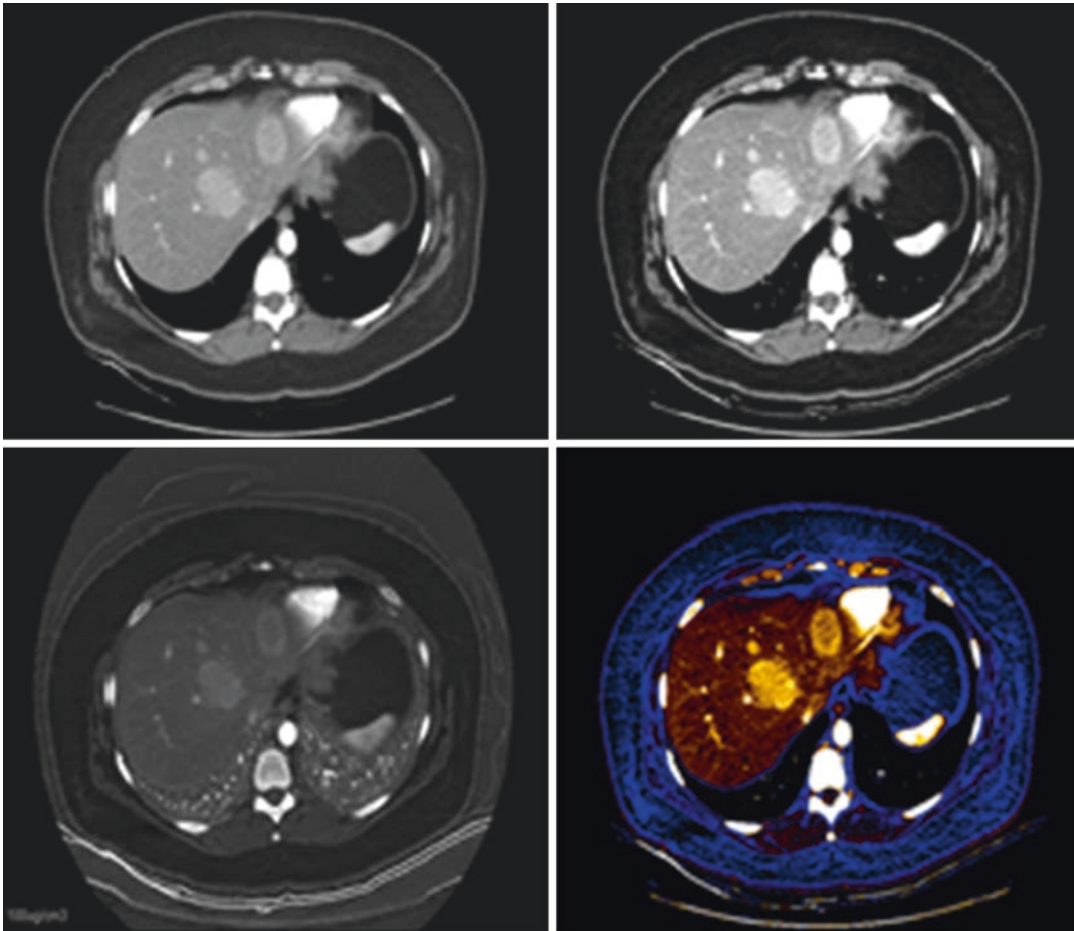


Fig. 16 Abdomen colorization of iodine in liver lesions

8.1 Photon Counting with Deep Silicon

Photon counting has emerged in recent years as a future alternative to dual-energy CT imaging. In photon counting, each X-ray is counted separately. The energy of each X-ray is measured using a number of programmable thresholds. In contrast to dual-energy CT, the number of energy levels can be selected in the design of the front-end electronics. For the deep silicon solution, we have eight threshold levels, meaning in principle that eight different materials can be separated in a so-called material basis decomposition. Typically, only three materials will be reconstructed, but having more thresholds increases dose efficiency and also means there is no need to change energy threshold levels for different

image cases. This increases usability. Deep silicon and other photon-counting solutions also offer significantly higher spatial resolution compared to state-of-the-art.

Silicon is the number one industry standard semiconductor substrate and very large volumes of high purity crystalline material are produced in a multitude of fabricators around the world. Due to the enormous investments in silicon production over many years, it is basically impossible for any other material to compete in terms of cost or quality. A proposed alternative to silicon is to use a cadmium-based detector, either cadmium telluride (CdTe) or cadmium zinc telluride (CZT). Those materials exist in prototype volumes, and an additional challenge is the environmental and health hazards associated with cadmium (World Health Organization 1992).

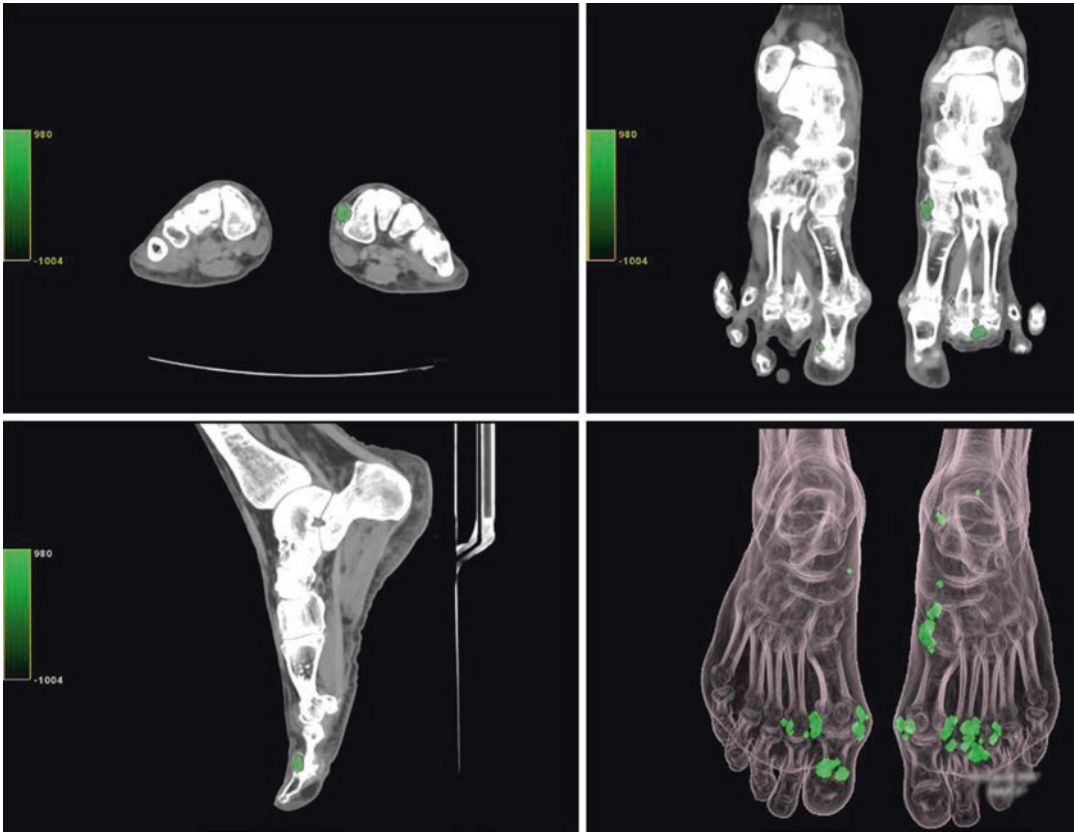


Fig. 17 Automated and advanced segmentation of gout crystals

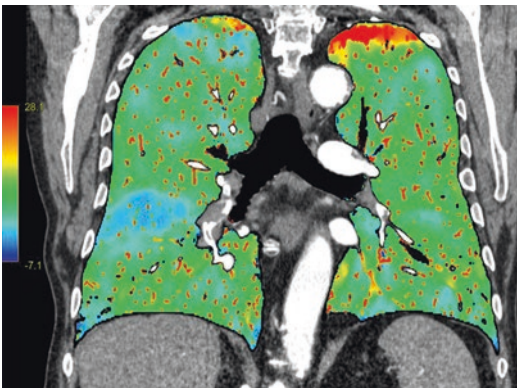


Fig. 18 Automated lung segmentation and colorization for pulmonary embolism studies

8.2 X-Ray Detection Efficiency for Deep Silicon

Since silicon has a low atomic number, a significant thickness is required to efficiently absorb incoming high energy X-rays in the diagnostic

range. Another factor that will impact the dose efficiency is the non-active “dead” layer at the surface, since there is never a perfect crystal structure all the way to the edge of the crystal and charge collection will be limited in this region. A low atomic number means that the sensitivity to any dead layer at the entrance surface of the detector is reduced. In Fig. 19, we show that the overall detection efficiency (DE) is very high.

8.3 X-Ray Scatter in the Detector

An advantage of silicon is that its low atomic number means there is a negligible probability for K-fluorescence, which deteriorates both energy resolution and spatial resolution, since energy deposition for one interaction is scattered over several pixels by the K-fluorescence photons. On the other hand, the cross section for Compton scatter is significant. All Compton

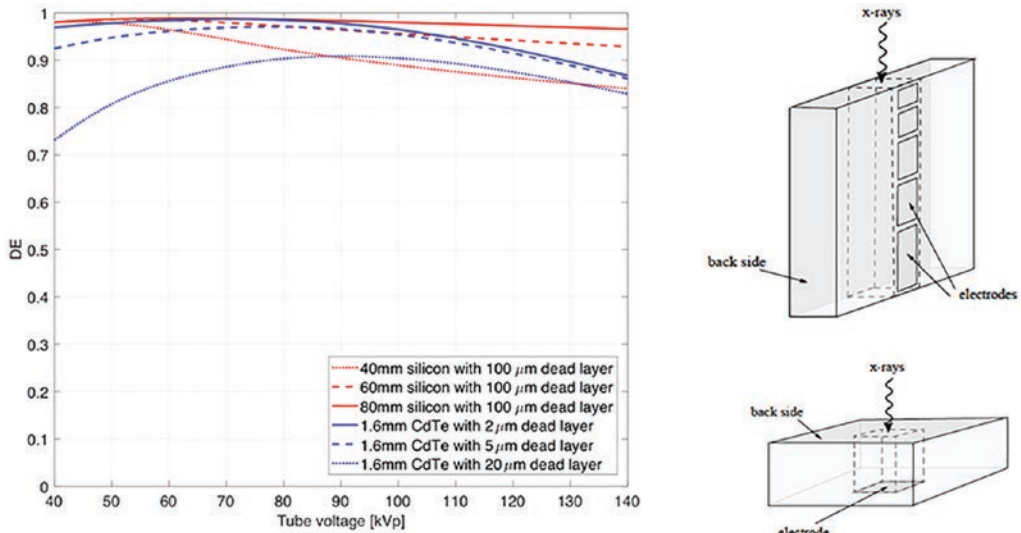


Fig. 19 X-ray detection efficiency for different detector geometries for photon-counting CT

scatter energy depositions above the minimum threshold will be counted and will contribute to the image. Energy deposited by Compton interactions will be recorded in the low energy bins, which allows these to be distinguished from the photoelectric interactions, which tend to be recorded in the higher energy bins. For X-rays with a primary Compton interaction, the energy resolution will be reduced since all energy is not deposited. For X-rays with a primary photo interaction, all the energy is deposited, and the energy resolution will be very high due to the high inherent energy resolution in silicon. Intersecting tungsten foils stop the scattered photons and work as a general anti-scatter collimator without loss of geometrical efficiency. In Fig. 20, we outline the distributions of different interactions in deep silicon for a 140 kVp spectrum, which is the worst-case diagnostic spectrum in that it produces the most Compton interactions. The point spread function in Fig. 21 confirms that Compton scattered pho-

tons are efficiently absorbed by the tungsten and have a negligible impact on spatial resolution.

8.4 Count Rate Performance

One significant challenge with photon-counting detectors has been the very high count rates, where the input flux can be up to 10^9 photons/mm²/s. In deep silicon, the depth of the silicon can be segmented into sub-voxels to decrease the count rate for each input channel. With a design using nine depth strata (with longer strata deeper in the detector), the count rate can be reduced by the same factor. The design shown in Fig. 22 outlines the depth strata together with the measured count rate response as a function of the X-ray¹. High count rate performance translates into reduced detective quantum efficiency (DQE) loss at high input flux and also enables a robust design, far from the point of detector saturation.

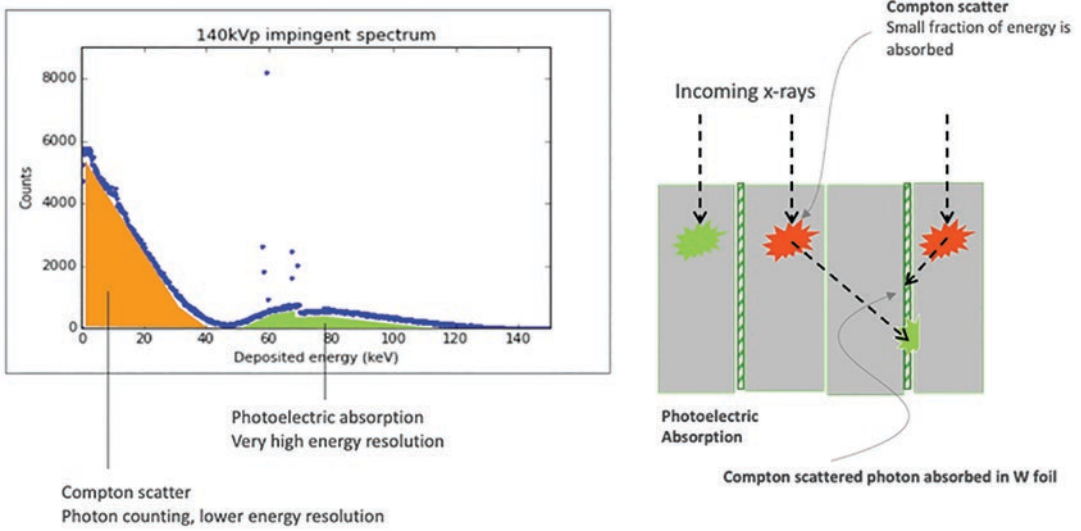


Fig. 20 Photoelectric and Compton interactions in deep silicon

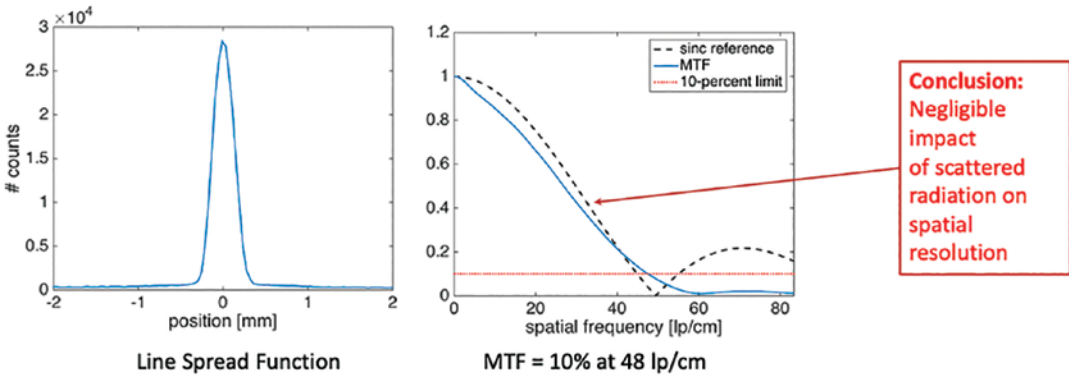


Fig. 21 Measured point spread function and MTF for deep silicon

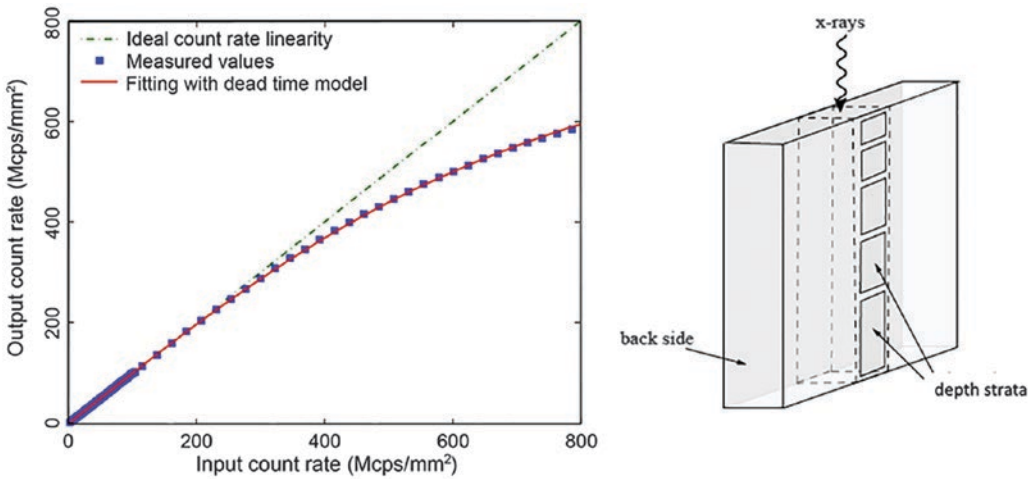


Fig. 22 Count Rate Performance and diagram of multi strata design

8.5 Deep Silicon Summary

In summary, the deep silicon approach to photon counting allows for the use of an industrial standard material with extremely high purity and crystal lattice quality. The depth of the silicon will result in high detection efficiency and enable depth strata for high and robust performance for high X-ray flux imaging cases. X-rays that are Compton scattered in the detector are absorbed by intersecting tungsten foils that also work as a collimator for object scatter. Charge collection in silicon is very fast, which translates into low diffusion of charges between pixels, resulting in high energy resolution. This in turn leads to high quantification accuracy and precision (for example, iodine concentration), and to dose-efficient three-material decomposition (Xu et al. 2013).

The deep silicon concept will deliver high spatial resolution combined with high energy resolution and spectral performance for tissue differentiation and quantification (Danielsson et al. 2021). One example is the evaluation of the degree of stenosis in blood vessels, when so-called “blooming artifacts” can be avoided and separation between calcium and iodine significantly improved. Another example is detection and follow-up of cancer.

Compliance with Ethical Standards

Disclosure of Interests Scott Slavic is an employee of GE Healthcare. Mats Danielsson is a consultant of GE Healthcare.

Ethical Approval In this review article, the authors obtained images from sites evaluating GE Healthcare devices with permission from the institutions. This article does not contain any studies with human participants performed by any of the authors.

References

- Agrawal MD et al (2014) Oncologic applications of dual-energy CT in the abdomen. *RadioGraphics* R34(3):589–612
- Alvarez RE, Macovski A (1976) Energy-selective reconstructions in X-ray computerized tomography. *Phys Med Biol* 21(5):733–744
- Alvarez RE, Seppi E (1979) A comparison of noise and dose in conventional and energy selective computed tomography. *IEEE Trans Nucl Sci NS-26(2):2853–2856*
- Bauer R, Frellesen C, Renker M et al (2011) Dual energy CT pulmonary blood volume assessment in acute pulmonary embolism: correlation with D-dimer level, right heart strain and clinical outcome. *Eur Radiol* 21(9):1914–1921
- Chae EJ, Seo JB, Jang YM et al (2010) Dual-energy CT for assessment of the severity of acute pulmonary embolism: pulmonary perfusion defect score compared with CT angiographic obstruction score and right ventricular/left ventricular diameter ratio. *AJR* 194:604–610
- Chandra N, Langan DA (2011) Gemstone detector: dual energy imaging via fast kVp switching. In: Johnson T, Fink C, Schönberg S, Reiser M (eds) *Dual energy CT in clinical practice*, Medical radiology. Springer, Berlin, Heidelberg. https://doi.org/10.1007/174_2010_35
- Danielsson M, Persson M, Sjölin M (2021) Photon-counting x-ray detectors for CT. *Phys Med Biol* 66(3):03TR01
- Dubourg B, Caudron J, Lestrat J et al (2014) Single-source dual-energy CT angiography with reduced iodine load in patients referred for aortoiliiofemoral evaluation before transcatheter aortic valve implantation: impact on image quality and radiation dose. *Eur Radiol* 24:2659–2668
- Fan J, Hsieh J, Sainath P, Crandall PS (2010) Head and Body CT DIw of dual energy x-ray CT with fast kVp switching. Paper 7622–69, SPIE Medical Imaging, San Diego
- Gauntt D (2019) A suggested method for setting up GSI profiles on GE Revolution CT Scanner. *Med Imaging*:169–179. <https://doi.org/10.1002/acm2.12754>
- Girijesh K, Pal D, Hsieh J (2014) Reduction of metal artifacts: beam hardening and photon starvation effects. *Proc. SPIE 9033*, Medical imaging 2014: physics of medical imaging, p 90332V
- Hsieh J et al (2013) Recent advances in CT image reconstruction. Technical report, General Electric Healthcare Company
- Lin X, Wu Z, Tao R et al (2012) Dual energy spectral CT imaging of insulinoma value in preoperative diagnosis compared with conventional multi-detector CT. *Eur J Radiol* 81:2487–2494
- Mileto A, Xiao J et al (2021) Virtual unenhanced dual-energy CT images obtained with a multimaterial decomposition algorithm: diagnostic value for renal mass and urinary stone evaluation. *Radiology* 298(3):611–619
- Morgan D et al (2013) Differentiation of high lipid content from low lipid content adrenal lesions using single-source rapid kilovolt (peak)-switching dual-energy multidetector CT. *J Comput Assist Tomogr* 37(6):937–943
- Pal D, Dong S, Genitsarios I, Hsieh J (2013a) Smart metal artifact reduction white paper. Technical report, General Electric Healthcare Company

- Pal D, Sen Sharma K, Hsieh J (2013b) Metal artifact correction algorithm for CT. In: Nuclear science symposium and medical imaging conference (NSS/MIC). IEEE, pp 1–4
- Patino M et al (2016) Material separation using dual-energy CT: current and emerging applications. *RadioGraphics* 36(4):1087–1105
- Pontana F, Faivre J, Remy-Jardin M et al (2008) Lung perfusion with dual-energy multidetector-row CT (MDCT): feasibility for the evaluation of acute pulmonary embolism in 117 consecutive patients. *Acad Radiol* 15(12):1494–1504
- Schuman W, Green D, Busey J et al (2014) Dual-energy liver CT: effect of monochromatic imaging on lesion detection, conspicuity, and contrast-to-noise ratio of hypervascular lesions on late arterial phase. *AJR Am J Roentgenol* 203:601–606
- Slavic S et al (2017) GSI Xtream on revolution CT. GE Healthcare, Waukesha
- World Health Organization (1992) Cadmium – environmental aspects. ECH 135
- Xu C et al (2013) Transactions on nuclear science. IEEE 60(1):437–445



Dual-Energy: The Canon Approach

Kirsten Boedeker, Jay Vaishnav, Ruoqiao Zhang,
Zhou Yu, and Satoru Nakanishi

Contents

1	Introduction	63
2	The Aquilion ONE Prism and Its Technology	64
2.1	Spectral Rapid kV Switching	64
2.2	Spectral Deep Learning Reconstruction	66
3	Spectral Performance	67
3.1	Spatial Resolution and CNR Performance	67
3.2	Wide Volume Detector	68
3.3	Virtual Monochromatic Images	68
3.4	Spectral Iodine Maps	69
3.5	Workflow	71
	References	72

1 Introduction

Canon Medical introduced the first multi-energy Computed Tomography (CT) system powered by deep learning artificial intelligence with the launch of Spectral Imaging on the Aquilion ONE Prism CT system in 2020. Spectral Imaging's multi-energy approach combines the benefits of Rapid

kV Switching technology with deep learning-based reconstruction to maximize the diagnostic value of every photon at each kV level, making routine and wide volume multi-energy imaging possible.

Spectral Imaging relies on the fundamental collection of data at two energies, a high and a low kV, that can be used to represent two basis materials, such as iodine and water, for material decomposition. The Aquilion ONE platform features a key design consideration for the optimal implementation of multi-energy CT: wide volume coverage. The Aquilion ONE Prism offers 16 cm of longitudinal coverage, allowing for acquisition of a whole organ, such as the head or heart, in a single rotation as well as a 50 cm mid-plane Field of View (FOV) (Fig. 1). Therefore, Spectral Imaging is designed to encompass both standard helical and wide volume coverage.

K. Boedeker · J. Vaishnav · S. Nakanishi
Canon Medical Systems Corporation,
Ottawara, Tochigi, Japan
e-mail: kboedeker@mru.medical.canon; jvaishnav@us.medical.canon; satoru.nakanishi@medical.canon

R. Zhang · Z. Yu (✉)
Canon Medical Research USA,
Vernon Hills, IL, USA
e-mail: rzhang@mru.medical.canon;
zyu@mru.medical.canon

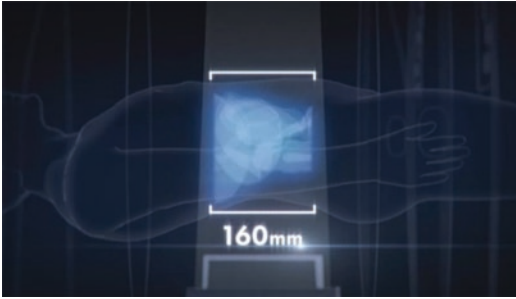


Fig. 1 The Aquilion ONE Prism offers 16 cm of longitudinal coverage, allowing for acquisition of a whole organ, such as the head or heart, in a single rotation as well as a 50 cm midplane Field of View (FOV)

Rapid kV Switching works by collecting interleaved projection views at each energy, generated by rapidly toggling between kV levels as the tube rotates around the patient. Rapid kV Switching minimizes spatial and temporal misalignment, permitting raw data-based material decomposition. Combining Rapid kV Switching with the image quality improvement capabilities of deep learning artificial intelligence permits the data to be acquired with tube current modulation, a key feature for optimizing radiation dose management. By infusing Rapid kV Switching with the power of deep learning, a full suite of clinical output—from crisp, clear iodine maps to low noise virtual monoenergetic images—can be generated for standard and wide volume CT.

2 The Aquilion ONE Prism and Its Technology

The Aquilion ONE wide volume CT system, first launched in 2007, offers 16 cm of longitudinal coverage that permits isotropic volumes of an entire organ to be acquired in a single rotation of the gantry. The Aquilion ONE Prism has 320 detector rows, each 0.5 mm thick. Canon Medical's Spectral CT is designed to combine the temporal resolution benefits of Rapid kV Switching with the ability of 16 cm coverage to reduce motion artifact throughout the volume. Performing Spectral CT on whole organs acquired in a single rotation provides increased diagnostic potential in applications such as spec-

tral cardiac CT. Spectral is also designed to be compatible with the entire 50 cm FOV in both standard helical modes and for wide volume modes. Sufficiently large field of view has become an important factor for CT systems, particularly when scanning large patients, as some anatomical structures may be missed with a limited FOV, such as the periphery of lung, liver, and bowel.

The Aquilion ONE Prism also utilizes Canon Medical's ^{SURE}Exposure Automatic Exposure Control (AEC) to vary the tube current applied during a scan, based on the size and composition of the individual patient being scanned. The purpose of AEC is to automatically optimize the CT scan exposure to reduce overall radiation dose while tailoring the dose distribution to yield consistent image quality. This technology is particularly relevant for radiosensitive subjects, such as chest and pediatric patients. Canon Medical's spectral CT is compatible with the routine use of AEC in both standard helical and wide volume scanning modes.

2.1 Spectral Rapid kV Switching

Every multi-energy CT system needs to generate two complete sinograms worth of raw data, one at each energy, to perform material decomposition, i.e., the process of separating the data into two basis materials. In order to acquire views at more than one energy, Rapid kV Switching operates by quickly and repeatedly switching the energy of the beam from high to low as the tube and detector rotate around the patient (Fig. 2). Rapid kV Switching minimizes the temporal delay between high and low energy measurements, resulting in images with minimal contrast delay and motion mismatch. In addition, Rapid kV Switching allows for the material decomposition process to take place in the raw data domain itself (Zou and Silver 2008), rather than post-reconstruction in the image domain. Raw data-based decomposition has been demonstrated to be less impacted by beam hardening and other biases that occur when material decomposition is performed in the image domain (Li et al. 2011).

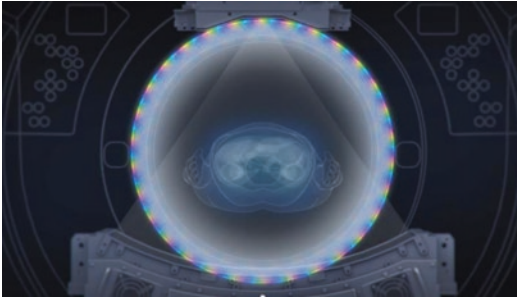


Fig. 2 Rapid kV Switching operates by quickly and repeatedly switching the energy of the beam from high to low as the tube and detector rotate around the patient

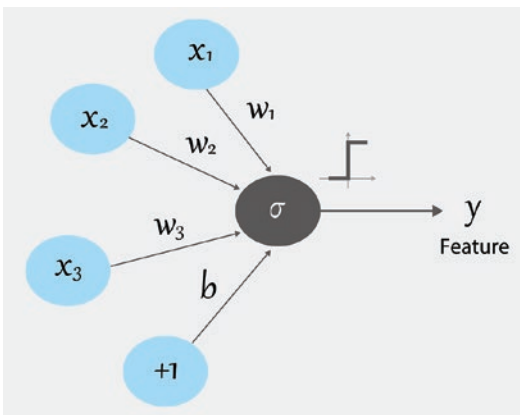


Fig. 3 A Deep Convolutional Neural Network (DCNN) comprised of layers of neurons is trained in the performance of a complex task. A neuron is a node where a mathematical operation takes places, the output of which is connected with other neurons, forming a network

Earlier implementations of kV switching using conventional reconstruction techniques are constrained by the need to acquire a large number of views at each energy to maintain spatial resolution. This requires highly specialized hardware that makes implementing dual-energy scanning across a variety of platforms difficult. In addition, the need to maintain energy separation between the high and low kV across such a large number of views requires conventional kV switching to operate at speeds that prohibit the use of AEC for radiation dose management. Furthermore, such approaches face significant challenges when the cone angle of the system is large, as required for wide volume coverage. Canon Medical’s deep

learning-based spectral reconstruction was developed to overcome these challenges associated with kV switching.

2.1.1 Deep Learning

Deep learning is a subfield of machine learning that takes advantage of multi-layered artificial neural network and represents the current state-of-the-art in Artificial Intelligence. Unlike conventional algorithms that are constrained by pre-programmed rules for performing a complex task, deep learning occurs when a neural network learns from its own intensive training process and develops its own logic structure. With deep learning, a Deep Convolutional Neural Network (DCNN) comprised of layers of neurons is trained in the performance of a complex task (Fig. 3). A neuron is a node where a mathematical operation takes places, the output of which is connected with other neurons, forming a network. The neural network derives its name from the neuron-synapse paradigm found in biology and mimics how humans draw conclusions, based on learning from examples. As the network “learns,” the mathematical parameters, known as weight and bias, applied by each neuron are adjusted until reaching a target level of performance. This ability to learn via a deep neural network gives deep learning algorithms the freedom to find the optimum way to perform the desired task.

The key to a successful DCNN lies in its training, the process by which the neural network learns how to successfully perform its function. The network must compare its output to a gold standard reference in order to gauge its performance and learn, i.e., adjust the weights and bias of its neurons. To accomplish this the DCNN uses a mathematical loss function to determine the amount of error between its output and the reference datasets.

Canon pioneered the successful application of deep learning in CT reconstruction with the introduction of the AiCE Deep Learning Reconstruction in 2018. The implementation of AiCE dramatically lowered image noise over conventional reconstruction as the AiCE neural network is able to distinguish and preserve signal

while reducing unwanted noise. On the Aquilion ONE Prism, AiCE is able to reduce noise by 32% compared to the standard hybrid iterative reconstruction approach.

2.2 Spectral Deep Learning Reconstruction

Spectral deep learning reconstruction is a deep learning-based reconstruction algorithm that uses projection views acquired with Rapid kV Switching to perform raw data-based material decomposition into basis pairs as well as reconstruct the resultant images. Spectral reconstruction allows for the highly precise spatial and temporal alignment of the high and low energy views associated with Rapid kV Switching, without sacrificing full anatomical coverage or automatic exposure control (Zhang et al. 2020).

A common challenge to all multi-energy CT technology is noise amplification of the material decomposition process. Computing the basis materials from the two kV measurements requires solving what is referred to in mathematics as an ill-posed inverse problem, meaning the solution and resulting image output is very sensitive to noise. Recently, deep learning technologies have been successfully applied in CT reconstruction, demonstrating great noise reduction capabilities and thus well-suited to advancing the state-of-the-art in multi-energy CT (Akagi et al. 2019).

Previous implementations of kV switching have relied on brute force hardware approaches to acquire enough views at each kV to both preserve image quality and effectively perform material decomposition. Rather than compromise wide volume coverage or AEC by greatly increasing view rates, spectral reconstruction takes advantage of the fact that much of the anatomical information contained in a high kV view and a low kV view is common to both views. The high spatial frequency information needed to maintain spatial resolution can be distilled from either energy; for high spatial resolution content the acquisition of a second independent sinogram is superfluous. The unique information provided by the high and low energy views is the degree to

which the X-ray beam is attenuated by the patient being scanned via Compton scattering and the photoelectric effect.

Spectral deep learning reconstruction takes advantage of the fact a deep learning neural network can be trained to convert the energy-dependent attenuation information associated with one kV into that of another kV. Therefore, spectral reconstruction works by generating Deep Learning Views (DLVs) created by transforming attenuation information in views acquired at one energy into that of the opposite energy. DLVs are generated by the trained neural network using measured data from both the opposite-energy views at a particular location and adjacent same-energy views. The DLVs then complement the measured views at each energy to generate a complete sinogram for each kV. Spectral deep learning reconstruction then performs material decomposition in the raw data domain and completes the reconstruction process, with a deep learning-based denoising step to create low noise spectral CT image data.

The neural network used in spectral deep learning reconstruction has a multi-scaled structure, similar to that of U-Net (Ronneberger et al. 2015). With multiple layers at different scales, the network creates a large receptive field and is capable of capturing a multitude spatial and spectral features in the data. As with all deep learning technologies, the key to successful reconstruction lies in the training of the neural network. Training of network parameters was conducted to minimize the mean absolute error loss function, as shown in (1), between training input and target data,

$$\hat{\Theta} = \underset{\Theta}{\operatorname{argmin}} \left\{ \frac{1}{N} \sum_n \|y_n^* - f(y_n | \Theta)\|_1 \right\}, \quad (1)$$

where Θ denotes the parameter set of the neural network, y_n and y_n^* represent the n th training input and target sample, respectively, from a total of N training sample pairs, and $f(y | \Theta)$ represents neural network processing using input data y with underlying parameter Θ .

Spectral deep learning reconstruction was trained on complete measured sinograms acquired

at each energy for a wide variety of patient and phantom attenuation levels with a broad range of exposure levels. The sinogram data used for training were processed with an array of sophisticated models, such as a statistical model for noise reduction. Other models utilized to ensure ultra-high quality training include spectral, anatomical, material, and advanced system models. Using these ultra-high quality sinograms, the neural network was trained to generate DLVs from measured opposite-energy views and adjacent same-energy views. Spectral deep learning reconstruction’s neural network has also been optimized for denoising in the image domain, using training data reconstructed with Canon’s AiCE reconstruction algorithm (Fig. 4). AiCE has been demonstrated to preserve high contrast spatial resolution while greatly reducing noise magnitude and producing a noise texture more similar to filtered backprojection than model-based iterative reconstruction approaches (Akagi et al. 2019). This denoising step plays a vital role in compen-

sating for non-equal flux at 80 kV vs 135 kV and improving the utility of low keV Virtual Monoenergetic Images (VMI). After the extensive training process, Spectral deep learning reconstruction was tested with independent validation datasets and hundreds of thousands of image results were reviewed extensively by engineers, medical physicists, and radiologists.

3 Spectral Performance

3.1 Spatial Resolution and CNR Performance

By using high frequency information from the views of both energies, spectral deep learning reconstruction is able to preserve the system’s high contrast spatial resolution, as shown in Fig. 5.

The denoising capabilities of spectral deep learning reconstruction boost the contrast-to-

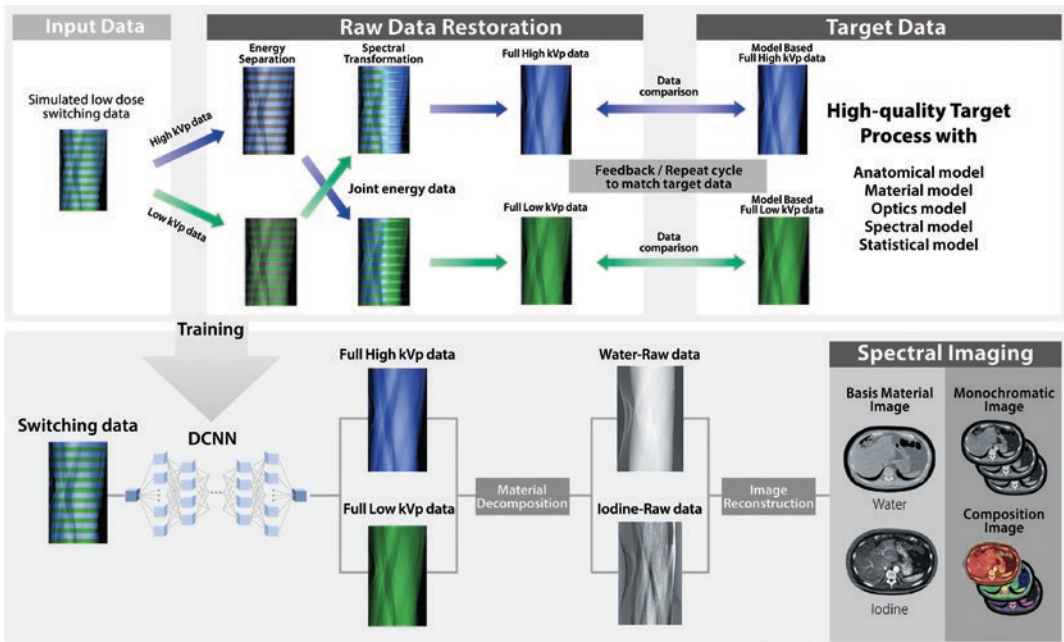


Fig. 4 This figure illustrates the process of spectral deep learning reconstruction algorithm (bottom) and the training of the neural networks (top). The kV switching data is input to the neural network. The neural network restores full sampled high kVp and low kVp views followed by

sinogram material decomposition. The material decomposition step produces basis material sinograms which can be reconstructed into material images and monochromatic images

noise (CNR) ratio of iodine. Below are CNR results for various densities in the 33 cm Gammex model 472, comparing Spectral CT across keV levels to single energy CT (Fig. 6).

3.2 Wide Volume Detector

Canon Medical’s Spectral CT can be used in combination with the full 16 cm wide volume detector coverage available on the Aquilion ONE

Prism, providing multi-energy imaging of entire organs in a single rotation. This capability is particularly useful in cardiac CT where, in the last 10 years, contrast-enhanced ECG gated CT has become important in imaging the coronary arteries. As an adjunct to coronary artery assessment, multi-energy CT is of increasing interest for evaluating myocardial blood supply (Vliegenthart et al. 2012).

Below is an example of the image quality and uniform temporal resolution that can be achieved for cardiac imaging when spectral CT is combined with the use of a wide volume detector (Fig. 7). Virtual monochromatic Images can be used to enhance contrast in the coronary arteries.

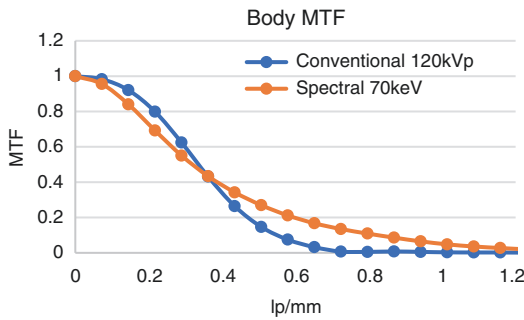


Fig. 5 This graph compares the MTF of a monochromatic image at 70 keV from a Spectral Body scan with a 120 kVp single energy Body scan

3.3 Virtual Monochromatic Images

Conventional single energy acquisitions are specified in terms of a peak kilovoltage, or kVp, in which the indicated value refers to the maximum energy contained in wide spectrum. The CT Number, or Hounsfield Unit (HU), for a given

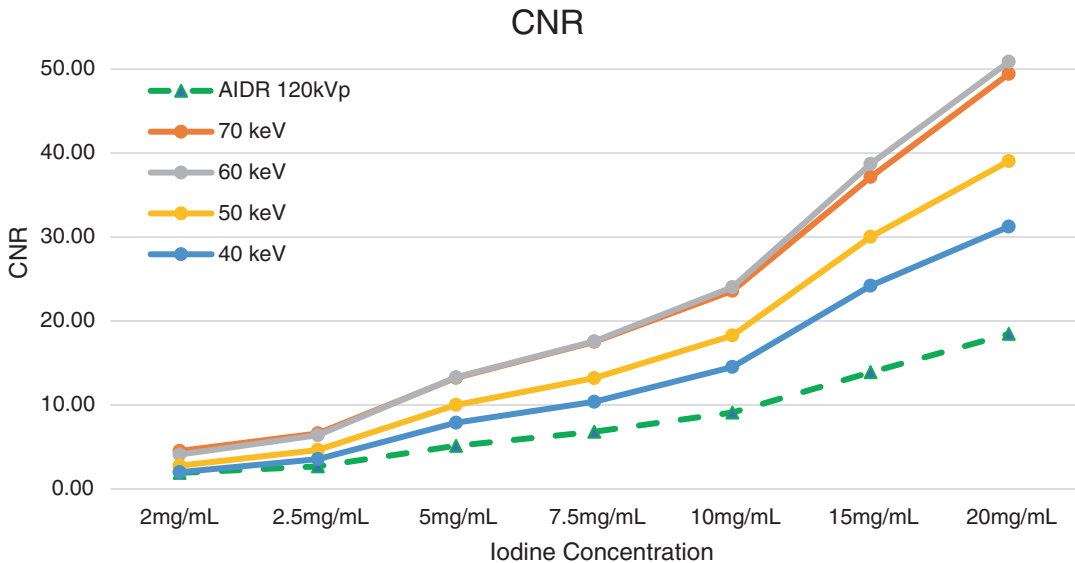


Fig. 6 This graph shows CNR results for various densities in the 33 cm Gammex model 472, comparing spectral CT across keV levels to single energy CT. The results

show spectral CT consistently achieve higher CNR compared to single energy CT

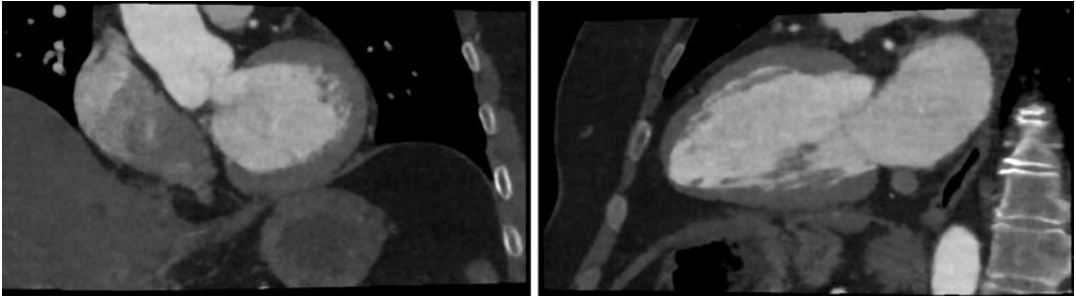


Fig. 7 Virtual monoenergetic (70 keV) image of a spectral cardiac scan. The left image shows the left ventricle in an approximate short axis view. The right image shows a two-chamber view. These are examples of images that can be obtained with a wide volume detector and are notable

for the uniform temporal resolution. 70 keV DL Spectral. Rapid-kV switching (135–80 kVp); AEC; Spectral Body; CTDIvol: 9.6 mGy; DLP 153.4; 2.1 mSV *k-factor 0.014. (Courtesy Prof. Roy and Prof. Ohana, University Hospital of Strasbourg)

pixel is largely determined by two energy-dependent physical interactions between photons and matter, viz. the photoelectric effect and Compton effect. The photoelectric effect is dominated at lower energies while the Compton effect is stronger at higher energies. In clinical practice, these two effects are discussed in terms of a representative material basis pair, such as iodine and water. Acquiring images with two energy levels allows for the individual impact each of basis material on attenuation to be determined. This material-specific information can then be combined to represent CT Numbers not just at the effective energy levels used for acquisition but also at other energies in a spectrum, from 35–200 keV on the Aquilion ONE Prism. Because images generated by recombining basis material information represent data associated with single point in the polyenergetic beam spectrum they are called Virtual Monoenergetic Images (VMIs).

While the ability to create VMIs at keV levels that yield improved contrast for various materials has existed for some time, the promise of multi-energy CT VMIs for improving patient care has been stymied by the concomitant generation of noise (Hanson et al. 2018; Yu et al. 2011). The CT Number of iodine increases over 15-fold in reducing from 120 keV to 40 keV, but as the share of photons comprising the recombined VMI image decreases the image noise increases and can be prohibitive to visualization of low contrast objects. Conventional denoising tech-

niques can diminish both high contrast spatial resolution and the noise texture. Spectral CT takes advantage of the powerful noise reduction capabilities of deep learning to improve the utility of VMIs of all keVs for patient care. Phantom experiments show noise can be reduced by over 50% at 70 keV relative to a conventional single energy scan while maintaining fine texture and that the CNR of iodine is increased by 50%, even at 40 keV (Fig. 8).

While contrast CT is helpful for diagnosing GI pathology, contrast-induced nephropathy is a concern for patients with compromised renal function. Low energy virtual monochromatic images can enhance the contrast, and Canon's spectral solution is designed to offer low noise and fine grain texture across the monochromatic spectrum (Fig. 9).

3.4 Spectral Iodine Maps

In addition to structural information, spectral CT provides functional information. Images in Fig. 10 show iodine maps on which a perfusion defect is apparent as a large wedge-shaped region of hypoperfusion. An iodine map can both serve as a check on the original image, and also provide supporting information. An ROI placed on the iodine map can quantify the iodine concentration, enabling a more detailed understanding of the local perfusion (Fig. 10).

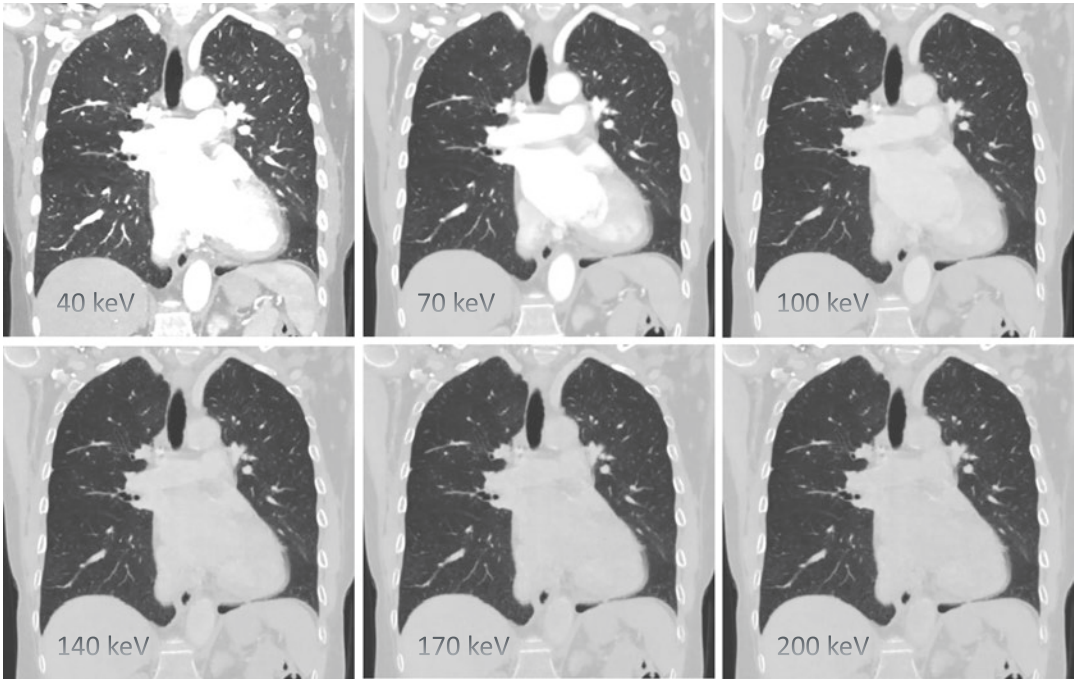


Fig. 8 Virtual monochromatic images of a pulmonary thromboembolism case. Canon's Spectral CT allows the generation of virtual monochromatic images for the 165 energy levels between 35 and 200 keV. Spectral CT allows easy tuning of the energy to suppress or enhance contrast,

or optimize the contrast difference between two adjacent structures. Rapid kV switching (135–80 kVp); 550; Spectral Body; CTDIvol: 13 mGy; DLP 548; 7.7 mSV *k-factor 0.014. (Courtesy Prof. Yokoyama and Associate Prof. Machida, Kyorin University, Japan)

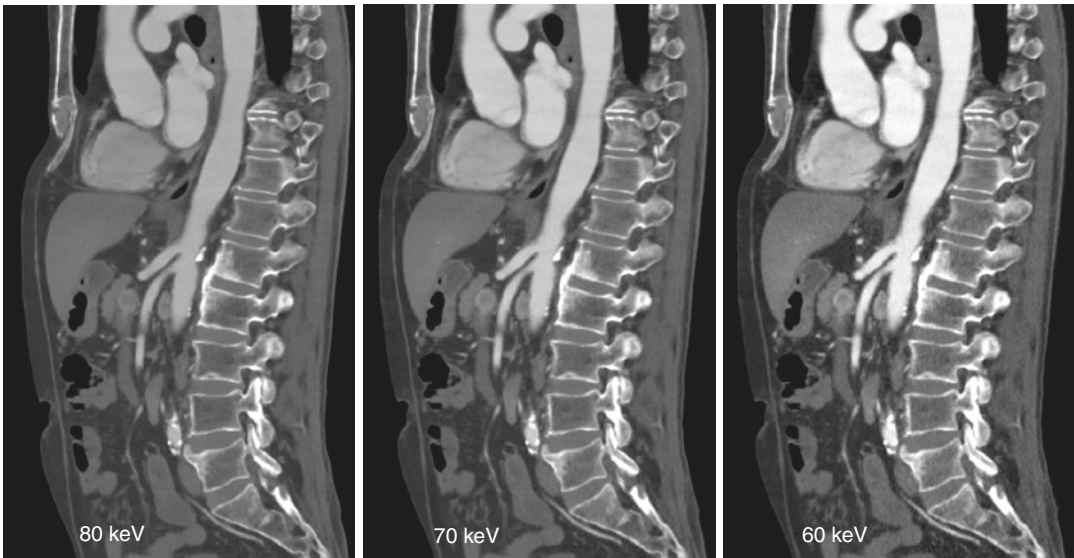


Fig. 9 This post-nephrectomy patient with low renal function was administered a reduced bolus of low density iodinated contrast. Spectral imaging was used to enhance

vasculature with monochromatic imaging. (Courtesy Prof. Roy and Prof. Ohana, University Hospital of Strasbourg)

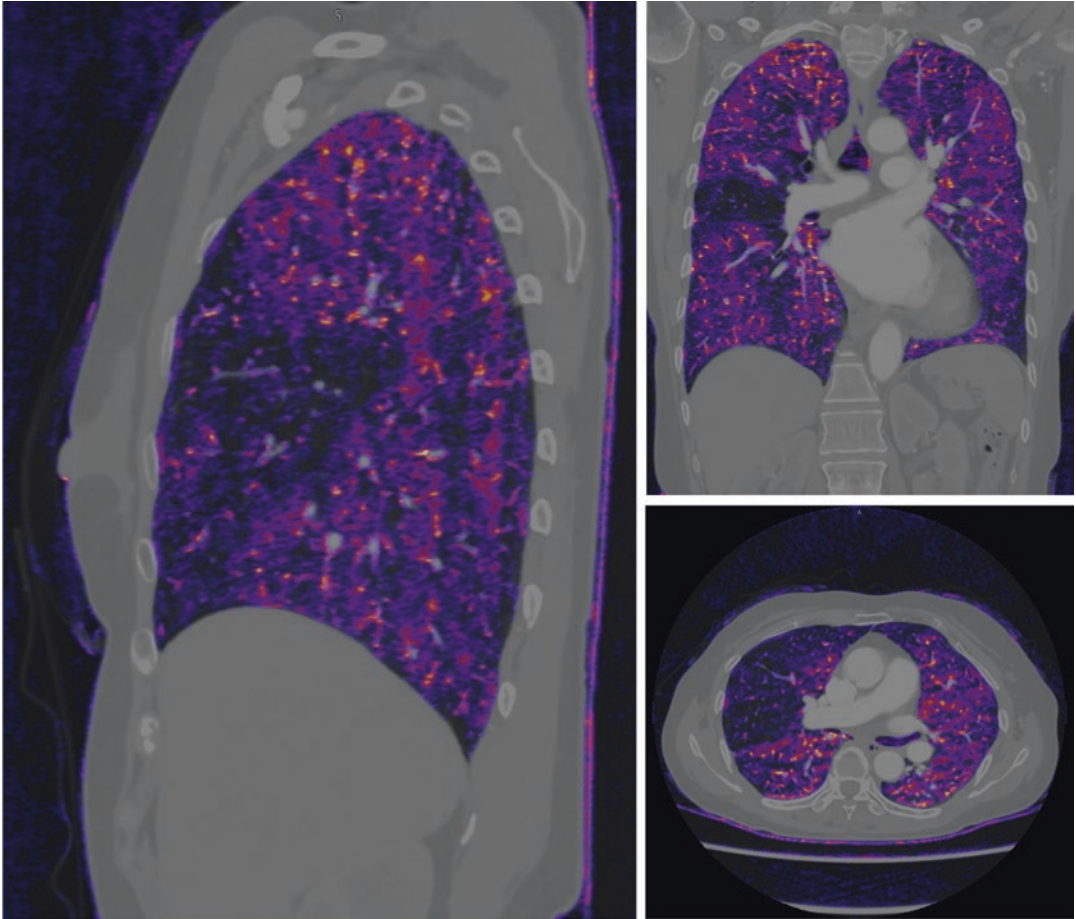


Fig. 10 Iodine maps of a pulmonary thromboembolism case. These images show iodine maps on which a perfusion defect is apparent as a large wedge-shaped region of hypoperfusion. Rapid-kV switching (135–80 kVp);

550 mA; Spectral Body; CTDIvol: 13 mGy; DLP 548; 7.7 mSV *k-factor 0.014. (Courtesy Prof. Yokoyama and Associate Prof. Machida, Kyorin University, Japan)

3.5 Workflow

Rapid kV Switching with spectral deep learning reconstruction produces a wealth of spectral CT data for clinicians to enhance diagnosis. Spectral CT offers automatically generated monoenergetic images, material-specific reconstructions, and iodine maps, requiring no additional effort or training for the technologist. Images are delivered directly to the reading station, making a rich array of information readily available to assist the radiologist with patient diagnosis.

Postprocessing software applications offer the ability to quantify images, as well as create multi-layered images (Fig. 11).

Compliance with Ethical Standards

Disclosure of Interests subsidiaries.

Ethical Approval This article does not contain any studies with human participants performed by any of the authors.

This article does not contain any studies with animals performed by any of the authors.



Fig. 11 An example of a spectral abdominal image, processed on Vitrea™. Upper left: Virtual monochromatic image. Upper center: Iodine blend image with one ROI selected. Upper right: Virtual non-contrast image. Bottom: spectral curve. An ROI is placed in the liver to measure the concentration of iodine in the iodine fusion image. The spectral curve offers an additional dimension of mate-

rial characterization; the blue curve shows increased enhancement at low energy as compared to the yellow curve. This information is helpful in understanding perfusion differences in different parts of the liver. (Courtesy Prof. Roy and Prof. Ohana, University Hospital of Strasbourg)

References

- Akagi M, Nakamura Y, Higaki T, Narita K, Honda Y, Zhou J, Yu Z, Akino N, Awai K (2019) Deep learning reconstruction improves image quality of abdominal ultra-high-resolution CT. *Eur Radiol* 29(11):6163–6171
- Hanson GJ, Michalak GJ, Childs R, McCollough B, Kurup AN, Hough DM, Frye JM, Fidler JL, Venkatesh SK, Leng S, Yu L, Halaweish AF, Harmen WS, McCollough CH, Fletcher JG (2018) Low kV versus dual-energy virtual monoenergetic CT imaging for proven liver lesions: what are the advantages and trade-offs in conspicuity and image quality? A pilot study. *Abdom Radiol* 43(6):1404–1412
- Li B, Yadava G, Hsieh J (2011) Quantification of head and body CT DIvol of dual-energy x-ray CT with fast-kVp switching. *Med Phys* 38(5):2595–2601
- Ronneberger O, Fischer P, Brox T (2015) U-net: convolutional networks for biomedical image segmentation. In International conference on medical image computing and computer-assisted intervention 2015 Oct 5 (pp 234–241)
- Vliegenthart R, Pelgrim GJ, Ebersberger U, Rowe GW, Oudkerk M, Schoepf UJ (2012) Dual-energy CT of the heart. *AJR Am J Roentgenol* 199(5 Suppl):S54–S63
- Yu L, Christner JA, Leng S, Wang J, Fletcher JG, McCollough CH (2011) Virtual monochromatic imaging in dual-source dual-energy CT: radiation dose and image quality. *Med Phys* 38(12):6371–6379
- Zhang R, Zhou J, Yu Z, Nemoto T (2020) A cascaded deep-learning reconstruction method for sparse-view kV-switching dual-energy CT. In *Medical imaging 2020: physics of medical imaging 2020 Mar 16* (vol. 11312, p 1131223)
- Zou Y, Silver MD (2008) Analysis of fast kV-switching in dual energy CT using a pre-reconstruction decomposition technique. In *Medical imaging 2008: physics of medical imaging 2008 Mar 18* (vol 6913, p 691313)



Basic Principles and Clinical Applications of Photon-Counting CT

Thomas Flohr, Martin Petersilka, Stefan Ulzheimer, Bernhard Schmidt, Klaus Erhard, Bernhard Brendel, Marjorie Villien, Philippe Coulon, Salim Si-Mohamed, and Sara Boccalini

Contents

1	Principles of Photon-Counting CT	73
1.1	Properties of Current Solid-State Scintillation Detectors	73
1.2	Properties of Photon-Counting Detectors	75
1.3	Challenges for Photon-Counting Detectors	77
2	Material Decomposition for Photon-Counting CT	79
3	Pre-clinical Evaluation of Photon-Counting CT	81
	References	90

T. Flohr (✉) · M. Petersilka · S. Ulzheimer · B. Schmidt
Siemens Healthcare GmbH, Computed Tomography, Forchheim, Germany
e-mail: flohr@siemens-healthineers.com

K. Erhard · B. Brendel
Philips GmbH Innovative Technologies, Research Laboratories Hamburg, Hamburg, Germany

M. Villien · P. Coulon
Philips Healthcare, Computed Tomography, PA, Best, The Netherlands

S. Si-Mohamed · S. Boccalini
Hospices Civils de Lyon, Department of Radiology, Lyon, France

1 Principles of Photon-Counting CT

This review article gives an overview of the basic principles of photon-counting detector CT, its spectral capabilities, and of the clinical experience gained so far in pre-clinical installations. Other reviews of photon-counting detector CT may be found in Taguchi and Iwanczyk (2013), Taguchi (2017), Willemink et al. (2018), Leng et al. (2019), and Si-Mohamed et al. (2017a).

1.1 Properties of Current Solid-State Scintillation Detectors

To understand the properties of photon-counting CT detectors it is helpful to recapitulate the prop-

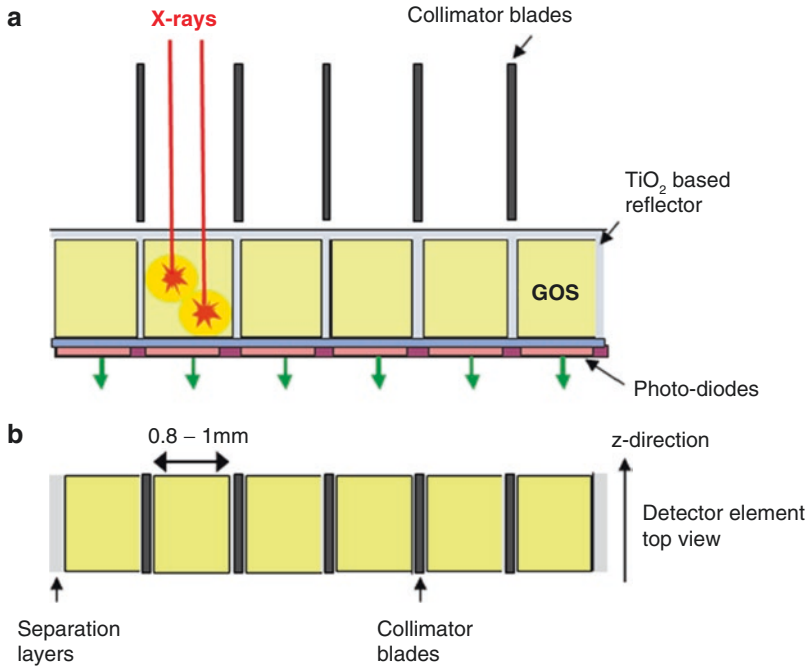


Fig. 1 Schematic drawing of an energy-integrating scintillator detector. (a) Side view, (b) top view. The z-direction is the patient's longitudinal direction. Detector cells made of a scintillator such as GOS absorb the X-rays (red arrows) and convert their energy into visible light (orange circles). This light is detected by photodiodes and

converted into an electrical current (two-step conversion). The individual detector cells are separated by optically intransparent layers (e.g., based on TiO_2) to prevent optical crosstalk. Collimator blades above the separation layers suppress scattered radiation

erties of solid-state scintillation detectors as they are used in all medical CT scanners today. Solid-state scintillation detectors consist of detector elements with a side length of 0.8–1 mm and a depth of 1.2–2 mm, made of a scintillator (e.g., gadolinium-oxysulfide GOS) with a photodiode attached to its backside, see Fig. 1. The X-rays are absorbed in the scintillator. They produce visible light which is registered by the photodiode and converted into an electrical current. Both the intensity of the scintillation light and the amplitude of the induced current pulse are proportional to the energy E of the absorbed X-ray photon. A CT scanner acquires 1000 and more projections (readings) during one rotation of the measurement system around the patient. For each of the detector elements, all current pulses registered during the time of one projection are integrated. X-rays with lower energy E , which carry most of the low-contrast-information, contribute less to the integrated detector signal than X-rays with

higher energy as consequence of the energy-proportional weighting. In more mathematical terms, the detector responsivity $D(E)$, a function describing the generated photocurrent per incident X-ray flux at energy E , is proportional to E , see Fig. 2. The contrast-to-noise ratio (CNR) in the CT images is negatively affected, in particular in CT scans with iodinated contrast agent—the X-ray absorption of iodine is highest at lower energies closely above its K-edge at 33 keV, see Fig. 2.

Furthermore, scintillation detectors cannot provide spectrally resolved signals—all medical CT scanners today capable of dual-energy imaging rely on special acquisition techniques to mitigate this limitation, be it dual source CT, fast kV switching, or use of dual layer detectors.

The low-level analog electric signal of the photodiodes is distorted by electronic noise which becomes larger than the quantum noise (Poisson noise) of the X-ray photons at low X-ray

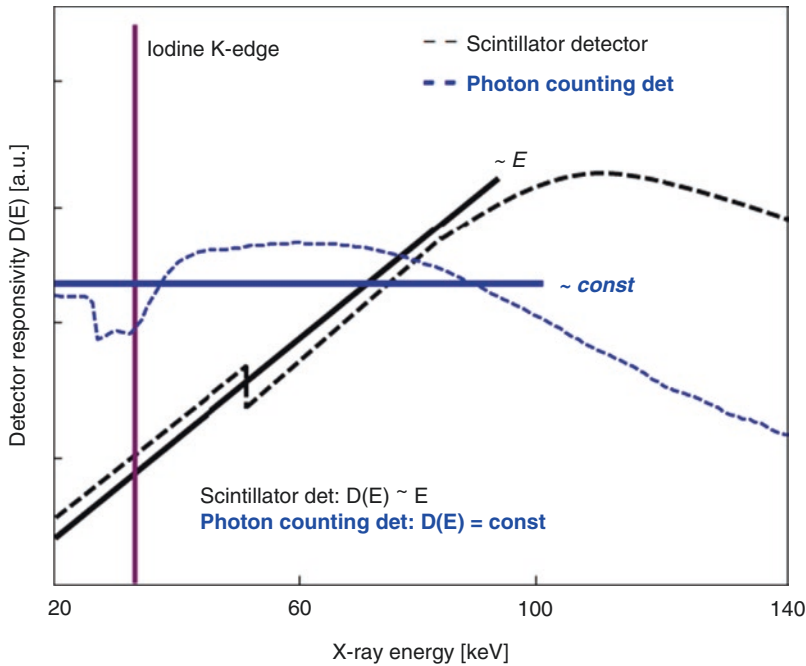


Fig. 2 Detector responsivity $D(E)$ as a function of the X-ray energy E for a GOS scintillator detector (dotted black line, approximation solid black line) and a CdTe photon-counting detector (dotted blue line, approximation solid blue line). The iodine K-edge at 33 keV is indicated

by a vertical line. Low-energy X-rays closely above the K-edge of iodine contribute less to the detector signal of a scintillator detector than of a photon-counting detector. The iodine contrast in the image is therefore lower for a scintillator detector than for a photon-counting detector

flux and causes a disproportional increase of image noise and instability of low CT-numbers. Electronic noise is, e.g., responsible for noise streaks in shoulder and pelvis images. The prevalence of electronic noise at low X-ray flux sets a limit to potential further radiation dose reduction in CT.

The detector elements are separated by optically in-transparent layers with a width of about 0.1 mm to prevent optical crosstalk between them which would significantly reduce spatial resolution. X-ray photons absorbed in the separation layers do not contribute to the measured signal even though they have passed through the patient—from a radiation dose perspective they are wasted dose. The ratio of active detector cell size and total size (including separation layers) is called geometric dose efficiency. Current medical CT detectors with an active cell size of about $0.8 \times 0.8 \text{ mm}^2$ to $1 \times 1 \text{ mm}^2$ (Willemink et al. 2018) have geometric dose efficiencies of 0.7–0.8 (70–80%). Significantly reducing the size of

the scintillators to increase spatial resolution while keeping the width of the separation layers constant will reduce the geometric efficiency—therefore, it is problematic to increase the spatial resolution of solid-state scintillation detectors beyond today’s performance levels (Flohr et al. 2007).

1.2 Properties of Photon-Counting Detectors

Photon-counting detectors are made of semiconductors such as cadmium-telluride (CdTe), cadmium-zinc-telluride (CZT), or silicon (Si). We will focus on CdTe- and CZT-based photon-counting detectors.

High voltage (800–1000 V) is applied between the cathode on top and pixelated anode electrodes at the bottom of a CdTe/CZT layer with a thickness of 1.4–2 mm, see Fig. 3. The absorbed X-rays produce electron-hole pairs which are

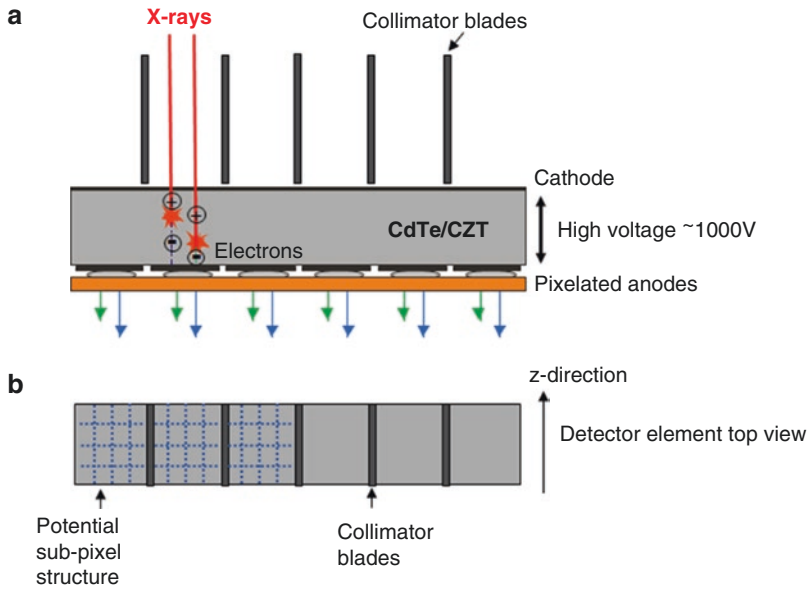


Fig. 3 Schematic drawing of a direct converting photon-counting detector. (a) Side view, (b) top view. The X-rays (red arrows) absorbed in CdTe or CZT produce electron-hole pairs that are separated in a strong electric field between cathode and pixelated anodes. The detector pixels are formed by the pixelated anodes and the electric

field without additional separation layers between them. Collimator blades are needed to suppress scattered radiation. A potential division of the “macro pixels” between two collimator blades into smaller sub-pixels is indicated for the three left detector cells. The pixelated anodes must then be correspondingly structured (not shown here)

separated in the strong electric field. The electrons drift to the anodes and induce short current pulses (10^{-9} s). A pulse-shaping circuit transforms the current pulses to voltage pulses with a full width at half maximum (FWHM) of 10–15 nanoseconds. The pulse height of the voltage pulses is proportional to the energy E of the absorbed X-rays. As soon as the pulses exceed a threshold they are counted, see Fig. 4.

Photon-counting detectors have several advantages compared to solid-state scintillation detectors. The detector elements are defined by the strong electric field between common cathode and pixelated anodes (Fig. 3) without additional separation layers. The geometric dose efficiency is only reduced by anti-scatter collimator blades or grids. Different from scintillator detectors each “macro pixel” confined by collimator blades can be divided into smaller sub-pixels which are read-out separately if needed (see Fig. 3b) to improve spatial resolution.

All current pulses produced by absorbed X-rays are counted as soon as they exceed a

threshold energy $T_0 \sim 20\text{--}25$ keV. Low-amplitude baseline noise is well below this level and does not trigger counts—even at low X-ray flux only the statistical Poisson noise of the X-ray quanta is present in the signal. CT scans at very low radiation dose or CT scans of obese patients show therefore less image noise, less streak artifacts, and more stable CT-numbers than the corresponding scans with a scintillation detector, and radiation dose reduction beyond today’s limits seems possible.

The detector responsivity $D(E)$ in the X-ray energy range from 30 to 100 keV is approximately constant (see Fig. 2)—all X-ray photons contribute equally to the measured signal regardless of their energy E , as soon as E exceeds T_0 . There is no down-weighting of lower-energy X-ray photons as in solid-state scintillation detectors. Photon-counting detectors can provide CT images with potentially improved CNR, in particular in CT scans with iodinated contrast agent, see Fig. 2.

In a more advanced read-out mode, several counters operating at different threshold energies

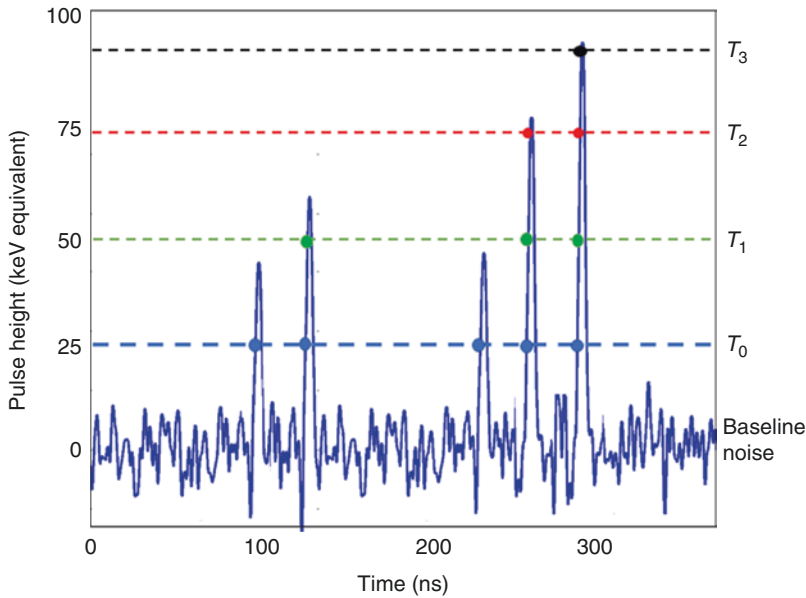


Fig. 4 The electrons produced by absorbed X-rays in a photon-counting detector induce signal pulses at the anodes with a pulse height proportional to the X-ray energy. The pulses are counted as soon as they exceed a threshold T_0 (dashed blue line, “counting” is indicated by a blue dot). T_0 has a typical energy of 25 keV, well above

the low-amplitude baseline noise. Three additional thresholds at higher energies (T_1 at 50 keV, T_2 at 75 keV, T_3 at 90 keV) are also indicated—simultaneous read-out of the counts exceeding different thresholds (in this example 4) provides spectrally resolved detector signals

can be introduced for energy discrimination, see Fig. 4. Up to 6 different thresholds have so far been realized in prototype settings (Schlomka et al. 2008). In the example of Fig. 4, 4 different energy thresholds T_0 , T_1 , T_2 , and T_3 are realized. During the measurement time of one projection, counter 1 counts all X-ray pulses with an energy exceeding T_0 , while counter 2 simultaneously counts all X-ray pulses with an energy exceeding T_1 , and so on. The photon-counting detector simultaneously provides 4 signals S_0 , S_1 , S_2 , and S_3 with different lower-energy thresholds T_0 , T_1 , T_2 , and T_3 . CT images reconstructed from these raw data are shown in Fig. 5. By subtracting the detector signals with adjacent lower-energy thresholds, “energy bin” data can be produced. Energy bin $b_0 = S_1 - S_0$ as an example contains all X-ray photons detected in the energy range between T_1 and T_0 . Physically, the thresholds are realized by different voltages which are fed into pulse-height comparator circuits.

The simultaneous read-out of CT data in different energy bins opens the potential of spectrally resolved measurements and material differentiation in any CT scan.

1.3 Challenges for Photon-Counting Detectors

Despite their benefits, CdTe- or CZT-based photon-counting detectors need to cope with several challenges. Their spectral separation is reduced by unavoidable physical effects. The current pulses produced by X-rays absorbed close to pixel borders are split between adjacent detectors cells (“charge sharing”). This leads to erroneous counting of a high-energy X-ray photon as several lower-energy hits. Incident X-rays at an energy E may kick-out K-electrons of the detector material (Cd and Te have K-edges at 26.7 and 31.8 keV, respectively). The empty

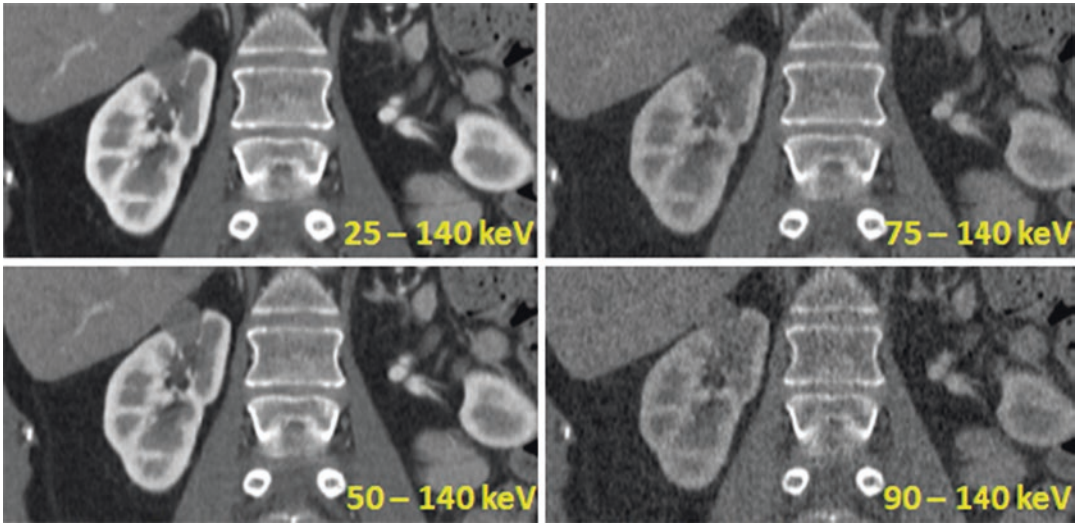
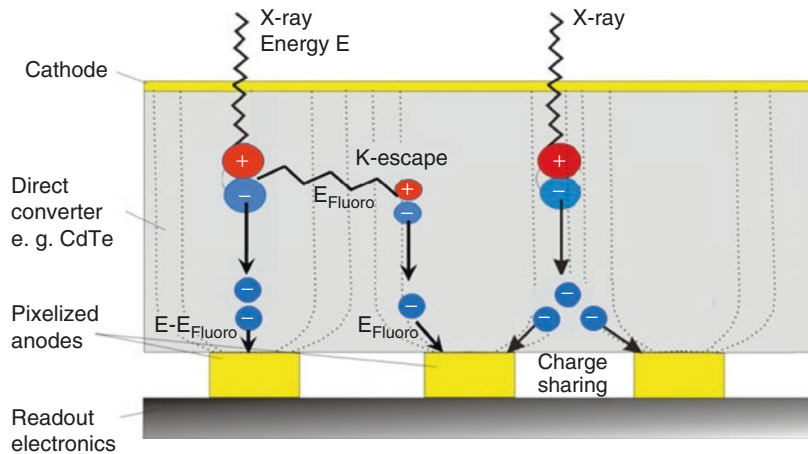


Fig. 5 Contrast-enhanced kidney scan acquired with a pre-clinical hybrid dual source CT prototype with 4 energy thresholds (25, 50, 75, and 90 keV, as indicated in Fig. 4), operated at an X-ray tube voltage of 140 kV. The higher the low-energy threshold, the lower is the iodine

contrast and the higher is the image noise in the reconstructed images, because fewer low-energy X-ray photons contribute to the image. Courtesy of National Institute of Health NIH, Bethesda, MD, USA

Fig. 6 Schematic illustration of charge sharing at pixel boundaries and loss of energy due to K-escape, which lead to double counting of X-ray pulses at wrong energies and reduction of spectral separation. E_{Fluoro} is the K-shell fluorescence X-ray energy



K-shells are immediately refilled, and characteristic X-rays at the K-shell fluorescence energy E_{Fluoro} are released which are re-absorbed and counted in the detector cell itself or in neighboring detector cells (“K-escape”). The incident X-rays at the primary interaction site lose the energy E_{Fluoro} and are counted at energy $E - E_{\text{Fluoro}}$. Charge sharing, fluorescence, and K-escape are

illustrated in Fig. 6. In summary, high-energy X-ray photons are wrongly counted at lower energies, and spectral separation as well as spatial resolution are reduced. The low-energy bins of the detector will contain wrong high-energy information (“high-energy tails” as shown in Fig. 7). For a realistic detector model including charge sharing, fluorescence, and K-escape, the

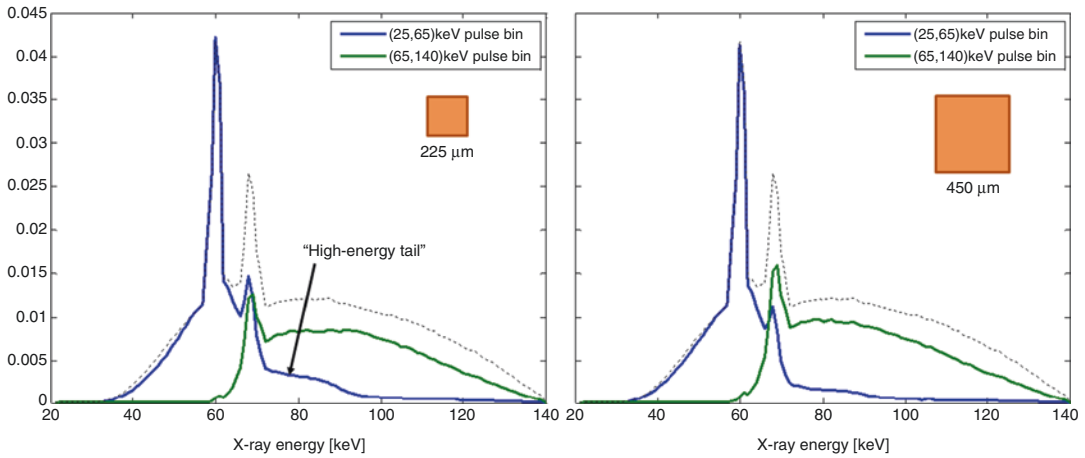


Fig. 7 Computer simulation of the X-ray spectra recorded in the 2 energy bins of a realistic photon-counting detector for an incident 140 kV spectrum (bin: 25–65 keV, blue line; bin: 65–140 keV, green line). The dotted line is the incident X-ray spectrum. Left: pixel size $0.225 \times 0.225 \text{ mm}^2$.

Right: pixel size $0.45 \times 0.45 \text{ mm}^2$. Increasing the pixel size reduces the characteristic “high-energy tail” of the low-energy bin caused by charge sharing and other effects such as K-escape

spectral separation with two energy bins is equivalent to existing dual-energy techniques (Kappler et al. 2010).

Increasing the size of the detector pixels improves spectral separation, because boundary effects such as charge sharing and K-escape contribute less to the total detector signal, see Fig. 7. The maximum size of the detector pixels is unfortunately limited by pulse pile-up. Medical CTs are operated at high X-ray flux rates up to 10^9 counts per s and mm^2 —if the detector pixels are too large, too many X-ray photons hit them too closely in time to be registered separately (the width of the voltage pulses after pulse-shaping is at least 10 ns). Several overlapping pulses are then counted as one hit only at a too high energy (“pulse pile-up”). Pulse pile-up leads to non-linear detector count rates and finally to detector saturation. It can be reduced by making the detector pixels smaller—however, smaller pixels lead to more charge sharing and K-escape. Finding the optimum size of the detector cells to balance pulse pile-up, charge sharing, and K-escape is one of the most challenging tasks in designing a photon-counting detector (Blevins 2020).

2 Material Decomposition for Photon-Counting CT

As the spectral X-ray attenuation of most materials in the relevant energy regime from 30 to 140 keV can be well approximated by a linear combination of the attenuation due to the photoelectric effect and Compton scattering, data acquisition with two energy bins and a decomposition into two base materials are often sufficient in the material decomposition task. Today’s established dual-energy applications are based on decomposition into two base materials such as calcium and water, iodine and water, or iodine and calcium.

Data acquisition with more than two energy bins enables multi-material decomposition under certain preconditions. Separation into two basis materials plus an additional element with its K-edge position in the energy range of the source spectrum of a clinical CT, such as gadolinium or gold, requires the spectral data acquisition to comprise at least three energy bins. The K-edge attenuation needs to be represented by an additional base material for an accurate and consis-

tent material decomposition of the spectral data. Unfortunately, these K-edge materials do not naturally occur in the human body. Multi-material decomposition will therefore be limited to clinical scenarios in which K-edge elements are introduced into the human body, e.g., to separate different contrast agents (e.g., iodine and gadolinium, or iodine and bismuth), or to compute material maps of other heavy elements (e.g., tungsten, or gold).

The computation of material-specific images from spectral projection data can essentially be achieved with three different methods: image-domain decomposition, projection-domain decomposition, and one-step inversion. In image-domain decomposition, each individual energy bin is first reconstructed separately and the actual material decomposition is performed in the image domain with linear approximations (Maaß et al. 2009). Prior knowledge on the object can be easily incorporated in these methods (Liu et al. 2016); however, beam-hardening artifacts are difficult to be corrected in an image-domain decomposition approach and are better handled with a projection-domain decomposition algorithm.

In projection-domain decomposition (Roessl and Proksa 2007), the spectral information, given by the measurements of the photon counts in the various energy bins, is first decomposed into the base materials directly in the projection domain, for example with a maximum likelihood algorithm. Then, the material-specific sinograms are separately reconstructed to provide the material-specific images in the image domain. This approach allows the incorporation of a statistical noise model and beam-hardening effects are properly modeled by the system model (Schirra et al. 2013). Compared to image-domain decomposition methods, prior (image domain) information and additional constraints are less easy to implement in the projection domain.

Finally, one-step inversion methods aim at combining the material decomposition and reconstruction task into one single step and solve this problem iteratively (Mory et al. 2018). In this way, the unknown base material images are

reconstructed jointly with the use of a forward model, which compares the current base material estimates with the measured spectral projection data and minimizes the residual error in an iterative procedure. Both additional constraints on the basis material images as well as statistical noise models can therefore be easily incorporated at the cost of a computationally more expensive algorithm (Mory et al. 2018).

One difference between dual-energy spectral CT systems and photon-counting spectral CT systems regarding material decomposition is that in photon-counting CT systems the number of spectral acquisitions (i.e., the number of energy bins) is often higher than the number of basis materials that should be decomposed. Thus, the decomposition task is over-determined, and the question especially for projection-domain decomposition arises how to make optimal use of the spectral information during decomposition. A common option to use the spectral information optimally in a projection-based decomposition is the maximum likelihood material decomposition (Schlomka et al. 2008), an iterative minimization algorithm that aims to find the basis material line integrals, which best match the measured photon counts in the energy bins considering the noise distribution of the measured data. A major ingredient of the maximum likelihood decomposition is a spectral forward model that is used to calculate for a given combination of material line integrals the expectation values of the measured photon counts. The spectral forward model comprises the photon emission of the tube, the photon attenuation by the object, and the photon detection process by the photon-counting detector. Assuming that tube emission spectrum, material attenuation spectra, and detector model are given, the only unknown in the decomposition are the basis material line integrals. If for a set of energy bins measured photon counts are available, the according basis material line integrals can be determined by minimizing the deviation between the measured counts and the expectation values of the counts, determined with the spectral forward model. In maximum likelihood approaches, the deviation is minimized in a statistical sense.

For this, a model describing the noise in the measurements is needed. Commonly, it is assumed that the noise of the measured photon counts follows a Poisson noise distribution.

Different strategies have been proposed to solve the minimization problem (Schlomka et al. 2008). The final results of all strategies are virtually the same. Thus, main selection criterion is the computation time, since material decomposition can be time-consuming. Pre-computation methods, look-up tables, and neural networks may be applied for speed-up (Zimmerman and Petschke 2017).

The spectral image formation in a single-source spectral photon-counting CT prototype (SPCCT - Philips Healthcare, Haifa, Israel) follows a two-step approach, with the material decomposition performed in the projection domain. To this end, the photon counts from the five energy bins are first decomposed into two or three basis materials using a maximum likelihood-based algorithm as described above (Schlomka et al. 2008; Roessl and Proksa 2007). In a subsequent step, basis material images are reconstructed. For example, each basis material image can be reconstructed separately using a filtered back-projection reconstruction algorithm (Grass 2001; Heuscher 2004).

For standard spectral image reconstruction in other photon-counting CT prototypes (Siemens Healthcare GmbH, Forchheim), the photon counts from the four energy bins are combined into two effective energy bins and statistically decorrelated. Then, an iterative beam-hardening correction in the projection domain is performed based on a two-material decomposition into water and iodine—the result are pseudo-monoenergetic projection data at two distinct energies. The pseudo-monoenergetic projection data provide the basis for the established dual-energy applications, not only for direct reconstruction of monoenergetic images at arbitrary energies, but also for subsequent material decomposition into water and iodine, water and iron, or calcium and iodine. For research, the projection data of the four energy bins can be read-out separately and decomposed into two, three, or four basis materials.

3 Pre-clinical Evaluation of Photon-Counting CT

Currently, CT scanner prototypes based on CdTe/CZT detectors are used to evaluate the potential and limitations of photon-counting CT in clinical practice.

A small-bore spectral micro-CT equipped with a Medipix detector with 8 energy channels has been translated to a large-bore photon-counting CT capable of obtaining diagnostic spectral CT images of a human within a clinical radiation dose level (Panta et al. 2018); however, no further results have been published yet.

Recently, a clinical single-source spectral photon-counting CT system (SPCCT—Philips Healthcare, Haifa, Israel) with a full field-of-view (FOV) of 50 cm has been installed (Si-Mohamed et al. 2020). The system is equipped with tiles of 2 mm thick CZT sensors with a $500\ \mu\text{m} \times 500\ \mu\text{m}$ pixel pitch, bonded to the proprietary ChromAIX2 application-specific integrated circuit (ASIC) (Steadman et al. 2017). Each channel offers pulse-height discrimination with five programmable energy thresholds with windows between 30 and 120 keV, which are advantageous with respect to achievable signal-to-noise ratio (SNR) even if only two or three different materials should be discriminated (Alvarez 2011). The single-source system acquires data from 64 rows to reconstruct a 50 cm FOV with a z-coverage of 17.6 mm at the iso-center. The system supports both axial and helical scan modes with a shortest gantry rotation time of 0.33 s and 2400 projections per rotation. Furthermore, the scanner is equipped with an ASG and can be operated at clinically relevant flux levels for large animal and human studies. A previous pre-clinical single-source photon-counting CT system (Philips Healthcare, Haifa, Israel) provided an in-plane field-of-view of 168 mm and a z-coverage of 2.5 mm, with a rotation time of 1 s (Kopp et al. 2018).

A pre-clinical hybrid dual source CT scanner prototype equipped with a conventional scintillation detector and a CdTe photon-counting detector (Siemens Healthcare GmbH, Forchheim, Germany) was described and evaluated in

Kappler et al. (2012, 2013, 2014). The photon-counting detector consists of sub-pixels with a size of $0.225 \times 0.225 \text{ mm}^2$. The detector provides 2 energy thresholds per sub-pixel. 2×2 sub-pixels can be binned to a “UHR pixel” with a pixel size of $0.45 \times 0.45 \text{ mm}^2$, 4×4 sub-pixels can be binned to a “macro pixel” with a size of $0.9 \times 0.9 \text{ mm}^2$ comparable to today’s medical CT systems. By assigning alternating low-energy and high-energy thresholds to adjacent detector sub-pixels in a “chess pattern mode,” the detector provides 4 energy thresholds in “macro pixels.” The in-plane FOV of the photon-counting detector is 275 mm, the z-coverage is 8–16 mm, depending on the read-out mode. A completion scan with the energy-integrating sub-system can be used to extend the photon-counting FOV to 500 mm. The shortest rotation time of the system is 0.5 s.

A clinical single-source CT scanner prototype (Siemens Healthcare GmbH, Forchheim, Germany) is equipped with a CdTe photon-counting detector consisting of sub-pixels with a size of $0.275 \times 0.322 \text{ mm}^2$. Its FOV is 500 mm at the iso-center. 2×2 sub-pixels can be binned to a “macro pixel” in the “standard” mode, the z-coverage is then 57.6 mm ($144 \times 0.4 \text{ mm}$ at the iso-center). The sub-pixels can as well be read out separately in the “UHR” mode, the z-coverage is then limited to 24 mm ($120 \times 0.2 \text{ mm}$ at the iso-center). The detector provides 4 energy thresholds per sub-pixel. The shortest rotation time of the system is 0.3 s (Flohr et al. 2020). The system is installed in three pre-clinical settings and operated using typical clinical scan protocols (Ferda et al. 2021).

The imaging performance of the pre-clinical hybrid dual source CT was evaluated by means of phantom and cadaver scans (Yu et al. 2016a; Gutjahr et al. 2016), confirming clinical image quality at clinically realistic levels of X-ray photon flux. In contrast-enhanced abdominal scans of human volunteers, similar qualitative and quantitative image quality scores as with conventional CT were achieved, with the addition of spectral information for material decomposition (Pourmorteza et al. 2016).

An improvement of iodine CNR by 11–38% with photon-counting CT was confirmed by measurements in 4 anthropomorphic phantoms simulating 4 patient sizes (Gutjahr et al. 2016). Improved iodine CNR can potentially be translated into reduced radiation dose, or reduced amount of contrast agent. Better differentiation of gray and white brain matter was demonstrated in a brain CT study with 21 human volunteers (Pourmorteza et al. 2017) and attributed to both higher soft-tissue contrasts ($10.3 \pm 1.9 \text{ HU}$ versus $8.9 \pm 1.8 \text{ HU}$), and lower image noise for photon-counting CT.

The impact of missing electronic noise on image quality was assessed for various clinical applications at low radiation dose. Less streaking artifacts in shoulder images acquired with the photon-counting detector of the pre-clinical hybrid dual source CT as compared to its scintillation detector were demonstrated (Yu et al. 2016b), as well as better Hounsfield unit stability in a lung phantom in combination with better reproducibility (Symons et al. 2017a). This is an important pre-requisite for further reduced radiation dose in lung imaging, e.g., in the context of lung cancer screening. In a study with 30 human subjects undergoing dose-reduced chest CT imaging (Symons et al. 2017b), photon-counting CT demonstrated higher diagnostic quality with significantly better image quality scores, fewer beam-hardening artifacts, lower image noise, and higher CNR for lung nodule detection, see Fig. 8.

Improved quality of coronary artery calcium (CAC) scoring with photon-counting CT at low radiation dose was shown in a combined phantom, ex vivo and in vivo study (Symons et al. 2019). The authors concluded that photon-counting CT technology may play a role in further reducing the radiation dose of CAC scoring.

Different photon-counting detector manufacturers are using different compromises to balance pulse pile-up and charge sharing effects, but all use pixel sizes smaller than integrating detectors. This results in increased spatial resolution, typically over 30 lp/cm or 0.15 mm (Kopp et al. 2018). It is important to notice that with small detector pixel size, the size of the X-ray tube

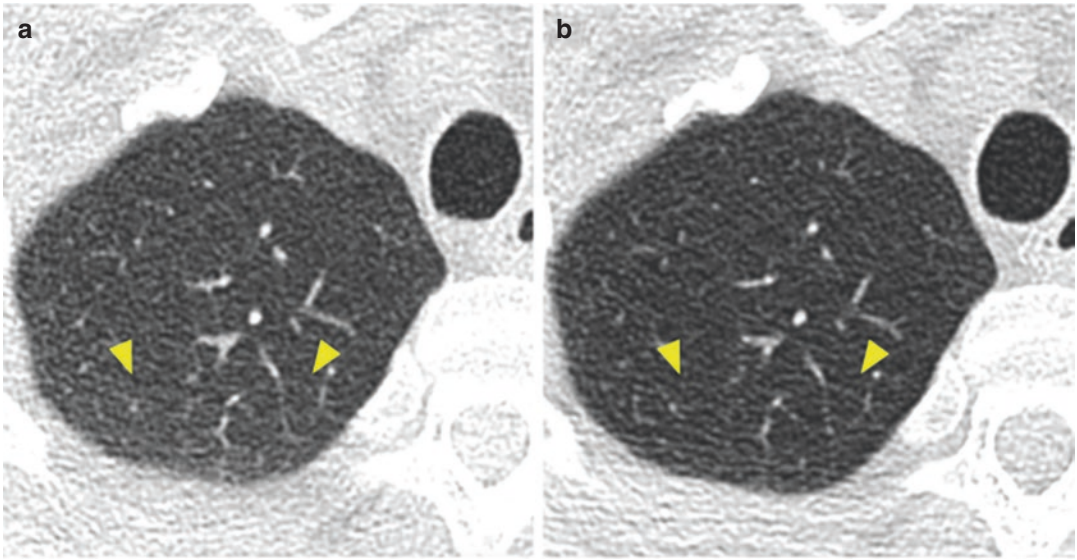


Fig. 8 Example of a low-dose lung scan acquired with the pre-clinical hybrid dual source CT prototype. (a) Energy-integrating detector image. (b) Photon-counting detector image, demonstrating less image noise (arrow-

heads) at low radiation dose because of the absence of electronic noise. (Courtesy of R Symons, NIH, Bethesda, USA)

focal spot practically determines the spatial resolution. Small focal spots can allow 30 lp/cm, but at the expense of a reduced maximum X-ray flux or mA. Increased spatial resolution enabled by the smaller detector pixels of photon-counting CT was evaluated in several phantom studies. 0.15 mm in-plane spatial resolution and minimum slice widths down to 0.41 mm were demonstrated for the pre-clinical hybrid dual source CT prototype, and better spatial resolution was confirmed in clinical images of the lung, shoulder, and temporal bone (Leng et al. 2018). At equal spatial resolution, photon-counting images had less image noise than conventional CT images because of the better modulation transfer function (MTF) of the measurement system (Leng et al. 2018). Significant improvements of coronary stent lumen were found (Symons et al. 2018a), as well as superior qualitative and quantitative image characteristics for coronary stent imaging when using a dedicated sharp convolution kernel (von Spiczak et al. 2018). In a phantom study (Bratke et al. 2020) spectral photon-counting CT allowed for the noninvasive

evaluation of intra-stent restenosis with reliable results regarding the residual lumen for most tested stents and the clear identification or suspicion of stenosis for all stents when, in contrast, the residual lumen could not be detected for a single stent using dual layer CT. The benefit of spectral photon-counting CT for the assessment of stents was also demonstrated in vivo on rabbits as illustrated in Fig. 9. Figures 10 and 11 show first images of patient carotid and coronary CTA, illustrating the added value of spectral photon-counting CT for the assessment of atherosclerotic plaques. The clinical benefits of this superior visualization of plaques in small vessels still need to be validated but preliminary results are promising.

Kopp et al. (2018) demonstrated on a phantom and animal study that spectral photon-counting CT has the potential to improve the assessment of lung structures due to higher resolution compared to conventional CT.

Improved spatial resolution and less image noise with the “UHR mode” of the pre-clinical hybrid dual source CT were also demonstrated

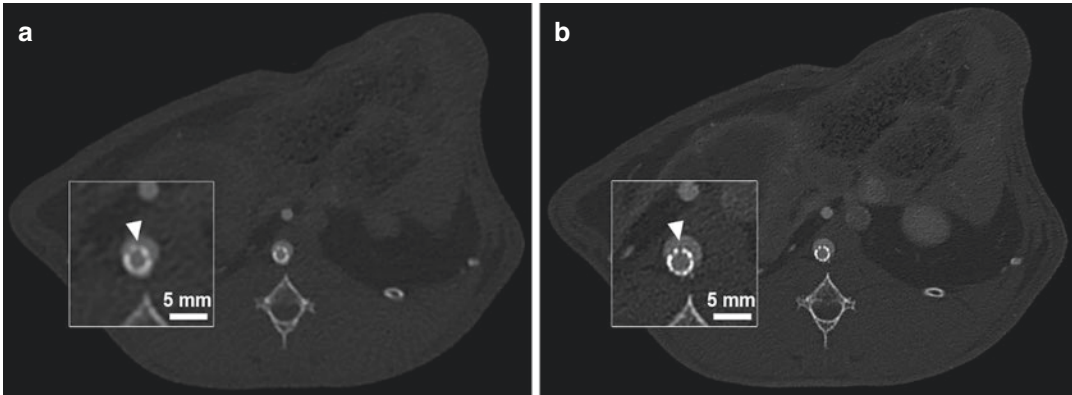


Fig. 9 Comparison of spectral photon-counting CT and conventional CT for in vivo stent assessment in a rabbit. Ultra-High Spatial Resolution images from SPCCT (b) show a significantly improved visualization of the stent

lumen (about 5 mm diameter) compared to conventional CT (a). Especially the stent's struts and intra-stent lumen can be better visualized. (Courtesy of S. Si-Mohamed, Hospices Civils de Lyon, France)

for CT scans of the brain, the thorax, and the kidneys (Pourmorteza et al. 2018), as well as for temporal bone anatomy (Zhou et al. 2018a).

Superior visualization of higher-order bronchi and third-/fourth-order bronchial walls at preserved lung nodule conspicuity compared with clinical reference images was demonstrated in 22 adult patients referred for clinically indicated high-resolution chest CT (Bartlett et al. 2019). According to the authors, photon-counting CT is beneficial for high-resolution imaging of airway diseases, and potentially for other pathologies, such as fibrosis, honeycombing, and emphysema.

The achievable image quality with a photon-counting detector in high-resolution chest CT is demonstrated in Fig. 12. Figure 13 illustrates the resolution improvement for temporal bone anatomy.

The spectral performance of the pre-clinical hybrid dual source prototype with photon-counting detector was evaluated in phantom studies (Leng et al. 2017). CT number accuracy in virtual monoenergetic images (VMIs) and iodine quantification accuracy were found to be comparable to dual source dual-energy CT. According to the authors, photon-counting CT offers additional advantages, such as high spatial resolution, and improved CNR. In an anthropomorphic head phantom containing tubes filled with aqueous

solutions of iodine (0.1–50 mg/ml) excellent agreement between actual iodine concentrations and iodine concentrations measured in the iodine maps was observed (Symons et al. 2018b). The authors assessed the use of iodine maps and VMIs in head and neck CTA in 16 asymptomatic volunteers and proposed VMIs as a method to enhance plaque detection and characterization as well as grading of stenosis by reconstructing images at different keV.

The routine availability of VMIs with photon-counting CT may pave the way to further standardization of CT protocols, provided that CNR and image quality of the VMIs are enhanced by refined processing (see e.g. Grant et al. 2014). In this approach, VMIs at standardized keV levels tailored to the clinical question (e.g., 55–60 keV for contrast-enhanced examinations of parenchymal organs, 45–55 keV for CT angiographic studies) are the primary output of any CT scan regardless of the acquisition protocol. Going one step further, the acquisition protocol may be standardized as well. Some authors (Zhou et al. 2018b) already recommend a standardized acquisition protocol with 140 kV X-ray tube voltage for contrast-enhanced abdominal CT examinations in all patient sizes, with standardized VMI reconstruction at 50 keV. According to the authors, optimal or near optimal iodine CNR for

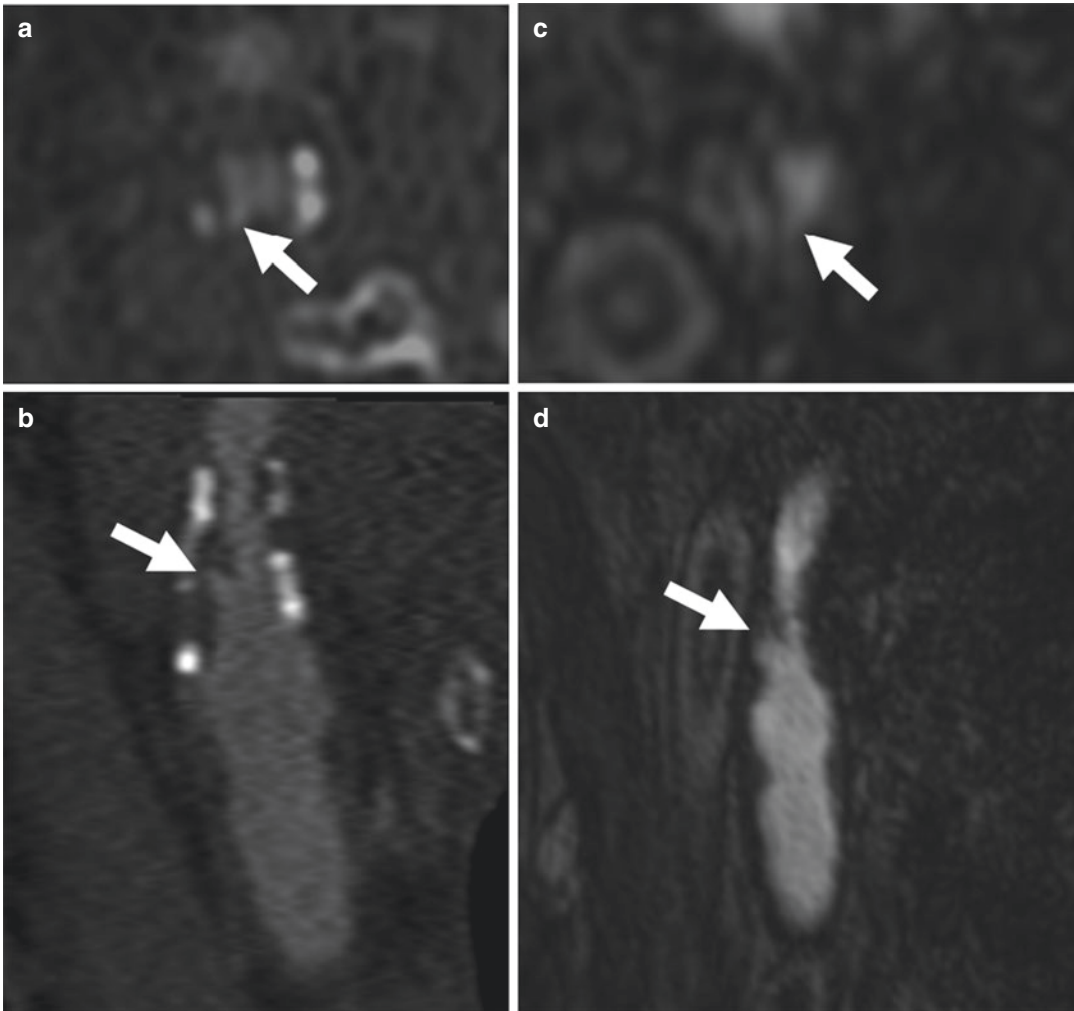


Fig. 10 Axial (a, c) and modified sagittal (b, d) images of the right carotid artery of a 55-year-old asymptomatic man having undergone radiotherapy of the neck for Hodgkin lymphoma, acquired with a single-source CT prototype with photon-counting detector (a, b) and angiography (c, d). The injection protocol for the photon-counting CT was of 40 mL of Iomeron 400 followed by 20 mL of saline at 4 mL/s. Data acquisition: helical mode with

64 × 0.27 mm collimation, 0.33 s rotation time, $CTDI_{vol} = 15.9$ mGy, $DLP = 332.7$ mGy.cm. Image reconstruction: soft reconstruction kernel, 1024 × 1024 image matrix, 0.25 mm slice width. Excellent visualization of the lumen of the carotid as well as plaques in both their soft and calcific parts. The arrows show an ulceration confirmed by angiography. (Courtesy of S. Boccalini, Hospices Civils de Lyon, France)

all patient sizes is obtained with this protocol. Figure 14 shows spectral image types that can be routinely reconstructed for each thoraco-abdominal CT scan.

Several authors assessed the performance of spectral photon-counting CT for detection and characterization of kidney stones, another established dual-energy CT application (Gutjahr et al. 2017; Ferrero et al. 2018; Marcus et al. 2018).

They found comparable overall performance to state-of-the-art dual-energy CT in differentiating stone composition, while photon-counting CT was better able to help characterize small renal stones (Marcus et al. 2018).

Figure 15 demonstrates a promising dual-energy processing technique for vascular imaging—the computation of virtual non-calcium images based on a two-material decomposition

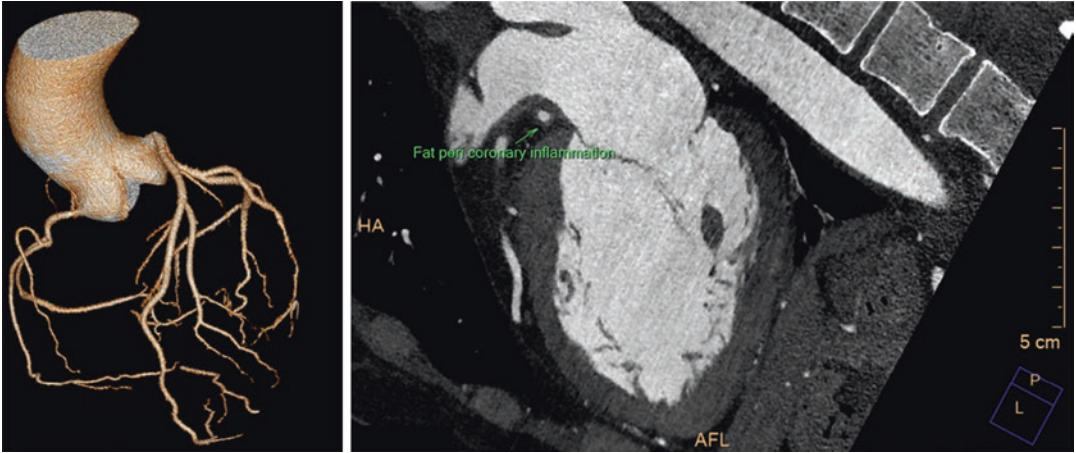


Fig. 11 Cardiac images of a 48-year-old woman with chest pain, acquired with a single-source CT prototype with photon-counting detector, after injection of 45 ml of iodine (400 mg/ml) at a rate of 4 ml/s. Data acquisition: ECG gated helical mode with 64×0.27 mm collimation, 0.33 s rotation time, $\text{CTDI}_{\text{vol}} = 25.7$ mGy,

$\text{DLP} = 475.7$ mGy.cm. Image reconstruction: sharp reconstruction kernel, 1024×1024 image matrix, 0.25 mm slice width. Excellent visualization of the coronary tree including small branches and small fat peri-coronary inflammation. (Courtesy of Prof. Douek, Hospices Civils de Lyon, France)

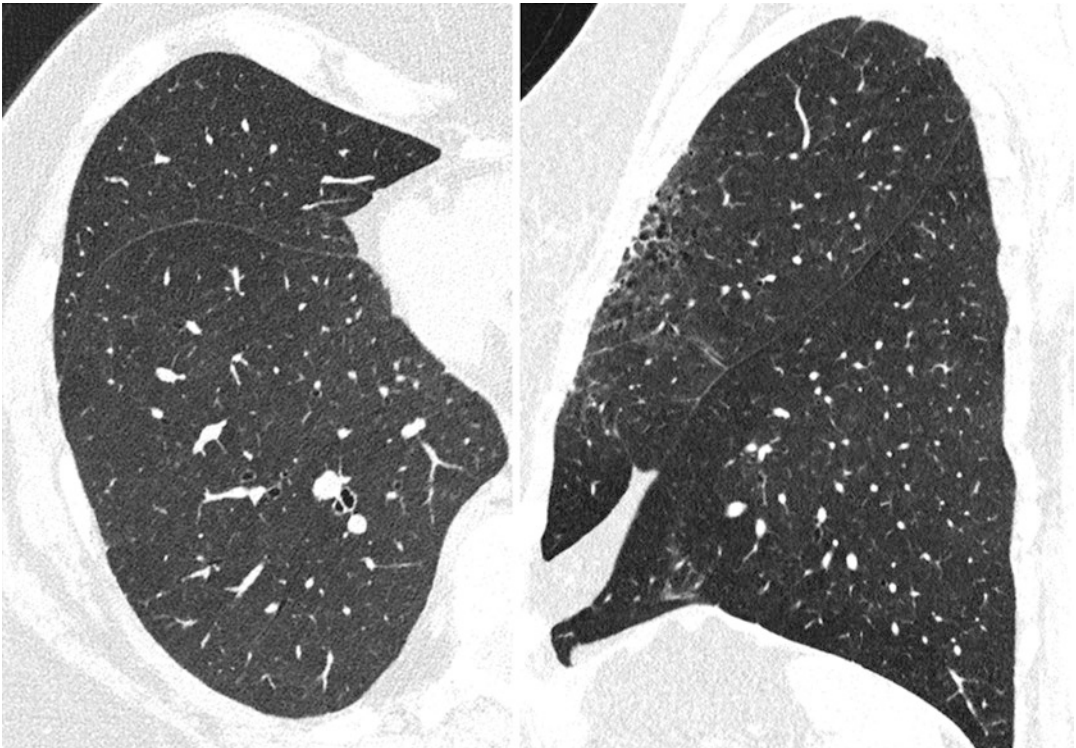


Fig. 12 Lung images of a 74-year-old woman with breast cancer and signs of fibrosis after radiation therapy, acquired with a single-source CT prototype with photon-counting detector. Data acquisition: “UHR” mode, 120×0.2 mm collimation, 0.3 s rotation time,

$\text{CTDI}_{\text{vol}} = 3.89$ mGy, $\text{DLP} = 126$ mGy.cm. Image reconstruction: sharp convolution kernel, 1024×1024 image matrix, 0.4 mm slice width. Excellent visualization of fibrosis and fine details such as fissures. (Courtesy of J. Ferda, Pilsen, Czech Republic)

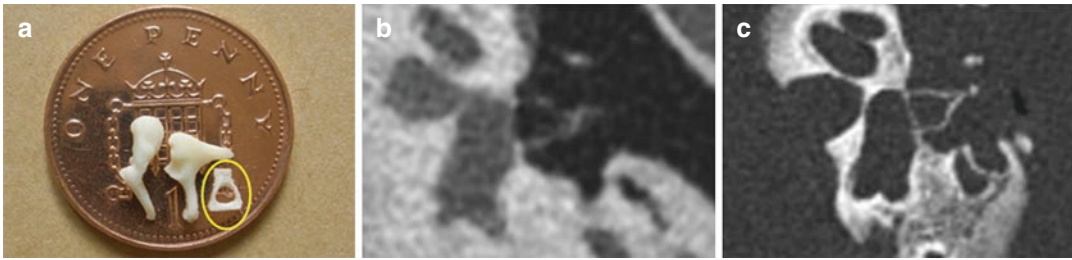


Fig. 13 (a) Bones of the middle ear—the stapes (yellow circle) has a size of about 2 mm × 3 mm. (b) Specimen image acquired with a state-of-the-art medical CT (SOMATOM Force, Siemens Healthcare). (c) Specimen image acquired with a single-source CT prototype with

photon-counting detector. Data acquisition: “UHR” mode, 120 × 0.2 mm collimation. Spatial resolution is significantly improved. (Courtesy of A Persson, CMIV, Linköping, Sweden)

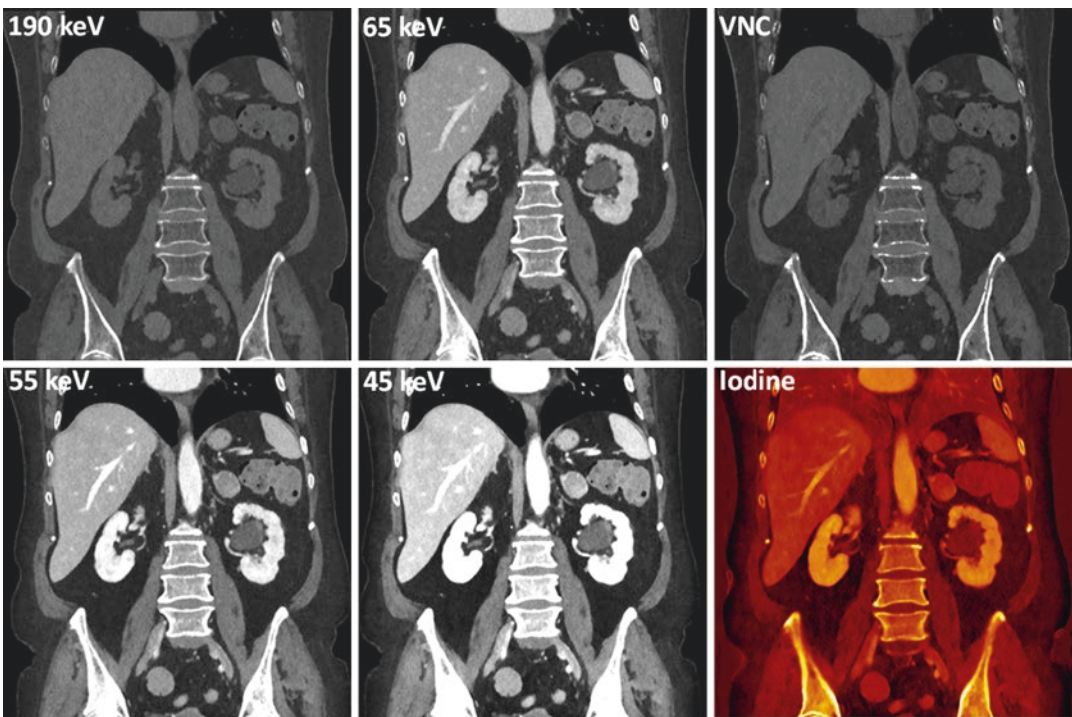


Fig. 14 Abdominal images of a 67-year-old woman with adrenal adenoma and parapelvic renal cyst, acquired with a single-source CT prototype with photon-counting detector. Data acquisition: “standard” mode, 144 × 0.4 mm collimation, 0.3 s rotation time, CTDI_{vol} = 10.2 mGy,

DLP = 450 mGycm. Image reconstruction: 0.4 mm slice width. VMIs at 190, 65, 55, and 45 keV, virtual non-contrast image VNC, and iodine image. (Courtesy of J. Ferda, Pilsen, Czech Republic)

into iodine and calcium images. In the iodine images—which correspond to virtual non-calcium images—calcified plaques are removed which hamper the assessment of the true vessel lumen in standard CT images, in particular for small vessels. In contrast to other processing

techniques removing calcified plaques, the lumen of the vessels is restored.

If the photon-counting detector is operated with more than two energy bins, multi-material decomposition is possible if K-edge elements are present. In a canine model of myocardial infarction,

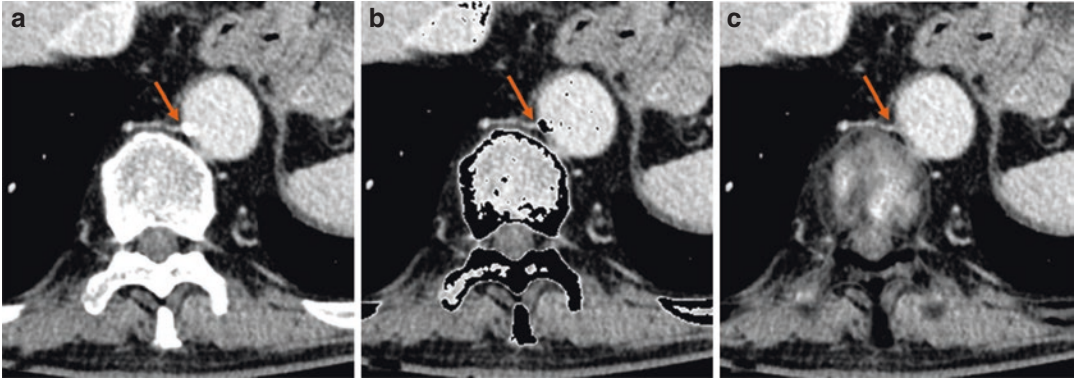


Fig. 15 Contrast-enhanced abdominal scan of a 73-year-old patient acquired with a single-source CT prototype with photon-counting detector. Data acquisition: “standard” mode, 144×0.4 mm collimation, 0.5 s rotation time, 120 kV, 130 eff. mAs, DLP = 316 mGycm. (a) Standard diagnostic image (VMI at 65 keV). A calcified plaque (arrow) prevents the assessment of the patency of

the small aortic branch. (b) Conventional HU threshold-based Ca-removal—reliable evaluation of the small vessel is still not possible (arrow). (c) Virtual non-Ca image—the calcified plaque is removed, and the true vessel lumen is restored (arrow). (Courtesy of J. Ferda, Pilsen, Czech Republic)

Symons et al. (2017c) performed dual-contrast agent imaging of the heart to simultaneously assess both first-pass and late enhancement of the myocardium. The authors concluded that combined first-pass iodine and late gadolinium maps allowed quantitative separation of blood pool, infarct scar, and remote myocardium. The same authors also investigated the feasibility of simultaneous material decomposition of three contrast agents (bismuth, iodine, and gadolinium) in vivo in a canine model (Symons et al. 2017d). They observed tissue enhancement at multiple phases in a single CT acquisition, opening the potential to replace multiphase CT scans by a single CT acquisition with multiple contrast agents, see Fig. 16.

Several phantom and animal studies have also demonstrated the feasibility of multiple contrast imaging using a combination of material decomposition and K-edge imaging. The concept of assessing the liver in different time phases from a single-scan, double injection of iodine and gadolinium contrast agents, was demonstrated in 2017 (Muenzel et al. 2017) in a simulation study. Si-Mohamed et al. (2019) demonstrated the feasibility of this dual-contrast multiphase liver

imaging by injecting iodinated and gadolinated contrast agents in healthy rabbits at different times so that the first contrast agent visualized the portal phase and the second the arterial phase.

The ability to perform absolute quantification of multiple contrast agents can be used for the simultaneous assessment of different pathophysiological processes. Spectral photon-counting CT has been used to image macrophages inside atherosclerotic plaque with gold nanoparticles, and simultaneously image the arterial lumen with an iodine contrast agent (Cormode et al. 2010). In a study from the same team, spectral photon-counting CT has been used in phantoms and in rabbits to simultaneously discriminate and quantify a gold blood pool agent (Au-NP) from an iodinated contrast agent imaging tissue and calcium-rich matter, from a single scan (Cormode et al. 2017). Si-Mohamed et al. (2018) have demonstrated that spectral photon-counting CT can be used to perform a complete peritoneal dual-contrast protocol, enabling a good assessment of the peritoneal cavity and abdominal organs in rats thanks to dual-contrast agents within peritoneal and blood compartments, see Fig. 17.

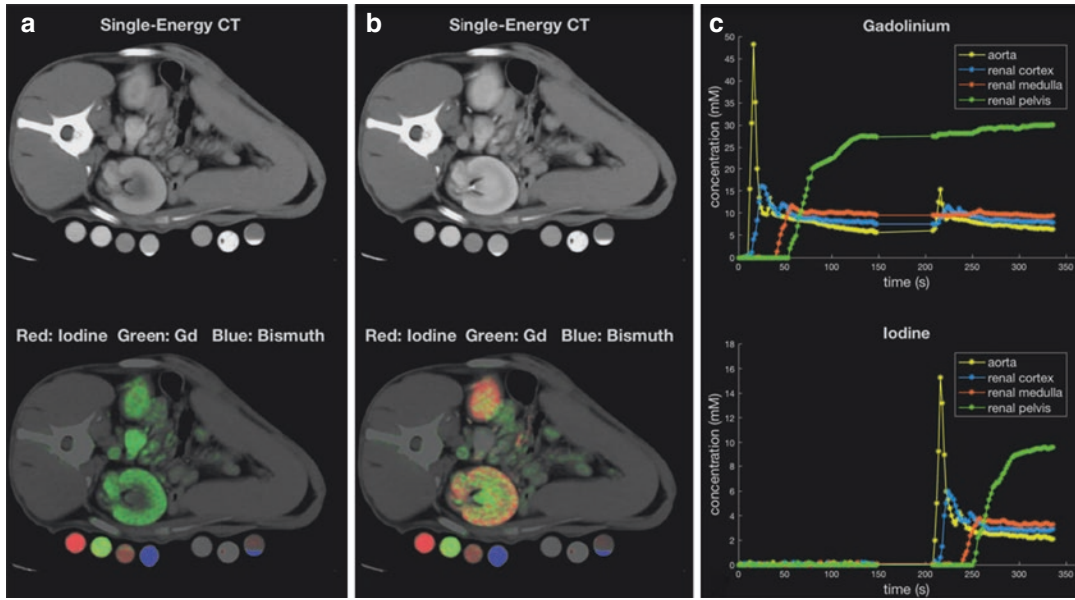


Fig. 16 Simultaneous imaging of 3 different contrast agents (iodine, gadolinium, and bismuth) by multi-material decomposition in a dog model. Scan data were acquired with the pre-clinical hybrid dual source CT prototype and read-out in four energy bins (25–50, 50–75, 75–90, and 90–140 keV). Bismuth was administered more than one day prior to scanning. Intravenous administration of gadolinium-based contrast agent was followed by intravenous administration of iodine-based contrast agent after 3 mins

to simultaneously visualize different phases of renal enhancement. (a) Image acquired at 30 s after start of gadolinium injection, at the peak of gadolinium enhancement in the renal cortex. (b) Image acquired at 220 s, at the peak of iodine enhancement in the renal cortex. (c) Enhancement curves of gadolinium and iodine in the aorta, renal cortex, medulla, and pelvis. (Courtesy of R Symons, NIH, Bethesda, MD, USA, see also Symons et al. 2017d)

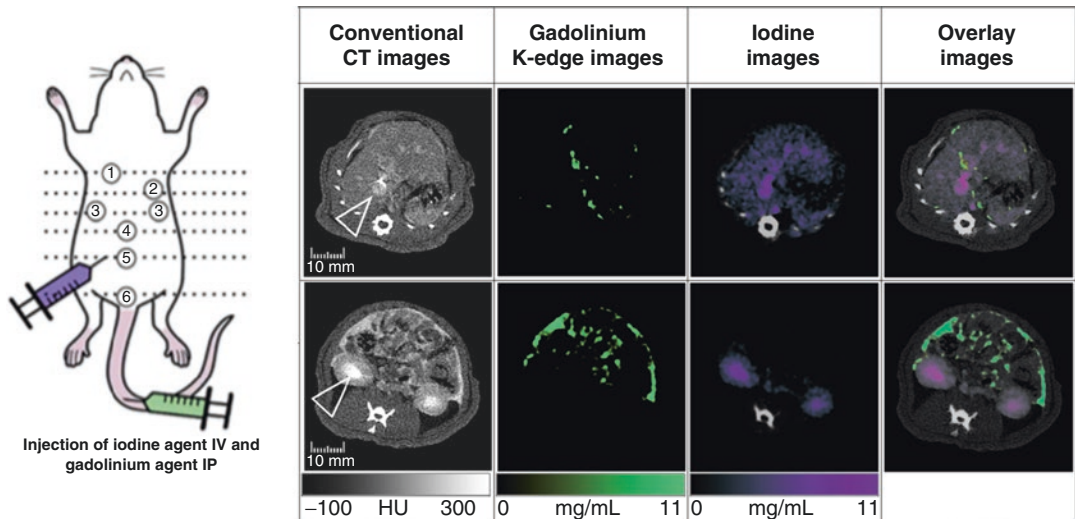


Fig. 17 Abdominopelvic spectral photon-counting CT images and contrast material images acquired post-IV injections of intraperitoneal gadolinium and intravenous iodine-based contrast agents. The contrast material images allowed a specific enhancement of the abdominal organs and vessels on the iodine map (top row, head arrow: hepatic vein; bottom row, head arrow: urinary cavity) (in

purple) and the peritoneal cavity on the gadolinium K-edge map (in green) for increasing the contrast in each compartment potentially enabling better lesion detection in comparison to conventional imaging. (Courtesy of S. Si-Mohamed, Hospices Civils de Lyon, France, see also Si-Mohamed et al. 2018; Thivolet et al. 2020)

While several novel imaging contrast agents based on high atomic number elements are being explored, iodine and gadolinium are particularly attractive because of their existing approval for clinical use. However, these iodinated agents have a number of limitations (nephropathy, gadolinium retention, non-specificity, K-edge at too low energy for iodine, etc.). Thus there is a compelling need to develop photon-counting specific contrast agents to expand the field of CT-based molecular imaging. Nanoparticles are a promising platform for contrast agent development. Cormode et al. (2017) described the biodistribution and pharmacokinetics of gold and iodine contrast agents. They found persistently high concentrations of the gold nanoparticles in the blood vessels of rabbits over the duration of the experiment (41 min), allowing both arterial and venous mapping. Photon-counting CT imaging may allow the use of blood pool agents for delayed steady-state imaging, and can simultaneously perform first-pass arterial imaging using a different contrast agent, such as iodine. Further potential applications of blood pool contrast agents include detection of bleeding, visualization of tumor vasculature, and quantification of tissue blood volume. In another study, Riederer et al. (2019) have investigated a tantalum-based contrast agent (K-edge energy of tantalum is 67.4 keV). They were able to demonstrate in a phantom study that spectral photon-counting CT can provide tantalum density maps and allows for material decomposition and differentiation between tantalum and iodine in vitro which may enable for an improved follow-up diagnosis in patients after vascular occlusion therapy.

Photon-counting CT can also be used to study the biodistribution of nanoparticles in vivo over time. In particular, longitudinal imaging of the biodistribution of nanoparticles would be highly attractive for their clinical translation. Spectral photon-counting CT allowed repetitive and quick acquisitions in vivo, and follow-up of changes in the Au-NP biodistribution over time as demonstrated in 2017 (Si-Mohamed et al. 2017b). In another study from Badea et al. (2019) the team investigated the in vivo discrimination of iodine and gadolinium nanoparticle contrast agents using both dual-energy micro-CT with energy-

integrating detectors and photon-counting detector based spectral micro-CT. The material concentration maps confirmed expected biodistributions of contrast agents in the blood, liver, spleen, and kidneys. Photon-counting CT demonstrated to be useful for functional characterization of solid tumors and could aid in the characterization of nanoparticles that show promise in the developing field of cancer theranostics.

In clinical practice, the use of multi-material maps may be hampered by the unavoidable increase of image noise in a multi-material decomposition. Similar to ultra-high resolution scanning non-linear data and image denoising techniques will play a key role to fully exploit the potential of multi-material decomposition in clinical routine, see, e.g., Tao et al. (2018).

Compliance with Ethical Standards

Ethical Approval This is a review article. No patient scans were performed for this chapter.

References

- Alvarez RE (2011) Estimator for photon counting energy selective x-ray imaging with multibin pulse height analysis. *Med Phys* 38(5):2324–2334
- Badea CT, Clark DP, Holbrook M, Srivastava M, Mowery Y, Ghaghada KB (2019) Functional imaging of tumor vasculature using iodine and gadolinium-based nanoparticle contrast agents: a comparison of spectral micro-CT using energy integrating and photon counting detectors. *Phys Med Biol* 64(6):065007. <https://doi.org/10.1088/1361-6560/ab03e2>
- Bartlett DJ, Koo WC, Bartholmai BJ et al (2019) High-resolution chest computed tomography imaging of the lungs: impact of 1024 matrix reconstruction and photon-counting detector computed tomography. *Investig Radiol* 54(3):129–137
- Blevis I (2020) Chapter 10: X ray detectors for spectral photon counting CT. In: Taguchi K, Blevis I, Iniewski K (eds) *Spectral, photon counting computed tomography technology and applications*, 1st edn. CRC Press, Boca Raton. <https://doi.org/10.1201/9780429486111>. First Published 2020; eBook Published 15 July 2020. See Chapter 10
- Bratke G, Hicethier T, Bar-Ness D et al (2020) Spectral photon-counting computed tomography for coronary stent imaging: evaluation of the potential clinical impact for the delineation of in-stent restenosis. *Investig Radiol* 55(2):61–67

- Cormode DP, Roessler E, Thran A et al (2010) Atherosclerotic plaque composition: analysis with multicolor CT and targeted gold nanoparticles. *Radiology* 256:774–782
- Cormode DP, Si-Mohamed S, Bar-Ness D et al (2017) Multicolor spectral photon-counting computed tomography: in vivo dual contrast imaging with a high count rate scanner. *Sci Rep* 7:4784. <https://doi.org/10.1038/s41598-017-04659-9>
- Ferda J, Vendiš T, Flohr T et al (2021) Computed tomography with a full FOV photon-counting detector in a clinical setting, the first experience. *Eur J Radiol* 137:109614. <https://doi.org/10.1016/j.ejrad.2021.109614>. Online ahead of print
- Ferrero A, Gutjahr R, Halaweish AF, Leng S, McCollough CH (2018) Characterization of urinary stone composition by use of whole-body, photon-counting detector CT. *Acad Radiol* 25(10):1270–1276
- Flohr TG, Stierstorfer K, Süß C et al (2007) Novel ultra-high resolution data acquisition and image reconstruction for multi-detector row CT. *Med Phys* 34(5):1712–1723
- Flohr T, Petersilka M, Henning A, Ulzheimer S, Ferda J, Schmidt B (2020) Photon counting CT review. *Phys Med* 79:126–136
- Grant KL, Flohr TG, Krauss B et al (2014) Assessment of an advanced image-based technique to calculate virtual monoenergetic computed tomographic images from a dual-energy examination to improve contrast-to-noise ratio in examinations using iodinated contrast media. *Investig Radiol* 49(9):586–592
- Grass M (2001) Angular weighted hybrid cone-beam CT reconstruction for circular trajectories. *Phys Med Biol* 46(6):1595–1610
- Gutjahr R, Halaweish AF, Yu Z et al (2016) Human imaging with photon-counting-based computed tomography at clinical dose levels: contrast-to-noise ratio and cadaver studies. *Investig Radiol* 51(7):421–429
- Gutjahr R, Polster C, Henning A et al (2017) Dual-energy CT kidney stone differentiation in photon-counting computed tomography. *Proc SPIE Int Soc Opt Eng* 10132
- Heuscher D (2004) Redundant data and exact helical cone-beam reconstruction. *Phys Med Biol* 49(11):2219–2238
- Kappler S, Niederlöhner D, Stierstorfer K, Flohr T (2010) Contrast-enhancement, image noise and dual-energy simulations for quantum-counting clinical CT. In: *Proceedings of the SPIE medical imaging conference 2010*, Vol 7622, pp 76223H
- Kappler S, Hannemann T, Kraft E et al (2012) First results from a hybrid prototype CT scanner for exploring benefits of quantum-counting in clinical CT. In: *Medical imaging 2012: physics of medical imaging* 83130X
- Kappler S, Henning A, Krauss B, et al (2013) Multi-energy performance of a research prototype CT scanner with small-pixel counting detector. In: *Medical imaging 2013: physics of medical imaging* 86680O
- Kappler S, Henning A, Kreisler B, et al (2014) Photon-counting CT at elevated x-ray tube currents: contrast stability, image noise and multi-energy performance. In: *Medical imaging 2014: physics of medical imaging* 90331C
- Kopp FK, Daerr H, Si-Mohamed S et al (2018) Evaluation of a preclinical photon-counting CT prototype for pulmonary imaging. *Sci Rep* 8(1):1738
- Leng S, Zhou W, Yu Z et al (2017) Spectral performance of a whole-body research photon-counting detector CT: quantitative accuracy in derived image sets. *Phys Med Biol* 62(17):7216–7232
- Leng S, Rajendran K, Gong H et al (2018) 150- μm spatial resolution using photon-counting detector computed tomography technology: technical performance and first patient images. *Investig Radiol* 53(11):655–662
- Leng S, Bruesewitz M, Tao S et al (2019) Photon-counting detector CT: system design and clinical applications of an emerging technology. *Radiographics* 39(3):729–743
- Liu J, Ding H, Molloy S, Zhang X, Gao H (2016) TICMR: Total image constrained material reconstruction via nonlocal total variation regularization for spectral CT. *IEEE Trans Med Imaging* 35(12):2578–2586
- Maaß C, Baer M, Kachelrieß M (2009) Image-based dual energy CT using optimized pre-correction functions: a practical new approach of material decomposition in image domain. *Med Phys* 36(8):3818–3829
- Marcus RP, Fletcher JG, Ferrero A et al (2018) Detection and characterization of renal stones by using photon-counting-based CT. *Radiology* 289(2):436–442
- Mory C, Sixou B, Si-Mohamed S, Bousset L, Rit S (2018) Comparison of five one-step reconstruction algorithms for spectral CT. *Phys Med Biol* 63(23):235001
- Muenzel D, Daerr H, Proksa R et al (2017) Simultaneous dual-contrast multi-phase liver imaging using spectral photoncounting computed tomography: a proof-of-concept study. *Eur Radiol Exp* 1:25
- Panta RK, Butler APH, de Ruyter NJA et al (2018) First human imaging with MARS photon-counting CT. In: *2018 IEEE nuclear science symposium and medical imaging conference proceedings (NSS/MIC)*
- Pourmorteza A, Symons R, Sandfort V et al (2016) Abdominal imaging with contrast-enhanced photon-counting CT: first human experience. *Radiology* 279(1):239–245
- Pourmorteza A, Symons R, Reich DS, Bagheri M, Cork TE, Kappler S, Ulzheimer S, Bluemke DA (2017) Photon-counting CT of the brain: in vivo human results and image-quality assessment. *AJNR Am J Neuroradiol* 38(12):2257–2263
- Pourmorteza A, Symons R, Henning A, Ulzheimer S, Bluemke DA (2018) Dose efficiency of quarter-millimeter photon-counting computed tomography: first-in-human results. *Investig Radiol* 53(6):365–372
- Riederer I, Bar-Ness D, Kimm M et al (2019) Liquid embolic agents in spectral X-ray photon-counting computed tomography using tantalum K-edge imaging. *Sci Rep* 9:5268. <https://doi.org/10.1038/s41598-019-41737-6>
- Roessler E, Proksa R (2007) K-edge imaging in x-ray computed tomography using multi-bin photon counting detectors. *Phys Med Biol* 52(15):4679–4696

- Schirra CO, Roessl E, Koehler T et al (2013) Statistical reconstruction of material decomposed data in spectral CT. *IEEE Trans Med Imaging* 32(7):1249–1257
- Schlomka JP, Roessl E, Dorscheid R et al (2008) Experimental feasibility of multi-energy photon-counting K-edge imaging in pre-clinical computed tomography. *Phys Med Biol* 53(15):4031–4047
- Si-Mohamed S, Bar-Ness D, Sigovan M et al (2017a) Review of an initial experience with an experimental spectral photon counting computed tomography system. *NIMA* 873:27–35
- Si-Mohamed S, Cormode DP, Bar-Ness D et al (2017b) Evaluation of spectral photon counting computed tomography K-edge imaging for determination of gold nanoparticle biodistribution in vivo. *Nanoscale* 9(46):18246–18257
- Si-Mohamed S, Thivolet A, Bonnot P et al (2018) Improved peritoneal cavity and abdominal organ imaging using a biphasic contrast agent protocol and spectral photon counting computed tomography K-edge imaging. *Investig Radiol* 53(10):629–639
- Si-Mohamed S, Tatar-Leitman V, Laugerette A et al (2019) Spectral Photon-Counting Computed Tomography (SPCCT): in-vivo single-acquisition multi-phase liver imaging with a dual contrast agent protocol. *Sci Rep* 9:8458. <https://doi.org/10.1038/s41598-019-44821-z>
- Si-Mohamed S, Boussel L, Douek P (2020) Clinical perspectives of spectral photon-counting CT. In: *Spectral, photon counting computed tomography: technology and applications*. CRC Press, Taylor & Francis Group, Boca Raton, p 97
- Steadman R, Herrmann C, Livne A (2017) Chro-mAIX2: a large area, high count-rate energy-resolving photon counting ASIC for a spectral CT prototype. *Nucl Instrum Methods Phys Res, Sect A* 862:18–24
- Symons R, Cork T, Sahbaee P et al (2017a) Low-dose lung cancer screening with photon-counting CT: a feasibility study. *Phys Med Biol* 62(1):202–213
- Symons R, Pourmorteza A, Sandfort V et al (2017b) Feasibility of dose-reduced chest CT with photon-counting detectors: initial results in humans. *Radiology* 285(3):980–989
- Symons R, Cork TE, Lakshmanan MN et al (2017c) Dual-contrast agent photon-counting computed tomography of the heart: initial experience. *Int J Cardiovasc Imaging* 33:1253–1261
- Symons R, Krauss B, Sahbaee P et al (2017d) Photon-counting CT for simultaneous imaging of multiple contrast agents in the abdomen: an in vivo study. *Med Phys* 44(10):5120–5127
- Symons R, de Bruecker Y, Roosen J et al (2018a) Quarter-millimeter spectral coronary stent imaging with photon-counting CT: initial experience. *J Cardiovasc Comput Tomogr* 12:509–515
- Symons R, Reich DS, Bagheri M et al (2018b) Photon-counting computed tomography for vascular imaging of the head and neck: first in vivo human results. *Investig Radiol* 53(3):135–142
- Symons R, Sandfort V, Mallek M, Ulzheimer S, Pourmorteza A (2019) Coronary artery calcium scoring with photon-counting CT: first in vivo human experience. *Int J Cardiovasc Imaging* 35(4):733–739
- Taguchi K (2017) Energy-sensitive photon-counting detector-based X-ray computed tomography. *Radiol Phys Technol* 10(1):8–22
- Taguchi K, Iwanczyk JS (2013) *Vision 20/20: single photon-counting x-ray detectors in medical imaging*. *Med Phys* 40(10):100901
- Tao S, Rajendran K, McCollough CH, Leng S (2018) Material decomposition with prior knowledge aware iterative denoising (MD-PKAID). *Phys Med Biol* 63(19):195003
- Thivolet A, Si-Mohamed S, Bonnot P et al (2020) Spectral photon-counting CT imaging of colorectal peritoneal metastases: initial experience in rats. *Sci Rep* 10:13394. <https://doi.org/10.1038/s41598-020-70282-w>
- von Spiczak J, Mannil M, Peters B et al (2018) Photon-counting computed tomography with dedicated sharp convolution kernels – tapping the potential of a new technology for stent imaging. *Investig Radiol* 53(8):486–494
- Willeminck MJ, Persson M, Pourmorteza A, Pelc NJ, Fleischmann D (2018) Photon-counting CT: technical principles and clinical prospects. *Radiology* 289(2):293–312
- Yu Z, Leng S, Jorgensen SM et al (2016a) Evaluation of conventional imaging performance in a research CT system with a photon-counting detector array. *Phys Med Biol* 61:1572–1595
- Yu Z, Leng S, Kappler S et al (2016b) Noise performance of low-dose CT: comparison between an energy integrating detector and a photon-counting detector using a whole-body research photon-counting CT scanner. *J Med Imaging* 3(4):043503
- Zhou W, Lane JJ, Carlson ML et al (2018a) Comparison of a photon-counting-detector CT with an energy-integrating-detector CT for temporal bone imaging: a cadaveric study. *AJNR Am J Neuroradiol* 39(9):1733–1738
- Zhou W, Abdurakhimova D, Bruesewitz M et al (2018b) Impact of photon-counting detector technology on kV selection and diagnostic workflow in CT. *Proc SPIE Int Soc. Opt Eng.* 10573. pii: 105731C. <https://doi.org/10.1117/12.2294952>
- Zimmerman KC, Petschke A (2017) Empirical neural network forward model for maximum likelihood material decomposition in spectral CT. In: *Medical imaging 2017: physics of medical imaging* 101323S



Contrast Media for Modern Computed Tomography

Hubertus Pietsch and Gregor Jost

Contents

1	Introduction	93
2	Iodinated Contrast Media: Current Standard in Safety and Tolerability	94
2.1	Structure and Physicochemistry	94
2.2	Tolerability and Safety	95
2.3	LOCM, the Reference Standard	95
3	The Technology Is a Determining Factor for the Efficiency of Contrast Media	95
4	Pharmacokinetics of Iodinated Contrast Media and Their Relevance for Modern CT	97
4.1	Volume of Distribution and Excretion	97
4.2	Basic Mechanisms of Contrasting Inside the Body	99
5	Contrast Media in Dual-Energy CT	99
6	Clinical Applications of Dual-Energy Material Decomposition	101
6.1	Oncology Applications	101
6.2	Cardiovascular Applications	102
6.3	Pulmonary Applications	102
7	Summary and Outlook	103
	References	104

H. Pietsch (✉)
Bayer AG, MR and CT Contrast Media Research,
Berlin, Germany

Universitätsklinikum Essen, Institute of Diagnostic
and Interventional Radiology and Neuroradiology,
Essen, Germany
e-mail: hubertus.pietsch@bayer.com

G. Jost
Bayer AG, MR and CT Contrast Media Research,
Berlin, Germany

1 Introduction

Contrast media are an important element in modern computed tomography and are the basis for a profound diagnosis. The number of computed tomography (CT) examinations performed is increasing by approximately 5% each year. In 2020, roughly 280 million CT scans were performed worldwide, and about 50% of these CT examinations were contrast enhanced.

Intravenous iodine-containing low- and iso-osmolar contrast media, such as iopromide or iodixanol, are standard and are commonly used for contrast enhancement in CT imaging (Pietsch et al. 2012).

Thus, the physical properties of these contrast media for X-ray attenuation are limited exclusively to one element—iodine. One option for the future would be the development of contrast media with other contrasting elements, preferably with a much higher atomic number (Nowak et al. 2011; Pietsch et al. 2009).

Such contrast media would be more suitable for higher voltage ranges of the X-ray tube used in CT. On the one hand, this would allow more flexibility in imaging protocols, allowing examinations with lower radiation doses to be made with equivalent diagnostic value (Nowak et al. 2011; Roessler et al. 2016). In addition, these contrast media could allow new applications or indications due to optimized spectral differentiation in X-ray attenuation compared to iodine. Furthermore, iodine-free contrast media would have advantages for patients with known reactions to contrast media or with thyroid disorders.

The continuous technological progress in X-ray imaging and CT should be an incentive for the development of a new dedicated contrast media, as new technologies in detectors and tubes, as well as the application of artificial intelligence algorithms will further develop and improve the next generation of CT scanners in the long term.

2 Iodinated Contrast Media: Current Standard in Safety and Tolerability

Iodinated nonionic contrast media are the standard in contrast-enhanced CT. They were clinically approved and established over 40 years ago. Millions of patients with a wide variety of diseases, multimorbid elderly patients, patients with severe diseases such as generalized atherosclero-

sis, acute cerebral or myocardial infarction, advanced cancer, severe heart failure, impaired renal or hepatic function, and also pregnant women as well as newborns have been given these contrast media via all conceivable routes of administration.

2.1 Structure and Physicochemistry

All currently available iodinated contrast media are based on the tri-iodinated benzene ring. They are classified, based on the presence of 1 or 2 tri-iodinated benzene rings, as monomeric or dimeric, and based on the electric charge of the molecule, as ionic and nonionic contrast media, respectively (Pietsch et al. 2012; Schöckel et al. 2020).

The structure and charge of the molecule define the two main physicochemical properties of contrast media:

1. Osmotic pressure or osmolality

High osmolality ionic contrast media (HOCM) such as sodium diatrizoate (Urografin) has an osmolality up to five times higher than that of human blood. In contrast, nonionic low osmolality CM (LOCM) have a markedly lower osmolality than HOCM, which is nonetheless higher than that of blood. Nonionic iso-osmolar contrast media (IOCM) have an osmolality the equivalent to that of blood.

2. Viscosity

The viscosity is a crucial parameter for the flow properties of solutions, which increases with increasing concentration and decreasing temperature in a non-linear relationship. In practice, this factor is relevant for the possible speed of injection of contrast media through a needle or catheter.

At comparable concentrations, dimeric contrast media are much more viscous than monomeric at similar concentrations. All new contrast media developments must take

into account, in addition to excellent tolerability, the physicochemical parameters which are crucial for the application of such agents in CT (Behrendt et al. 2013).

2.2 Tolerability and Safety

In general, iodinated CM have a very high tolerability and safety profile (Rosovsky et al. 1996; Palkowitsch et al. 2013; Dawson 2006). The known types of adverse reactions after application can in principle be divided according to their pathophysiology into idiosyncratic dose-independent hypersensitivity reactions or organotoxic dose-dependent reactions. Hypersensitivity reactions are allergy-like and are not immunomodulated. Direct biological reactions to the administration of the molecules of iodinated CM solution and their physicochemical properties are, for example, contrast media-induced nephropathy (CIN) following intra-arterial administration (e.g., cerebral angiography). Furthermore, reactions involving thyroid function due to free iodide can also be regarded as such. Mild and transient adverse reactions are observed in up to 3% of patients after intravenous injection of nonionic compounds. Nevertheless, some rare but occasionally serious adverse reactions to iodine-containing contrast media may occur. In patients with a serious thyroid dysfunction, these include the effects of free iodide, which may be present in contrast media in the smallest traces or may be generated in the body itself following administration. Adverse reactions are usually observed more frequently with ionic than with nonionic contrast media (Schöckel et al. 2020; Kopp et al. 2008).

Adverse effects of contrast media are also categorized according to the time of their occurrence:

- acute (up to 1 h following injection),
- delayed/late (between 1 h and 7 days following injection),
- very late reactions (more than 1 week following injection of an iodine-containing CM).

By far the most common reactions occur within 1 h and are usually mild and self-limiting (Dawson 2006).

2.3 LOCM, the Reference Standard

The properties of LOCM, in particular, its safety profile, set a high standard. All new contrast media to be developed for CT must have comparable characteristics. The molecules must be characterized by a high hydrophilicity and solubility in order to achieve a low viscosity and low osmolality in the final formulation, combined with high stability (important for manufacturing, basic requirement for autoclavability).

The important basics for good tolerability *in vivo* are lowest possible protein binding, and no metabolism in the body as a basis for rapid and complete renal elimination (Jost et al. 2009).

A new contrast agent must compete with all these important properties.

3 The Technology Is a Determining Factor for the Efficiency of Contrast Media

The diagnostic capabilities and performance of today's contrast media is still largely dependent on or influenced by the radiological technology used and has changed drastically and effectively over the evolutionary stages, particularly of CT machine development. Compared with conventional X-ray, computed tomography has significantly improved the effectiveness of iodinated CM (Schockel et al. 2020).

In CT, in addition to the concentration of the contrasting element on site, the high sensitivity of the CT techniques is also the basis for the detection and spatially resolved visualization of iodinated CM. In contrast, in standard projection X-ray procedures, such as angiography, only the amount of iodine present along the path of the X-ray radiation penetrating the object is relevant (Fig. 1).

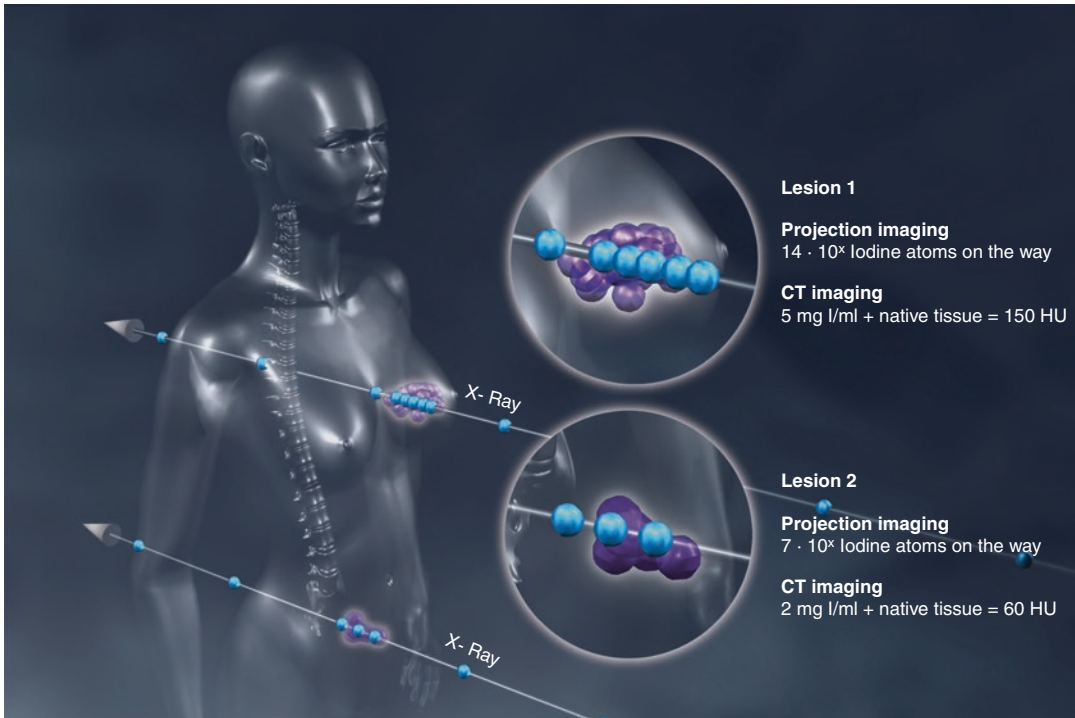


Fig. 1 Comparison of the contrast in 2D radiography versus CT

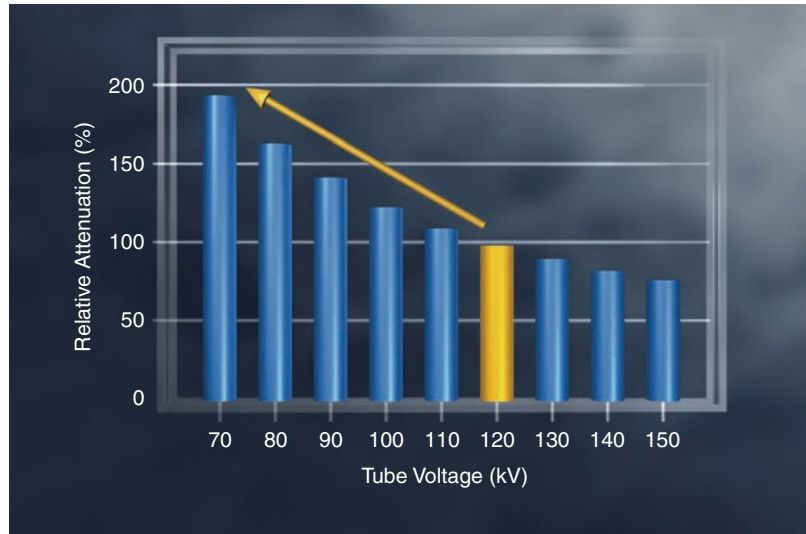
The modern CT is much more sensitive to iodine than conventional X-ray imaging. Projection radiography requires at least 20 mg iodine/ml to visualize tissue with a thickness of 1 cm (Langer et al. 1985). This is demonstrated by an example of angiography: despite very high dosages of contrast media, which are rapidly and locally injected, intravenous DSA has a relatively low sensitivity to iodine. In contrast, CT is able to clearly visualize iodine concentrations of 1 mg/ml in a volume of less than 0.1 ml. The CT attenuation given in Hounsfield units (HU) is based on the linear attenuation coefficient μ , which describes how monochromatic X-rays are attenuated when they pass through an object along the path they cross. However, it is not identical to this as μ strongly depend on the X-ray energy and in turn to the X-ray tube spectrum. Therefore, on the HU scale the CT values are normalized to the attenuation of water to correct for different X-ray tube voltages and filtrations.

Today, modern CT uses tube voltages between 70 and 150 kV (Lusic and Grinstaff 2013). The use of tube voltages in the range of 70–100 kV yields greater iodine attenuations up to a factor of two compared to 120 kV (Fig. 2). The resulting increase in sensitivity to contrast media can be used to reduced radiation dose and/or contrast media dose specifically to the patient or to increase image quality in certain indications (Fleischmann et al. 2018). The introduction of high-power X-ray tubes allows CT imaging at lower kV for multiple indications and for a broad patient population.

The development and widespread use of interactive reconstruction techniques further increased the sensitivity for visualization of iodine enhancement by reducing the image noise level.

A further step is the wide availability of different dual-energy technologies and the introduction of counting detectors in CT, with the potential for spectral imaging. This offers great opportunities and will change the use and spectrum of contrast media (Flohr et al. 2006).

Fig. 2 Increasing attenuation of iodine at lower tube voltages. Samples of Ultravist containing solutions were investigated in a human equivalent body phantom. Measurement was performed in a dual-source CT Siemens Somatom Force



4 Pharmacokinetics of Iodinated Contrast Media and Their Relevance for Modern CT

With the introduction of CT, the clinical significance and the huge diagnostic benefit of contrast media became evident, as the majority of necessary diagnoses in CT can only be achieved with the use of contrast media. The first clinical application of iodine-containing contrast media after intravenous injection was visualization of the urinary tract. In addition to urography, contrast media were also used from the beginning to visualize open and enclosed body cavities and blood vessels because they could easily mix with the contents of the organ or body cavities.

4.1 Volume of Distribution and Excretion

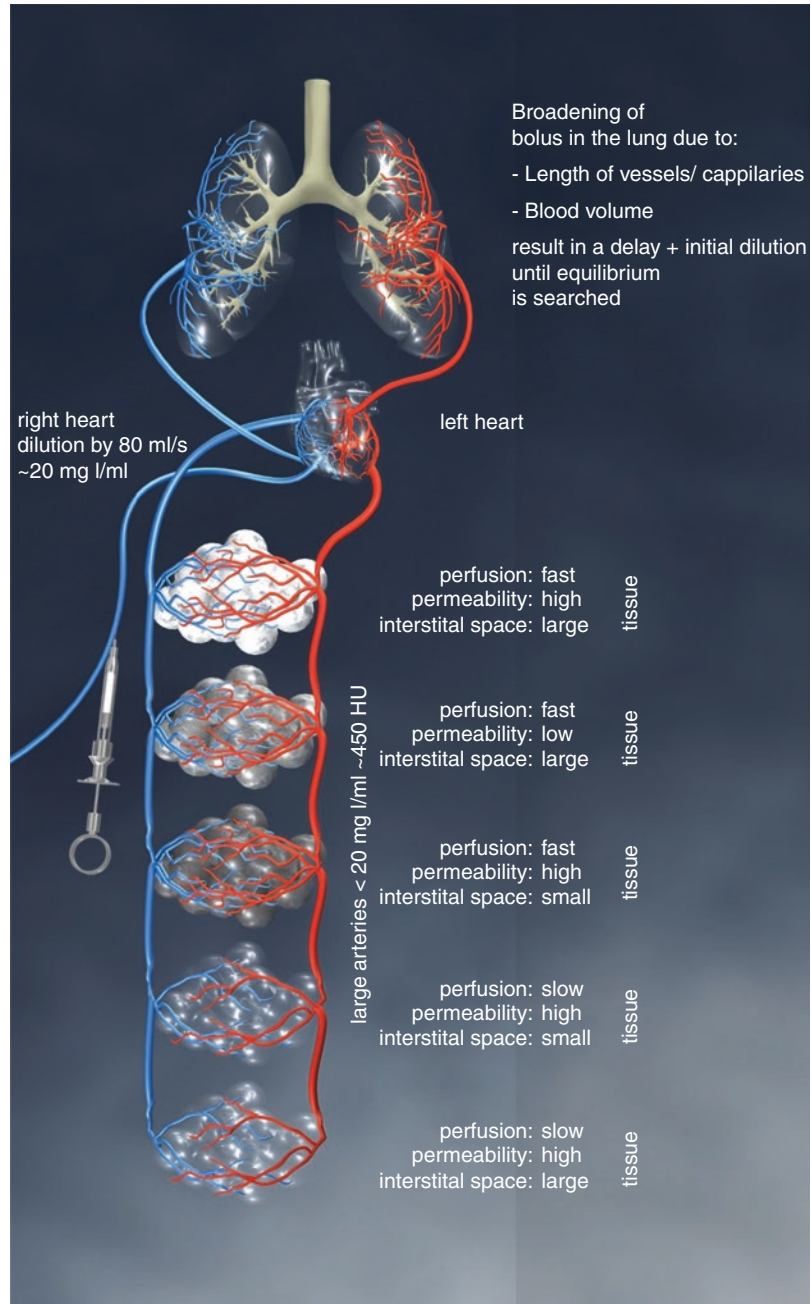
Contrast media cannot pass through cell membranes due to their hydrophilicity. In general, these molecules are very small and do not interact with any parts, membranes or cells of the body, nor should they affect its functionality. Due to their size, they are able to diffuse through tiny pores. The general distribution takes place with the blood flow analogously to the blood circula-

tion of the body. Finally, the contrast media molecules are filtered by the glomeruli, concentrated in the renal tubules, and excreted in the urine (Pietsch et al. 2012).

Because iodinated contrast media can neither penetrate cells of the body nor pass through biological barriers such as the blood–brain barrier, they are also termed extracellular CM (Claussen et al. 1984). This is important for the physician and the patient because these agents are neither absorbed enterically nor do they accumulate in healthy organs or tissues other than the kidney to an extent that can be used for diagnostic purposes. Thus, the iodine-containing contrast media are non-specific in the broadest sense, as they can be circulated throughout the body, with the exception of the central nervous system due to the blood–brain barrier. On the other hand, precisely this feature is the basis for visualizing pathologies within the body, such as inflammation, necrosis, or tumors. All changes or processes in the body that are associated with an increase in the number of blood vessels (angiogenesis), an increase in the permeability of the vessel walls, size changes of the interstitial space, or simply an increased blood perfusion can be visualized with extracellular contrast media (Bae et al. 2000, 2004).

Figure 3 illustrates the pathway of the contrast media into the body following intravenous

Fig. 3 Dilution and early pharmacokinetics of extracellular contrast agents after intravenous injection depend on the perfusion, vascular permeability and size of the interstitial space of the respective tissue
 * Tissue: The interstitial space includes the plasma volume (e.g. 5% of tissue volume, contributing to about 30 HU) and the interstitial space between the cells of the solid tissue (e.g. 10% of tissue volume).



administration and also visualizes the basic mechanisms of the contrasting pathological tissues. Based on a standard human dosage of approximately 1 ml/kg body weight, extracellular CM is injected intravenously at a rate of 3–8 ml/s at concentrations of 300–370 mg iodine/ml. Dilution by the cardiac circulation (–

80 ml/s) and passage through the lungs reduces or dilutes the concentration in the arterial system to about 10 to <20 mg iodine/ml. However, this concentration is still sufficient to result in a contrast enhancement of several 100 Hounsfield units in the arterial blood on CT (Claussen et al. 1984).

4.2 Basic Mechanisms of Contrasting Inside the Body

In addition to the intrinsic perfusion of the tissue, the ability of the contrast medium to diffuse through the tiny pores in the capillaries into the interstitial space is an important prerequisite for contrasting pathological processes in the body. This provides information about the nature of the tissue, as well as the pathophysiological changes characteristic of many diseases. For example, blood flow differs between different tissues in the body and is often increased in inflammation or fast-growing tumors. In contrast, it is heavily reduced in ischemia, in certain tumors and severely restricted or non-existent in necroses or cysts.

The permeability of the vessels can also be described by the contrast medium—which could also differ in the respective tissues of the body. For example, inflammation, angiogenesis, special tumors as well as disruptions of the blood–brain barrier are characterized by an increase in the permeability of the vessels, which in turn leads to altered contrast media concentrations in the interstitial space.

However, this specific distribution is transient, sometimes only for seconds after intravascular injection or during the first passage of the contrast medium through the tissues. It can already disappear in the recirculation phase. The great advantage of CT is the ability to scan the respective organ or the entire body quickly and repeatedly in order to use the specific dynamics and the early distribution pattern of the contrast medium efficiently for diagnosis.

Two fundamental attributes of contrast media are the basic prerequisites for their use in CT: the ability to efficiently absorb X-rays due to the element iodine and, due to the physicochemical properties of the molecules, to depict numerous organs or systems and pathologically altered structures within the human body via the pharmacokinetics. The next step would be to change fundamental properties such as the distribution spaces by adjusting the size of the molecules. It is possible to change the spectral attenuation properties. This can be achieved by replacing the

iodine with elements with a higher atomic number, ideally tuned to the emission spectrum of a modern CT tube. This approach is highly interesting and offers attractive opportunities in the field of dual-energy imaging towards photon-counting detector technology (Flohr et al. 2006; Frenzel et al. 2015; Gutjahr et al. 2016).

5 Contrast Media in Dual-Energy CT

Important clinical applications of dual-energy (DE) CT are contrast-enhanced procedures, for example, the quantification of the iodine uptake in oncology, the evaluation of lung perfusion in case of suspected pulmonary embolism or the characterization of myocardial perfusion defects. The physical basis of these applications is the spectral X-ray attenuation characteristic of iodine, the attenuating element in clinically available X-ray contrast media. In the energy range of CT, the iodine mass attenuation coefficient shows a large energy dependence with a relatively low K-edge energy at 33.2 keV (Fig. 4, upper left). Consequently, the CT attenuation strongly depends on the X-ray tube spectrum, mainly on tube potential and filtering but, to a lesser extent, also on the object composition and size (Fig. 2). Measurements using Ultravist in a thoracic phantom revealed an attenuation of 50.6 HU per mgI/mL at 70 kV that continuously decreased with tube voltage to 21.6 HU per mgI/mL at 150 kV. This more than 2.3-fold difference can be further increased using dedicated filters; the additional 0.6 mm tin filtration available for the third-generation dual-source CT results in a further decrease of attenuation to 11.8 HU per mg I/ml at 150 kV. The improved spectral separation allows a better material decomposition of iodine vs. soft tissue that showed no significant change in attenuation in dependent on the kV setting and filtering. Notably, many innovations in dual-energy CT technology are tailored to the spectral attenuation profile of iodine.

An alternate approach for dual-energy CT is the change of the contrast media attenuating element. Elements with higher K-edge energy

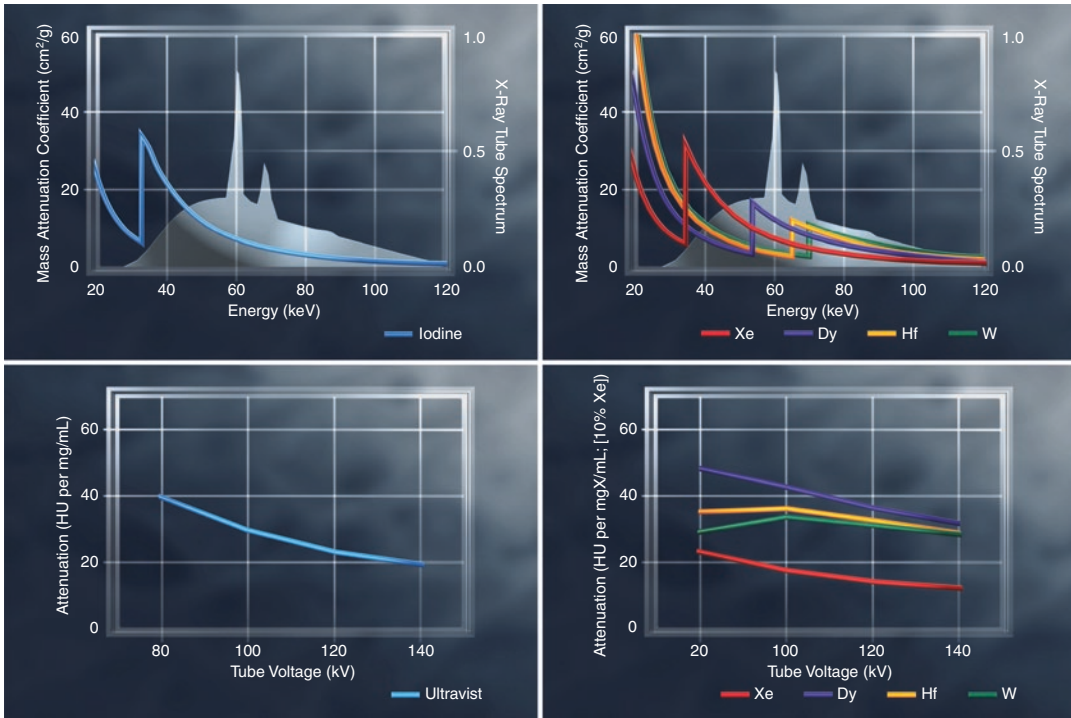


Fig. 4 Spectral X-ray attenuation of Ultravist (Iodine) and alternative promising elements with different k-edge energies as Dysprosium (Dy), Hafnium (Hf), Tungsten (W) and Xenon (Xe). Energy dependent mass attenuation

coefficient superimposed with a typical 120 kV X-Ray spectrum (upper row). Respective CT attenuations at different tube voltages (lower row)

such as dysprosium (53.8 keV), hafnium (65.4 keV), or tungsten (69.5 keV) possess a different spectral mass attenuation coefficient that better match the photon energy distribution of the X-ray tube (Fig. 4; upper right). This results in more similar CT attenuations for the different tube voltages, particularly for tungsten and hafnium. Tungsten, for example, has almost identical attenuations for 70/150 kV or 80/140 kV (Fig. 4, lower right). The total attenuation per mass concentration (mg Dy/mL) is highest for dysprosium. However, the attenuation also shows a significance dependence on tube voltage albeit not at the level of iodine. Another interesting element is xenon (K-edge = 34.65 keV), which possesses a similar attenuation profile with comparable signal ratios between high and low kV than iodine.

Dual-energy adds additional information to the visualization of morphology in CT images. In the context of contrast media, this is realized by computation of a material map usually containing the amount and distribution of contrast media and virtual non-contrast (VNC) images containing anatomical information. Different material decomposition algorithms exist but all require different spectral attenuation characteristics of the materials to be separated. Two-material decomposition algorithms can separate contrast media from endogenous tissues (e.g., iodine and VNC) or a specific endogenous material from contrast media and tissue (e.g., calcium and tungsten/tissue) or even two contrast media (e.g., xenon and tungsten/tissue). Higher order material decomposition algorithms are feasible but also require a higher order of input data and can lead to high image noise levels.

6 Clinical Applications of Dual-Energy Material Decomposition

6.1 Oncology Applications

Iodine, with its large spectral attenuation difference between low and high X-ray energies, can be effectively separated from tissue that has a low or almost no energy-dependent difference in attenuation (Fig. 5, upper right). One of the early dual-source CT studies was the calculation of iodine maps and virtual non-contrast (VNC) images in an experimental liver tumor rabbit model using an investigational iodine-based liver contrast medium to visualize hepatocytes (Fig. 5, lower left). This investigation on a first-generation dual-source CT demonstrated that

the full information about morphology and iodine uptake can be provided by a single dual-energy scan (Flohr et al. 2006). This approach was further evaluated for treatment response monitoring in oncology. Targeted anti-tumor drug therapies as antiangiogenetic drugs or tyrosine kinase inhibitors primarily induce changes in the tumor microvasculature rather than a decrease in tumor size. In an experimental glioma model in rats, treatment effects were successfully monitored with Ultravist enhanced dual-energy CT followed by the quantification of the iodine uptake in the tumor. Notably, the dual-energy method was more effective than conventional single energy CT and showed comparable results at much lower radiation dose than dynamic-contrast enhanced CT (Knobloch et al. 2014).

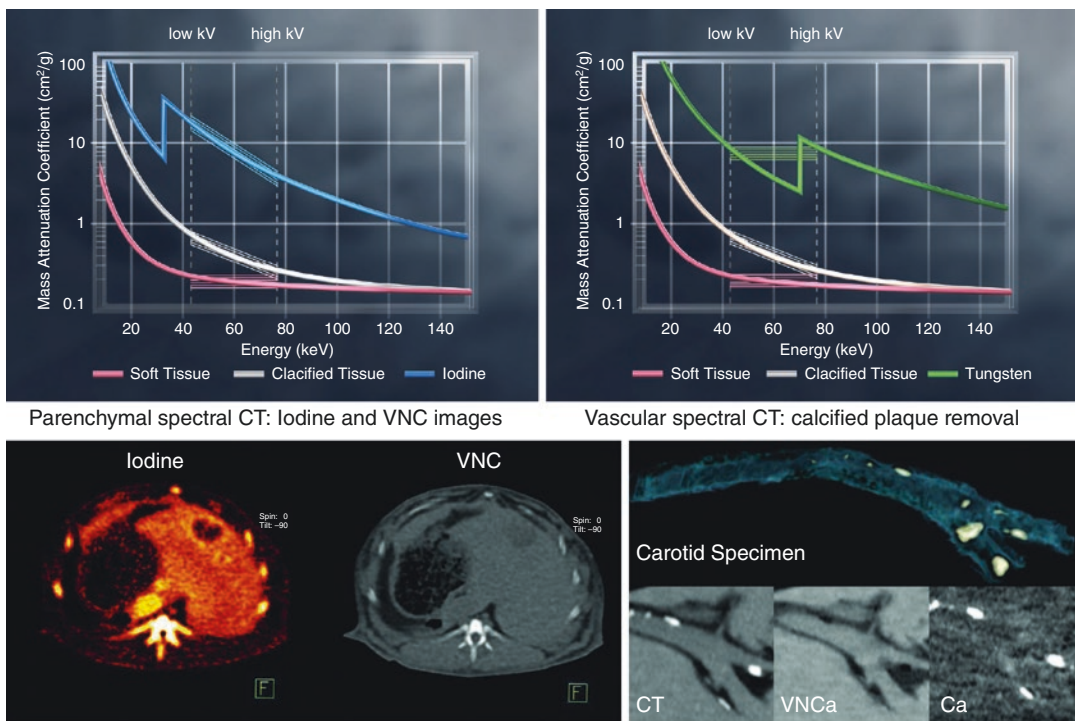


Fig. 5 Spectral X-ray attenuation of iodine, tungsten in comparison to soft and calcified tissues (upper row). The different spectral behavior of iodine and tungsten between low and high tube potentials (marked with triple lines) enables different applications. Material decomposition is used for computation of iodine and virtual non-contrast (VNC) images in parenchymal dual-energy CT. In the rabbit tumor model (lower row left) the iodine map clearly shows

the tumor, while the VNC images shows the morphology (Flohr et al. 2006). In vascular spectral CT tungsten offers accurate calcified plaque removal. In the human carotid artery specimen (lower right) investigated in experimental tungsten-based contrast media solution (15mgW/ml) the lumen narrowing is visible on the virtual non calcium reconstruction (VNCa) and calcium (Ca) burden is visible on the calcium reconstruction map (Sartoretto et al. 2021)

6.2 Cardiovascular Applications

Cardiovascular diseases represent a second major indication for contrast-enhanced CT. Important clinical questions for CT angiography (CTA) are, for example, the accurate assessment of vascular stenosis and the characterization of arteriosclerotic plaques. Dual-energy has a great potential for improving CTA image quality and diagnostic confidence by reducing the negative effects of blooming and beam hardening often induced by calcified plaques. The efficacy of material decomposition between iodinated contrast media and calcified structures is limited, however. The spectral attenuation characteristic of the two materials is similar, resulting in comparable ratios between high and low X-ray energies (Fig. 5, upper left). Contrast media with higher K-edge energies such as tungsten and hafnium can close this gap as they offer a significantly different dual-energy pattern than calcified tissues (Fig. 5., upper right). This in turn improves the material decomposition into virtual non-calcium (VNCA) images containing a contrast medium-soft tissue mixture and a calcium map containing the calcified tissue. The resulting better plaque removal in the VNCA reconstructions and the lower image noise in these images can significantly increase the diagnostic accuracy of vascular imaging. This was demonstrated with a coronary artery stenosis phantom mimicking different degrees of stenosis at different plaque density levels (Sartoretti et al. 2020). The vessel lumen was filled with different investigational contrast media based on tungsten, hafnium, bismuth, holmium, or iodine. Dual-energy imaging was performed with a photon-counting detector CT prototype at energy thresholds optimized for the specific element of the contrast medium. Qualitative and quantitative image evaluation performed on the VNCA images revealed improved image quality and diagnostic evaluability of stenosis for tungsten, hafnium, and bismuth compared to iodinated contrast media. Furthermore, the used tungsten- and hafnium-containing contrast media result in lower VNCA image noise levels. Further experimental evidence was obtained in a similar study on a human carotid artery specimen with athero-

sclerotic plaques (Fig. 5, lower right). In this study the noise levels in the VNCA images were significantly improved by using an experimental tungsten (W_3O_2)-based contrast medium compared to Ultravist as the iodine reference standard (Sartoretti et al. 2021). This results in superior vessel visualization and better vessel wall delineation. Thus, tungsten and hafnium-based contrast media would offer new promising opportunities for cardiovascular dual-energy CT (Berger et al. 2017; Sülzle et al. 2015; Yu and Watson 1999).

6.3 Pulmonary Applications

Several lung diseases such as chronic obstructive pulmonary disease (COPD) are associated with regional ventilation disorders that are difficult to assess with global pulmonary function tests such as spirometry or gas transfer tests. On the other hand, new therapeutic options such as implantation of endobronchial valves or improved lung volume reduction surgery require a precise definition of regional lung function. Xenon-enhanced CT can be used for spatially resolved imaging of lung ventilation. Xenon is a radiopaque gas that can be safely inhaled in concentrations of about 30%. This results in an image enhancement of 20–30 HU (120 kV) in normally ventilated regions. However, subtraction between unenhanced and Xe-enhanced images is challenging because imaging cannot be performed at exactly identical respiration levels. Dual-energy CT circumvents this procedure since the xenon enhancement can be determined at a single time-point (Thieme et al. 2008, 2009). The spectral attenuation of xenon is comparable to that of iodine, leading to a large change in attenuation between low and high X-ray energies (Fig. 4). Thus, a xenon and a lung parenchyma image can be reconstructed using material decomposition techniques.

Another important parameter that can be affected by disease is lung perfusion. Iodine-enhanced dual-energy CT significantly improved the diagnostic workup, as this enables the reconstruction of morphological images and functional

images that visualize perfusion (Dawson 2006). In terms of physiological aspects, pulmonary function depends on lung ventilation and lung perfusion to ensure an effective gas exchange. Both can be affected by disease, i.e., a ventilation/perfusion mismatch is a typical characteristic in COPD patient. The degree of this mismatch and its regional distribution have a potential to improve the diagnosis and therapeutic decisions.

To date, such ventilation and perfusion measurements can be made by means of nuclear medicine method such as SPECT, using radiolabeled gases and tracers in sequential mode. Dual-energy CT might be a promising alternative that may even enable simultaneous lung ventilation and perfusion imaging. Furthermore, it would offer a much higher spatial resolution, an easier examination taking at much less time, and importantly also a high availability of scanning units. However, xenon for ventilation and iodine for perfusion imaging have a very similar attenuation profile and cannot be separated using dual-energy methods. This requires the sequential application of Xe and iodine resulting in repeated scanning and images acquired at different breathing phases or breath-hold levels (Thieme et al. 2008). This might be overcome, however, by using contrast media elements with high K-edge energies such as hafnium and tungsten to visualize pulmonary

perfusion. These elements only show as little or almost no dependence of attenuation on the tube potential and can be effectively separated from xenon by dual-energy material decomposition (Fig. 6a). The feasibility of this approach was demonstrated in a study on healthy pigs. The anesthetized animals were ventilated with a 30% xenon, 70% oxygen mixture for 120 s and an investigational tungsten-based contrast medium was injected in temporal coordination. Repeated dual-energy imaging (80/140 kV) was performed to capture the lung during different contrast medium phases on a third-generation dual-source CT. A xenon material map and a virtual non-xenon (VNXe) image, containing soft tissue and tungsten were reconstructed for each time-point (Fig. 6b). Xenon and tungsten could be clearly separated enabling simultaneous assessment of lung ventilation and perfusion.

7 Summary and Outlook

There had already been systematic investigations of alternatives to iodine as a contrasting element in the early days of X-ray imaging. Since then, numerous contrast media approaches with elements other than iodine have been explored. For a variety of reasons, however, none has made it to

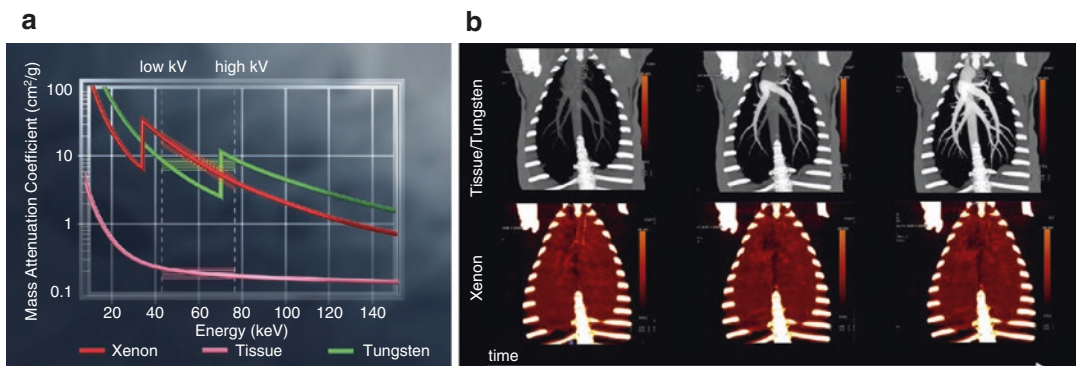


Fig. 6 Separation of two contrast materials. (a) Spectral X-ray attenuation of xenon, tungsten and tissue. The different spectral behavior of xenon and tungsten between low and high tube potentials (marked with triple lines) enables dual-energy-based material decomposition of both contrasting materials. (b) Functional imaging (third

generation Dual Source CT) of the lung in a porcine model. Inhalation of 30% xenon for 2 min followed by intravenous administration of an experimental tungsten-based contrast medium. Xenon and tungsten could be clearly separated enabling simultaneous assessment of lung ventilation and lung perfusion

the market. As described earlier, the advantage of such elements is the higher attenuation of X-rays compared to iodine, which depends on the mass attenuation coefficient of the contrast element and the energy distribution of the X-ray spectrum. Elements with higher atomic numbers and thus higher k-edge energies better fit to the CT tube energy spectrum than iodine. Therefore, elements such as the lanthanides, hafnium, tantalum, tungsten, or even gold are better suited as contrasting elements.

In the recent past, there have been very promising investigations of hafnium with the aim of reducing the radiation exposure in contrast-enhanced CT imaging (Frenzel et al. 2015, 2016; Berger et al. 2017). In this context, the element hafnium was combined with a strongly chelating polydentate ligand. Both the physicochemical properties and the tolerance in animal studies were encouraging. A new generation of multi-dentate tungsten metal clusters with high chemical stability, generally, an essential requirement for CM, was also found (Sülzle et al. 2015). These compounds also proved to be quite well tolerated and showed high solubility in order to achieve high tungsten concentrations comparable to the iodine concentrations of commercial CM.

Another interesting approach are nanoparticles (NPs) which contain the absorbing element in a very high density. Depending on their size and coating, nanoparticles have a different pharmacokinetic profile and biodistribution compared to currently available iodinated CM, thus limiting their distribution to the intravascular space (Dong et al. 2019). One concern is the slow and incomplete elimination of NPs from the body. Gold as a source material for NPs has been experimented with again and again. The problem of rapid and sufficient excretion via the kidneys and the high cost have limited the progress of gold-based NPs for use in humans (Allijn et al. 2013; Cormode et al. 2010).

CT imaging has great clinical utility and can only be partially replaced by other radiation-free techniques. Therefore, reducing the radiation exposure required for CT is an important goal (Schockel et al. 2020; Lusic and Grinstaff 2013; Dong et al. 2019; Shahid et al. 2020). Here, too,

such contrast media could make an important contribution by improving the contrast enhancement per molecule, which would allow, on the one hand, a reduction of the radiation dose with an acceptably higher noise level but the same contrast-to-noise ratio. Alternatively, a better image quality in respect of contrast-to-noise can be obtained with the same radiation dose. Both would allow the use of contrast-enhanced CT in further clinical areas.

In view of the rapid developments in CT technology, the use of CM will continue to be of central importance as an integral part of clinical routine. In particular, the trend spectral CT through photon-counting CT technology will expand the application possibilities of new contrast media with higher atomic numbers. Their spectral attenuation characteristics will certainly allow completely new ways of improved material separation and tissue characterization. This holds great potential to increase diagnostic performance and to enable additional clinical fields and indications.

The development of X-ray technology has always gone hand in hand with the development and continuous improvement of suitable contrast media (Barrs 2006). This will no doubt also continue in the future.

Compliance with Ethical Standards

The manuscript has not been submitted to more than one publication simultaneously. The submitted work is original and has not been published elsewhere in any form or language (partial or complete). The authors have followed the rules for obtaining, selecting, and processing data and have not presented any data, texts, or theories of other authors as if they were their own.

References

- Allijn IE et al (2013) *ACS Nano* 7:9761
- Bae KT, Tran HQ, Heiken JP (2000) *Radiology* 216:872
- Bae KT, Tran HQ, Heiken JP (2004) *Radiology* 231:732
- Barrs TJ (2006) *Am J Health Syst Pharm* 63:2248
- Behrendt FF et al (2013) *AJR Am J Roentgenol* 200:1151
- Berger M et al (2017) *Inorg Chem* 56:5757
- Claussen CD, Banzer D, Pfretzschner C, Kalender WA, Schorner W (1984) *Radiology* 153:365

- Cormode DP et al (2010) *Radiology* 256:774
- Dawson P (2006) *BMJ* 333:663
- Dong YC et al (2019) *Sci Rep* 9:14912
- Fleischmann U et al (2018) *Investig Radiol* 53:264
- Flohr T et al. (2006) Paper presented at the RSNA; 2006, Chicago 2006
- Frenzel T et al (2015) *Investig Radiol* 50:671
- Frenzel T et al (2016) *Investig Radiol* 51:776
- Gutjahr R et al (2016) *Investig Radiol* 51:421
- Jost G et al (2009) *Investig Radiol* 44:114
- Knobloch G, Jost G, Huppertz A, Hamm B, Pietsch H (2014) *Eur Radiol* 24:1896
- Kopp AF et al (2008) *Acta Radiol* 49:902
- Langer M, Felix R, Keysser R, Speck U, Banzer D (1985) *Digitale Bilddiagn* 5:154
- Lusic H, Grinstaff MW (2013) *Chem Rev* 113:1641
- Nowak T, Hupfer M, Brauweiler R, Eisa F, Kalender WA (2011) *Med Phys* 38:6469
- Palkowitsch PK, Bostelmann S, Lengsfeld P (2013) *Acta Radiol* 55:707
- Pietsch H et al (2009) *Eur J Radiol* 80:349
- Pietsch H, Hübner-Steiner U, Seidensticker P (2012) *Ullmann's encyclopedia of industrial chemistry*, 7th edn. Wiley-VCH, Weinheim
- Roessler AC et al (2016) *Investig Radiol* 51:249
- Rosovsky MA et al (1996) *Radiology* 200:119
- Sartoretti T et al (2020) *Invest Radiol*
- Sartoretti T et al (2021) *Atherosclerosis* 310:11
- Schöckel L et al (2020) *Investig Radiol* 55:592
- Shahid I, Lancelot E, Desche P (2020) *Investig Radiol* 55:598
- Sülzle D, Bauser M, Frenzel T (2015) *J Clust Sci* 26
- Thieme SF et al (2008) *Eur J Radiol* 68:369
- Thieme SF et al (2009) *Eur Radiol* 20:2882
- Yu SB, Watson AD (1999) *Chem Rev* 99:2353

Part II

Clinical Applications



Neuroradiological Imaging

Sebastian Winklhofer, Dominik Nakhostin,
and Mohammed Fahim Mohammed

Contents

1	Introduction	110
2	Technical Background and Workflow Considerations	110
2.1	Background	110
2.2	Training Considerations for Technologists and Radiologists	110
2.3	Patient Selection and Scan Acquisition	111
2.4	Protocol and Dose Optimization	112
2.5	Image Reconstruction and Storage	112
2.6	Considerations for Image Interpretation	115
3	Clinical Applications	115
3.1	Introduction to Clinical Applications	115
3.2	Differentiation Between Contrast Staining and Intracranial Hemorrhage	115
3.3	Further Material and Tissue Differentiation	115
3.4	Image Quality, Radiation Dose, and Artifact Reduction	118
3.5	Other Applications of DECT in Emergency Neuroradiology	121
4	Photon Counting	122
5	Outlook and Conclusion	122
	References	123

S. Winklhofer (✉)
Department of Neuroradiology, Clinical
Neuroscience Center, University Hospital Zurich,
University of Zurich, Zurich, Switzerland
e-mail: sebastian.winklhofer@usz.ch

D. Nakhostin
Department of Neuroradiology, Clinical
Neuroscience Center, University Hospital Zurich,
University of Zurich, Zurich, Switzerland

Department of Diagnostic and Interventional
Radiology, University Hospital Zurich, University of
Zurich, Zurich, Switzerland
e-mail: dominik.nakhostin@usz.ch

M. F. Mohammed
Medical Imaging Department – CR and Corporate
Clinical Performance and Innovation Department,
Ministry of the National Guard Health Affairs,
Riyadh, Saudi Arabia
e-mail: mohammedm22@ngha.med.sa

Abstract

Dual-energy computed tomography (DECT) has proven itself as an important innovation in neuroimaging. Technical aspects and practical considerations to incorporate dual-energy scanning into routine practice including patient selection, recommendations for reconstructions, and image interpretation for routine head CT examinations are discussed. Selected established or newly introduced applications have found their way into daily clinical routine, which include various topics such as emergency neuroradiology, stroke imaging, or applications affecting the image quality or radiation dose. In addition, this chapter provides an outlook to the future of spectral neuroimaging including photon-counting detector-based CT and applications for artificial intelligence.

1 Introduction

A new tool in computed tomography based neuroimaging? Yes! Spectral imaging, in particular dual-energy computed tomography (DECT), has proven itself as an important innovation in neuroimaging. DECT has come a long way from its first experimental studies and today is a well-understood and clinically applicable technology in neuroradiology. Current literature does not only demonstrate the feasibility of clinical DECT applications, but also the evidence-based value for the patient. This in itself is very exciting as just a few decades ago the future of CT in neuroimaging in particular was believed to be limited and that the wide availability of MRI would overshadow it in clinical practice.

CT has made great advances and is now increasingly in the focus of modern diagnostic and therapeutical clinical guidelines. One example is the rapidly evolving topic of stroke imaging, where highly relevant clinical decisions (i.e., the decision to treat the patient with a certain therapy such as mechanical thrombectomy or not) are mainly based on CT imaging. Another

example is trauma and emergency imaging, where CT plays a major role in the rapid and accurate triage and diagnosis of patients. DECT might not only add benefit for image interpretation in such clinical situations, but may also reduce the required radiation dose or the number of required follow-up imaging, and therefore might result in a reduction of costs for the health-care system (Wong et al. 2020).

2 Technical Background and Workflow Considerations**2.1 Background**

Here we will discuss technical aspects and practical considerations to incorporate dual-energy scanning into routine practice including patient selection, approaches to image reconstruction, issues related to image storage and recommended reconstructions for routine head CT examinations.

The precise technical principles of the image acquisition are described in detail in the first part of this book. In summary, several dual-energy CT systems are available today which are suitable for neuroimaging. They can be broadly classified into scanner systems with two x-ray sources (dual-source DECT) or with one x-ray source (single-energy DECT). The latter includes several different technical backgrounds including the fast kV switching, the dual-layer detector, the twin-beam or the dual-spiral approach. All of these commercially available techniques of the main scanner vendors have found their way into clinical routine DECT in neuroimaging today.

2.2 Training Considerations for Technologists and Radiologists

To ensure the smooth introduction of a new service, the involvement of key stakeholders and the engagement of technologically and clinically well-trained professionals is essential. Identifying

these dedicated colleagues and training them to be super-users will facilitate an improved transition to the launch of any new service. Assigning a handful of technologists to become super-users by training them on scanning techniques and concepts through in-service lectures, simulated training with the vendors, and hands-on scanning and reconstruction techniques by application specialists or through workshops are all essential to build capacity and improve confidence so that they may scan and troubleshoot as needed. It would also provide them with the judgment needed to adjust protocols as clinically appropriate. They can then transfer knowledge to colleagues and ensure that the service is running efficiently from a technical standpoint.

Similarly, training and capacity building of radiologists begins with an introduction of the applications of DECT through lectures and scientific meetings. Familiarity with the applications can be improved through hands-on or online workshops.

2.3 Patient Selection and Scan Acquisition

The decision to acquire dual-energy scans must be made prospectively on nearly all the current DECT platforms available on the market—the exception being the dual-layer (or “sandwich”) detector DECT platform which can display DECT data retrospectively as the low and high energy x-ray spectra are split at the detector level.

Patients could be selected based on referral departments (e.g., all patients from the oncology or the emergency department), specific clinical indications (e.g., post intra-arterial thrombectomy for stroke, intracranial hemorrhage assessment, etc.) or based on broader criteria, such as the anatomic area assessed (such as all adult brain CTs). To ensure a smooth adoption within the department, the selection criteria must be agreed upon by all stakeholders and a clear algorithm must be created, including what should be the default protocols for certain indications and details on when it is acceptable to switch to single-energy scan mode (for example, in the

case of a highly agitated patient that cannot lay still). Having these algorithms clearly outlined can streamline workflows and avoid confusion at the time of scanning.

Although selective scanning may have the benefit of limiting the workflow impact of introducing DECT into a department’s practice, it is sometimes impossible to predict which patients may benefit from a dual-energy scan. As the list of clinically validated indications of DECT of the head continues to grow beyond what is highlighted in this chapter, it might become extremely challenging to continue updating patient selection criteria based on an indication or prospectively predicted benefit. Alternatively, routine implementation of DECT scans for all patients may be more feasible, especially after gaining more experience with DECT scanning and understanding any potential impact on both technologist and radiologist workflows.

The number and physical distribution of DE-capable scanners is an important consideration in designing the DECT workflow. For example, in practices that have a mix of DE-capable scanners and SECT-only scanners, it may be more practical to scan all or the majority of patients on the DE-capable scanners in DE mode in order to streamline the workflow and improve technologist familiarity with DE techniques and protocols.

However, if a practice or division only has access to a single scanner that offers DECT capabilities (such as a scanner in the emergency department or outpatient imaging centers), the scanner’s technical limitations may guide the decision to selectively scan in the dual-energy mode. For example, while dual-energy scanning time is generally comparable to single-energy acquisitions, some scanners such as earlier rapid-kV switching scanners may have prolonged reconstruction times which may impact patient flow through the department and must be taken into consideration, particularly in emergency settings.

Due to the comparatively small field of view (FOV) associated with scanning of the head, the scanner’s FOV is of little concern when considering single- or dual-energy scan modes.

2.4 Protocol and Dose Optimization

In the last few years, there has been a proliferation of various DE/Spectral CT systems on the market (at least seven by the authors' count), all with unique approaches to image acquisition and data reconstruction. Hence, it would be beyond the scope of this chapter to provide a comprehensive list of protocols suitable for each scanner type. Instead, engaging the vendors is essential. When creating new DECT protocols, we recommend creating a team consisting of a radiologist, technologist, medical physicist, and application specialist from the vendor. A clear expectation of image quality and radiation dose must be outlined at the start. With this approach, protocols can be created with a specific benchmark in mind. The protocols then can be tested on various phantoms to ensure appropriate image quality, noise levels, and radiation dose as outlined by government or institutional guidelines. We recommend testing the protocols on dedicated DECT phantoms which are commercially available. Optimal image parameters have to be adapted according to the available imaging system and to the individual situation and needs of each radiology department.

Similar aspects are valid regarding the injection of contrast materials. However, the amount and the injection rate of iodine are quite similar compared to standard SECT protocols.

It is important to note that DE/Spectral CT scans are either dose-neutral or dose-negative for the majority of indications as compared to SECT scans (van Ommen et al. 2019; Pomerantz et al. 2013a; Neuhaus et al. 2017).

2.5 Image Reconstruction and Storage

Following the acquisition of the raw data, the images are processed and a "single-energy equivalent" image is generated to mimic a 120 kVp acquisition. This may be generated by linear-blended (weighted average or mixed images) techniques which mix data from low and high

energy acquisitions to simulate a single-energy acquisition. Alternatively, virtual monoenergetic images (VMI) reconstructed at 65–70 keV are considered 120 kVp equivalents as well. These basic images should automatically be generated for every scan and sent to PACS for primary interpretation.

The more advanced dual-energy reconstructions may be generated through several approaches, each offering various advantages and drawbacks. Broadly, we can divide reconstruction approaches to automated reconstructions, technologist-driven reconstructions, and radiologist-driven reconstructions. Automated reconstructions may be performed on the CT console or on a dedicated workstation depending on the vendor and the reconstruction options available. For example, the CT console may allow for VMI reconstructions or gray-scale virtual non-contrast images but not colored overlay maps or multiplanar reformats. In addition, scanner console-based reconstruction may limit access to the CT scanner and delay imaging of the next patient, in which case this approach may be unfavorable especially in an already busy department operating near capacity. Hence, workstation-based automation is preferred by the authors whenever available. Another drawback of automated reconstructions is a significant increase in number of images generated per study. In our practice, the number of images in a head CT has increased from an average of 300–400 to 1200–1500 images. This will increase the amount of storage needed and may have a negative impact on study interpretation if the radiologists are not familiar with the additional reconstructions or their clinical use. However, the presence of images at the time of study interpretation increases the likelihood of utilization of DECT reconstructions, especially when radiologists are aware of the clinical applications and method of interpretation.

Technologist-driven image reconstructions could be performed manually at the CT console or on a dedicated workstation, especially if the department has a 3D/advanced imaging lab. The main advantage of this approach is that the reconstructions can be generated on-demand and as

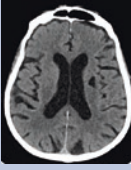
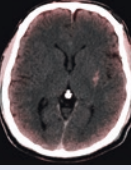

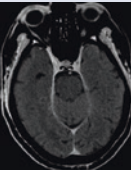
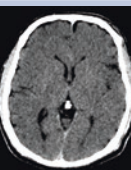
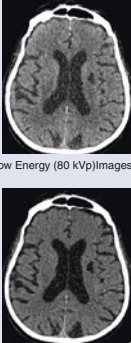
needed based on the findings on the images provided by the available raw data. This may also reduce the load on PACS storage as not all studies will have advanced reconstructions sent for archiving. However, this approach may increase the workload of technologists which may delay scanning of patients or increase turn-around time in the CT room. It also requires that technologists are well trained on DECT systems and their dedicated reconstruction techniques. Another disadvantage of this approach is the possible low utilization of advanced DECT reconstructions by radiologists if they are not readily available at the time of interpretation as they may not be aware that the images were acquired using a DE technique. This could be the case if the image data are not labeled appropriately or due to the loss in productivity by requesting the reconstructions and waiting for them to be sent over to the PACS.

The radiologist-driven approach is usually initiated at the time of image interpretation. The images may be reconstructed at a stand-alone workstation; however, it is in the authors' experience that this approach is the least likely to drive utilization or engagement as it takes away from the task of interpreting the study and negatively affects productivity, particularly in a high-volume radiology setting, such as an emergency radiology department. A more practical approach is the utilization of a thin client—a server-based version of the advanced imaging workstation that can be accessed through the internal hospital network or over the internet—integrated into the PACS. This would allow the radiologist to process the DECT data while interpreting the study. This approach would likely have the lowest impact on the number of images sent for permanent archiving as the radiologist could select and send only the significant and pertinent images, ignoring the rest. It would also improve the radiologist's understanding of DECT reconstructions, improving confidence and encouraging experimentation. However, this approach also has the largest negative impact on the productivity of the radiologist, as each study that requires DECT data reconstruction has to be loaded into the thin client and each algorithm must be processed and assessed individually.

For all cases, the single-energy equivalent images should always be sent to the PACS. Additionally, it is strongly recommended that the DE raw data are sent to PACS as well. This will allow for any additional advanced DE reconstructions should the need arise, enable research, and allow for retrospective application of any new techniques added to the reconstruction software. Additionally, in the case of a non-contrast head CT, we recommend the inclusion of a 65 keV VMI series to improve overall image quality, a 190 keV VMI series to improve detection of intracranial hemorrhage and decrease metal artifacts or streaking artifacts in the posterior fossa and finally, a brain hemorrhage algorithm to differentiate between hemorrhage or calcium. In the case of post intra-arterial thrombectomy, the addition of a colored iodine map and virtual non-contrast (VNC) images is recommended. For post-contrast studies (CTA, CTV, or routine post-contrast), the addition of bone-subtraction images and low keV (40–50 keV) VMI images add value to interpretation (Table 1).

Each practice must identify the scope and goals of implementing a DECT service in their practice. A careful assessment of the pros and cons of each approach and an understanding of how each might impact or compliment the current workflow is essential to the successful integration of DECT into practice. At one of our institutions, a high-volume academic practice, the service was launched by intensive training of the residents and fellows on DECT concepts, techniques, reconstruction methods, and the use of the thin client. The required images were generated by the resident at the time of primary interpretation and were reassessed by the attending radiologist during the final readout. Any additionally required images were generated at readout by the attending. Currently with the increase in familiarity with DECT, the practice has shifted to automated generation of the highest impact reconstructions based on experience and literature, so that the reconstructions are available to all at the time of interpretation without delays in workflow. The projected storage requirements have also been scaled to consider the increase in number of images per study.

Table 1 Commonly utilized DECT reconstructions in clinical practice and their practical applications

DECT Recommended Reconstructions for Head CT	Reconstruction Type	Description	Function	Image Example
	Standard Mixed Images	Single-energy equivalent	First line image assessment	
	Iodine Overlay Images	A fused set of images that displays the distribution of iodine content overlaid on a grey-scale image	<ul style="list-style-type: none"> Assessment of contrast enhancement Differentiating blood vs. iodine 	
	Virtual Monoenergetic Images (VMI)	Extrapolated images that simulate tissue behavior at a single selected energy level (keV)	<p>Intermediate Energy VMI (65-70 keV):</p> <ul style="list-style-type: none"> Improved image quality Reduced posterior fossa artifacts <p>High Energy VMI (140-190 keV):</p> <ul style="list-style-type: none"> Reduced artifacts Improved conspicuity of hemorrhage <p>Low Energy VMI (40-50 keV):</p> <ul style="list-style-type: none"> Increase tissue contrast Increase iodine attenuation 	 <p>190 keV Image to improve detection of subdural hematomas</p>
	Bone-subtracted Images	Subtraction of calvarial bone based on dual-energy material identification and decomposition	<ul style="list-style-type: none"> Allows for improved image reconstruction in post contrast studies May also contribute to improved detection of hemorrhage along the calvarium 	
	Virtual Non-Contrast Images (VNC)	Subtraction of iodine; based on dual-energy material identification and decomposition	<ul style="list-style-type: none"> Complimentary to iodine overlay images Differentiates hemorrhage or calcium from iodine 	 <p>VNC image of the above post-thrombectomy case</p>
	Raw Data	Raw data file or source images used for dual-energy reconstruction	<ul style="list-style-type: none"> Allows for prospective DECT reconstructions 	 <p>Low Energy (80 kVp) Images</p> <p>High Energy (Sn140 kVp) Images</p>

2.6 Considerations for Image Interpretation

When implementing a DECT service for the first time, there may be some apprehension from colleagues due to the sudden introduction of several unfamiliar images into routine imaging studies. It is essential to communicate clearly what changes will be taking place, which images will be included, the clinical value of any additions based on current literature, and how to best utilize any additional images. It is also normal and expected that there will be a learning curve at the launch of the service which may increase the time spent on each study. Creating awareness early on will help with adoption.

A systematic approach to image interpretation will reduce errors. It is our recommendation that for any study, the single-energy equivalent images be utilized for primary interpretation in a similar way to standard practice. The dual-energy reconstructions can then be used as a secondary read and for problem-solving depending on the specific clinical scenario.

3 Clinical Applications

3.1 Introduction to Clinical Applications

A number of promising clinical DECT applications have been introduced and developed in the past years. Selected established and proven applications have found their way into daily clinical routine, which include various topics such as emergency neuroradiology, stroke imaging, or applications affecting the image quality or radiation dose. These may add value to already existing imaging concepts or show new CT applications in neuroimaging.

3.2 Differentiation Between Contrast Staining and Intracranial Hemorrhage

One of the most widely used and accepted applications of DECT in neuroradiology is the differ-

entiation of hyperdensities in a non-enhanced CT (NECT), which could signify both intracranial hemorrhage (ICH) and contrast extravasation (after prior administration of intravenous contrast agent, such as in diagnostic angiographies (DSA)). Zauoak et al. (Zauoak et al. 2020) reported a specificity and accuracy of up to 100% for the differentiation between cerebral hemorrhage and iodine leakage due to a disturbed blood–brain barrier after neurointerventional procedures. A large meta-analysis by Choi et al. (Choi et al. 2020) published in 2020 confirmed the excellent diagnostic performance of DECT in said regard, however showing a relatively large risk of publication bias. In addition, said interventional application also has a direct clinical impact: Chen et al. (Chen et al. 2020) showed that contrast extravasation is a predictor of poor clinical outcomes in patients undergoing endovascular therapy for acute ischemic stroke (Fig. 1).

Furthermore, the generation of virtual non-contrast (VNC) images from contrast-enhanced CT images (particularly CT angiographies) promises to be a valuable tool in order to generate precontrast images without the additional radiation dose of acquiring a true non-contrast image. However, a study from Bonatti et al. from 2017 (Bonatti et al. 2017) showed that intracranial hemorrhages were somewhat less conspicuous on VNC images compared to true non-contrast images and particularly the extent of an ICH might be underestimated in VNC images.

An application which yet has to be scientifically evaluated but shows great potential benefit in contrast-enhanced DECT is the differentiation between hemorrhage and neoplastic contrast enhancing cerebral lesions (hyperdense) within a tumor associated (hyperdense) surrounding hemorrhage, as seen in Fig. 2.

3.3 Further Material and Tissue Differentiation

In addition to differentiating between hemorrhage and iodine from contrast agents, DECT can also differentiate between iodine and cal-

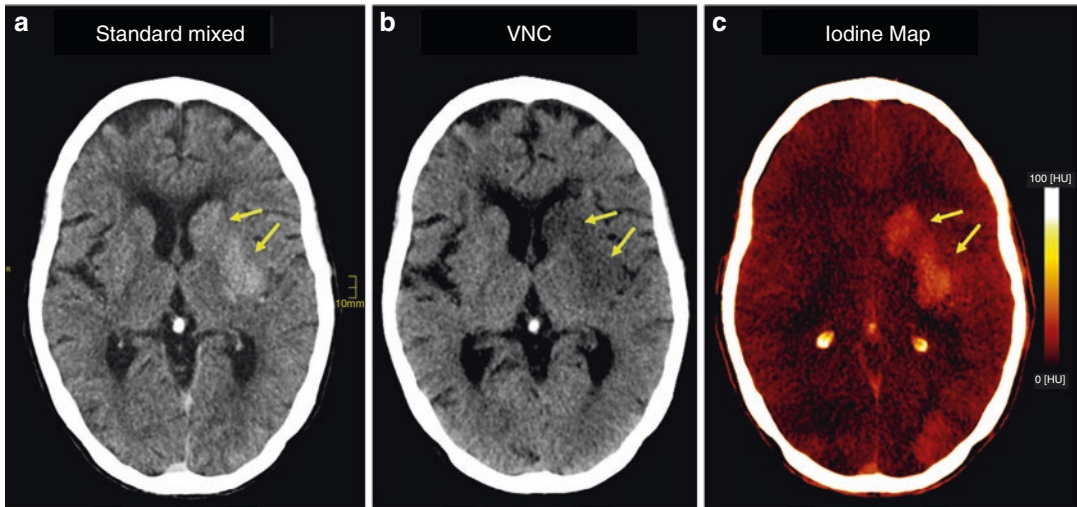


Fig. 1 Dual-energy CT after mechanical thrombectomy in a patient with acute left-sided ischemic stroke. Parenchymal hyperdensities are visible in the left lenticular and caudate nucleus in standard mixed images (a). In this case, it is unclear whether these hyperdensities are due to hemorrhage or iodine extravasation from the previ-

ous thrombectomy. In VNC images (b), the hyperdensities are not visible anymore, indicating the absence of hemorrhage. Iodine images (c) demonstrate color coded hyperdensities in the area of the hyperdensities seen in the mixed images. These findings indicate an iodine extravasation without any intracranial hemorrhage

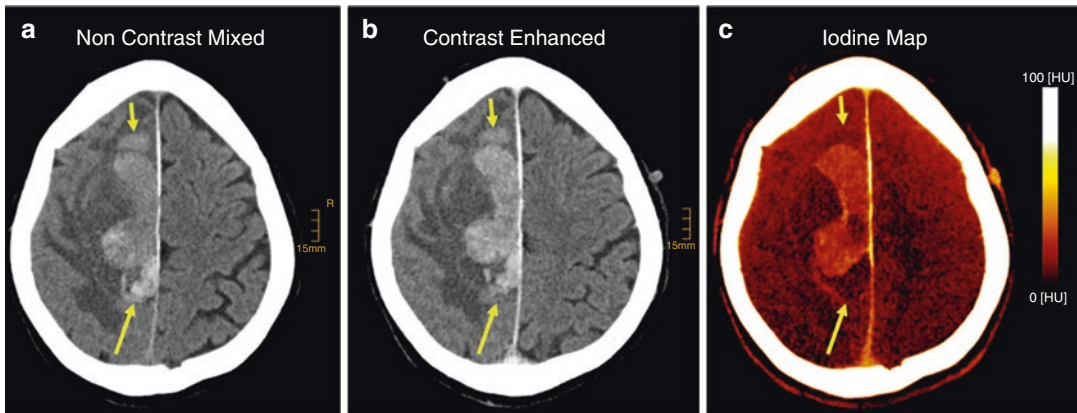


Fig. 2 (a) Non-contrast CT of the head demonstrates a right-sided parenchymal hyperdensity with a perifocal hypodense edema. This scan was interpreted as an intracranial hyperdensity with a potential underlying tumor or vascular malformation. (b) Contrast-enhanced scan demonstrated no obvious enhancement. (c) The iodine map

from DECT demonstrates a color coded part within the hyperdensity in A and B indicating a contrast enhancing tumor. Parts of the hyperdense lesion in A and B do not show iodine uptake in C, indicating hemorrhagic components (arrows). The patient received surgery and histopathology revealed an atypical teratoid rhabdoid tumor

cium containing structures in NECT (Tran et al. 2009). This possibility leads to several clinical applications, among the most frequently used ones being the detection of (intraosseous) calcium and subsequent bone removal (bone subtraction) in CT angiography, providing clear

virtual rendering technique (VRT) or maximum intensity projection (MIP) images for an improved (clinical) vessel visualization (Figs. 3 and 4). Bone subtraction with DECT can be used to avoid artifacts adjacent to the vessel from bony or calcified structures so that vascu-

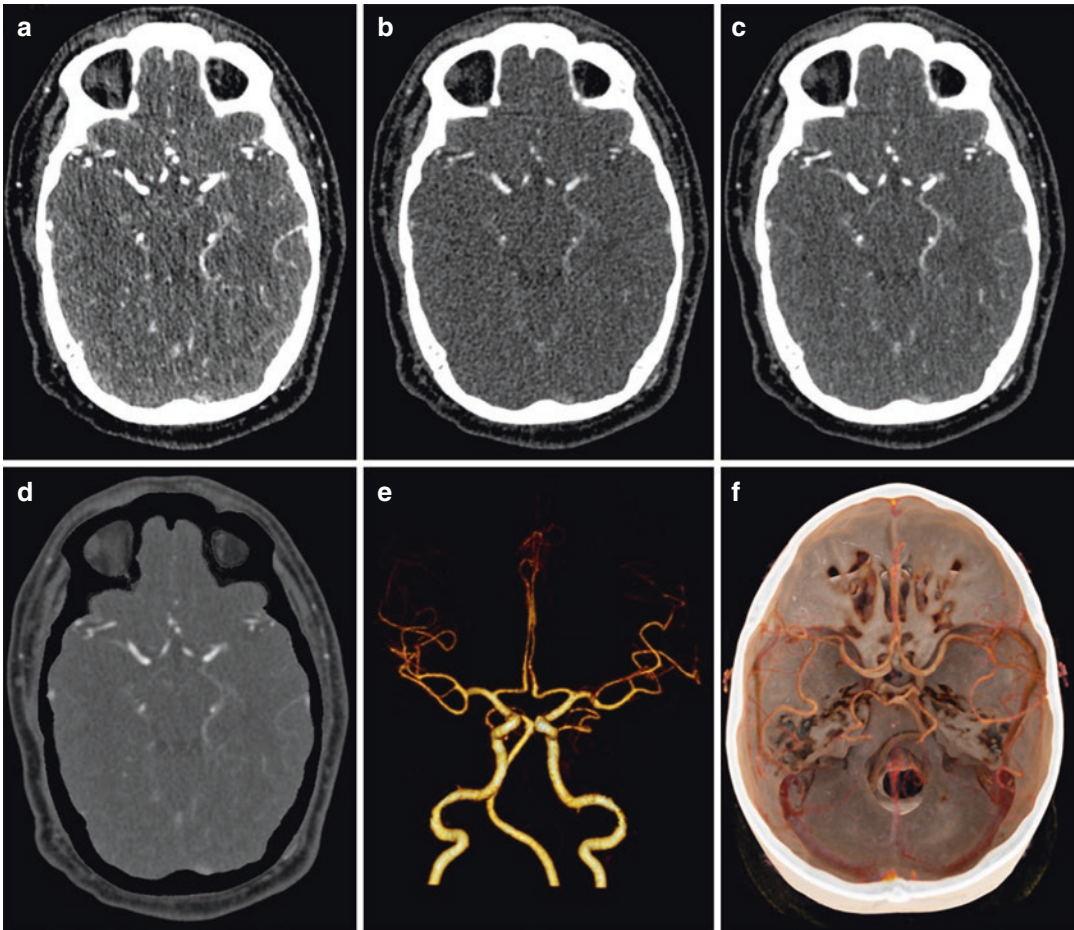


Fig. 3 Arterial phase dual-energy CT angiography with bone subtraction of the intracranial arteries. (a) 80 kVp acquisition, (b) 150 kVp acquisition, (c) mixed (weighted)

image, (d) bone subtraction, (e) volume rendering technique (VRT) for advanced 3-dimensional visualization, (f) cinematic rendering reconstruction

lar pathologies such as aneurysms or vessel stenoses can be nicely visualized (Zhang et al. 2010; Korn et al. 2015) in particular by using VRT or other 3-dimensional rendering techniques. The problem of a potential blooming-associated overestimation of the grade of a vessel stenosis could be overcome by applying an improved and modified 3-material decomposition algorithm for calcium removal as shown by Mannil et al. (Mannil et al. 2017). This approach increases the accuracy of calcified plaques removal and shows similar stenosis degrees as compared to the gold standard of digital subtraction angiography (DSA) images as reference.

Another often encountered problem in neuroradiology, particularly in the emergency setting, is the uncertainty of differentiation of hyperdense foci into (benign) calcifications and intracranial hemorrhage (Fig. 5). Wiggins et al. showed in their 2019 paper that with the application of DECT and subsequent reconstruction of virtual non-calcium and calcium overlay images, the diagnostic accuracies can be improved substantially (Wiggins et al. 2020).

By using a 3-material decomposition in DECT postprocessing with parameters adjusted to suppress the gray/white matter contrast, these reconstructions are able to more accurately detect edema and the end-infarct volume as compared

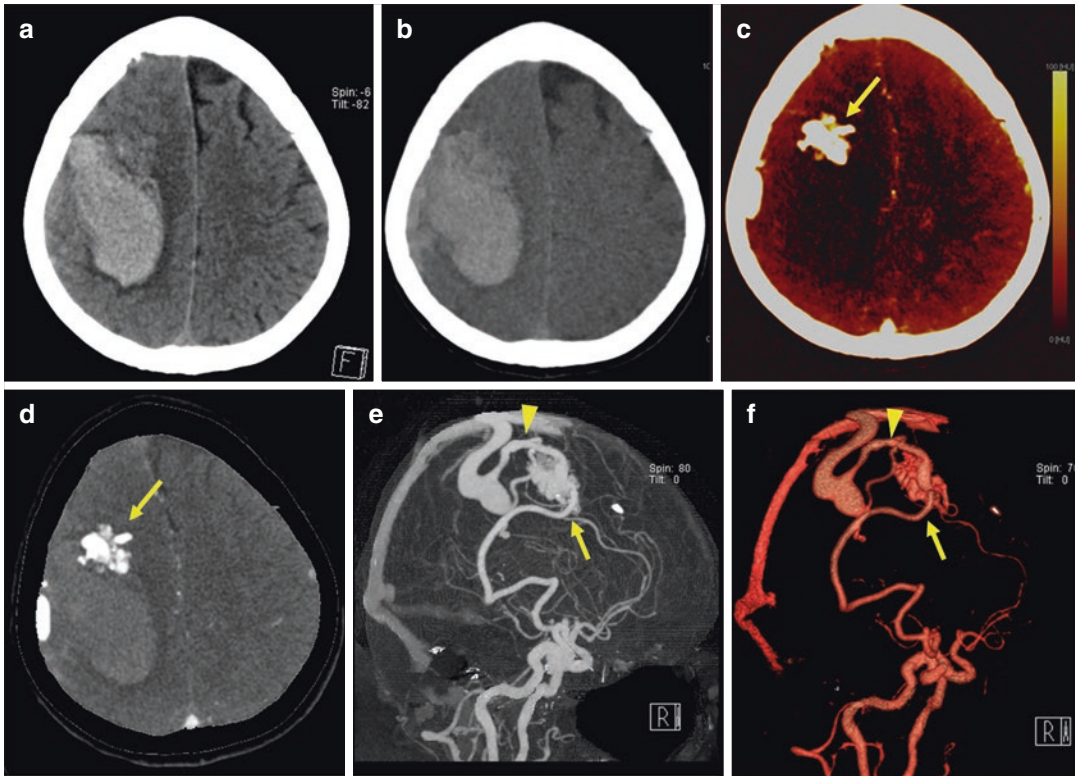


Fig. 4 A patient with a large acute parenchymal hemorrhage seen in a single-energy CT scan of the head (a). Virtual non-contrast (VNC) images (b) reconstructed from the dual-energy CT angiography confirm the presence of hemorrhagic hyperdensities. Iodine images (c) demonstrate a clear iodine containing anterior part of the lesion with a tubular structure. These findings are better

visible in the bone removal images (d) where one can also see enlarged veins indicating an arterio-venous malformation (AVM). 3-D maximum intensity projection (MIP) (e) and volume rendering technique (VRT) (f) reconstructions from DECT allow for a better understanding of the complex malformation with the arterial inflow (arrow) and the venous outflow (arrowhead)

with the initial true non-contrast images. This approach might allow for a better assessment of the degree and extent of infarction and may further serve to better guide stroke therapy (Mohammed et al. 2018; Grams et al. 2018; Taguchi et al. 2018; Hopf-Jensen et al. 2020) (Fig. 6). Other studies showed similar potential benefits for the detection of ischemic brain parenchyma also based on other DECT systems (Lennartz et al. 2018) or DECT reconstructions such as virtual monoenergetic reconstructions (van Ommen et al. 2021).

Furthermore, DECT has been shown to be beneficial for the diagnosis of ischemia in the posterior fossa. The latter is a region which is frequently affected by artifacts due to beam hardening and photon starvation. With DECT, not only

the image quality for the edema assessment can be improved, but DECT also allows to reduce the mentioned artifacts which can be helpful to delineate posterior fossa ischemia. However, sensitivity from DECT is still lower compared to MRI, so that MRI remains to be the preferred modality for lesions in this region (Hixson et al. 2016).

3.4 Image Quality, Radiation Dose, and Artifact Reduction

A prerequisite for the implementation of DECT in everyday clinical practice is an image quality that meets the clinical requirements while at the same time keeping the radiation dose as low as possible. Even if additional information is gained

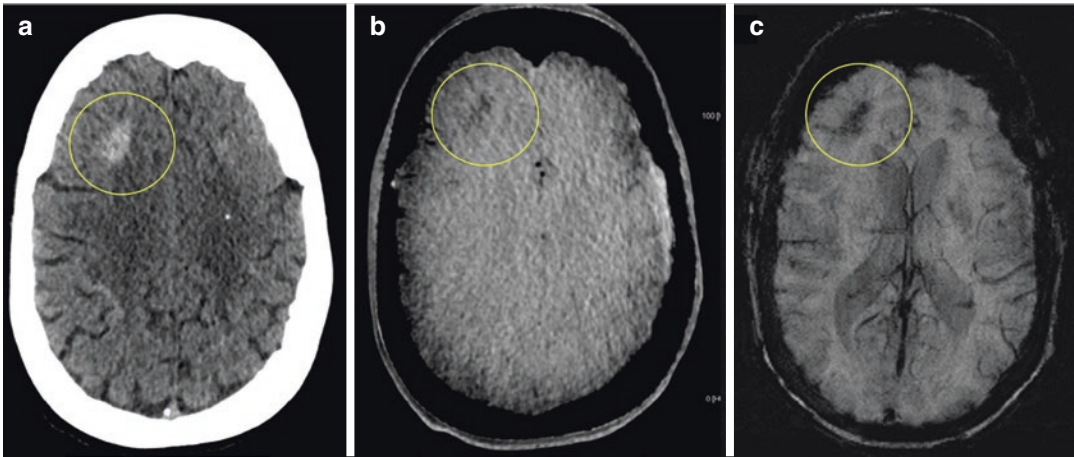


Fig. 5 Differentiation intracranial hemorrhage versus calcifications by using DECT. A faint parenchymal hyperdensity in the right frontal brain which is not easy to be classified as hemorrhage or calcification in standard brain CT (a). Dual-energy can help to answer this challenging question by using virtual non-calcium images (b). The

former hyperdensity is no longer visible, indicating that this is in fact a calcified lesion. This was confirmed by a previous MRI scan in the susceptibility weighted image (SWI) (c) from two years prior to the CT, which was not available at the time of the initial CT (a) evaluation by the radiologist

from spectral imaging, it must be ensured that the two main aspects, image quality and radiation dose, correspond mostly to a standard SECT image acquisition. The SECT equivalent standard weighted (mixed) image reconstruction of the head is used for first-line image evaluation; hence, its quality should be prioritized so that it is indistinguishable from a true SECT acquisition and must be able to show subtle changes of the brain parenchyma for example, as in the case of an acute ischemic stroke.

Weighted average DECT images of the brain have been shown to yield less artifacts at lower radiation doses compared to standard SECT acquisitions. At a comparable dose level, the signal to noise ratio (SNR) has also been shown to be higher and the image noise has been shown to be lower in DECT. However, when comparing the gray matter/white matter (GM/WM) contrast-to-noise ratio (CNR), SECT was superior to DECT (Dodig et al. 2020). Nevertheless, in several studies it has been shown that the latter disadvantage could be compensated by monoenergetic DECT reconstructions and CNR could even be improved compared to polychromatic SECT CT with the same or even lower radiation doses (Neuhaus et al. 2017; Pomerantz et al. 2013b; Zhao et al. 2018; Kamiya

et al. 2013). Furthermore, DECT also has potential image quality applications in pediatric patients. Weinmann et al. showed that DECT can at least maintain or even improve the image quality in pediatric head CT while at the same time significantly reduce the radiation dose (Weinman et al. 2019).

Another often encountered challenge is the differentiation between naturally occurring beam hardening artifacts close to the neurocranium and actual intracranial hemorrhage. Beam hardening occurs when a polychromatic x-ray beam passes through a very dense object (such as the bone in the calvaria), leading to preferential attenuation of low-energy photons and consequent artifacts, such as streaking artifacts. The reconstruction of virtual monochromatic images (at different keV values) allows to virtually reconstruct images which minimize artifacts (particularly in the posterior fossa), while at the same time maintaining a high CNR and signal to noise ratio. Pomerantz et al. showed in their work that the maximum CNR and SNR values were observed at 65 keV while posterior fossa artifacts were best reduced at 75 keV (Pomerantz et al. 2013a).

In addition, another clinical challenge in neuroradiology is beam hardening artifacts associated with surgical clips or endovascular coils

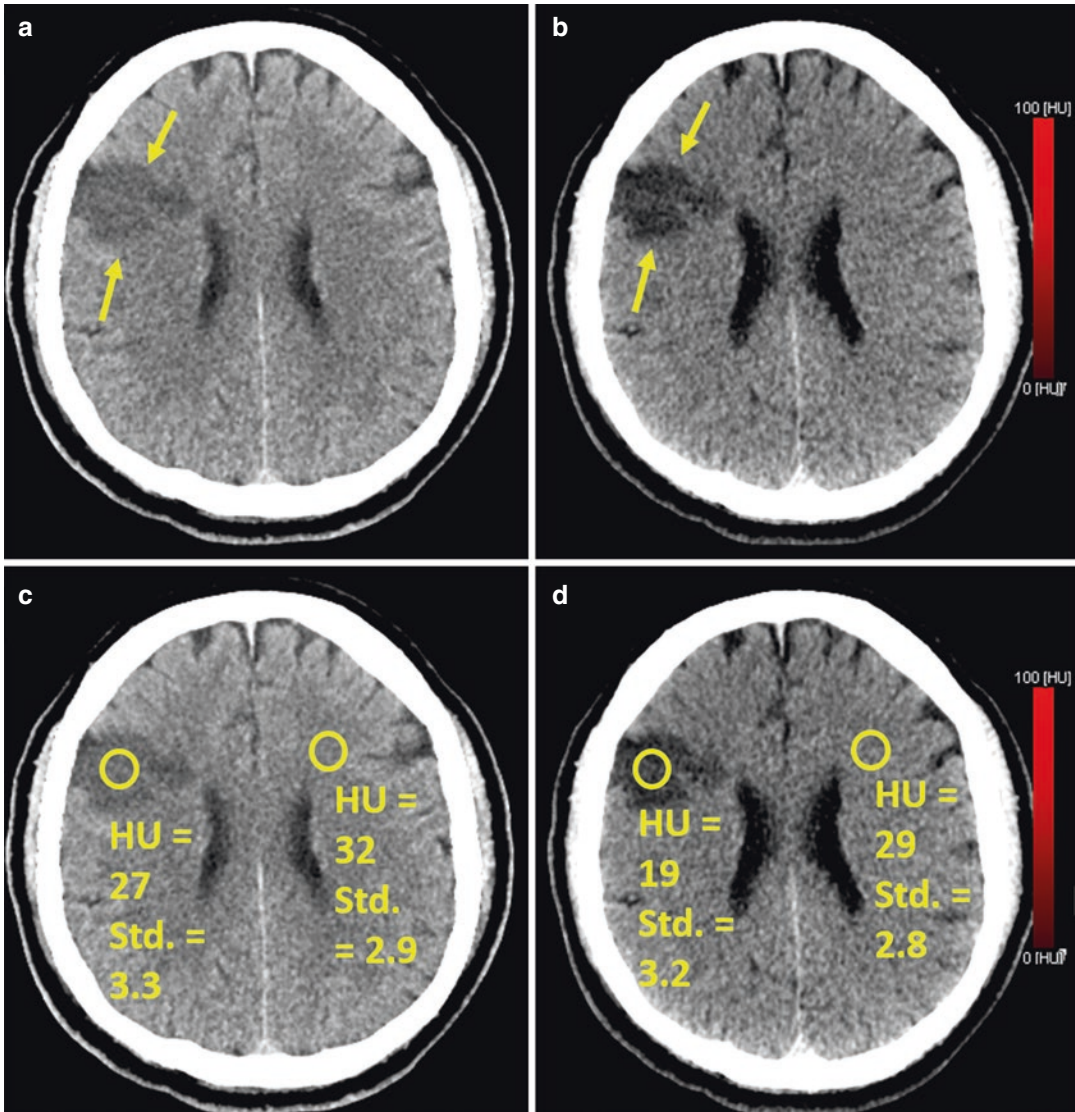


Fig. 6 Improved visibility of ischemic brain parenchyma in a patient with right-sided acute ischemic stroke after mechanical thrombectomy. Standard DECT mixed image (a) demonstrates faint hypodensities (arrows) which are better visible in the VNC images (b) (arrows). Quantitative region of interest (ROI) measurements confirm the

improved visibility of the ischemic stroke with a higher difference between the HU in the ROI in the ischemic parenchyma versus in the healthy parenchyma in the contralateral side in VNC (c) images (difference = 10 HU) compared to standard mixed images (d) (difference = 5 HU)

used for the treatment of intracranial aneurysms. Using DECT and monoenergetic reconstructions (e.g., 95 keV), artifacts from surgical clips can be reduced relatively well, whereas artifacts from endovascular coils can hardly be reduced (Mocanu et al. 2018) (Fig. 7). In another study, it was shown that the usage of virtual monoener-

getic extrapolation from DECT leads to a significant reduction of clip artifacts, especially when used in combination with iterative reconstruction methods (Winklhofer et al. 2018).

The generation of virtual monoenergetic images has numerous other implications for clinical practice, for instance in improving the detec-

tion of early ischemic changes in stroke patients. Ståhl et al. showed in their 2020 work (Ståhl et al. 2020) that with the generation of VMI, a very high diagnostic accuracy regarding early ischemic changes in the cerebral parenchyma could be achieved, with the best result at 70 keV. Karino et al. demonstrated the value of VMI images for the investigation of brain metastasis by DECT. They described an improved tumor visibility with optimal VMI (63 keV) which can supplement an accurate delineation of brain metastases (Karino et al. 2020). Lastly, VMI (particularly at low keV levels) can also lead to superior quantitative image quality in carotid and intracerebral angiography (Leithner et al. 2018).

3.5 Other Applications of DECT in Emergency Neuroradiology

As of recently, DECT has also found its way into the acute setting of emergency radiology. It has been shown that there are several applications regarding the evaluation of intracranial hemorrhages. By using monoenergetic reconstructions from DECT, the reliability to detect traumatic intracranial hemorrhages can be increased compared to standard 120 kV Images. Subdural and epidural hematomas in particular as well as contusions can be better visualized in high keV images (190 keV) as shown by Bodanapally et al. (Bodanapally et al. 2019a). This can be attributed

to the reduced beam hardening artifacts, increased contrast index (CI, a measure of relative prominence compared to background HU) of the hematoma at blood–brain interface, improved spatial resolution, and decreased partial volume averaging rendered by thin-section images.

Bodanapally et al. showed in another paper from 2019 (Bodanapally et al. 2019b) that a pseudohematoma after traumatic hemorrhagic contusion (by means of quantifying iodine leakage in DECT head scans) is a reliable marker of post-traumatic blood–brain barrier permeability, which in turn is predictive of subsequent neurosurgical management. Pseudohematoma was defined as an enhancing penumbra caused by iodine leakage on follow-up 120 kV images. In another paper by the same authors, it could be shown that by analyzing conventional 120 kV images, the size of hemorrhagic cerebral contusions is routinely overestimated, which in turn can be corrected by using a 190 keV image set (Bodanapally et al. 2018). Furthermore, Can et al. showed that in DECT scans by means of properly identifying quantification of iodine extravasation, hematoma expansion in acute cerebral hemorrhage could be reliably predicted (Tan et al. 2019).

If DECT is appropriately included in the clinical workflow, it might not only add benefit by increasing the radiologist image interpretation confidence but also might reduce the need for follow-up imaging as shown in a larger study with 3159 emergency CT scans from all body regions (Wong et al. 2020).

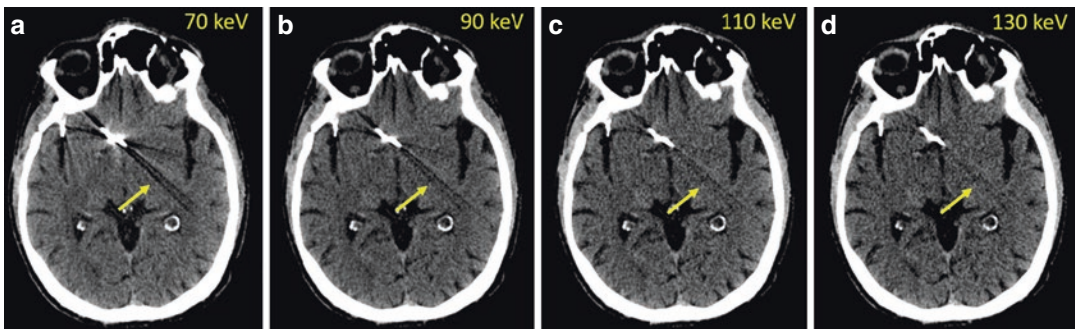


Fig. 7 Dual-energy CT for metal artifact reduction. Severe hypodense streak artifacts are seen in a patient after surgical aneurysm clipping in the standard 70 keV image (a). DECT allows to reconstruct various virtual

monoenergetic images (VMI) with higher or lower keV levels. b–d demonstrate higher keV levels (90–130 keV) with markedly decreasing artifacts (arrows)

4 Photon Counting

Photon-Counting Detector-Based CT (PCD-CT) is currently the subject of intense investigations and is a promising and emerging new development in CT which is based on a high resolution, multi-energy imaging technique. In contrast to DECT where the conventional detector converts x-rays to light and consequently to an electrical signal, photon-counting detectors do not convert the x-ray photons to light, but directly to electrical pulses. The energy of the x-ray of each photon is determined by the magnitude of the electrical pulse. This results in the ability to also register spectral information with multiple (more than two) energies (Rajendran and McCollough 2020; Willeminck et al. 2018). Details about the technical background of PCD-CT can be found in the chapters “Basic Principles and Clinical Applications of Photon-Counting CT” and “Photon-Counting CT: Initial Clinical Experience” of this book. Several prototypes of PCD-CT are currently under investigation and the first commercial systems for clinical applications available. The major advantages are the increased spatial resolution and the potentially lower radiation dose compared to conventional single-energy or current DECT systems (McCollough et al. 2015; Rajiah et al. 2020; Zhou et al. 2019). This ultra-high resolution capability enables a substantially better delineation of fine anatomy, e.g., for the temporal bones or the sinuses compared to standard clinical CT imaging with even a potentially lower radiation dose (Rajendran et al. 2020; Zhou et al. 2018). A higher soft-tissue contrast and lower image noise for photon-counting CT allows for an improved gray-white matter contrast compared with conventional CT as shown by Pourmorteza et al. (Pourmorteza et al. 2017). Other potential applications of PCD-CT include advanced metal artifact reduction (Do et al. 2020; Sigovan et al. 2019), the differentiation of blood and iodine (Riederer et al. 2019), and improved vascular imaging (Harvey et al. 2019) (Mannil et al. 2018).

5 Outlook and Conclusion

With the increasing availability and implementation of DECT systems, its future impact in clinical neuroimaging will further increase. New DECT techniques might be available and already established systems will be improved.

One example is the recent revival of the dual-spiral technique by one of the major vendors which is actually the earliest and simplest way to obtain DECT data, in which the patient is examined using two CT spirals in quick succession. What initially started as the beginning of DECT imaging could now be optimized so that the spectral examination can be performed in a dose-neutral fashion with high quality on single source DECT scanners.

New DECT or multi-energy contrast agents are currently under investigation as specific disease biomarkers or for local disease determination (Gutjahr et al. 2021). Biocompatible high-atomic number contrast materials with a different biodistribution and a different x-ray attenuation than iodine might expand the diagnostic power of DECT or multi-energy CT without an increase of the scan time or the radiation dose (Yeh et al. 2017).

Also, AI might play a role for DECT by means of data acquisition, data postprocessing, and data reconstruction. One example is the application of Deep Learning to improve the image quality while reducing the required radiation dose at the same time in pediatric patients (Lee et al. 2020). Another truly interesting aspect has been recently investigated: DECT information could be generated from SECT images by using Deep Learning approaches. This could allow to gain the benefits of DECT such as monoenergetic reconstructions or material differentiation from a non-DECT single-energy acquisition (Liu et al. 2021; Kawahara et al. 2021; Cong et al. 2020). The results of the preliminary research indicate great potential; however, the approach has to be clinically validated in the future, but might heavily influence future CT imaging with several potential applications.

With the upcoming implementation of clinical photon-counting scanners, multi-energy CT imaging will reach a new era and as a result, these technical advantages may be translated into advantages for the patients.

Spectral imaging has developed into a powerful tool in neuroimaging and potential applications have been increasing over the past decade with many other highly interesting and promising projects currently under development. A growing number of studies are available which demonstrate that physicians and subsequently patients substantially benefit from selected technical innovations implemented in clinical routine. A key driver of this adoption will be an optimization and standardization of workflows in the future. To increase the utilization of spectral neuroimaging, vendor-neutral approaches must be adopted, and the ability to seamlessly view and process DECT images within PACS is of utmost importance.

Nevertheless, the implementation of these advantages into the daily operation of a radiology institute requires some effort which emphasizes the need for further technical improvements and an optimized workflow in each individual radiology department.

Compliance with Ethical Standards

Disclosure of Interests No financial disclosure. No ethical conflict.

References

- Bodanapally UK, Shanmuganathan K, Issa G, Dreizin D, Li G, Sudini K et al (2018) Dual-energy CT in hemorrhagic progression of cerebral contusion: overestimation of hematoma volumes on standard 120-kV images and rectification with virtual high-energy monochromatic images after contrast-enhanced whole-body imaging. *AJNR Am J Neuroradiol* 39(4):658–662
- Bodanapally UK, Archer-Arroyo KL, Dreizin D, Shanmuganathan K, Schwartzbauer G, Li G et al (2019a) Dual-energy computed tomography imaging of head: virtual high-energy monochromatic (190 keV) images are more reliable than standard 120 kV images for detecting traumatic intracranial hemorrhages. *J Neurotrauma* 36(8):1375–1381
- Bodanapally UK, Shanmuganathan K, Gunjan YP, Schwartzbauer G, Kondaveti R, Feiter TR (2019b) Quantification of iodine leakage on dual-energy CT as a marker of blood-brain barrier permeability in traumatic hemorrhagic contusions: prediction of surgical intervention for intracranial pressure management. *AJNR Am J Neuroradiol* 40(12):2059–2065
- Bonatti M, Lombardo F, Zamboni GA, Pernter P, Pozzi Mucelli R, Bonatti G (2017) Dual-energy CT of the brain: comparison between DECT angiography-derived virtual unenhanced images and true unenhanced images in the detection of intracranial haemorrhage. *Eur Radiol* 27(7):2690–2697
- Chen Z, Zhang Y, Su Y, Sun Y, He Y, Chen H (2020) Contrast extravasation is predictive of poor clinical outcomes in patients undergoing endovascular therapy for acute ischemic stroke in the anterior circulation. *J Stroke Cerebrovascular Dis Off J Natl Stroke Assoc* 29(1):104494
- Choi Y, Shin N-Y, Jang J, Ahn K-J, Kim B-S (2020) Dual-energy CT for differentiating acute intracranial hemorrhage from contrast staining or calcification: a meta-analysis. *Neuroradiology* 62(12):1617–1626
- Cong W, Xi Y, Fitzgerald P, De Man B, Wang G (2020) Virtual monoenergetic CT imaging via deep learning. *Patterns (N Y)* 1(8):100128
- Do TD, Sawall S, Heinze S, Reiner T, Ziener CH, Stiller W et al (2020) A semi-automated quantitative comparison of metal artifact reduction in photon-counting computed tomography by energy-selective thresholding. *Sci Rep* 10(1):21099
- Dodig D, Kovačić S, Matana Kaštelan Z, Žuža I, Benić F, Slaven J et al (2020) Comparing image quality of single- and dual-energy computed tomography of the brain. *Neuroradiol J* 33(3):259–266
- Grams AE, Djurdjevic T, Rehwald R, Schiestl T, Dazinger F, Steiger R et al (2018) Improved visualisation of early cerebral infarctions after endovascular stroke therapy using dual-energy computed tomography oedema maps. *Eur Radiol* 28(11):4534–4541
- Gutjahr R, Bakker RC, Tiessens F, van Nimwegen SA, Schmidt B, Nijsen JFW (2021) Quantitative dual-energy CT material decomposition of holmium microspheres: local concentration determination evaluated in phantoms and a rabbit tumor model. *Eur Radiol* 31(1):139–148
- Harvey EC, Feng M, Ji X, Zhang R, Li Y, Chen GH et al (2019) Impacts of photon counting CT to maximum intensity projection (MIP) images of cerebral CT angiography: theoretical and experimental studies. *Phys Med Biol* 64(18):185015
- Hixson HR, Leiva-Salinas C, Sumer S, Patrie J, Xin W, Wintermark M (2016) Utilizing dual energy CT to improve CT diagnosis of posterior fossa ischemia. *J Neuroradiol* 43(5):346–352
- Hopf-Jensen S, Anraths M, Lehrke S, Szymczak S, Hasler M, Müller-Hülsbeck S (2020) Early prediction of final infarct volume with material decomposition images of dual-energy CT after mechanical thrombectomy. *Neuroradiology*

- Kamiya K, Kunimatsu A, Mori H, Sato J, Akahane M, Yamakawa T et al (2013) Preliminary report on virtual monochromatic spectral imaging with fast kVp switching dual energy head CT: comparable image quality to that of 120-kVp CT without increasing the radiation dose. *Jpn J Radiol* 31(4):293–298
- Karino T, Ohira S, Kanayama N, Wada K, Ikawa T, Nitta Y et al (2020) Determination of optimal virtual monochromatic energy level for target delineation of brain metastases in radiosurgery using dual-energy CT. *Br J Radiol* 93(1106):20180850
- Kawahara D, Saito A, Ozawa S, Nagata Y (2021) Image synthesis with deep convolutional generative adversarial networks for material decomposition in dual-energy CT from a kilovoltage CT. *Comput Biol Med* 128:104111
- Korn A, Bender B, Brodoefel H, Hauser TK, Danz S, Ernemann U et al (2015) Grading of carotid artery stenosis in the presence of extensive calcifications: dual-energy CT angiography in comparison with contrast-enhanced MR angiography. *Clin Neuroradiol* 25(1):33–40
- Lee S, Choi YH, Cho YJ, Lee SB, Cheon JE, Kim WS et al (2020) Noise reduction approach in pediatric abdominal CT combining deep learning and dual-energy technique. *Eur Radiol*
- Leithner D, Mahmoudi S, Wichmann JL, Martin SS, Leng L, Albrecht MH et al (2018) Evaluation of virtual monoenergetic imaging algorithms for dual-energy carotid and intracerebral CT angiography: effects on image quality, artefacts and diagnostic performance for the detection of stenosis. *Eur J Radiol* 99:111–117
- Lennartz S, Laukamp KR, Neuhaus V, Große Hokamp N, Le Blanc M, Maus V et al (2018) Dual-layer detector CT of the head: initial experience in visualization of intracranial hemorrhage and hypodense brain lesions using virtual monoenergetic images. *Eur J Radiol* 108:177–183
- Liu CK, Liu CC, Yang CH, Huang HM (2021) Generation of brain dual-energy CT from single-energy CT using deep learning. *J Digit Imaging*
- Mannil M, Ramachandran J, Vittoria de Martini I, Wegener S, Schmidt B, Flohr T et al (2017) Modified dual-energy algorithm for calcified plaque removal: evaluation in carotid computed tomography angiography and comparison with digital subtraction angiography. *Investig Radiol* 52(11):680–685
- Mannil M, Hickethier T, von Spiczak J, Baer M, Henning A, Hertel M et al (2018) Photon-counting CT: high-resolution imaging of coronary stents. *Investig Radiol* 53(3):143–149
- McCullough CH, Leng S, Yu L, Fletcher JG (2015) Dual- and multi-energy CT: principles, technical approaches, and clinical applications. *Radiology* 276(3):637–653
- Mocanu I, Van Wettere M, Absil J, Bruneau M, Lubicz B, Sadeghi N (2018) Value of dual-energy CT angiography in patients with treated intracranial aneurysms. *Neuroradiology* 60(12):1287–1295
- Mohammed MF, Marais O, Min A, Ferguson D, Jalal S, Khosa F et al (2018) Unenhanced dual-energy computed tomography: visualization of brain edema. *Investig Radiol* 53(2):63–69
- Neuhaus V, Abdullayev N, Große Hokamp N, Pahn G, Kabbasch C, Mpotsaris A et al (2017) Improvement of image quality in unenhanced dual-layer CT of the head using virtual Monoenergetic images compared with Polyenergetic single-energy CT. *Investig Radiol* 52(8):470–476
- Pomerantz SR, Kamalian S, Zhang D, Gupta R, Rapalino O, Sahani DV et al (2013a) Virtual monochromatic reconstruction of dual-energy unenhanced head CT at 65-75 keV maximizes image quality compared with conventional polychromatic CT. *Radiology* 266(1):318–325
- Pomerantz SR, Kamalian S, Zhang D, Gupta R, Rapalino O, Sahani DV et al (2013b) Virtual monochromatic reconstruction of dual-energy unenhanced head CT at 65-75 keV maximizes image quality compared with conventional polychromatic CT. *Radiology* 266(1):318–325
- Pourmorteza A, Symons R, Reich DS, Bagheri M, Cork TE, Kappler S et al (2017) Photon-counting CT of the Brain: in vivo human results and image-quality assessment. *AJNR Am J Neuroradiol* 38(12):2257–2263
- Rajendran K, McCollough CH (2020) Photon-counting detector-based computed tomography. In: Mannil M, Winklhofer SFX (eds) *Neuroimaging techniques in clinical practice: physical concepts and clinical applications*. Springer, Cham, pp 87–94
- Rajendran K, Voss BA, Zhou W, Tao S, DeLone DR, Lane JI et al (2020) Dose reduction for sinus and temporal bone imaging using photon-counting detector CT with an additional tin filter. *Investig Radiol* 55(2):91–100
- Rajiah P, Parakh A, Kay F, Baruah D, Kambadakone AR, Leng S (2020) Update on multienergy CT: physics, principles, and applications. *Radiographics* 40(5):1284–1308
- Riederer I, Si-Mohamed S, Ehn S, Bar-Ness D, Noël PB, Fingerle AA et al (2019) Differentiation between blood and iodine in a bovine brain-initial experience with spectral photon-counting computed tomography (SPCCT). *PLoS One* 14(2):e0212679
- Sigovan M, Si-Mohamed S, Bar-Ness D, Mitchell J, Langlois JB, Coulon P et al (2019) Feasibility of improving vascular imaging in the presence of metallic stents using spectral photon counting CT and K-edge imaging. *Sci Rep* 9(1):19850
- Ståhl F, Gontu V, Almqvist H, Mazya MV, Falk DA (2020) Performance of dual layer dual energy CT virtual monoenergetic images to identify early ischemic changes in patients with anterior circulation large vessel occlusion. *J Neuroradiol = Journal De Neuroradiologie*
- Taguchi K, Itoh T, Fuld MK, Fournie E, Lee O, Noguchi K (2018) “X-Map 2.0” for edema signal enhancement for acute ischemic stroke using non-contrast-enhanced dual-energy computed tomography. *Investig Radiol* 53(7):432–439

- Tan CO, Lam S, Kuppens D, Bergmans RHJ, Parameswaran BK, Forghani R et al (2019) Spot and diffuse signs: quantitative markers of intracranial hematoma expansion at dual-energy CT. *Radiology* 290(1):179–186
- Tran DN, Straka M, Roos JE, Napel S, Fleischmann D (2009) Dual-energy CT discrimination of iodine and calcium: experimental results and implications for lower extremity CT angiography. *Acad Radiol* 16(2):160–171
- van Ommen F, de Jong HWAM, Dankbaar JW, Bennink E, Leiner T, Schilham AMR (2019) Dose of CT protocols acquired in clinical routine using a dual-layer detector CT scanner: a preliminary report. *Eur J Radiol* 112:65–71
- van Ommen F, Dankbaar JW, Zhu G, Wolman DN, Heit JJ, Kauw F et al (2021) Virtual monochromatic dual-energy CT reconstructions improve detection of cerebral infarct in patients with suspicion of stroke. *Neuroradiology* 63(1):41–49
- Weinman JP, Mirsky DM, Jensen AM, Stence NV (2019) Dual energy head CT to maintain image quality while reducing dose in pediatric patients. *Clin Imaging* 55:83–88
- Wiggins WF, Potter CA, Sodickson AD (2020) Dual-energy CT to differentiate small foci of intracranial hemorrhage from calcium. *Radiology* 294(1):129–138
- Willeminck MJ, Persson M, Pourmorteza A, Pelc NJ, Fleischmann D (2018) Photon-counting CT: technical principles and clinical prospects. *Radiology* 289(2):293–312
- Winklhofer S, Hinzpeter R, Stocker D, Baltsavias G, Michels L, Burkhardt J-K et al (2018) Combining monoenergetic extrapolations from dual-energy CT with iterative reconstructions: reduction of coil and clip artifacts from intracranial aneurysm therapy. *Neuroradiology* 60(3):281–291
- Wong WD, Mohammed MF, Nicolaou S, Schmiedeskamp H, Khosa F, Murray N et al (2020) Impact of dual-energy CT in the emergency department: increased radiologist confidence, reduced need for follow-up imaging, and projected cost benefit. *AJR Am J Roentgenol* 215(6):1528–1538
- Yeh BM, FitzGerald PF, Edic PM, Lambert JW, Colborn RE, Marino ME et al (2017) Opportunities for new CT contrast agents to maximize the diagnostic potential of emerging spectral CT technologies. *Adv Drug Deliv Rev* 113:201–222
- Zaouak Y, Sadeghi N, Sarbu N, Ligot N, Lubicz B (2020) Differentiation between cerebral hemorrhage and contrast extravasation using dual energy computed tomography after intra-arterial neuro interventional procedures. *J Belgian Soc Radiol* 104(1):70
- Zhang LJ, Wu SY, Niu JB, Zhang ZL, Wang HZ, Zhao YE et al (2010) Dual-energy CT angiography in the evaluation of intracranial aneurysms: image quality, radiation dose, and comparison with 3D rotational digital subtraction angiography. *AJR Am J Roentgenol* 194(1):23–30
- Zhao XM, Wang M, Wu RZ, Dharaiya E, Feng F, Li ML et al (2018) Dual-layer spectral detector CT monoenergetic reconstruction improves image quality of non-contrast cerebral CT as compared with conventional single energy CT. *Eur J Radiol* 103:131–138
- Zhou W, Lane JI, Carlson ML, Bruesewitz MR, Witte RJ, Koeller KK et al (2018) Comparison of a photon-counting-detector CT with an energy-integrating-detector CT for temporal bone imaging: a cadaveric study. *AJNR Am J Neuroradiol* 39(9):1733–1738
- Zhou W, Bartlett DJ, Diehn FE, Glazebrook KN, Kotsenas AL, Carter RE et al (2019) Reduction of metal artifacts and improvement in dose efficiency using photon-counting detector computed tomography and tin filtration. *Investig Radiol* 54(4):204–211



Head and Neck Imaging

David Zopfs

Contents

1	Head and Neck Oncology	128
1.1	Delineation and Visibility of Tumors.....	128
1.2	Lymph Node Imaging.....	131
2	Salivary Glands	131
3	Inflammation	132
4	Metal Artifact Reduction	132
5	Thyroid and Parathyroid Lesions	135
6	Angiography of the Head and Neck	135
7	Future Directions: Assessment of Therapy Response and Prediction of Recurrence	137
	References	139

Abstract

CT is an important imaging method in the head and neck region and accumulating evidence indicates an added value of dual-energy CT (DECT) reconstructions in this area, especially for head and neck cancer. In general, DECT derived low keV virtual monoenergetic images (VMI) facilitate an increased contrast and subsequently an improved delineation of tumor tissue and its boundaries, vessels, and lymph

nodes. High keV VMI are an established tool in the metal artifact reduction arsenal and are beneficial in the assessment of tumorous cartilage invasion. Material-specific DECT reconstructions, such as quantitative iodine maps might allow for a better tissue characterization or distinction of benign and metastatic lymph nodes. While VMI and iodine maps are both relatively well researched and already in frequent clinical use, data on radiomics is comparatively sparse and principal application across different platforms is not yet given.

Overall, a multiparametric approach of various DECT reconstructions seems most promising to develop a clinically relevant advantage over conventional CT, allowing for

D. Zopfs (✉)
Institute for Diagnostic and Interventional Radiology,
University Hospital Cologne, Cologne, Germany
e-mail: david.zopfs@uk-koeln.de

a more accurate imaging of head and neck pathologies to achieve the best possible patient treatment. The following chapter will provide an overview of the most significant applications of multiparametric DECT in head and neck imaging and outline challenges and obstacles to further deployment, as well as future developments.

1 Head and Neck Oncology

Head and neck cancer causes up to 300.000 cancer deaths each year, representing the 7th most common cancer in men worldwide. Squamous cell carcinomas account for the largest proportion of head and neck cancer (Bray et al. 2018; Forghani 2019). Precise imaging of the head and neck region is essential for initial, pretreatment workup as well as follow-up examinations to allow for adequate treatment decisions. In the initial assessment of newly diagnosed head and neck cancer, one of the crucial points of radiological imaging is to determine the extent of tumor growth and to assess metastatic spread, which both may not be detected in clinical and endoscopic evaluation, thus resulting in a potential upstaging (Forghani 2019). Compared to MRI, CT is more widely available; however, due to its limited soft tissue contrast, precise tumor delineation in CT of the head and neck region may be challenging. Moreover, the head and neck region has a rather difficult anatomy and the tumors are often close to many important anatomical structures - there is no other region where the human body is as narrow in its cross-section. Different DECT derived reconstructions seem a promising tool to mitigate this issue and facilitate a more accurate staging.

1.1 Delineation and Visibility of Tumors

Contrast enhancement and tissue asymmetry are among the underlying mechanisms integral to head and neck cancer identification in cervical

CT examinations. Numerous studies demonstrated the ability of DECT derived low keV virtual monoenergetic images (VMI) to boost contrast in vascularized tumors, resulting in an increased signal-to-noise (SNR) and contrast-to-noise ratio (CNR) of tumorous tissue compared to conventional image reconstructions (Albrecht et al. 2015; Forghani 2019; Forghani et al. 2017; Lohöfer et al. 2018; Roele et al. 2017; Wichmann et al. 2014). While in general 40 keV VMI tend to yield highest SNR and CNR in head and neck cancer, image noise might simultaneously increase at 40 keV, depending on the applied denoising algorithms and technical approach to DECT (Forghani 2019; Große Hokamp et al. 2020). Beyond improved quantitative improvement, low keV VMI similarly enhance subjective image analysis. For example, May et al. reported superior image quality in 40 keV VMI in comparison to conventional images and other VMI levels for a dual-source DECT system (May et al. 2019). Albrecht et al. recommended 55 keV for clinical practice in patients with head and neck cancer (Albrecht et al. 2015). The improvement in detection and delineation of head and neck cancer by low-energy VMI in staging CT examinations has been widely described in many studies. Toepker et al. highlighted the capability of low keV VMI to improve the depiction of tumor margins, which might be especially beneficial in initial assessment of T-stage or for surgical resection planning (Toepker et al. 2014). In general, VMI at 40–60 keV are to be favored when assessing head and neck cancer with individual adjustment depending on the case. While many retrospective studies have demonstrated the benefits of various DECT reconstructions, larger-scale prospective, preferably cross vendor studies exploring the impact on patient treatment and disease outcome are still lacking. Figure 1 illustrates the increase in contrast of hyper vascularized tumor areas in low keV VMI and an enhanced delineation in iodine overlay maps.

1.1.1 Invasion of Cartilage

Adequate assessment of potential cartilage invasion is a cornerstone in the workup of patients with hypopharyngeal or laryngeal cancers, in

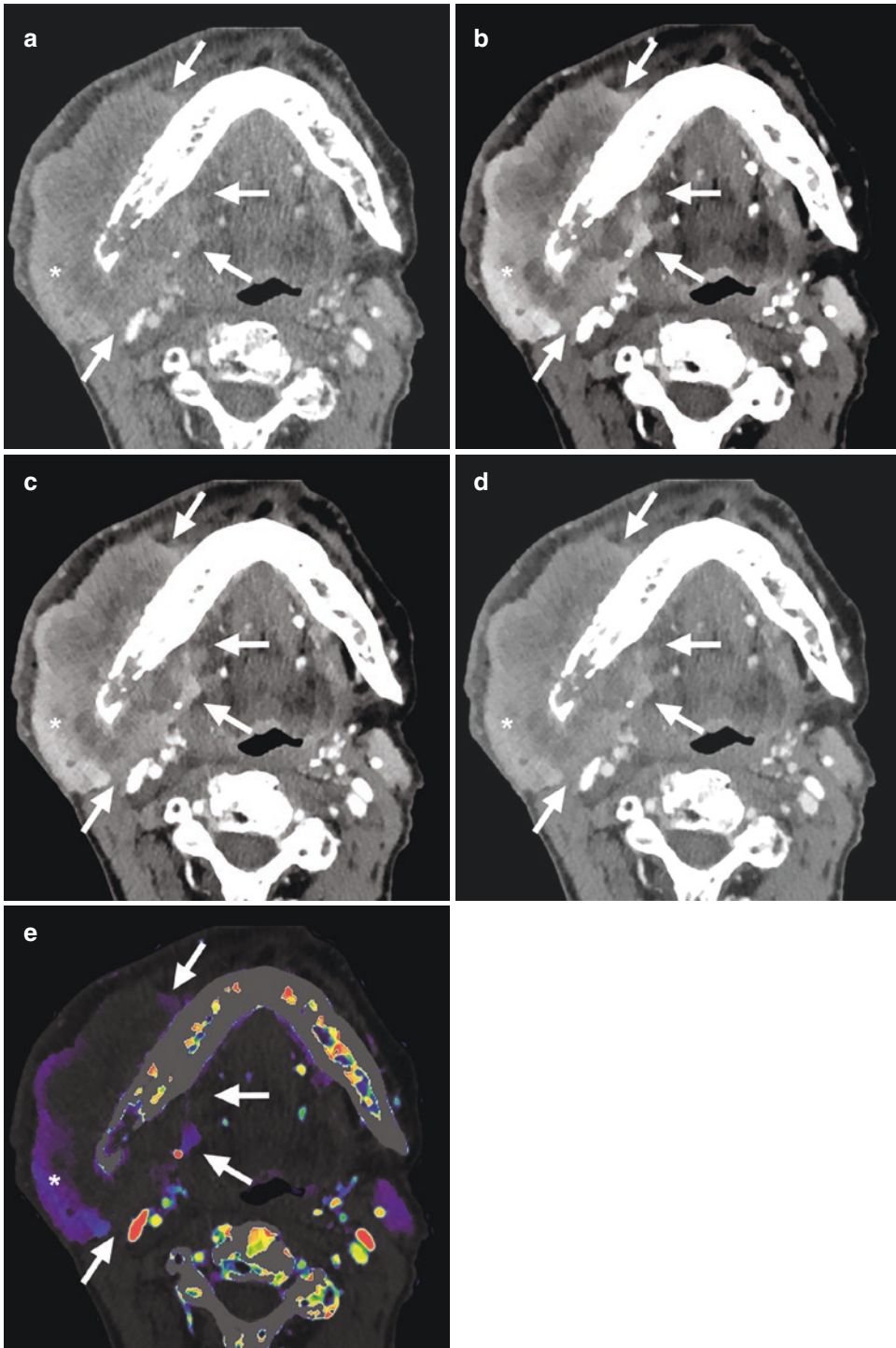


Fig. 1 Initial imaging study of a 73-year-old male patient with histopathological proven squamous cell carcinoma in conventional image reconstruction (a) the contrast between the lesions and liver parenchyma is gradually increased with decreasing keV levels from 70 keV (b) to

60 keV (c), 50 keV (d), down to 40 keV (e). Improved delineation of tumor boundaries (white arrows) can be appreciated in low keV VMI and iodine overlay maps compared to CI. Iodine overlay maps depict areas of necrosis and hypervascularization (white asterisk)

particular detection of thyroid cartilage invasion (Kuno et al. 2014; Pérez-Lara and Forghani 2018). The reason for that being that the presence/absence of cartilage invasion has a direct impact on treatment strategies: If cartilage invasion is present, more aggressive surgical treatment is needed while larynx-preserving strategies may be advantageous in patients without cartilage invasion (Kuno et al. 2012, 2014; Roele et al. 2017; Sheahan 2014). Detection of cartilage invasion with CT is challenging, as non-ossified cartilage and tumor show a considerable overlap in HU values (Kuno et al. 2012; Roele et al. 2017), rendering accurate delineation rather difficult. Furthermore, hyaline cartilage ossifies with age, which causes healthy laryngeal cartilage to differ in appearance from patient to patient, further complicating accurate differentiation between healthy cartilage and adjacent tumor. In this respect, Kuno et al. reported that the combination of DECT derived iodine overlay maps and weighted-average images (which are similar to conventional CT images) significantly improved specificity of detection of cartilage invasion compared to weighted-average images only, while sensitivity did not decrease (Kuno et al. 2012). Additionally, inter-observer agreement increased when using the combination of

DECT derived iodine overlay maps and weighted-average images (Kuno et al. 2012). Iodine overlay maps facilitate the depiction of iodine distribution in contrast enhances scans and thereby are likely to diminish the rate of false positive diagnoses for tumor infiltration in hyaline cartilage (Kuno et al. 2012; Zopfs et al. 2021). Kuno et al. demonstrated in a follow-up study a higher specificity of iodine overlay maps and weighted-average images compared to MRI with similar sensitivity (Kuno et al. 2018). Another promising approach to differentiate hyaline cartilage and tumor tissue was demonstrated by Forghani et al.: High keV of ≥ 95 keV enabled a reliable, attenuation-based method for differentiation (see Fig. 2). This is due to the relatively high intrinsic attenuation of hyaline cartilage, which is not decreased in high keV contrary to the attenuation of vascularized tumor tissue, in which enhancement largely depends on iodinated contrast media (Forghani et al. 2015; Roele et al. 2017).

Given the results of these studies, implementation of low keV and high keV VMI as well as iodine maps in clinical routine represents a clear benefit over conventional single energy CT images in the staging of laryngeal and hypopharyngeal cancer.

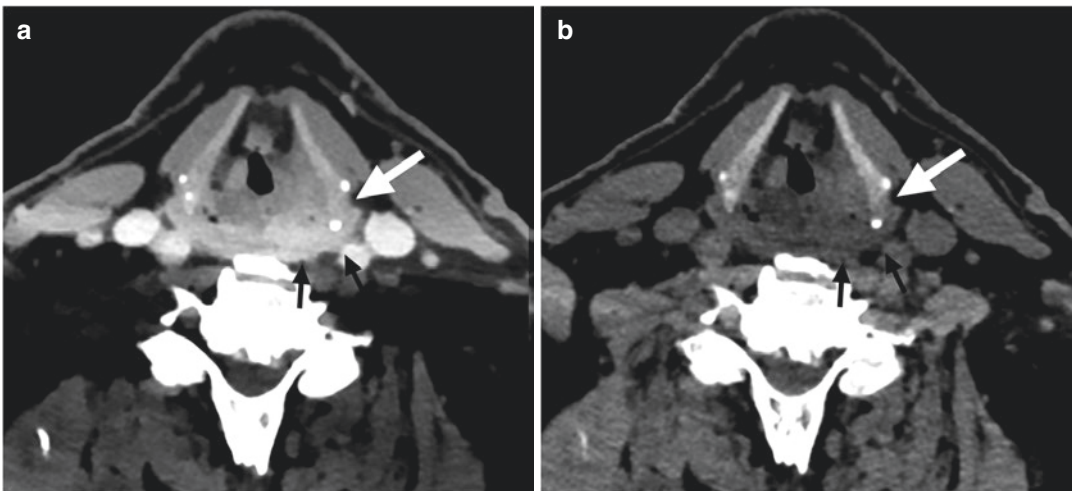


Fig. 2 Virtual monoenergetic image (VMI) reconstruction at 50 keV (a) display a hyperattenuating tumor (black arrows) adjacent to the posterior part of the left thyroid cartilage with considerable overlap of attenuation to the

bordering cartilage (white arrow). At 150 keV VMI (b), the attenuation of the tumor is reduced, while the attenuation of the cartilage remains high and the delineation of the cartilage boundary is improved

1.2 Lymph Node Imaging

Presence/Absence of lymph node metastases is an important prognostic factor in head and neck cancer (Axelsson et al. 2017; Magnano et al. 1997). Thus, accurate imaging of metastatic cervical lymph nodes is crucial to detect clinically not palpable lymph nodes, to evaluate the extent of lymph node metastases or to confirm a N0 status in follow-up examinations. However, in daily radiological routine reliable delineation and detection of cervical lymph nodes may be difficult due to the proximity of anatomical structures in the neck region. Unfortunately, enlargement of lymph nodes is neither sensitive nor specific enough to facilitate an accurate classification of lymph nodes as malignant, as up to 20% of lymph nodes are reactively increased in size or are hyperplastic (Tawfik et al. 2014). Therefore, imaging biomarkers allowing for a more precise assessment of ambiguous lymph nodes are highly desirable. In this regard, Tawfik et al. demonstrated that DECT derived iodine concentration significantly varies between healthy, inflammatory, and metastatic lymph nodes (Tawfik et al. 2014). Similarly, Liu et al. reported differences in normalized iodine concentration and the slope of the spectral Hounsfield unit curve between

healthy and metastatic lymph nodes in patients with papillary thyroid cancer (Liu et al. 2015). However, while Tawfik et al. reported significant lower iodine concentrations in metastatic lymph nodes, Liu et al. contrary found an increased normalized iodine concentration associated with malignant lymph nodes (Liu et al. 2015; Tawfik et al. 2014). In this context it is important to consider factors influencing iodine concentration, such as intra- and inter-individual as well as inter-scanner differences (Lennartz et al. 2021; Zopfs et al. 2020a, b). The current body of evidence is not yet sufficient to distinguish benign from metastatic lymph nodes based on absolute iodine concentrations with high confidence (Fig. 3).

2 Salivary Glands

Sialolithiasis is the most frequent disease of the major salivary glands and CT can be helpful in visualizing complications or facilitate treatment planning, especially if conventional intraoral radiographs are not well assessable. While unenhanced CT images are preferred to depict sialolithiasis, contrast-enhanced CT enables a better assessment of glandular parenchyma and possible

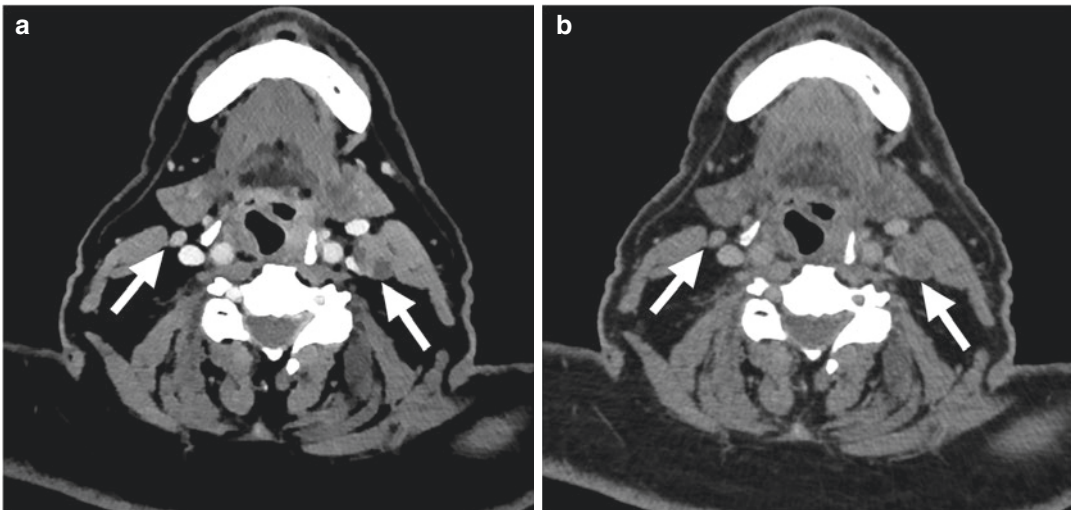


Fig. 3 Improved delineation of metastatic lymph node (right white arrow) and healthy appearing lymph nodes (left white arrow) in low keV virtual monoenergetic

images at 40 keV (a) compared to conventional image reconstructions (b)

inflammatory complications. However, focal spots of hyperenhancement or cross-sections of vessels may mimic lithiasis, thus leading to false positive findings (Pulickal et al. 2019; Rzymaska-Grala et al. 2010). Regarding this matter, virtual non-contrast (VNC) images reconstructed from contrast-enhanced DECT have been reported to be instrumental for delineation of sialolithiasis (Beland et al. 2019; Pulickal et al. 2019). Beland et al. reported comparable accuracy in the detection of sialolithiasis between true non-contrast images and VNC images derived from rapid kVp switching DECT (Beland et al. 2019). Therefore, a single phase, contrast-enhanced DECT examination protocol with reconstruction of VNC images may allow omitting true non-contrast images which could lead to significant radiation dose reduction (Beland et al. 2019; Pulickal et al. 2019). However, validation in studies with larger patient collectives and different technical approaches to DECT is needed prior to routine clinical application.

3 Inflammation

Peritonsillar abscesses represent the most frequent deep infection in the head and neck region in adolescent patients. While clinical examination is most important for diagnosis, CT is the main imaging modality chosen to visualize the extent and localization of the abscess (Roele et al. 2017; Steyer 2002). Scholtz et al. demonstrated an increased soft tissue enhancement and improved delineation of inflammatory changes in patients with peritonsillar abscesses using low-tube-voltage 80 kVp dual-source DECT (Scholtz et al. 2015). Furthermore, DECT derived iodine overlay maps might be helpful in depicting inhomogeneous iodine distribution of salivary gland tissue in sialadenitis (Chawla et al. 2017). Due to the very limited available studies regarding this topic and the lacking literature evidence, the clinical application of DECT in this field remains exploratory. However, an increased contrast of the hypervascularized abscess rim and an improved delineation of boundaries in low keV VMI and iodine overlay maps seem suggestive (see Fig. 4).

4 Metal Artifact Reduction

In daily routine, image quality of head and neck CT examinations is often severely hampered by artifacts arising from different forms of metallic hardware, especially dentures and dental implants. This limitation is aggravated with demographic change, as more and more older patients are undergoing CT examinations and the frequent presence of metallic dental hardware in these patients. Thus, the oral cavity and the maxillofacial region are particularly affected by artifacts. Metal artifacts mainly arise for three reasons: (1) beam hardening artifacts, result from the absorption of low-energy photons of the polyenergetic X-ray beam, (2) photon starvation, which are caused by the complete absorption of photons, and (3) scatter artifacts, which occur from major differences in attenuation between highly attenuating metallic implants and the adjacent soft tissue. These phenomena result in different kind of artifacts, i.e. hypo- and hyperdense areas adjacent to the metallic structure, streaking artifacts that can spread over the whole CT image and an increase in image noise (Große Hokamp et al. 2018; Mori et al. 2013; Roele et al. 2017; Zopfs et al. 2020c). Especially the combination of these effects can result in strong interferences, which may severely impair diagnostic assessment. In this regard, DECT has been found an efficient resource to reduce metal artifacts and improve subjective image assessment. Especially virtual monoenergetic images at high energy levels have proven to be a powerful tool for artifact reduction in various studies, irrespective of the technical approach to dual-energy CT (Bamberg et al. 2011; Cha et al. 2017; Große Hokamp et al. 2018; Lee et al. 2012; Morsbach et al. 2013; Stolzmann et al. 2013; Tanaka et al. 2013) (Fig. 5). For example, Stolzmann et al. and Große Hokamp et al. found a significant reduction of metal artifacts from dental implants in VMI with higher keV while simultaneously improving diagnostic assessment of the oral cavity (Große Hokamp et al. 2018; Stolzmann et al. 2013). The optimal keV level for artifact reduction was stated at 108 ± 17 keV and 145 ± 15 keV, respectively (Große Hokamp et al. 2018; Stolzmann

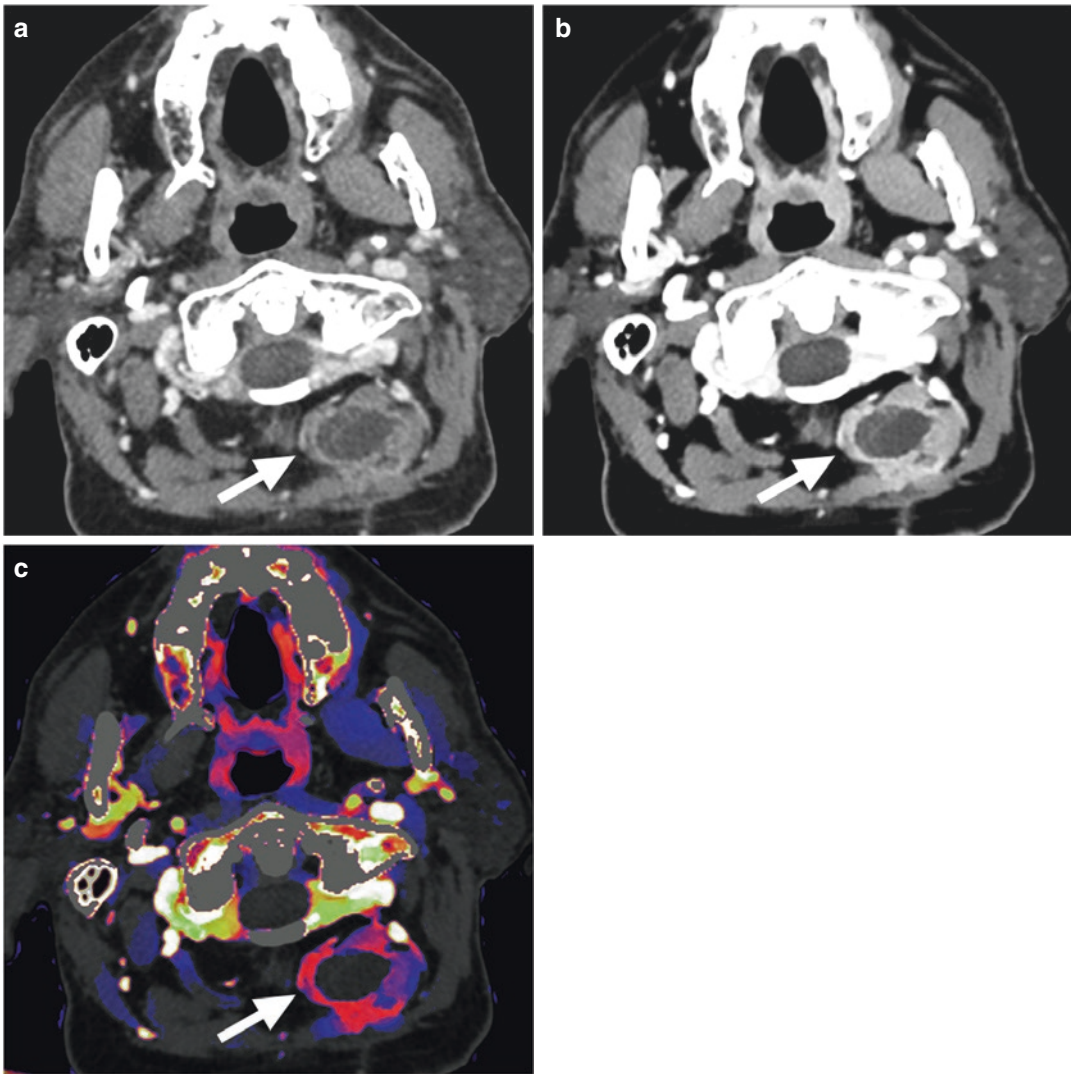


Fig. 4 Nuchal abscess (white arrow) in conventional image reconstructions (a), virtual monoenergetic images (VMI) at 40 keV (b) and iodine overlay maps (c). The

strong contrast enhancement of the hyper vascularized abscess rim is highlighted in 40 keV VMI and iodine overlay maps

et al. 2013). Zhou et al. and Guggenberger et al. investigated the usefulness of high keV VMI to reduce metal artifacts arising from spinal implants (Guggenberger et al. 2012; Roele et al. 2017; Zhou et al. 2011). Similar to artifacts from dental artifacts, both studies found VMI at around 130 keV best suited for improving image quality (Guggenberger et al. 2012; Zhou et al. 2011).

Altogether, the optimal VMI level for artifact reduction in the head and neck region seems to range between 100 and 150 keV, yet individual

adjustment is necessary depending on the specific patient, type of implant, and artifact localization (Bamberg et al. 2011; Große Hokamp et al. 2018; Guggenberger et al. 2012; Laukamp et al. 2019; Roele et al. 2017; Stolzmann et al. 2013; Tanaka et al. 2013; Zhou et al. 2011). Recent studies suggested that a combination of dedicated metal artifact reduction algorithms (MAR) and virtual monoenergetic images may yield an additional benefit compared to the sole use of one of the techniques (Große Hokamp

et al. 2020; Guggenberger et al. 2012; Tanaka et al. 2013). Laukamp et al. demonstrated that especially hyperdense artifacts can be effectively reduced using a combination of VMI between

140 and 200 keV and MAR (Laukamp et al. 2019). However, this combined approach holds the risk of overcorrection and new artifacts (Laukamp et al. 2019; Zopfs et al. 2020c).

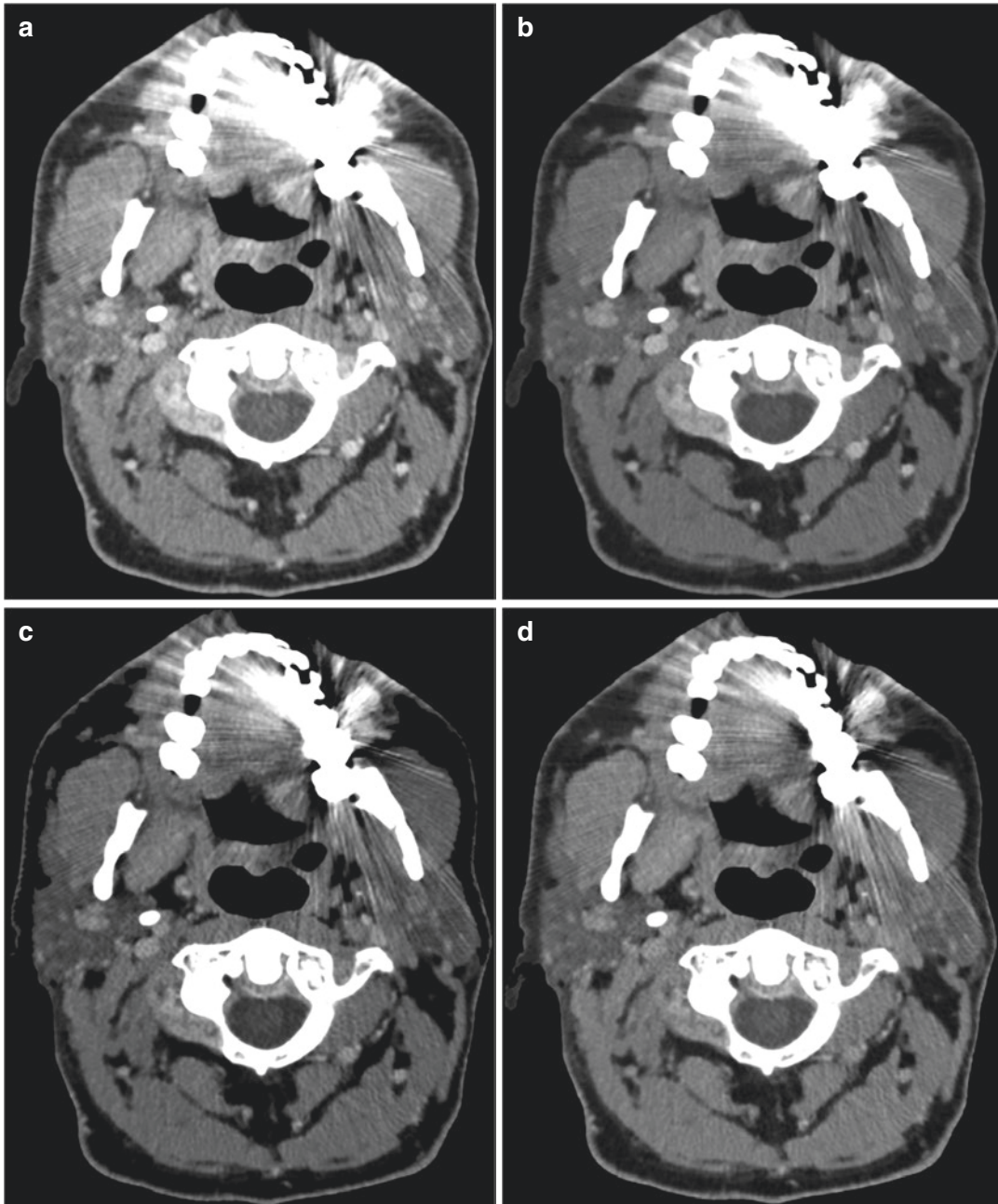


Fig. 5 Contrast-enhanced scan of the oral cavity in venous phase with significant artifacts arising from metallic dental hardware. Hyper- and hypodense artifact streaks

are reduced with higher keV virtual monoenergetic images (70 keV [b], 100 keV [c], 130 keV [d], 170 keV [e], and 200 keV [f]) compared to conventional images (a)

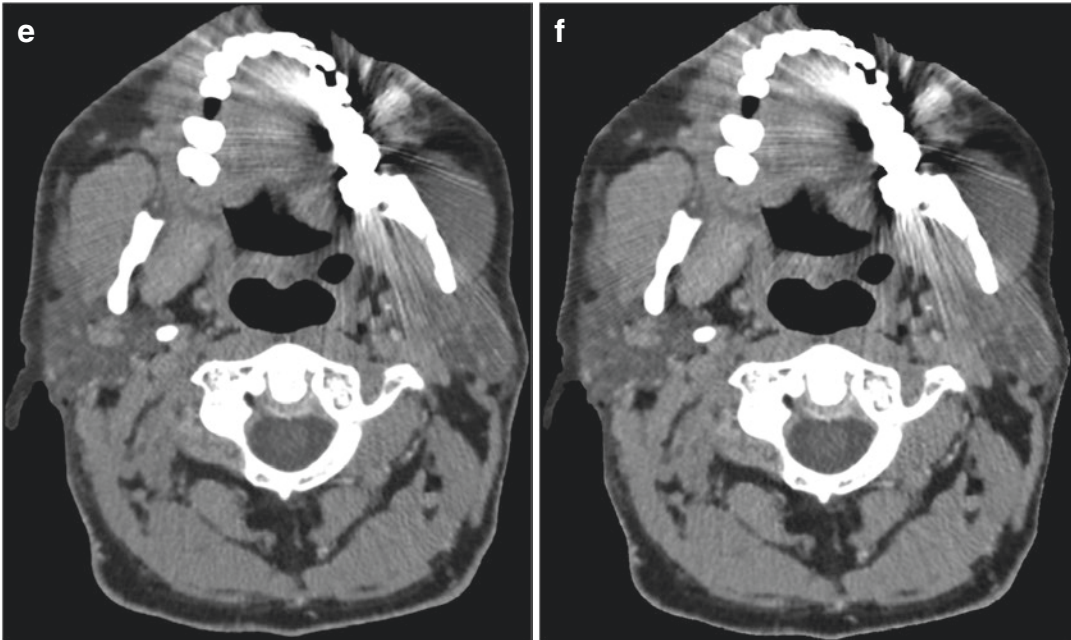


Fig. 5 (continued)

5 Thyroid and Parathyroid Lesions

Thyroid nodules are a common finding in CT examinations of the head and neck, whereas incidental thyroid cancer is rare. Their high prevalence and the associated cost of patient workup renders a reliable differentiation in CT highly desirable (Youser et al. 1997). VMI and iodine maps have been investigated for distinguishing malignant from benign focal thyroid lesions in different studies (Gao et al. 2016; Lee et al. 2019; Li et al. 2012). Yet, the body of evidence is relatively small.

Parathyroid adenomas are the leading cause of primary hyperparathyroidism (Duan et al. 2015). As treatment is surgical, accurate pretherapeutic assessment of size and location is important. Whereas ultrasonography of the neck and Technetium-99m-Sestamibi scintigraphy of the parathyroid comprise the most established imaging methods for characterization of parathyroid adenomas, various comparative studies described a superior performance of multiphasic CT to evaluate parathyroid adenomas. Currently, CT is especially used if results of previous examinations are inconsistent, however, utilization of CT is limited due to the considerable radiation exposure resulting from

a multiphasic protocol (Forghani et al. 2016; Woisetschläger et al. 2020). In this regard, DECT derived VNC reconstructions may reduce radiation exposure. Leiva-Salinas et al. reported a comparable diagnostic accuracy of a monophasic DECT protocol with reconstruction of VNC images compared to a conventional biphasic protocol, resulting in a considerable dose reduction (Leiva-Salinas et al. 2016). Forghani et al. found an additional value of different DECT reconstructions in the detection of parathyroid adenomas, such as iodine concentration, SHUAC curves, and effective Z, which might increase diagnostic accuracy, especially in equivocal cases (Forghani et al. 2016).

6 Angiography of the Head and Neck

CT-Angiography of the head and neck is frequently used to detect stenosed or occluded cervical arteries, evaluate atherosclerotic plaques or vascular malformations (Anzidei et al. 2012). Numerous studies demonstrated a boost of vessel contrast in CT-Angiographies of the head and neck in low keV VMI compared to conventional images (see Fig. 6) (Leithner et al. 2018; Martin

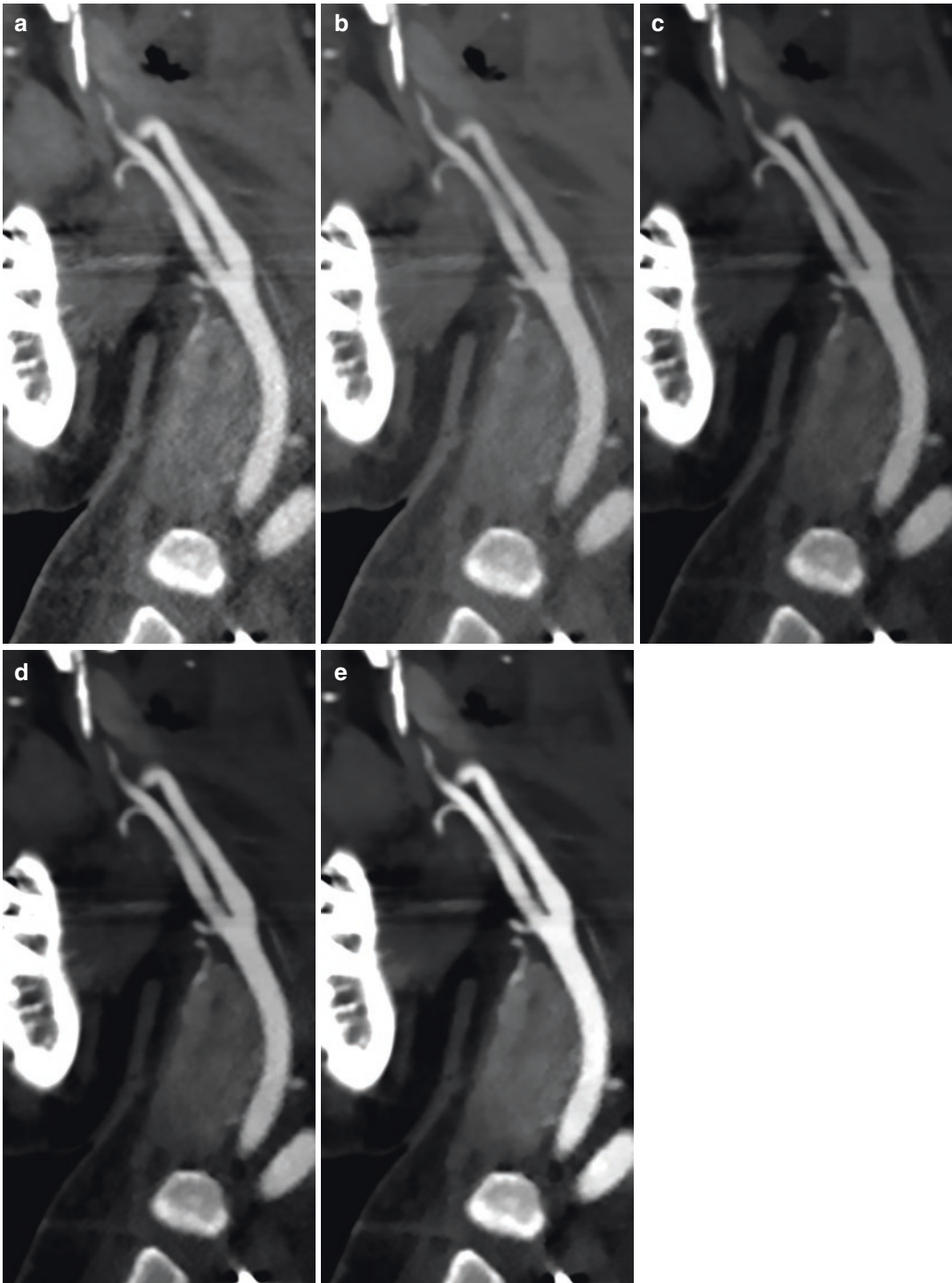


Fig. 6 Sagittal reconstructions of a CT-Angiography of the head and neck with depiction of the common carotid artery and the proximal external and internal carotid artery in conventional images (a) and virtual monoenergetic

images (VMI) at 70 keV (b), 60 keV (c), 50 keV (d), and 40 keV (e). Improved subjective image quality can be appreciated in low keV VMI

et al. 2017; Zopfs et al. 2018). This increase in iodine attenuation facilitates an improvement of objective image quality, such as SNR and CNR accompanied with a subjective superior vessel delineation and assessment (Riffel et al. 2016; Zopfs et al. 2018). Most studies report ideal keV levels of 40–60 keV, varying with the technical approach to DECT and examination protocols (Albrecht et al. 2019; Leithner et al. 2018; Zopfs et al. 2018). Neuhaus et al. found low keV VMI especially useful to assess arteries nearby the skull base and smaller arterial branches (Neuhaus et al. 2018). Furthermore, VMI at 40 keV were found to be useful for increasing vessel contrast in venous phase examinations of the neck (see Fig. 7), reaching an image quality comparable to that of conventional angiographic CT scans (Zopfs et al. 2018). This allows for an equivalent assessment of incidental carotid stenosis in venous phase staging examinations compared to dedicated CT-Angiographies, thus possibly decreasing the number of subsequent follow-up examinations to evaluate the extent of carotid artery stenosis. While few studies reported differences in the quantification of the degree of carotid artery stenosis in low keV, most studies found no significant differences compared to conventional studies (Leithner et al. 2018; Paul et al. 2013; Saba et al. 2019; Zopfs et al. 2018). However, calcified plaques of the carotid arteries and bone frequently hamper the assessment of cervical arteries and the determination of stenosis grades as blooming artifacts may lead to an overestimation of stenosis in conventional CT-Angiography. In this regard, different studies demonstrated a benefit of DECT based virtual calcium or bone removal (Deng et al. 2009; Kaemmerer et al. 2016; Kamalian et al. 2017; Mannil et al. 2017).

7 Future Directions: Assessment of Therapy Response and Prediction of Recurrence

Whereas the vast majority of research has been focused on the assessment of newly diagnosed head and neck cancer so far, only a few studies

addressed on the capability of DECT to differentiate between recurrent disease and benign post-treatment changes in patients with history of treated head and neck cancer undergoing follow-up examinations. In a study from Takumi et al., VMI at 40 keV and iodine concentration were both significantly higher in recurrent tumor compared to post-therapeutic tissue (Takumi et al. 2020). Similarly, several other studies found the spectral HU curve and iodine quantification helpful to distinguish and benign reactive changes after treatment (Roele et al. 2017; Srinivasan et al. 2013; Yamauchi et al. 2016). Thus, these DECT derived reconstructions might assist in the diagnosis of recurrent head and neck cancer and decrease the number of biopsies needed.

Recently, an increasing number of studies demonstrated that radiomics can be employed to generate an additional value from the wide range of quantitative DECT data (Agarwal et al. 2020; Forghani et al. 2019; Guo et al. 2020; Tomita et al. 2020). A study from Agarwal et al. indicated that the radiomics parameter medium texture entropy is predictive of local control and laryngectomy free survival (Agarwal et al. 2020). Forghani et al. demonstrated that multi-energy texture analysis, i.e. on different VMI levels, allows for prediction of cervical lymph node metastases (Forghani et al. 2019). A retrospective study of Tomita et al. suggested that texture analysis of DECT derived VMI might facilitate an differentiation of benign and malignant thyroid nodules (Tomita et al. 2020). Additionally, different radiomics features based on absolute iodine concentration correlated significantly with tumor recurrence in a preliminary study from Bahig et al. (2019). However, inter-individual physiological and longitudinal intra-individual changes of iodine concentrations should be taken into account before providing absolute cut-off values to distinguish malignant and benign tissue or predict outcome, especially in studies with rather small patient collectives (Lennartz et al. 2021; Zopfs et al. 2020a, b).

In general, however, most of the studies dealing with the significance of radiomics analysis are retrospective and limited in their sample size. Therefore, a basic practical clinical applicability is not given yet.

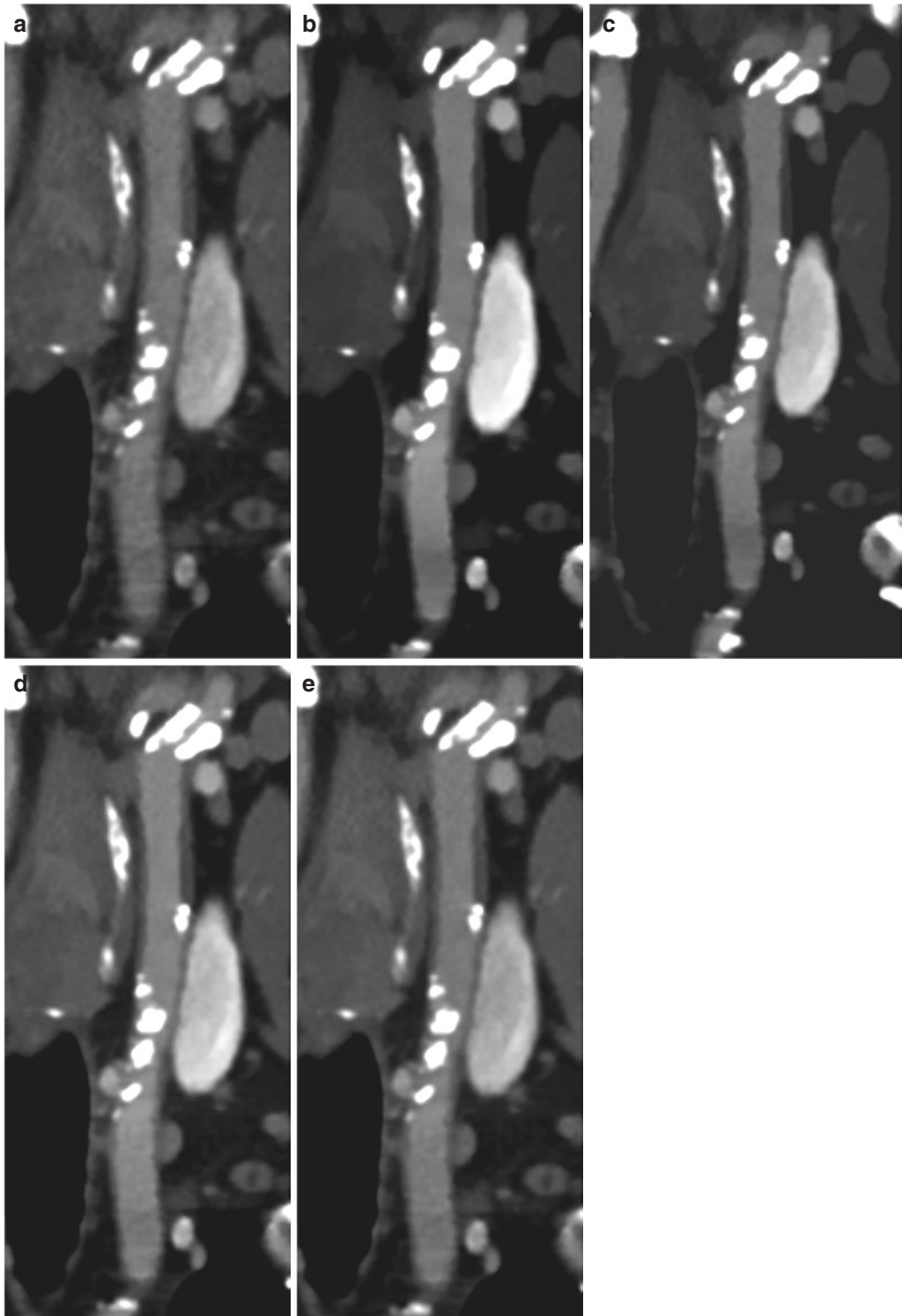


Fig. 7 Sagittal reconstructions of the common carotid artery and the proximal internal carotid artery in a venous phase oncologic staging examination of the head and

neck. Low keV virtual monoenergetic images at 40 keV (b), 50 keV (c), 60 keV (d), and 70 keV (e) increase vessel contrast compared to conventional images (a)

Compliance with Ethical Standards

Funding None.

Disclosure of Interests David Zopfs receives research support from Philips Healthcare.

Ethical Approval This article does not contain any studies with human participants performed by any of the authors.

References

- Agarwal JP, Sinha S, Goda JS et al (2020) Tumor radiomic features complement clinico-radiological factors in predicting long-term local control and laryngectomy free survival in locally advanced laryngopharyngeal cancers. *Br J Radiol* 93:20190857. <https://doi.org/10.1259/bjr.20190857>
- Albrecht MH, Scholtz J-E, Kraft J et al (2015) Assessment of an advanced monoenergetic reconstruction technique in dual-energy computed tomography of head and neck cancer. *Eur Radiol* 25:2493–2501. <https://doi.org/10.1007/s00330-015-3627-1>
- Albrecht MH, Vogl TJ, Martin SS et al (2019) Review of clinical applications for virtual monoenergetic dual-energy CT. *Radiology* 293:260–271. <https://doi.org/10.1148/radiol.2019182297>
- Anzidei M, Napoli A, Zaccagna F et al (2012) Diagnostic accuracy of colour Doppler ultrasonography, CT angiography and blood-pool-enhanced MR angiography in assessing carotid stenosis: a comparative study with DSA in 170 patients. *Radiol Med* 117:54–71. <https://doi.org/10.1007/s11547-011-0651-3>
- Axelsson L, Nyman J, Haugen-Cange H et al (2017) Prognostic factors for head and neck cancer of unknown primary including the impact of human papilloma virus infection. *J Otolaryngol Head Neck Surg* 46:45. <https://doi.org/10.1186/s40463-017-0223-1>
- Bahig H, Lapointe A, Bedwani S et al (2019) Dual-energy computed tomography for prediction of loco-regional recurrence after radiotherapy in larynx and hypopharynx squamous cell carcinoma. *Eur J Radiol* 110:1–6. <https://doi.org/10.1016/j.ejrad.2018.11.005>
- Bamberg F, Dierks A, Nikolaou K et al (2011) Metal artifact reduction by dual energy computed tomography using monoenergetic extrapolation. *Eur Radiol* 21:1424–1429. <https://doi.org/10.1007/s00330-011-2062-1>
- Beland B, Levental M, Srinivasan A et al (2019) Practice variations in salivary gland imaging and utility of virtual unenhanced dual energy CT images for the detection of major salivary gland stones. *Acta Radiol* 60:1144–1152. <https://doi.org/10.1177/0284185118817906>
- Bray F, Ferlay J, Soerjomataram I et al (2018) Global cancer statistics 2018: GLOBOCAN estimates of incidence and mortality worldwide for 36 cancers in 185 countries. *CA Cancer J Clin* 68:394–424. <https://doi.org/10.3322/caac.21492>
- Cha J, Kim H-J, Kim ST et al (2017) Dual-energy CT with virtual monochromatic images and metal artifact reduction software for reducing metallic dental artifacts. *Acta Radiol* 58:1312–1319. <https://doi.org/10.1177/0284185117692174>
- Chawla A, Srinivasan S, Lim T-C et al (2017) Dual-energy CT applications in salivary gland lesions. *Br J Radiol* 90. <https://doi.org/10.1259/bjr.20160859>
- Deng K, Liu C, Ma R et al (2009) Clinical evaluation of dual-energy bone removal in CT angiography of the head and neck: comparison with conventional bone-subtraction CT angiography. *Clin Radiol* 64:534–541. <https://doi.org/10.1016/j.crad.2009.01.007>
- Duan K, Gomez Hernandez K, Mete O (2015) Clinicopathological correlates of hyperparathyroidism. *J Clin Pathol* 68:771–787. <https://doi.org/10.1136/jclinpath-2015-203186>
- Forghani R (2019) An update on advanced dual-energy CT for head and neck cancer imaging. *Expert Rev Anticancer Ther* 19:633–644. <https://doi.org/10.1080/14737140.2019.1626234>
- Forghani R, Levental M, Gupta R et al (2015) Different spectral hounsfield unit curve and high-energy virtual monochromatic image characteristics of squamous cell carcinoma compared with nonossified thyroid cartilage. *AJNR Am J Neuroradiol* 36:1194–1200. <https://doi.org/10.3174/ajnr.A4253>
- Forghani R, Roskies M, Liu X et al (2016) Dual-energy CT characteristics of parathyroid adenomas on 25- and 55-second 4D-CT acquisitions: preliminary experience. *J Comput Assist Tomogr* 40:806–814. <https://doi.org/10.1097/RCT.0000000000000442>
- Forghani R, Kelly H, Yu E et al (2017) Low-energy virtual monochromatic dual-energy computed tomography images for the evaluation of head and neck squamous cell carcinoma: a study of tumor visibility compared with single-energy computed tomography and user acceptance. *J Comput Assist Tomogr* 41:565–571. <https://doi.org/10.1097/RCT.0000000000000571>
- Forghani R, Chatterjee A, Reinhold C et al (2019) Head and neck squamous cell carcinoma: prediction of cervical lymph node metastasis by dual-energy CT texture analysis with machine learning. *Eur Radiol* 29:6172–6181. <https://doi.org/10.1007/s00330-019-06159-y>
- Gao S-Y, Zhang X-Y, Wei W et al (2016) Identification of benign and malignant thyroid nodules by in vivo iodine concentration measurement using single-source dual energy CT: a retrospective diagnostic accuracy study. *Medicine (Baltimore)* 95:e4816. <https://doi.org/10.1097/MD.00000000000004816>

- Große Hokamp N, Laukamp KR, Lennartz S et al (2018) Artifact reduction from dental implants using virtual monoenergetic reconstructions from novel spectral detector CT. *Eur J Radiol* 104:136–142. <https://doi.org/10.1016/j.ejrad.2018.04.018>
- Große Hokamp N, Maintz D, Shapira N et al (2020) Technical background of a novel detector-based approach to dual-energy computed tomography. *Diagn Interv Radiol* 26:68–71. <https://doi.org/10.5152/dir.2019.19136>
- Guggenberger R, Winklhofer S, Osterhoff G et al (2012) Metallic artefact reduction with monoenergetic dual-energy CT: systematic ex vivo evaluation of posterior spinal fusion implants from various vendors and different spine levels. *Eur Radiol* 22:2357–2364. <https://doi.org/10.1007/s00330-012-2501-7>
- Guo R, Guo J, Zhang L et al (2020) CT-based radiomics features in the prediction of thyroid cartilage invasion from laryngeal and hypopharyngeal squamous cell carcinoma. *Cancer Imaging* 20:81. <https://doi.org/10.1186/s40644-020-00359-2>
- Kaemmerer N, Brand M, Hammon M et al (2016) Dual-energy computed tomography angiography of the head and neck with single-source computed tomography: a new technical (split filter) approach for bone removal. *Investig Radiol* 51:618–623. <https://doi.org/10.1097/RLI.0000000000000290>
- Kamalian S, Lev MH, Pomerantz SR (2017) Dual-energy computed tomography angiography of the head and neck and related applications. *Neuroimaging Clin N Am* 27:429–443. <https://doi.org/10.1016/j.nic.2017.04.009>
- Kuno H, Onaya H, Iwata R et al (2012) Evaluation of cartilage invasion by laryngeal and hypopharyngeal squamous cell carcinoma with dual-energy CT. *Radiology* 265:488–496. <https://doi.org/10.1148/radiol.12111719>
- Kuno H, Onaya H, Fujii S et al (2014) Primary staging of laryngeal and hypopharyngeal cancer: CT, MR imaging and dual-energy CT. *Eur J Radiol* 83:e23–e35. <https://doi.org/10.1016/j.ejrad.2013.10.022>
- Kuno H, Sakamaki K, Fujii S et al (2018) Comparison of MR imaging and dual-energy CT for the evaluation of cartilage invasion by laryngeal and hypopharyngeal squamous cell carcinoma. *AJNR Am J Neuroradiol* 39:524–531. <https://doi.org/10.3174/ajnr.A5530>
- Laukamp KR, Zopfs D, Lennartz S et al (2019) Metal artifacts in patients with large dental implants and bridges: combination of metal artifact reduction algorithms and virtual monoenergetic images provides an approach to handle even strongest artifacts. *Eur Radiol* 29:4228–4238. <https://doi.org/10.1007/s00330-018-5928-7>
- Lee YH, Park KK, Song H-T et al (2012) Metal artefact reduction in gemstone spectral imaging dual-energy CT with and without metal artefact reduction software. *Eur Radiol* 22:1331–1340. <https://doi.org/10.1007/s00330-011-2370-5>
- Lee DH, Lee YH, Seo HS et al (2019) Dual-energy CT iodine quantification for characterizing focal thyroid lesions. *Head Neck* 41:1024–1031. <https://doi.org/10.1002/hed.25524>
- Leithner D, Mahmoudi S, Wichmann JL et al (2018) Evaluation of virtual monoenergetic imaging algorithms for dual-energy carotid and intracerebral CT angiography: effects on image quality, artefacts and diagnostic performance for the detection of stenosis. *Eur J Radiol* 99:111–117. <https://doi.org/10.1016/j.ejrad.2017.12.024>
- Leiva-Salinas C, Flors L, Durst CR et al (2016) Detection of parathyroid adenomas using a monophasic dual-energy computed tomography acquisition: diagnostic performance and potential radiation dose reduction. *Neuroradiology* 58:1135–1141. <https://doi.org/10.1007/s00234-016-1736-4>
- Lennartz S, Parakh A, Cao J et al (2021) Inter-scan and inter-scanner variation of quantitative dual-energy CT: evaluation with three different scanner types. *Eur Radiol*. <https://doi.org/10.1007/s00330-020-07611-0>
- Li M, Zheng X, Li J et al (2012) Dual-energy computed tomography imaging of thyroid nodule specimens: comparison with pathologic findings. *Investig Radiol* 47:58–64. <https://doi.org/10.1097/RLI.0b013e318229fef3>
- Liu X, Ouyang D, Li H et al (2015) Papillary thyroid cancer: dual-energy spectral CT quantitative parameters for preoperative diagnosis of metastasis to the cervical lymph nodes. *Radiology* 275:167–176. <https://doi.org/10.1148/radiol.14140481>
- Lohöfer FK, Kaissis GA, Köster FL et al (2018) Improved detection rates and treatment planning of head and neck cancer using dual-layer spectral CT. *Eur Radiol* 28:4925–4931. <https://doi.org/10.1007/s00330-018-5511-2>
- Magnano M, de Stefani A, Lerda W et al (1997) Prognostic factors of cervical lymph node metastasis in head and neck squamous cell carcinoma. *Tumori* 83:922–926
- Mannil M, Ramachandran J, Vittoria de Martini I et al (2017) Modified dual-energy algorithm for calcified plaque removal: evaluation in carotid computed tomography angiography and comparison with digital subtraction angiography. *Investig Radiol* 52:680–685. <https://doi.org/10.1097/RLI.0000000000000391>
- Martin SS, Albrecht MH, Wichmann JL et al (2017) Value of a noise-optimized virtual monoenergetic reconstruction technique in dual-energy CT for planning of transcatheter aortic valve replacement. *Eur Radiol* 27:705–714. <https://doi.org/10.1007/s00330-016-4422-3>
- May MS, Wiesmueller M, Heiss R et al (2019) Comparison of dual- and single-source dual-energy CT in head and neck imaging. *Eur Radiol* 29:4207–4214. <https://doi.org/10.1007/s00330-018-5762-y>
- Mori I, Machida Y, Osanai M et al (2013) Photon starvation artifacts of X-ray CT: their true cause and a solution. *Radiol Phys Technol* 6:130–141. <https://doi.org/10.1007/s12194-012-0179-9>
- Morsbach F, Wurnig M, Kunz DM et al (2013) Metal artefact reduction from dental hardware in carotid

- CT angiography using iterative reconstructions. *Eur Radiol* 23:2687–2694. <https://doi.org/10.1007/s00330-013-2885-z>
- Neuhaus V, Große Hokamp N, Abdullayev N et al (2018) Comparison of virtual monoenergetic and polyenergetic images reconstructed from dual-layer detector CT angiography of the head and neck. *Eur Radiol* 28:1102–1110. <https://doi.org/10.1007/s00330-017-5081-8>
- Paul J, Tan MML, Farhang M et al (2013) Dual-energy CT spectral and energy weighted data sets: carotid stenosis and plaque detection. *Acad Radiol* 20:1144–1151. <https://doi.org/10.1016/j.acra.2013.02.019>
- Pérez-Lara A, Forghani R (2018) Spectral computed tomography: technique and applications for head and neck cancer. *Magn Reson Imaging Clin N Am* 26:1–17. <https://doi.org/10.1016/j.mric.2017.08.001>
- Pulickal GG, Singh D, Lohan R et al (2019) Dual-source dual-energy CT in submandibular sialolithiasis: reliability and radiation burden. *AJR Am J Roentgenol* 213:1291–1296. <https://doi.org/10.2214/AJR.19.21299>
- Riffel P, Haubenreisser H, Meyer M et al (2016) Carotid dual-energy CT angiography: evaluation of low keV calculated monoenergetic datasets by means of a frequency-split approach for noise reduction at low keV levels. *Eur J Radiol* 85:720–725. <https://doi.org/10.1016/j.ejrad.2016.01.015>
- Roele ED, Timmer VCML, Vaassen LAA et al (2017) Dual-energy CT in head and neck imaging. *Curr Radiol Rep* 5:19. <https://doi.org/10.1007/s40134-017-0213-0>
- Rzyska-Grala I, Stopa Z, Grala B et al (2010) Salivary gland calculi - contemporary methods of imaging. *Pol J Radiol* 75:25–37
- Saba L, Argioas GM, Lucatelli P et al (2019) Variation of degree of stenosis quantification using different energy level with dual energy CT scanner. *Neuroradiology* 61:285–291. <https://doi.org/10.1007/s00234-018-2142-x>
- Scholtz J-E, Hüßers K, Kaup M et al (2015) Evaluation of image quality and dose reduction of 80 kVp neck computed tomography in patients with suspected peritonsillar abscess. *Clin Radiol* 70:e67–e73. <https://doi.org/10.1016/j.crad.2015.04.009>
- Sheahan P (2014) Management of advanced laryngeal cancer. *Rambam Maimonides Med J* 5:e0015. <https://doi.org/10.5041/RMMJ.10149>
- Srinivasan A, Parker RA, Manjunathan A et al (2013) Differentiation of benign and malignant neck pathologies: preliminary experience using spectral computed tomography. *J Comput Assist Tomogr* 37:666–672. <https://doi.org/10.1097/RCT.0b013e3182976365>
- Steyer TE (2002) Peritonsillar abscess: diagnosis and treatment. *Am Fam Physician* 65:93–96
- Stolzmann P, Winklhofer S, Schwendener N et al (2013) Monoenergetic computed tomography reconstructions reduce beam hardening artifacts from dental restorations. *Forensic Sci Med Pathol* 9:327–332. <https://doi.org/10.1007/s12024-013-9420-z>
- Takumi K, Hakamada H, Nagano H et al (2020) Usefulness of dual-layer spectral CT in follow-up examinations: diagnosing recurrent squamous cell carcinomas in the head and neck. *Jpn J Radiol*. <https://doi.org/10.1007/s11604-020-01071-8>
- Tanaka R, Hayashi T, Ike M et al (2013) Reduction of dark-band-like metal artifacts caused by dental implant bodies using hypothetical monoenergetic imaging after dual-energy computed tomography. *Oral Surg Oral Med Oral Pathol Oral Radiol* 115:833–838. <https://doi.org/10.1016/j.oooo.2013.03.014>
- Tawfik AM, Razeq AA, Kerl JM et al (2014) Comparison of dual-energy CT-derived iodine content and iodine overlay of normal, inflammatory and metastatic squamous cell carcinoma cervical lymph nodes. *Eur Radiol* 24:574–580. <https://doi.org/10.1007/s00330-013-3035-3>
- Toepker M, Czerny C, Ringl H et al (2014) Can dual-energy CT improve the assessment of tumor margins in oral cancer? *Oral Oncol* 50:221–227. <https://doi.org/10.1016/j.oraloncology.2013.12.001>
- Tomita H, Kuno H, Sekiya K et al (2020) Quantitative assessment of thyroid nodules using dual-energy computed tomography: iodine concentration measurement and multiparametric texture analysis for differentiating between malignant and benign lesions. *Int J Endocrinol* 2020:5484671. <https://doi.org/10.1155/2020/5484671>
- Wichmann JL, Nöske E-M, Kraft J et al (2014) Virtual monoenergetic dual-energy computed tomography: optimization of kiloelectron volt settings in head and neck cancer. *Investig Radiol* 49:735–741. <https://doi.org/10.1097/RLI.0000000000000077>
- Woisetschläger M, Gimm O, Johansson K et al (2020) Dual energy 4D-CT of parathyroid adenomas not clearly localized by sestamibi scintigraphy and ultrasonography - a retrospective study. *Eur J Radiol* 124:108821. <https://doi.org/10.1016/j.ejrad.2020.108821>
- Yamauchi H, Buehler M, Goodsitt MM et al (2016) Dual-energy CT-based differentiation of benign post-treatment changes from primary or recurrent malignancy of the head and neck: comparison of spectral Hounsfield units at 40 and 70 keV and iodine concentration. *AJR Am J Roentgenol* 206:580–587. <https://doi.org/10.2214/AJR.15.14896>
- Yousem DM, Huang T, Loevner LA et al (1997) Clinical and economic impact of incidental thyroid lesions found with CT and MR. *AJNR Am J Neuroradiol* 18:1423–1428
- Zhou C, Zhao YE, Luo S et al (2011) Monoenergetic imaging of dual-energy CT reduces artifacts from implanted metal orthopedic devices in patients with fractures. *Acad Radiol* 18:1252–1257. <https://doi.org/10.1016/j.acra.2011.05.009>
- Zopf D, Lennartz S, Laukamp K et al (2018) Improved depiction of atherosclerotic carotid artery stenosis in virtual monoenergetic reconstructions of venous phase

- dual-layer computed tomography in comparison to polyenergetic reconstructions. *Eur J Radiol* 100:36–42. <https://doi.org/10.1016/j.ejrad.2018.01.008>
- Zopfs D, Reimer RP, Sonnabend K et al (2020a) Intraindividual consistency of iodine concentration in dual-energy computed tomography of the chest and abdomen. *Investig Radiol*. <https://doi.org/10.1097/RLI.0000000000000724>
- Zopfs D, Graffe J, Reimer RP et al (2020b) Quantitative distribution of iodinated contrast media in body computed tomography: data from a large reference cohort. *Eur Radiol*. <https://doi.org/10.1007/s00330-020-07298-3>
- Zopfs D, Lennartz S, Pennig L et al (2020c) Virtual monoenergetic images and post-processing algorithms effectively reduce CT artifacts from intracranial aneurysm treatment. *Sci Rep* 10:6629. <https://doi.org/10.1038/s41598-020-63574-8>
- Zopfs D, Große Hokamp N, Reimer R et al (2021) Value of spectral detector CT for pretherapeutic, locoregional assessment of esophageal cancer. *Eur J Radiol* 134:109423. <https://doi.org/10.1016/j.ejrad.2020.109423>



Clinical Applications in Cardiac Imaging

Basel Yacoub, Josua Decker, U. Joseph Schoepf,
Tilman Emrich, Jon F. Aldinger,
and Akos Varga-Szemes

Contents

1	History of Cardiac Imaging	144
2	Benefits and Applications of Cardiac CT Imaging	145
3	Functional Applications for Cardiac CT	146
4	Advantages of Spectral Imaging	146
4.1	Optimizing Image Quality	146
4.2	Artifact Reduction	146
4.3	Reducing Contrast Media	146
4.4	Virtual Reconstructions to Lower Radiation Dose	147
5	Coronary Arteries	147
5.1	Improvement of Imaging Quality and Artifact Reduction	147
5.2	General Improvements of Image Quality	147
5.3	Reducing Calcium Blooming Artifacts	148
5.4	Improved Visualization of Coronary Artery Stents	148
5.5	Improved Plaque Imaging	148
5.6	Calcium Scoring	149

B. Yacoub · U. J. Schoepf (✉) · J. F. Aldinger ·
A. Varga-Szemes
Division of Cardiovascular Imaging, Department of
Radiology and Radiological Science, Medical
University of South Carolina, Charleston, SC, USA
e-mail: yacoubb@muscc.edu; schoepf@muscc.edu;
aldingej@muscc.edu; vargaasz@muscc.edu

J. Decker
Division of Cardiovascular Imaging, Department of
Radiology and Radiological Science, Medical
University of South Carolina, Charleston, SC, USA
Department of Diagnostic and Interventional
Radiology, University Hospital Augsburg,
Augsburg, Germany
e-mail: deckejos@muscc.edu

T. Emrich
Division of Cardiovascular Imaging, Department of
Radiology and Radiological Science, Medical
University of South Carolina, Charleston, SC, USA
Department of Diagnostic and Interventional
Radiology, University Medical Center of the
Johannes Gutenberg University Mainz,
Mainz, Germany
German Centre for Cardiovascular Research
(DZHK), Partner Site Rhine-Main, Mainz, Germany
e-mail: emrich@muscc.edu

6	Myocardial Characterization	150
6.1	Myocardial Fibrosis	150
6.2	Iron Overload	150
6.3	Perfusion Imaging	151
6.4	Scar Imaging	152
7	Cardiac Valves	152
8	Cardiac Masses	153
9	Outlook Cardiac CT	153
9.1	Artificial Intelligence and Radiomics	153
9.2	Photon-Counting CT	154
9.3	Conclusion	155
	References	155

Abstract

Cardiac computed tomography (CT) is an indispensable tool for evaluating cardiovascular structures. Its widespread use has increasingly gained momentum in the past decade as results from large-scale trials became available, and it steadily found its way to become the guidelines' recommended first-line imaging test for various cardiac conditions. Spectral imaging capabilities in cardiac CT first became possible with the introduction of dual-energy computed tomography (DECT) scanners. Cardiac CT examinations obtained using dual-energy techniques benefit from improved image quality, which enhances the diagnostic value of these scans. Additionally, DECT enables the generation of advanced postprocessed image reconstructions that may be utilized to reduce the radiation and contrast media doses required in patients, thus making cardiac CT scans safer overall. The latest emerging advancement in CT imaging is photon-counting CT (PCCT) scanning that employs state-of-the-art photon detectors. This technology promises higher spatial resolution and lower image noise, which are critical in visualizing the small structures of the heart such as coronary arteries and stents. That said, the use of PCCT for cardiac imaging is still under investigation with very few research scans performed in human subjects. As more validation studies are performed, time will tell whether PCCT is set to become the next frontier of cardiac CT imaging.

1 History of Cardiac Imaging

The value and potential of computed tomography (CT) in cardiac imaging was realized soon after the first cardiovascular CT scans were performed in the early 1980s. At that time, imaging options for the heart included angiography, radiography, early forms of magnetic resonance imaging (MRI), and echocardiography, the last of which was considered to be the reference standard. These cutting-edge cardiovascular CT scans were initially limited to diagnosing aortic dissections and evaluating patency of coronary artery bypass grafts as it was evident that they had better diagnostic performances for those purposes than echocardiography. Within the following few years, the use of cardiovascular CT expanded and found its way into clinical practice as an imaging modality for various cardiovascular abnormalities, including the evaluation of coronary arteries, myocardial perfusion, ischemic cardiomyopathy, and intra-cardiac thrombi (Brundage and Lipton 1982).

More so than other organ systems, cardiovascular structures are particularly challenging to image, and therefore they are rarely, if ever, the first organ system to be the center of investigations by new imaging modalities and techniques. There are several reasons for this distinguished status, and the severity of the resulting limitations vary by modality. The most prominent challenge to overcome is the heart's perpetual movement originating from myocardial contraction, motion of cardiac valves, and respiration. There are three

possibilities to mitigate the impact of motion on the quality of the resulting images. One would be to stop the movement of the heart, which is not performed in humans for obvious reasons. A second option is to acquire images instantaneously, as in echocardiography. The third method is to synchronize acquisition of the images to the rhythm of the heart, as in ECG-gated CT or MRI. Another challenging attribute that makes imaging of the heart more problematic is its position. Being located deep within the thorax and protected by the rib cage, it is one of the two most shielded organs in the human body, along with the brain. This attribute limits acoustic windows on ultrasonography, increases image noise on CT, and reduces radiofrequency signal for MRI. All these encountered difficulties are not prominent when imaging other structures of the body.

An ever-increasing demand for medical diagnostic tools has fueled technological advances in the field of radiology, which in turn has greatly expanded utilization of non-invasive cardiac imaging. Today's physicians have several prominent options of imaging modalities for the cardiovascular system, such as CT, MRI, nuclear stress testing, and echocardiography; each having its own specific indications for appropriate use. This chapter will explore the use of dual-energy computed tomography (DECT), discuss benefits of multi-energy imaging, and provide an outlook on the future role and applications of photon-counting computed tomography (PCCT) in cardiac imaging.

2 Benefits and Applications of Cardiac CT Imaging

Cardiac CT has come a long way since its early days and has grown significantly in complexity and clinical utility. Technical innovations have significantly reduced radiation doses associated with CT imaging, and safety concerns previously raised over exposure to ionizing radiation have dwindled. Over the past decade, advanced DECT scanners have gained wide-

spread popularity at many medical centers as the utilization of CT imaging continued to climb. These scanners offer high temporal resolution, necessary to image moving structures such as the myocardium and heart valves, and high spatial resolution, needed to differentiate small structures such as the coronary arteries. The practicality and attractiveness for the use of CT lies in the relative ease and speed in performing examinations, making them particularly useful for patients presenting to emergency departments.

While no single modality offers a “one-stop-shop” for all cardiac imaging purposes, CT has become the guidelines' recommended first-line imaging test for various heart conditions. Coronary CT angiography (CCTA) is deemed a first-line test for stable chest pain as recommended by the American College of Cardiology/American Heart Association guideline of 2012 and European Society of Cardiology guideline of 2019 (Knuuti et al. 2020; Fihn et al. 2012). CCTA is also a first-line investigation recommended in patients presenting with acute chest pain, who are at low to intermediate risk of acute coronary syndrome (ACS), by a joint guideline published in 2010 by multiple medical societies spearheaded by the American College of Cardiology (Taylor et al. 2010). This guideline also deems the use of cardiac CT appropriate for evaluation of systolic function, ventricular morphology, intra- and extra-cardiac structures, adult congenital heart diseases, as well as for preoperative assessment prior to various cardiac procedures. The United Kingdom's National Institute for Health and Care Excellence guideline published in 2017 also recommends CCTA as a first-line investigation for all patients presenting with chest pain due to suspected coronary artery disease (CAD) (Moss et al. 2017). Apart from being a tool to provide a diagnosis, cardiac CT is also used to calculate coronary artery calcium score and has also been incorporated into guidelines for risk assessment of cardiovascular adverse events (Grundy et al. 2019).

3 Functional Applications for Cardiac CT

Cardiac CT imaging was predominantly used solely for anatomical assessment, particularly in evaluating the severity of CAD. Recent innovations in CT technology have increased cardiac CT's potential applications. One of these ventures has been a cardiac functional application of CCTA to predict fractional flow reserve (FFR) by applying computational fluid dynamics. This can be processed and evaluated from a standard CCTA without the need for additional image acquisitions (Baumann et al. 2021; Schwartz et al. 2019). Another use for cardiac CT in functional assessment of the heart has been for the measurement of blood perfusion before and after myocardial stress. This technique can provide valuable information on the hemodynamic significance of coronary artery stenoses (Cannaò et al. 2015). In addition to detecting coronary plaque and indicating its burden, CCTA can also provide detailed characterization of plaque morphology which can aid in cardiac risk assessment (Nerlekar et al. 2018; Motoyama et al. 2015).

4 Advantages of Spectral Imaging

4.1 Optimizing Image Quality

The capacity to acquire CT images at more than one energy level and combining data obtained from all energy levels enables benefits that would not be possible on single-energy acquisitions. Information from each energy level image set is then postprocessed to create blended CT images. Basic postprocessing algorithms use linear blending and are based on blending image sets with a specific ratio assigned to each energy level (Cavedon and Rudin 2015). The resulting images will have characteristics similar to those that would have been obtained at an energy level intermediate to those of the image sets used, depending on ratios assigned (Johnson et al.

2007). More advanced non-linear algorithms are better able to optimize the blending process in order to improve enhancement and reduce image noise. This is done by selectively combining low- and high-energy image sets with varying ratios for different regions of the CT dataset based on attenuation.

4.2 Artifact Reduction

Dual- and multi-energy imaging can assess material differential attenuation at each energy level, which enables the measurement of the fractions of materials in each voxel. With this material-specific information on hand, the attenuation of each voxel can be extrapolated to any desired energy level using complex algorithms to generate virtual monoenergetic images (VMI). These images reduce beam hardening at higher energy levels, which consequently reduces high attenuation artifacts such as metal artifacts from stents and blooming artifacts from coronary artery calcification (Mangold et al. 2016a).

4.3 Reducing Contrast Media

In turn, low-energy VMI are able to substantially increase contrast enhancement, which is especially useful in CT scans where the contrast media bolus is suboptimally timed. This can enable a reduction in the volume and concentration of the contrast media administered while still achieving adequate enhancement in the lumen of vessels and myocardium. However, these low-energy VMI may suffer from an increase in image noise as a tradeoff for higher contrast attenuation (Albrecht et al. 2019). Newer processing algorithms known as VMI plus offer a solution for this limitation as they provide the ability to decompose data from each energy level. This serves to combine the benefits of high contrast enhancement on low-energy image sets with the low noise information on high-energy image sets, in contrast enhanced acquisitions (Lenga et al. 2017).

4.4 Virtual Reconstructions to Lower Radiation Dose

With material decomposition information available through the analysis of element dependent attenuation on multi-energy imaging, it is possible to create material-specific color overlay maps of the CT dataset. These can be used to generate iodine maps for measuring its concentration in tissue, for example. It is also possible to remove the iodine overlay maps to generate virtual non-contrast (VNC) images which can potentially eliminate the need for a true non-contrast (TNC) acquisition, thus reducing both scan times and the patients' exposure to radiation. These VNC images have been shown to have excellent correlation with TNC images (Yamada et al. 2014). Given its higher energy discriminating capabilities, the use of PCCT can provide even more discrete information on spectral attenuation than DECT. Theoretically, this can be utilized to achieve more accurate material decomposition (McCullough et al. 2015).

The major restricting factor in reducing radiation dose in scans acquired on single- or dual-energy CT is the resulting increase in image noise. This limitation may be ameliorated by the physical capabilities of PCCT which enable it to discriminate the low-amplitude signals causing electronic image noise and to exclude them by adjusting the low-energy threshold. Thus, the use of PCCT results in improved image quality and higher contrast-to-noise ratios (Wang et al. 2012; Rajagopal et al. 2020). This capacity serves to increase the diagnostic quality on low-dose CT scans, particularly in morbidly obese patients who require higher radiation doses to obtain diagnostic quality images (den Harder et al. 2016).

5 Coronary Arteries

5.1 Improvement of Imaging Quality and Artifact Reduction

With CCTA being established as the first-line test in the workup of patients presenting with sus-

pected CAD, a lot of effort has been placed into improving and optimizing the diagnostic quality of its images. Using spectral imaging, the lynchpin of further improvements is the generation of VMI reconstructions. In short, information from multi-energy CT datasets is used to reconstruct approximated VMI that represent CT images as they would be obtained using a true monoenergetic X-ray beam at specific tube voltages (Yu et al. 2011). Different studies have demonstrated that when using VMI, overall image quality is improved as compared to conventional 120 kVp images or polychromatic CT (Matsumoto et al. 2011; Pomerantz et al. 2013). Specific approaches in which spectral imaging, especially using VMI, can enhance the diagnostic value of CCTA are described here.

5.2 General Improvements of Image Quality

Inadequate CCTA image quality may be caused by various factors such as insufficient contrast density within the coronary arteries due to patient's obesity, inaccurate scan timing, insufficient contrast volume or contrast extravasation. The resulting diagnostic limitations due to poor image signal-to-noise ratio (SNR) and contrast-to-noise ratio (CNR) may potentially necessitate a repeat scan with additional contrast administration and radiation exposure (Yan et al. 2013). Low-energy VMI at 40 keV have been shown to boost iodine attenuation in suboptimal vascular studies, improve both objective and subjective image quality and obviate the need to repeat scans (Yu et al. 2011; Arendt et al. 2020; Grant et al. 2014; Kalisz et al. 2017). Furthermore, using VMI generated at 40–50 keV showed improved image quality, evaluability, and diagnostic accuracy compared to single-energy CCTA (Albrecht et al. 2016; Yi et al. 2019; Andreini et al. 2015). The amplification of iodine contrast may also be utilized in administration of smaller volumes of contrast media. Two studies reported equivalent coronary image quality in CCTA using only half of contrast media and amplifying iodine contrast using VMI at 50–60 keV

(Carrascosa et al. 2015; Huang et al. 2020). Mangold et al. investigated the use of DECT in obese patients and reported a routinely obtainable diagnostic image quality of CCTA (Mangold et al. 2016b). Ohta et al. described that coronary lumen in general is best assessed on 70 keV VMI, which showed the overall best SNC and CNR (Ohta et al. 2017).

5.3 Reducing Calcium Blooming Artifacts

Another advantage of multi-energy imaging is the ability to reduce calcium blooming artifacts. Such artifacts may potentially cause an overestimation of stenosis on CCTA and possibly lead to unnecessary invasive coronary angiography in patients with suspected CAD (Yan et al. 2013; Brodoefel et al. 2008; Cademartiri et al. 2005; Kruk et al. 2014; Zhang et al. 2008). Using high-energy VMI, earlier studies by Boll et al. and Scheffel et al. reported a reduction in calcium blooming artifacts and improvement in lumen visualization when extensive calcifications were present (Boll et al. 2008a; Scheffel et al. 2006). Several following studies showed that calcium blooming artifacts are significantly diminished on VMI generated at 80–90 keV, decreasing the stenotic grading and increasing luminal dimensions which led to more accurate assessments of coronary artery stenosis (Foley et al. 2016; Kang et al. 2010; Scheske et al. 2013; Van Hedent et al. 2018; Wang et al. 2011). A different approach in reducing calcium blooming artifacts involves using calcium subtraction images generated using spectral CT data. These have also been shown to improve coronary lumen visualization and diagnostic performance in patients with heavily calcified lesions (De Santis et al. 2018; Yunaga et al. 2017).

5.4 Improved Visualization of Coronary Artery Stents

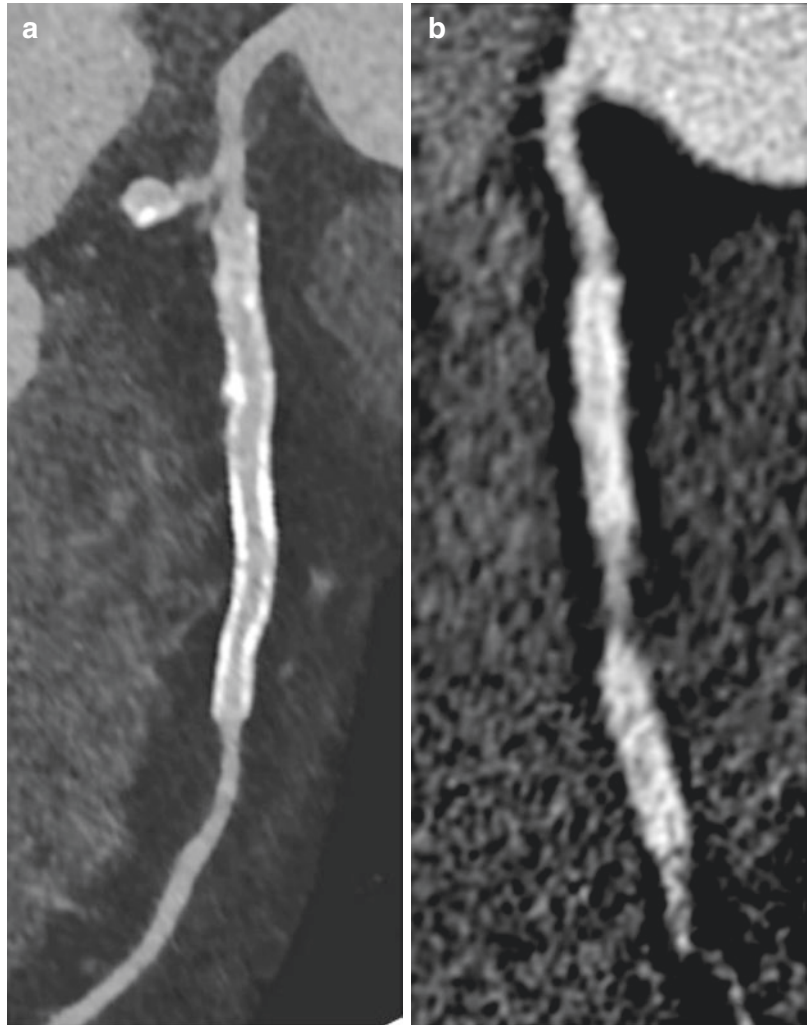
Similar to calcium blooming artifacts, high attenuation artifacts from metallic stents in coronary

arteries limit diagnostic quality, particularly when needing to evaluate the stent lumen. This may restrict performing a full assessment which is important given that in-stent restenosis is reported in about 5–10% of coronary artery stents (Gogas et al. 2013). Again, the use of high-energy VMI have been shown to improve image quality by reducing noise and beam hardening artifacts (Fig. 1) (Fuchs et al. 2013; Kuchenbecker et al. 2015; Pessis et al. 2013; Secchi et al. 2015; Yu et al. 2012; Zou and Silver 2009). Several groups have reported reliable stent imaging with improved in-lumen visibility using VMI generated at 80–130 keV acquired using DECT as compared to reconstructions from single-energy CT (Mangold et al. 2016a; Boll et al. 2008b; Hickethier et al. 2017; Stehli et al. 2015).

5.5 Improved Plaque Imaging

It is an established fact that different histomorphologic characteristics of coronary artery plaques have distinct prognostic implications (Narula et al. 2013). Using CCTA, it may be possible to identify several plaque features such as plaque burden, positive remodeling, napkin ring sign, and small spotty calcifications which have been associated with instability and high risk for ACS (Andreini et al. 2020; Danad et al. 2015; Ferencik et al. 2018; Hoffmann et al. 2006; Williams et al. 2019). Promising earlier ex vivo studies showed very good potential for DECT in further differentiation of certain plaque features. Barreto et al. compared 80 and 140 kVp images to show changes in attenuation of densely calcified and fibrocalcific plaques (Barreto et al. 2008). The ability to discriminate between lipid-rich and fibrous plaques using both 80 and 140 kVp images has been reported by Tanami et al. (Tanami et al. 2010). Zachrisson et al. described better discrimination of soft tissues occurring in plaques with DECT (Zachrisson et al. 2010). Furthermore, Obaid et al. showed improved differentiation of necrotic core and fibrous plaque in ex vivo arteries using DECT that was not, however, translated to in vivo imaging due to reduced image quality (Obaid et al. 2014). A different

Fig. 1 Curved multiplanar reconstruction (MPR) from (a) 120 keV reconstruction generated from DECT and (b) SECT. VMI reconstructions on DECT reduce image noise and beam hardening artifacts in imaging of coronary stents and improve the overall visibility of the lumen which is important to assess for in-stent restenosis



approach by Haghighi et al. showed the potential of DECT to investigate the composition of non-calcified plaques using electron density and effective atomic numbers (Haghighi et al. 2015). VMI reconstructions at varying energy levels may also provide increased accuracy in diagnosing stenoses in regard to plaque composition. For example, Stehli et al. reported that 90 keV VMI provided the best luminal evaluation when calcified and mixed plaques are present (Stehli et al. 2016). More recent literature also reported that spectral CT imaging can further improve CNR and the differentiation of plaque components on CCTA, which aids in more accurate assessment of plaque vulnerability (Boussel et al. 2014; Mandal et al. 2018; Symons et al. 2018a).

However, such findings are yet to be applied in practice for clinical assessments.

5.6 Calcium Scoring

Using multi-energy CT data, VNC images can be generated from contrast enhanced CT scans by subtracting the component of the iodine attenuation from the CT attenuation number (Fig. 2) (McCollough et al. 2015). These images had gained a special interest since they have potential to reduce both radiation dose and scan time and to eliminate the need for pre-contrast scans of the heart when assessing coronary artery calcium (CAC) burden (Yamada et al. 2014; Kay 2020;

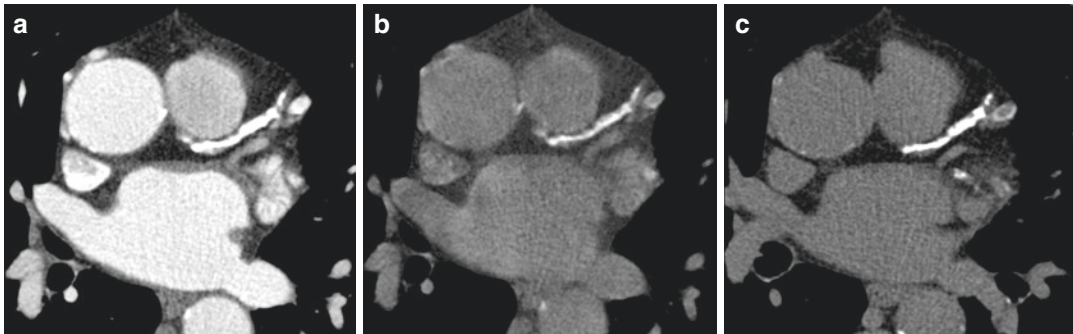


Fig. 2 (a) Contrast enhanced, (b) virtual non-contrast (VNC), and (c) true non-contrast (TNC) acquisitions from a patient with coronary artery calcifications in the LAD. The quality of the VNC image is comparable to that

of TNC and the calcifications can be easily visualized without necessitating an additional non-enhanced CT acquisition

Kim et al. 2009). Different studies showed high correlation between TNC and VNC images, however, all of them reported lower CAC values when reading VNC images, which led to a more limited clinical applicability (Yamada et al. 2014; Fuchs et al. 2014; Schwarz et al. 2012; Song et al. 2016). A recent study by Nadjiri et al. reported that VNC underestimated CAC volume and plaque density and that CAC scores obtained from VNC are approximately half of those from TNC images (Nadjiri et al. 2018). The results of these studies demonstrate that there is potential to reliably calculate CAC scores using VNC images, but further validation is required before they can be implemented in clinical practice.

6 Myocardial Characterization

6.1 Myocardial Fibrosis

Myocardial extracellular volume (ECV) fraction is increased as a result of myocardial remodeling and subsequent fibrosis, which are hallmarks of several cardiomyopathies. Conventionally, MRI has been used to evaluate ECV with a both true non-contrast and delayed contrast phase acquisitions (Schoepf 2019). Given the wider availability of CT, its shorter examination times, and the shortfalls of MRI in patients with metal implants, several groups have examined and found good correlation between CT and MRI derived ECV

values (Nacif et al. 2012, 2013; Kurita et al. 2016). Through material decomposition capabilities of multi-energy imaging, which allow the differentiation of iodine attenuation at more than one energy level, it is possible to quantify iodine content and distribution and to use it as a surrogate marker for blood volume (Fig. 3). This has led to more investigations assessing ECV values derived from a single delayed phase DECT acquisition with processing of VNC images. Van Assen et al. demonstrated the feasibility of this approach and its ability to differentiate diseased from healthy myocardium (van Assen et al. 2019a). Furthermore, Abadia et al. quantified myocardial ECV using iodine maps without VNC or TNC images and established the cutoff values that may be used to identify diseased tissue. (Abadia et al. 2020).

6.2 Iron Overload

Myocardial iron deposition is caused by iron overload states such as hemochromatosis, certain hematologic diseases or frequent blood transfusions. These form another spectrum of conditions for which DECT may be a fast and reliable diagnostic tool. Although the gold standard for diagnosing iron overload in organs is tissue biopsy, imaging with MRI has been widely utilized in clinical practice due to its non-invasive nature (Chu et al. 2012). An early feasibility study by

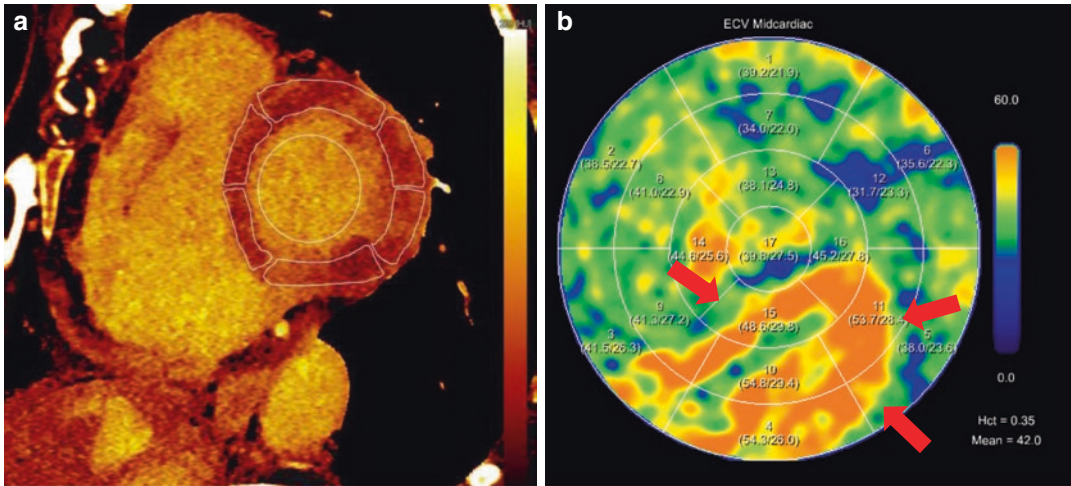


Fig. 3 (a) An illustration of an iodine map obtained from a delayed contrast-enhanced DECT scan showing manually performed segmentations of the left ventricular and blood pool (b) Myocardial extracellular volume (ECV)

polar map, generated by a fully automated method, showing a regional elevation in ECV readings (arrows) that indicate myocardial scarring from cardiomyopathy

Hazirolan et al. on cardiac DECT performed in thalassemia patients showed good correlation for HU values from the septal muscles with corresponding T2* values in MRI. Later phantom studies evaluating iron content in porcine cardiac tissue and tube phantoms also found very high correlations for measurements performed on DECT and MRI scans (Tsai et al. 2014; Ibrahim and Bowman 2014). Conversely, a more recent study by Ma et al. assessing iron overload with DECT and MRI in patients with histories of myelodysplastic syndrome or aplastic anemia failed to show a good correlation in myocardial iron content measurements. This is despite finding a strong correlation in liver iron content measurements obtained from both modalities (Ma et al. 2020).

6.3 Perfusion Imaging

Adding functional assessment of the heart in addition to the anatomical evaluation that is traditionally reported on every cardiac CT scan provides a more comprehensive representation of cardiac physiology. It can provide valuable information on the hemodynamic relevance of coronary stenosis and allow physicians to timely

select appropriate treatments and interventions (Pijls et al. 2010). There are two technical approaches for analyzing myocardial perfusion on cardiac CT using rest and stress images. The first and more basic approach is the static “single-shot” scan with image acquisition performed in a narrow temporal window within the early first-pass arterial phase. The second approach is a dynamic one that uses several consecutive acquisitions throughout the cardiac cycle and captures the first pass of contrast during wash-in and wash-out phases which makes quantitative analysis of myocardial blood flow possible.

Dynamic CT for myocardial perfusion has been shown to have a clear advantage over static CT and shows high diagnostic accuracy in detecting ischemia when compared to MRI and SPECT (Bamberg et al. 2014; Sørgaard et al. 2016; Caruso et al. 2016). The added benefit for DECT over SECT in perfusion imaging is its ability to evaluate the distribution of blood using iodine maps, which more accurately reflect its content, rather than through the measurement of contrast attenuation on CT images which is utilized in SECT (Schoepf 2019). This is supported by the results of Arnoldi et. el. that examined the accuracy for detection of myocardial perfusion deficits on SECT and DECT scans and concluded

that iodine maps from DECT showed better correlation with SPECT findings in diagnosing myocardial hypoperfusion (Arnoldi et al. 2011). As such, iodine concentration has the potential to differentiate between ischemic and normal myocardium (van Assen et al. 2019b).

6.4 Scar Imaging

Delayed gadolinium enhancement on CMR has been the go-to imaging test for evaluating myocardial scarring given its higher sensitivity and CNR compared to delayed enhanced SECT (Nieman et al. 2008). Yet, spectral imaging CT using VMI reconstructions can slightly improve the performance of CT for that use (Fig. 4). Sandfort et al. conducted a DECT study on human and canine subjects to evaluate CNR values in infarcted myocardial tissue. They concluded that VMI plus reconstructions at 40 keV improved infarct delineation in canine subjects, with histology as a reference standard, by up to 25% compared to conventional VMI. These reconstructions also provided higher CNR compared to conventional VMI and linearly blended images, yet their values did not exceed 4.2. In contrast, CNR values from delayed gadolinium enhancement on MRI are generally greater than 10 (Sandfort et al. 2017). Undeterred by underwhelming results for a role for VMI plus in scar imaging, Ohta et al. evaluated the use of iodine density images against MRI in detecting and classifying myocardial scarring patients with heart failure. They reported

that these images had a mean CNR of 9.14 with a sensitivity and specificity of 92% and 98%, respectively, in detecting the myocardial delayed enhancement that represents scar tissue (Ohta et al. 2018).

7 Cardiac Valves

Cardiac CT provides a comprehensive modality for non-invasive anatomical examination of the cardiac valves. This makes it an optimal tool for pre-procedural planning in patients scheduled to undergo transcatheter aortic valve replacement (TAVR). CT examinations for this purpose involve measurements of geometrical dimensions of the aortic valve, its degree of calcification and its distance from the coronary ostia. These values are necessary to appropriately select prosthesis model and size, which is of paramount importance in improving post-operative outcomes (Binder et al. 2013; Tops et al. 2008). Multi-energy imaging has been thoroughly evaluated in this particular patient group and its potential and added value in improving the CT protocols has been examined.

The value of noise-optimized VMI reconstructions was assessed in the prospective Spectral CT Assessment Prior to TAVR (SPECTACULAR) study which showed the feasibility of using VMI with administering lower contrast media doses while ensuring a comprehensive evaluation of vessel access and aortic root dimensions (Cavallo et al. 2020). Reducing the risk of acute kidney

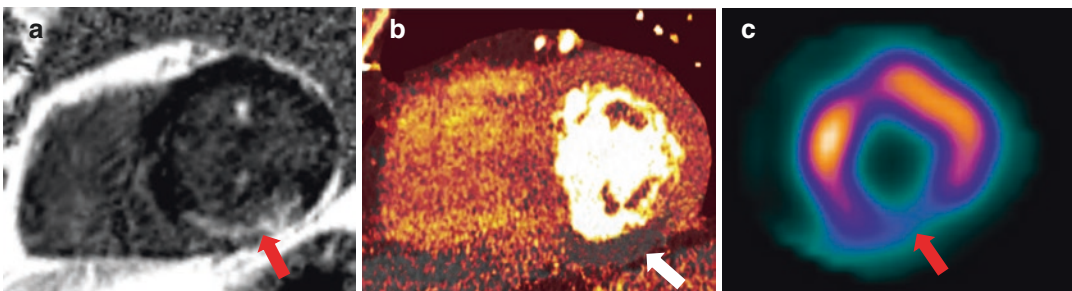


Fig. 4 (a) Phase sensitive inversion recovery (PSIR) sequence on delayed enhancement MRI, (b) iodine map from DECT, and (c) single-photon emission computed tomography (SPECT). Perfusion abnormality (arrows) in

the inferior ventricular wall is observed on all three modalities. The defect is illustrated as hyperenhancement in (a), reduction of iodine content in (b), and reduction in radiotracer uptake in (c)

injury is particularly desired in TAVR candidates as renal dysfunction is present in about half of this patient group (Faggiano et al. 2012). The image quality of noise-optimized VMI plus reconstructions was evaluated in a study by Martin et al. where it was compared to traditional VMI reconstructions as well as standard linearly blended images. It concluded that these advanced reconstructions significantly increased CNR and SNR over the others (Martin et al. 2017).

Given that metallic aortic valves demonstrate moderate to severe high attenuation artifact, assessment for post-procedural complications such as valve thrombosis or paravalvular leaks may become complicated on CT (Suchá et al. 2015). For this purpose, Schwartz et al. conducted a study on 80 patients with aortic valve replacement to quantify metal artifact and reported that high keV VMI offered up to 17.2% artifact reduction when compared with standard SECT (Schwartz et al. 2020). Finally, dual source CT scanners may also be operated in single-energy mode at low-tube-voltage acquisitions to safely and effectively evaluate TAVR candidates using a lower radiation dose (Felmly et al. 2017).

8 Cardiac Masses

Intra-cardiac masses such as lipomas, fibromas, myxomas, and thrombi are very rare entities found in less than 0.1% of autopsy studies and are often assessed by echocardiography as a first-line diagnostic modality. Not infrequently, another confirmatory imaging modality would be requested when echocardiography is inconclusive due to poor acoustic windows or artifacts (Mankad and Herrmann 2016). CT offers a high-resolution volumetric evaluation of the heart and can explore a cardiac tumor's relationship with adjacent structures such as chambers, arteries, valves, myocardium or epicardium. It can also offer a comprehensive four-dimensional anatomical assessment in planning for surgical resection of cardiac tumors if indicated (Young et al. 2019). Hur et al. evaluated the diagnostic performance of cardiac DECT in detecting left atrial appendage thrombi, using the findings from the gold-

standard transesophageal echocardiography (TEE) as a reference, and reported each of the sensitivity, specificity, negative predictive value, and positive predicted value to exceed 95% (Hur et al. 2012). As such, DECT can provide an excellent alternative for diagnosis given that TEE is often uncomfortable to patients and requires specialized skills to perform it and interpret its results. Additionally, material composition capabilities of DECT are useful in differentiating between cardiac masses. Results from Hong et al. illustrate that iodine concentrations on DECT were significantly higher in cardiac myxomas compared to thrombi, while attenuation values in Hounsfield units showed no difference between the two (Hong et al. 2014).

9 Outlook Cardiac CT

9.1 Artificial Intelligence and Radiomics

Being in a medical specialty that is heavily reliant on technology, radiologists are often among the pioneering physicians who openly embrace and incorporate new innovations into their practice. As with other sectors of industry, the rise of artificial intelligence (AI) promises to revolutionize many workplaces, including departments of radiology. AI has found its way into cardiac CT workflows and has been used for applications such as the automated detection of coronary artery calcium, measurement of myocardial perfusion, and measurement of CT derived FFR (Monti et al. 2020; Fischer et al. 2020; Tesche and Gray 2020). Besides its use in detection or measurement of findings, AI has also been utilized for optimizing scanning protocols for individual patient requirements and for improving CT image quality and reducing image noise (Wang et al. 2019; Sharma et al. 2020). Radiomics is another discipline whose potential in cardiac CT is also being explored. This developing field aims to utilize spatial and texture information from every voxel on a CT image for use in quantitative analysis in order to identify biomarkers that can expand diagnostic and predictive abili-

ties based on imaging (Kolossváry et al. 2018). A recent study by Kolossváry et al. demonstrated that cluster analysis of radiomic features of coronary plaque on CCTA differentiated between patients with traditional cardiovascular risk factors and those with nontraditional risk factors such as cocaine use and HIV. This enables morphologic phenotyping of CAD and provides more insight into the pathogenesis of CAD (Kolossváry et al. 2021). Such new developments hold great promise for use in cardiac CT and will continue to modernize the practice of radiology in the coming years and may even be the driving force for a new era of personalized precision medicine in management of cardiac disease (Schoepf and Emrich 2021).

9.2 Photon-Counting CT

A principal development of PCCT over DECT lies in its photon detector systems used. The advanced physical properties of detectors in PCCT scanners enable them to have higher dose efficiency and be smaller in size. This in turn vastly improves spatial resolution and quality of the resulting images when compared side-by-side with those obtained from DECT scans that use identical tube voltage, tube current, and reconstruction parameters (Mannil et al. 2018). Thus, PCCT leads to overall increased diagnostic abilities and confidence when assessing miniscule structures such as small coronary plaques or the distal coronary arteries.

At the time of writing of this chapter, the field of cardiac PCCT is still in its infancy. The number of published articles evaluating the heart using this novel technology remains in the single digits with only one article describing the use of PCCT for imaging of the heart human volunteers. Hence the information on its use in cardiac imaging derives from pre-clinical phantom studies, as well as from extrapolating experiences with dual-energy spectral imaging. The major technical advantages for use of PCCT lie in its increased spatial resolution and lower noise levels leading to better quality images. Image noise is a restrict-

ing factor when trying to reduce radiation dose in CT imaging and the optimized noise properties of PCCT images may be the key to overcome that limitation. Given the physical abilities of detectors in PCCT, they have to ability to significantly decrease spectral overlap. This in turn leads to improved CNR compared to DECT which further enhances its spectral imaging capabilities such as material decomposition (Sandfort et al. 2020).

First pre-clinical PCCT studies reported improved SNR in iodine enhanced scans that may translate to further reductions in the contrast doses necessary in CT imaging (Leng et al. 2017). Increased spatial resolution and multi-material composition bear the possibility to further improve imaging of the coronary arteries and to aid in reducing calcium blooming artifacts (Holmes et al. 2020; Leng et al. 2018). Increased spatial resolution has also been shown to improve visualization of coronary artery stents and stent-lumen evaluation, which allows for non-invasive assessment of in-stent restenosis (Mannil et al. 2018; Bratke et al. 2020; Sigovan et al. 2019; Symons et al. 2018b). Another promising field of PCCT is the assessment of CAC score. Having a CAC score of zero has been described as a 15-year warranty period against mortality in asymptomatic patients (Valenti et al. 2015). Because of this, it is important to identify patients with ultra-low calcium scores and further discriminate between patients with zero and near zero CAC scores that may still be at risk (Hsieh et al. 2020; Senoner et al. 2020). First in vivo experiences by Symons et al. showed that PCCT can significantly improve CAC scoring and might even reduce radiation dose while maintaining diagnostic quality (Symons et al. 2019). It was shown that PCCT has the potential to accurately quantify the mass and density of CAC lesions which might quickly translate into its use in clinical practice, and to obsolescence of the currently necessary TNC cardiac CT scans (Juntunen et al. 2020). Also, further discrimination of calcified lesions by their density, shape and distribution could enhance risk assessment models and lead to more personalized management plans of patients (Sandfort et al. 2020).

9.3 Conclusion

Cardiac CT is a fundamental tool for imaging of the heart. It is the guideline-recommended first-line test in a variety of cardiac conditions, plays an essential role in planning of cardiac procedures, and is utilized in cardiovascular risk stratification of patients. It has gradually developed from a static and purely anatomical image modality and is now able to provide us with functional information on the heart. Additionally, the rise of spectral imaging capabilities in CT with dual-energy scanners has enabled the differentiation of materials based on atomic numbers, as well as the development of complex post-processing image reconstructions algorithms. These may be used to make CT a safer option for patients by reducing the contrast and radiation doses necessary. More recent advancements in photon detector technologies of CT systems have led to the introduction of PCCT scanners that have a promising potential for cardiac imaging due to their higher spatial resolution and the advantages that they carry for improved visualization of the coronary arteries. The refinement of these CT systems as well as research on their use in human subjects is still ongoing. Based on findings over the next few years, we may be witnessing the steady surge of PCCT to become the mainstream of cardiac CT imaging.

Compliance with Ethical Standards

Disclosure of Interests U. Joseph Schoepf has received institutional research support, consulting fees, and/or speaker honoraria from Bayer, Bracco, Elucid, GE, Guerbet, HeartFlow Inc., Keya Medical, and Siemens. Tilman Emrich has received a speaker fee and travel support from Siemens. Akos Varga-Szemes receives institutional research support from Siemens and is a consultant for Bayer and Elucid Bioimaging. The other authors have no potential conflict of interest to disclose.

Funding This book chapter did not receive any grant from funding agencies in the public, commercial, or not-for-profit sectors.

References

Abadia AF, van Assen M, Martin SS, Vingiani V, Griffith LP, Giovagnoli DA, Bauer MJ, Schoepf UJ (2020) Myocardial extracellular volume fraction to differenti-

- ate healthy from cardiomyopathic myocardium using dual-source dual-energy CT. *J Cardiovasc Comput Tomogr* 14(2):162–167. <https://doi.org/10.1016/j.jcct.2019.09.008>
- Albrecht MH, Trommer J, Wichmann JL, Scholtz J-E, Martin SS, Lehnert T, Vogl TJ, Bodelle B (2016) Comprehensive comparison of virtual monoenergetic and linearly blended reconstruction techniques in third-generation dual-source dual-energy computed tomography angiography of the thorax and abdomen. *Investig Radiol* 51(9):582–590. <https://doi.org/10.1097/RLI.0000000000000272>
- Albrecht MH, Vogl TJ, Martin SS, Nance JW, Duguay TM, Wichmann JL, De Cecco CN, Varga-Szemes A, van Assen M, Tesche C, Schoepf UJ (2019) Review of clinical applications for virtual monoenergetic dual-energy CT. *Radiology* 293(2):260–271. <https://doi.org/10.1148/radiol.2019182297>
- Andreini D, Pontone G, Mushtaq S, Bertella E, Conte E, Segurini C, Giovannardi M, Baggiano A, Annoni A, Formenti A, Petullà M, Beltrama V, Volpato V, Bartorelli AL, Trabattini D, Fiorentini C, Pepi M (2015) Diagnostic accuracy of rapid kilovolt peak-switching dual-energy CT coronary angiography in patients with a high calcium score. *JACC Cardiovasc Imaging* 8(6):746–748. <https://doi.org/10.1016/j.jcmg.2014.10.013>
- Andreini D, Magnoni M, Conte E, Masson S, Mushtaq S, Berti S, Canestrari M, Casolo G, Gabrielli D, Latini R, Marraccini P, Moccetti T, Modena MG, Pontone G, Gorini M, Maggioni AP, Maseri A (2020) Coronary plaque features on CTA can identify patients at increased risk of cardiovascular events. *JACC Cardiovasc Imaging* 13(8):1704–1717. <https://doi.org/10.1016/j.jcmg.2019.06.019>
- Arendt CT, Czwikla R, Lenga L, Wichmann JL, Albrecht MH, Booz C, Martin SS, Leithner D, Tischendorf P, Blandino A, Vogl TJ, D'Angelo T (2020) Improved coronary artery contrast enhancement using noise-optimised virtual monoenergetic imaging from dual-source dual-energy computed tomography. *Eur J Radiol* 122:108666. <https://doi.org/10.1016/j.ejrad.2019.108666>
- Arnoldi E, Lee YS, Ruzsics B, Weininger M, Spears JR, Rowley CP, Chiaramida SA, Costello P, Reiser MF, Schoepf UJ (2011) CT detection of myocardial blood volume deficits: dual-energy CT compared with single-energy CT spectra. *J Cardiovasc Comput Tomogr* 5(6):421–429. <https://doi.org/10.1016/j.jcct.2011.10.007>
- Bamberg F, Marcus RP, Becker A, Hildebrandt K, Bauner K, Schwarz F, Greif M, von Ziegler F, Bischoff B, Becker HC, Johnson TR, Reiser MF, Nikolaou K, Theisen D (2014) Dynamic myocardial CT perfusion imaging for evaluation of myocardial ischemia as determined by MR imaging. *JACC Cardiovasc Imaging* 7(3):267–277. <https://doi.org/10.1016/j.jcmg.2013.06.008>
- Barreto M, Schoenhagen P, Nair A, Amatangelo S, Milite M, Obuchowski NA, Lieber ML, Halliburton SS (2008) Potential of dual-energy computed tomography

- to characterize atherosclerotic plaque: ex vivo assessment of human coronary arteries in comparison to histology. *J Cardiovasc Comput Tomogr* 2(4):234–242. <https://doi.org/10.1016/j.jcct.2008.05.146>
- Baumann S, Kaeder F, Schoepf UJ, Golden JW, Kryeziu P, Tesche C, Renker M, Jannsen S, Weiss C, Hetjens S, Schoenberg SO, Borggreffe M, Akin I, Lossnitzer D, Overhoff D (2021) Prognostic value of coronary computed tomography angiography-derived morphologic and quantitative plaque markers using semiautomated plaque software. *J Thorac Imaging* 36(2):108–115. <https://doi.org/10.1097/rti.0000000000000509>
- Binder RK, Webb JG, Willson AB, Urena M, Hansson NC, Norgaard BL, Pibarot P, Barbanti M, Larose E, Freeman M, Dumont E, Thompson C, Wheeler M, Moss RR, Yang TH, Pasian S, Hague CJ, Nguyen G, Raju R, Toggweiler S, Min JK, Wood DA, Rodés-Cabau J, Leipsic J (2013) The impact of integration of a multidetector computed tomography annulus area sizing algorithm on outcomes of transcatheter aortic valve replacement: a prospective, multicenter, controlled trial. *J Am Coll Cardiol* 62(5):431–438. <https://doi.org/10.1016/j.jacc.2013.04.036>
- Boll DT, Merkle EM, Paulson EK, Mirza RA, Fleiter TR (2008a) Calcified vascular plaque specimens: assessment with cardiac dual-energy multidetector CT in anthropomorphically moving heart phantom. *Radiology* 249(1):119–126. <https://doi.org/10.1148/radiol.2483071576>
- Boll DT, Merkle EM, Paulson EK, Fleiter TR (2008b) Coronary stent patency: dual-energy multidetector CT assessment in a pilot study with anthropomorphic phantom. *Radiology* 247(3):687–695. <https://doi.org/10.1148/radiol.2473070849>
- Boussel L, Coulon P, Thran A, Roessler E, Martens G, Sigovan M, Douek P (2014) Photon counting spectral CT component analysis of coronary artery atherosclerotic plaque samples. *BJR* 87(1040):20130798. <https://doi.org/10.1259/bjr.20130798>
- Bratke G, Hickehier T, Bar-Ness D, Bunck AC, Maintz D, Pahn G, Coulon P, Si-Mohamed S, Douek P, Sigovan M (2020) Spectral photon-counting computed tomography for coronary stent imaging: evaluation of the potential clinical impact for the delineation of in-stent stenosis. *Investig Radiol* 55(2):61–67. <https://doi.org/10.1097/RLI.0000000000000610>
- Brodoefel H, Burgstahler C, Tsiflikas I, Reimann A, Schroeder S, Claussen CD, Heuschmid M, Kopp AF (2008) Dual-source CT: effect of heart rate, heart rate variability, and calcification on image quality and diagnostic accuracy. *Radiology* 247(2):346–355. <https://doi.org/10.1148/radiol.2472070906>
- Brundage BH, Lipton MJ (1982) The emergence of computed tomography as a cardiovascular diagnostic technique. *Am Heart J* 103(2):313–316. [https://doi.org/10.1016/0002-8703\(82\)90517-8](https://doi.org/10.1016/0002-8703(82)90517-8)
- Cademartiri F, Mollet NR, Runza G, Bruining N, Hamers R, Somers P, Knaapen M, Verheye S, Midiri M, Krestin GP, de Feyter PJ (2005) Influence of intracoronary attenuation on coronary plaque measurements using multislice computed tomography: observations in an ex vivo model of coronary computed tomography angiography. *Eur Radiol* 15(7):1426–1431. <https://doi.org/10.1007/s00330-005-2697-x>
- Cannaò PM, Schoepf UJ, Muscogiuri G, Wichmann JL, Fuller SR, Secchi F, Varga-Szemes A, De Cecco CN (2015) Technical prerequisites and imaging protocols for dynamic and dual energy myocardial perfusion imaging. *Eur J Radiol* 84(12):2401–2410. <https://doi.org/10.1016/j.ejrad.2015.02.010>
- Carrascosa P, Leipsic JA, Capunay C, Deviggiano A, Vallejos J, Goldsmit A, Rodriguez-Granillo GA (2015) Monochromatic image reconstruction by dual energy imaging allows half iodine load computed tomography coronary angiography. *Eur J Radiol* 84(10):1915–1920. <https://doi.org/10.1016/j.ejrad.2015.06.019>
- Caruso D, Eid M, Schoepf UJ, Jin KN, Varga-Szemes A, Tesche C, Mangold S, Spandorfer A, Laghi A, De Cecco CN (2016) Dynamic CT myocardial perfusion imaging. *Eur J Radiol* 85(10):1893–1899. <https://doi.org/10.1016/j.ejrad.2016.07.017>
- Cavallo AU, Patterson AJ, Thomas R, Alaiti MA, Attizzani GF, Laukamp K, Große Hokamp N, Bezerra H, Gilkeson R, Rajagopalan S (2020) Low dose contrast CT for transcatheter aortic valve replacement assessment: results from the prospective SPECTACULAR study (spectral CT assessment prior to TAVR). *J Cardiovasc Comput Tomogr* 14(1):68–74. <https://doi.org/10.1016/j.jcct.2019.06.015>
- Cavedon C, Rudin S (2015) Cardiovascular and neurovascular imaging: physics and technology. CRC Press, Boca Raton
- Chu WC, Au WY, Lam WW (2012) MRI of cardiac iron overload. *J Magn Reson Imaging* 36(5):1052–1059. <https://doi.org/10.1002/jmri.23628>
- Danad I, Fayad ZA, Willemink MJ, Min JK (2015) New applications of cardiac computed tomography. *JACC Cardiovasc Imaging* 8(6):710–723. <https://doi.org/10.1016/j.jcmg.2015.03.005>
- De Santis D, Jin KN, Schoepf UJ, Grant KL, De Cecco CN, Nance JW, Vogl TJ, Laghi A, Albrecht MH (2018) Heavily calcified coronary arteries: advanced calcium subtraction improves luminal visualization and diagnostic confidence in dual-energy coronary computed tomography angiography. *Investig Radiol* 53(2):103–109. <https://doi.org/10.1097/RLI.0000000000000416>
- den Harder AM, Willemink MJ, de Jong PA, Schilham AM, Rajiah P, Takx RA, Leiner T (2016) New horizons in cardiac CT. *Clin Radiol* 71(8):758–767. <https://doi.org/10.1016/j.crad.2016.01.022>
- Faggiano P, Frattini S, Zilioli V, Rossi A, Nistri S, Dini FL, Lorusso R, Tomasi C, Cas LD (2012) Prevalence of comorbidities and associated cardiac diseases in patients with valve aortic stenosis. Potential implications for the decision-making process. *Int J Cardiol* 159(2):94–99. <https://doi.org/10.1016/j.ijcard.2011.02.026>
- Felmly LM, De Cecco CN, Schoepf UJ, Varga-Szemes A, Mangold S, McQuiston AD, Litwin SE, Bayer RR 2nd, Vogl TJ, Wichmann JL (2017) Low contrast

- medium-volume third-generation dual-source computed tomography angiography for transcatheter aortic valve replacement planning. *Eur Radiol* 27(5):1944–1953. <https://doi.org/10.1007/s00330-016-4537-6>
- Ferencik M, Mayrhofer T, Bittner DO, Emami H, Puchner SB, Lu MT, Meyersohn NM, Ivanov AV, Adami EC, Patel MR, Mark DB, Udelson JE, Lee KL, Douglas PS, Hoffmann U (2018) Use of high-risk coronary atherosclerotic plaque detection for risk stratification of patients with stable chest pain: a secondary analysis of the PROMISE randomized clinical trial. *JAMA Cardiol* 3(2):144. <https://doi.org/10.1001/jamacardio.2017.4973>
- Fihn SD, Gardin JM, Abrams J, Berra K, Blankenship JC, Dallas AP, Douglas PS, Foody JM, Gerber TC, Hinderliter AL, King SB 3rd, Kligfield PD, Krumholz HM, Kwong RY, Lim MJ, Linderbaum JA, Mack MJ, Munger MA, Prager RL, Sabik JF, Shaw LJ, Sikkema JD, Smith CR Jr, Smith SC Jr, Spertus JA, Williams SV, Anderson JL (2012) 2012 ACCF/AHA/ACP/AATS/PCNA/SCAI/STS guideline for the diagnosis and management of patients with stable ischemic heart disease: a report of the American College of Cardiology Foundation/American Heart Association task force on practice guidelines, and the American College of Physicians, American Association for Thoracic Surgery, Preventive Cardiovascular Nurses Association, Society for Cardiovascular Angiography and Interventions, and Society of Thoracic Surgeons. *Circulation* 126(25):e354–e471. <https://doi.org/10.1161/CIR.0b013e318277d6a0>
- Fischer AM, Eid M, De Cecco CN, Gulsun MA, van Assen M, Nance JW, Sahbaee P, De Santis D, Bauer MJ, Jacobs BE, Varga-Szemes A, Kabakus IM, Sharma P, Jackson LJ, Schoepf UJ (2020) Accuracy of an artificial intelligence deep learning algorithm implementing a recurrent neural network with long short-term memory for the automated detection of calcified plaques from coronary computed tomography angiography. *J Thorac Imaging* 35:S49–S57. <https://doi.org/10.1097/rti.0000000000000491>
- Foley WD, Shuman WP, Siegel MJ, Sahani DV, Boll DT, Bolus DN, De Cecco CN, Kaza RK, Morgan DE, Schoepf UJ, Vrtiska TJ, Yeh BM, Berland LL (2016) White paper of the Society of Computed Body Tomography and Magnetic Resonance on dual-energy CT, part 2: radiation dose and iodine sensitivity. *J Comput Assist Tomogr* 40(6):846–850. <https://doi.org/10.1097/RCT.0000000000000539>
- Fuchs TA, Stehli J, Fiechter M, Dougoud S, Gebhard C, Ghadri JR, Husmann L, Gaemperli O, Kaufmann PA (2013) First experience with monochromatic coronary computed tomography angiography from a 64-slice CT scanner with gemstone spectral imaging (GSI). *J Cardiovasc Comput Tomogr* 7(1):25–31. <https://doi.org/10.1016/j.jcct.2013.01.004>
- Fuchs TA, Stehli J, Dougoud S, Sah B-R, Bull S, Clerc OF, Possner M, Buechel RR, Gaemperli O, Kaufmann PA (2014) Coronary artery calcium quantification from contrast enhanced CT using gemstone spectral imaging and material decomposition. *Int J Cardiovasc Imaging* 30(7):1399–1405. <https://doi.org/10.1007/s10554-014-0474-0>
- Gogas BD, Garcia-Garcia HM, Onuma Y, Muramatsu T, Farooq V, Bourantas CV, Serruys PW (2013) Edge vascular response after percutaneous coronary intervention. *J Am Coll Cardiol Interv* 6(3):211–221. <https://doi.org/10.1016/j.jcin.2013.01.132>
- Grant KL, Flohr TG, Krauss B, Sedlmair M, Thomas C, Schmidt B (2014) Assessment of an advanced image-based technique to calculate virtual monoenergetic computed tomographic images from a dual-energy examination to improve contrast-to-noise ratio in examinations using iodinated contrast media. *Investig Radiol* 49(9):586–592. <https://doi.org/10.1097/RLI.0000000000000060>
- Grundy SM, Stone NJ, Bailey AL, Beam C, Birtcher KK, Blumenthal RS, Braun LT, de Ferranti S, Faiella-Tommasino J, Forman DE, Goldberg R, Heidenreich PA, Hlatky MA, Jones DW, Lloyd-Jones D, Lopez-Pajares N, Ndumele CE, Orringer CE, Peralta CA, Saseen JJ, Smith SC Jr, Sperling L, Virani SS, Yeboah J (2019) 2018 AHA/ACC/AACVPR/AAPA/ABC/ACPM/ADA/AGS/APhA/ASPC/NLA/PCNA guideline on the management of blood cholesterol: executive summary: a report of the American College of Cardiology/American Heart Association Task Force on Clinical Practice Guidelines. *J Am Coll Cardiol* 73(24):3168–3209. <https://doi.org/10.1016/j.jacc.2018.11.002>
- Haghighi RR, Chatterjee S, Tabin M, Sharma S, Jagia P, Ray R, Singh RP, Yadav R, Sharma M, Krishna K, Vani VC, Lakshmi R, Mandal SR, Kumar P, Arava S (2015) DECT evaluation of noncalcified coronary artery plaque. *Med Phys* 42(10):5945–5954. <https://doi.org/10.1118/1.4929935>
- Hickethier T, Baeßler B, Kroeger JR, Doerner J, Pahn G, Maintz D, Michels G, Bunck AC (2017) Monoenergetic reconstructions for imaging of coronary artery stents using spectral detector CT: in-vitro experience and comparison to conventional images. *J Cardiovasc Comput Tomogr* 11(1):33–39. <https://doi.org/10.1016/j.jcct.2016.12.005>
- Hoffmann U, Moselewski F, Nieman K, Jang I-K, Ferencik M, Rahman AM, Cury RC, Abbara S, Joneidi-Jafari H, Achenbach S, Brady TJ (2006) Noninvasive assessment of plaque morphology and composition in culprit and stable lesions in acute coronary syndrome and stable lesions in stable angina by multidetector computed tomography. *J Am Coll Cardiol* 47(8):1655–1662. <https://doi.org/10.1016/j.jacc.2006.01.041>
- Holmes T, Ulzheimer S, Pourmorteza A (2020) Dose-efficient ultra-high-resolution imaging of calcified coronary artery stenoses with photon-counting Ct. *J Cardiovasc Comput Tomogr* 14(3):S69. <https://doi.org/10.1016/j.jcct.2020.06.133>
- Hong YJ, Hur J, Kim YJ, Lee HJ, Hong SR, Suh YJ, Kim HY, Lee JW, Choi BW (2014) Dual-energy cardiac computed tomography for differentiating cardiac myxoma from thrombus. *Int J Cardiovasc Imaging* 30(Suppl 2):121–128. <https://doi.org/10.1007/s10554-014-0490-0>

- Hsieh SS, Leng S, Rajendran K, Tao S, McCollough CH (2020) Photon counting CT: clinical applications and future developments. *IEEE Trans Radiat Plasma Med Sci*:1–1. <https://doi.org/10.1109/TRPMS.2020.3020212>
- Huang X, Gao S, Ma Y, Lu X, Jia Z, Hou Y (2020) The optimal monoenergetic spectral image level of coronary computed tomography (CT) angiography on a dual-layer spectral detector CT with half-dose contrast media. *Quant Imaging Med Surg* 10(3):592–603. <https://doi.org/10.21037/qims.2020.02.17>
- Hur J, Kim YJ, Lee HJ, Nam JE, Hong YJ, Kim HY, Lee JW, Choi BW (2012) Cardioembolic stroke: dual-energy cardiac CT for differentiation of left atrial appendage thrombus and circulatory stasis. *Radiology* 263(3):688–695. <https://doi.org/10.1148/radiol.12111691>
- Ibrahim E-SH, Bowman AW (2014) Evaluation of iron overload: dual-energy computed tomography versus magnetic resonance imaging. *J Cardiovasc Magn Reson* 16(1):O92. <https://doi.org/10.1186/1532-429X-16-S1-O92>
- Johnson TR, Krauss B, Sedlmair M, Grasruck M, Bruder H, Morhard D, Fink C, Weckbach S, Lenhard M, Schmidt B, Flohr T, Reiser MF, Becker CR (2007) Material differentiation by dual energy CT: initial experience. *Eur Radiol* 17(6):1510–1517. <https://doi.org/10.1007/s00330-006-0517-6>
- Juntunen MAK, Inkinen SI, Ketola JH, Kotiaho A, Kauppinen M, Winkler A, Nieminen MT (2020) Framework for photon counting quantitative material decomposition. *IEEE Trans Med Imaging* 39(1):35–47. <https://doi.org/10.1109/TMI.2019.2914370>
- Kalisz K, Halliburton S, Abbara S, Leipsic JA, Albrecht MH, Schoepf UJ, Rajiah P (2017) Update on cardiovascular applications of multienergy CT. *RadioGraphics* 37(7):1955–1974. <https://doi.org/10.1148/rg.2017170100>
- Kang DK, Schoepf UJ, Bastarrika G, Nance JW, Abro JA, Ruzsics B (2010) Dual-energy computed tomography for integrative imaging of coronary artery disease: principles and clinical applications. *Semin Ultrasound CT MRI* 31(4):276–291. <https://doi.org/10.1053/j.sult.2010.05.004>
- Kay FU (2020) Dual-energy CT and coronary imaging. *Cardiovasc Diagn Ther* 10(4):1090–1107. <https://doi.org/10.21037/cdt.2020.04.04>
- Kim KP, Einstein AJ, Berrington de González A (2009) Coronary artery calcification screening: estimated radiation dose and cancer risk. *Arch Intern Med* 169(13):1188. <https://doi.org/10.1001/archinternmed.2009.162>
- Knuuti J, Wijns W, Saraste A, Capodanno D, Barbato E, Funck-Brentano C, Prescott E, Storey RF, Deaton C, Cuisset T, Agewall S, Dickstein K, Edvardsen T, Escaned J, Gersh BJ, Svitil P, Gilard M, Hasdai D, Hatala R, Mahfoud F, Masip J, Muneretto C, Valgimigli M, Achenbach S, Bax JJ (2020) 2019 ESC guidelines for the diagnosis and management of chronic coronary syndromes. *Eur Heart J* 41(3):407–477. <https://doi.org/10.1093/eurheartj/ehz425>
- Kolossváry M, Kellermayer M, Merkely B, Maurovich-Horvat P (2018) Cardiac computed tomography radiomics: a comprehensive review on radiomic techniques. *J Thorac Imaging* 33(1):26–34. <https://doi.org/10.1097/rti.0000000000000268>
- Kolossváry M, Gerstenblith G, Bluemke DA, Fishman EK, Mandler RN, Kickler TS, Chen S, Bhatia S, Lai S, Lai H (2021) Contribution of risk factors to the development of coronary atherosclerosis as confirmed via coronary CT angiography: a longitudinal radiomics-based study. *Radiology* 299(1):97–106. <https://doi.org/10.1148/radiol.2021203179>
- Kruk M, Noll D, Achenbach S, Mintz GS, Pęgowski J, Kaczmarska E, Kryczka K, Pracoń R, Dzielińska Z, Śleszycka J, Witkowski A, Demkow M, Rużyło W, Kępka C (2014) Impact of coronary artery calcium characteristics on accuracy of CT angiography. *JACC Cardiovasc Imaging* 7(1):49–58. <https://doi.org/10.1016/j.jcmg.2013.07.013>
- Kuchenbecker S, Faby S, Sawall S, Lell M, Kachelrieß M (2015) Dual energy CT: how well can pseudo-monochromatic imaging reduce metal artifacts?: DECT: can monoenergetic imaging remove metal artifacts? *Med Phys* 42(2):1023–1036. <https://doi.org/10.1118/1.4905106>
- Kurita Y, Kitagawa K, Kurobe Y, Nakamori S, Nakajima H, Dohi K, Ito M, Sakuma H (2016) Estimation of myocardial extracellular volume fraction with cardiac CT in subjects without clinical coronary artery disease: a feasibility study. *J Cardiovasc Comput Tomogr* 10(3):237–241. <https://doi.org/10.1016/j.jcct.2016.02.001>
- Leng S, Zhou W, Yu Z, Halaweish A, Krauss B, Schmidt B, Yu L, Kappler S, McCollough C (2017) Spectral performance of a whole-body research photon counting detector CT: quantitative accuracy in derived image sets. *Phys Med Biol* 62(17):7216–7232. <https://doi.org/10.1088/1361-6560/aa8103>
- Leng S, Rajendran K, Gong H, Zhou W, Halaweish AF, Henning A, Kappler S, Baer M, Fletcher JG, McCollough CH (2018) 150- μ m spatial resolution using photon-counting detector computed tomography technology: technical performance and first patient images. *Investig Radiol* 53(11):655–662. <https://doi.org/10.1097/RLI.0000000000000488>
- Lenga L, Albrecht MH, Othman AE, Martin SS, Leithner D, D'Angelo T, Arendt C, Scholtz JE, De Cecco CN, Schoepf UJ, Vogl TJ, Wichmann JL (2017) Monoenergetic dual-energy computed tomographic imaging: cardiothoracic applications. *J Thorac Imaging* 32(3):151–158. <https://doi.org/10.1097/rti.0000000000000259>
- Ma Q, Hu J, Yang W, Hou Y (2020) Dual-layer detector spectral CT versus magnetic resonance imaging for the assessment of iron overload in myelodysplastic syndromes and aplastic anemia. *Jpn J Radiol* 38(4):374–381. <https://doi.org/10.1007/s11604-020-00921-9>
- Mandal SR, Bharati A, Haghghi RR, Arava S, Ray R, Jagia P, Sharma S, Chatterjee S, Tabin M, Sharma M, Sharma S, Kumar P (2018) Non-invasive characterization of coronary artery atherosclerotic plaque using dual energy CT: explanation in ex-vivo sam-

- ples. *Phys Med* 45:52–58. <https://doi.org/10.1016/j.ejmp.2017.12.006>
- Mangold S, Cannaó PM, Schoepf UJ, Wichmann JL, Canstein C, Fuller SR, Muscogiuri G, Varga-Szemes A, Nikolaou K, De Cecco CN (2016a) Impact of an advanced image-based monoenergetic reconstruction algorithm on coronary stent visualization using third generation dual-source dual-energy CT: a phantom study. *Eur Radiol* 26(6):1871–1878. <https://doi.org/10.1007/s00330-015-3997-4>
- Mangold S, Wichmann JL, Schoepf UJ, Litwin SE, Canstein C, Varga-Szemes A, Muscogiuri G, Fuller SR, Stubenrauch AC, Nikolaou K, De Cecco CN (2016b) Coronary CT angiography in obese patients using 3rd generation dual-source CT: effect of body mass index on image quality. *Eur Radiol* 26(9):2937–2946. <https://doi.org/10.1007/s00330-015-4161-x>
- Mankad R, Herrmann J (2016) Cardiac tumors: echo assessment. *Echo Res Pract* 3(4):R65–r77. <https://doi.org/10.1530/erp-16-0035>
- Mannil M, Hieckthier T, von Spiczak J, Baer M, Henning A, Hertel M, Schmidt B, Flohr T, Maintz D, Alkadhi H (2018) Photon-counting CT: high-resolution imaging of coronary stents. *Investig Radiol* 53(3):143–149. <https://doi.org/10.1097/RLL.0000000000000420>
- Martin SS, Albrecht MH, Wichmann JL, Hüsters K, Scholtz JE, Booz C, Bodelle B, Bauer RW, Metzger SC, Vogl TJ, Lehnert T (2017) Value of a noise-optimized virtual monoenergetic reconstruction technique in dual-energy CT for planning of transcatheter aortic valve replacement. *Eur Radiol* 27(2):705–714. <https://doi.org/10.1007/s00330-016-4422-3>
- Matsumoto K, Jinzaki M, Tanami Y, Ueno A, Yamada M, Kuribayashi S (2011) Virtual monochromatic spectral imaging with fast kilovoltage switching: improved image quality as compared with that obtained with conventional 120-kVp CT. *Radiology* 259(1):257–262. <https://doi.org/10.1148/radiol.11100978>
- McCullough CH, Leng S, Yu L, Fletcher JG (2015) Dual- and multi-energy CT: principles, technical approaches, and clinical applications. *Radiology* 276(3):637–653. <https://doi.org/10.1148/radiol.2015142631>
- Monti CB, Codari M, van Assen M, De Cecco CN, Vliegenthart R (2020) Machine learning and deep neural networks applications in computed tomography for coronary artery disease and myocardial perfusion. *J Thorac Imaging* 35:S58–S65. <https://doi.org/10.1097/rti.0000000000000490>
- Moss AJ, Williams MC, Newby DE, Nicol ED (2017) The updated NICE guidelines: cardiac CT as the first-line test for coronary artery disease. *Curr Cardiovasc Imaging Rep* 10(5):15. <https://doi.org/10.1007/s12410-017-9412-6>
- Motoyama S, Ito H, Sarai M, Kondo T, Kawai H, Nagahara Y, Harigaya H, Kan S, Anno H, Takahashi H, Naruse H, Ishii J, Hecht H, Shaw LJ, Ozaki Y, Narula J (2015) Plaque characterization by coronary computed tomography angiography and the likelihood of acute coronary events in mid-term follow-up. *J Am Coll Cardiol* 66(4):337–346. <https://doi.org/10.1016/j.jacc.2015.05.069>
- Nacif MS, Kawel N, Lee JJ, Chen X, Yao J, Zavodni A, Sibley CT, Lima JA, Liu S, Bluemke DA (2012) Interstitial myocardial fibrosis assessed as extracellular volume fraction with low-radiation-dose cardiac CT. *Radiology* 264(3):876–883. <https://doi.org/10.1148/radiol.12112458>
- Nacif MS, Liu Y, Yao J, Liu S, Sibley CT, Summers RM, Bluemke DA (2013) 3D left ventricular extracellular volume fraction by low-radiation dose cardiac CT: assessment of interstitial myocardial fibrosis. *J Cardiovasc Comput Tomogr* 7(1):51–57. <https://doi.org/10.1016/j.jcct.2012.10.010>
- Nadjiri J, Kaissis G, Meurer F, Weis F, Laugwitz K-L, Straeter AS, Muenzel D, Noël PB, Rummey EJ, Rasper M (2018) Accuracy of calcium scoring calculated from contrast-enhanced coronary computed tomography angiography using a dual-layer spectral CT: a comparison of calcium scoring from real and virtual non-contrast data. *PLoS One* 13(12):e0208588. <https://doi.org/10.1371/journal.pone.0208588>
- Narula J, Nakano M, Virmani R, Kolodgie FD, Petersen R, Newcomb R, Malik S, Fuster V, Finn AV (2013) Histopathologic characteristics of atherosclerotic coronary disease and implications of the findings for the invasive and noninvasive detection of vulnerable plaques. *J Am Coll Cardiol* 61(10):1041–1051. <https://doi.org/10.1016/j.jacc.2012.10.054>
- Nerlekar N, Ha FJ, Cheshire C, Rashid H, Cameron JD, Wong DT, Seneviratne S, Brown AJ (2018) Computed tomographic coronary angiography-derived plaque characteristics predict major adverse cardiovascular events: a systematic review and meta-analysis. *Circ Cardiovasc Imaging* 11(1):e006973. <https://doi.org/10.1161/circimaging.117.006973>
- Nieman K, Shapiro MD, Ferencik M, Nomura CH, Abbara S, Hoffmann U, Gold HK, Jang IK, Brady TJ, Cury RC (2008) Reperfused myocardial infarction: contrast-enhanced 64-Section CT in comparison to MR imaging. *Radiology* 247(1):49–56. <https://doi.org/10.1148/radiol.2471070332>
- Obaid DR, Calvert PA, Gopalan D, Parker RA, West NEJ, Goddard M, Rudd JHF, Bennett MR (2014) Dual-energy computed tomography imaging to determine atherosclerotic plaque composition: a prospective study with tissue validation. *J Cardiovasc Comput Tomogr* 8(3):230–237. <https://doi.org/10.1016/j.jcct.2014.04.007>
- Ohta Y, Kitao S, Watanabe T, Kishimoto J, Yamamoto K, Ogawa T (2017) Evaluation of image quality of coronary artery plaque with rapid kVp-switching dual-energy CT. *Clin Imaging* 43:42–49. <https://doi.org/10.1016/j.clinimag.2017.01.014>
- Ohta Y, Kitao S, Yunaga H, Fujii S, Mukai N, Yamamoto K, Ogawa T (2018) Myocardial delayed enhancement CT for the evaluation of heart failure: comparison to MRI. *Radiology* 288(3):682–691. <https://doi.org/10.1148/radiol.2018172523>
- Pessis E, Campagna R, Sverzut J-M, Bach F, Rodallec M, Guerini H, Feydy A, Drapé J-L (2013) Virtual monochromatic spectral imaging with fast kilovoltage switching: reduction of metal artifacts at

- CT. *Radiographics* 33(2):573–583. <https://doi.org/10.1148/rg.332125124>
- Pijls NH, Fearon WF, Tonino PA, Siebert U, Ikeno F, Bornschein B, van't Veer M, Klauss V, Manoharan G, Engström T, Oldroyd KG, Ver Lee PN, MacCarthy PA, De Bruyne B (2010) Fractional flow reserve versus angiography for guiding percutaneous coronary intervention in patients with multivessel coronary artery disease: 2-year follow-up of the FAME (Fractional Flow Reserve Versus Angiography for Multivessel Evaluation) study. *J Am Coll Cardiol* 56(3):177–184. <https://doi.org/10.1016/j.jacc.2010.04.012>
- Pomerantz SR, Kamalian S, Zhang D, Gupta R, Rapalino O, Sahani DV, Lev MH (2013) Virtual monochromatic reconstruction of dual-energy unenhanced head CT at 65–75 keV maximizes image quality compared with conventional polychromatic CT. *Radiology* 266(1):318–325. <https://doi.org/10.1148/radiol.12111604>
- Rajagopal JR, Farhadi F, Solomon J, Sahbaee P, Saboury B, Pritchard WF, Jones EC, Samei E (2020) Comparison of low dose performance of photon-counting and energy integrating CT. *Acad Radiol*. <https://doi.org/10.1016/j.acra.2020.07.033>
- Sandfort V, Palanisamy S, Symons R, Pourmorteza A, Ahlman MA, Rice K, Thomas T, Davies-Venn C, Krauss B, Kwan A, Pandey A, Zimmerman SL, Bluemke DA (2017) Optimized energy of spectral CT for infarct imaging: experimental validation with human validation. *J Cardiovasc Comput Tomogr* 11(3):171–178. <https://doi.org/10.1016/j.jcct.2017.02.003>
- Sandfort V, Persson M, Pourmorteza A, Noël PB, Fleischmann D, Willemlink MJ (2020) Spectral photon-counting CT in cardiovascular imaging. *J Cardiovasc Comput Tomogr*. <https://doi.org/10.1016/j.jcct.2020.12.005>
- Scheffel H, Alkadhhi H, Plass A, Vachenaer R, Desbiolles L, Gaemperli O, Schepis T, Frauenfelder T, Schertler T, Husmann L, Grunenfelder J, Genoni M, Kaufmann PA, Marincek B, Leschka S (2006) Accuracy of dual-source CT coronary angiography: first experience in a high pre-test probability population without heart rate control. *Eur Radiol* 16(12):2739–2747. <https://doi.org/10.1007/s00330-006-0474-0>
- Scheske JA, O'Brien JM, Earls JP, Min JK, LaBounty TM, Cury RC, Lee T-Y, So A, Hague CJ, Al-Hassan D, Kuriyabashi S, Dowe DA, Leipsic JA (2013) Coronary artery imaging with single-source rapid kilovolt peak-switching dual-energy CT. *Radiology* 268(3):702–709. <https://doi.org/10.1148/radiol.13121901>
- Schoepf UJ (2019) CT of the heart. Humana Press, Totowa
- Schoepf UJ, Emrich T (2021) A brave new world: toward precision phenotyping and understanding of coronary artery disease using radiomics plaque analysis. *Radiology* 299(1):107–108. <https://doi.org/10.1148/radiol.2021204456>
- Schwartz FR, Koweek LM, Nørgaard BL (2019) Current evidence in cardiothoracic imaging: computed tomography-derived fractional flow reserve in stable chest pain. *J Thorac Imaging* 34(1):12–17. <https://doi.org/10.1097/rti.0000000000000369>
- Schwartz FR, Tailor T, Gaca JG, Kiefer T, Harrison K, Hughes GC, Ramirez-Giraldo JC, Marin D, Hurwitz LM (2020) Impact of dual energy cardiac CT for metal artefact reduction post aortic valve replacement. *Eur J Radiol* 129:109135. <https://doi.org/10.1016/j.ejrad.2020.109135>
- Schwarz F, Nance JW, Ruzsics B, Bastarrika G, Sterzik A, Schoepf UJ (2012) Quantification of coronary artery calcium on the basis of dual-energy coronary CT angiography. *Radiology* 264(3):700–707. <https://doi.org/10.1148/radiol.12112455>
- Secchi F, De Cecco CN, Spearman JV, Silverman JR, Ebersberger U, Sardanelli F, Schoepf UJ (2015) Monoenergetic extrapolation of cardiac dual energy CT for artifact reduction. *Acta Radiol* 56(4):413–418. <https://doi.org/10.1177/0284185114527867>
- Senoner T, Plank F, Beyer C, Langer C, Birkel K, Steinkohl F, Widmann G, Barbieri F, Adukauskaite A, Friedrich G, Dichtl W, Feuchtner GM (2020) Does coronary calcium score zero reliably rule out coronary artery disease in low-to-intermediate risk patients? A coronary CTA study. *J Cardiovasc Comput Tomogr* 14(2):155–161. <https://doi.org/10.1016/j.jcct.2019.09.009>
- Sharma P, Suehling M, Flohr T, Comaniciu D (2020) Artificial intelligence in diagnostic imaging: status quo, challenges, and future opportunities. *J Thorac Imaging* 35(Suppl 1):S11–s16. <https://doi.org/10.1097/rti.0000000000000499>
- Sigovan M, Si-Mohamed S, Bar-Ness D, Mitchell J, Langlois J-B, Coulon P, Roessl E, Blevis I, Rokni M, Rioufol G, Douek P, Bussel L (2019) Feasibility of improving vascular imaging in the presence of metallic stents using spectral photon counting CT and K-edge imaging. *Sci Rep* 9(1):19850. <https://doi.org/10.1038/s41598-019-56427-6>
- Song I, Yi JG, Park JH, Kim SM, Lee KS, Chung MJ (2016) Virtual non-contrast CT using dual-energy spectral CT: feasibility of coronary artery calcium scoring. *Korean J Radiol* 17(3):321. <https://doi.org/10.3348/kjr.2016.17.3.321>
- Sørgaard MH, Kofoed KF, Linde JJ, George RT, Rochitte CE, Feuchtner G, Lima JA, Abdulla J (2016) Diagnostic accuracy of static CT perfusion for the detection of myocardial ischemia. A systematic review and meta-analysis. *J Cardiovasc Comput Tomogr* 10(6):450–457. <https://doi.org/10.1016/j.jcct.2016.09.003>
- Stehli J, Fuchs TA, Singer A, Bull S, Clerc OF, Possner M, Gaemperli O, Buechel RR, Kaufmann PA (2015) First experience with single-source, dual-energy CCTA for monochromatic stent imaging. *Eur Heart J Cardiovasc Imaging* 16(5):507–512. <https://doi.org/10.1093/ehjci/jeu282>
- Stehli J, Clerc OF, Fuchs TA, Possner M, Gräni C, Benz DC, Buechel RR, Kaufmann PA (2016) Impact of monochromatic coronary computed tomography angiography from single-source dual-energy CT on coronary stenosis quantification. *J Cardiovasc Comput*

- Tomogr 10(2):135–140. <https://doi.org/10.1016/j.jcct.2015.12.008>
- Suchá D, Symersky P, Tanis W, Mali WP, Leiner T, van Herwerden LA, Budde RP (2015) Multimodality imaging assessment of prosthetic heart valves. *Circ Cardiovasc Imaging* 8(9):e003703. <https://doi.org/10.1161/circimaging.115.003703>
- Symons R, Choi Y, Cork TE, Ahlman MA, Mallek M, Bluemke DA, Sandfort V (2018a) Optimized energy of spectral coronary CT angiography for coronary plaque detection and quantification. *J Cardiovasc Comput Tomogr* 12(2):108–114. <https://doi.org/10.1016/j.jcct.2018.01.006>
- Symons R, De Bruecker Y, Roosen J, Van Camp L, Cork TE, Kappler S, Ulzheimer S, Sandfort V, Bluemke DA, Pourmorteza A (2018b) Quarter-millimeter spectral coronary stent imaging with photon-counting CT: initial experience. *J Cardiovasc Comput Tomogr* 12(6):509–515. <https://doi.org/10.1016/j.jcct.2018.10.008>
- Symons R, Sandfort V, Mallek M, Ulzheimer S, Pourmorteza A (2019) Coronary artery calcium scoring with photon-counting CT: first in vivo human experience. *Int J Cardiovasc Imaging* 35(4):733–739. <https://doi.org/10.1007/s10554-018-1499-6>
- Tanami Y, Ikeda E, Jinzaki M, Satoh K, Nishiwaki Y, Yamada M, Okada Y, Kuribayashi S (2010) Computed tomographic attenuation value of coronary atherosclerotic plaques with different tube voltage: an ex vivo study. *J Comput Assist Tomogr* 34(1):58–63. <https://doi.org/10.1097/RCT.0b013e3181b66c41>
- Taylor AJ, Cerqueira M, Hodgson JM, Mark D, Min J, O’Gara P, Rubin GD (2010) ACCF/SCCT/ACR/AHA/ASE/ASNC/NASCI/SCAI/SCMR 2010 appropriate use criteria for cardiac computed tomography. A report of the American College of Cardiology Foundation Appropriate Use Criteria Task Force, the Society of Cardiovascular Computed Tomography, the American College of Radiology, the American Heart Association, the American Society of Echocardiography, the American Society of Nuclear Cardiology, the North American Society for Cardiovascular Imaging, the Society for Cardiovascular Angiography and Interventions, and the Society for Cardiovascular Magnetic Resonance. *J Cardiovasc Comput Tomogr* 4(6):407.e401–433. <https://doi.org/10.1016/j.jcct.2010.11.001>
- Tesche C, Gray HN (2020) Machine learning and deep neural networks applications in coronary flow assessment: the case of computed tomography fractional flow reserve. *J Thorac Imaging* 35:S66–S71. <https://doi.org/10.1097/rti.0000000000000483>
- Tops LF, Wood DA, Delgado V, Schuijf JD, Mayo JR, Pasupati S, Lamers FP, van der Wall EE, Schalij MJ, Webb JG, Bax JJ (2008) Noninvasive evaluation of the aortic root with multislice computed tomography implications for transcatheter aortic valve replacement. *JACC Cardiovasc Imaging* 1(3):321–330. <https://doi.org/10.1016/j.jcmg.2007.12.006>
- Tsai YS, Chen JS, Wang CK, Lu CH, Cheng CN, Kuo CS, Liu YS, Tsai HM (2014) Quantitative assessment of iron in heart and liver phantoms using dual-energy computed tomography. *Exp Ther Med* 8(3):907–912. <https://doi.org/10.3892/etm.2014.1813>
- Valenti V, ó Hartaigh B, Heo R, Cho I, Schulman-Marcus J, Gransar H, Truong QA, Shaw LJ, Knapper J, Kelkar AA, Sandesara P, Lin FY, Sciarretta S, Chang H-J, Callister TQ, Min JK (2015) A 15-year warranty period for asymptomatic individuals without coronary artery calcium. *JACC Cardiovasc Imaging* 8(8):900–909. <https://doi.org/10.1016/j.jcmg.2015.01.025>
- van Assen M, De Cecco CN, Sahbaee P, Eid MH, Griffith LP, Bauer MJ, Savage RH, Varga-Szemes A, Oudkerk M, Vliegenthart R, Schoepf UJ (2019a) Feasibility of extracellular volume quantification using dual-energy CT. *J Cardiovasc Comput Tomogr* 13(1):81–84. <https://doi.org/10.1016/j.jcct.2018.10.011>
- van Assen M, Lavra F, Schoepf UJ, Jacobs BE, Williams BT, Thompson ZM, Varga-Szemes A, Ruzsics B, Oudkerk M, Vliegenthart R, De Cecco CN (2019b) Iodine quantification based on rest / stress perfusion dual energy CT to differentiate ischemic, infarcted and normal myocardium. *Eur J Radiol* 112:136–143. <https://doi.org/10.1016/j.ejrad.2019.01.017>
- Van Hedent S, Große Hokamp N, Kessner R, Gilkeson R, Ros PR, Gupta A (2018) Effect of virtual monoenergetic images from spectral detector computed tomography on coronary calcium blooming. *J Comput Assist Tomogr* 42(6):912–918. <https://doi.org/10.1097/RCT.0000000000000811>
- Wang R, Yu W, Wang Y, He Y, Yang L, Bi T, Jiao J, Wang Q, Chi L, Yu Y, Zhang Z (2011) Incremental value of dual-energy CT to coronary CT angiography for the detection of significant coronary stenosis: comparison with quantitative coronary angiography and single photon emission computed tomography. *Int J Cardiovasc Imaging* 27(5):647–656. <https://doi.org/10.1007/s10554-011-9881-7>
- Wang X, Zamyatin A, Shi D (2012) Dose reduction potential with photon counting computed tomography. In: *Medical imaging 2012: physics of medical imaging*. International Society for Optics and Photonics, p 831349
- Wang Y, Yu M, Wang M, Wang Y, Kong L, Yi Y, Wang M, Li Y, Jin Z (2019) Application of artificial intelligence-based image optimization for computed tomography angiography of the aorta with low tube voltage and reduced contrast medium volume. *J Thorac Imaging* 34(6):393–399. <https://doi.org/10.1097/rti.0000000000000438>
- Williams MC, Moss AJ, Dweck M, Adamson PD, Alam S, Hunter A, Shah ASV, Pawade T, Weir-McCall JR, Roditi G, van Beek EJR, Newby DE, Nicol ED (2019) Coronary artery plaque characteristics associated with adverse outcomes in the SCOT-HEART study. *J Am Coll Cardiol* 73(3):291–301. <https://doi.org/10.1016/j.jacc.2018.10.066>

- Yamada Y, Jinzaki M, Okamura T, Yamada M, Tanami Y, Abe T, Kuribayashi S (2014) Feasibility of coronary artery calcium scoring on virtual unenhanced images derived from single-source fast kVp-switching dual-energy coronary CT angiography. *J Cardiovasc Comput Tomogr* 8(5):391–400. <https://doi.org/10.1016/j.jcct.2014.08.005>
- Yan RT, Miller JM, Rochitte CE, Dewey M, Niinuma H, Clouse ME, Vavere AL, Brinker J, Lima JAC, Arbab-Zadeh A (2013) Predictors of inaccurate coronary arterial stenosis assessment by CT angiography. *JACC Cardiovasc Imaging* 6(9):963–972. <https://doi.org/10.1016/j.jcmg.2013.02.011>
- Yi Y, Zhao X-M, Wu R-Z, Wang Y, Vembar M, Jin Z-Y, Wang Y-N (2019) Low dose and low contrast medium coronary CT angiography using dual-layer spectral detector CT: low keV versus low kVp. *Int Heart J* 60(3):608–617. <https://doi.org/10.1536/ihj.18-340>
- Young PM, Foley TA, Araoz PA, Williamson EE (2019) Computed tomography imaging of cardiac masses. *Radiol Clin N Am* 57(1):75–84. <https://doi.org/10.1016/j.rcl.2018.08.002>
- Yu L, Christner JA, Leng S, Wang J, Fletcher JG, McCollough CH (2011) Virtual monochromatic imaging in dual-source dual-energy CT: radiation dose and image quality: monochromatic imaging in dual-source dual-energy CT. *Med Phys* 38(12):6371–6379. <https://doi.org/10.1118/1.3658568>
- Yu L, Leng S, McCollough CH (2012) Dual-energy CT-based monochromatic imaging. *Am J Roentgenol* 199(5_supplement):S9–S15. <https://doi.org/10.2214/AJR.12.9121>
- Yunaga H, Ohta Y, Kaetsu Y, Kitao S, Watanabe T, Furuse Y, Yamamoto K, Ogawa T (2017) Diagnostic performance of calcification-suppressed coronary CT angiography using rapid kilovolt-switching dual-energy CT. *Eur Radiol* 27(7):2794–2801. <https://doi.org/10.1007/s00330-016-4675-x>
- Zachrisson H, Engström E, Engvall J, Wigström L, Smedby Ö, Persson A (2010) Soft tissue discrimination ex vivo by dual energy computed tomography. *Eur J Radiol* 75(2):e124–e128. <https://doi.org/10.1016/j.ejrad.2010.02.001>
- Zhang S, Levin DC, Halpern EJ, Fischman D, Savage M, Walinsky P (2008) Accuracy of MDCT in assessing the degree of stenosis caused by calcified coronary artery plaques. *Am J Roentgenol* 191(6):1676–1683. <https://doi.org/10.2214/AJR.07.4026>
- Zou Y, Silver MD (2009) Elimination of blooming artifacts off stents by dual energy CT. In: Samei E, Hsieh J (eds) *SPIE medical imaging, 2009*, Lake Buena Vista, FL, vol 72581X. <https://doi.org/10.1117/12.811696>



Dual-Energy CT Angiography

Matthias Stefan May and Armin Muttke

Contents

1	Dual-Energy CT Angiography	163
1.1	Image Contrast	163
1.2	Contrast Agent	165
1.3	Virtual Unenhanced	166
1.4	Plaques	167
1.5	Clinical Applications	169
	References	175

1 Dual-Energy CT Angiography

Successful CT imaging of the vascular system requires contrast media injection. High vessel contrast is vital to obtain high diagnostic image quality. Besides optimized injection protocols, the energy level of the X-ray source has a high impact on the imaging results. A significant limitation of CT angiography is the limited evaluability in highly calcified plaque burden. Unfortunately, low photon energy levels further decrease the evaluability of the vessel lumen in precisely these patients because of increased blooming artifacts. Dual-energy (DE) is a promising tool to overcome this dilemma by simultaneously addressing image contrast and material decomposition. This chapter will first review the

general technical considerations of Dual-Energy CT Angiography and then evaluate the respective clinical applications.

1.1 Image Contrast

The image quality from DE examinations is superior to conventional acquisitions at 120 kV tube voltage potential if the low and the high energy dataset are blended to obtain polychromatic images (PI). Non-linear blending techniques provide the best results with the highest contrast to noise ratios. Modified sigmoid functions provide the optimum contrast from this raw data (Li et al. 2014). Ahead of blending techniques, extrapolating the simulated energy levels with virtual monoenergetic image reconstructions (VMI) can further increase image contrast. The high vessel contrast from low-energy reconstructions can achieve two primary goals: to improve the diagnostic performance

M. S. May (✉) · A. Muttke
Department of Radiology, University Hospital
Erlangen, Erlangen, Germany
e-mail: Matthias.May@uk-erlangen.de

or to reduce the contrast agent dose. Also, a combination of both effects can be helpful, depending on the clinical situation and the intention for imaging. The lowest available VMI levels provide the highest vessel contrast (Fig. 1). Forty kiloelectron Volt (keV) is the value that approaches the K-edge of iodine the closest (Yoshida et al. 2020). Vessel reproduction in these images and contrast to noise ratio (CNR) is substantially superior to the PI and conventional Single Energy (SE) acquisitions at 120 kVp (Murphy et al. 2019). The objective vessel image quality is also superior to low tube voltage acquisitions, but subjective and overall image quality is favorable in the low kV images (Yoshida et al. 2020). Therefore, low tube voltages could always be a good selection if DE is unavailable.

However, the additional flexibility to apply various other reconstruction types to DE data favors DE acquisitions over SE techniques. In some studies, moderately low monoenergetic reconstructions between 50 and 70 keV had better subjective image quality than 40 keV despite lower objective image quality in CNR (Martin et al. 2017a). So, the implementation of very low (40 keV) or moderately low reconstructions (50–70 keV) in the clinical routine setting seems more a matter of individual taste than evidence-based medicine. Early reconstruction algorithms suffered from a substantial increase in image noise, especially in the very low VMI. The next generation, the so-called advanced monoenergetic reconstructions (VMI+), solved these drawbacks using frequency selective techniques. These advanced algorithms do not affect the image con-

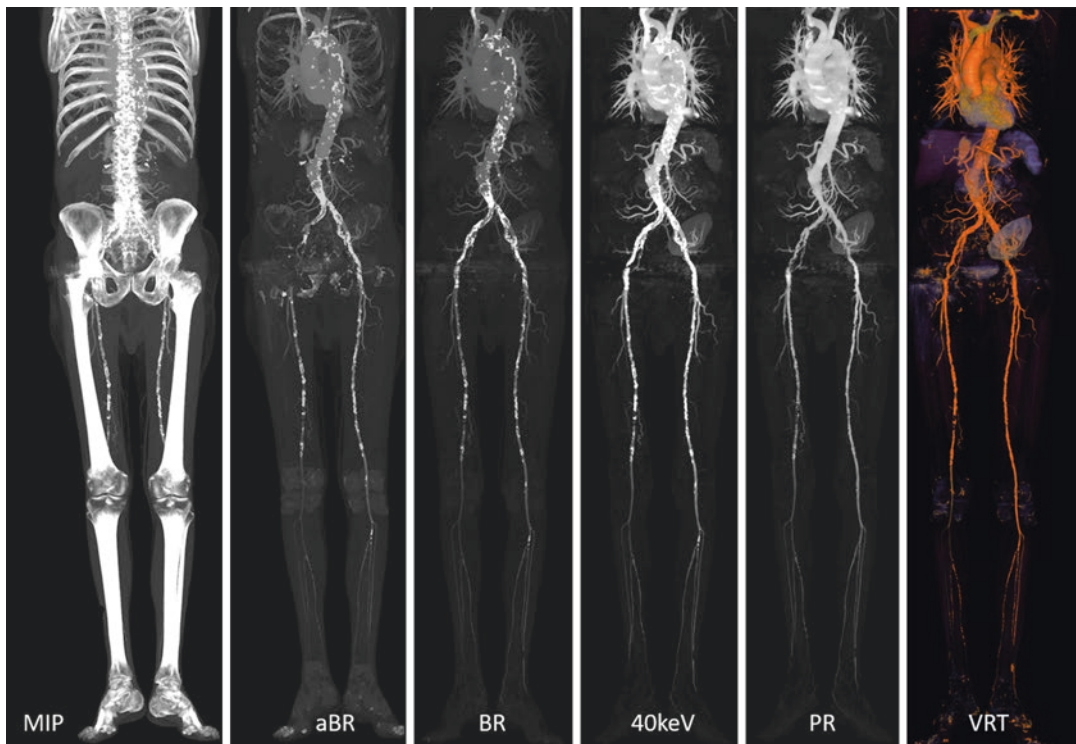


Fig. 1 Visualization of dual-energy CT angiographies: maximum intensity projections (MIP) suffer from bone and calcified plaque superposition. Dual-energy can reduce the error rates of automated bone removal (aBR) compared to conventional techniques. Therefore, the required time for manual post-processing to obtain overview images with bone removal (BR) is also reduced.

Very low virtual monoenergetic reconstructions (40 keV) provide the best vessel contrast. Improved quality of plaque removal techniques (PR) helps to achieve high diagnostic accuracies (right superficial femoral artery stenosis in this case) but often require manual adaptations before a comprehensive demonstration in MIP or volume rendering techniques (VRT) is possible

trast but significantly reduce the image noise. This effect substantially improves the CNR in the 40 keV images (Riffel et al. 2016).

Conventional window settings from standard SE acquisitions are inappropriate for the vessels' very high attenuation values in these contrast optimized VMI, with up to far more than 1000 HU. Some studies evaluated the subjective and calculated optimum window setting (D'Angelo et al. 2018, 2020; Caruso et al. 2017). The suggested values differed between different vessel regions and injection protocols. With mean attenuation values around 1000 HU in the carotids, width values (W) around 1600 HU, and level values (L) around 550 HU seemed most appropriate. This combination was higher than recommended evaluating the pulmonary arteries (mean attenuation around 650 HU, suggested W/L = 1100/400 HU). However, two independent studies about the abdominal arteries suggested different window levels, such as W/L = 1400/450 HU for a mean attenuation around 700 HU and W/L = 1600/700 for a mean attenuation of 1100 HU. This roughly copies the recommendations in the literature for attenuation-adapted adjustments of the window settings for conventional acquisition techniques (Saba and Mallarin 2009). Thus, presets could support the implementation into the routine workflow and adapt to the local technique of contrast injection and timing.

The image quality of VMI reconstructions seems to be relatively stable to different acquisition techniques. All methods to generate DE datasets follow a common trend, independent from the vendor and the scanner generation. Different acquisition speeds and tube power mainly account for potential limitations and differences. Time gaps between the high- and the low-energy exposure may induce artifacts based on the movement of structures, like the heart or the digestive tract, in the meantime. These artifacts are most pronounced in the very low VMI and can be neglected in the PI (Eichler et al. 2020; May et al. 2019a). Luckily, the impact on vessel evaluation is shallow in most regions beyond the ascending Aorta. Increased image noise may hamper especially the assess-

ment of smaller vessel branches in obese patients. Therefore, a high power capacity of the X-ray tube is required to obtain DE datasets in a large collective. This need is also essential to increase the radiation dose efficiency by reduction of the tube voltage. Savings up to 46% at constant CNR are possible by voltage reduction of the main tube from 100 kV to 80 kV in Dual Source scanners (Li et al. 2017). Automated attenuation-based kV pair selection may be an attractive technique for future scanner generations to improve the individualization of vascular DE protocols (Renapurkar et al. 2017). Another way to overcome image noise problems in DE angiography is the combination with iterative reconstructions. The effects are comparable to the impact on SE data (Lee et al. 2016).

1.2 Contrast Agent

Generally, the lowest dose of contrast medium consistent with a diagnostic result for all patients should be favored (van der Molen et al. 2018). The limit to not exceed the volume injection in mL above the threefold glomerular filtration rate may be challenging in patients with impaired kidney function. DE can help to provide diagnostic vascular image quality, also in very low contrast agent dose protocols. The range of reported reduction rates is vast (28–75%) (Xin et al. 2015; Meier et al. 2016, 2017). Different study designs can explain this discrepancy. Rather conservative trials reported a simultaneously increased objective image quality. Some of the more aggressive studies used unequal intensities of iterative reconstructions to obtain similar objective image quality at matched radiation dose (Shuman et al. 2017). Lowest reported total volume is 15 mL and the lowest total iodine dose is 6 g for imaging of the pulmonary arteries, and 28 mL or 9.8 g for the Aorta (Meier et al. 2016, 2017; Hou et al. 2017; Carrascosa et al. 2014). The authors recommend adapting the bolus dynamics in these protocols by diluting the contrast agent using dual head injectors or choosing contrast agents with lower iodine concentrations. The combina-

tion of 60% contrast dose reduction and VMI at 50–60 keV was reported to best match a 120 kV SE acquisition in a systematic dilution series over different collectives (Carrascosa et al. 2014). Overall, most clinical trials outweighed the expectations from phantom trials (40% reduction), probably due to an additional effect of the systemic circulation, dilution processes, and bolus dynamics in vivo. On the other side, DE acquisitions can help overcome these uncertainties of unpredictable image contrast levels in a clinical collective. Individual retrospective selection of the VMI level, based on the mean attenuation values, could help to standardize the image quality in the respective collective (Hou et al. 2017).

Gadolinium-containing contrast agents may serve as an alternative in case of contraindications for iodine-containing contrast agents. Few authors described this feasibility in one animal trial and one single translational clinical trial. PI with 150% and 250% gadopentetate dimeglumine injection in rabbits provided a sound reproduction of healthy and obstructed pulmonary vessels. The clinical examinations used single-dose injections (Zhang et al. 2011). Standard reconstructions could not provide diagnostic image quality in the aortic system in this setting in humans, but VMI allowed for diagnostic data. Like with iodine, 40 keV has the highest impact on vessel contrast and is best suitable for patients undergoing iodine-free contrast-enhanced CT angiography. This result is astonishing regarding the K-edge of Gadolinium at 50.2 keV. Here, the extrapolation algorithm in VMI detaches the image contrast from the physical principles of X-ray absorption (Nadjiri et al. 2018).

1.3 Virtual Unenhanced

DE data also allows for material decomposition. This technique can separate the iodine-containing contrast agents from the tissues. The resulting images display iodine concentration quantitatively on one side, which is not so much in the

scope of CT angiograms, and virtual unenhanced vessels and tissues on the other side. The use of these virtual unenhanced images to replace actual unenhanced images may help to reduce the radiation dose for the patient but is discussed controversially in the literature. Some authors reported significant differences in objective and subjective image quality compared to the reference (Lehti et al. 2018). Especially the very high iodine concentrations in the large vessels pose problems. The virtual unenhanced datasets contain significantly increased attenuation values and significantly increased image noise in these locations (Pinho et al. 2013). Therefore, late arterial or portal-venous phase images are more appropriate for these reconstructions in multiphase studies than the arteriograms (Lehti et al. 2019). The problem is also more pronounced in the thoracic aorta, and pulsation artifacts may further hamper the evaluation. On the contrary, the image quality of virtual unenhanced data in the abdominal aorta seems suitable for a clinical diagnosis. So, patients prone to radiation dose can benefit from reduced phase acquisitions (Shaïda et al. 2012).

1.3.1 Bones

One of MR angiography's primary advantages over CT angiography is the easily obtained maximum intensity projection overview of the examined vessels. These are very useful for demonstrations and quick identification of the regions requiring intensified thin-slice workup. Threshold-based bone removal of SE CT data requires intensive manual corrections and, therefore, high post-processing times. Error rates of automated bone removal algorithms without manual corrections are high. Literature reports that up to more than 90% of the captured bones may be missed (Morhard et al. 2009). DE promises to overcome this problem because the material decomposition technique can specifically detect calcium. Automated bone removal reconstructions are available and tested for a variety of regions. All of the studies found substantially reduced missing rates of bone detection ranging from 0 to 46% (Fig. 1) (Sommer et al. 2009;

Meyer et al. 2008). Most problems occur with the ribcage (error rate 46%) and the patella (error rate 25%). Also, the head and neck region remains challenging, with reported error rates of 12% (Morhard et al. 2009). Supportive metal artifact reconstructions before automated DE bone removal are beneficial in around 60% of all cases and should be used routinely for this region (Kaemmerer et al. 2016). Primary error rates for all other regions are below 5%. The resulting time effort for manual corrections is also significantly lower than with the threshold method and can be consistently around 2–4 min, compared to 4–6 min. The resulting vessel contrast from DE studies was simultaneously better than in the SE acquisitions (Schulz et al. 2012). However, in severe vessel calcifications, new vessel irregularities may occur from the DE bone removal algorithms (Yamamoto et al. 2009). This artifact should be known and respected during post-processing and interpretation. Higher tube voltages during acquisition may reduce these artificial vessel erosions in Dual Source DE examinations of the supra-aortic arteries (Korn et al. 2015). This principle especially accounts for the lower segments, the internal carotid artery, and the V3/4 segments of the vertebral artery, which remains problematic.

1.4 Plaques

Calcified plaques pose another main difficulty of overview images derived from CT angiography compared to MR. Automated calcified plaque removal by material decomposition is required to derive a true luminogram and avoid unevaluable segments. Systematic phantom trials found that in vessels with a diameter equal to or above 5 mm, DE with automated plaque removal reconstruction can provide reliable results. Vessels below 2 mm may be deleted entirely from the images in case of severe calcifications. Other negatively influencing factors for plaque removal are low iodine concentration in the lumen and high density of the plaques.

Interestingly, the calcium plaque thickness does not influence the vessel lumen visualiza-

tion (Jin et al. 2017). The overall underestimation of the proper lumen area can still be up to 50% in stenotic segments. However, these results are much better than those from SE evaluation of stenosis by calcified plaques, severely suffering from blooming artifacts (Li et al. 2020). A toxic combination of conditions with small vessels, poor lumen contrast, and severe calcifications is often present below the knee. Poor diagnostic results for this body region have been described (Meyer et al. 2008). Notably, algorithms for calcified plaque removal improved over time, with the most recently published diagnostic accuracy up to 96.5%. The increased specificity and negative predictive value contribute to the superiority over conventional evaluation without plaque removal (Fig. 1) (de Santis et al. 2019). Non-significant differences to invasive digital subtraction angiography are possible. The immediate success of automated plaque removal can be around 40–75%. Still, about one-fourth of all datasets can suffer from insufficiently high residual calcifications, limiting the overview visualization as maximum intensity projection. There are no reported negative influences of the plaque removal algorithms on the overall image quality (Mannil et al. 2017).

Another critical issue in plaque imaging is the influence of different VMI reconstructions. It is well known that lower tube voltages in SE acquisitions come along with increased vessel contrast, but with the drawback of higher blooming artifacts (Grimes et al. 2015). Low keV VMI from DE examinations of the carotids copied this effect in an evaluation with fixed window levels (width 850 HU, level 300 HU). The mean effect was as high as a 30% increase of the grade of diameter stenosis in 66 keV VMI compared to 86 keV (Fig. 2) (Saba et al. 2019). Conversely, in an evaluation with adjustments of the window level according to the reader's discretion for each case, no influence on the total plaque burden, the vessel diameter, or the reported grade of stenosis was found (Bai et al. 2020). This finding further emphasizes the need for adjustments of the window level for the interpretation of VMI. A considerable additional effect is an improved

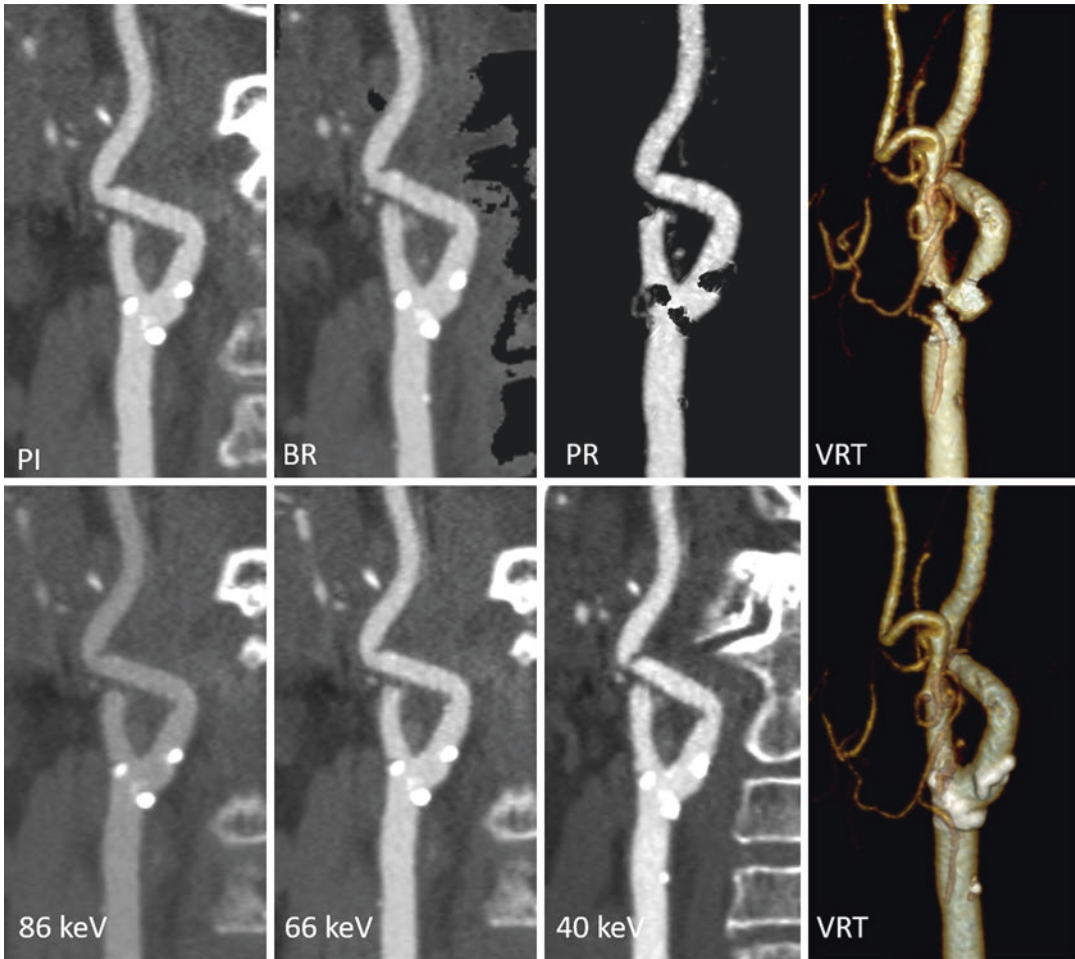


Fig. 2 Flexibility of dual-energy reconstructions: bone removal (BR) and plaque removal (PR) support a comprehensive demonstration of carotid stenosis using volume rendering techniques (VRT). Different energy levels of

virtual monoenergetic reconstructions allow for reduced blooming artifacts (86 keV) or increased vessel contrast (40 keV)

contrast in low VMI that can support the differentiation of the plaque composition, such as a fibrous cap, large lipid core, and intraplaque hemorrhage. Also, it is easier to delineate non-calcified plaque margins from the surrounding adipose tissue and delineate calcified plaque margins from the contrast agent-filled lumen at the same time (Reynoso et al. 2017). Quantification of the plaque composition is fea-

sible by calculation of the mean atomic number (Z). Low Z -values inversely correlate with the areas of fibro-fatty components in vulnerable plaques derived from virtual histology intravascular ultrasound (Shinohara et al. 2015). Therefore, DE provides a high convenience for subjective plaque evaluation in general and an objective quantification tool to identify patients at risk simultaneously (Fig. 3).

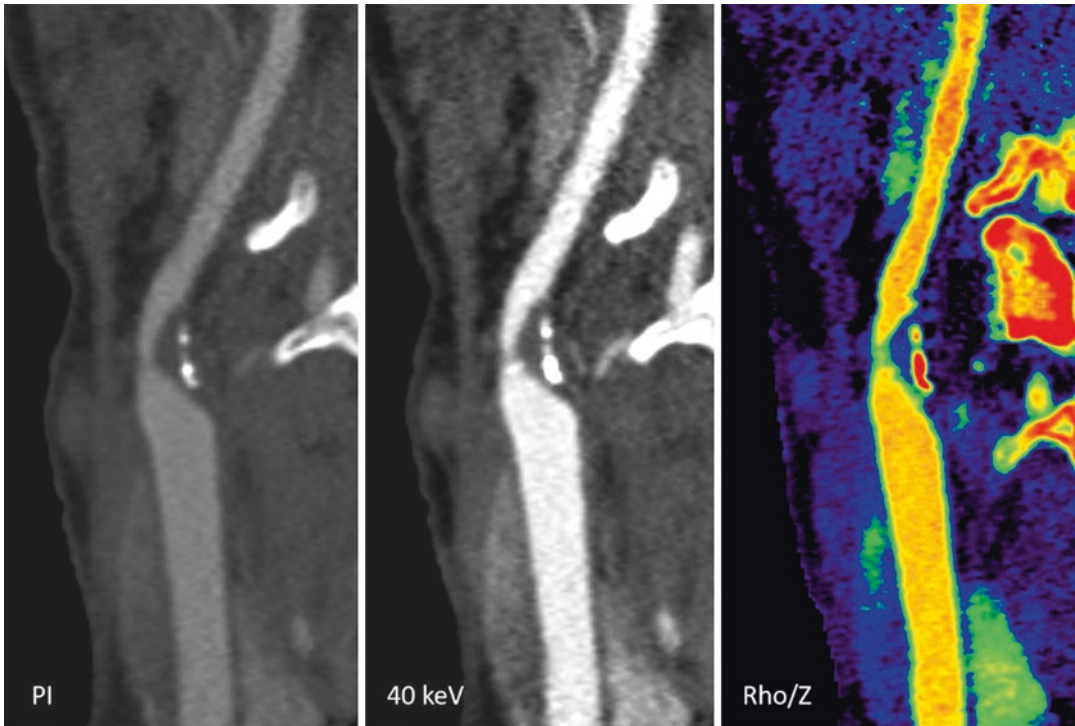


Fig. 3 Plaque imaging with dual-energy: different calcified and non-calcified plaque composition areas can be better differentiated by increased contrast from low virtual monoenergetic reconstructions (40 keV) compared to the reference polychromatic images (PI). Simultaneously the

contrast of the lumen stenosis and the delineation of the plaque from the surrounding adipose tissue are increased. Z-value and electron density (Rho/Z) maps allow for plaque quantification

1.5 Clinical Applications

1.5.1 Pulmonary Angiography

Pulmonary angiography is performed frequently in the emergency setting and remains one of the radiology enigmas. No matter how well one prepares the examination, how intense one calculates circulation times, or how much contrast one injects, sometimes the vessel contrast is inferior. Venous capacity, collateral flow, cardiac function, intravascular volume, and last but not least—alternating intra-thoracic pressures by forced respiration may influence the bolus dynamics in pulmonary angiograms. Abrupt breathing commands and well-behaved patients taking deep breaths can have devastating effects, even if the bolus is detected automatically in the target vessel. This failure becomes incredibly disruptive for the evaluation of the smaller vessels.

Therefore, contrast improvements are often required, and retrospective options are frequently welcome. More than 90% of retrospectively selected, non-diagnostic pulmonary angiograms with attenuation values below 200 HU could be salvaged by VMI reconstructions compared to the PI (Ghandour et al. 2018). In particular, the sensitivity increases substantially from 80% to 92% and adds to the increased diagnostic performance. The specificity is as high as 94–97% in that situation (Bae et al. 2018). Other studies reported the sensitivity and specificity for detecting pulmonary embolism in portal-venous phase images as high as 90/100%. The subjectively selected monoenergetic level was 48.5 keV (Foti et al. 2021). This approach appears to be an attractive bail-out strategy in oncologic staging patients, where incidental pulmonary embolism is as frequent as 4% and overlooked in about one-

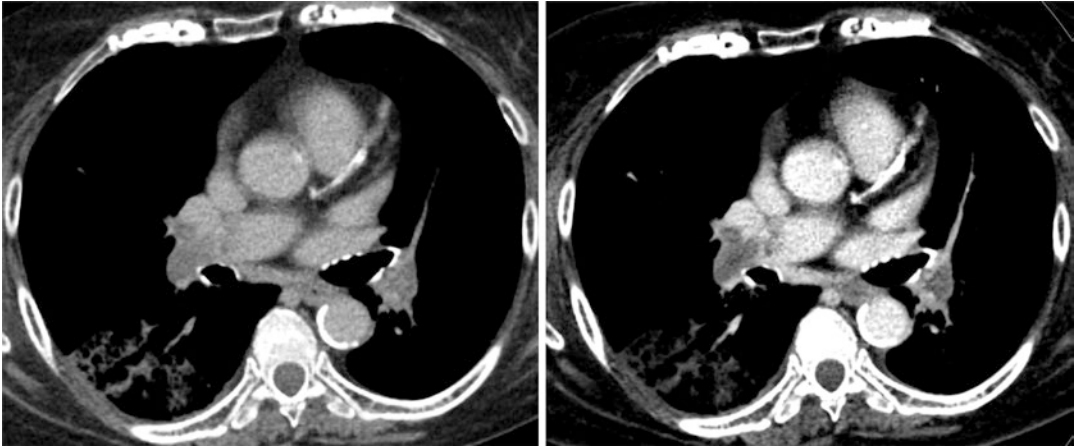


Fig. 4 Enhanced iodine contrast: The bilateral pulmonary embolism in portal-venous phase staging CT could easily be overlooked. Low kiloelectron voltage reconstructions, 40 keV in this case, help to delineate the thrombi

fourth of cases (Fig. 4) (Gladish et al. 2006). The impact of DE, mainly due to the detection of smaller subsegmental embolism, was indicated to double the detection rate (Uhrig et al. 2018). The best visualization of the relatively small bronchial arteries was found at 63 keV in pulmonary angiograms with bolus detection in the descending Aorta (Ma et al. 2016a). However, also in regular pulmonary embolism examinations, low VMI seem to support the reader. The best diagnostic performance (>96%) was reported for 60 keV images, while 40 keV had the highest subjective diagnostic confidence (Sauter et al. 2020). More is probably not always better in DE, even if the differences were only subtle. Advanced VMI+ are potentially able to overcome this non-linear pattern by further lowering the image noise. Some authors found that this technique could lower artifacts in the pulmonary arteries, but structured performance evaluation compared to the preceding generation is missing in the literature (Meier et al. 2015). The increased contrast allows for substantial contrast agent dose reductions and comes along with only a moderate increase of image noise. Therefore, substantial radiation dose reductions are also feasible with this advanced reconstruction technique (Petritsch et al. 2017). A hundred percent diagnostic accuracy was found for a protocol with 83% iodine dose reduction (5.4 g instead of 32 g) in a collective with acute or chronic renal insufficiency

(Meyer et al. 2018). In contrast, radiation dose reduction by more than 50% is possible for pregnant and postpartum women. The rate of images with limited or non-diagnostic quality was simultaneously reduced from 37% to 10% using DE (McDermott et al. 2018). Notably, the positive effect on the diagnostic image quality is not limited to radiologists. The higher contrast levels of VMI improve the accuracy of computer-aided detection (CAD) algorithms, especially in insufficient contrast levels with the standard reconstructions (Kröger et al. 2017). In a systematic evaluation, between 40 and 80 keV, intermediate low energies of 65 keV appear to be the best trade-off between high sensitivity (84%) and a low rate of false positives (12%) (Ma et al. 2019). This compromise may underline the potential of DE images to adapt the image quality to the individual. Future concepts certainly need to combine all available technologies, from physics over medical history to artificial intelligence, to achieve the best results to support clinicians and improve the patients' outcomes (Huang et al. 2020).

1.5.2 Carotid Angiography

Angiography of the carotid arteries is critical to read due to two disturbing factors: calcified plaques and bones. The calcifications in the carotid sinus and the proximal internal carotid artery can be vast and dense. Lumen evaluation

can be challenging in these cases on one side. However, there is strong evidence in the literature about the carotid plaque composition as a risk factor on the other side. Radiologists should therefore love and hate carotid plaques at the same time. Hypodense plaques are associated with embolic cerebrovascular stroke and are therefore considered vulnerable (Mikail et al. 2021). Microcalcifications are known to be associated with plaque instability. Paradoxically, macrocalcifications seem to stabilize the plaque (Montanaro et al. 2021). CT angiography is the only method to assess the plaque composition reliably. DE has proven a good sensitivity of 100% for detecting calcification, 89% for mixed plaques, and 85% for low-density fatty plaques correlated with histopathology (Das et al. 2009). Radiologists should be aware that the historically established threshold levels (130 HU) for assessing the calcified plaque volume may be inappropriate in DE reconstructions (Agatston et al. 1990). A comparative study with unenhanced SE acquisitions reported that the conventional calculation methods may yield underestimations and that 180 HU could provide higher consistency (Watanabe et al. 2011). Moreover, VMI can increase the intraplaque contrast and allow a better differentiation (Fig. 3) (Reynoso et al. 2017). Studies, for example, found an increasing negative correlation of plaque density with the extent of leukoaraiosis using DE (Saba et al. 2017). Some also speculated that contrast enhancement of these critical plaques could be assessed by DE as well. In general, lower energies can improve the objective and subjective image quality of the cervical, petrous and intracranial vessels compared to PI. The vascular contrast increases and significantly improves the assessment of arteries close to the skull base and small arterial branches. The lowest energy levels provide the best results (Neuhaus et al. 2018). However, the diagnostic performance seems to remain unaffected by VMI alone (Leithner et al. 2018). Objective image quality comparable to the standard PI from arterially triggered examinations is even feasible in venous phase acquisitions. The slightly increasing blooming artifacts at lower energy levels do not affect the grade of stenosis in the internal

carotid artery (Zopfs et al. 2018). The advanced methods for bone and plaque removal additionally promise to ease up the cumbersome reporting process in the vicinity of dense bones or severe vessel wall calcifications. Sensitivity and specificity of 100% and 92% to detect hemodynamically relevant (>70%) stenosis can be achieved with combined bone and hard plaque removal (Fig. 2) (Uotani et al. 2009). Overestimation of the grade of stenosis in maximum intensity projections of the carotid bifurcation after plaque and bone removal was only 6% compared to digital subtraction angiography, but a considerable amount of pseudo-occlusions should be expected (Korn et al. 2011). In general, vessel reproduction below the skull base seems superior in DE bone removal techniques compared to conventional image registration bone subtraction. However, disadvantages for the intra-osseous and intracranial sections were found (Lell et al. 2009). Stenosis grade overestimation especially happens in the course of the internal carotid artery through the skull base and in the V3/4 segments of the vertebral artery. Hence, it remains always recommended to review these areas in MPR mode using the images without calcium removal techniques (Buerke et al. 2009). Especially the ophthalmic artery was mentioned in the literature to be usually eliminated (Lell et al. 2010).

1.5.3 Aortic Angiography

A wide variety of indications exists for CT angiography of the aorta. Acute aortic syndromes and traumatic injuries of the aorta have a different scope than aneurysm evaluation, treatment planning, and surveillance. The aortic root often suffers from motion artifacts in non-gated examinations, posing a diagnostic problem in the emergency setting (Qanadli et al. 1999). ECG-gated DE examinations can provide motion-free images of the coronary arteries. The diagnostic image quality in a frequency-controlled collective was comparable to SE acquisitions (98.4% vs. 99.1% diagnostic segments), simultaneously increasing CNR (Kerl et al. 2011). Unfortunately, no study has evaluated the DE image quality of the aortic root in the emergency setting so far,

where higher and probably irregular heart rates are frequent. Recently, the visualization of intramural hematomas of the thoracic aorta by a custom-made two-material decomposition algorithm to obtain dark blood images provided appealing results. Subjective image scores were substantially outranging the actual non-contrast images for delineation of the healthy vessel wall as well as for hematomas (Rotzinger et al. 2020).

Trials that aimed to use DE three-material decomposition techniques for radiation dose reduction by replacing an unenhanced acquisition in patients with an acute aortic syndrome reported only limited success for the image quality of virtual non-contrast reconstructions (Lehti et al. 2018). Disturbing aspects are an increased image noise, incomplete iodine removal from the vessel lumen with higher attenuation values, elimination of calcifications or stent material, reduced overall subjective image quality, and motion artifacts in the aortic root.

Other authors reported the feasibility of virtual unenhanced images to differentiate calcifications from endoleaks in patients after endovascular aortic replacement (EVAR) (Godoy et al. 2010). However, the indicated error rate of calcification subtraction in virtual unenhanced reconstructions in this scenario was 70% (Sommer et al. 2010). Luckily, the detection rate will be unaffected by this technique and will range from 96 to 100% if applied on venous or late phase acquisitions (Buffa et al. 2014). Some authors recommend using a split bolus approach with 40% injection of the total volume 35 s earlier to allow contrast agent accumulation in the endoleak sac (Javor et al. 2017). The respective radiation dose reduction is around 40% compared to a biphasic protocol and 60% compared to a triphasic protocol. VMI+ reconstructions can obtain the best results for the sometimes subtle contrast of endoleaks at 40 keV. This advanced reconstruction algorithm also has a measurable positive effect on the detection rate compared to conventional VMI and PI (Martin et al. 2017b). The further increase of the CNR can be 50–100% compared to classic VMI, mainly delivered by image noise reduction. The lowest energy levels (40/50 keV) and the relatively high energy levels (100 keV) achieve the

maximum extent of this effect. The very high vessel contrast in minimum energy VMI is objectively also superior to SE examinations with the lowest tube voltages of 70 kV. However, the subjective overall image quality and also the detection rate of endoleaks were slightly inferior (Beeres et al. 2016). A similar discrepancy was also reported between the highest objective image quality with 40 keV VMI and the highest subjective image quality with 60 keV VMI in the pre-interventional workup for transarterial valve replacements (TAVR). The main reason for this difference was the altered image noise texture (Martin et al. 2017a). Therefore, maximum vessel contrast seems to be not the only limiting factor for evaluating the large vessels, and relatively moderate energy levels may be appropriate in the clinical setting, depending on the individual taste of image impression.

1.5.4 Abdominal Angiography

The caliber of the abdominal arteries is quickly decreasing after their point of origin in the abdominal aorta. The lowest energy VMI have the most pronounced advantages for the subjective delineation of the small abdominal branches (Fig. 5) (Albrecht et al. 2016a). Also, a systematic review of the liver arteries found the best results at 40 keV (Marin et al. 2015). These results were only limited in obese patients, where image noise exceeded the diagnostically acceptable level. The PI reconstructions did not suffer from this limitation. In general, DE can also help to reduce radiation dose and maintain high image quality in obese collectives compared to conventional SE examinations (Liu et al. 2016). Studies without VMI proved a relevant impact of DE on the hepatic vessel representation compared to conventional 120 kV acquisitions. The delineation of the right gastric artery, the vessels of the liver segment IV, and potential extrahepatic non-target vessels for the workup before radioembolization is easier with PI (Altenbernd et al. 2015). Like for the aorta, the best objective image quality can be expected in the minimum energy VMI datasets, too. The CNR can be increased by factor 3 compared to PI (Albrecht et al. 2016b). However, moderately decreased energy levels,

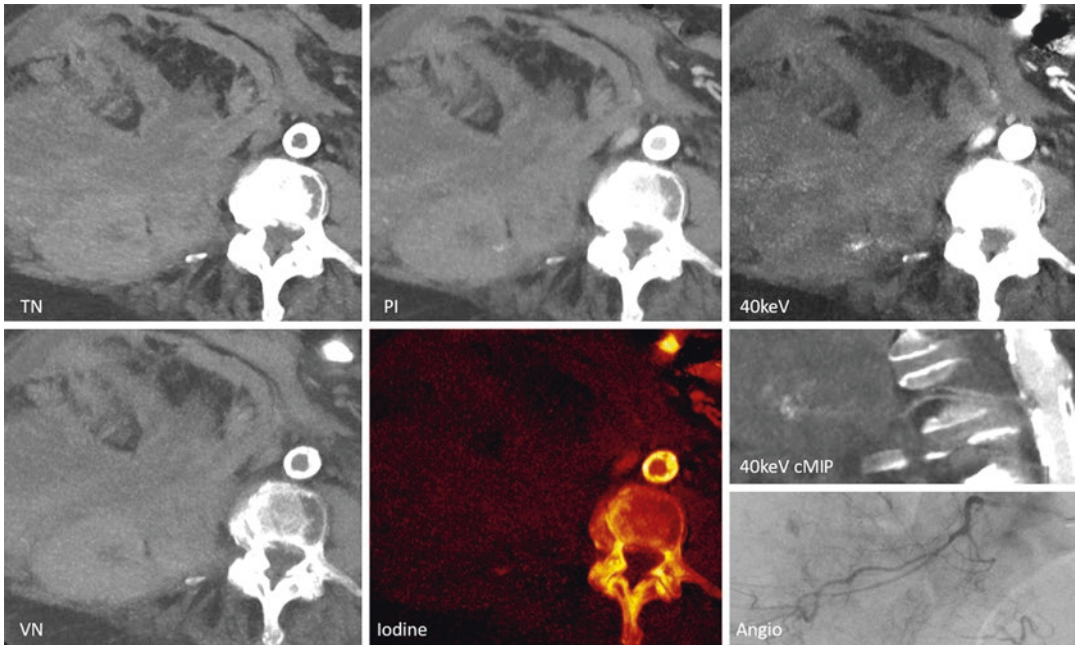


Fig. 5 Increased precision: virtual non-contrast (VN) reconstructions from dual-energy acquisitions of the abdomen are comparable to true non-contrast (TN) images. Additionally, the slight Iodine extravasation from a lumbar artery, in this case, is explicitly detected in the

iodine map. The lowest virtual monoenergetic reconstructions (40 keV) and curved maximum intensity projections (cMIP) helped to detect and locate the bleeding and the feeding vessel for immediate embolization therapy (Angio)

like 60–70 keV, provide the abdomen's best overall subjective vessel image quality (Gao et al. 2016). Especially motion artifacts from the small intestine can further reduce the image quality at 40 keV (Eichler et al. 2020). Several studies examined the potential of VMI to reduce contrast agent dose in the abdomen. Values between 15 and 25% were reported without affecting the vessel reproduction of the renal arteries and the splanchnic arteries (Liu et al. 2014; He et al. 2015). A study about simultaneous arteriovenous CT angiography of the kidneys was even able to demonstrate a positive impact on kidney function in a large collective (Zhou et al. 2017). Patients with abnormal renal function, defined as estimated glomerular filtration rate between 30 and 90 mL/min 1.73 m², had a significantly lower incidence of contrast-induced nephropathy in the group with the lower contrast agent concentration. No measurable difference was found for patients without reduced renal function before CT. The image quality was comparable if the

optimum kiloelectron voltage reconstructions are used (mean 53 keV). The optimum energy level for evaluating the tiny branches of the inferior epigastric artery before deep-inferior-epigastric-perforator (DIEP) flap transplantation was 63 keV in another study (Gao et al. 2016). Notably, DE was the modality with the highest diagnostic detection rate of the tiny anterior spinal artery in abdominal angiography (82%) when compared to SE CT angiography (81%), MR angiography (75%), and invasive catheter angiography (60%) (Abdelbaky et al. 2019).

Abdominal vessel evaluation is also often required in the emergency setting. I assume it happens to every radiologist at least once in his career that he thinks about intestinal ischemia after the scan of a patient with an acute abdomen was finalized in the portal-venous phase only. In precisely this situation, you would give your kingdom for a DE exam. VMI can provide contrast values in the superior mesenteric artery from portal-venous acquisitions that can exceed the

contrast values from arterial series (Hickethier et al. 2018). Embolic occlusions should therefore be fully evaluable. Care must be taken during the evaluation of stenosis grade by atherosclerotic lesions because overestimations can occur at 40 keV. Another emergency to trade kingdoms is acute bleedings, especially if an unenhanced examination was forgotten in the examination protocol. Luckily, the diagnostic performance of virtual non-contrast reconstructions was non-inferior to actual non-contrast examinations before contrast-enhanced acquisitions in an evaluation in the acute emergency setting (Fig. 5) (Sun et al. 2015). Moreover, bleeding detection has a higher precision with VMI reconstructions from portal-venous examinations than with the respective PI (area under the curve 0.96 vs. 0.82) (Martin et al. 2017c).

1.5.5 Peripheral Angiography

Imaging of the peripheral arteries has to deal with two different challenges. First, the vessel diameter in the proximal sections is often larger than 3 mm and relatively easy to visualize. Some authors found 100% sensitivity and specificity for high-grade stenosis (>75%) in the iliac arteries (Schabel et al. 2015). However, solid calcifications or stent material can lead to an overestimated degree of stenosis and limit diagnostic accuracy. A trade-off between high iodine contrast and blooming artifacts seems appropriate for these vessels. It seems that 90 keV VMI are appropriate for stent lumen visualization, while 40 keV VMI provide the best contrast and 100 keV VMI the most extensive in-stent lumen reproduction (Zhang et al. 2020). VMI+ come along with slightly lower optimum energy results. Here, moderate energies of 70–80 keV provide the best in-stent lumen reproduction directly compared with the gold standard from invasive catheter digital subtraction angiography (Mangold et al. 2016). These VMI+ significantly improved the diagnostic accuracy compared to PI (96% vs. 89%).

Second, the small vessels in the periphery of the forearm and the lower leg can be challenging to capture on one side and difficult to evaluate on the other side. Image contrast plays an important

role here. The drop in diagnostic accuracy below the knee was determined to be around 10% compared to lesions above in PI images from DE acquisitions (Schabel et al. 2015). Other authors reported even lower accuracies for MIP-only evaluations with abysmal results for the pedal arteries. The respective accuracy drop can be as high as 20–30% for that region, but the results for bypass segments were comparable to above the knee (Kau et al. 2011). Especially the rate of false positives increases in the lower leg (Brockmann et al. 2009). Therefore it was recommended to use the lowest available VMI+ reconstruction for this area, which provides increased diagnostic accuracy over VMI and PI (Wichmann et al. 2016). Some authors also claimed diagnostic accuracies above 90% by this technique for stenosis and occlusion of the lower leg. The direct comparison with conventional CT was also significantly superior (Jia et al. 2020). The lowest VMI also substantially improved the evaluation of the very small peroneal artery perforators before autologous transplantation in head and neck surgery. Manual vessel segmentation and multiplanar unfolding have the potential to support this benefit further (May et al. 2019b). A transfer of this fundamental principle of maximum contrast optimization for evaluating small peripheral arteries to other regions is possible. The subclavian artery branches and the arterial supply to the nipple-areola-complex before nipple-sparing mastectomy in case of breast cancer are just one example in the literature (Zeng et al. 2020).

Workflow is another crucial issue in CT angiography of the peripheral arteries. The long scan range and the transversal physics of CT scanners ensure high diagnostic image quality for evaluating the vessel diameter in general. However, it is time-consuming to evaluate a large stack of thin-slice axial images. Unfortunately, the appropriateness for coronal overview images is very limited, especially if compared with MR angiography, because of the superposition of bones and calcified plaques. Thus, especially workflow issues need to be addressed in CT of the peripheral vessels. Evidence exists in the literature that implementing bone and plaque removal algorithms

based on DE acquisitions can provide coronal overview images with high sensitivities (94–98%, Fig. 1) (Klink et al. 2017). The required time for post-processing DE datasets seems affordable (1–2 min) and roughly 50% below the duration of conventional techniques (Brockmann et al. 2009). There was no relevant difference in the literature than for conventional MPR, MIP, curved MPR, and automated assessment, making it a reasonable method for rapid assessment and demonstration. However, specificity remains the Achilles' heel of this technique (67–75%) and can be below 50% in case of severe calcifications. Therefore, additional detailed evaluation of questionable sections in MPR mode is recommended in a two-part workflow to achieve acceptable specificities (92%) (Kosmala et al. 2020). Also, a direct comparison of two commercially available products claimed a strong dependence of the diagnostic accuracy from the vessel segmentation and bone removal algorithm (Kostrzewa et al. 2016). Future software may hopefully further improve the workflow and diagnostic performance.

1.5.6 Venous System

Venography often suffers from poor contrast due to the free diffusion of contrast agents across the blood–tissue barrier and low Iodine concentration in the venous backflow, especially compared to arteriography. So it is hardly surprising that some studies in the literature targeted the contrast improvements by low kiloelectron voltage VMI from DE acquisitions (Kulkarni et al. 2012). For example, 40–50 keV VMI provide the best CNR in the pelvic veins, and the diagnostic performance and confidence for detection of deep venous thrombosis is best in these images (Tanoue et al. 2020). This advantage is of particular interest because the documented prevalence of isolated pelvic thrombosis, thus thrombosis that CT exclusively sees, is as low as 0.1–0.7% (Reichert et al. 2011). The respective radiation dose is considerably high (5–10 mSv). Therefore, if performed at all, the radiation dose efficiency should be as high as possible. Other authors reported enhanced visualization for the superficial veins of the legs before coronary artery bypass graft surgery by VMI+ (Schmoe et al.

2020). Also, adrenal vein delineation, before catheter-based adrenal vein sampling in patients with primary aldosteronism, benefits from high CNR and subjective image quality (Nakayama et al. 2020). The detection rate was 100% and improved compared to the 92% reported in the literature (Onozawa et al. 2016). The sampling success rate with DE was 95% and comparable to the results from other studies. Contrast agent concentration in a portal-venous system is even more insufficient. Early studies found that non-linear blending in PI increases the rate of patients with visible 5th to 6th generation branches of the portal vein from 36% to 76% (Wang et al. 2013). These images were also better than VMI for a combined evaluation of the portal and hepatic veins (Wang et al. 2014). However, low-energy VMI+ were recommended in deplorable contrast conditions, such as late phase imaging or cirrhotic patients, to visualize the venous systems in the liver (Schabel et al. 2014). Also, it was reported that low VMI (50–60 keV) could help to reduce the contrast agent dose by 25–52% (Han et al. 2019; Ma et al. 2016b). In general, enhanced iodine contrast in the venous system can help obtain diagnostic image quality in conventionally unevaluable cases. Especially the retrospective, spontaneous application of contrast-enhancing algorithms, like VMI+, to portal venous or late phase datasets can direct the radiologists' decision and increase their confidence level.

Compliance with Ethical Standards

Disclosure of Interests All authors declare they have no conflict of interest.

Ethical Approval This article does not contain any studies with human participants performed by any of the authors.

References

- Abdelbaky M, Zafar MA, Saeyeldin A et al (2019) Routine anterior spinal artery visualization prior to descending and thoracoabdominal aneurysm repair: high detection success. *J Card Surg* 34(12):1563–1568. <https://doi.org/10.1111/jocs.14310>

- Agatston AS, Janowitz WR, Hildner FJ, Zusmer NR, Viamonte M, Detrano R (1990) Quantification of coronary artery calcium using ultrafast computed tomography. *J Am Coll Cardiol* 15(4):827–832. [https://doi.org/10.1016/0735-1097\(90\)90282-t](https://doi.org/10.1016/0735-1097(90)90282-t)
- Albrecht MH, Trommer J, Wichmann JL et al (2016a) Comprehensive comparison of virtual monoenergetic and linearly blended reconstruction techniques in third-generation dual-source dual-energy computed tomography angiography of the thorax and abdomen. *Investig Radiol* 51(9):582–590. <https://doi.org/10.1097/RLL.0000000000000272>
- Albrecht MH, Scholtz J-E, Hüßers K et al (2016b) Advanced image-based virtual monoenergetic dual-energy CT angiography of the abdomen: optimization of kiloelectron volt settings to improve image contrast. *Eur Radiol* 26(6):1863–1870. <https://doi.org/10.1007/s00330-015-3970-2>
- Altenbernd J-C, Stein I, Wetter A et al (2015) Impact of dual-energy CT prior to radioembolization (RE). *Acta Radiol* 56(11):1293–1299. <https://doi.org/10.1177/0284185114558973>
- Bae K, Jeon KN, Cho SB et al (2018) Improved opacification of a suboptimally enhanced pulmonary artery in chest CT: experience using a dual-layer detector spectral CT. *AJR Am J Roentgenol* 210(4):734–741. <https://doi.org/10.2214/AJR.17.18537>
- Bai X, Gao P, Zhang D et al (2020) Plaque burden assessment and attenuation measurement of carotid atherosclerotic plaque using virtual monoenergetic images in comparison to conventional polyenergetic images from dual-layer spectral detector CT. *Eur J Radiol* 132:109302. <https://doi.org/10.1016/j.ejrad.2020.109302>
- Beeres M, Trommer J, Frellesen C et al (2016) Evaluation of different keV-settings in dual-energy CT angiography of the aorta using advanced image-based virtual monoenergetic imaging. *Int J Cardiovasc Imaging* 32(1):137–144. <https://doi.org/10.1007/s10554-015-0728-5>
- Brockmann C, Jochum S, Sadick M et al (2009) Dual-energy CT angiography in peripheral arterial occlusive disease. *Cardiovasc Intervent Radiol* 32(4):630–637. <https://doi.org/10.1007/s00270-008-9491-5>
- Buerke B, Wittkamp G, Seifarth H, Heindel W, Kloska SP (2009) Dual-energy CTA with bone removal for transcranial arteries: intraindividual comparison with standard CTA without bone removal and TOF-MRA. *Acad Radiol* 16(11):1348–1355. <https://doi.org/10.1016/j.acra.2009.05.007>
- Buffa V, Solazzo A, D'Auria V et al (2014) Dual-source dual-energy CT: dose reduction after endovascular abdominal aortic aneurysm repair. *Radiol Med* 119(12):934–941. <https://doi.org/10.1007/s11547-014-0420-1>
- Carrascosa P, Capunay C, Rodriguez-Granillo GA, Deviggiano A, Vallejos J, Leipsic JA (2014) Substantial iodine volume load reduction in CT angiography with dual-energy imaging: insights from a pilot randomized study. *Int J Cardiovasc Imaging* 30(8):1613–1620. <https://doi.org/10.1007/s10554-014-0501-1>
- Caruso D, Parinella AH, Schoepf UJ et al (2017) Optimization of window settings for standard and advanced virtual monoenergetic imaging in abdominal dual-energy CT angiography. *Abdom Radiol* 42(3):772–780. <https://doi.org/10.1007/s00261-016-0963-9>
- D'Angelo T, Bucher AM, Lenga L et al (2018) Optimisation of window settings for traditional and noise-optimised virtual monoenergetic imaging in dual-energy computed tomography pulmonary angiography. *Eur Radiol* 28(4):1393–1401. <https://doi.org/10.1007/s00330-017-5059-6>
- D'Angelo T, Lenga L, Arendt CT et al (2020) Carotid and cerebrovascular dual-energy computed tomography angiography: optimization of window settings for virtual monoenergetic imaging reconstruction. *Eur J Radiol* 130:109166. <https://doi.org/10.1016/j.ejrad.2020.109166>
- Das M, Braunschweig T, Mühlenbruch G et al (2009) Carotid plaque analysis: comparison of dual-source computed tomography (CT) findings and histopathological correlation. *Eur J Vasc Endovasc Surg* 38(1):14–19. <https://doi.org/10.1016/j.ejvs.2009.03.013>
- de Santis D, de Cecco CN, Schoepf UJ et al (2019) Modified calcium subtraction in dual-energy CT angiography of the lower extremity runoff: impact on diagnostic accuracy for stenosis detection. *Eur Radiol* 29(9):4783–4793. <https://doi.org/10.1007/s00330-019-06032-y>
- Eichler M, May M, Wiesmueller M et al (2020) Single source split filter dual energy: image quality and liver lesion detection in abdominal CT. *Eur J Radiol* 126:108913. <https://doi.org/10.1016/j.ejrad.2020.108913>
- Foti G, Silva R, Faccioli N et al (2021) Identification of pulmonary embolism: diagnostic accuracy of venous-phase dual-energy CT in comparison to pulmonary arteries CT angiography. *Eur Radiol* 31(4):1923–1931. <https://doi.org/10.1007/s00330-020-07286-7>
- Gao Z, Meng D, Lu H, Yao B, Huang N, Ye Z (2016) Utility of dual-energy spectral CT and low-iodine contrast medium in DIEP angiography. *Int J Clin Pract* 70(9):64–71. <https://doi.org/10.1111/ijcp.12855>
- Ghandour A, Sher A, Rassouli N, Dhanantwari A, Rajiah P (2018) Evaluation of virtual monoenergetic images on pulmonary vasculature using the dual-layer detector-based spectral computed tomography. *J Comput Assist Tomogr* 42(6):858–865. <https://doi.org/10.1097/RCT.0000000000000748>
- Gladish GW, Du Choe H, Marom EM, Sabloff BS, Broemeling LD, Munden RF (2006) Incidental pulmonary emboli in oncology patients: prevalence, CT evaluation, and natural history. *Radiology* 240(1):246–255. <https://doi.org/10.1148/radiol.2401051129>
- Godoy MCB, Naidich DP, Marchiori E et al (2010) Single-acquisition dual-energy multidetector computed tomography: analysis of vascular enhancement and postprocessing techniques for evaluating the thoracic aorta. *J Comput Assist Tomogr* 34(5):670–677. <https://doi.org/10.1097/RCT.0b013e3181e10627>

- Grimes J, Duan X, Yu L et al (2015) The influence of focal spot blooming on high-contrast spatial resolution in CT imaging. *Med Phys* 42(10):6011–6020. <https://doi.org/10.1118/1.4931053>
- Han D, Chen X, Lei Y et al (2019) Iodine load reduction in dual-energy spectral CT portal venography with low energy images combined with adaptive statistical iterative reconstruction. *Br J Radiol* 92(1100):20180414. <https://doi.org/10.1259/bjr.20180414>
- He J, Wang Q, Ma X, Sun Z (2015) Dual-energy CT angiography of abdomen with routine concentration contrast agent in comparison with conventional single-energy CT with high concentration contrast agent. *Eur J Radiol* 84(2):221–227. <https://doi.org/10.1016/j.ejrad.2014.11.025>
- Hickethier T, Byrtus J, Hauger M et al (2018) Utilization of virtual mono-energetic images (MonoE) derived from a dual-layer spectral detector CT (SDCT) for the assessment of abdominal arteries in venous contrast phase scans. *Eur J Radiol* 99:28–33. <https://doi.org/10.1016/j.ejrad.2017.12.007>
- Hou P, Feng X, Liu J et al (2017) Iterative reconstruction in single-source dual-energy CT angiography: feasibility of low and ultra-low volume contrast medium protocols. *Br J Radiol* 90(1075):20160506. <https://doi.org/10.1259/bjr.20160506>
- Huang S-C, Pareek A, Zamanian R, Banerjee I, Lungren MP (2020) Multimodal fusion with deep neural networks for leveraging CT imaging and electronic health record: a case-study in pulmonary embolism detection. *Sci Rep* 10(1):22147. <https://doi.org/10.1038/s41598-020-78888-w>
- Javor D, Wressnegger A, Unterhumer S et al (2017) Endoleak detection using single-acquisition split-bolus dual-energy computer tomography (DECT). *Eur Radiol* 27(4):1622–1630. <https://doi.org/10.1007/s00330-016-4480-6>
- Jia X, Li X, Li J et al (2020) Improving diagnostic accuracy for arteries of lower extremities with dual-energy spectral CT imaging. *Eur J Radiol* 128:109061. <https://doi.org/10.1016/j.ejrad.2020.109061>
- Jin KN, Chung JW, Park E-A, Lee W (2017) Dual-energy computed tomography angiography: virtual calcified plaque subtraction in a vascular phantom. *Acta Radiol Open* 6(7):2058460117717765. <https://doi.org/10.1177/2058460117717765>
- Kaemmerer N, Brand M, Hammon M et al (2016) Dual-energy computed tomography angiography of the head and neck with single-source computed tomography: a new technical (split filter) approach for bone removal. *Investig Radiol* 51(10):618–623. <https://doi.org/10.1097/RLL.0000000000000290>
- Kau T, Eicher W, Reiterer C et al (2011) Dual-energy CT angiography in peripheral arterial occlusive disease-accuracy of maximum intensity projections in clinical routine and subgroup analysis. *Eur Radiol* 21(8):1677–1686. <https://doi.org/10.1007/s00330-011-2099-1>
- Kerl JM, Bauer RW, Maurer TB et al (2011) Dose levels at coronary CT angiography--a comparison of dual energy-, dual source- and 16-slice CT. *Eur Radiol* 21(3):530–537. <https://doi.org/10.1007/s00330-010-1954-9>
- Klink T, Wilhelm T, Roth C, Heverhagen JT (2017) Dual Energy CTA bei Patienten mit symptomatischer pAVK: Studie über die diagnostische Genauigkeit und limitierende Faktoren. *Röfo* 189(5):441–452. <https://doi.org/10.1055/s-0043-101526>
- Korn A, Bender B, Thomas C et al (2011) Dual energy CTA of the carotid bifurcation: advantage of plaque subtraction for assessment of grade of the stenosis and morphology. *Eur J Radiol* 80(2):120–125. <https://doi.org/10.1016/j.ejrad.2010.08.028>
- Korn A, Bender B, Schabel C et al (2015) Dual-source dual-energy CT angiography of the supra-aortic arteries with tin filter: impact of tube voltage selection. *Acad Radiol* 22(6):708–713. <https://doi.org/10.1016/j.acra.2015.01.016>
- Kosmala A, Weng AM, Schmid A et al (2020) Dual-energy CT angiography in peripheral arterial occlusive disease: diagnostic accuracy of different image reconstruction approaches. *Acad Radiol*. <https://doi.org/10.1016/j.acra.2020.10.028>
- Kostrzewa M, Rathmann N, Hesser J, Huck K, Schönberg SO, Diehl SJ (2016) automated vessel segmentation in dual energy computed tomography data of the pelvis and lower extremities. *In Vivo* 30(5):651–655
- Kröger JR, Hickethier T, Pahn G, Gerhardt F, Maintz D, Bunck AC (2017) Influence of spectral detector CT based monoenergetic images on the computer-aided detection of pulmonary artery embolism. *Eur J Radiol* 95:242–248. <https://doi.org/10.1016/j.ejrad.2017.08.034>
- Kulkarni NM, Sahani DV, Desai GS, Kalva SP (2012) Indirect computed tomography venography of the lower extremities using single-source dual-energy computed tomography: advantage of low-kiloelectron volt monochromatic images. *J Vasc Interv Radiol* 23(7):879–886. <https://doi.org/10.1016/j.jvir.2012.04.012>
- Lee JW, Lee G, Lee NK et al (2016) Effectiveness of adaptive statistical iterative reconstruction for 64-slice dual-energy computed tomography pulmonary angiography in patients with a reduced iodine load: comparison with standard computed tomography pulmonary angiography. *J Comput Assist Tomogr* 40(5):777–783. <https://doi.org/10.1097/RCT.0000000000000443>
- Lehti L, Söderberg M, Höglund P, Nyman U, Gottsäter A, Wassélius J (2018) Reliability of virtual non-contrast computed tomography angiography: comparing it with the real deal. *Acta Radiol Open* 7(7-8):2058460118790115. <https://doi.org/10.1177/2058460118790115>
- Lehti L, Söderberg M, Höglund P, Wassélius J (2019) Comparing arterial- and venous-phase acquisition for optimization of virtual noncontrast images from dual-energy computed tomography angiography. *J Comput Assist Tomogr* 43(5):770–774. <https://doi.org/10.1097/RCT.0000000000000903>
- Leithner D, Mahmoudi S, Wichmann JL et al (2018) Evaluation of virtual monoenergetic imaging algo-

- rhythms for dual-energy carotid and intracerebral CT angiography: effects on image quality, artefacts and diagnostic performance for the detection of stenosis. *Eur J Radiol* 99:111–117. <https://doi.org/10.1016/j.ejrad.2017.12.024>
- Lell MM, Kramer M, Klotz E, Villablanca P, Ruehm SG (2009) Carotid computed tomography angiography with automated bone suppression: a comparative study between dual energy and bone subtraction techniques. *Investig Radiol* 44(6):322–328. <https://doi.org/10.1097/RLL.0b013e31819e8ad9>
- Lell MM, Hinkmann F, Nkenke E et al (2010) Dual energy CTA of the supraaortic arteries: technical improvements with a novel dual source CT system. *Eur J Radiol* 76(2):6–12. <https://doi.org/10.1016/j.ejrad.2009.09.022>
- Li S, Wang C, Jiang X, Xu G (2014) Effects of dual-energy CT with non-linear blending on abdominal CT angiography. *Korean J Radiol* 15(4):430–438. <https://doi.org/10.3348/kjr.2014.15.4.430>
- Li X, Chen GZ, Zhao YE et al (2017) Radiation optimized dual-source dual-energy computed tomography pulmonary angiography: intra-individual and inter-individual comparison. *Acad Radiol* 24(1):13–21. <https://doi.org/10.1016/j.acra.2016.09.009>
- Li Z, Leng S, Halaweish AF et al (2020) Overcoming calcium blooming and improving the quantification accuracy of percent area luminal stenosis by material decomposition of multi-energy computed tomography datasets. *J Med Imaging* 7(5):53501. <https://doi.org/10.1117/1.JMI.7.5.03501>
- Liu J, Lv P-J, Wu R et al (2014) Aortic dual-energy CT angiography with low contrast medium injection rate. *J Xray Sci Technol* 22(5):689–696. <https://doi.org/10.3233/XST-140454>
- Liu Y, Liu A, Liu L et al (2016) Feasibility of spectral imaging with low-concentration contrast medium in abdominal CT angiography of obese patients. *Int J Clin Pract* 70(9):37–43. <https://doi.org/10.1111/ijcp.12856>
- Ma G, He T, Yu Y, Duan H, Yang C (2016a) Improving image quality of bronchial arteries with virtual monochromatic spectral CT images. *PLoS One* 11(3):e0150985. <https://doi.org/10.1371/journal.pone.0150985>
- Ma C-L, Chen X-X, Lei Y-X et al (2016b) Clinical value of dual-energy spectral imaging with adaptive statistical iterative reconstruction for reducing contrast medium dose in CT portal venography: in comparison with standard 120-kVp imaging protocol. *Br J Radiol* 89(1062):20151022. <https://doi.org/10.1259/bjr.20151022>
- Ma G, Dou Y, Dang S et al (2019) Influence of monoenergetic images at different energy levels in dual-energy spectral CT on the accuracy of computer-aided detection for pulmonary embolism. *Acad Radiol* 26(7):967–973. <https://doi.org/10.1016/j.acra.2018.09.007>
- Mangold S, Cecco CN, Schoepf UJ et al (2016) A noise-optimized virtual monochromatic reconstruction algorithm improves stent visualization and diagnostic accuracy for detection of in-stent re-stenosis in lower extremity run-off CT angiography. *Eur Radiol* 26(12):4380–4389. <https://doi.org/10.1007/s00330-016-4304-8>
- Mannil M, Ramachandran J, Vittoria de Martini I et al (2017) Modified dual-energy algorithm for calcified plaque removal: evaluation in carotid computed tomography angiography and comparison with digital subtraction angiography. *Investig Radiol* 52(11):680–685. <https://doi.org/10.1097/RLL.0000000000000391>
- Marin D, Caywood DT, Mileto A et al (2015) Dual-energy multidetector-row computed tomography of the hepatic arterial system: optimization of energy and material-specific reconstruction techniques. *J Comput Assist Tomogr* 39(5):721–729. <https://doi.org/10.1097/RCT.0000000000000259>
- Martin SS, Albrecht MH, Wichmann JL et al (2017a) Value of a noise-optimized virtual monoenergetic reconstruction technique in dual-energy CT for planning of transcatheter aortic valve replacement. *Eur Radiol* 27(2):705–714. <https://doi.org/10.1007/s00330-016-4422-3>
- Martin SS, Wichmann JL, Weyer H et al (2017b) Endoleaks after endovascular aortic aneurysm repair: Improved detection with noise-optimized virtual monoenergetic dual-energy CT. *Eur J Radiol* 94:125–132. <https://doi.org/10.1016/j.ejrad.2017.06.017>
- Martin SS, Wichmann JL, Scholtz J-E et al (2017c) Noise-optimized virtual monoenergetic dual-energy CT improves diagnostic accuracy for the detection of active arterial bleeding of the abdomen. *J Vasc Interv Radiol* 28(9):1257–1266. <https://doi.org/10.1016/j.jvir.2017.06.011>
- May MS, Wiesmueller M, Heiss R et al (2019a) Comparison of dual- and single-source dual-energy CT in head and neck imaging. *Eur Radiol* 29(8):4207–4214. <https://doi.org/10.1007/s00330-018-5762-y>
- May MS, Wetzl M, Wust W, et al (2019b) Advanced visualization of peroneal artery perforators prior to autologous transplantation in head and neck surgery by dual-energy CT and multiplanar vessel unfolding. *Radiological Society of North America*. RC612-09
- McDermott S, Otrakji A, Flores EJ, Kalra MK, Shepard J-AO, Digumarthy SR (2018) Should dual-energy computed tomography pulmonary angiography replace single-energy computed tomography pulmonary angiography in pregnant and postpartum patients? *J Comput Assist Tomogr* 42(1):25–32. <https://doi.org/10.1097/RCT.0000000000000655>
- Meier A, Wurnig M, Desbiolles L, Leschka S, Frauenfelder T, Alkadhi H (2015) Advanced virtual monoenergetic images: improving the contrast of dual-energy CT pulmonary angiography. *Clin Radiol* 70(11):1244–1251. <https://doi.org/10.1016/j.crad.2015.06.094>
- Meier A, Higashigaito K, Martini K et al (2016) Dual energy CT pulmonary angiography with 6g Iodine-A propensity score-matched study. *PLoS One* 11(12):e0167214. <https://doi.org/10.1371/journal.pone.0167214>
- Meier A, Higashigaito K, Martini K et al (2017) Correction: dual energy CT pulmonary angiography

- with 6g Iodine-A propensity score-matched study. *PLoS One* 12(2):e0172251. <https://doi.org/10.1371/journal.pone.0172251>
- Meyer BC, Werncke T, Hopfenmüller W, Raatschen HJ, Wolf K-J, Albrecht T (2008) Dual energy CT of peripheral arteries: effect of automatic bone and plaque removal on image quality and grading of stenoses. *Eur J Radiol* 68(3):414–422. <https://doi.org/10.1016/j.ejrad.2008.09.016>
- Meyer M, Haubenreisser H, Schabel C et al (2018) CT pulmonary angiography in patients with acute or chronic renal insufficiency: evaluation of a low dose contrast material protocol. *Sci Rep* 8(1):1995. <https://doi.org/10.1038/s41598-018-20254-y>
- Mikail N, Meseguer E, Lavallée P et al (2021) Evaluation of non-stenotic carotid atherosclerotic plaques with combined FDG-PET imaging and CT angiography in patients with ischemic stroke of unknown origin. *J Nucl Cardiol*. <https://doi.org/10.1007/s12350-020-02511-8>
- Montanaro M, Scimeca M, Anemona L et al (2021) The paradox effect of calcification in carotid atherosclerosis: microcalcification is correlated with plaque instability. *Int J Mol Sci* 22(1):395. <https://doi.org/10.3390/ijms22010395>
- Morhard D, Fink C, Graser A, Reiser MF, Becker C, Johnson TRC (2009) Cervical and cranial computed tomographic angiography with automated bone removal: dual energy computed tomography versus standard computed tomography. *Investig Radiol* 44(5):293–297. <https://doi.org/10.1097/RLI.0b013e31819b6fba>
- Murphy A, Cheng J, Pratap J, Redman R, Couchner J (2019) Dual-energy computed tomography pulmonary angiography: comparison of vessel enhancement between linear blended and virtual monoenergetic reconstruction techniques. *J Med Imaging Radiat Sci* 50(1):62–67. <https://doi.org/10.1016/j.jmir.2018.10.009>
- Nadjiri J, Pfeiffer D, Straeter AS et al (2018) Spectral computed tomography angiography with a gadolinium-based contrast agent: first clinical imaging results in cardiovascular applications. *J Thorac Imaging* 33(4):246–253. <https://doi.org/10.1097/RTI.0000000000000335>
- Nakayama K, Shimohira M, Nakagawa M et al (2020) Advanced monoenergetic reconstruction technique in dual-energy computed tomography for evaluation of vascular anatomy before adrenal vein sampling. *Acta Radiol* 61(2):282–288. <https://doi.org/10.1177/0284185119860226>
- Neuhaus V, Große Hokamp N, Abdullayev N et al (2018) Comparison of virtual monoenergetic and polyenergetic images reconstructed from dual-layer detector CT angiography of the head and neck. *Eur Radiol* 28(3):1102–1110. <https://doi.org/10.1007/s00330-017-5081-8>
- Onozawa S, Murata S, Yamaguchi H et al (2016) Can an enhanced thin-slice computed tomography delineate the right adrenal vein and improve the success rate? *Jpn J Radiol* 34(9):611–619. <https://doi.org/10.1007/s11604-016-0564-0>
- Petrtsch B, Kosmala A, Gassenmaier T et al (2017) Diagnostik der akuten Lungenarterienembolie: Vergleich von single-source CT und Dritt-generation dual-source CT unter Einsatz eines dual-energy protokolls – Bildqualität und Strahlenexposition. *Röfo* 189(6):527–536. <https://doi.org/10.1055/s-0043-103089>
- Pinho DF, Kulkarni NM, Krishnaraj A, Kalva SP, Sahani DV (2013) Initial experience with single-source dual-energy CT abdominal angiography and comparison with single-energy CT angiography: image quality, enhancement, diagnosis and radiation dose. *Eur Radiol* 23(2):351–359. <https://doi.org/10.1007/s00330-012-2624-x>
- Qanadli SD, El Hajjam M, Mesurolle B et al (1999) Motion artifacts of the aorta simulating aortic dissection on spiral CT. *J Comput Assist Tomogr* 23(1):1–6. <https://doi.org/10.1097/00004728-199901000-00001>
- Reichert M, Henzler T, Krissak R et al (2011) Venous thromboembolism: additional diagnostic value and radiation dose of pelvic CT venography in patients with suspected pulmonary embolism. *Eur J Radiol* 80(1):50–53. <https://doi.org/10.1016/j.ejrad.2010.12.101>
- Renapurkar RD, Primak A, Azok J et al (2017) Attenuation-based kV pair selection in dual source dual energy computed tomography angiography of the chest: impact on radiation dose and image quality. *Eur Radiol* 27(8):3283–3289. <https://doi.org/10.1007/s00330-016-4714-7>
- Reynoso E, Rodriguez-Granillo GA, Capunay C, Deviggiano A, Meli F, Carrascosa P (2017) Spectral signal density of carotid plaque using dual-energy computed tomography. *J Neuroimaging* 27(5):511–516. <https://doi.org/10.1111/jon.12440>
- Riffel P, Haubenreisser H, Meyer M et al (2016) Carotid dual-energy CT angiography: evaluation of low keV calculated monoenergetic datasets by means of a frequency-split approach for noise reduction at low keV levels. *Eur J Radiol* 85(4):720–725. <https://doi.org/10.1016/j.ejrad.2016.01.015>
- Rotzinger DC, Si-Mohamed SA, Shapira N, Douek PC, Meuli RA, Bousset L (2020) “Dark-blood” dual-energy computed tomography angiography for thoracic aortic wall imaging. *Eur Radiol* 30(1):425–431. <https://doi.org/10.1007/s00330-019-06336-z>
- Saba L, Mallarin G (2009) Window settings for the study of calcified carotid plaques with multidetector CT angiography. *AJNR Am J Neuroradiol* 30(7):1445–1450. <https://doi.org/10.3174/ajnr.A1509>
- Saba L, Sanfilippo R, Balestrieri A et al (2017) Relationship between carotid computed tomography dual-energy and brain leukoaraiosis. *J Stroke Cerebrovasc Dis* 26(8):1824–1830. <https://doi.org/10.1016/j.jstrokecerebrovasdis.2017.04.016>
- Saba L, Argioas GM, Lucatelli P, Lavra F, Suri JS, Wintermark M (2019) Variation of degree of stenosis quantification using different energy level with dual

- energy CT scanner. *Neuroradiology* 61(3):285–291. <https://doi.org/10.1007/s00234-018-2142-x>
- Sauter AP, Shapira N, Kopp FK et al (2020) CTPA with a conventional CT at 100 kVp vs. a spectral-detector CT at 120 kVp: comparison of radiation exposure, diagnostic performance and image quality. *Eur J Radiol Open* 7:100234. <https://doi.org/10.1016/j.ejro.2020.100234>
- Schabel C, Bongers M, Sedlmair M et al (2014) Assessment of the hepatic veins in poor contrast conditions using dual energy CT: evaluation of a novel monoenergetic extrapolation software algorithm. *Röfo* 186(6):591–597. <https://doi.org/10.1055/s-0034-1366423>
- Schabel C, Bongers MN, Ketelsen D et al (2015) Diagnostische Genauigkeit der Dual-energy-CT-Angiographie bei Patienten mit Diabetes mellitus. *Radiologe* 55(4):314–322. <https://doi.org/10.1007/s00117-014-2721-8>
- Schmoe J, Dirrichs T, Fehrenbacher K et al (2020) Virtual monoenergetic images (VMI+) in dual-source dual-energy CT venography (DSDE-CTV) of the lower extremity prior to coronary artery bypass graft (CABG): a feasibility study. *Acad Radiol* 27(9):1249–1254. <https://doi.org/10.1016/j.acra.2019.11.005>
- Schulz B, Kuehling K, Kromen W et al (2012) Automatic bone removal technique in whole-body dual-energy CT angiography: performance and image quality. *AJR Am J Roentgenol* 199(5):W646–W650. <https://doi.org/10.2214/AJR.12.9176>
- Shaida N, Bowden DJ, Barrett T et al (2012) Acceptability of virtual unenhanced CT of the aorta as a replacement for the conventional unenhanced phase. *Clin Radiol* 67(5):461–467. <https://doi.org/10.1016/j.crad.2011.10.023>
- Shinohara Y, Sakamoto M, Kuya K et al (2015) Assessment of carotid plaque composition using fast-kV switching dual-energy CT with gemstone detector: comparison with extracorporeal and virtual histology-intravascular ultrasound. *Neuroradiology* 57(9):889–895. <https://doi.org/10.1007/s00234-015-1541-5>
- Shuman WP, O'Malley RB, Busey JM, Ramos MM, Koprowicz KM (2017) Prospective comparison of dual-energy CT aortography using 70% reduced iodine dose versus single-energy CT aortography using standard iodine dose in the same patient. *Abdom Radiol* 42(3):759–765. <https://doi.org/10.1007/s00261-016-1041-z>
- Sommer WH, Johnson TR, Becker CR et al (2009) The value of dual-energy bone removal in maximum intensity projections of lower extremity computed tomography angiography. *Investig Radiol* 44(5):285–292. <https://doi.org/10.1097/RLL.0b013e31819b70ba>
- Sommer WH, Graser A, Becker CR et al (2010) Image quality of virtual noncontrast images derived from dual-energy CT angiography after endovascular aneurysm repair. *J Vasc Interv Radiol* 21(3):315–321. <https://doi.org/10.1016/j.jvir.2009.10.040>
- Sun H, Hou X-Y, Xue H-D et al (2015) Dual-source dual-energy CT angiography with virtual non-enhanced images and iodine map for active gastrointestinal bleeding: image quality, radiation dose and diagnostic performance. *Eur J Radiol* 84(5):884–891. <https://doi.org/10.1016/j.ejrad.2015.01.013>
- Tanoue S, Nakaura T, Iyama Y et al (2020) Diagnostic performance of dual-layer computed tomography for deep vein thrombosis in indirect computed tomography venography. *Circ J* 84(4):636–641. <https://doi.org/10.1253/circj.CJ-19-0722>
- Uhrig M, Simons D, Schlemmer H-P (2018) Incidental pulmonary emboli in stage IV melanoma patients: Prevalence in CT staging examinations and improved detection with vessel reconstructions based on dual energy CT. *PLoS One* 13(7):e0199458. <https://doi.org/10.1371/journal.pone.0199458>
- Uotani K, Watanabe Y, Higashi M et al (2009) Dual-energy CT head bone and hard plaque removal for quantification of calcified carotid stenosis: utility and comparison with digital subtraction angiography. *Eur Radiol* 19(8):2060–2065. <https://doi.org/10.1007/s00330-009-1358-x>
- van der Molen AJ, Reimer P, Dekkers IA et al (2018) Post-contrast acute kidney injury. Part 2: risk stratification, role of hydration and other prophylactic measures, patients taking metformin and chronic dialysis patients: recommendations for updated ESUR Contrast Medium Safety Committee guidelines. *Eur Radiol* 28(7):2856–2869. <https://doi.org/10.1007/s00330-017-5247-4>
- Wang Q, Shi G, Liu X, Wu R, Wang S (2013) Optimal contrast of computed tomography portal venography using dual-energy computed tomography. *J Comput Assist Tomogr* 37(2):142–148. <https://doi.org/10.1097/RCT.0b013e31827cd656>
- Wang Q, Gaofeng S, Xueli F, Lijia W, Runze W (2014) Comparative study of hepatic venography using non-linear-blending images, monochromatic images and low-voltage images of dual-energy CT. *Br J Radiol* 87(1042):20140220. <https://doi.org/10.1259/bjr.20140220>
- Watanabe Y, Nakazawa T, Higashi M, Itoh T, Naito H (2011) Assessment of calcified carotid plaque volume: comparison of contrast-enhanced dual-energy CT angiography and native single-energy CT. *AJR Am J Roentgenol* 196(6):796–799. <https://doi.org/10.2214/AJR.10.4938>
- Wichmann JL, Gillott MR, Cecco CN et al (2016) Dual-energy computed tomography angiography of the lower extremity runoff: impact of noise-optimized virtual monochromatic imaging on image quality and diagnostic accuracy. *Investig Radiol* 51(2):139–146. <https://doi.org/10.1097/RLL.0000000000000216>
- Xin L, Yang X, Huang N et al (2015) The initial experience of the upper abdominal CT angiography using low-concentration contrast medium on dual energy spectral CT. *Abdom Imaging* 40(7):2894–2899. <https://doi.org/10.1007/s00261-015-0462-4>
- Yamamoto S, McWilliams J, Arellano C et al (2009) Dual-energy CT angiography of pelvic and lower extremity arteries: dual-energy bone subtraction versus manual

- bone subtraction. *Clin Radiol* 64(11):1088–1096. <https://doi.org/10.1016/j.crad.2009.07.009>
- Yoshida M, Nakaura T, Sentaro T et al (2020) Prospective comparison of 70-kVp single-energy CT versus dual-energy CT: which is more suitable for CT angiography with low contrast media dosage? *Acad Radiol* 27(5):116–122. <https://doi.org/10.1016/j.acra.2019.07.016>
- Zeng X, Wang X, Chen H et al (2020) Evaluating the image quality of monoenergetic images from dual-energy computed tomography with low-concentration and low-flow-rate contrast media for the arterials supply to the nipple-areola complex in breast cancer compared with conventional computed tomography angiography. *J Comput Assist Tomogr* 44(6):921–927. <https://doi.org/10.1097/RCT.0000000000001063>
- Zhang LJ, Wang ZJ, Lu L, Chen B, Lu GM (2011) Feasibility of gadolinium-enhanced dual energy CT pulmonary angiography: a pilot study in rabbits. *Int J Cardiovasc Imaging* 27(7):1069–1080. <https://doi.org/10.1007/s10554-010-9755-4>
- Zhang D, Xie Y, Wang Y et al (2020) Initial clinical experience of virtual monoenergetic imaging improves stent visualization in lower extremity run-off CT angiography by dual-layer spectral detector CT. *Acad Radiol* 27(6):825–832. <https://doi.org/10.1016/j.acra.2019.07.022>
- Zhou K, He J, Qu F et al (2017) Comparison of 270 versus 320 mg I/mL of Iodixanol in I image assessment of both renal arteries and veins with dual-energy spectral CT imaging in late arterial phase and their influence on renal function. *J Comput Assist Tomogr* 41(5):798–803. <https://doi.org/10.1097/RCT.0000000000000595>
- Zopfs D, Lennartz S, Laukamp K et al (2018) Improved depiction of atherosclerotic carotid artery stenosis in virtual monoenergetic reconstructions of venous phase dual-layer computed tomography in comparison to polyenergetic reconstructions. *Eur J Radiol* 100:36–42. <https://doi.org/10.1016/j.ejrad.2018.01.008>



Thoracic Imaging: Ventilation/ Perfusion

Hye Jeon Hwang, Sang Min Lee,
and Joon Beom Seo

Contents

1	Perfusion Dual-Energy CT	184
1.1	Imaging Protocol	184
1.2	Clinical Applications	184
2	Ventilation Dual-Energy CT	188
2.1	Technical Aspects	188
2.2	Clinical Applications	190
3	Comprehensive Assessment of Morphology, Pulmonary Ventilation, Perfusion, and Relationship of Ventilation and Perfusion Using Dual-Energy CT	194
3.1	Concept	194
3.2	Clinical Application: Pulmonary Embolism, COPD	194
4	Perspective and Conclusion	197
	References	197

Abstract

Various lung diseases cause structural or reflex changes in the lungs, resulting in changes in ventilation or perfusion status, which lead to ventilation–perfusion imbalances. Various imaging methods, including magnetic resonance imaging (MRI), gamma camera-based planar scintigraphy, single-photon emission computed tomography (SPECT), or positron emission tomography (PET) have been used

to evaluate and visualize the pulmonary perfusion or ventilation status. The above methods have limitations of spatial resolution and present challenges in the generation of the radioactive tag. Multidetector computed tomography is the modality of choice in lung imaging for anatomic evaluation by providing excellent spatial resolution; however, it requires repeated CT scans for evaluating pulmonary ventilation or perfusion, which may result in increased radiation exposure and potential misregistration of images. With the advance of dual-energy computed tomography (DECT), it has become possible to provide pulmonary functional information such as pulmonary perfusion or ventilation map

H. J. Hwang · S. M. Lee · J. B. Seo (✉)
Department of Radiology and Research Institute of
Radiology, University of Ulsan College of Medicine,
Asan Medical Center, Seoul, South Korea
e-mail: seojb@amc.seoul.kr

and high-resolution morphologic information within a single CT scan. This advantage of DECT may facilitate the acquisition of coregistered structural and functional information within a clinical setting's constraints. This chapter will present the clinical applications for the assessment of pulmonary perfusion, ventilation, and ventilation–perfusion imbalance using DECT in various lung diseases.

1 Perfusion Dual-Energy CT

1.1 Imaging Protocol

Lung perfusion or pulmonary blood volume (PBV) image is based on quantification of the enhancement in tissue and blood at certain time points after IV administration of contrast media (Gorgos et al. 2009). This image is not true perfusion but reflects the regional volume of blood to which fresh blood is being delivered. If this fresh blood is equilibrated with iodine, then the regional iodine concentration measured by DECT reflects the regional PBV. As increased blood flow to a region of lung may serve to dilate the capillary beds and recruit new capillaries, a measure of regional PBV may serve as a surrogate for pulmonary parenchymal perfusion.

For accurate assessment of PBV, there are several important considerations (Hwang et al. 2017). First, PBV can be affected by the amount of breathing volume at the time of breath-hold. And important assumption of PBV is that an amount of iodine is equilibrated in the blood at the time of imaging and that equilibrated iodine concentration remains constant during the scanning of the lung. In calculating PBV, it is important to standardize the regional measurements by the iodine signal within the feeding pulmonary artery.

Lung perfusion image from DECT provides an iodine map of the lung microcirculation which represents a measurement at one time point only. Though this image shows only blood volume at certain time points, this modality provides high-quality morphologic and functional information

on the pulmonary circulation from the same data set. Many factors influence the enhancement within lung microvessels: the volume and flow rate of the contrast media, the contrast media administration site, and the anatomic structures through which the iodinated contrast media courses (Thieme et al. 2009). Another factor is the systemic circulation, because of its role in collateral supply and the numerous anastomoses within the pulmonary circulation.

1.2 Clinical Applications

1.2.1 Pulmonary Vascular Diseases (Pulmonary Embolism and Pulmonary Hypertension)

Pulmonary embolism (PE) is a common disease cardiovascular disease. The emboli, migrated from deep vein thrombosis of the lower limb, cause either total or partial blockage of the pulmonary arteries. Because outcomes without proper treatment are poor, accurate and fast diagnosis of PE is essential. CT pulmonary angiography (CTPA) can visualize emboli and the ancillary findings associated with PE. CTPA has been accepted as the method of choice for imaging suspected PE. However, CTPA does not provide functional assessment of lung, which can be evaluated with ventilation/perfusion scintigraphy.

With a single scan of DECT, both the high spatial/temporal resolution axial image and the PBV map can be acquired simultaneously with similar radiation dose of CTPA (Fig. 1). PBV map can provide perfusion defects in the lung parenchyma for the diagnosis of acute PE. Perfusion defects distal to the occlusion usually have the typical wedge shape.

In acute PE, the PBV map of DECT shows strong correlation with pulmonary perfusion scintigraphy and SPECT images (Thieme et al. 2008, 2012a). The additional information of parenchymal perfusion impairment from DECT can improve the diagnosis of acute PE (Okada et al. 2015). In clinical practice, it is difficult to detect small thrombi in the segmental or subsegmental pulmonary arteries on conventional CT angiography. With the postprocessing of DECT

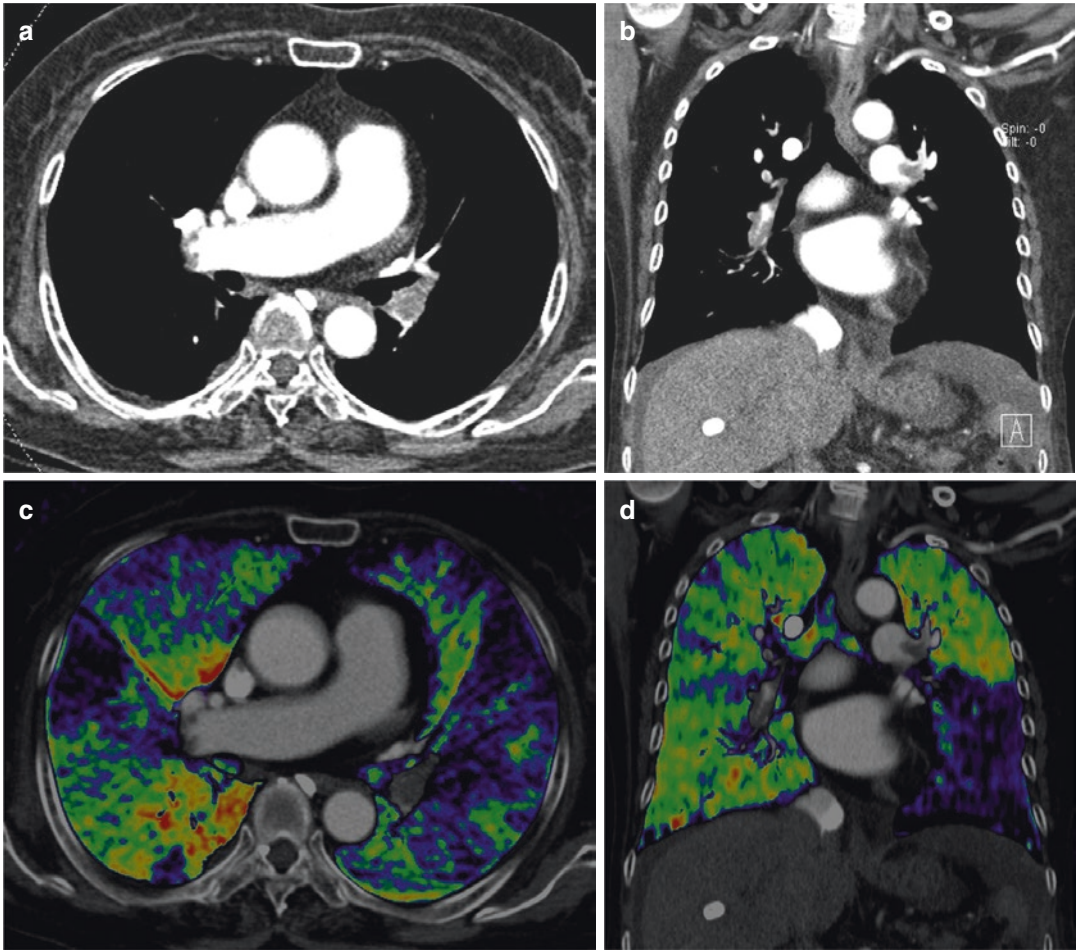


Fig. 1 Example of CTPA using DECT in a 71-year-old man with acute pulmonary embolism. (a, b) Axial and coronal CTPA images show large clots in both lobar and segmental pulmonary arteries. (c, d) Axial and coronal

fusion images of PBV maps show wedge shape perfusion defects in the right middle lobe and left lingular segment of the left upper lobe. A large perfusion defect is also noted in the left lower lobe

image, the direct color-coded differentiation of thrombosed vessels and contrast-filled non-thrombosed vessels can be assessed. The perfusion impairment of PBV and the differentiation of thrombosed/non-thrombosed vessels map help detection of small endovascular thrombi (Lee et al. 2011) (Fig. 2).

Using the perfusion defects on PBV map, the severity of acute PE can be investigated. The visually assessed perfusion defects score from the PBV map showed correlation with established CT parameters of PE severity such as RV/LV ratio and CT angiography obstruction score (Chae et al. 2010a). And visual scoring system of

DECT-based perfusion defects in patients with PE correlated with clinical parameters of acute PE severity (Thieme et al. 2012b). The quantification assessment of perfusion defect volume of the PBV map was correlated with established CT parameters (Meinel et al. 2013a; Sakamoto et al. 2014).

Chronic PE may show a mosaic pattern of lung attenuation due to redistribution of blood flow (Remy-Jardin et al. 2010). DECT can differentiate ground glass attenuation of vascular origin with high iodine contents from ground glass attenuation of other origin. DECT provides virtual non-contrast (VNC) image which

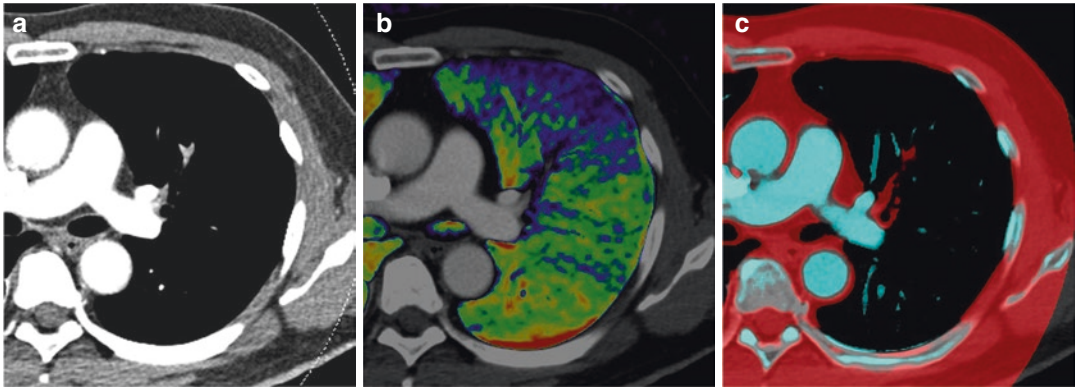


Fig. 2 Example of detection of small peripheral embolism in a 56-year-old man with elevated d-dimer using DECT. (a) Axial CT pulmonary angiography shows low attenuated small vessels compared with other normally enhanced small vessels in the left upper lobe, suspicious of peripheral embolic clots. (b) PBV map shows a wedge-

shaped perfusion defect distal to the small indecisive vessel. (c) The color-coded CT image with the dedicated dual-energy software, “Lung Vessels,” shows these small vessels in red, representing thrombosed vessels without iodine

can detect calcification in chronic clots. In chronic PE, the bronchial circulation and systemic circulation may be increased due to decreased pulmonary flow and ischemia. Two-phase DECT can differentiate acute and chronic PE (Hong et al. 2013). In delayed second phase PBV map, lung area with systemic collateral circulation showed increased enhancement compared with arterial phase PBV map. Using DECT, enhancement values of pulmonary artery and whole lung parenchyma can be quantified, and the derived central-to-peripheral ratio can help to detect chronic thromboembolic pulmonary hypertension (Ameli-Renani et al. 2014).

1.2.2 Diffuse Parenchymal/Airway Disease

With the assessment of PBV map, pulmonary vascular dysfunction can be evaluated as a possible role in the etiology of smoking associated emphysema. In smokers with normal pulmonary function tests (PFTs), the smokers with centriacinar emphysema on CT showed nearly double heterogeneity of parenchymal perfusion than smokers without early emphysema (Alford et al. 2010). This increased heterogeneity of PBV can be reversible with a single oral dose of 20 mg of

sildenafil in emphysema susceptible normal smokers (Iyer et al. 2016). These data show that vascular heterogeneity of smokers is not due to a fixed remodeling but is the result of an active vasoconstriction.

In COPD, regional perfusion can be impaired due to loss of capillary beds from emphysematous destruction or chronic inflammation and hypoxic vasoconstriction (Barbera et al. 2003). DECT can be helpful to assess patients with COPD, because the severity of anatomic destruction and the change of parenchymal perfusion make the functional effect of the disease. The regional lung perfusion change on PBV map is matched to the parenchymal destruction and quantitative information of parenchymal destruction and perfusion can be provided simultaneously using DECT (Lee et al. 2012; Pansini et al. 2009). Enhanced CT cannot be used for quantification of emphysema; however, VNC image showed moderate correlation with PFTs (Lee et al. 2012). Using the automated quantified PBV value, pulmonary perfusion in emphysema can be assessed (Meinel et al. 2013b). The quantified PBV showed correlation with PFTs and carbon monoxide diffusing capacity (DL_{CO}). The global PBV showed stronger correlation with DL_{CO} than emphysema severity.

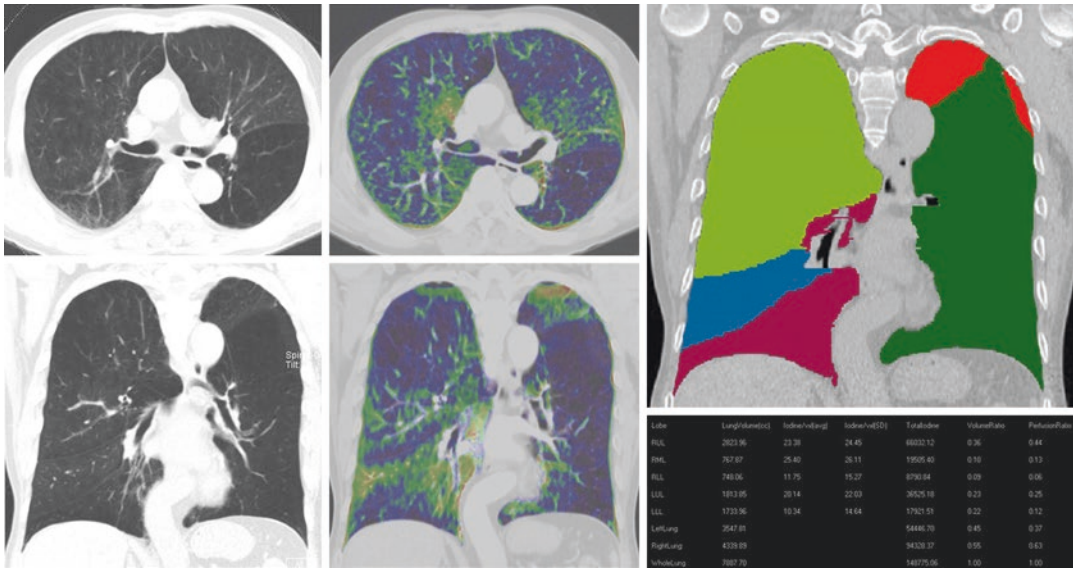


Fig. 3 Perfusion DECT in a 66-year-old man with severe emphysema shows hyperinflation and decreased parenchymal perfusion in the left lower lobe. After lobe segmentation, perfusion ratio of LLL (12%) is more decreased than volume ratio of LLL (22%). Considering the conventional CT findings and perfusion map of perfu-

sion DECT, the left lower lobe was selected for the target lobe of bronchoscopic lung volume reduction. Bronchoscopic lung volume reduction was performed successfully in this patient, and the percent predicted FEV₁ was improved from 18% to 32%

In severe COPD patients, assessment of emphysema distribution and regional perfusion using DECT can help target lobe selection of surgical or bronchoscopic lung volume reduction (Park et al. 2014) (Fig. 3). Most hyperinflated and least perfused lobe of the emphysematous lung on DECT was selected as the target lobe. Additionally, CT image can provide fissure integrity of the target lobe.

In interstitial lung disease (ILD), DECT can be used for assessing ILD and predicting prognosis with assessment of texture pattern-based quantification and the PBV map (Moon et al. 2016). Perfusion and morphologic assessments on DECT were correlated with clinical parameters such as PFTs, DLco, or 6-min walk test and can predict survival of ILD patients.

1.2.3 Lung Cancer

The lobar perfusion ratio on perfusion scintigraphy is widely used to predict postoperative forced expiratory volume during 1 s (FEV₁) for preoperative risk stratification (Brunelli and Fianchini 1997; Pierce et al. 1994). DECT with PBV map

can be used for prediction of postoperative lung function in patients undergoing lung resection and can predict more accurately than perfusion scintigraphy, because DECT can do the precise segmentation and measurement of lobar perfusion on high-resolution CT imaging and perfectly matched PBV maps (Chae et al. 2013) (Fig. 4).

The maximum iodine-related attenuation of lung cancer on DECT showed a moderate correlation with the maximum standardized uptake value (SUV_{max}) on FDG-PET/CT. Especially non-small cell lung cancer showed a strong correlation between SUV_{max} and maximum iodine-related attenuation (Schmid-Bindert et al. 2012). The maximum iodine-related attenuation on DECT may be a useful surrogate parameter for assessment of therapy response in non-small cell lung cancer patient.

Dual-phase DECT can assess therapeutic effect after conservative therapy including anti-angiogenesis therapy for not only primary lesions, but also mediastinal lymph node metastases in non-small cell lung cancer (Baxa et al. 2014, 2016). Quantification of arterial iodine

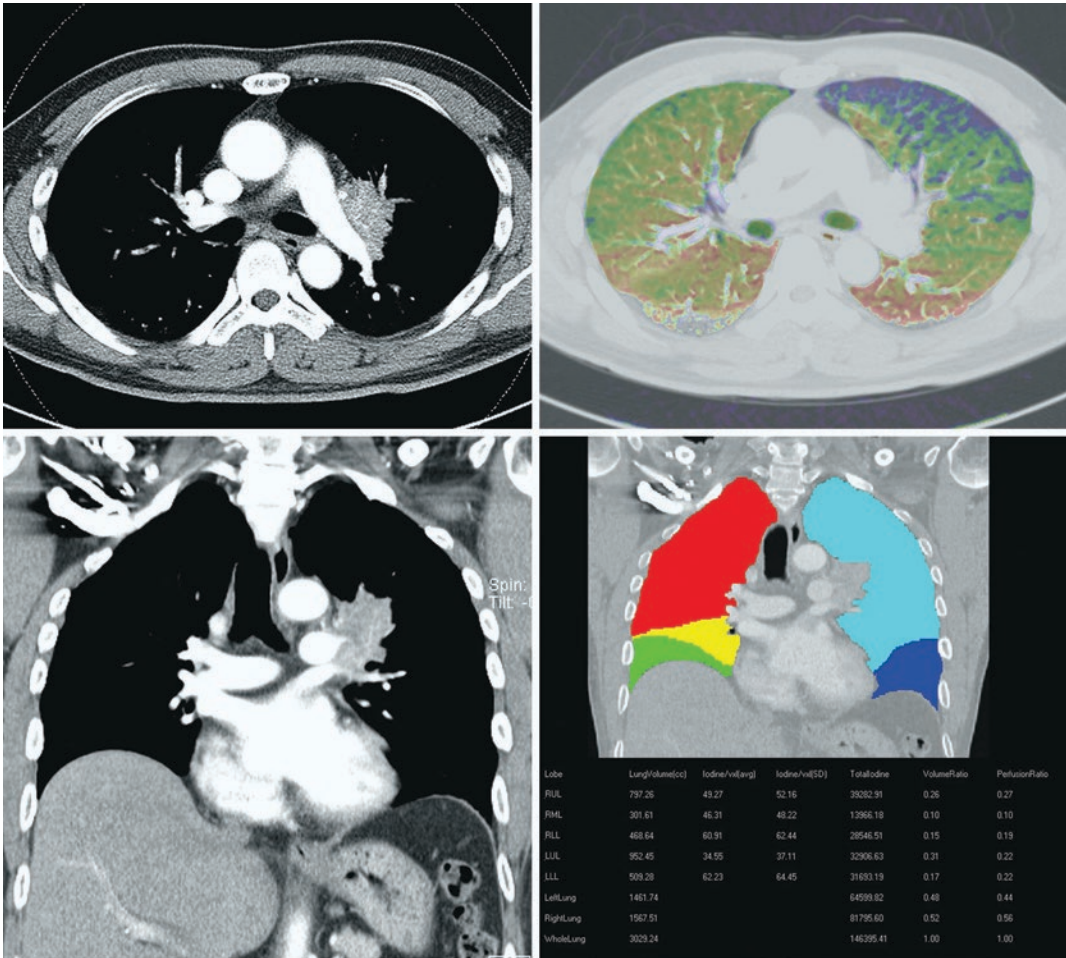


Fig. 4 Perfusion DECT in a 56-year-old man with a central lung mass in the left lower lobe abutting to left main pulmonary artery. After lobe segmentation, perfusion ratio of Lt. lung is 44%. Preoperative FEV₁ was 2.79L (76%)

and predicted postoperative FEV₁ using perfusion DECT was 1.56L (43%). After 3 months from left pneumonectomy, postoperative FEV₁ was 1.65L (45%)

uptake can predict and assess therapeutic effect. In addition, ratio of early and late iodine uptake quantification can evaluate function of mediastinal lymph node.

2 Ventilation Dual-Energy CT

2.1 Technical Aspects

2.1.1 Noble Gas Contrast Agents

For ventilation imaging with DECT, two stable gases, xenon and krypton are eligible as inhala-

tion contrast agents (Gur et al. 1979; Herbert et al. 1982; Chae et al. 2010b; Chon et al. 1985; Hong et al. 2016). These are radio-opaque gases with high atomic numbers (54 for xenon and 36 for krypton) that resemble the X-ray absorption characteristics of iodine. Their concentration in the airspaces of the lung including alveolar space can be measured based on the CT attenuation, and it has been shown that local xenon concentration is linearly related to CT attenuation (Gur et al. 1979; Murphy et al. 1989). Xenon has anesthetic properties and respiratory depression effect at a concentration of over 30–40% (Bedi et al.

2002; Latchaw et al. 1987; Tonner 2006); thus, the 30% concentration of xenon gas is clinically used in ventilation imaging. Other side effects included headache, somnolence nausea and vomiting, and physiologic effects, such as lightheadedness and labile emotion (Latchaw et al. 1987; Yonas et al. 1981). These adverse effects are mostly mild and uncommon and not resulted in any persistent neurologic change or other sequelae. Stable krypton gas can be an alternative to xenon gas for ventilation imaging, and its potential usefulness as an inhalation contrast agent for ventilation imaging has been investigated in several studies (Hong et al. 2016; Chung et al. 2014; Winkler et al. 1977). Krypton gas is less radio-opaque than xenon gas (Chon et al. 1985); however, it has no anesthetic properties like xenon gas. With improvements in spectral separation and detector sensitivity of scanners, krypton is expected to become a viable alternative to xenon gas (Chung et al. 2014).

2.1.2 Imaging Protocol

Xenon ventilation DECT can be successfully performed using the dual-source CT scanners (Somatom Definition scanner and Somatom Definition FLASH, Siemens Healthcare, Forchheim, Germany) (Chae et al. 2010b, 2008; Goo et al. 2008; Park et al. 2010).

Patients inhale xenon gas using the close-fitting face mask designed to deliver positive pressure ventilation treatment (Chae et al. 2010b, 2008; Hong et al. 2016; Park et al. 2010; Hwang et al. 2020). As Chae et al. (2008) demonstrated, a xenon concentration of 30% is sufficient for an adequate CT attenuation, and many studies used the mixture of 30% xenon and 70% oxygen with the use of an inhalation system (Chae et al. 2010b, 2008; Goo et al. 2008; Park et al. 2010; Hwang et al. 2020). The patient may inhale a high concentration (>60%) of oxygen for 2–3 min before inhaling xenon gas to reduce the probability of respiratory difficulties. The inhalation times vary depending on imaging protocols, and it is recommended not to exceed 2 min, because most adverse effects have occurred after inhalation lasting longer than 4 min (Latchaw et al. 1987; Winkler et al. 1977). The inhalation times

may vary depending on study protocols; and the multiple breath-in method for less than 2 min has been used in most of the studies for patients' safety and sufficient CT attenuation for visual and quantitative analyses (Chae et al. 2010b; Park et al. 2010; Hwang et al. 2020). However, the multiple breath-in method might obscure the mild degree of ventilation abnormalities that can be identified on ^3He MRI with the single breath-in method. In recent years, xenon ventilation DECT using a single vital capacity inhalation of 35% xenon gas also has been tried (Honda et al. 2012; Kyoyama et al. 2017). Monitoring of respiratory rate, oxygen saturation, and blood pressure of patients, and xenon concentrations within inhaled and exhaled gas and carbon dioxide concentrations within exhaled gas are recommended throughout the study.

Ventilation DECT scanning with either single static or dynamic acquisition protocols is available depending on the purpose of the ventilation imaging. The single static scan is usually performed with multiple breath-in method, and CT image acquisition is usually performed with full lung coverage at the end of the wash-in period, and an additional CT scan with full lung coverage may be performed at the end of the wash-out period. This method can fully answer whether a region of the lung is or is not being ventilated, although the minor regional ventilation heterogeneity may be obscured. The dynamic scan of ventilation DECT during wash-in and wash-out of xenon gas may provide more detailed information of regional ventilation, reflecting real ventilation, as pathologies of various airway diseases affect the outflow of the air, as well as the inflow of the air. However, additional radiation exposure is required in this protocol. In a dynamic acquisition protocol, CT images are usually obtained every 18–30 s during both the wash-in and wash-out period with limited or targeted coverage, and single CT scans that covered the whole thorax are performed at the end of the wash-in and washout periods. Chae et al. (Chae et al. 2008) performed a dynamic examination using xenon ventilation DECT in the limited area of the lung and analyzed the DECT data with a single-compartment model based on the Kety model, which assumes that the

xenon wash-in rate is equal to the xenon wash-out rate. This study showed the diseased lung areas showed the different dynamics of wash-out as well as wash-in xenon curves compared with the normal lung areas, showing an irregular delayed and redistributed pattern. As the different ventilation dynamics can be assessed depending upon the scanning protocols, it is crucial to determine the physiologic question to be evaluated in implementing a DECT imaging protocol using xenon or krypton gases. The appropriate protocols to assess regional ventilation change remain an important topic for further investigation.

2.1.3 Postprocessing

The image reconstruction system provides low- and high-kVp images and weighted average images from the acquired data from both detectors. The weighted average images integrate both low- and high-kVp data in a certain proportion for diagnostic and morphologic assessment, and the proportion of data from both acquisitions can be adjusted using dedicated postprocessing software. Usually, 30% image information from 80-kVp series and 70% from 140-kVp series are used to get an average weighted series corresponding to a 120-kVp image, and 50% for each 140- and 100-kVp images.

For the generation of ventilation maps, the dedicated dual-energy postprocessing software (Syngo Dual-Energy software; Siemens Healthcare) analyzes the density values in the corresponding low- and high-kVp separate series using a three-material decomposition algorithm for air, soft tissue, and xenon. By which, xenon can be differentiated from other materials in the lung such as air and soft tissue, and the distribution of xenon within lung parenchyma is displayed with color-coded map. The preset material parameters for xenon extraction are set to -1000 HU for air at both photon energies, $60/56$ HU at $80/100$ kVp and $54/52$ HU at $140/\text{Sn}140$ kVp for soft tissue, minimum value, -960 HU; and maximum value, -600 HU, a slope of 2.00 for $140/80$ kVp or 2.18 for $100/\text{Sn}140$ kVp. These parameters are based on the empirical observation of dual-energy scans.

2.2 Clinical Applications

2.2.1 Chronic Obstructive Pulmonary Disease

Chronic Obstructive Pulmonary Disease (COPD) is characterized by airflow limitation that is caused by airway obstruction due to persistent inflammation and emphysematous alveolar destruction (Hogg et al. 2004; Mead et al. 1967). The diagnosis of COPD is based on clinical symptoms and the results of pulmonary function test (PFT), and the severity of COPD is also graded on the basis of the results of PFT. Although obviously useful, PFT provides a global measure of lung function inferred from primary structural and functional alterations in the lung and does not demonstrate the regional distribution of structural and functional abnormalities. Conventional CT scan is also widely used in COPD patients to assess the regional distribution of low attenuation areas, but when assessed as a single full inspiratory scan, it is limited because it provides only structural information of the lung parenchyma and airways. With the introduction of a dual-energy CT technique, which can provide high-resolution anatomic information and functional information such as parenchymal ventilation, concurrently, many investigators have tried to evaluate pulmonary ventilation in COPD patients as well as structural changes using DECT (Fig. 5).

Chae et al. reported the first clinical study with xenon ventilation imaging using DECT in four patients with lung disease including COPD and eight healthy volunteers (Chae et al. 2008). The study has reported the heterogeneous xenon enhancement of the lung parenchyma in a patient with COPD. Park et al. performed two-phase (wash-in and wash-out phase) xenon ventilation imaging with DECT in 32 COPD patients. This study has shown that regionally quantified value of xenon enhancement in low attenuating lung areas on wash-in and wash-out phases showed inverse correlation with PFT results, and the xenon value of low attenuating lung areas on wash-out phase (suggesting abnormal xenon retention in a diseased lung) showed a better correlation with FEV_1 than CT density based quanti-

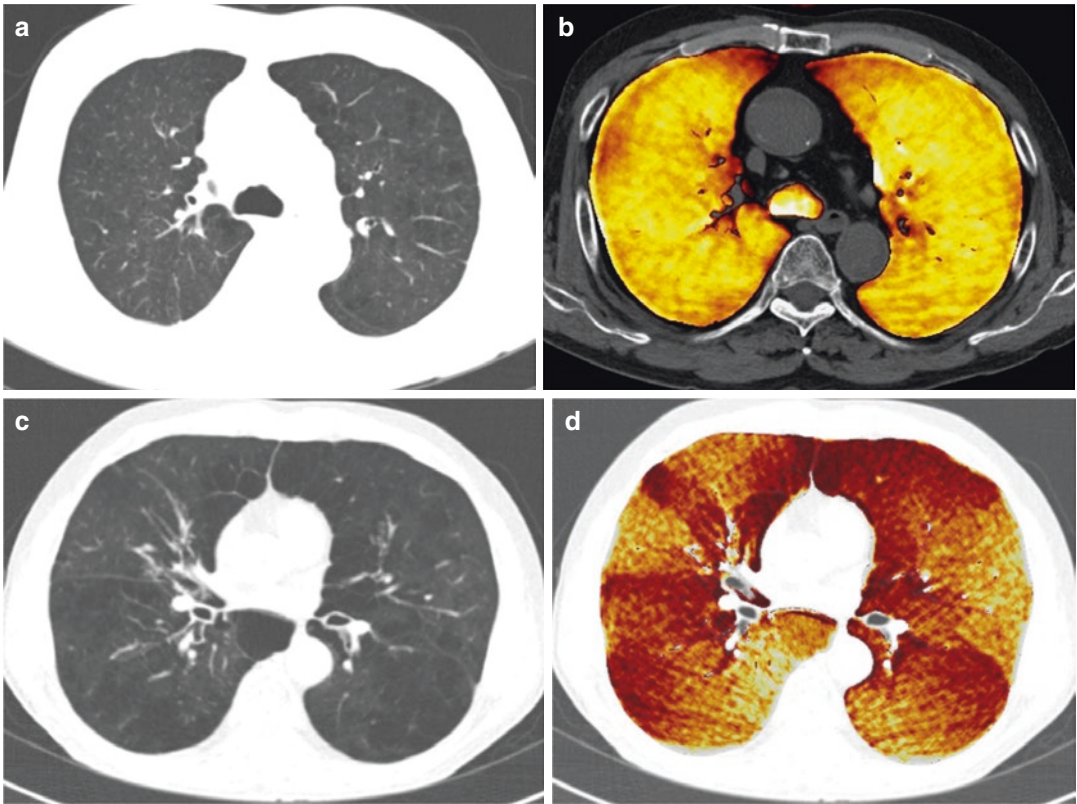


Fig. 5 Xenon ventilation DECTs in a patient with COPD in 66-year-old male with mild emphysema (a, b) and 58-year-old male with moderate to severe emphysema (c, d). (a) Xenon ventilation DECT shows mild centrilobular emphysema on axial VNC image and (b) homogeneous xenon enhancement throughout both upper lobes but

slightly decreased xenon enhancement at the periphery on xenon ventilation map. (c) Axial VNC image shows severe emphysema with diffuse bronchial wall thickening in both lungs. (d) On the xenon ventilation map, multifocal areas with decreased xenon enhancement are identified in both lungs

fication of emphysema severity (Park et al. 2010). The authors categorized the lung ventilation abnormalities on two-phase xenon imaging into four patterns. Visual analysis showed the areas with emphysema exhibited iso-attenuation or high attenuation in both wash-in and the wash-out phase, while the areas with predominant airway disease showed low attenuation during the wash-in period and various attenuation during the wash-out period. Thus, this categorization correlated well with conventional CT imaging findings for the components of COPD. Lee et al. also performed two-phase (wash-in inspiration CT and wash-out expiration CT) xenon ventilation DECT in 52 COPD patients (Lee et al. 2017a). The authors compared between the xenon dynamic of wash-in and wash-out phase xenon ventilation

CTs and the parenchymal attenuation changes between inspiration/expiration CTs.

Hachulla et al. have performed ventilation DECT imaging using krypton gas in COPD patients. The maximum level of krypton enhancement in the lung parenchyma was 18.5 HU. This value is lower than that reported with xenon gas, with an average maximum degree of xenon enhancement of 23.78 HU; however, it is sufficient to visualize ventilation abnormalities, with significant differences of krypton attenuation between the normal and emphysematous lungs (Hachulla et al. 2012).

2.2.2 Asthma

Asthma is characterized by a reversible airway obstructive disease with increased airway hyper-

responsiveness and chronic airway inflammation (ATS Board of Directors 1987). The clinical diagnosis of bronchial asthma is mainly based on clinical symptoms and pulmonary function test results. Conventional CT imaging can show the parenchymal changes including bronchial wall thickening, varying degrees of air trapping, and airway mucus (Lee et al. 2004; Svenningsen et al. 2019), however, clinically, CT has been mainly used to evaluate the complications and associated conditions in patients with asthma.

In the study by Chae et al., xenon ventilation imaging with DECT has shown the ventilation defects in the mid to lower lung periphery, usually pleural based, frequently wedge-shaped, and varied in size from tiny to segment in asthma patients (Chae et al. 2010b). The configuration and location of the ventilation defects on xenon ventilation DECT were similar to the description of ventilation defects on ^3He -MR studies (Altes et al. 2001; de Lange et al. 2006). In this study, ventilation defect scores are also correlated with PFT results, including FEV₁/forced vital capacity (FVC), total lung capacity, functional residual volume, and residual volume. Xenon ventilation DECT can also provide the changes in airflow dynamic in response to inhalation drugs such as methacholine or salbutamol in asthma patients. In several studies, xenon ventilation DECT has demonstrated the changes in xenon ventilation map, including compensatory hyperventilation which occurred adjacent to the ventilation defects after methacholine inhalation and improved regional ventilation defects after inhalation of bronchodilator in asthma patients (Goo and Yu 2011; Kim et al. 2012). Also, in the study by Jung et al., the authors evaluated the change in airflow dynamics after inhalation of methacholine and salbutamol in 43 non-smoking asthmatics (Jung et al. 2013). This study showed that xenon trapings in the wash-out phase after salbutamol inhalation were correlated with various clinical symptoms including the asthma control test scores, wheezing, or night symptoms; whereas FEV₁ showed no significant correlation with asthma symptoms. The degrees of ventilation defects were also positively correlated with FEV₁ improvement after 3 months of treatment. These

findings suggested that ventilation abnormalities assessed using xenon-enhanced DECT may be used as novel parameters that reflect the asthma status and predict therapeutic responses.

2.2.3 Other Ventilation Related Diseases: Asthma-COPD Overlap Syndrome, Bronchiolitis Obliterans

Xenon ventilation DECT may be applicable to other obstructive airway diseases such as asthma-COPD overlap syndrome (ACOS) and bronchiolitis obliterans (BO). Although asthma and COPD have characteristic features, they share similar physiologic and clinical features (Gibson and Simpson 2009; Hardin et al. 2014; Zeki et al. 2011). Thus, the phenotype that shows persistent airflow limitation with several features of both asthma and COPD is referred to as ACOS (Hwang et al. 2020). In 2017, the American Thoracic Society and the National Heart, Lung, and Blood Institute published a joint workshop report on asthma-COPD overlap (Woodruff et al. 2017). Hwang et al. have evaluated the regional ventilation status in twenty-one ACOS patients using xenon ventilation DECT, and to compare it to that in COPD patients (Hwang et al. 2020). In this study, most patients with ACOS showed the peripheral wedge/diffuse defect on xenon maps, which is frequently seen on various ventilation images performed in asthmatics, whereas patients with COPD commonly showed the diffuse heterogeneous defect or lobar/segmental/subsegmental defect (Fig. 6). The airway wall thickening (Pi10) and severity of emphysema (emphysema index) were also quantified on virtual non-contrast (VNC) images of xenon ventilation DECT, and the measured Pi10 was significantly higher in ACOS patients than in COPD patients, while emphysema index was not significantly different between two group. Xenon ventilation DECT may demonstrate the difference in the physiologic change of ventilation in ACOS patients compared to COPD patients.

Bronchiolitis obliterans (BO) is a chronic obstructive lung disease following an injury to the small airways due to various etiologies including lower respiratory infection, organ

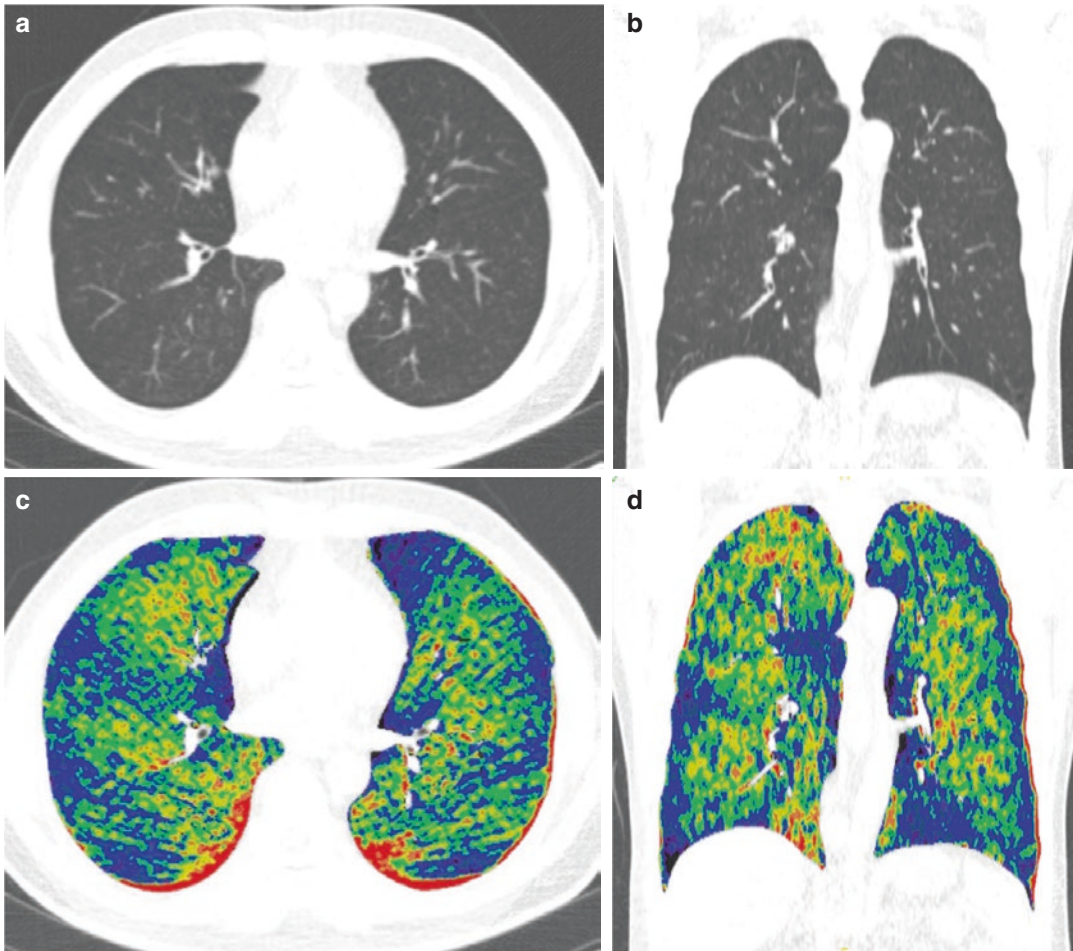


Fig. 6 Xenon ventilation DECT in a 54-year-old man with ACOS. (a, b) Axial and coronal VNC images of DECT show diffuse bronchial wall thickening with minimal centrilobular emphysema. (c, d) Axial and coronal

xenon ventilation maps show multifocal wedge-shaped or patchy areas showing blue-to-purple color in peripheral lung areas, indicating ventilation defects

transplantation, and others. BO is usually diagnosed based on the typical clinical presentation, the finding of fixed airway obstruction in pulmonary function tests, and characteristic CT findings. Conventional CT image is quite sensitive and specific in the evaluation of BO, showing characteristic CT findings including bronchial wall thickening, central bronchiectasis, centrilobular opacities, and mosaic parenchymal attenuation due to air trapping. However, for the comprehensive and accurate evaluation of BO, paired inspiratory and expiratory chest CT scans may be required, and such paired CT examina-

tions would increase the radiation exposure. Goo et al. performed xenon ventilation DECT in 17 children with BO (Goo et al. 2010). They demonstrated heterogeneously impaired ventilation in lung regions with BO on xenon ventilation map. Additionally, measured xenon and CT density values showed a positive correlation for the whole lung and the hyperlucent regions. The indexed volumes and volume percentages of hyperlucent areas and xenon ventilation defects have shown correlation with PFTs, including FEV₁, FEV₁/FVC, and forced mid expiratory flow rate. Thus, xenon-enhanced DECT can help

identify regional ventilation defects as well as morphologic abnormalities of BO without additional radiation exposure.

3 Comprehensive Assessment of Morphology, Pulmonary Ventilation, Perfusion, and Relationship of Ventilation and Perfusion Using Dual-Energy CT

3.1 Concept

With the introduction of DECT, pulmonary parenchymal perfusion and ventilation impairment have been evaluated independently with DECT in various lung diseases. However, pulmonary ventilation and perfusion often change concurrently, and both ventilation and perfusion are crucial for efficient gas exchange. Combined ventilation–perfusion DECT can provide comprehensive information of regional ventilation, perfusion, and ventilation–perfusion relationship as well as high-resolution anatomic information in various pulmonary diseases.

Based on our own experience and the results previously reported by Thieme et al., combined xenon ventilation and perfusion DECT can be successfully performed using the dual-source CT scanners (Somatom Definition scanner and Somatom Definition FLASH, Siemens Healthcare, Forchheim, Germany) (Hwang et al. 2016, 2019; Lee et al. 2017b; Thieme et al. 2010). For evaluating both ventilation and perfusion using DECT, the xenon ventilation DECT is performed, followed by iodine-contrast perfusion DECT. After xenon ventilation DECT and before perfusion DECT, patients should inhale room air for more than 10 min to wash out xenon gas. Because xenon is moderately soluble, the question may arise about whether vascular uptake and redistribution back to the lung of inhaled xenon may affect the background level lung density of pulmonary PBV map. However, Hoag et al. have been demonstrated with the unilateral ventilation of xenon in intubated canines that the redistribution of inhaled xenon via the circulation is negli-

gible and does not warrant correction (Hoag et al. 2007). Then, for evaluating the ventilation–perfusion relationship, registration of VNC image of perfusion CT to VNC image of ventilation CT is performed, and with this information ventilation, map, registered perfusion map, and then ventilation/perfusion ratio (V/Qratio) map area are generated (Fig. 7).

Recently, Sauter et al. have tried to simultaneously evaluate pulmonary ventilation and perfusion during a single CT scan in an animal model using three-material differentiation in a dual-layer CT scan (IQon Spectral CT, Philips Healthcare, Netherlands) (Sauter et al. 2019).

3.2 Clinical Application: Pulmonary Embolism, COPD

There are few studies on the clinical application of combined ventilation and perfusion imaging with DECT. Thieme et al. have reported the potential of DECT to provide both pulmonary ventilation and perfusion imaging by investigating ten patients with various diseases (e.g., lung transplantation, acute respiratory distress syndrome, aortic dissection, gastric cancer) from an anesthesiological intensive care unit (Thieme et al. 2010). Zhang et al. have applied this examination in patients with suspected pulmonary embolism (Zhang et al. 2013). In that study, ventilation and PBV maps have shown the ventilation–perfusion mismatch in most areas with pulmonary embolism, and the authors hypothesized that the combined ventilation and perfusion DECT might provide higher sensitivity for detecting peripheral pulmonary embolism compared to conventional CT pulmonary angiography.

In COPD patients, the imbalances between alveolar ventilation and pulmonary blood flow are the critical features that result in arterial hypoxemia. Thus, combined ventilation–perfusion DECT has the potential for the evaluation of ventilation–perfusion imbalances as well as morphologic changes in COPD patients. Hwang et al. have applied the combined xenon ventilation and iodine perfusion DECT in 52 COPD patients

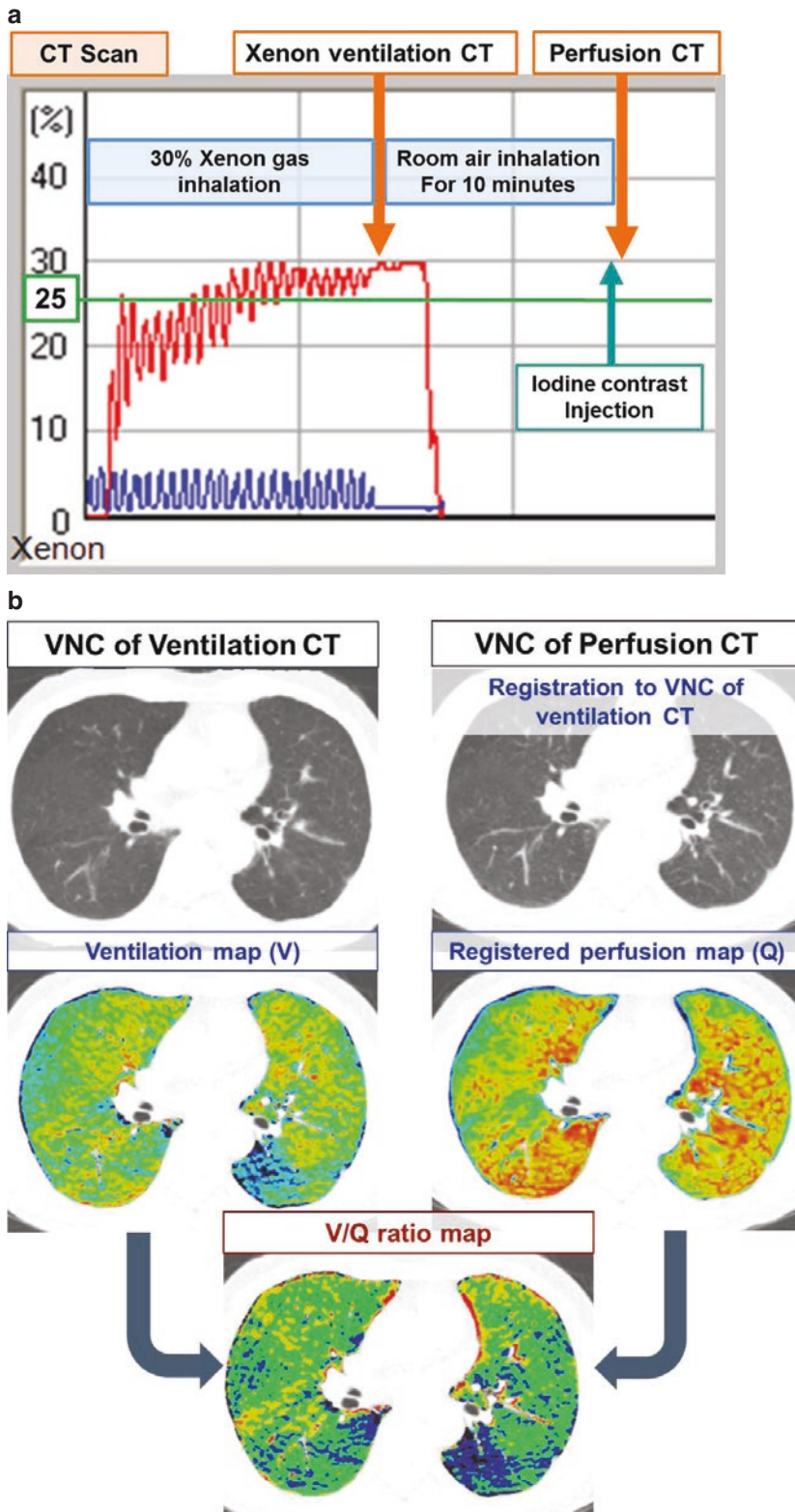


Fig. 7 The graph shows the CT scanning protocol for combined xenon ventilation and contrast-enhanced perfusion DECT. (a) Red and blue curves denote tidal xenon and CO₂ concentrations in the exhaled gas, respectively.

(b) From ventilation and coregistered perfusion maps, a coregistered ventilation/perfusion ratio map is generated for evaluating the ventilation–perfusion relationship

(Hwang et al. 2016). In this study, ventilation, perfusion, and ventilation/perfusion maps and VNC images were used for the visual analysis of regional ventilation, perfusion, and ventilation–perfusion relationships along with the morphologic evaluation in COPD patients. On visual analysis, in the normal appearing lung areas on VNC images, parenchymal ventilation and perfusion were preserved, resulting in a matched ventilation–perfusion relationship. However, in the areas of bronchial wall thickening, ventilation was often decreased while perfusion was preserved, resulting in a ventilation–perfusion mismatch (reversed mismatch). In areas with emphysema, there were no dominant ventilation or perfusion patterns. Furthermore, quantified DECT parameters for ventilation, perfusion, and ventilation–perfusion relationships are significantly correlated with PFT results. Using this combined DECT imaging, the functional and physiologic changes after bronchoscopic lung volume reduction in COPD patients have been demonstrated. In 30 COPD patients who under-

went bronchoscopic lung volume reduction, DECT showed improved pulmonary ventilation and ventilation–perfusion mismatch after bronchoscopic lung volume reduction (Lee et al. 2017b). This combined DECT imaging has also demonstrated change in the functional changes after pharmacologic treatment in COPD patients (Hwang et al. 2019). In this study, 52 COPD patients underwent combined ventilation and perfusion DECT in the baseline and after 3 months of pharmacologic treatment. The combined DECT analysis showed improved ventilation–perfusion imbalance after the pharmacological treatment in COPD patients, although the parenchymal disease patterns remained unchanged (Fig. 8). This comprehensive evaluation of parenchymal destruction and regional ventilation–perfusion relationships using DECT in COPD patients may provide useful information to the clinician, such as for the assessment of response to medical treatment or the target lobe selection for lung volume reduction treatment.

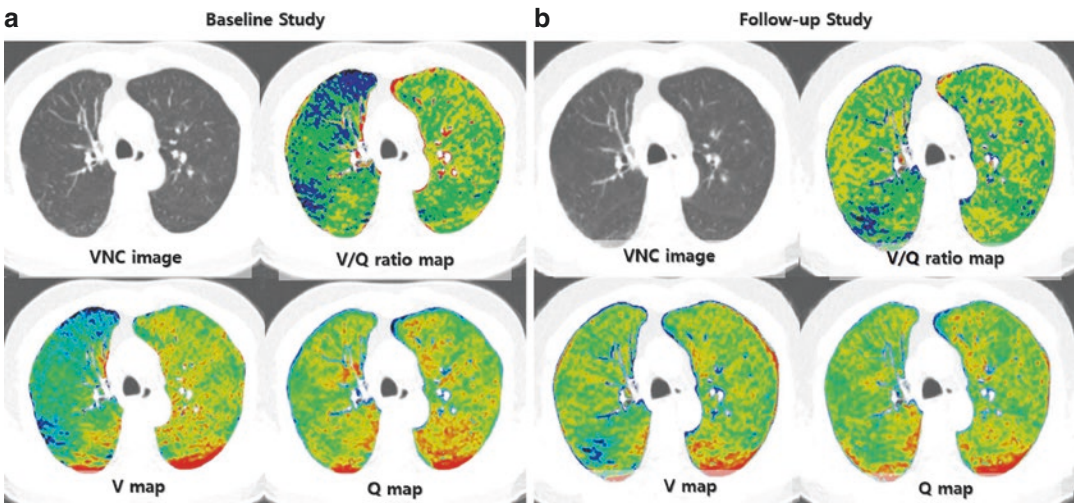


Fig. 8 A 63-year-old male COPD patient. On a VNC image of xenon ventilation CT, minimal centrilobular emphysema and bronchial wall thickening are notable in both upper lobes. (a) On baseline study, multifocal patchy decreased ventilation is noted in the right upper lobe, while perfusion is preserved, resulting in the reversed mismatched V/Q on the V/Qratio map. (b) After 3 months of medical treatment, ventilation is improved on follow-

up studies, resulting in the matched V/Q pattern on the V/Qratio map in most areas of the right upper lobe. In the posterior segment of the right upper lobe, ventilation remained decreased on ventilation map, while perfusion is preserved, resulting in the persistent reversed mismatched V/Q on the V/Qratio map. In this patient, the percent predicted FEV₁ increased by 20%

4 Perspective and Conclusion

Ventilation or perfusion imaging using DECT is a novel technique for perfusion and ventilation assessment of various pulmonary diseases along with morphologic assessment with high-resolution CT information without additional radiation exposure. DECT analysis can help us diagnose disease, assess disease severity more accurately, and understand unrevealed pathophysiologies related to lung function in various lung diseases. However, there is still insufficient evidence that DECT analysis can add clinically valuable information in addition to anatomic information, change the treatment plans, and predict therapeutic response or prognosis. Therefore, further research will be needed to solidify the evidence of the values and roles of DECT imaging methods for improved diagnosis and outcomes assessment in diseases associated with the lung function alteration. More investigations will also be needed to establish appropriate imaging protocols that can be applied to a clinical diagnostic work-up. With the continued development of image acquisition protocols, post-processing techniques, and scanner designs, DECT will be applied widely to assessing various lung diseases in clinical practices and research.

Compliance with Ethical Standards

Funding None.

Disclosure of Interests All authors declare they have no conflict of interest.

Studies involving human

Ethical Approval This article does not contain any specific studies with human participants performed by any of the authors.

Informed Consent Informed consent was not needed for this chapter.

References

Alford SK, van Beek EJ, McLennan G, Hoffman EA (2010) Heterogeneity of pulmonary perfusion as a mechanistic image-based phenotype in emphy-

- sema susceptible smokers. *Proc Natl Acad Sci U S A* 107(16):7485–7490. <https://doi.org/10.1073/pnas.0913880107>
- Altes TA, Powers PL, Knight-Scott J, Rakes G, Platts-Mills TA, de Lange EE, Alford BA, Mugler JP, Brookeman JR (2001) Hyperpolarized ^3He MR lung ventilation imaging in asthmatics: preliminary findings. *J Magn Reson Imaging* 13(3):378–384. <https://doi.org/10.1002/jmri.1054>
- Ameli-Renani S, Ramsay L, Bacon JL, Rahman F, Nair A, Smith V, Baskerville K, Devaraj A, Madden B, Vlahos I (2014) Dual-energy computed tomography in the assessment of vascular and parenchymal enhancement in suspected pulmonary hypertension. *J Thorac Imaging* 29(2):98–106. <https://doi.org/10.1097/RTI.0000000000000061>
- ATS Board of Directors (1987) Standards for the diagnosis and care of patients with chronic obstructive pulmonary disease (COPD) and asthma. *Am Rev Respir Dis* 136(1):225–244. <https://doi.org/10.1164/ajrccm/136.1.225>
- Barbera JA, Peinado VI, Santos S (2003) Pulmonary hypertension in chronic obstructive pulmonary disease. *Eur Respir J* 21(5):892–905. <https://doi.org/10.1183/09031936.03.00115402>
- Baxa J, Vondrakova A, Matouskova T, Ruzickova O, Schmidt B, Flohr T, Sedlmair M, Ferda J (2014) Dual-phase dual-energy CT in patients with lung cancer: assessment of the additional value of iodine quantification in lymph node therapy response. *Eur Radiol* 24(8):1981–1988. <https://doi.org/10.1007/s00330-014-3223-9>
- Baxa J, Matouskova T, Krakorova G, Schmidt B, Flohr T, Sedlmair M, Bejcek J, Ferda J (2016) Dual-phase dual-energy CT in patients treated with erlotinib for advanced non-small cell lung cancer: possible benefits of iodine quantification in response assessment. *Eur Radiol* 26(8):2828–2836. <https://doi.org/10.1007/s00330-015-4092-6>
- Bedi A, McCarroll C, Murray JM, Stevenson MA, Fee JP (2002) The effects of subanaesthetic concentrations of xenon in volunteers. *Anaesthesia* 57(3):233–241. <https://doi.org/10.1046/j.0003-2409.2001.02455.x>
- Brunelli A, Fianchini A (1997) Predicted postoperative FEV1 and complications in lung resection candidates. *Chest* 111(4):1145–1146. <https://doi.org/10.1378/chest.111.4.1145>
- Chae EJ, Seo JB, Goo HW, Kim N, Song KS, Lee SD, Hong SJ, Krauss B (2008) Xenon ventilation CT with a dual-energy technique of dual-source CT: initial experience. *Radiology* 248(2):615–624. <https://doi.org/10.1148/radiol.2482071482>
- Chae EJ, Seo JB, Jang YM, Krauss B, Lee CW, Lee HJ, Song KS (2010a) Dual-energy CT for assessment of the severity of acute pulmonary embolism: pulmonary perfusion defect score compared with CT angiographic obstruction score and right ventricular/left ventricular diameter ratio. *AJR Am J Roentgenol* 194(3):604–610. <https://doi.org/10.2214/AJR.09.2681>
- Chae EJ, Seo JB, Lee J, Kim N, Goo HW, Lee HJ, Lee CW, Ra SW, Oh YM, Cho YS (2010b) Xenon venti-

- lation imaging using dual-energy computed tomography in asthmatics: initial experience. *Investig Radiol* 45(6):354–361. <https://doi.org/10.1097/RLI.0b013e3181dfdae0>
- Chae EJ, Kim N, Seo JB, Park JY, Song JW, Lee HJ, Hwang HJ, Lim C, Chang YJ, Kim YH (2013) Prediction of postoperative lung function in patients undergoing lung resection: dual-energy perfusion computed tomography versus perfusion scintigraphy. *Invest Radiol* 48(8):622–627.
- Chon D, Beck KC, Simon BA, Shikata H, Saba OI, Hoffman EA (1985) Effect of low-xenon and krypton supplementation on signal/noise of regional CT-based ventilation measurements. *J Appl Physiol* 102(4):1535–1544. <https://doi.org/10.1152/jappphysiol.01235.2005>
- Chung YE, Hong SR, Lee MJ, Lee M, Lee HJ (2014) Krypton-enhanced ventilation CT with dual energy technique: experimental study for optimal krypton concentration. *Exp Lung Res* 40(9):439–446. <https://doi.org/10.3109/01902148.2014.946630>
- de Lange EE, Altes TA, Patrie JT, Gaare JD, Knake JJ, Mugler JP, Platts-Mills TA (2006) Evaluation of asthma with hyperpolarized helium-3 MRI: correlation with clinical severity and spirometry. *Chest* 130(4):1055–1062. <https://doi.org/10.1378/chest.130.4.1055>
- Gibson PG, Simpson JL (2009) The overlap syndrome of asthma and COPD: what are its features and how important is it? *Thorax* 64(8):728–735. <https://doi.org/10.1136/thx.2008.108027>
- Goo HW, Yu J (2011) Redistributed regional ventilation after the administration of a bronchodilator demonstrated on xenon-inhaled dual-energy CT in a patient with asthma. *Korean J Radiol* 12(3):386–389. <https://doi.org/10.3348/kjr.2011.12.3.386>
- Goo HW, Chae EJ, Seo JB, Hong SJ (2008) Xenon ventilation CT using a dual-source dual-energy technique: dynamic ventilation abnormality in a child with bronchial atresia. *Pediatr Radiol* 38(10):1113–1116. <https://doi.org/10.1007/s00247-008-0914-x>
- Goo HW, Yang DH, Hong SJ, Yu J, Kim BJ, Seo JB, Chae EJ, Lee J, Krauss B (2010) Xenon ventilation CT using dual-source and dual-energy technique in children with bronchiolitis obliterans: correlation of xenon and CT density values with pulmonary function test results. *Pediatr Radiol* 40(9):1490–1497. <https://doi.org/10.1007/s00247-010-1645-3>
- Gorgos A, Remy-Jardin M, Duhamel A, Faivre JB, Tacelli N, Delannoy V, Remy J (2009) Evaluation of peripheral pulmonary arteries at 80 kV and at 140 kV: dual-energy computed tomography assessment in 51 patients. *J Comput Assist Tomogr* 33(6):981–986. <https://doi.org/10.1097/RCT.0b013e3181a5cd0f>
- Gur D, Drayer BP, Borovetz HS, Griffith BP, Hardesty RL, Wolfson SK (1979) Dynamic computed tomography of the lung: regional ventilation measurements. *J Comput Assist Tomogr* 3(6):749–753
- Hachulla AL, Pontana F, Wemeau-Stervinou L, Khung S, Faivre JB, Wallaert B, Cazaubon JF, Duhamel A, Perez T, Devos P, Remy J, Remy-Jardin M (2012) Krypton ventilation imaging using dual-energy CT in chronic obstructive pulmonary disease patients: initial experience. *Radiology* 263(1):253–259. <https://doi.org/10.1148/radiol.12111211>
- Hardin M, Cho M, McDonald ML, Beatty T, Ramsdell J, Bhatt S, van Beek EJ, Make BJ, Crapo JD, Silverman EK, Hersh CP (2014) The clinical and genetic features of COPD-asthma overlap syndrome. *Eur Respir J* 44(2):341–350. <https://doi.org/10.1183/09031936.00216013>
- Herbert DL, Gur D, Shabason L, Good WF, Rinaldo JE, Snyder JV, Borovetz HS, Mancini MC (1982) Mapping of human local pulmonary ventilation by xenon enhanced computed tomography. *J Comput Assist Tomogr* 6(6):1088–1093. <https://doi.org/10.1097/00004728-198212000-00006>
- Hoag JB, Fuld M, Brown RH, Simon BA (2007) Recirculation of inhaled xenon does not alter lung CT density. *Acad Radiol* 14(1):81–84. <https://doi.org/10.1016/j.acra.2006.10.012>
- Hogg JC, Chu F, Utokaparch S, Woods R, Elliott WM, Buzatu L, Cherniack RM, Rogers RM, Sciurba FC, Coxson HO, Pare PD (2004) The nature of small-airway obstruction in chronic obstructive pulmonary disease. *N Engl J Med* 350(26):2645–2653. <https://doi.org/10.1056/NEJMoa032158>
- Honda N, Osada H, Watanabe W, Nakayama M, Nishimura K, Krauss B, Otani K (2012) Imaging of ventilation with dual-energy CT during breath hold after single vital-capacity inspiration of stable xenon. *Radiology* 262(1):262–268. <https://doi.org/10.1148/radiol.11110569>
- Hong YJ, Kim JY, Choe KO, Hur J, Lee HJ, Choi BW, Kim YJ (2013) Different perfusion pattern between acute and chronic pulmonary thromboembolism: evaluation with two-phase dual-energy perfusion CT. *AJR Am J Roentgenol* 200(4):812–817. <https://doi.org/10.2214/AJR.12.8697>
- Hong SR, Chang S, Im DJ, Suh YJ, Hong YJ, Hur J, Kim YJ, Choi BW, Lee HJ (2016) Feasibility of single scan for simultaneous evaluation of regional Krypton and iodine concentrations with dual-energy CT: an experimental study. *Radiology* 281(2):597–605. <https://doi.org/10.1148/radiol.16152429>
- Hwang HJ, Seo JB, Lee SM, Kim N, Oh SY, Lee JS, Lee SW, Oh YM (2016) Assessment of regional xenon ventilation, perfusion, and ventilation-perfusion mismatch using dual-energy computed tomography in chronic obstructive pulmonary disease patients. *Investig Radiol* 51(5):306–315. <https://doi.org/10.1097/RLI.0000000000000239>
- Hwang HJ, Hoffman EA, Lee CH, Goo JM, Levin DL, Kauczor HU, Seo JB (2017) The role of dual-energy computed tomography in the assessment of pulmonary function. *Eur J Radiol* 86:320–334. <https://doi.org/10.1016/j.ejrad.2016.11.010>
- Hwang HJ, Lee SM, Seo JB, Lee JS, Kim N, Kim C, Oh SY, Lee SW (2019) Assessment of changes in regional xenon-ventilation, perfusion, and ventilation-perfusion mismatch using dual-energy computed tomography

- after pharmacological treatment in patients with chronic obstructive pulmonary disease: visual and quantitative analysis. *Int J Chron Obstruct Pulmon Dis* 14:2195–2203. <https://doi.org/10.2147/COPD.S210555>
- Hwang HJ, Lee SM, Seo JB, Lee JS, Kim N, Lee SW, Oh YM (2020) Visual and quantitative assessments of regional xenon-ventilation using dual-energy CT in asthma-chronic obstructive pulmonary disease overlap syndrome: a comparison with chronic obstructive pulmonary disease. *Korean J Radiol* 21(9):1104–1113. <https://doi.org/10.3348/kjr.2019.0936>
- Iyer KS, Newell JD Jr, Jin D, Fuld MK, Saha PK, Hansdottir S, Hoffman EA (2016) Quantitative dual-energy computed tomography supports a vascular etiology of smoking-induced inflammatory lung disease. *Am J Respir Crit Care Med* 193(6):652–661. <https://doi.org/10.1164/rccm.201506-1196OC>
- Jung JW, Kwon JW, Kim TW, Lee SH, Kim KM, Kang HR, Park HW, Lee CH, Goo JM, Min KU, Cho SH (2013) New insight into the assessment of asthma using xenon ventilation computed tomography. *Ann Allergy Asthma Immunol* 111(2):90–95. <https://doi.org/10.1016/j.anai.2013.04.019>
- Kim WW, Lee CH, Goo JM, Park SJ, Kim JH, Park EA, Cho SH (2012) Xenon-enhanced dual-energy CT of patients with asthma: dynamic ventilation changes after methacholine and salbutamol inhalation. *AJR Am J Roentgenol* 199(5):975–981. <https://doi.org/10.2214/AJR.11.7624>
- Kyoyama H, Hirata Y, Kikuchi S, Sakai K, Saito Y, Mikami S, Moriyama G, Yanagita H, Watanabe W, Otani K, Honda N, Uematsu K (2017) Evaluation of pulmonary function using single-breath-hold dual-energy computed tomography with xenon: Results of a preliminary study. *Medicine* 96(3):e5937. <https://doi.org/10.1097/MD.0000000000005937>
- Latchaw RE, Yonas H, Pentheny SL, Gur D (1987) Adverse reactions to xenon-enhanced CT cerebral blood flow determination. *Radiology* 163(1):251–254. <https://doi.org/10.1148/radiology.163.1.3823444>
- Lee YM, Park JS, Hwang JH, Park SW, Uh ST, Kim YH, Park CS (2004) High-resolution CT findings in patients with near-fatal asthma: comparison of patients with mild-to-severe asthma and normal control subjects and changes in airway abnormalities following steroid treatment. *Chest* 126(6):1840–1848. <https://doi.org/10.1378/chest.126.6.1840>
- Lee CW, Seo JB, Song JW, Kim MY, Lee HY, Park YS, Chae EJ, Jang YM, Kim N, Krauss B (2011) Evaluation of computer-aided detection and dual energy software in detection of peripheral pulmonary embolism on dual-energy pulmonary CT angiography. *Eur Radiol* 21(1):54–62. <https://doi.org/10.1007/s00330-010-1903-7>
- Lee CW, Seo JB, Lee Y, Chae EJ, Kim N, Lee HJ, Hwang HJ, Lim CH (2012) A pilot trial on pulmonary emphysema quantification and perfusion mapping in a single-step using contrast-enhanced dual-energy computed tomography. *Investig Radiol* 47(1):92–97. <https://doi.org/10.1097/RLI.0b013e318228359a>
- Lee SM, Seo JB, Hwang HJ, Kim N, Oh SY, Lee JS, Lee SW, Oh YM, Kim TH (2017a) Assessment of regional emphysema, air-trapping and Xenon-ventilation using dual-energy computed tomography in chronic obstructive pulmonary disease patients. *Eur Radiol* 27(7):2818–2827. <https://doi.org/10.1007/s00330-016-4657-z>
- Lee SW, Lee SM, Shin SY, Park TS, Oh SY, Kim N, Hong Y, Lee JS, Oh YM, Lee SD, Seo JB (2017b) Improvement in ventilation-perfusion mismatch after bronchoscopic lung volume reduction: quantitative image analysis. *Radiology* 285(1):250–260. <https://doi.org/10.1148/radiol.2017162148>
- Mead J, Turner JM, Macklem PT, Little JB (1967) Significance of the relationship between lung recoil and maximum expiratory flow. *J Appl Physiol* 22(1):95–108. <https://doi.org/10.1152/jappl.1967.22.1.95>
- Meinel FG, Graef A, Bamberg F, Thieme SF, Schwarz F, Sommer WH, Neurohr C, Kupatt C, Reiser MF, Johnson TR (2013a) Effectiveness of automated quantification of pulmonary perfused blood volume using dual-energy CTPA for the severity assessment of acute pulmonary embolism. *Investig Radiol* 48(8):563–569. <https://doi.org/10.1097/RLI.0b013e3182879482>
- Meinel FG, Graef A, Thieme SF, Bamberg F, Schwarz F, Sommer WH, Helck AD, Neurohr C, Reiser MF, Johnson TR (2013b) Assessing pulmonary perfusion in emphysema: automated quantification of perfused blood volume in dual-energy CTPA. *Investig Radiol* 48(2):79–85. <https://doi.org/10.1097/RLI.0b013e3182778f07>
- Moon JW, Bae JP, Lee HY, Kim N, Chung MP, Park HY, Chang Y, Seo JB, Lee KS (2016) Perfusion- and pattern-based quantitative CT indexes using contrast-enhanced dual-energy computed tomography in diffuse interstitial lung disease: relationships with physiologic impairment and prediction of prognosis. *Eur Radiol* 26(5):1368–1377. <https://doi.org/10.1007/s00330-015-3946-2>
- Murphy DM, Nicewicz JT, Zabbatino SM, Moore RA (1989) Local pulmonary ventilation using nonradioactive xenon-enhanced ultrafast computed tomography. *Chest* 96(4):799–804. <https://doi.org/10.1378/chest.96.4.799>
- Okada M, Kunihiro Y, Nakashima Y, Nomura T, Kudomi S, Yonezawa T, Suga K, Matsunaga N (2015) Added value of lung perfused blood volume images using dual-energy CT for assessment of acute pulmonary embolism. *Eur J Radiol* 84(1):172–177. <https://doi.org/10.1016/j.ejrad.2014.09.009>
- Pansini V, Remy-Jardin M, Faivre JB, Schmidt B, Dejardin-Bothelo A, Perez T, Delannoy V, Duhamel A, Remy J (2009) Assessment of lobar perfusion in smokers according to the presence and severity of emphysema: preliminary experience with dual-energy CT angiography. *Eur Radiol* 19(12):2834–2843. <https://doi.org/10.1007/s00330-009-1475-6>
- Park EA, Goo JM, Park SJ, Lee HJ, Lee CH, Park CM, Yoo CG, Kim JH (2010) Chronic obstructive pulmonary disease: quantitative and visual ventilation pattern

- analysis at xenon ventilation CT performed by using a dual-energy technique. *Radiology* 256(3):985–997. <https://doi.org/10.1148/radiol.10091502>
- Park TS, Hong Y, Lee JS, Lee SM, Seo JB, Oh YM, Lee SD, Lee SW (2014) Efficacy of bronchoscopic lung volume reduction by endobronchial valves in patients with heterogeneous emphysema: report on the first Asian cases. *J Korean Med Sci* 29(10):1404–1410. <https://doi.org/10.3346/jkms.2014.29.10.1404>
- Pierce RJ, Copland JM, Sharpe K, Barter CE (1994) Preoperative risk evaluation for lung cancer resection: predicted postoperative product as a predictor of surgical mortality. *Am J Respir Crit Care Med* 150(4):947–955. <https://doi.org/10.1164/ajrccm.150.4.7921468>
- Remy-Jardin M, Faivre JB, Pontana F, Hachulla AL, Tacelli N, Santangelo T, Remy J (2010) Thoracic applications of dual energy. *Radiol Clin N Am* 48(1):193–205. <https://doi.org/10.1016/j.rcl.2009.08.013>
- Sakamoto A, Sakamoto I, Nagayama H, Koike H, Sueyoshi E, Uetani M (2014) Quantification of lung perfusion blood volume with dual-energy CT: assessment of the severity of acute pulmonary thromboembolism. *AJR Am J Roentgenol* 203(2):287–291. <https://doi.org/10.2214/AJR.13.11586>
- Sauter AP, Hammel J, Ehn S, Achterhold K, Kopp FK, Kimm MA, Mei K, Laugerette A, Pfeiffer F, Rummeny EJ, Pfeiffer D, Noel PB (2019) Perfusion-ventilation CT via three-material differentiation in dual-layer CT: a feasibility study. *Sci Rep* 9(1):5837. <https://doi.org/10.1038/s41598-019-42330-7>
- Schmid-Bindert G, Henzler T, Chu TQ, Meyer M, Nance JW Jr, Schoepf UJ, Dinter DJ, Apfaltrer P, Krissak R, Manegold C, Schoenberg SO, Fink C (2012) Functional imaging of lung cancer using dual energy CT: how does iodine related attenuation correlate with standardized uptake value of 18FDG-PET-CT? *Eur Radiol* 22(1):93–103. <https://doi.org/10.1007/s00330-011-2230-3>
- Svenningsen S, Haider E, Boylan C, Mukherjee M, Eddy RL, Capaldi DPI, Parraga G, Nair P (2019) CT and functional MRI to evaluate airway mucus in severe asthma. *Chest* 155(6):1178–1189. <https://doi.org/10.1016/j.chest.2019.02.403>
- Thieme SF, Becker CR, Hacker M, Nikolaou K, Reiser MF, Johnson TR (2008) Dual energy CT for the assessment of lung perfusion—correlation to scintigraphy. *Eur J Radiol* 68(3):369–374. <https://doi.org/10.1016/j.ejrad.2008.07.031>
- Thieme SF, Johnson TR, Lee C, McWilliams J, Becker CR, Reiser MF, Nikolaou K (2009) Dual-energy CT for the assessment of contrast material distribution in the pulmonary parenchyma. *AJR Am J Roentgenol* 193(1):144–149. <https://doi.org/10.2214/AJR.08.1653>
- Thieme SF, Hoegl S, Nikolaou K, Fisahn J, Irlbeck M, Maxien D, Reiser MF, Becker CR, Johnson TR (2010) Pulmonary ventilation and perfusion imaging with dual-energy CT. *Eur Radiol* 20(12):2882–2889. <https://doi.org/10.1007/s00330-010-1866-8>
- Thieme SF, Graute V, Nikolaou K, Maxien D, Reiser MF, Hacker M, Johnson TR (2012a) Dual energy CT lung perfusion imaging—correlation with SPECT/CT. *Eur J Radiol* 81(2):360–365. <https://doi.org/10.1016/j.ejrad.2010.11.037>
- Thieme SF, Ashoori N, Bamberg F, Sommer WH, Johnson TR, Leuchte H, Becker A, Maxien D, Helck AD, Behr J, Reiser MF, Nikolaou K (2012b) Severity assessment of pulmonary embolism using dual energy CT—correlation of a pulmonary perfusion defect score with clinical and morphological parameters of blood oxygenation and right ventricular failure. *Eur Radiol* 22(2):269–278. <https://doi.org/10.1007/s00330-011-2267-3>
- Tonner PH (2006) Xenon: one small step for anaesthesia...? *Curr Opin Anaesthesiol* 19(4):382–384. <https://doi.org/10.1097/01.aco.0000236136.85356.13>
- Winkler SS, Holden JE, Sackett JF, Flemming DC, Alexander SC (1977) Xenon and krypton as radiographic inhalation contrast media with computerized tomography: preliminary note. *Investig Radiol* 12(1):19–20. <https://doi.org/10.1097/00004424-197701000-00007>
- Woodruff PG, van den Berge M, Boucher RC, Brightling C, Burchard EG, Christenson SA, Han MK, Holtzman MJ, Kraft M, Lynch DA, Martinez FD, Reddel HK, Sin DD, Washko GR, Wenzel SE, Punterieri A, Freemer MM, Wise RA (2017) *Am J Respir Crit Care Med* 196(3):375–381. <https://doi.org/10.1164/rccm.201705-0973WS>
- Yonas H, Grundy B, Gur D, Shabason L, Wolfson SK Jr, Cook EE (1981) Side effects of xenon inhalation. *J Comput Assist Tomogr* 5(4):591–592. <https://doi.org/10.1097/00004728-198108000-00029>
- Zeki AA, Schivo M, Chan A, Albertson TE, Louie S (2011) The asthma-COPD overlap syndrome: a common clinical problem in the elderly. *J Allergy* 2011:861926. <https://doi.org/10.1155/2011/861926>
- Zhang LJ, Zhou CS, Schoepf UJ, Sheng HX, Wu SY, Krazinski AW, Silverman JR, Meinel FG, Zhao YE, Zhang ZJ, Lu GM (2013) Dual-energy CT lung ventilation/perfusion imaging for diagnosing pulmonary embolism. *Eur Radiol* 23(10):2666–2675. <https://doi.org/10.1007/s00330-013-2907-x>



Thoracic Oncology

Philip Konietzke 

Contents

1	Artifact Reduction and Improved Image Quality	202
1.1	Metal Artifacts	202
1.2	Beam-Hardening Artifacts Due to Contrast Media	202
2	Imaging Pulmonary Nodules	203
2.1	Introduction	203
2.2	Detection of Pulmonary Nodules	204
2.3	Classification of Pulmonary Nodules	204
3	Imaging Lung Cancer	206
3.1	Introduction	206
3.2	Detecting Lung Cancer	206
3.3	Differentiate Lung Cancer and Inflammation	207
3.4	Characterization of Lung Cancer	208
3.5	Staging Lung Cancer	210
4	Therapy Evaluation of Lung Cancer	212
4.1	Introduction	212
4.2	Therapy Response with DECT	212
	References	215

Abstract

In recent years, dual-energy computed tomography (DECT) is increasingly used in routine clinical practice due to technical developments. DECT can provide both material-nonspecific and material-specific energy-dependent information like virtual monoenergetic or mono-

chromatic imaging (VMI), virtual non-contrast or unenhanced imaging (VNC), iodine concentration (IC) measurements, and the effective atomic number (Z_{eff}). In thoracic oncology, these applications might have additional benefits, in the diagnostic and therapy response evaluation of lung cancer, especially in the context with new treatments based on antiangiogenic agents and tyrosine kinase inhibitors. However, besides the problem that DECT parameter values are not uniform across studies, the DECT technique also has some general limitations. First, the use of DECT is limited in

P. Konietzke (✉)
Department of Diagnostic and Interventional
Radiology, University Hospital of Heidelberg,
Heidelberg, Germany
e-mail: Philip.Konietzke@med.uni-heidelberg.de

obese patients because of high image noise often interfering with structural and functional image analysis. Second, larger image datasets require increased data storage capabilities and appropriate adjustment of clinical workflows.

Photon-counting detector computed tomography (PCDCT) is an emerging technology, using energy-resolving X-ray detectors that differ substantially from conventional energy-integrating detectors. The results of initial studies indicate its potentially high impact on lung imaging by correcting for artifacts, having an excellent spatial resolution, reducing radiation exposure, and optimizing the use of contrast agents. However, till a broad use in clinical routines, further research is necessary.

1 Artifact Reduction and Improved Image Quality

1.1 Metal Artifacts

The photon absorption of metal objects leads to prominent metal- and beam-hardening artifacts. In thoracic oncology, these artifacts may hamper tumor delineation when patients have metal objects such as spinal stabilization implants close to the treatment area, causing problems in follow-up situations or planning radiation therapy.

With its virtual monochromatic imaging (VMI), DECT can improve image quality by decreasing metal or beam-hardening artifacts. However, if there is no desire to obtain material-specific information or correct metal or beam-hardening artifacts, it is better to perform a conventional single-energy scan at the optimal tube potential (Yu et al. 2012). VMI can be combined with a metal artifact reduction (MAR) algorithm to improve image quality further. Three studies investigated VMI and MAR for artifact reduction in the thorax. Gyobu et al. placed 12 simulated nodules randomly inside a chest phantom with a pacemaker. They reported that high energy VMIs of 100 or 140 keV reduced metal artifacts without influencing the capability to

detect pulmonary nodules. In contrast, low VMIs of 40 keV increased metal artifacts and worsen the nodule detection, at least in thick slices, concluding that high monochromatic energy images can reduce metal artifacts without nodule detection changes (Gyobu et al. 2013). Another group used specially designed phantoms containing dental, spine, and hip implants. They tested a MAR algorithm and two types of VMI reconstructions separately and in combination to identify the optimal technique for each implant site. Both methods significantly improved delineation accuracy, but the combination of 130 keV VMIs with MAR showed the best overall results. However, the optimal reconstruction technique depends on the type of metal implant (Kovacs et al. 2018). Finally, Liu et al. evaluated the clinical value of VMI combined with a MAR algorithm to assess small pulmonary nodules after the placement of microcoils before video-assisted thoracoscopic surgery (VATS). They reported that 74 keV was the optimal level for VMIs since it improved the image quality for microcoil localization in pulmonary nodules (Liu et al. 2018a). However, the presented results indicate that each situation's most suitable energy level is different depending on whether artifact reduction or improved signal-to-noise ratio is preferred. Therefore, the energy level needs to be adjusted depending on the situation.

PCDCT can also reduce metal- and beam-hardening artifacts by relying on multiple energy bins (Shikhaliyev 2005). However, there are currently only limited data available addressing artifact reduction in the specific setting of thoracic oncology imaging.

1.2 Beam-Hardening Artifacts Due to Contrast Media

DECT VMI can also reduce beam-hardening artifacts caused by contrast media in the thorax, particularly when assessing lesions in the upper mediastinum adjacent to the brachiocephalic vein (Fig. 1). In a retrospective study with 101 patients, Kim et al. determined the optimal energy level of VMIs for reducing beam-hardening artifacts

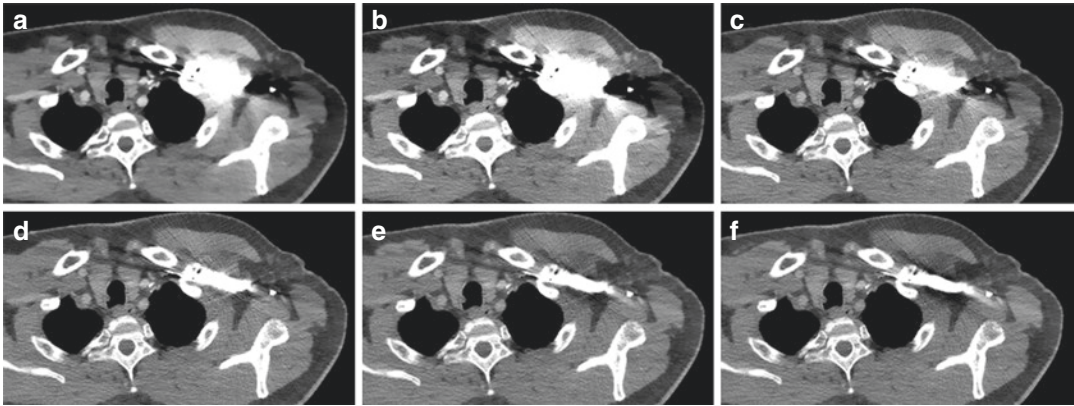


Fig. 1 Image (a) shows a conventional polychromatic reconstruction of the upper thoracic apparatus with a contrast bolus in the left subclavian vein. Images (b–f) are showing monochromatic reconstructions with ascending

keV levels (70, 90, 110, 130, 150). The best contrast with significantly reduced beam-hardening artifacts is achieved at KeV levels of 100 to 130 KeV

caused by contrast media. They compared VMIs at different energy levels with conventional polychromatic images and reported the best subjective image quality and image noise at an energy level of 100 and 130 keV (Kim et al. 2018).

2 Imaging Pulmonary Nodules

2.1 Introduction

Conventional contrast-enhanced or non-enhanced chest CT is the best imaging modality for diagnosing and characterizing pulmonary nodules (PN). Medium to large lung pulmonary nodules are consistently detected on clinical CT systems, but the interreader agreement and reader sensitivity diminish substantially if the nodule size is below 8–10 mm (Rubin 2015). Over the last decades, the case detection rates of pulmonary nodules have continuously increased and might rise even faster due to recent lung cancer screening recommendations (Kauczor et al. 2015). However, the correct management of detected pulmonary nodules is sometimes demanding.

On CT, the diagnostic evaluation of PN usually consists of two major parts: the degree and pattern of contrast enhancement and the morphologic features such as growth, size, and mar-

gins. Malignancy is often indicated by deep lobulated or coarse spiculated margins or a maximum attenuation of 20–60 Hounsfield units (HU), while smooth borders and a maximum attenuation of ≤ 15 HU make benignity more likely (Ohno et al. 2014). However, there is considerable overlap between benign and malignant PNs in imaging features, and oversimplifying can lead to misdiagnosis. Furthermore, the evaluation of contrast enhancement in pulmonary lesions with ground-glass attenuation (GGA) remains challenging with conventional imaging techniques.

However, there are some pitfalls when using DECT for PN evaluation. Harder et al. measured a total of 63 PN in 24 patients to assess the effect of different VMI reconstructions on iodine attenuation and pulmonary nodule volumetry, showing a good correlation between nodule attenuation and nodule volume ($R^2 = 0.77$). Furthermore, high energy VMI resulted in lower attenuation and nodule volumes, while low energy VMI resulted in higher attenuation and nodule volumes, which is probably caused by differences in nodules' peripheral enhancement at different energy levels. Therefore, readers should consider the possibility of over- or under-estimating pulmonary nodules volume while using VMI (den Harder et al. 2017).

2.2 Detection of Pulmonary Nodules

Leng et al. established an ultrahigh-resolution (UHR) data collection mode on a whole-body, research photon-counting detector computed tomography (PCDCT) system with 64 rows of $0.45 \text{ mm} \times 0.45 \text{ mm}$ detector pixels, which corresponded to a pixel size of $0.25 \text{ mm} \times 0.25 \text{ mm}$ at the isocenter (Leng et al. 2016). In a phantom study, the same group evaluated this UHR mode to assess its performance in volume quantification and shape differentiation for lung nodules. Therefore, they scanned 20 synthetic lung nodules with different sizes, shapes, and radiodensities to assess the influence of nodule properties and reconstruction kernels. The volume measurements of small or star-shape nodules were promising, demonstrating the advantages of PCDCT as a robust quantitative tool for lung nodule characterization. Moreover, the results indicated that the UHR mode has a high capability to differentiate sphere- from star-shaped nodules (Fig. 2). They concluded that the

improved spatial resolution of the evaluated PCDCT system could improve nodule growth measurements and nodule shape characterization (Zhou et al. 2017). Furthermore, SPCCT offers high-quality images at low radiation doses, which is advantageous in low-dose lung cancer screening (Symons et al. 2017a).

2.3 Classification of Pulmonary Nodules

2.3.1 Solid Pulmonary Nodules

DECT offers several parameters derived from iodine concentration (IC) measurements, providing additional information when evaluating pulmonary nodules (PN). Several studies investigated values of DECT to differentiate benign from malignant PN.

In a pilot study, Xiao et al. assessed the combination of low-dose DECT and ASIR (Adaptive Statistical Iterative Reconstruction) algorithm to classify solitary pulmonary nodules (SPN). Sixty-two patients with pathology-proved 42 benign

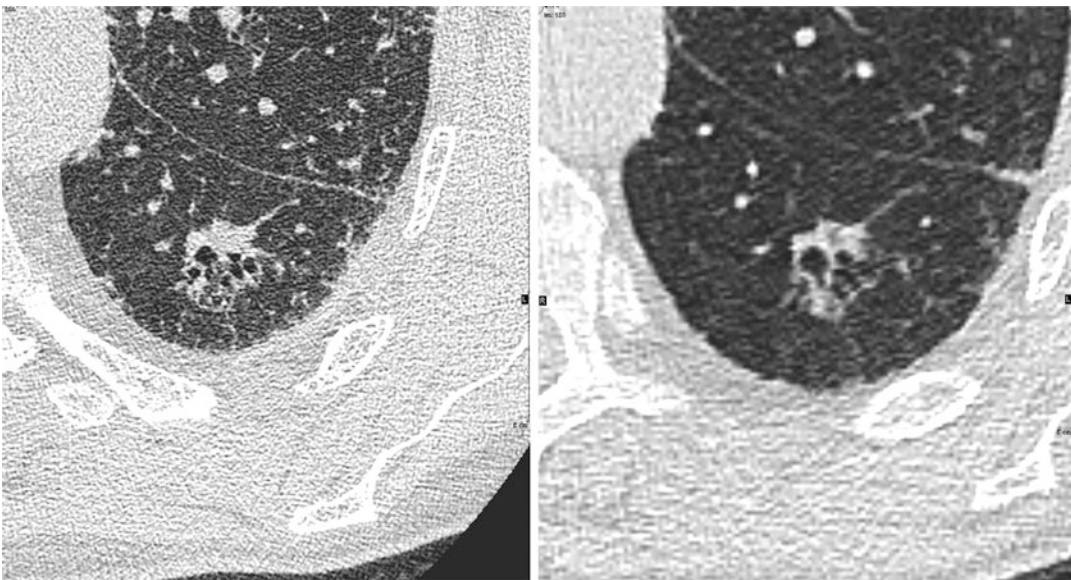


Fig. 2 Lung cancer in the left lower lung lobe showing spiculae and central cavitations. Left: Transverse photon-counting detector CT images using a U70 kernel and achieving a slice thickness of 0.25 mm. Right: Transverse images of the same lesion obtained with a conventional

CT scanner (Somatom Definition AS) using a I70 kernel and achieving a slice thickness of 1 mm. (Kindly provided by the DKFZ Heidelberg and the Thoraxklinik at University of Heidelberg)

and 20 malignant SPNs were scanned with arterial and venous phase DECT. The iodine and water concentration (IC and WC), the normalized iodine and water concentration (NIC and NWC) of the lesions were measured, and the normalized iodine and water concentration difference (ICD and WCD) between the arterial and venous phases (AP and VP) were calculated. The spectral HU curve was divided into three sections based on the energy (40–70, 70–100, and 100–140 keV), and the slopes (λ HU) in both phases were calculated. The results showed that iodine-related parameters (ICAP, IC_{VP}, NIC_{AP}, NIC_{VP}, and the ICD) of malignant SPN were significantly higher than that of benign SPN and that the three venous phase λ HU values in malignant SPN were higher than in benign SPN ($P < 0.05$). The water-related parameters showed no difference. Therefore, they concluded that iodine parameters are useful markers to distinguish benign from malignant lung diseases (Xiao et al. 2015). Wu et al. also used multiple DECT parameters to assess the spatial distribution of NIC in 39 malignant and 21 benign pulmonary SPNs. For this purpose, they calculated the difference (dNIC) between the proximal (NIC_{pro}) and the distal (NIC_{dis}) regions of the nodules, showing significant differences between malignant and benign nodules in the arterial and venous phase (Wu et al. 2018a).

Lin et al. analyzed 139 patients with pathology-proved SPNs who also underwent double-phase enhanced DECT scans. They divided the patients into an active inflammatory, a malignant, and a tuberculosis group. Normalized (NICs) and non-normalized iodine concentrations (ICs) were derived from iodine-based material decomposition CT images, and the slope rate was calculated from the spectral curve. The results showed that the mean slope rate, IC, and NIC for the active inflammatory group were significantly higher than for the malignant group, and the parameters of the malignant group were considerably higher than the tuberculosis group ($P < 0.05$) (Lin et al. 2016).

In summary, all three studies imply that DECT imaging provides a novel method for a better characterization of pulmonary nodules in double-phase contrast-enhanced scanning.

2.3.2 Ground-Glass Pulmonary Nodules

Pulmonary ground-glass attenuation (GGA) or lesions with GGA are still challenging with conventional imaging techniques since the evaluation of contrast enhancement is difficult.

In a phantom study, Kawai et al. used phantoms containing various iodine or calcium concentrations to simulate soft tissue and GGA to examine the relationship between iodine concentration and calculated iodine value contrast-mapping images (CMIs). They reported a good correlation between iodine value and iodine concentration in the soft tissue models ($r^2 = 0.996$) and the GGA models ($R^2 = 0.998$). In the next step, they applied the technique to clinical cases with lung lesions, showing that contrast enhancement on CMIs was visible in 22 adenocarcinomas but not in pulmonary hemorrhage and inflammatory changes (Kawai et al. 2011).

Liu et al. included 48 patients with lung adenocarcinoma in a retrospective study who underwent arterial phase DECT before treatment. The iodine concentration (IC) and water content (WC) of the GGO were measured and compared to the contralateral and ipsilateral normal lung tissue, finding significantly higher IC values in pGGO and mGGO ($P < 0.001$). Furthermore, IC, NIC, and WC values were compared between groups of pure ground-glass opacity (pGGO), mixed ground-glass opacity (mGGO), preinvasive lesions, minimally invasive adenocarcinoma (MIA), and invasive adenocarcinoma (IA). The NIC and WC values for pGGO and mGGO, and the WC values of the groups with preinvasive lesions and MIA and IA were statistically different ($P = 0.049$, $P < 0.001$, $P < 0.001$) (Liu et al. 2018b).

Chen et al. quantitatively assessed the DECT imaging's efficacy for differentiation of benign and malignant ground-glass nodules (GGN) and solid nodules (SN). The study included 114 patients with SPNs (61 GGNs and 53 SNs) who underwent DECT plain and enhanced scans in the arterial (a) and venous (v) phases. The spectral CT imaging parameters included: iodine concentrations (IC) of lesions in the arterial (IC_{La}) and venous (IC_{Lv}) phases; normalized IC (NIC_a/

NIC_v), the slope of the spectral curve ($\lambda\text{HU}_a/\lambda\text{HU}_v$), and VMI images on 40 and 70 keV (CT40keVa/v, CT70keVa/v). Pathology revealed 75 lung cancer cases, three metastatic nodules, 14 benign nodules, and 22 inflammatory nodules. Among the 53 SNs were 37 malignant and 16 benign nodules, while among the 61 GGNs were 41 malignant and 20 benign nodules. Overall, the CT40keVa, λHU_a , CT40keVv, λHU_v , and ICLv of benign SPNs were greater than those of malignant SPNs (all $P < 0.05$). For GGNs, CT40keVa/v, CT70keVa/v, $\lambda\text{HU}_a/\lambda\text{HU}_v$, and ICLv of malignant GGNs were all lower than those of benign GGNs (Chen et al. 2019).

All three studies mentioned above showed that DECT is a promising method for distinguishing malignant from benign GGN by indicating their blood supply status.

2.3.3 Calcified Pulmonary Nodules

The DESCT technique allows data acquisition at different kilovoltage settings, enabling reconstructing virtual non-contrast (VNC) images by subtracting the iodine content in contrast-enhanced images with CT numbers similar to true non-contrast imaging (TNC).

VNC has the potential to differentiate calcifications and strongly attenuating nodules without additional TNC, which can help characterize pulmonary nodes (Fig. 3). Chae et al. detected 17 out of 20 calcifications in SPN on VNC images without using TNC (Chae et al. 2008). Nevertheless, VNC can underestimate calcification's extent due to post-processing subtraction errors and influence the measured volume of pulmonary nodules. In this context, Harder et al. compared the volume of pulmonary nodules on VNC and conventional reconstructions, finding a significant reduction of 5.5% (2.6–11.2%, $P < 0.001$) on VNC (den Harder et al. 2017).

3 Imaging Lung Cancer

3.1 Introduction

Lung cancer is the leading cause of cancer-related deaths for both men and women across the devel-

oped world (Sung et al. 2021). Early-stage lung cancer can be treated with potentially curative intent, but most patients present at an advanced stage, which results in an overall low 5-year survival for all stages. Furthermore, the staging of lung cancer is essential because treatment options and prognosis differ significantly by stage.

Computed tomography (CT) plays an essential role in noninvasively characterizing pulmonary masses according to the morphology, interfaces, inner densities, and enhancement of masses (MacMahon et al. 2005). DECT has the potential to describe the contrast enhancement even further by depicting microvessel density and blood supply with IC measurements. In this context, significant correlations between the iodine uptake derived from DECT and perfusion parameters derived from first-pass dual-input perfusion computed tomography (DIPCT) have been reported (Chen et al. 2017). Several DECT parameters are available describing contrast enhancement, which can help detect lung cancer, differentiate lung cancer from inflammation, classify lung cancer subtypes, and identify lymph node metastasis:

1. Iodine concentration (IC) in enhanced arterial (AP) or venous phase (VP) images.
2. Normalized iodine concentration (NIC) as the ratio of the lesions IC and the IC of the artery at the same level.
3. The spectral attenuation curve slope (λHU) calculated with spectral images from 40 to 140 keV (spaced at 10 keV intervals).

3.2 Detecting Lung Cancer

DECT techniques may improve lung cancer detection by decreasing image noise and increasing the signal-to-noise and contrast-to-noise ratio. For this purpose, two studies explored the optimal energy level of virtual monochromatic imaging (VMI) to improve lung cancer imaging quality. Hou et al. scanned 50 lung cancer patients with DECT, generating monochromatic images at 50, 60, 70, and 80 keV energy levels. Subjective assessment about the overall image quality and

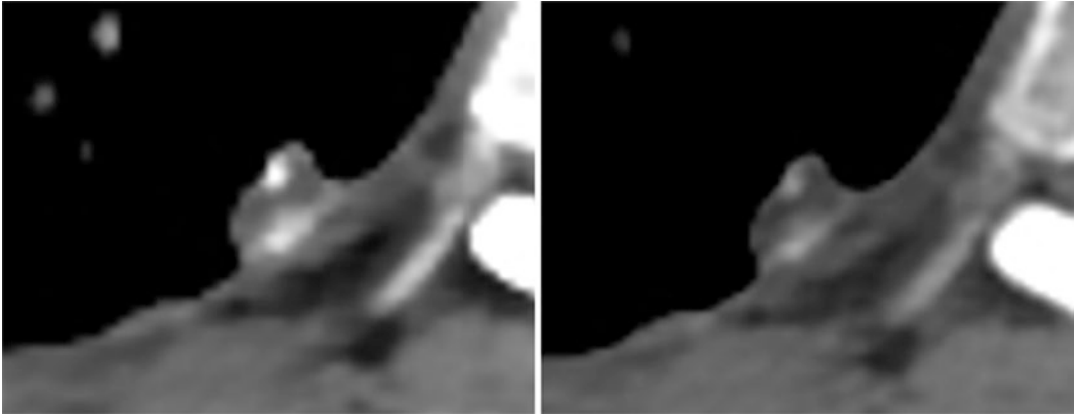


Fig. 3 Partially calcified hamartoma in the right lower lobe. The left image shows a conventional polychromatic reconstruction in the venous phase. The right image shows the same slice with same windowing as virtual non-

contrast reconstruction (VNC). Using VNC images, calcifications can be well separated from a possible nodular contrast enhancement within the lesion

inhomogeneity enhancement was performed by analyzing image noise, lesion-to-lung contrast-to-noise ratio, and CT number difference between central and peripheral regions of tumor (dCT value). The highest contrast-to-noise ratio value and the best subjective score of image quality were obtained at 70 keV ($P < 0.05$), whereas the highest subjective score of inhomogeneity evaluation was at 60 keV ($P < 0.05$). Therefore, the combination of 60 and 70 keV monochromatic images might be useful in lung cancer imaging (Hou et al. 2016). Kaup et al. reported comparable results. In their study, the scans of 59 lung cancer patients who underwent chest DECT were reconstructed at different energy levels (40, 60, 80, 100 keV) with VMI. After assessing each reconstruction's objective and subjective image qualities, the best performance for lung cancer imaging was reported at 60 keV (Kaup et al. 2016).

Central lung cancer often involves lobar or segmental bronchi, causing ventilation impairment in the distal lung parenchyma. The close relationship between pulmonary ventilation and perfusion may also cause perfusion deficits in the corresponding lung areas. Sun et al. investigated the capability of DECT to quantitatively evaluate lung perfusion defects that are induced by central lung cancer. They compared the iodine concentrations (IC) and

CT numbers in the distal lung of 32 patients with central lung cancer with the corresponding areas in the normal contralateral lung. The results showed that IC of the side with lung cancer (0.70 ± 0.42 mg/ml) was significantly lower than the corresponding area in the normal contralateral lung (1.19 ± 0.62 mg/ml) ($P < 0.001$), indicating that DECT is feasible and to identify perfusion defects that are induced by central lung cancer (Sun et al. 2013).

3.3 Differentiate Lung Cancer and Inflammation

Inflammatory masses with benign nature such as granulomatous inflammation, focal organizing pneumonia, and lung abscess are a common finding in chest CT. The differentiation against lung cancer is essential because inflammatory masses can be treated with high-dose steroids, irradiation, or antibiotics, and unnecessary pulmonary resection should be avoided. DECT parameters reflect the blood supply of lung masses. Granulomatous inflammation and organizing pneumonia are formed by the proliferation of inflammatory granulation tissue or acute inflammation residuals. The inflammation may stimulate rich and dilated capillaries leading to a high

and homogenous enhancement (Maldonado et al. 2007; Diederich et al. 2006). However, inappropriate angiogenesis and establishment of vascular networks may occur in lung cancer, leading to a subsequent reduction in oxygen delivery and an insufficient supply of fast-growing masses, thus explaining the inhomogeneous enhancement in lung cancer (Yi et al. 2004; Zhao et al. 2014).

Several studies investigate the value of DECT in differentiating malignant from inflammatory pulmonary masses. Wang et al. evaluated the feasibility of qualitative and quantitative information from Gemstone Spectral Imaging (GSI) to differentiate lung cancer and benign lung lesions. Sixty-eight patients, divided into pneumonia ($n = 24$) and malignant tumor groups ($n = 44$), were compared by iodine concentration (IC), water concentration (WP), spectral curve slope, and CT numbers at 40 keV, and significant differences were found for all parameters ($P < 0.05$) (Wang et al. 2014). Hou et al. analyzed 60 patients with 35 lung cancers and 25 inflammatory masses who underwent arterial phase (AP) and venous phase (VP) DECT. They measured the normalized iodine concentration (NIC), the slopes of spectral attenuation curves (λ_{HU}), and the CT numbers in 70 keV VMI in the central and the peripheral regions of lung masses and calculated the difference in CT numbers (dCT) between both regions. The results showed that NICs and CT numbers in the central and λ_{HU} values in the central and peripheral regions of lung cancers were significantly lower than those of inflammatory masses. In contrast, dCT values of lung cancers were higher than those of inflammatory masses. (Hou et al. 2015). Yu et al. explored the value of arterial phase (AP) and venous phase (VP) DECT in differentiating lung cancer from an inflammatory myofibroblastic tumor (IMT) in 96 patients with lung cancer and 16 with IMT. For this purpose, the normalized iodine concentration in AP (NIC_{AP}) and VP (NIC_{VP}), the slope of the spectral curve in AP (λ_{AP}) and VP (λ_{VP}), and the normalized iodine concentration difference between AP and VP (ICD) were calculated and compared. A significantly higher NIC_{AP} , NIC_{VP} , λ_{AP} , λ_{VP} , and ICD was found in IMT than in lung cancer ($P < 0.05$),

while the combination of these parameters achieved a sensitivity and specificity of 100% and 81.3% (Yu et al. 2019). In conclusion, these studies indicate that DESCT imaging can help to differentiate lung cancers from inflammatory masses.

3.4 Characterization of Lung Cancer

3.4.1 Virtual Biopsy with DECT

The heterogeneity and complexity of lung cancer are determined by genes that play a crucial role in its occurrence, type, development, and prognosis (Vogelstein et al. 2013). The lung tumor classification system of the World Health Organization divides lung carcinomas into non-small cell lung carcinoma (NSCLC) and small cell lung carcinoma (SCLC). NSCLCs are further classified into squamous cell carcinoma (SC), adenocarcinoma (AC), and large cell carcinoma (Travis et al. 2015). The definitive diagnosis for lung mass is achieved via invasive histological examination, such as thoracoscopic surgery, biopsy via bronchoscopy, or transthoracic puncture guided by ultrasonography. However, a non-invasive and accurate method for evaluating the histological type of lung cancer would be desirable since histological examination may be associated with complications in some cases.

Fehrenbach et al. showed that in 52 untreated primary NSCLC lesions, lung adenocarcinoma had significantly higher normalized iodine concentrations than (NIC: 19.37) squamous cell carcinoma (NIC: 12.03; $P = 0.035$) (Fehrenbach et al. 2019a). Jia et al. combined the quantitative DECT parameters CT numbers, the slope of the spectral attenuation curve (λ_{HU}), iodine concentration, water concentration, and the effective atomic number (Z_{eff}) with serum tumor markers to evaluate the lung cancer histology type. Tumor markers were the serum levels of carcinoembryonic antigen (CEA), neuron-specific enolase (NSE), squamous cell carcinoma antigen (SCC-Ag), and cytokeratin fragment CYFRA21-1. CEA and NSE levels were higher in adenocarcinoma and neuroendocrine tumors,

while SCC-Ag and CYFRA21-1 levels were higher in squamous cell cancer. There was no significant difference in CT number attenuation among the groups ($P > 0.05$), whereas $HU\lambda$ in the arterial phase and Z_{eff} and IC in the arterial and venous phases was significantly different among the groups ($P < 0.05$). The diagnostic efficiency of serum tumor markers was higher than that of CT spectral parameters, but combining serum markers and CT parameters showed a larger diagnostic efficiency than combined serum markers and combined CT parameters alone. Therefore, DECT parameters and serum tumor markers are valuable in evaluating histological types of lung cancer, and in combination, they can significantly improve diagnostic efficiency. Nevertheless, the accuracy of these two methods alone is still insufficient (Jia et al. 2018). DECT might also differentiate pulmonary metastases from different primary origins. Deniffel et al. demonstrated significant differences in the IC between pulmonary metastases of renal cell carcinoma, breast, colorectal, and head/neck carcinoma, as well as metastases of colorectal carcinoma, osteosarcoma, pancreato-biliary, and urinary tract carcinoma (Deniffel et al. 2019).

Angiogenesis is essential in the process of primary tumor growth, proliferation, and metastasis. In many cancers, including non-small cell lung cancer (NSCLC), tumor angiogenesis pathways have been identified as important therapeutic targets. Wu et al. used DECT parameters to characterize 60 histology confirmed lung squamous cell carcinoma (SC) and adenocarcinoma (AC) and correlated the findings with the expression of thyroid transcription factor-1 (TTF-1) and epidermal growth factor receptor (EGFR). They noted no significant differences in normalized iodine concentration (NIC) and the spectral attenuation curve slope (λHU) between the TTF-1-positive and TTF-1-negative groups. However, significant differences in NIC and λHU were noted between EGFR-positive and EGFR-negative SC and AC (Wu et al. 2018b). Li et al. explored the role of DECT in identifying epidermal growth factor receptor (EGFR) mutation status in a cohort of 120 patients with pulmonary adenocarcinoma, 66 with confirmed EGFR mutations. The patients

were divided into an EGFR mutation and an EGFR wild-type group. The evaluated DECT parameters were the CT numbers at 70 keV, normalized iodine concentration (NIC), normalized water concentration, and slopes of the spectral attenuation curves (λHU). The univariate analysis revealed that sex, smoking history, NIC, and slope λHU were significantly associated with EGFR mutation status ($P > 0.05$). Furthermore, smoking history and NIC were the two significant predictive factors associated with EGFR mutations (OR = 3.23, $P = 0.005$; OR = 58.026, $P = 0.049$). Based on this analysis, the smoking history and NIC were combined to determine the predictive value for EGFR mutations with the area under the curve of 0.702 (Li et al. 2019). Li et al. explored 48 patients with NSCLC who underwent DECT before surgical tumor resection. They correlated the expression level of vascular endothelial growth factor (VEGF) in non-small-cell lung cancer (NSCLC) with the DECT quantitative imaging parameters IC and CT values at 40 keV and λHU . They found significant differences in IC, λHU , and CT values at 40 KeV between NSCLCs with negative and moderately positive VEGF expression ($P = 0.001$) and between NSCLCs with mildly and moderately positive expression of VEGF ($P = 0.047-0.002$). Besides, all parameters displayed a significant and positive correlation with the level of VEGF expression ($R^2 = 0.458-0.393$, $P < 0.05$) (Li et al. 2016). All three studies imply that quantitative DECT parameters have the potential to predict EGFR and VEGF mutations in lung cancer, helping to evaluate the status of angiogenesis.

The grading of cancer is a histological method intended to help predict prognosis based on specific morphological features. It typically is based on architectural or cytological features (nuclear grade or the number of mitoses), or in some cases, a combination of both (Travis et al. 2016). Lin et al. investigated the correlation between pathological grades of non-small cell lung cancers (NSCLCs) and quantitative DECT parameters. They evaluated 53 patients with NSCLCs who underwent preoperative DECT, dividing them into a low-grade and a high-grade group

based on their histopathological differentiation. They measured arterial phase (AP) and venous phase (VP), iodine concentration (IC), the normalized iodine concentration (NIC), and slope of the spectral curve (λ HU), showing that NIC and λ HU in the AP and VP were significantly higher in the low-grade NSCLC than in the high-grade NSCLC ($P < 0.001$). Furthermore, there was a significant negative correlation between DECT parameters and pathological grades ($P < 0.001$). ROC analysis indicated that λ HU in VP provided the best diagnostic performance in distinguishing high-grade from low-grade cancers with an AUC of 0.914, a sensitivity of 85.7%, and a specificity of 84.4% (Lin et al. 2018).

3.4.2 PCDCT and Molecular Imaging

Molecular imaging using new types of targeted contrast agents is among the exciting possibilities that may become a reality using PCDCT (Taguchi and Iwaczyk 2013; Jaffer and Weissleder 2004). Molecular CT uses combined particles composed of a contrast agent labeled with nanoparticles, larger than conventional contrast agents, remaining in the cardiovascular system longer than 24 h (Fornaro et al. 2011). Moreover, these nanoparticles can carry targeting molecules for specific cells or enzymes, allowing target-specific imaging. Research has focused on nanoparticles labeled with gold, which can be detected with K-edge imaging even in the presence of other contrast agents, such as iodine (Si-Mohamed et al. 2017; Cormode et al. 2009; Roessl and Proksa 2007). In oncology, molecular CT may aid in early cancer diagnosis by quantifying small tumors' mass and size and determining the distribution of contrast agents and/or particles (Barber et al. 2015).

In 1967, Milne showed that lung tumors might have a dual blood supply by the pulmonary and the aortic system, with a trend toward histological type-specific circulatory patterns (Milne 1967). Furthermore, tumor cells can produce angiogenic factors that stimulate and generate many new blood vessels. These new blood vessels' wall is immature due to a lack of hemangio-

pericyte and smooth muscle tissue, increasing permeability of the blood vessels (Ruoslahti 2002). Therefore, the use of different contrast agents simultaneously (e.g., purely intravascular for the vascular supply and intra-/extracellular for the capillary leak) might offer new possibilities for lung tumors' characterization. PCDCT's K-edge imaging enables the differentiation between multiple contrast agents, making it possible to administer different contrast agents and simultaneously show their specific distribution (Cormode et al. 2017). Furthermore, multiple contrast agents could be administered at different time points while imaging is performed at a single time point (Fornaro et al. 2011). The arterial phase could be evaluated by removing the contrast agent administered first, and the portal phase could be assessed by removing the second contrast agent. Non-contrast images could be reconstructed by removing the contrast agents from the images. Symons et al. evaluated simultaneous imaging in a canine model with orally administered bismuth and intravenously injected gadolinium and iodine (Symons et al. 2017b, c). All these techniques may significantly impact lung tumor characterization and may offer new methods in evaluating tumor behavior, possibly leading to a more accurate tumor prognosis. However, extensive studies are necessary till these techniques may be part of the clinical routine.

3.5 Staging Lung Cancer

3.5.1 Lymph Node Metastasis

The correct staging of lung cancer is essential because treatment options and prognosis differ significantly by stage. However, conventional CT diagnostic criteria based on size (lymph node maximal short-axis diameter ≥ 10 mm) are still standard for judging metastatic lymph nodes, reaching accuracy of only about 60% (Silvestri et al. 2013).

Yang et al. investigated the value of DECT quantitative parameters for preoperative diagnosis of metastatic lymph nodes in patients with

non-small cell lung cancer (NSLC). They included 84 patients with suspected lung cancer, evaluating a total of 144 lymph nodes, of which 48 were metastatic, and 96 were non-metastatic. They measured the normalized iodine concentrations (NIC), water concentration, and slope of the spectral curve (λ HU) in the arterial and venous phases. The λ HU measured during both phases was significantly higher in metastatic than in benign lymph nodes ($P < 0.05$). The λ HU of the arterial phase (AP) with an optimal threshold value of λ HU of 2.75 reached a sensitivity of 88.2% and a specificity of 88.4% for metastatic lymph nodes, which is higher than for conventional CT-based qualitative size assessment (Yang et al. 2017).

Imaging the hilar lymph nodes using non-contrast-enhanced CT is difficult because X-ray absorption by the hilar nodes is similar to that of the neighboring pulmonary arteries and veins. Consequently, the hilar LNs are commonly evaluated using contrast-enhanced CT. Still, even with contrast agents, the detection of hilar lymphadenopathy can be difficult when the enhance-

ment of the pulmonary vessels and the lymph nodes is almost the same. Sekiguchi et al. evaluated the visibility of the hilar lymph nodes (LNs) by comparing virtual monoenergetic low-keV images with early-phase contrast-enhanced CT (Fig. 4). DECT was performed in 50 patients for evaluation of lung cancer at 20 and 60 s after administration of contrast media, and five reconstructions were made each (A: 20 s/120 kV; B: 60 s/40 keV; C: 60 s/50 keV; D: 60 s/120 kV; E: 60 s/100 keV). The authors measured the differences in CT numbers of the bilateral main pulmonary arteries (PAs), pulmonary veins (PVs), and hilar LNs and calculated the differences in CT number between the PA/PV and LNs (PA-LN and PV-LN contrast). They also evaluated the artifacts from the superior vena cava (SVC). The results showed that virtual monoenergetic 40-keV imaging at the delayed 60-s phase was beneficial for evaluating hilar lymph nodes since it had good PA-LN and PV-LN contrasts with low artifacts (Sekiguchi et al. 2019).

Virtual non-contrast imaging (VNC) can offer additional information when differentiating cal-

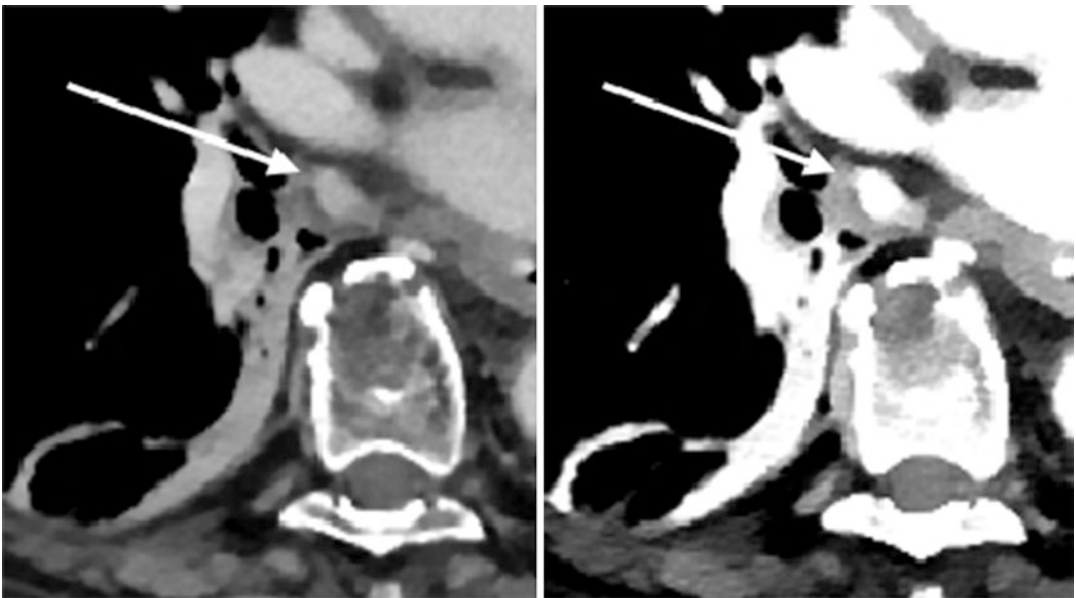


Fig. 4 Small lymph node in the lower mediastinum with contrast uptake. The left image shows a conventional polychromatic reconstruction in the venous phase. The

right image shows the same slice with same windowing as 40 keV VMI. The lymph node is better delineated on the VMI image

cifications and strongly enhancing lymph nodes without additional true non-contrast imaging (TNC). Yoo et al. evaluated VNC images' reliability compared with TNC images in determining high CT attenuation or calcification of mediastinal lymph nodes. Node attenuation in TNC and VNC images was compared in a total of 112 mediastinal nodes from 45 patients, objectively and subjectively, via computed tomography (CT) attenuation and visual scoring. CT attenuation in TNC and VNC had a mean absolute difference of 7.8 ± 7.6 HU and an absolute difference of equal to or less than 10 HU in 65.2% of cases, which corresponds to a moderate intraclass correlation coefficient of 0.612. The visual scores in TNC and VNC images showed fair agreement with a κ value of 0.335 (Yoo et al. 2013).

3.5.2 Bone Metastasis

Bone metastasis is a frequent finding in advanced lung cancer patients, and the spine is the most common location. The detection of a metastatic vertebral lesion in its early development stage is important because appropriate treatment can hinder complications due to advanced metastasis. However, the diagnosis of inconspicuous osteoblastic metastases (OBM) from lung cancer is a challenge in conventional CT images since they might have a similar density and are therefore not distinguishable from normal vertebrae. Yue et al. evaluated the optimal energy level of VMI in 35 patients to detect and diagnose OBMs of the vertebra. The CT number and standard deviation (SD) of lesions and adjacent normal bone and the SD value of subcutaneous fat were measured on the conventional polychromatic image (140 kVp) and a set of 11 VMI at different energy levels in the range of 40–140 keV (intervals of 10 keV). The contrast-to-noise ratio (CNR) was compared between the conventional and all VMI images. The lowest image noise was in 70 and 140 keV images, and the highest CNR was noted in 70 keV images, suggesting that VMI at 70 keV could be the best for diagnosing inconspicuous vertebral metastases (Yue et al. 2017).

4 Therapy Evaluation of Lung Cancer

4.1 Introduction

Computed tomography (CT) or magnetic resonance imaging (MRI) is usually used to evaluate tumor response to therapy. Combined chemotherapy and thoracic radiation therapy (i.e., chemoradiotherapy (CRT)) have proven their value in nonresectable NSCLC (Ramnath et al. 2013), but definitive external beam radiation therapy is associated with local recurrence rates of 55% to 70% (Jones et al. 2015). The success of radiation therapy highly depends on tumor vascularization and is limited in hypoxic tumor tissue (Salem et al. 2018).

The morphological criteria used by Response Evaluation Criteria in Solid Tumors (RECIST) 1.1 are limited to dimensional changes in tumor size, whereas other criteria such as density evaluation, functional or metabolic changes are not considered. However, radiation therapy can be successful without immediately changing the morphology of treated masses. Furthermore, new response criteria like immune-related response criteria (irRC) and modifications of RECIST will be necessary due to new treatments based on antiangiogenic agents and tyrosine kinase inhibitors. In this context, imaging techniques such as positron emission tomography (PET-CT), diffusion-weighted MRI, and DECT may offer some of the promising applications.

4.2 Therapy Response with DECT

4.2.1 Evaluation of RFA Therapy with DECT

Percutaneous radiofrequency ablation (RFA) is a minimally invasive therapy for treating advanced primary or metastatic lung cancers that are not suitable for surgical resection treatment and can also be combined with radiotherapy and chemotherapy (Ambrogi et al. 2006). Liu et al. evaluated the therapeutic efficacy of lung RFA in 30

patients with contrast-enhanced DECT images. Conventional CT images were used to obtain tumor size values, and on water-based and iodine-based material decomposition images, the densities of iodine and water in lung tumors were quantitatively analyzed. In 22 cases, tumor size increased after RFA while there was no detectable change in the remaining eight patients. The water content in the tumors increased significantly after RFA ($P < 0.05$), while the iodine content in the tumors was reduced from 2.49 ± 0.74 mg/ml before RFA to 0.45 ± 0.29 mg/ml in areas of necrosis after RFA ($P = 0.001$). The authors stated that by comparing the tumor size, water content, and iodine content before and after RFA, the metabolic states and therapeutic efficiency could be evaluated (Liu et al. 2016).

4.2.2 Evaluation of Anti-angiogenic Therapy with DECT

Baxa et al. investigate the changes of DECT parameters and tumor size in advanced non-small cell lung cancer (NSCLC) under anti-EGFR therapy (erlotinib). In 31 patients before and after treatment (mean 8 weeks as follow-up) the iodine uptake (IU) was quantified in the arterial and venous phases, and the arterial enhancement fraction (AEF) was calculated. The change of IU in responders and non-responders was compared with morphological changes in diameter and volume. A significant decrease of IU was proven in the venous phase in responders, whereas non-responders showed variable trends of developments and no substantial IU changes. AEF percentage also showed significant differences between both groups ($P < 0.05$). Based on the results, the authors assumed a decrease in vascularization in responding and non-significant variable development of vascularization in non-responding tumors. However, the most significant change was still observed using the anatomical parameter diameter and volume (Baxa et al. 2016). The same research group investigated the potential of DECT in staging and therapy response monitoring of metastatic lymph nodes. They analyzed 110 mediastinal lymph nodes in 27 patients with NSCLC with the same

methods described above. Correspondingly, before treatment significant differences of AEF were observed between enlarged (90.4%, 32.3–238.5%) and non-enlarged (72.7%, –37.5–237.5%) lymph nodes ($P = 0.044$). A significantly different change of AEF in responding (decrease of 26.3%; $P = 0.022$) and non-responding (increase of 43.0%; $P = 0.031$) lymph nodes was also demonstrated. Finally, a higher value of AEF before treatment was observed in lymph nodes with a subsequent favorable response (88.6% vs. 77.7%; $P = 0.122$), but this difference had no reach statistical significance (Baxa et al. 2014).

Kim et al. evaluated tumor response in 10 NSCLC patients treated with anti-angiogenic agents (bevacizumab) by assessing intratumoral changes with DECT. Tumor responses were evaluated and compared with the baseline CT results using both RECIST (size changes only) and Choi's criteria (reflecting net tumor enhancement). The weighted κ value for comparing the RECIST and Choi's criteria was 0.72, with discordant responses found in 5 of 31 lesions. Therefore, DECT may be a useful tool for response evaluation after anti-angiogenic treatment in NSCLC patients by providing information on the net enhancement. In the same study, iodine-enhanced images also allowed a distinction between tumor enhancement and hemorrhagic response (detected 4 of 29), which is important since intratumoral hemorrhage or necrosis during tumor treatment can make tumor response evaluation more challenging. The measurement of the net enhancement allows the discrimination between intratumoral hemorrhage, which can be otherwise regarded as a solid enhancing component, leading to an overestimation of tumor diameters (Kim et al. 2012).

4.2.3 Correlation of DECT and PET-CT in Therapy Evaluation

The information derived from PET-CT imaging enables treatment evaluation at the molecular/metabolic level, far ahead of the macroscopic visual change in RECIST 1.1. Therefore, the PET-CT response evaluation criterion in solid tumors (PERCIST) has been suggested as the

alternative to RECIST 1.1 (Wahl et al. 2009). Ren et al. showed that semiautomatic iodine-related quantitation in DECT correlated well with metabolism-based measurements in fluorine-18 fluorodeoxyglucose (F-FDG) PET/CT, suggesting that DECT-based iodine quantitation might be a feasible substitute for assessment of lung cancer response to chemoradiotherapy/radiotherapy. They acquired a total of 32 pairs of DECT and F-FDG PET/CT imaging from 13 patients with primary or metastatic lung cancers receiving either radiotherapy alone or chemoradiotherapy. Imaging examinations were performed before, immediately, and no later than 6 months after treatment for response evaluation. Iodine-related DECT parameters included the total iodine uptake (TIU) and vital volume (VIV), and metabolic metrics of F-FDG-PET/CT were the standardized uptake value normalized to lean body mass (SULpeak), metabolic tumor volume (MTV), and the total lesion glycolysis (TLG). Pretreatment imaging data revealed a strong correlation between DECT (RECIST, TIU, and VIV) and F-FDG PET/CT parameters (MTV, TLG) ($R^2 = 0.86$ to 0.90 , $P < 0.01$). After treatment, all DECT and PET/CT parameters significantly decreased, whereas the descending amplitude in RECIST was substantially smaller than that of the other parameters ($P < 0.05$). During follow-up examinations, all parameters followed a similar changing pattern, with a strong consistency between RECIST, TIU, VIV and SULpeak, MTV, TLG ($R^2 = 0.78$ – 0.96 , $P < 0.05$) (Ren et al. 2018).

4.2.4 Predicting Recurrence with DECT

CT, PET-CT, and clinical patient follow-up are used to detect recurrence. However, no examination is totally reliable, and recurrences might be diagnosed late, when the cancers are locally extended, or when the patients are metastatic.

Izaaryene et al. investigated the utility of DECT in order to assess therapeutic responses to RFA for lung neoplasia. The study included 70 patients in which the enhancement values of all scars were measured without establishing a prior threshold of positivity. At the 1 month follow-up, 53 nodules were analyzed with DECT and four nodules had recurred, all of which were detected

by DECT. The sensitivity, which was calculated at 100%, was excellent; the NPV was at 100% (CI: 91.62, 100) and the specificity was at 85.71% (CI: 73.33, 92.9). The diagnostic accuracy index was 86.79% (CI: 75.16, 93.45). Therefore, DECT could be a conceivable alternative for detecting early recurrence after lung RFA (Izaaryene et al. 2017).

Fehrenbach et al. analyzed the DECT parameters in 83 patients with advanced NSCLC treated by CRT who underwent single-phase, contrast-enhanced DECT. The evaluation included quantitative treatment response measurements (RECIST 1.1), iodine content (IC) measurements, and spectral slope analysis. Secondary outcome parameters were IC and spectral slopes in mediastinal lymph nodes ($n = 61$). The tumor response was evaluated by applying RECIST 1.1. 24 patients (29%) showed complete remission, 34 patients (41%) had stable disease (SD) or partial regression (PR), and 25 (30%) had progressive disease (PD). The corresponding hotspot analysis showed significantly higher iodine values in PD than in SD/PR. Ten patients (12%) with initially SD showed progressive disease during follow-up for up to 18 months (PDFU). These patients also had significantly higher hotspot iodine values in the initial scan compared to patients with SD throughout the follow-up period (SDFU) ($P < 0.001$). Enlarged lymph nodes showed significantly lower iodine content and a lower spectral slope pitch than normal-sized nodes ($P = 0.003$ – 0.029). Therefore, the authors concluded that SCT might improve tumor response evaluation and lymph node assessment in NSCLC patients treated with CRT. Iodine quantification can add information on tumor vascularization and detection of iodine hotspots indicating residual tumor vascularization has the potential to serve as an imaging marker to predict tumor progression (Fehrenbach et al. 2019b). Two other studies by Aoki et al. evaluated the correlation between DECT parameters and metabolic uptake in F-FDG PET-CT and the association with tumor recurrence, finding strong correlations between iodine concentration (IC), the maximum standardized uptake value (SUVmax), and local recurrence in NSCLC treated with stereotactic body radiotherapy (SBRT) (Aoki et al. 2016a,b).

Compliance with Ethical Standards

Conflict of Interest The author declares that he has no conflicts of interest.

References

- Ambrogi MC, Lucchi M, Dini P, Melfi F, Fontanini G, Faviana P, Fanucchi O, Mussi A (2006) Percutaneous radiofrequency ablation of lung tumours: results in the mid-term. *Eur J Cardiothorac Surg* 30:177–183
- Aoki M, Akimoto H, Sato M, Hirose K, Kawaguchi H, Hatayama Y, Seino H, Kakehata S, Tsushima F, Fujita H, Fujita T, Fujioka I, Tanaka M, Miura H, Ono S, Takai Y (2016a) Impact of pretreatment whole-tumor perfusion computed tomography and 18F-fluorodeoxyglucose positron emission tomography/computed tomography measurements on local control of non-small cell lung cancer treated with stereotactic body radiotherapy. *J Radiat Res* 57:533–540
- Aoki M, Hirose K, Sato M, Akimoto H, Kawaguchi H, Hatayama Y, Fujioka I, Tanaka M, Ono S, Takai Y (2016b) Prognostic impact of average iodine density assessed by dual-energy spectral imaging for predicting lung tumor recurrence after stereotactic body radiotherapy. *J Radiat Res* 57:381–386
- Barber WC, Wessel JC, Nygard E, Iwanczyk JS (2015) Energy dispersive CdTe and CdZnTe detectors for spectral clinical CT and NDT applications. *Nucl Instrum Methods Phys Res A* 784:531–537
- Baxa J, Vondráková A, Matoušková T, Růžicková O, Schmidt B, Flohr T, Sedlmair M, Ferda J (2014) Dual-phase dual-energy CT in patients with lung cancer: assessment of the additional value of iodine quantification in lymph node therapy response. *Eur Radiol* 24:1981–1988
- Baxa J, Matouskova T, Krakorova G, Schmidt B, Flohr T, Sedlmair M, Bejcek J, Ferda J (2016) Dual-phase dual-energy CT in patients treated with erlotinib for advanced non-small cell lung cancer: possible benefits of iodine quantification in response assessment. *Eur Radiol* 26:2828–2836
- Chae EJ, Song J-W, Seo JB, Krauss B, Jang YM, Song K-S (2008) Clinical utility of dual-energy CT in the evaluation of solitary pulmonary nodules: initial experience. *Radiology* 249:671–681
- Chen X, Xu Y, Duan J, Li C, Sun H, Wang W (2017) Correlation of iodine uptake and perfusion parameters between dual-energy CT imaging and first-pass dual-input perfusion CT in lung cancer. *Medicine* 96:e7479
- Chen ML, Li XT, Wei YY, Qi LP, Sun YS (2019) Can spectral computed tomography imaging improve the differentiation between malignant and benign pulmonary lesions manifesting as solitary pure ground glass, mixed ground glass, and solid nodules? *Thorac Canc* 10:234–242
- Cormode DP, Skajaa T, Fayad ZA, Mulder WJ (2009) Nanotechnology in medical imaging: probe design and applications. *Arterioscler Thromb Vasc Biol* 29:992–1000
- Cormode DP, Si-Mohamed S, Bar-Ness D, Sigovan M, Naha PC, Balegamire J, Lavenne F, Coulon P, Roessel E, Bartels M, Rokni M, Bleviss I, Bousset L, Douek P (2017) Multicolor spectral photon-counting computed tomography: in vivo dual contrast imaging with a high count rate scanner. *Sci Rep* 7:4784
- den Harder AM, Bangert F, van Hamersvelt RW, Leiner T, Milles J, Schilham AMR, Willeminck MJ, de Jong PA (2017) The effects of iodine attenuation on pulmonary nodule volumetry using novel dual-layer computed tomography reconstructions. *Eur Radiol* 27:5244–5251
- Deniffel D, Sauter A, Dangelmaier J, Fingerle A, Rummeny EJ, Pfeiffer D (2019) Differentiating intrapulmonary metastases from different primary tumors via quantitative dual-energy CT based iodine concentration and conventional CT attenuation. *Eur J Radiol* 111:6–13
- Diederich S, Theegarten D, Stamatis G, Lüthen R (2006) Solitary pulmonary nodule with growth and contrast enhancement at CT: inflammatory pseudotumour as an unusual benign cause. *Br J Radiol* 79:76–78
- Fehrenbach U, Kahn J, Böning G, Feldhaus F, Merz K, Frost N, Maurer MH, Renz D, Hamm B, Streitparth F (2019a) Spectral CT and its specific values in the staging of patients with non-small cell lung cancer: technical possibilities and clinical impact. *Clin Radiol* 74:456–466
- Fehrenbach U, Feldhaus F, Kahn J, Böning G, Maurer MH, Renz D, Frost N, Streitparth F (2019b) Tumour response in non-small-cell lung cancer patients treated with chemoradiotherapy - can spectral CT predict recurrence? *J Med Imaging Radiat Oncol* 63:641–649
- Fornaro J, Leschka S, Hibbeln D, Butler A, Anderson N, Pache G, Scheffel H, Wildermuth S, Alkadhi H, Stolzmann P (2011) Dual- and multi-energy CT: approach to functional imaging. *Insights Imaging* 2:149–159
- Gyobu T, Honda O, Kawata Y, Kikuyama A, Miki H, Yanagawa M, Sumikawa H, Koyama M, Tomiyama N (2013) The effect of the virtual monochromatic spectral imaging for the metallic artifact and the pulmonary nodule detection. *J Comput Assist Tomogr* 37:707–711
- Hou WS, Wu HW, Yin Y, Cheng JJ, Zhang Q, Xu JR (2015) Differentiation of lung cancers from inflammatory masses with dual-energy spectral CT imaging. *Acad Radiol* 22:337–344
- Hou W, Sun X, Yin Y, Cheng J, Zhang Q, Xu J, Li Y, Zhou W, Wu H (2016) Improving image quality for lung cancer imaging with optimal monochromatic energy level in dual energy spectral computed tomography. *J Comput Assist Tomogr* 40:243–247
- Izaaryene J, Vidal V, Bartoli JM, Loundou A, Gaubert JY (2017) Role of dual-energy computed tomography in detecting early recurrences of lung tumours

- treated with radiofrequency ablation. *Int J Hyperth* 33:653–658
- Jaffer FA, Weissleder R (2004) Seeing within: molecular imaging of the cardiovascular system. *Circ Res* 94:433–445
- Jia Y, Xiao X, Sun Q, Jiang H (2018) CT spectral parameters and serum tumour markers to differentiate histological types of cancer histology. *Clin Radiol* 73:1033–1040
- Jones GC, Kehrer JD, Kahn J, Koneru BN, Narayan R, Thomas TO, Camphausen K, Mehta MP, Kaushal A (2015) Primary treatment options for high-risk/medically inoperable early stage NSCLC patients. *Clin Lung Cancer* 16:413–430
- Kauczor HU, Bonomo L, Gaga M, Nackaerts K, Peled N, Prokop M, Remy-Jardin M, von Stackelberg O, Sculier JP (2015) ESR/ERS white paper on lung cancer screening. *Eur Respir J* 46:28–39
- Kaup M, Scholtz JE, Engler A, Albrecht MH, Bauer RW, Kerl JM, Beeres M, Lehnert T, Vogl TJ, Wichmann JL (2016) Dual-energy computed tomography virtual monoenergetic imaging of lung cancer: assessment of optimal energy levels. *J Comput Assist Tomogr* 40:80–85
- Kawai T, Shibamoto Y, Hara M, Arakawa T, Nagai K, Ohashi K (2011) Can dual-energy ct evaluate contrast enhancement of ground-glass attenuation?: phantom and preliminary clinical studies. *Acad Radiol* 18:682–689
- Kim YN, Lee HY, Lee KS, Seo JB, Chung MJ, Ahn MJ, Park K, Kim TS, Yi CA (2012) Dual-energy CT in patients treated with anti-angiogenic agents for non-small cell lung cancer: new method of monitoring tumor response? *Korean J Radiol* 13:702–710
- Kim C, Kim D, Lee KY, Kim H, Cha J, Choo JY, Cho PK (2018) The optimal energy level of virtual monochromatic images from spectral CT for reducing beam-hardening artifacts due to contrast media in the thorax. *AJR Am J Roentgenol* 211:557–563
- Kovacs DG, Rechner LA, Appelt AL, Berthelsen AK, Costa JC, Friberg J, Persson GF, Bangsgaard JP, Specht L, Aznar MC (2018) Metal artefact reduction for accurate tumour delineation in radiotherapy. *Radiother Oncol* 126:479–486
- Leng S, Yu Z, Halaweish A, Kappler S, Hahn K, Henning A, Li Z, Lane J, Levin DL, Jorgensen S, Ritman E, McCollough C (2016) Dose-efficient ultrahigh-resolution scan mode using a photon counting detector computed tomography system. *J Med Imaging (Bellingham)* 3:043504
- Li GJ, Gao J, Wang GL, Zhang CQ, Shi H, Deng K (2016) Correlation between vascular endothelial growth factor and quantitative dual-energy spectral CT in non-small-cell lung cancer. *Clin Radiol* 71:363–368
- Li M, Zhang L, Tang W, Jin Y-J, Qi L-L, Wu N (2019) Identification of epidermal growth factor receptor mutations in pulmonary adenocarcinoma using dual-energy spectral computed tomography. *Eur Radiol* 29:2989–2997
- Lin JZ, Zhang L, Zhang CY, Yang L, Lou HN, Wang ZG (2016) Application of gemstone spectral computed tomography imaging in the characterization of solitary pulmonary nodules: preliminary result. *J Comput Assist Tomogr* 40:907–911
- Lin LY, Zhang Y, Suo ST, Zhang F, Cheng JJ, Wu HW (2018) Correlation between dual-energy spectral CT imaging parameters and pathological grades of non-small cell lung cancer. *Clin Radiol* 73(412):e412.e1–e412.e7
- Liu L, Zhi X, Liu B, Zhang Y (2016) Utilizing gemstone spectral CT imaging to evaluate the therapeutic efficacy of radiofrequency ablation in lung cancer. *Radiol Med* 121:261–267
- Liu Z, Zhang Z, Chen C, Hong N (2018a) Value of virtual monochromatic spectral images with metal artifact reduction algorithm in dual-energy computed tomography-guided microcoil localization of pulmonary nodules. *Medicine* 97:e11562
- Liu G, Li M, Li G, Li Z, Liu A, Pu R, Cao H, Liu Y (2018b) Assessing the blood supply status of the focal ground-glass opacity in lungs using spectral computed tomography. *Korean J Radiol* 19:130–138
- MacMahon H, Austin JH, Gamsu G, Herold CJ, Jett JR, Naidich DP, Patz EF Jr, Swensen SJ (2005) Guidelines for management of small pulmonary nodules detected on CT scans: a statement from the Fleischner Society. *Radiology* 237:395–400
- Maldonado F, Daniels CE, Hoffman EA, Yi ES, Ryu JH (2007) Focal organizing pneumonia on surgical lung biopsy: causes, clinicoradiologic features, and outcomes. *Chest* 132:1579–1583
- Milne EN (1967) Circulation of primary and metastatic pulmonary neoplasms. A postmortem microarteriographic study. *Am J Roentgenol Radium Therapy, Nucl Med* 100:603–619
- Ohno Y, Nishio M, Koyama H, Miura S, Yoshikawa T, Matsumoto S, Sugimura K (2014) Dynamic contrast-enhanced CT and MRI for pulmonary nodule assessment. *AJR Am J Roentgenol* 202:515–529
- Ramnath N, Dilling TJ, Harris LJ, Kim AW, Michaud GC, Balekian AA, Diekemper R, Detterbeck FC, Arenberg DA (2013) Treatment of stage III non-small cell lung cancer: diagnosis and management of lung cancer, 3rd ed: American College of Chest Physicians evidence-based clinical practice guidelines. *Chest* 143:e314S–e340S
- Ren Y, Jiao Y, Ge W, Zhang L, Hua Y, Li C, Zhai W, Tang X, He W, Fang M, Zheng X (2018) Dual-energy computed tomography-based iodine quantitation for response evaluation of lung cancers to chemoradiotherapy/radiotherapy: a comparison with fluorine-18 fluorodeoxyglucose positron emission tomography/computed tomography-based positron emission tomography/computed tomography response evaluation criterion in solid tumors. *J Comput Assist Tomogr* 42:614–622
- Roessl E, Proksa R (2007) K-edge imaging in x-ray computed tomography using multi-bin photon counting detectors. *Phys Med Biol* 52:4679–4696

- Rubin GD (2015) Lung nodule and cancer detection in computed tomography screening. *J Thorac Imaging* 30:130–138
- Ruoslahti E (2002) Specialization of tumour vasculature. *Nat Rev Cancer* 2:83–90
- Salem A, Asselin MC, Reymen B, Jackson A, Lambin P, West CML, O'Connor JPB, Faivre-Finn C (2018) Targeting hypoxia to improve non-small cell lung cancer outcome. *J Natl Cancer Inst* 110. <https://doi.org/10.1093/jnci/djx160>
- Sekiguchi T, Ozawa Y, Hara M, Nakagawa M, Goto T, Shibamoto Y (2019) Visibility of the hilar lymph nodes using advanced virtual monoenergetic low-keV images for preoperative evaluation of lung cancer. *Br J Radiol* 92:20180734
- Shikhaliyev PM (2005) Beam hardening artefacts in computed tomography with photon counting, charge integrating and energy weighting detectors: a simulation study. *Phys Med Biol* 50:5813–5827
- Silvestri GA, Gonzalez AV, Jantz MA, Margolis ML, Gould MK, Tanoue LT, Harris LJ, Detterbeck FC (2013) Methods for staging non-small cell lung cancer: diagnosis and management of lung cancer, 3rd ed: American College of Chest Physicians evidence-based clinical practice guidelines. *Chest* 143:e211S–e250S
- Si-Mohamed S, Cormode DP, Bar-Ness D, Sigovan M, Naha PC, Langlois JB, Chalabreysse L, Coulon P, Bleviss I, Roessl E, Erhard K, Boussel L, Douek P (2017) Evaluation of spectral photon counting computed tomography K-edge imaging for determination of gold nanoparticle biodistribution in vivo. *Nanoscale* 9:18246–18257
- Sun YS, Zhang XY, Cui Y, Tang L, Li XT, Chen Y, Zhang XP (2013) Spectral CT imaging as a new quantitative tool? Assessment of perfusion defects of pulmonary parenchyma in patients with lung cancer. *Chin J Canc Res* 25:722–728
- Sung H, Ferlay J, Siegel RL, Laversanne M, Soerjomataram I, Jemal A, Bray F (2021) Global cancer statistics 2020: GLOBOCAN estimates of incidence and mortality worldwide for 36 cancers in 185 countries. *CA Cancer J Clin* 71(3):209–249
- Symons R, Cork TE, Sahbaee P, Fuld MK, Kappler S, Folio LR, Bluemke DA, Pourmorteza A (2017a) Low-dose lung cancer screening with photon-counting CT: a feasibility study. *Phys Med Biol* 62:202–213
- Symons R, Krauss B, Sahbaee P, Cork TE, Lakshmanan MN, Bluemke DA, Pourmorteza A (2017b) Photon-counting CT for simultaneous imaging of multiple contrast agents in the abdomen: an in vivo study. *Med Phys* 44:5120–5127
- Symons R, Cork TE, Lakshmanan MN, Evers R, Davies-Venn C, Rice KA, Thomas ML, Liu CY, Kappler S, Ulzheimer S, Sandfort V, Bluemke DA, Pourmorteza A (2017c) Dual-contrast agent photon-counting computed tomography of the heart: initial experience. *Int J Cardiovasc Imaging* 33:1253–1261
- Taguchi K, Iwanczyk JS (2013) Vision 20/20: single photon counting x-ray detectors in medical imaging. *Med Phys* 40:100901
- Travis WD, Brambilla E, Nicholson AG, Yatabe Y, Austin JHM, Beasley MB, Chiriac LR, Dacic S, Duhig E, Flieder DB, Geisinger K, Hirsch FR, Ishikawa Y, Kerr KM, Noguchi M, Pelosi G, Powell CA, Tsao MS, Wistuba I (2015) The 2015 world health organization classification of lung tumors: impact of genetic, clinical and radiologic advances since the 2004 classification. *J Thorac Oncol* 10:1243–1260
- Travis WD, Brambilla E, Geisinger KR (2016) Histological grading in lung cancer: one system for all or separate systems for each histological type? *Eur Respir J* 47:720
- Vogelstein B, Papadopoulos N, Velculescu VE, Zhou S, Diaz LA, Kinzler KW (2013) Cancer genome landscapes. *Science* 339:1546
- Wahl RL, Jacene H, Kasamon Y, Lodge MA (2009) From RECIST to PERCIST: evolving considerations for PET response criteria in solid tumors. *J Nucl Med* 50:122S
- Wang G, Zhang C, Li M, Deng K, Li W (2014) Preliminary application of high-definition computed tomographic Gemstone Spectral Imaging in lung cancer. *J Comput Assist Tomogr* 38:77–81
- Wu L, Cao G, Zhao L, Tang K, Lin J, Miao S, Lin T, Sun J, Zheng X (2018a) Spectral CT analysis of solitary pulmonary nodules for differentiating malignancy from benignancy: the value of iodine concentration spatial distribution difference. *Biomed Res Int* 2018:4830659
- Wu F, Zhou H, Li F, Wang JT, Ai T (2018b) Spectral CT imaging of lung cancer: quantitative analysis of spectral parameters and their correlation with tumor characteristics. *Acad Radiol* 25:1398–1404
- Xiao H, Liu Y, Tan H, Liang P, Wang B, Su L, Wang S, Gao J (2015) A pilot study using low-dose Spectral CT and ASIR (Adaptive Statistical Iterative Reconstruction) algorithm to diagnose solitary pulmonary nodules. *BMC Med Imaging* 15:54
- Yang F, Dong J, Wang X, Fu X, Zhang T (2017) Non-small cell lung cancer: spectral computed tomography quantitative parameters for preoperative diagnosis of metastatic lymph nodes. *Eur J Radiol* 89:129–135
- Yi CA, Lee KS, Kim EA, Han J, Kim H, Kwon OJ, Jeong YJ, Kim S (2004) Solitary pulmonary nodules: dynamic enhanced multi-detector row CT study and comparison with vascular endothelial growth factor and microvessel density. *Radiology* 233:191–199
- Yoo SY, Kim Y, Cho HH, Choi MJ, Shim SS, Lee JK, Baek SY (2013) Dual-energy CT in the assessment of mediastinal lymph nodes: comparative study of virtual non-contrast and true non-contrast images. *Korean J Radiol* 14:532–539
- Yu L, Leng S, McCollough CH (2012) Dual-energy CT-based monochromatic imaging. *AJR Am J Roentgenol* 199:S9–s15
- Yu Y, Wang X, Shi C, Hu S, Zhu H, Hu C (2019) Spectral computed tomography imaging in the differential

- diagnosis of lung cancer and inflammatory myofibroblastic tumor. *J Comput Assist Tomogr* 43:338–344
- Yue D, Ru Xin W, Jing C, Fan Rong C, Li Fei S, Ai Lian L, Hong LY (2017) Virtual monochromatic spectral imaging for the evaluation of vertebral inconspicuous osteoblastic metastases from lung. *Acta Radiol* 58:1485–1492
- Zhao F, Yan SX, Wang GF, Wang J, Lu PX, Chen B, Yuan J, Zhang SZ, Wang YX (2014) CT features of focal organizing pneumonia: an analysis of consecutive histopathologically confirmed 45 cases. *Eur J Radiol* 83:73–78
- Zhou W, Montoya J, Gutjahr R, Ferrero A, Halaweish A, Kappler S, McCollough C, Leng S (2017) Lung nodule volume quantification and shape differentiation with an ultra-high resolution technique on a photon-counting detector computed tomography system. *J Med Imaging (Bellingham)* 4:043502



Gastrointestinal Imaging: Oncology (Liver, Pancreas, Bowel Cancer, and Treatment Response)

Simon Lennartz and Nils Große Hokamp

Contents

1	Introduction	220
2	Clinical Applications of Dual-Energy CT for Oncologic Imaging of the Liver	220
2.1	Imaging Protocols.....	220
2.2	Challenges in Imaging the Liver.....	221
2.3	Liver Lesion Detection and Delineation.....	221
2.4	Liver Lesion Characterization.....	224
2.5	Response Assessment of Hepatocellular Carcinoma.....	224
3	Dual-Energy Imaging Applications for Pancreatic Imaging	224
3.1	Imaging Protocols.....	224
3.2	Imaging of Pancreatic Lesions.....	225
3.3	Imaging of Pancreatic Cancer.....	226
4	Oncologic Imaging of the Gastrointestinal System with Dual-Energy CT	226
4.1	Imaging Protocols.....	226
4.2	Upper GI Tract.....	227
4.3	Lower Intestinal Tract.....	227
5	Oncologic Applications of DECT in the Abdomen outside of Parenchymal Organs	229
6	The Role of Dual-Energy CT for Assessing Oncologic Treatment Response	230
6.1	Assessment of Treatment Response After Locoregional Therapy.....	230
6.2	Assessment of Treatment Response After Antiangiogenic Treatment.....	231
	References	232

Abstract

S. Lennartz · N. Große Hokamp (✉)
Institute for Diagnostic and Interventional Radiology,
University Hospital Cologne, Cologne, Germany
e-mail: simon.lennartz@uk-koeln.de; nils.grosse-hokamp@uk-koeln.de

Oncologic diseases of the gastrointestinal tract encompass a wide variety of tumors and pathological conditions. Dual-Energy CT can be tremendously helpful in this instance, par-

ticularly with regard to visualization of subtle tumor masses in parenchymal organs such as the liver or the pancreas. In this context, low-keV virtual monoenergetic images and iodine maps play an important role. Other application fields of dual-energy CT for diagnosing oncologic diseases of the gastrointestinal tract include CT colonography, assessment of peritoneal lesions and evaluation of treatment response. This chapter will provide a conclusive overview on the most important clinical use cases as well as scientific concepts that are still pending clinical implementation.

1 Introduction

Dual-energy CT (DECT) is a clinically useful technique for a wide range of oncologic imaging applications of the hepatobiliary system, the pancreas, and the gastrointestinal tract. Regarding oncologic imaging of the abdomen, both the qualitative improvement of iodine and soft tissue contrast and the option for material quantification provided by DECT have been extensively investigated and can be of clinical use. While the first mentioned provides a more accurate lesion delineation, lesion detection, and assessment of tumor infiltration, the second may be useful for quantitative lesion characterization.

Despite substantial technical developments of CT in the past decades including multidetector CT and 3D volumetric rendering, lesion detection and delineation in parenchymal organs such as the liver and pancreas in CT is still challenging due to its inherently limited soft tissue contrast. This particularly accounts for small and/or intermediate lesions with similar CT characteristics as the surrounding organ parenchyma. Therefore, the capability of DECT to increase the lesion-to-parenchyma contrast by means of low energy virtual monoenergetic images as well as material-specific images such as iodine maps adds clinical value in many diagnostic scenarios. Moreover, the option of DECT-derived material quantification allows among others reconstructing iodine maps as well as virtual unenhanced images. They can help characterizing incidentally detected ambiguous or intermediate lesions

when there is no unenhanced acquisition available. Moreover, iodine maps have been explored as an alternate method for characterization of and assessment of response to anticancer treatment.

This chapter will focus on the most important DECT applications for imaging of the gastrointestinal and hepatobiliary system as well as the pancreas with a focus on oncologic imaging. Further, it will include a review of current data on the potential of quantitative characteristics of DECT for characterization and treatment response assessment in oncologic diseases of the abdomen.

2 Clinical Applications of Dual-Energy CT for Oncologic Imaging of the Liver

2.1 Imaging Protocols

In imaging of the liver, administration of i.v.-contrast is usually required, while administration of oral contrast (positive or negative) depends on the clinical question and field of view. Pertaining to imaging phases, the portal venous phase is the “standard” phase at most institutions. Depending on the question in focus, early/late arterial (e.g. unknown hepatic malignancy, hepatocellular carcinoma, cholangiocellular carcinoma, known cancer with possibly hypervascular metastasis, prior surgery) or late phases (e.g. unknown hepatic malignancy, hepatocellular carcinoma, cholangiocellular carcinoma) might be acquired in addition. Unenhanced examinations can provide incremental information in select cases (e.g. pre-/post local ablative therapy), however, are not considered standard in imaging of the liver (Prokop and Galanski 2002). The need for a true-unenhanced phase furthermore can be questioned if VNC from any DECT acquisition can be reconstructed. In a consensus paper published by Patel et al. in 2016, DECT acquisition is suggested for the arterial phase for DSCT and kVp-switching DECT, while this selection naturally is not required for dual-layer detector DECT and photon counting detector CT.

Specific use cases of VNC, low keV virtual monoenergetic images, and material-specific maps for imaging of the liver are elucidated hereafter and summarized in Table 1.

Table 1 Overview on key applications of different DECT-derived reconstructions in liver imaging

Reconstruction	Application
Low keV virtual monoenergetic images	Detection and delineation of hypoattenuating and hyperattenuating liver lesions Evaluation of vessels, e.g. prior to surgery
Virtual noncontrast images	Possible replacement for true-unenhanced images for assessment of lesion enhancement in dedicated multiphasic protocols
Iodine maps	Liver lesion characterization

2.2 Challenges in Imaging the Liver

There are three key diagnostic challenges at CT imaging of the liver: first, the accurate detection and delineation of lesions at oncologic staging or follow-up; second, the differential diagnosis (i.e. accurate characterization) of these lesions; and third, staging and response assessment of hepatic tumors, the last of which will be addressed in the dedicated subsection below about DECT-enabled therapy response assessment.

2.3 Liver Lesion Detection and Delineation

Many studies have elucidated the capability of DECT to improve the contrast of hyper- and hypoattenuating liver lesions and to thereby allow for an improved lesion detection and delineation (Robinson et al. 2010). While the underlying principle of highlighting the iodine contrast in DECT is the same for improving the assessment of both hypo- and hyperattenuating lesions, the contrast improvement of hyperattenuating lesions is based on the increased attenuation of the lesion itself, while for hypoattenuating lesions, the higher contrast of the circumjacent organ parenchyma and the relatively lower iodine contrast enhancement of the lesion are exploited. Whereas earlier generation DECT systems showed a higher image noise in virtual monoenergetic images at low energy levels, recent

improvements in hard- and software as well as the introduction of novel technical approaches to DECT resulted in significant noise reductions in low keV virtual monoenergetic images which is why these reconstructions can be used as clinical “screening” tools, allowing for an optimal lesion-to-parenchyma contrast without noticeable increase in image noise (Grant et al. 2014; Große Hokamp et al. 2019).

Hypoattenuating hepatic lesions are frequently encountered incidentally in routine, portal venous phase CT examinations of the abdomen. While many of these lesions fall in the category “too small to characterize” and eventually turn out benign, the probability of underlying malignancy or a small liver metastasis can be higher depending on the patient’s history (Fig. 1). Detecting hypoattenuating lesions in clinical routine is the first step for further lesion characterization and clinical decision making on the necessity of additional imaging (e.g. dedicated liver MRI or contrast-enhanced ultrasound) or follow-up examinations. Many studies found that the improved contrast of hypoattenuating liver lesions in low keV virtual monoenergetic images facilitates improvements in their detection and delineation (Husarik et al. 2015; Altenbernd et al. 2016a; Hanson et al. 2018; Große Hokamp et al. 2018a). Conversely, it was described that in patients with liver steatosis, the advantage of low energy virtual monoenergetic images for imaging hypoattenuating lesions might be lower or even nullified (Nattenmüller et al. 2015). Opposed to this, Grosse Hokamp et al. demonstrated in an ex-vivo set-up that benefits from low keV imaging may be leveraged even in poorly attenuating livers and mildly hypodense lesions; however, systematic validation of these findings in vivo is necessary to clarify this case (Große Hokamp et al. 2018b).

Hyperattenuating lesions of the liver comprise a wide spectrum of differential diagnoses ranging from benign lesions with often characteristic appearance (e.g. focal nodular hyperplasia, hemangioma) to liver metastasis or primary tumors such as hepatocellular carcinoma. Whereas detection of hypervascular lesions may often be effortless in case of a distinctive enhancement, lesions with a more subtle enhancement or a

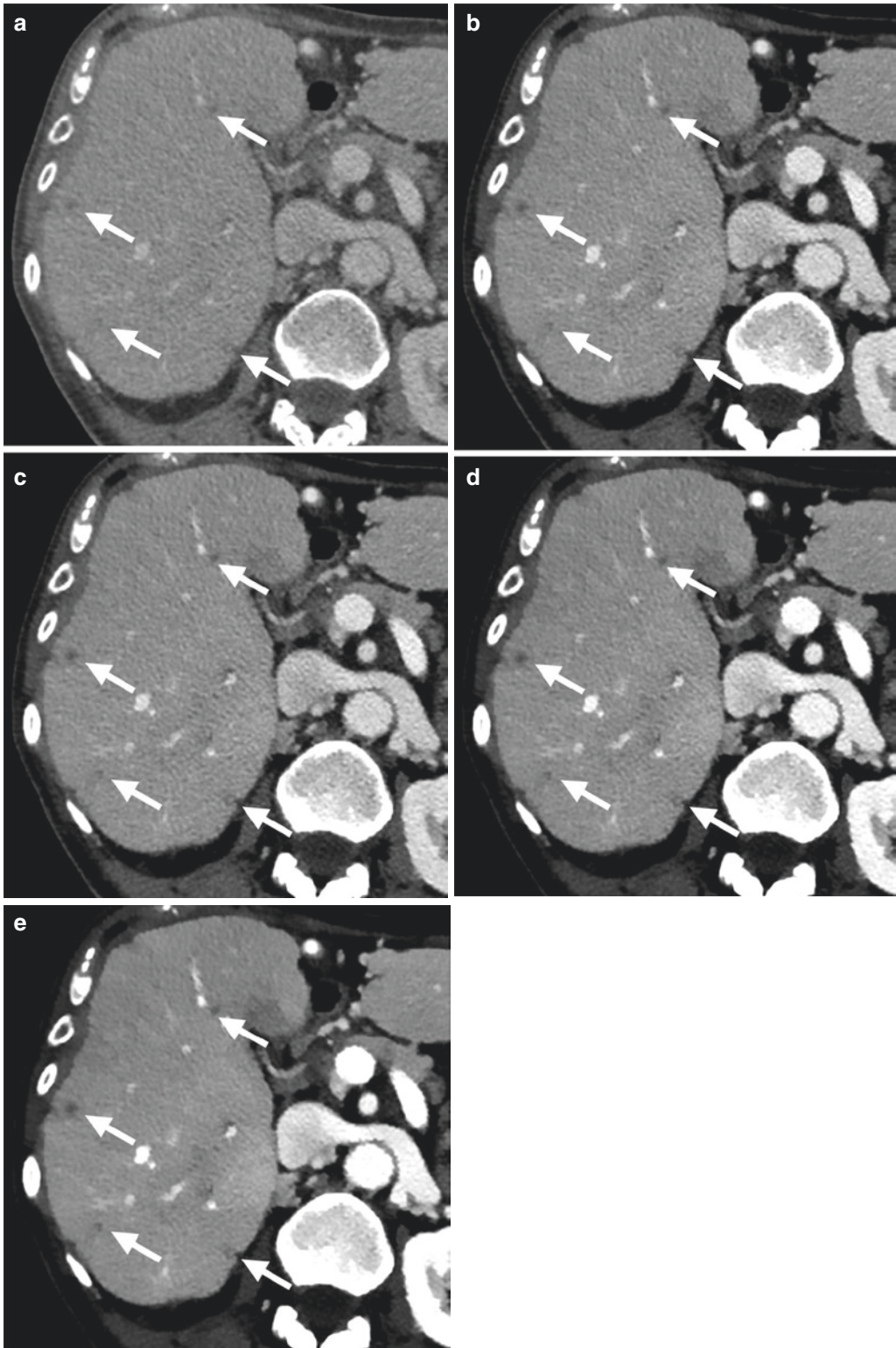


Fig. 1 Patient with new appearance of hypodense liver lesions suspicious for metastatic disease. While these lesions are very subtle in the conventional image equivalent:

(a) the contrast between the lesions and liver parenchyma is gradually increased with decreasing keV level from 70 keV (b) down to 40 keV (e)

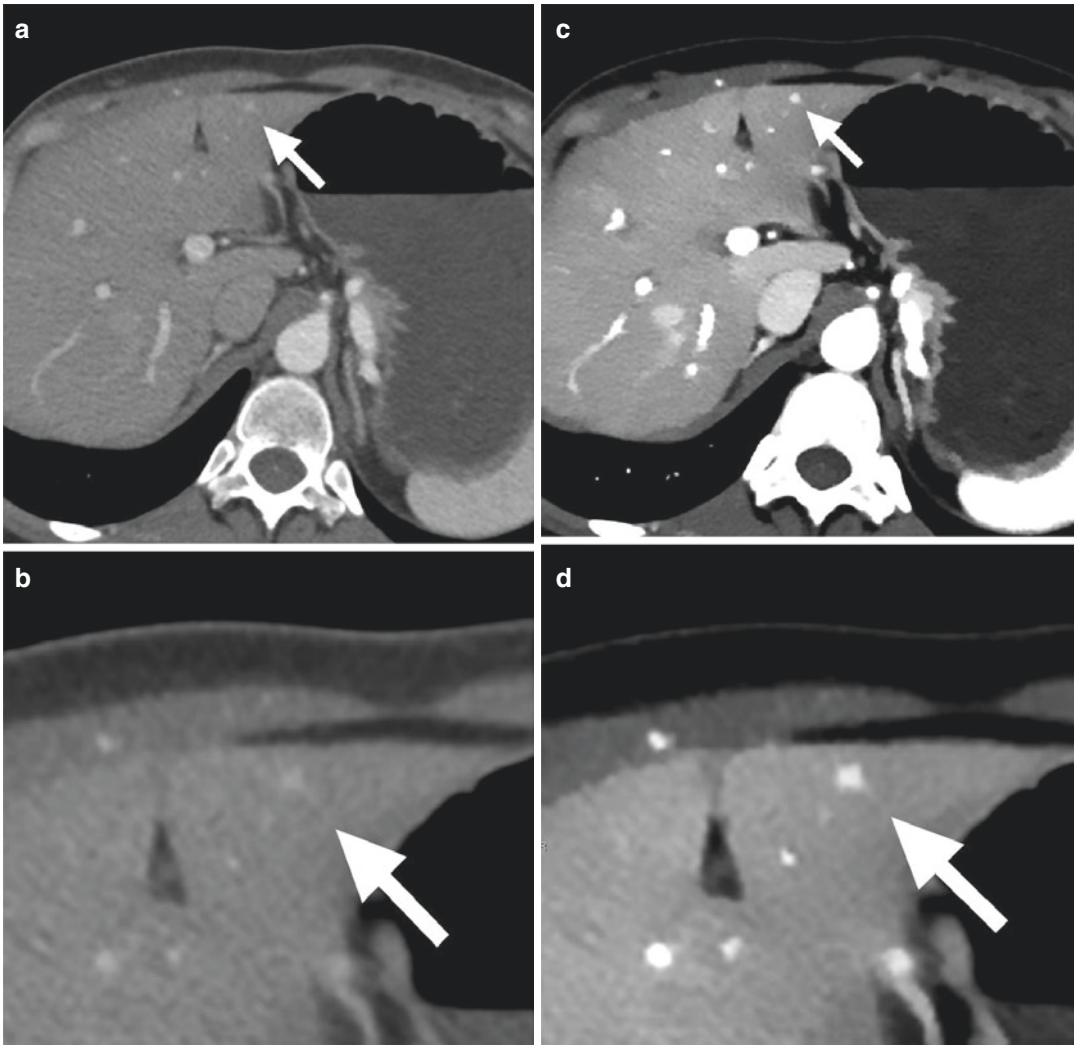


Fig. 2 Patient with incidentally detected hyperdense lesion in the left liver lobe. The lesion is only subtle with low contrast to circumjacent parenchyma (**a, b**), whereas

dual-energy CT derived virtual monoenergetic images 40 keV (**b, c**) allow for improved delineation by increasing the lesion-to-parenchyma contrast

smaller size might still be missed, hampering accurate diagnosis. DECT can highlight the iodine hyperenhancement of lesions in comparison to the surrounding liver parenchyma in low keV virtual monoenergetic images or low kVp acquisitions, respectively (Altenbernd et al. 2011; Shuman et al. 2014; Große Hokamp et al. 2018b). This effect facilitates an improved delineation and conspicuity of hypervascular lesions of the liver (Fig. 2), more accurate measurements of hyperattenuating lesion components, and a

more accurate distinction between characteristic enhancement patterns.

To facilitate and optimize diagnostic assessment of any focal lesions, dedicated window settings have been proposed for a long time. Historically, this arose from the lacking possibility to adjust window settings on a printed film; however, quickly became implemented in the DICOM standard. For conventional images, a window center of 100 and a width of 150 have been proposed and commonly accepted (Mayo-

Smith et al. 1999); however, considering the altered contrast characteristics in low keV virtual monoenergetic images it is obvious that adjustments become necessary. They further report that appropriate window settings can be semi-automatically obtained from simple attenuation measurements using linear models (Große Hokamp et al. 2018c), e.g. a center of 200 and a width of 405 are suggested when interpreting 40 keV virtual monoenergetic images for hepatic lesions in portal venous phase. Naturally, such settings have to be adjusted to the individual examination protocol; however, this can easily be done using suggested conversion formulas (e.g.: center = $HU_{liver} + 15$; width = $6 \times HU_{liver} + 12$; with HU_{liver} being measured in the respective reconstruction). Similar strategies have been suggested for imaging of other organ regions (Hickethier et al. 2018).

2.4 Liver Lesion Characterization

Apart from the qualitative improvements in the assessment of liver lesions that can be attained by means of low keV virtual monoenergetic images, the material decomposition and quantification capabilities of DECT further allow for a more accurate characterization of hepatic lesions as compared to conventional, single-energy CT. However, it should be acknowledged that these approaches employing quantitative thresholds mostly have not been validated across available DECT scanner types and should therefore be constrained in regard to their clinical application to the original scanner type on which the corresponding study was performed. In one study, Kaltenbach et al. suggested that metastases from hepatic neuroendocrine tumors may be distinguished from hepatocellular carcinoma by means of (normalized) iodine uptake and attenuation measurements in early arterial phase, with iodine-based measurements being superior (Kaltenbach et al. 2018); the metastases from neuroendocrine tumors showed a significantly lower normalized iodine concentration. Yu et al., in another study focused on discerning HCC from frequent differential diagnoses, found that iodine quantification

could differentiate HCC from focal nodular hyperplasia (Yu et al. 2013). The latter showed a significantly higher normalized iodine concentration both when the lesions were normalized to physiologically appearing liver parenchyma and to the abdominal aorta. In another study, it was reported that iodine maps were more accurate in differentiating small hepatic hemangioma from HCC as compared to qualitative differentiation using conventional CT (Lv et al. 2011). Patel et al. found that malignant lesions were detected more accurately among incidentally found hypoattenuating liver lesions when using an iodine-based threshold as compared to a HU-based threshold. They reported a significantly higher iodine concentration of 1.7 mg/ml in hypoattenuating lesions with underlying malignancy as opposed to a mean iodine concentration of 0.6 mg/ml in hypoattenuating lesions that were benign (Patel et al. 2018). Last, Reimer et al. recently reported that low keV imaging is superior in detecting washout phenomena in an HCC population (Reimer et al. 2020).

2.5 Response Assessment of Hepatocellular Carcinoma

As a tumor for which its enhancement patterns are among the most important diagnostic criteria, hepatocellular carcinoma has been subject to several studies investigating the potential benefit of using low keV virtual monoenergetic images and iodine maps for response assessment particularly after locoregional therapy. This topic will be addressed in Sect. 6.

3 Dual-Energy Imaging Applications for Pancreatic Imaging

3.1 Imaging Protocols

Protocols for pancreatic imaging are subject of an ongoing discussion and most recommendations directly transfer to DECT imaging in suspected pancreatic disease (Table 2). Fasting prior

Table 2 Overview on applications of different DECT-derived reconstructions for imaging of the pancreas

Reconstruction	Application
Low keV virtual monoenergetic images	Detection and delineation of incidental lesions Assessment of neuroendocrine and other hypervascular tumors of the pancreas Delineation of pancreatic cancer Evaluation of tumor extension and (vascular) infiltration in pancreatic cancer
Iodine maps	Differentiation of pancreatic cancer and mass-forming pancreatitis (explorative)
Virtual noncontrast	Detection of calcifications in chronic pancreatitis

to examination is commonly conducted. Most sites suggest negative oral contrast (1000–1500 ml) including 250 ml immediately prior to image acquisition. Furthermore, administration of buscopan is often advocated for. Dependent on the clinically suspected condition suggested contrast phases include unenhanced (pancreatitis), early and late arterial (suspected carcinoma, neuroendocrine tumor), and parenchymatous or portal venous phases (aforementioned and trauma); however, the specific protocols settings (including timing) as well as contrast media application (including rate, volume, concentration) vary largely between institutions (Prokop and Galanski 2002).

Omitting an unenhanced phase can be considered when another series is acquired in DECT mode and therefore virtual noncontrast image reconstructions are available. When examining a patient on an emission-based DECT system, the phase in which DECT data is acquired needs to be chosen. In this context, a balance between radiation-dose, biological and technological presets has to be found. It appears that most institutions chose the arterial phase to serve as DECT acquisition (Mastrodicasa et al. 2019).

Image reconstructions used in assessment of pancreatic disease include virtual noncontrast, low energy virtual monoenergetic (e.g. 50 keV), and iodine density maps (possibly as fused recon-

structions) in addition to blended or true conventional images.

3.2 Imaging of Pancreatic Lesions

In CT imaging of the pancreas, the accurate detection of incidental lesions is important as some of them may require additional imaging, e.g. with MRI or follow-up examinations to rule out malignancy. While lesions with a high contrast to the surrounding parenchyma such as typical hypervascular neuroendocrine tumors and poorly vascularized, clearly hypodense pancreatic adenomas may be easy to depict even in single-energy, contrast-enhanced CT, many pancreatic lesions such as isoattenuating or mildly hypoattenuating pancreatic adenocarcinomas as well as hypovascular neuroendocrine tumors are more subtle and can easily be missed, particularly when they are of smaller size. This accounts even more for incidental detection in portal venous phase examinations without a dedicated pancreatic phase in which the contrast even of typical lesions is often sub-optimal. DECT can enable improved depiction of such lesions following the same principle that is exploited for liver imaging: increasing soft tissue and iodine enhancement to highlight differences herein between the lesion itself and the surrounding parenchyma (Table 2). Consequently, multiple studies using many different DECT systems have concordantly shown that low keV virtual monoenergetic images improve conspicuity and diagnostic assessment of focal pancreatic lesions (McNamara et al. 2015; Quiney et al. 2015; El Kayal et al. 2019)—this principle accounts for iso- to hypoattenuating lesions such as pancreatic adenocarcinoma (Bhosale et al. 2015; Quiney et al. 2015), cystic pancreatic lesions (Laukamp et al. 2021) as well as hypervascularized lesions such as neuroendocrine tumors (Lin et al. 2012). Of note, it has been shown that low energy virtual monoenergetic images improve detection of small and isoattenuating pancreatic ductal adenocarcinomas and hypovascular/isoattenuating

neuroendocrine tumors as well (Lin et al. 2012; Patel et al. 2017).

Compared to the unequivocal evidence on improved qualitative lesion assessment which has been reported for most available dual-energy CT scanner types, data on quantitative differentiation of pancreatic lesions is sparser. For example, Chu et al. suggested that iodine maps may be helpful for distinguishing between solid and cystic pancreatic lesions. Moreover, virtual unenhanced images may be used to differentiate calcifications from linear iodine enhancement in cystic pancreatic lesions (Chu et al. 2012).

3.3 Imaging of Pancreatic Cancer

Pancreatic cancer greatly contributes to cancer mortality. The majority of pancreatic cancers show metastatic spread at the time of diagnosis. However, surgical resection of the tumor often still yields the best chance of attaining long-term survival. In assessing pancreatic cancer, DECT can help tackling three important challenges: detecting subtle primary tumors, delineating tumor margins, and assessing possible infiltration of other anatomical structures (Gupta et al. 2016).

CT plays an important role in the presurgical staging of pancreatic cancer, particularly with regard to the accurate assessment of potential infiltration of extrapancreatic structures such as circumjacent vessels. Allowing abdominal surgeons to evaluate resectability requires an accurate assessment of it and to which degree vessels are affected by the tumor. Due to the highlighting of intravascular contrast, low energy virtual monoenergetic images allow for an improved assessment of vessel infiltration in pancreatic cancer (Bellini et al. 2017; Nagayama et al. 2020).

Another possible benefit of DECT for pancreatic cancer imaging might be the capability to differentiate pancreatic adenocarcinoma from chronic mass-forming pancreatitis, an important imaging differential diagnosis. In this regard, a pilot study by Yin et al. showed that normalized iodine concentration in combination with spec-

tral slopes may distinguish between these two entities (Yin et al. 2015).

4 Oncologic Imaging of the Gastrointestinal System with Dual-Energy CT

Staging of malignancies of the gastrointestinal tract often requires the use of different modalities including CT or PET/CT for assessment of distant metastasis and presurgical planning as well as endoscopy for assessment of tumor infiltration or metastatic spread to locoregional lymph nodes. However, there are various potential applications of DECT that may benefit oncologic imaging of the gastrointestinal system including improved tumor detection, e.g. of esophageal cancer or neuroendocrine tumors, as well as DECT colonography (Table 3).

4.1 Imaging Protocols

Various institutional protocols are available for GI imaging. Little alterations from standard CT protocols are required with regard to luminal contrast. In this context it needs to be acknowledged that the bowel wall assessment is hampered by administration of positive oral contrast. Besides, this being an issue well known from conventional CT, the impairment naturally is aggravated in low keV imaging. In the authors' institution and supported by increasing evidence, positive oral contrast is therefore avoided whenever possible (Kammerer et al. 2015).

Table 3 Overview on applications of different DECT-derived reconstructions for imaging of the GI system

Reconstruction	Application
Low keV virtual monoenergetic images	Improved detection and delineation of focal masses
Iodine maps	Improved detection, particularly of small lesions Differentiation between different entities
Virtual noncontrast images	Lesion characterization Fecal tagging, particularly in DECT colonography

Pertaining to the type of positive contrast medium, Gabbai et al. reported that differentiating iodine and barium is possible to some extent in an *ex vivo* setting; however, evidence with regard to *in vivo* applicability is missing (Gabbai et al. 2015).

For evaluation of the GI tract, usually a single contrast phase is sufficient; therefore, no decision on DECT acquisition phase must be made. If, however, an early arterial or angiographic phase is required (e.g. prior to surgery), as elucidated earlier, most institutions perform the earlier acquisition in dual-energy mode (if using an emission-based DECT system).

4.2 Upper GI Tract

Assessing the upper GI tract naturally is not the primary domain of CT; however, particularly in oncologic disease, CT remains standard of care to assess tumor burden. Zopfs et al. recently reported that 40 keV virtual monoenergetic images hold value in assessing esophageal cancer locoregionally. They demonstrated that these reconstructions can be helpful in qualitative assessment of the primary tumor and furthermore in depiction of locoregional lymph nodes. Yet, they also found that the inherited limitation of CT in detecting tumor infiltration is not overcome (Zopfs et al. 2021). Figure 3 neatly demonstrate this benefit in terms of qualitative assessment. Figure 3c furthermore illustrates a possible benefit from iodine maps in this context; however, their clinical impact in assessing esophageal cancer is subject of ongoing investigations.

Similar findings account for gastric malignancy. Here, however, imaging of gastrointestinal stromal tumors (GIST) illustrates the potential iodine maps hold for assessing treatment response (see Sect. 6).

As elucidated above, low keV imaging particularly is useful in hypervascular lesions and therefore considered to be of particular benefit in assessing neuroendocrine tumors. Benefits of these images in assessing pancreatic NET are described in the corresponding section. Intestinal manifestations of NET are most commonly

located in the jejunum or duodenum, while ileal manifestations are rare. Despite missing literature evidence in this context, the theoretical benefit from low keV virtual monoenergetic images and iodine map (overlays) translates to this application.

4.3 Lower Intestinal Tract

Note, this section deals with DECT applications for lower GI tumors only, while other diseases of the lower GI are discussed in the chapter “Bowel Imaging.”

Again, DECT imaging, particularly low keV virtual monoenergetic images and iodine maps (overlays), is promising means to improve detection and delineation of tumors (Fulwadhva et al. 2016). In this respect, it was reported that iodine maps and weighted average images derived from DECT facilitated detection of colorectal cancers with a sensitivity of 96.7% even without bowel preparation or insufflation (Boellaard et al. 2013). However, these findings are still subject to larger-scale validation.

In regard to quantitative use of iodine maps for lower intestinal tract imaging, researchers from China recently reported that arterial phase information in terms of iodine concentration were found helpful in image-based differentiation between well- and poorly differentiated colon cancers in 47 patients (Chuang-Bo et al. 2017). Al-Najami et al. performed a proof-of-concept investigation on lymph node characterization in rectal cancer using small samples of patients undergoing surgery. Patients were examined with iodinated contrast media intraoperatively immediately prior to resection. The specimen then underwent re-examination using a kVp-switching dual-energy CT. The authors suggest a cut-off of 2.58 mg/cc for their specific setting and small cohort, resulting in a sensitivity and specificity of 86% and 92%, respectively (Al-Najami et al. 2016). Yet, such cut-offs have not been validated on a larger scale and therefore should not be used for clinical decision making. In this context, the authors would like to draw attention to Sect. 6.

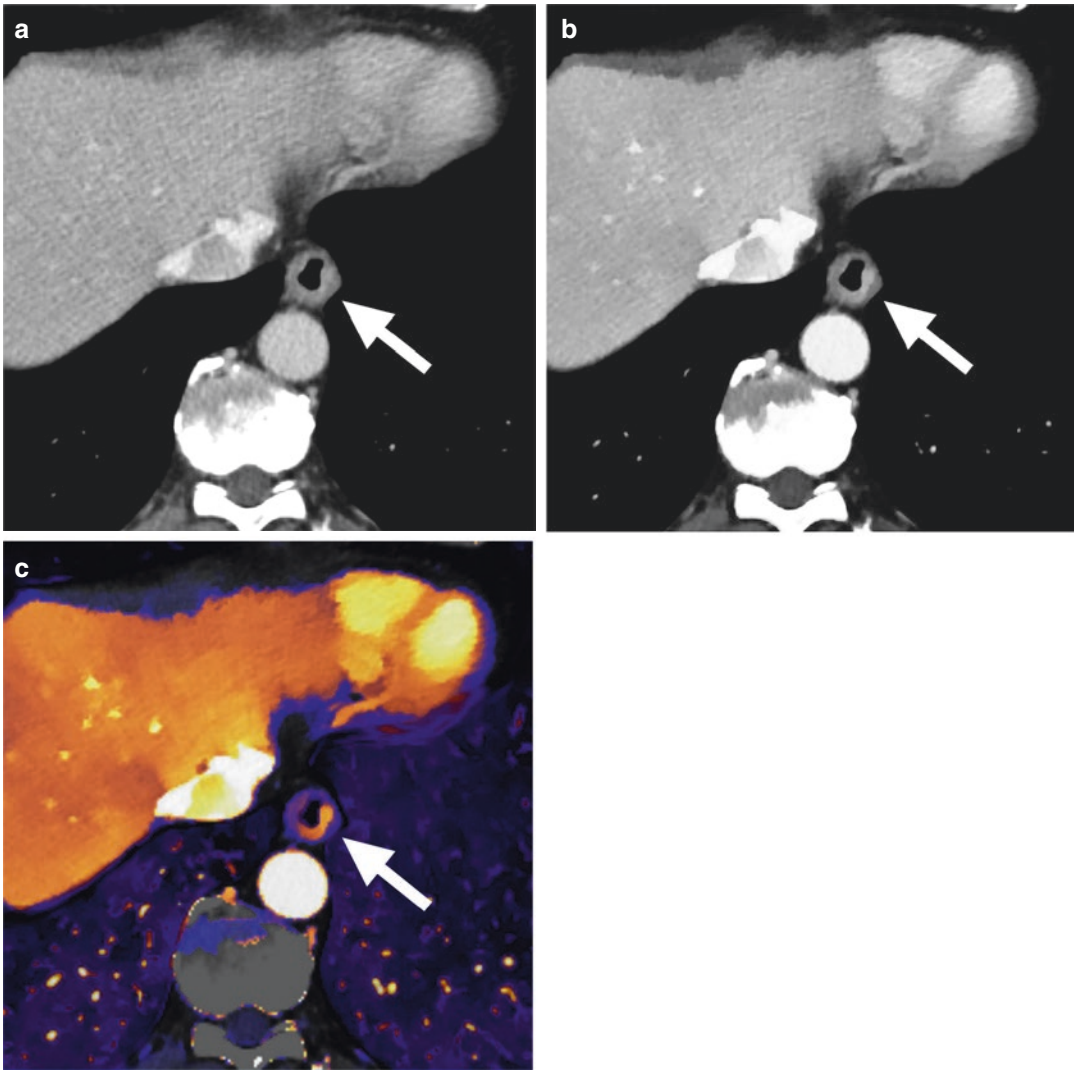


Fig. 3 Patient with path-proven esophageal cancer. At initial DECT staging, the contrast-enhancing semicircular thickening of the distal esophagus can be well appreciated in the virtual monoenergetic images at 40 keV (b) as well

as the iodine overlay image (c) whereas barely being perceivable in the conventional image (a). The localization correlated well with primary tumor localization determined with endoscopic ultrasound

4.3.1 Dual-Energy Colonography

CT colonography has been suggested as an alternative to optical colonoscopy for screening and diagnosis of colorectal carcinoma. There are two areas in which DECT may be useful for improving the diagnostic assessment in CT colonography: First, by using it for a procedure known as “electronic cleansing,” in which stool

is tagged previously to the examination and then virtually subtracted by DECT post-processing, facilitating accurate assessment of the bowel wall (Cai et al. 2013). Second, to differentiate findings such as stool, lipomas or adenomas from colorectal cancer by means of material-specific images such as iodine maps (Schaeffer et al. 2014).

5 Oncologic Applications of DECT in the Abdomen outside of Parenchymal Organs

Apart from improved lesion delineation or characterization within parenchymal organs, DECT can also enhance the assessment of abdominal oncologic disease manifestations outside of organs (Table 4). It has been shown that iodine overlay image may improve the assessment of peritoneal disease compared to a scenario where only conventional images are available (Fig. 4)

(Lennartz et al. 2019b, 2020). Similar results were found for virtual monoenergetic images at lower keV levels (Darras et al. 2019). However, it is

Table 4 Overview on applications of different DECT-derived reconstructions for imaging of the abdominal cavity

Reconstruction	Application
Low keV virtual monoenergetic images	Detection and delineation of small lesions
Iodine maps	Detection of peritoneal disease and differentiation from postoperative changes Lymph node characterization

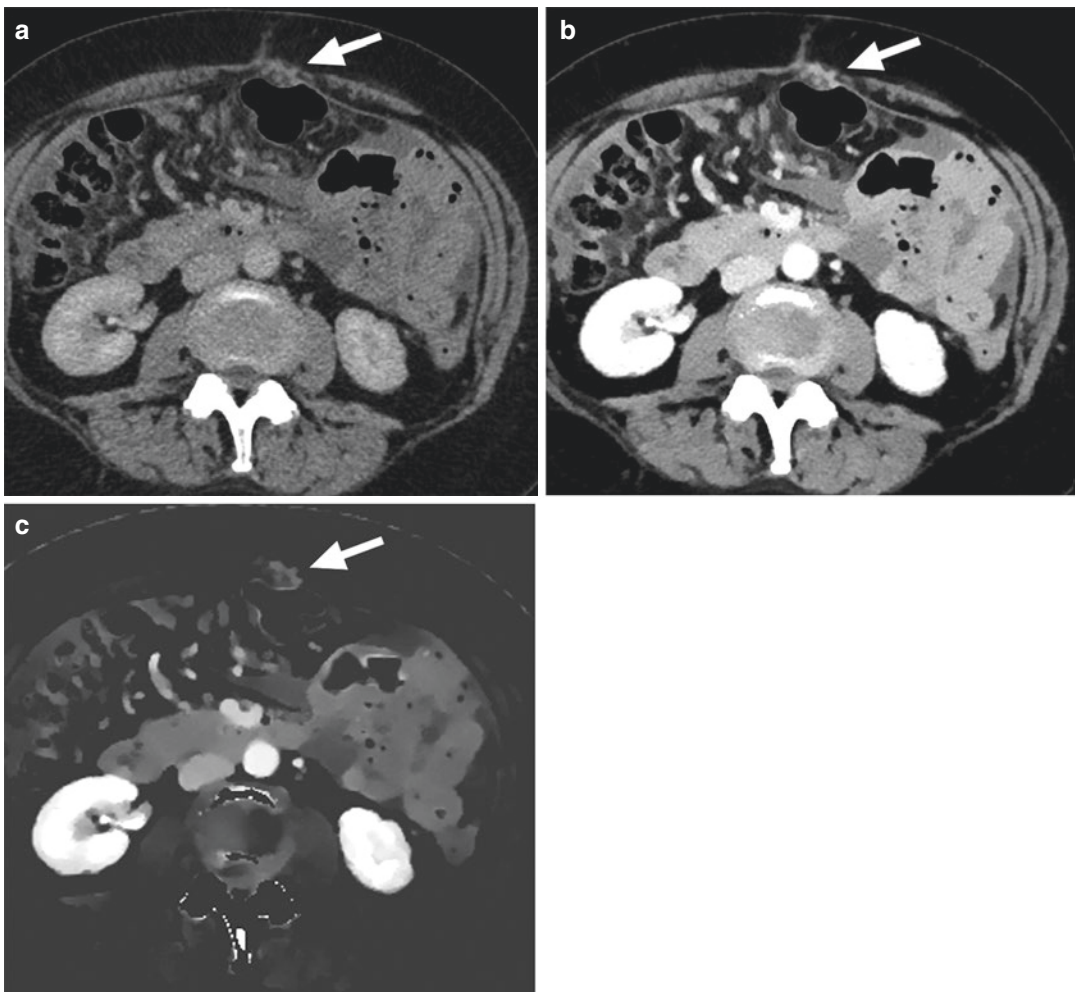


Fig. 4 Patient with newly diagnosed nodular peritoneal metastases adjacent to the anterior abdominal wall. Whereas the lesions are relatively subtle in the conven-

tional polyenergetic image (a), they are clearly depicted in the virtual monoenergetic image at 40 keV (b) as well as the iodine map (c)

worth noting that the attenuation of peritoneal lesions in contrast-enhanced CT may vary depending on factors such as the underlying disease, lesion size, or the individual patterns of disease spread in the abdominal cavity. Therefore, the diagnostic benefits provided by DECT-derived virtual monoenergetic or iodine overlay images remain to be verified at a larger scale. Another field of application at which DECT might complement the diagnostic assessment outside of dedicated parenchymal organs is the detection of nodal disease. In this respect, an explorative study on patients with known rectal cancer demonstrated that quantitative DECT parameters yielded a comparable accuracy in determining N-stage as MRI (Al-Najami et al. 2017). In another study, Sun et al. demonstrated that iodine concentration and fat fraction derived from DECT could help diagnosing lymph node metastasis in patients with esophageal cancer: here, the fat fraction was much lower in metastatic nodes and showed accuracies of around 80% in differentiating metastatic from non-metastatic nodes, while their short axis diameter was not significantly different (Sun et al. 2020). Another clinically challenging scenario that may occur is that it is unclear whether a nodal mass is due to metastatic spread from a particular tumor or if this mass is representing a nodal manifestation of lymphoma. In this regard, Marin et al. revealed that the iodine concentration as well as the fat fraction was significantly higher in lymphomas as compared to lymph node metastasis and that an iodine threshold of 2.0 mg/ml could differentiate these two malignant diseases with a sensitivity/specificity of 87% and 89%, respectively (Martin et al. 2018). It is important to note that the results of most of these studies on material quantification for assessing extraorganic disease are pending validation at a larger scale.

6 The Role of Dual-Energy CT for Assessing Oncologic Treatment Response

The rapid developments that took place in oncology over the past decade have revolutionized patient care in many areas. While being an

important pillar of oncologic follow-up, the radiological assessment of treatment response is still largely reliant on simple size measurements which often do not adequately reflect the tumor heterogeneity and the biological response to novel treatment options outside the realm of traditional cytotoxic therapies. A plethora of novel imaging biomarkers has therefore been investigated in this regard, among which quantitative DECT has shown promising results for assessing treatment response. Here, iodine concentration measurements performed on iodine maps is the most commonly applied approach.

The ex vivo validity of iodine map-based measurements has been thoroughly investigated and confirmed for all clinically available scanner types. Adapting these data into clinical routine has led to mixed observations; most authors highlight the dependency of iodine measurements on cardiac output. In recent, large scale studies our group suggested to utilize normalized iodine concentration measurements as this reduces the inter-individual variability, age, and gender-dependency and (which is of utmost importance for treatment response assessment) the intra-individual consistency of quantitative iodine measurements (Lennartz et al. 2019a; Zopfs et al. 2020). The mentioned studies performed normalization to the abdominal aorta and focused on portal venous phase acquisitions. It needs to be emphasized that this approach still is investigational while the clinical adoption is subject of ongoing research.

However, it is worth noting that few applications, particularly pertaining to treatment response assessment have been employed clinically yet as described in the consecutive sections.

6.1 Assessment of Treatment Response After Locoregional Therapy

One important area in which DECT may be a promising approach is the response assessment of patients undergoing locoregional therapy of

hepatocellular carcinoma. DECT-derived iodine maps reflect the iodine enhancement more accurately than conventional single-energy acquisitions. Therefore, they can serve as a surrogate parameter for lesion perfusion (Skornitzke et al. 2018). In this respect, several studies have shown that DECT-derived iodine maps facilitate depiction of presence or absence of residual tumor perfusion of hepatocellular carcinoma more accurately than conventional images. For response assessment of patients with radioembolization of hepatocellular carcinoma, Altenbernd et al. described that more patients were classified as having a stable disease as opposed to a progressive disease compared to an assessment based on AASLD criteria (Altenbernd et al. 2016b). In another pilot study, Bargellini et al. described that volumetric iodine uptake after Yttrium-90 radioembolization of hepatocellular carcinoma was highly reproducible and that patients that were defined as responders as per post-therapeutic reduction in volumetric iodine showed a significantly higher overall survival compared to the patients deemed as responders as per RECIST 1.1 or mRECIST (Bargellini et al. 2018). Pertaining to radiofrequency ablation, Vandenbroucke et al. outlined that DECT-derived features may help distinguish successful from unsuccessful ablative procedures by allowing an improved differentiation of residual tumors from post-interventional inflammatory changes (Vandenbroucke et al. 2015). Zhang et al. reported that volumetric iodine concentration more accurately predicted therapeutic response after microwave ablation in a rabbit model (Zhang et al. 2018).

Whereas most studies focusing on the use of DECT in locoregional therapy response assessment were focused on the liver, Parakh et al. furthermore reported that the additional use of iodine maps helped to distinguish postsurgical changes from local tumor recurrence in patients who underwent resection of pancreatic adenocarcinoma (Parakh et al. 2018).

6.2 Assessment of Treatment Response After Antiangiogenic Treatment

The capability of DECT to assess lesion perfusion has led to several studies investigating its potential use for assessing response by highlighting antiangiogenic treatment effects. Hellbach et al. reported that iodine quantification allowed for an improved characterization of response to tyrosine kinase inhibitors in patients with metastatic renal cell cancer: the iodine quantification of renal cell carcinoma metastasis was significantly more sensitive in detecting antiangiogenic treatment effects than the corresponding Hounsfield unit measurements (Hellbach et al. 2017). Similarly, Schramm et al. and Apfaltrer et al. highlighted a potential benefit of DECT in assessing response to targeted treatment in gastrointestinal stroma tumors (Schramm et al. 2011). Correspondingly, Meyer et al. reported that DECT allowed an improved prediction of response to tyrosine-kinase-inhibitor treatment than established response evaluation criteria such as RECIST and Choi criteria (Meyer et al. 2013).

Compliance with Ethical Standards

Funding None.

Disclosure of Interests Nils Große Hokamp receives speaker's fees and research support from Philips Healthcare. Nils Große Hokamp is consultant for Bristol-Myers Squibb. Nils Große Hokamp, and Simon Lennartz are on the editorial board of *European Radiology*.

Studies involving human

Ethical Approval This chapter does not contain any studies with human participants performed by any of the authors.

References

- Al-Najami I, Beets-Tan RGH, Madsen G, Baatrup G (2016) Dual-energy CT of rectal cancer specimens: a CT-based method for mesorectal lymph node characterization. *Dis Colon Rectum* 59:640–647. <https://doi.org/10.1097/DCR.0000000000000601>
- Al-Najami I, Lahaye MJ, Beets-Tan RGH, Baatrup G (2017) Dual-energy CT can detect malignant lymph nodes in rectal cancer. *Eur J Radiol* 90:81–88. <https://doi.org/10.1016/j.ejrad.2017.02.005>
- Altenbernd J, Heusner TA, Ringelstein A et al (2011) Dual-energy-CT of hypovascular liver lesions in patients with HCC: investigation of image quality and sensitivity. *Eur Radiol* 21:738–743. <https://doi.org/10.1007/s00330-010-1964-7>
- Altenbernd J, Forsting M, Lauenstein T, Wetter A (2016a) Improved image quality and detectability of hypovascular liver metastases on DECT with different adjusted window settings. *RöFo – Fortschritte auf dem Gebiet der Röntgenstrahlen und der Bildgeb Verfahren* 189:228–232. <https://doi.org/10.1055/s-0042-115571>
- Altenbernd J, Wetter A, Forsting M, Umutlu L (2016b) Treatment response after radioembolisation in patients with hepatocellular carcinoma—an evaluation with dual energy computed-tomography. *Eur J Radiol Open* 3:230–235. <https://doi.org/10.1016/j.ejro.2016.08.002>
- Bargellini I, Crocetti L, Turini FM et al (2018) Response assessment by volumetric iodine uptake measurement: preliminary experience in patients with intermediate-advanced hepatocellular carcinoma treated with Yttrium-90 radioembolization. *Cardiovasc Intervent Radiol* 41:1373–1383. <https://doi.org/10.1007/s00270-018-1962-8>
- Bellini D, Gupta S, Ramirez-Giraldo JC et al (2017) Use of a noise optimized monoenergetic algorithm for patient-size independent selection of an optimal energy level during dual-energy CT of the pancreas. *J Comput Assist Tomogr* 41:39–47. <https://doi.org/10.1097/RCT.0000000000000492>
- Bhosale P, Le O, Balachandran A et al (2015) Quantitative and qualitative comparison of single-source dual-energy computed tomography and 120-kVp computed tomography for the assessment of pancreatic ductal adenocarcinoma. *J Comput Assist Tomogr* 39:907–913. <https://doi.org/10.1097/RCT.0000000000000295>
- Boellaard TN, Henneman ODF, Streekstra GJ et al (2013) The feasibility of colorectal cancer detection using dual-energy computed tomography with iodine mapping. *Clin Radiol* 68:799–806. <https://doi.org/10.1016/j.crad.2013.03.005>
- Cai W, Kim SH, Lee JG, Yoshida H (2013) Informatics in radiology: dual-energy electronic cleansing for fecal-tagging CT colonography. *Radiographics* 33:891–912. <https://doi.org/10.1148/rg.333125039>
- Chu AJ, Lee JM, Lee YJ et al (2012) Dual-source, dual-energy multidetector CT for the evaluation of pancreatic tumours. *Br J Radiol* 85. <https://doi.org/10.1259/bjr/26129418>
- Chuang-Bo Y, Tai-Ping H, Hai-Feng D et al (2017) Quantitative assessment of the degree of differentiation in colon cancer with dual-energy spectral CT. *Abdom Radiol (New York)* 42:2591–2596. <https://doi.org/10.1007/s00261-017-1176-6>
- Darras KE, Clark SJ, Kang H et al (2019) Virtual monoenergetic reconstruction of contrast-enhanced CT scans of the abdomen and pelvis at 40 keV improves the detection of peritoneal metastatic deposits. *Abdom Radiol* 44:422–428. <https://doi.org/10.1007/s00261-018-1733-7>
- El Kayal N, Lennartz S, Ekdawi S et al (2019) Value of spectral detector computed tomography for assessment of pancreatic lesions. *Eur J Radiol* 118:215–222. <https://doi.org/10.1016/j.ejrad.2019.07.016>
- Fulwadhva UP, Wortman JR, Sodickson AD (2016) Use of dual-energy CT and iodine maps in evaluation of bowel disease. *Radiographics* 36:393–406. <https://doi.org/10.1148/rg.2016150151>
- Gabbai M, Leichter I, Mahgerefteh S, Sosna J (2015) Spectral material characterization with dual-energy CT: comparison of commercial and investigative technologies in phantoms. *Acta Radiol* 56:960–969. <https://doi.org/10.1177/0284185114545150>
- Grant KL, Flohr TG, Krauss B et al (2014) Assessment of an advanced image-based technique to calculate virtual monoenergetic computed tomographic images from a dual-energy examination to improve contrast-to-noise ratio in examinations using iodinated contrast media. *Investig Radiol* 49:586–592. <https://doi.org/10.1097/RLI.0000000000000060>
- Große Hokamp N, Höink AJ, Doerner J et al (2018a) Assessment of arterially hyper-enhancing liver lesions using virtual monoenergetic images from spectral detector CT: phantom and patient experience. *Abdom Radiol* 43:2066–2074. <https://doi.org/10.1007/s00261-017-1411-1>
- Große Hokamp N, Obmann VC, Kessner R et al (2018b) Improved visualization of hypodense liver lesions in virtual monoenergetic images from spectral detector CT: proof of concept in a 3D-printed phantom and evaluation in 74 patients. *Eur J Radiol* 109:114–123. <https://doi.org/10.1016/j.ejrad.2018.11.001>
- Große Hokamp N, Obmann VC, Kessner R et al (2018c) Virtual monoenergetic images for diagnostic assessment of hypodense lesions within the liver: semiautomatic estimation of window settings using linear models. *J Comput Assist Tomogr* 42:925–931. <https://doi.org/10.1097/RCT.0000000000000794>
- Große Hokamp N, Gilkeson R, Jordan MK et al (2019) Virtual monoenergetic images from spectral detector CT as a surrogate for conventional CT images: unaltered attenuation characteristics with reduced image noise. *Eur J Radiol* 117:49–55. <https://doi.org/10.1016/j.ejrad.2019.05.019>

- Gupta S, Wagner-Bartak N, Jensen CT et al (2016) Dual-energy CT of pancreatic adenocarcinoma: reproducibility of primary tumor measurements and assessment of tumor conspicuity and margin sharpness. *Abdom Radiol* 41:1317–1324. <https://doi.org/10.1007/s00261-016-0689-8>
- Hanson GJ, Michalak GJ, Childs R et al (2018) Low kV versus dual-energy virtual monoenergetic CT imaging for proven liver lesions: what are the advantages and trade-offs in conspicuity and image quality? A pilot study. *Abdom Radiol* 43:1404–1412. <https://doi.org/10.1007/s00261-017-1327-9>
- Hellbach K, Sterzik A, Sommer W et al (2017) Dual energy CT allows for improved characterization of response to antiangiogenic treatment in patients with metastatic renal cell cancer. *Eur Radiol* 27:2532–2537. <https://doi.org/10.1007/s00330-016-4597-7>
- Hickethier T, Iuga A-I, Lennartz S et al (2018) Virtual monoenergetic images from a novel dual-layer spectral detector computed tomography scanner in portal venous phase: adjusted window settings depending on assessment focus are essential for image interpretation. *J Comput Assist Tomogr* 42:350–356. <https://doi.org/10.1097/RCT.0000000000000711>
- Husarik DB, Gordic S, Desbiolles L et al (2015) Advanced virtual monoenergetic computed tomography of hyperattenuating and hypoattenuating liver lesions: ex-vivo and patient experience in various body sizes. *Investig Radiol* 50:695–702. <https://doi.org/10.1097/RLI.0000000000000171>
- Kaltenbach B, Wichmann JL, Pfeifer S et al (2018) Iodine quantification to distinguish hepatic neuroendocrine tumor metastasis from hepatocellular carcinoma at dual-source dual-energy liver CT. *Eur J Radiol* 105:20–24. <https://doi.org/10.1016/j.ejrad.2018.05.019>
- Kammerer S, Höink AJ, Wessling J et al (2015) Abdominal and pelvic CT: is positive enteric contrast still necessary? Results of a retrospective observational study. *Eur Radiol* 25:669–678. <https://doi.org/10.1007/s00330-014-3446-9>
- Laukamp KR, Tirumani SH, Lennartz S et al (2021) Evaluation of equivocal small cystic pancreatic lesions with spectral-detector computed tomography. *Acta Radiol* 62:172–181. <https://doi.org/10.1177/0284185120917119>
- Lennartz S, Abdullayev N, Zopfs D et al (2019a) Intra-individual consistency of spectral detector CT-enabled iodine quantification of the vascular and renal blood pool. *Eur Radiol* 29:6581–6590. <https://doi.org/10.1007/s00330-019-06266-w>
- Lennartz S, Große Hokamp N, Abdullayev N et al (2019b) Diagnostic value of spectral reconstructions in detecting incidental skeletal muscle metastases in CT staging examinations. *Cancer Imaging* 19:1–8. <https://doi.org/10.1186/s40644-019-0235-3>
- Lennartz S, Zopfs D, Abdullayev N et al (2020) Iodine overlays to improve differentiation between peritoneal carcinomatosis and benign peritoneal lesions. *Eur Radiol*. <https://doi.org/10.1007/s00330-020-06729-5>
- Lin XZ, Wu ZY, Tao R et al (2012) Dual energy spectral CT imaging of insulinoma – value in preoperative diagnosis compared with conventional multi-detector CT. *Eur J Radiol* 81:2487–2494. <https://doi.org/10.1016/j.ejrad.2011.10.028>
- Lv P, Lin XZ, Li J et al (2011) Differentiation of small hepatic hemangioma from small hepatocellular carcinoma: recently introduced spectral CT method. *Radiology* 259:720–729. <https://doi.org/10.1148/radiol.11101425>
- Martin SS, Czwikla R, Wichmann JL et al (2018) Dual-energy CT-based iodine quantification to differentiate abdominal malignant lymphoma from lymph node metastasis. *Eur J Radiol* 105:255–260. <https://doi.org/10.1016/j.ejrad.2018.06.017>
- Mastrodicasa D, Delli Pizzi A, Patel BN (2019) Dual-energy CT of the pancreas. *Semin Ultrasound CT MRI* 40:509–514. <https://doi.org/10.1053/j.sult.2019.05.002>
- Mayo-Smith WW, Gupta H, Ridlen MS et al (1999) Detecting hepatic lesions: the added utility of CT liver window settings. *Radiology* 210:601–604. <https://doi.org/10.1148/radiology.210.3.r99mr07601>
- McNamara MM, Little MD, Alexander LF et al (2015) Multireader evaluation of lesion conspicuity in small pancreatic adenocarcinomas: complimentary value of iodine material density and low keV simulated monoenergetic images using multiphasic rapid kVp-switching dual energy CT. *Abdom Imaging* 40:1230–1240. <https://doi.org/10.1007/s00261-014-0274-y>
- Meyer M, Hohenberger P, Apfaltrer P et al (2013) CT-based response assessment of advanced gastrointestinal stromal tumor: dual energy CT provides a more predictive imaging biomarker of clinical benefit than RECIST or Choi criteria. *Eur J Radiol* 82:923–928. <https://doi.org/10.1016/j.ejrad.2013.01.006>
- Nagayama Y, Tanoue S, Inoue T et al (2020) Dual-layer spectral CT improves image quality of multiphase pancreas CT in patients with pancreatic ductal adenocarcinoma. *Eur Radiol* 30:394–403. <https://doi.org/10.1007/s00330-019-06337-y>
- Nattenmüller J, Hosch W, Nguyen T-T et al (2015) Hypodense liver lesions in patients with hepatic steatosis: do we profit from dual-energy computed tomography? *Eur Radiol* 25:3567–3576. <https://doi.org/10.1007/s00330-015-3772-6>
- Parakh A, Patino M, Muenzel D et al (2018) Role of rapid kV-switching dual-energy CT in assessment of post-surgical local recurrence of pancreatic adenocarcinoma. *Abdom Radiol (New York)* 43:497–504. <https://doi.org/10.1007/s00261-017-1390-2>
- Patel BN, Alexander L, Allen B et al (2017) Dual-energy CT workflow: multi-institutional consensus on standardization of abdominopelvic MDCT protocols. *Abdom Radiol (NY)* 42:676. <https://doi.org/10.1007/s00261-016-0966-6>
- Patel BN, Rosenberg M, Vernuccio F et al (2018) Characterization of small incidental indeterminate

- hypoattenuating hepatic lesions: added value of single-phase contrast-enhanced dual-energy CT material attenuation analysis. *Am J Roentgenol* 211:571–579. <https://doi.org/10.2214/AJR.17.19170>
- Prokop M, Galanski M (2002) Spiral and multislice computed tomography of the body. Thieme, Leipzig
- Quiney B, Harris A, McLaughlin P, Nicolaou S (2015) Dual-energy CT increases reader confidence in the detection and diagnosis of hypoattenuating pancreatic lesions. *Abdom Imaging* 40:859–864. <https://doi.org/10.1007/s00261-014-0254-2>
- Reimer RP, Große Hokamp N, Fehrmann Efferoth A et al (2020) Virtual monoenergetic images from spectral detector computed tomography facilitate washout assessment in arterially hyper-enhancing liver lesions. *Eur Radiol*. <https://doi.org/10.1007/s00330-020-07379-3>
- Robinson E, Babb J, Chandarana H, Macari M (2010) Dual source dual energy MDCT. *Investig Radiol* 45:413–418. <https://doi.org/10.1097/RLI.0b013e3181dfda78>
- Schaeffer B, Johnson TRC, Mang T et al (2014) Dual-energy CT colonography for preoperative “one-stop” staging in patients with colonic neoplasia. *Acad Radiol* 21:1567–1572. <https://doi.org/10.1016/j.acra.2014.07.019>
- Schramm N, Schlemmer M, Enghart E et al (2011) Dual energy CT for monitoring targeted therapies in patients with advanced gastrointestinal stromal tumor: initial results. *Curr Pharm Biotechnol* 12:547–557. <https://doi.org/10.2174/138920111795164066>
- Shuman WP, Green DE, Busey JM et al (2014) Dual-energy liver CT: effect of monochromatic imaging on lesion detection, conspicuity, and contrast-to-noise ratio of hypervascular lesions on late arterial phase. *Am J Roentgenol* 203:601–606. <https://doi.org/10.2214/AJR.13.11337>
- Skornitzke S, Fritz F, Mayer P et al (2018) Dual-energy CT iodine maps as an alternative quantitative imaging biomarker to abdominal CT perfusion: determination of appropriate trigger delays for acquisition using bolus tracking. *Br J Radiol* 91. <https://doi.org/10.1259/bjr.20170351>
- Sun X, Niwa T, Ozawa S, et al (2020) Detecting lymph node metastasis of esophageal cancer on dual-energy computed tomography. *Acta Radiol* 028418512098014. <https://doi.org/10.1177/0284185120980144>
- Vandenbroucke F, Van Hedent S, Van Gompel G et al (2015) Dual-energy CT after radiofrequency ablation of liver, kidney, and lung lesions: a review of features. *Insights Imaging* 6:363–379. <https://doi.org/10.1007/s13244-015-0408-y>
- Yin Q, Zou X, Zai X et al (2015) Pancreatic ductal adenocarcinoma and chronic mass-forming pancreatitis: differentiation with dual-energy MDCT in spectral imaging mode. *Eur J Radiol* 84:2470–2476. <https://doi.org/10.1016/j.ejrad.2015.09.023>
- Yu Y, Lin X, Chen K et al (2013) Hepatocellular carcinoma and focal nodular hyperplasia of the liver: differentiation with CT spectral imaging. *Eur Radiol* 23:1660–1668. <https://doi.org/10.1007/s00330-012-2747-0>
- Zhang L, Wang N, Mao J et al (2018) Dual-energy CT-derived volumetric iodine concentration for the assessment of therapeutic response after microwave ablation in a rabbit model with intrahepatic VX2 tumor. *J Vasc Interv Radiol* 29:1455–1461. <https://doi.org/10.1016/j.jvir.2018.04.019>
- Zopfs D, Graffe J, Reimer RP et al (2021) Quantitative distribution of iodinated contrast media in body computed tomography: data from a large reference cohort. *Eur Radio* 31(4):2340–2348. <https://doi.org/10.1007/s00330-020-07298-3>. Epub 2020 Sep 30. PMID: 32997173, PMCID: PMC7979665
- Zopfs D, Große Hokamp N, Reimer R et al (2021) Value of spectral detector CT for pretherapeutic, locoregional assessment of esophageal cancer. *Eur J Radiol* 134. <https://doi.org/10.1016/j.ejrad.2020.109423>



Gastrointestinal Imaging: Liver Fat and Iron Quantification

Malte Niklas Bongers

Contents

1	Clinical Background	235
2	Physical Background	237
3	Scan Protocol and Contrast Injection	238
4	Post-processing	239
5	Diagnostic Evaluation and Scientific Evidence	240
5.1	Liver Fat	240
5.2	Liver Iron	241
6	Conclusion	243
	References	243

1 Clinical Background

The liver, as the major metabolic organ, plays the crucial role in both amino acid and carbohydrate metabolism as well as in fat and iron balance in humans. The underlying pathophysiology of diffuse liver parenchymal diseases is typically due to the dysfunction of one of these metabolic pathways.

Diffuse liver parenchymal disease can generally be divided into storage disease, vascular disease, and inflammatory disease. The main causes are hepatitis B or C, non-alcoholic fatty liver dis-

ease (NAFLD), alcoholic fatty liver disease, and autoimmune diseases (Chundru et al. 2013). The main causes of diffuse liver disease differ significantly worldwide. In Asia and Africa, viral infections dominate, while in Europe and North America, NAFLD is the leading medical cause (Blachier et al. 2013).

Due to the increasing incidence of diabetes, obesity, and resulting metabolic syndrome worldwide, the prevalence of NAFLD in particular is increasing dramatically. Two subentities of NAFLD can be differentiated as follows. The non-alcoholic fatty liver is characterized by an increased storage of triglycerides in the hepatocytes and the so-called non-alcoholic steatohepatitis (NASH), in which an inflammatory reaction prevails in addition to the increased fat storage. In addition, chemotherapeutic drugs can also

M. N. Bongers (✉)
Department of Diagnostic and Interventional
Radiology, University Hospital of Tuebingen,
Tuebingen, Germany
e-mail: Malte.Bongers@med.uni-tuebingen.de

cause increased fat storage and inflammatory reaction of the liver (chemotherapy-induced steatohepatitis = CASH) (Meunier and Larrey 2020). Any liver disease that directly or indirectly induces an inflammatory response causes fibrosis of the liver parenchyma in the longer term. Increasing fibrosis may develop into liver cirrhosis with the typical consequences of portal hypertension, hepatic insufficiency, and increased risk of developing hepatocellular carcinoma. The time course of development from hepatic steatosis to liver fibrosis and then to cirrhosis is variable and depends on the underlying cause. Therefore, determination of liver fat content is crucial for prognostic assessment and for treatment planning. With adequate therapy of the underlying cause, regression of hepatic steatosis and even liver fibrosis is possible in the long term (Byrne and Targher 2015).

In addition, the liver is also the main producer of enzymes and proteins to maintain systemic iron balance. Physiologically, an adult person has about 4–5 g of iron. Of this, 80% is bound in the red blood cells in the form of hemoglobin. Hepatic ferritin and hemosiderin primarily serve as proteins for iron storage (1–2 g) and can be mobilized from hepatocytes during increased metabolic demand. Complex feedback mechanisms regulate intestinal iron absorption and iron recycling from aged red blood cells in response to systemic iron demand. Dysregulation of these metabolic pathways leads to the so-called iron-associated diseases, of which the iron storage diseases are relevant to this article (Brissot and Loreal 2016).

In iron storage diseases, primary forms, such as hereditary hemochromatosis, are distinguished from secondary forms, which are predominantly associated with ineffective erythropoiesis. Hereditary hemochromatosis is an autosomal recessive disorder and a common cause of hepatic iron overload. Numerous genes encoding metabolic processes of iron balance have now been identified, allowing the differentiation of 5 subtypes of this disease. In secondary hemochromatosis, repeated blood transfusions are used therapeutically, which can lead to hepatic iron overload in the long term. Secondary hema-

matoses include numerous forms of anemia, such as thalassemia, sickle cell anemia, sideroblastic anemia, myelodysplastic syndrome, aplastic anemia, and rare enzyme or protein deficiency syndromes (Marx 2000). Mention should also be made of the newly discovered dysmetabolic iron overload syndrome, which is associated with metabolic syndrome characteristics such as obesity and type 2 diabetes mellitus but also excessive alcohol consumption and hepatitis C (Fargion 1999). Iron overload has been observed in 15% of patients with metabolic syndrome, in 50% of patients with NAFLD, and in over 40% of patients with chronic hepatitis C infection. Excessive liver iron overload can lead to tissue damage and loss of organ function. As far as known until today, free iron in combination with reactive oxygen species causes an increase in hydroxyl radicals. These lead to cell damage, liver fibrosis, and cirrhosis and increase the risk of developing hepatocellular carcinoma.

To date, invasive liver biopsy is considered the gold standard in the diagnosis of diffuse liver parenchymal disease. Besides the typical risks of invasive methods, such as bleeding and infection, liver biopsy results are only representative for the biopsied parenchymal area and cannot necessarily be generalized to the entire organ. Furthermore, liver biopsy is unsuitable as a screening and monitoring method, as repeatability is limited (Tapper and Lok 2017). Thus, the need for non-invasive methods to adequately assess the liver parenchyma with respect to diffuse liver parenchymal disease is evident.

Sonography, computed tomography, and magnetic resonance imaging already play an important role in the diagnosis of diffuse liver parenchymal disease. Increasingly, quantitative examination results can be obtained with these methods.

In general, for the non-invasive determination of liver fat content, proton magnetic resonance spectroscopy (H-MRS) can be considered as a non-invasive reference standard due to its high accuracy. The disadvantage of H-MRS is the limitation to the analysis of a cuboidal volume element and the need for repeated measurements in different parts of the liver to obtain a representative

result for the entire liver. However, chemical shift relaxometry of MRI now allows quantitative results to be obtained for the determination of liver fat content even for the total organ. Here, the so-called proton-density-fat fraction shows good agreement with both H-MRS and liver biopsy (Reeder and Sirlin 2010).

Sonography is also suitable for determining the fat content of the liver. In standard abdominal sonography, this is done purely visually by comparing the echogenicity of the liver and kidney, which is increased in fatty conditions. However, quantitative methods for fat quantification in sonography now also exist. Here, backscatter or attenuation coefficients are calculated to draw conclusions about the degree of fatty liver conversion. Nevertheless, residual inaccuracy remains with sonographic methods due to non-ideal interobserver agreement (Ferraioli and Soares Monteiro 2019).

In single-energy computed tomography, a semiquantitative determination of liver fat content is possible using the Hounsfield units, which decrease with increasing fat content. However, since the Hounsfield units represent a sum attenuation coefficient, there is a strong influence, e.g. by iodine-containing contrast medium or iron deposits that can lead to incorrect estimation of the liver fat content (Kodama et al. 2007). With the introduction of dual-energy computed tomography (DECT), it is now possible to accurately determine liver fat content even in contrast-enhanced CT examinations based on material-specific attenuation properties (Fischer et al. 2011; Hyodo et al. 2017a).

In non-invasive diagnosis of hepatic iron overload, methods of MR relaxometry have become established over the last decades. Initial approaches to determine liver iron content by analysis of the transverse relaxation rate (also called R2) were highly vulnerable to artifacts due to long acquisition times. However, the superparamagnetic properties of hemosiderin lead to focal inhomogeneity of the main magnetic field, which can now be measured very precisely with R2* relaxometry, allowing accurate quantification of liver iron content (Labranche et al. 2018).

With the introduction of DECT and material-specific decomposition algorithms, it is now possible to robustly determine liver iron content in native DECT examinations. In particular, due to the short examination time, but also in the case of occasional contraindications to MRI (pacemakers, etc.), DECT may be used in the future as an alternative method for determining liver iron content (Abadia et al. 2017).

2 Physical Background

In conventional single-energy CT (SECT), examinations are acquired with fixed tube voltages. The detected X-ray attenuation is given in Hounsfield units and displayed as gray values. In these SECT images, there is a high structural information content with respect to the material being radiographed. However, since the gray values depicted only represent the linear attenuation coefficient of the radiographed material, the material-specific information content is very low. Applied to the liver, this means that under physiological normal conditions in contrast-enhanced SECT, the linear attenuation coefficient is composed of the attenuation of the liver parenchyma and the intravenously applied iodine. However, both the amount of iodine present in the liver parenchyma and, in particular, the composition of the liver parenchyma can vary considerably. Here, for example, the acquired contrast medium phase and administered contrast medium quantity play a role. In addition, there are effects, such as the deposition of iron or copper components and fatty degeneration of the liver, which have an opposite effect on the linear attenuation coefficient and may thus completely compensate each other.

With the introduction of DECT, it is possible to obtain material-specific information about the material being radiographed. The basic principle of DECT imaging is based on the fact that different materials have energy-dependent different mass attenuation coefficients when interacting with X-rays (for details, see Part I: Physical Implementation: Physical Background).

Due to the availability of only two attenuation profiles, it is in general only possible to adequately separate a mixture of two materials using DECT. In order to be able to separate three materials from each other, further criteria are required to solve an equation with three unknowns on the basis of the information from only two attenuation profiles. Meanwhile, there are some slightly different approaches to this. One solution is to assume that the sum of the individual volumes of the three materials to be distinguished is equivalent to the volume of the mixture of the three materials, which is not true in every case. A more generalizable solution is based on the law of conservation of mass and describes the assumption that the sum of the three materials to be differentiated is equivalent to the mass of the mixture of these three materials (for details, see Part I: Physical Implementation: Dual-Energy Algorithms and Post-processing Techniques). The two required attenuation profiles with high and low energy can be acquired today with all common scanner designs, such as dual-source DECT (*ds*DECT), fast kV switching DECT (*fks*DECT), and dual-layer DECT (*dl*DECT) (for details, see Part I: Physical). Theoretically, the sequential DECT technique is also capable of generating the required attenuation profiles, but this is not suitable for liver imaging due to the time latency between acquisitions and resulting artifacts from patient motion.

Depending on the DECT technology used, the material-specific information is obtained at the image domain level from the low- and high-energy images (*ds*DECT) or from the low- and high-energy sinograms (*fks*DECT and *dl*DECT) before image reconstruction.

The basic materials of interest should have clearly differentiated mass attenuation coefficients for adequate DECT differentiation. Applied to the liver, this highlights the problem that the simultaneous presence of iron overload and intravenously applied iodine due to overlapping mass attenuation coefficients make simultaneous determination of liver fat and liver iron content problematic in contrast-enhanced DECT.

3 Scan Protocol and Contrast Injection

At the beginning of the clinical DECT era, quantification of liver fat content was only possible using a two-compartment model based on native DECT acquisitions. By implementing the three-material models, it is now possible to determine liver fat content even in contrast-enhanced DECT acquisitions. The contrast medium phase used is of secondary importance, but the greatest experience is with DECT acquisitions in portal venous contrast medium phase. Further development of the DECT scanners, e.g. by introducing an additive tin filter in the dual-source technique to reduce the soft radiation components in the polychromatic X-ray spectrum, has led to a further improvement in spectral separation. Thus, for a second-generation dual-source scanner (SOMATOM Definition Flash, Siemens Healthcare, Erlangen, Germany), it is recommended to examine the liver with a scanning protocol that includes 100 kV as low energy and 140 kV with additive tin filter (selective photon shield, Sn140 kV) as high energy. For a third-generation dual-source scanner (SOMATOM Force, Siemens Healthcare, Erlangen, Germany), the standard protocol to be favored for examining the liver, depending on the patient's diameter, is 100 or 90 kV and 150 kV, also with additive tin filter, resulting in dose neutrality compared with SECT acquisition. For routine abdominal examinations, a total collimation of 0.6×64 mm (second-generation scanner) or 0.6×128 mm (third-generation scanner) and a pitch of 0.6 with a rotation time of 0.5 s are suitable.

When using the latest *dl*DECT scanner (IQon and CT 7500, Philips Healthcare, Best, The Netherlands), the primary acquisition of the liver is performed at 120 kV. With the brand new *dl*DECT scanner (CT 7500, Philips Healthcare), however, it is now also possible to perform DECT examinations at 100 kV, which is preferable for abdominal examinations of slim persons, for example. Acquisition at 140 kV, which is possible with both scanners, is not recommended for the liver. With a collimation of 128×0.625 mm or 256×0.625 mm, a pitch between 0.5 and 1.7,

and a rotation time of 0.33 or 0.27 s, reconstructions with a slice thickness of 1–5 mm are computed with a medium soft standard kernel (B). When using interactive reconstruction algorithms, level 1 is recommended for the model-based method (IMR, Philips Healthcare) and level 3–4 for the statistical method (iDose, Philips Healthcare).

When using DECT devices with the latest generation fast kV switching technology (Revolution Apex, GE Healthcare, Waukesha, Wisconsin), a switch between the low voltage of 80 kV and the high voltage of 140 kV is performed every 25 ms. A collimation of 128×0.625 mm with a pitch of 0.992 at a rotation time of 0.5 s is suitable for examining the liver. The device-specific noise index should be between 19 and 23 for a slice thickness of 0.625 mm and between 13 and 15 for 2.5 mm.

All scan protocols should have automatic tube current modulation to accommodate the varying body dimensions of patients. By default, we recommend reconstructing slice thicknesses between 1 and 3 mm as a compromise between spatial resolution and the need for PACS storage space. For the exclusive determination of liver fat and liver iron content, slice thicknesses of 3–10 mm are certainly acceptable, too. To ensure correct post-processing of the DECT images, quantitative kernels (Q or Qr) are used in *ds*DECT. Post-processing of the DECT data is mainly done in the raw data space for both *dI*DECT and *fks*DECT, so no special kernels need to be used here beyond the standard kernels. In general, low and medium levels of vendor-specific reconstruction algorithms, both on an iterative basis and using machine learning techniques, produce an image impression that most radiologists describe as familiar.

For the determination of liver iron content, the acquisition of DECT images in native technique without intravenous application of iodine-containing contrast medium is required, since it is methodologically impossible to differentiate two materials with high atomic number from each other.

In rare cases, when in clinical practice a DECT examination of the liver is performed immedi-

ately after a contrast-enhanced MRI examination, errors may occur in the quantification of both liver fat and liver iron content due to the remaining gadolinium from the MRI contrast medium in the body.

4 Post-processing

Independent of the primary acquisition based on *ds*DECT, *dI*DECT, or *fks*DECT, the final post-processing for material differentiation is based on the information of a high- and a low-energy image data set. In order to be able to separate and effectively quantify materials using DECT, the materials must be known and defined as accurately as possible. In detail, post-processing to quantify liver fat content involves a three-material decomposition of fat, liver tissue, and iodine. For quantification of liver iron content, iodine has to be replaced by iron in this analysis. Since iodine and iron are high atomic number materials (Z is 53 and 26, respectively) compared to human body tissue, there is an overlap in the three-material decomposition preventing simultaneous differentiation of both using DECT.

The underlying process of the modified three-material decomposition is best understood by a graphical illustration (see Fig. 1). For this purpose, the CT numbers obtained from the high- and low-energy data sets are plotted against each other, with the ordinate representing the low-energy information. To quantify liver fat content, a coordinate point can be defined for pure fat that has negative CT numbers (orange dot in Fig. 1). Another point for pure liver parenchyma can be defined by positive CT numbers (blue dot in Fig. 1). On a direct line connecting these two points, the CT numbers of a continuous mixture of these two materials (fat and liver tissue) can be expected. The closer the measured point on the line connecting fat and liver tissue to pure fat, the higher the relative fat content. In contrast-enhanced DECT, however, the X-ray attenuation of intravenously applied iodine must also be taken into account. As mentioned above, in DECT post-processing, it is critical that the materials to be quantified are precisely known. Thus,

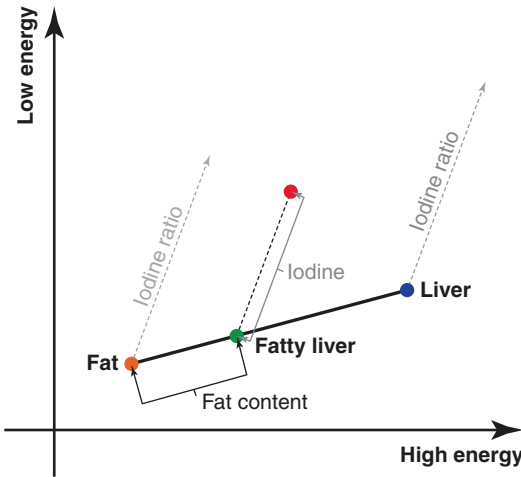


Fig. 1 Visualization of the DECT three-material decomposition in the form of a low-high energy diagram. Calculating the amount of the distance between the green dot, which represents the measured X-ray attenuation without the iodine component, and the orange dot, which represents pure adipose tissue, allows the liver fat content to be determined

for iodine, the material-specific DECT ratio, which is the slope of a straight line that can be obtained from the information of a DECT scanned dilution series, must be known (dotted gray lines in Fig. 1). If the information from a contrast-enhanced DECT is now plotted in the coordinate system described above, a point (red dot in Fig. 1) is created above the described connecting line between pure fat and liver tissue. Starting from this point, a straight line with the specific slope of iodine (dotted line in Fig. 1) can be drawn. The intersection point (green dot in Fig. 1) between this line and the line connecting pure fat and liver tissue reflects the measured point without the iodine attenuation. By determining the absolute value of the distance between this intersection point (green dot in Fig. 1) and the point for pure fat (orange dot in Fig. 1), the liver fat content can now be quantified. The absolute value of the distance on the straight line between the determined intersection point (green dot in Fig. 1) and the measured starting point (red dot in Fig. 1) represents the amount of iodine from the applied contrast medium.

When quantifying liver iron content, the above-described post-processing has to be

adapted to obtain iron in the three-material decomposition instead of iodine. The material-specific slope of iron is slightly flatter than that of iodine. To quantify the iron content, the absolute value of the distance between the measurement point and the intersection point on the line between fat and liver tissue has to be calculated.

5 Diagnostic Evaluation and Scientific Evidence

5.1 Liver Fat

The first scientific paper on liver fat quantification using DECT was published in 1991 by Raptopoulos et al. At that time, they could show using sequential DECT technique that differentiation of fatty infiltration of the liver from low density liver lesions is possible, but this was only successful if the liver iron content was low (Raptopoulos et al. 1991). In subsequent years, numerous authors have published papers comparing the accuracy of DECT-based liver fat quantifications with tissue histology from liver biopsies, proton magnetic resonance spectroscopy (h-MRS), chemical shift relaxometry of MRI, and SECT (Fig. 2).

Here, the extent of fatty liver degeneration is generally classified into histological grades. A liver fat content of 0–33% is considered as mild, 33–66% as moderate, and >66% as severe fatty liver infiltration (Brunt et al. 1999).

The correlation analyses performed show good agreement in the vast majority of studies. Numerous study results from small animal models are available. In rabbits, mice, and rats, excellent agreement with histology was repeatedly demonstrated using sequential and *fks*DECT in native studies (Wang et al. 2003; Artz et al. 2012; Sun et al. 2014). By further developing the algorithms for material decomposition from two- to three-material models (Mendonca et al. 2013), Hur et al. in 2014 also succeeded in achieving high agreement with histology in contrast-enhanced DECT examinations in the rabbit model when quantifying liver fat content using *fks*DECT (Hur et al. 2014). Hyodo et al. showed in an experimental ex vivo work on three-material decomposition by

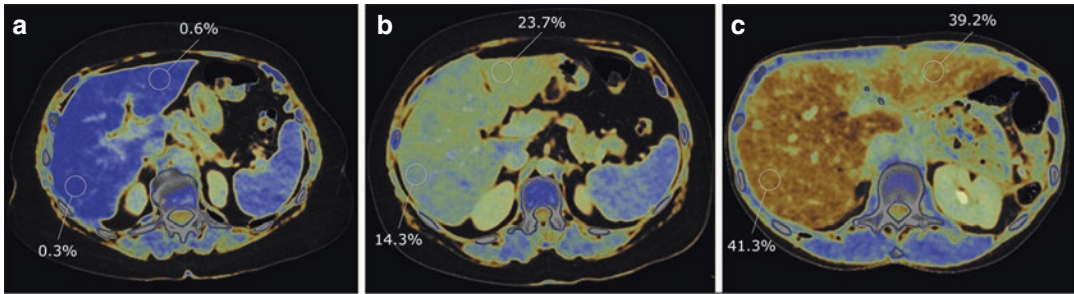


Fig. 2 Color-coded fat maps of three clinical cases with different degrees of fatty liver infiltration. (a) An overweight man aged 66 years shows no relevant hepatic fatty infiltration. (b) A 50-year-old female patient with obesity reveals moderate but inhomogeneous hepatic fatty infil-

tration with values ranging from 14% to 24%. (c) A 53-year-old female patient undergoing chemotherapy for breast cancer presents with a marked, increasingly inhomogeneous fatty liver (CASH) by 40%

*fs*DECT that object size has a small effect on the accuracy of liver fat quantification; however, iron deposition (and other metals with high atomic number such as copper in Wilson's disease) can lead to a relevant underestimation of liver fat content (Hyodo et al. 2017b). In a prospective study, the same authors demonstrated in a collective of 33 patients with NAFLD that three-material decomposition in *fs*DECT for determination of liver fat content can achieve high agreement with both h-MRS and liver biopsy and, moreover, very good reproducibility (Hyodo et al. 2017a).

When comparing DECT-based liver fat quantification with the two methods of MRI, volume-selective h-MRS should be considered separately from chemical shift relaxometry.

In native *fs*DECT studies, no superiority over SECT compared to H-MRS could be found in the quantification of liver fat content (Kramer et al. 2017). It should be noted that hepatic iron overload can lead to a relevant underestimation of liver fat content in both native SECT and DECT (Hyodo et al. 2017b), which can be quantified by DECT post-processing as described in the second part of this chapter.

In the meantime, however, experimental *ex vivo* approaches exist to determine liver fat content in native and especially contrast-enhanced DECT examinations sufficiently by means of further developed three-material models even in the presence of iron deposition (Fischer et al. 2011; Ma et al. 2014).

5.2 Liver Iron

Some studies are already available on DECT-based determination of liver iron content. Overall, the scientific evidence is still low due to the lack of studies with large cohorts and systematic comparison with liver biopsy and the established methods of MRI. To date, the greatest experience is in the use of *ds*DECT to determine liver iron content (Fig. 3).

For the first time, a study on the quantification of hepatic iron content by *ds*DECT in eight patients with primary hemochromatosis was published by Chapman and colleagues in 1980. They were able to demonstrate a strong correlation of 0.993 between DECT-based values for the assessment of hepatic iron content and chemical analyses of liver biopsies (Chapman et al. 1980).

In 1988, Leighton et al. described the clinically reliable quantification of liver iron in a study of 78 children suffering from thalassemia. Using the data obtained, they developed a method for calibrating conventional CT scanners to allow acquisition of DECT data sets (Leighton et al. 1988).

Then, in 1992, it was shown by Nielsen et al. in a small animal model that although there was a pronounced correlation between the bioptically confirmed iron content of the liver and that from DECT examinations, there is insufficient sensitivity of the DECT method at clinically relevant iron concentrations around 1–3 mg/g wet liver tissue (Nielsen et al. 1992).

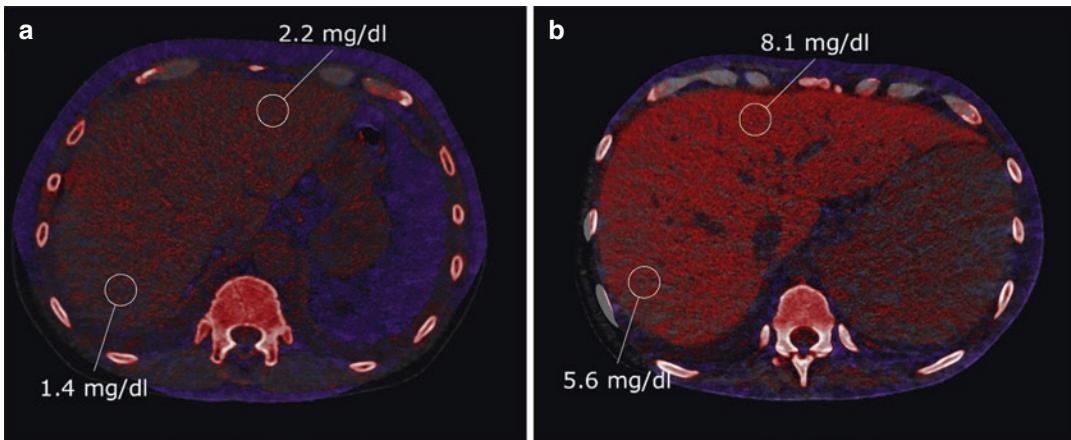


Fig. 3 Color-coded iron maps of *ds*DECT calculated with manufacturer-specific prototype software (DE IronVNC; Syngo.Via Frontier; Siemens Healthineers, Forchheim, Germany). (a) A 76-year-old female patient with myelodysplastic syndrome shows a slightly elevated

liver iron content of 1.4–2.2 mg/dl already after infusion of a single red cell concentrate. (b) A 67-year-old patient shows inhomogeneous liver iron overload of 5.6–8.1 mg/dl after recurrent blood transfusions due to acute myeloid leukemia

These early studies used CT acquisitions in sequential technique, which are prone to motion artifacts.

The research group led by Oelckers and colleagues undertook a vendor-independent model calculation in 1996 and showed that the DECT-based method for determining liver iron could in theory detect even lower amounts of iron than MR-based methods, but that there was an unclear susceptibility to error, e.g. due to artifacts or parallel prevailing liver fatty degeneration (Oelckers and Graeff 1996).

The clinical introduction of the first generation *ds*DECT scanner in 2006 enabled simultaneous acquisition of the low- and high-energy image data for the first time, minimizing patient motion artifacts and opening a new era of DECT.

In 2011, Joe et al. analyzed iron-associated X-ray attenuation of liver parenchyma for the first time based on *ds*DECT acquisitions. The research group was able to show that the difference in attenuation values between low- and high-energy correlates with the extent of hepatic iron overload and has an accuracy equal to MR relaxometry for the determination of liver iron in the clinically relevant ranges and, furthermore, is not relevantly influenced by the degree of liver fatty degeneration (Joe et al. 2012).

Luo et al. showed in a prospective study that equivalent sensitivity and specificity values can be obtained by means of three-material decomposition in *ds*DECT compared with MR relaxometry for the clinically relevant manifestations of hepatic iron overload. However, with the small limitation that this does not prove true for low iron overloads below the therapy-relevant threshold of 7 mg iron/g dry liver weight (Luo et al. 2015).

In a retrospective study, Werner et al. demonstrated that *ds*DECT can adequately quantify liver iron overload in a collective of patients with hematologic diseases and that there is a strong correlation with serum ferritin and the number of transfused red blood cell concentrates (Werner et al. 2019).

The *fls*DECT technology also succeeded in determining the hepatic iron content, however, according to a first study, coexisting liver fat seems to cause a slight underestimation of the hepatic iron content (Xie et al. 2019).

Abadia et al. showed that second-generation *ds*DECT scanners even succeed in imaging local iron distribution in the liver parenchyma (Abadia et al. 2017).

A study by Ma et al. in 2020 showed that *dI*DECT technology can be used to present a

strong, linear correlation with R^2 values from MR relaxometry by calculating virtual monoenergetic images and quantifying the attenuation difference between 50 and 120 keV to determine liver iron content (Ma et al. 2020).

Due to the current lack of commercially available DECT post-processing algorithms for liver iron quantification by all three major vendors, MR methods should continue to be preferred to quantify iron overload in routine clinical diagnostics up to now. In the future, with the availability of the appropriate post-processing software, DECT may also become a suitable alternative to MRI methods for determining liver iron content, especially when contraindications to MRI examination exist.

6 Conclusion

With all today available DECT scanner designs of dual-source, fast-kV switching, and dual-layer technique, it is possible to accurately quantify the liver fat content in vivo. With the advancement of post-processing algorithms from two- to three-material models, liver fat quantification is also successful in contrast-enhanced CT examinations. A very good agreement can be obtained in comparison with both liver biopsy and MRI methods, with H-MRS being the non-invasive reference standard. The software required to evaluate DECT examinations is commercially available from the device manufacturers and approved for routine clinical diagnostics.

DECT-based determination of liver iron methodologically requires acquisition of native DECT examinations, which is a rarity in routine daily use and therefore requires dedicated examination planning. Numerous studies have shown that reliable determination of liver iron content is possible with all currently available DECT scanners and that there is good agreement with results from liver biopsies and MRI methods. The greatest experience is in the use of *ds*DECT scanners; for *dI*DECT and *fks*DECT, further studies are needed for methodological establishment. In general, the DECT post-processing algorithms for quantification of liver iron are still at an

experimental status and are not yet commercially available. Therefore, MRI methods are currently still favored in routine clinical diagnostics for quantification of liver iron.

Compliance with Ethical Standards

Ethical Approval All procedures performed in studies involving human participants were in accordance with the ethical standards of the institutional and/or national research committee and with the 1964 Helsinki declaration and its later amendments or comparable ethical standards. Informed consent was obtained from all individual participants included in the study.

References

- Abadia AF, Grant KL, Carey KE et al (2017) Spatial distribution of iron within the normal human liver using dual-source dual-energy CT imaging. *Investig Radiol* 52(11):693–700
- Artz NS, Hines CD, Brunner ST et al (2012) Quantification of hepatic steatosis with dual-energy computed tomography: comparison with tissue reference standards and quantitative magnetic resonance imaging in the ob/ob mouse. *Investig Radiol* 47(10):603–610
- Blachier M, Leleu H, Peck-Radosavljevic M et al (2013) The burden of liver disease in Europe: a review of available epidemiological data. *J Hepatol* 58(3):593–608
- Brissot P, Loreal O (2016) Iron metabolism and related genetic diseases: a cleared land, keeping mysteries. *J Hepatol* 64(2):505–515
- Brunt EM, Janney CG, Di Bisceglie AM et al (1999) Nonalcoholic steatohepatitis: a proposal for grading and staging the histological lesions. *Am J Gastroenterol* 94(9):2467–2474
- Byrne CD, Targher G (2015) NAFLD: a multisystem disease. *J Hepatol* 62(1 Suppl):S47–S64
- Chapman RW, Williams G, Bydder G et al (1980) Computed tomography for determining liver iron content in primary haemochromatosis. *Br Med J* 280(6212):440–442
- Chundru S, Kalb B, Arif-Tiwari H et al (2013) MRI of diffuse liver disease: the common and uncommon etiologies. *Diagn Interv Radiol* 19(6):479–487
- Fargion S (1999) Dysmetabolic iron overload syndrome. *Haematologica* 84(2):97–98
- Ferraioli G, Soares Monteiro LB (2019) Ultrasound-based techniques for the diagnosis of liver steatosis. *World J Gastroenterol* 25(40):6053–6062
- Fischer MA, Gnannt R, Raptis D et al (2011) Quantification of liver fat in the presence of iron and iodine: an ex-vivo dual-energy CT study. *Investig Radiol* 46(6):351–358

- Hur BY, Lee JM, Hyunsik W et al (2014) Quantification of the fat fraction in the liver using dual-energy computed tomography and multimaterial decomposition. *J Comput Assist Tomogr* 38(6):845–852
- Hyodo T, Yada N, Hori M et al (2017a) Multimaterial decomposition algorithm for the quantification of liver fat content by using fast-kilovolt-peak switching dual-energy CT: clinical evaluation. *Radiology* 283(1):108–118
- Hyodo T, Hori M, Lamb P et al (2017b) Multimaterial decomposition algorithm for the quantification of liver fat content by using fast-kilovolt-peak switching dual-energy CT: experimental validation. *Radiology* 282(2):381–389
- Joe E, Kim SH, Lee KB et al (2012) Feasibility and accuracy of dual-source dual-energy CT for noninvasive determination of hepatic iron accumulation. *Radiology* 262(1):126–135
- Kodama Y, Ng CS, Wu TT et al (2007) Comparison of CT methods for determining the fat content of the liver. *AJR Am J Roentgenol* 188(5):1307–1312
- Kramer H, Pickhardt PJ, Kliewer MA et al (2017) Accuracy of liver fat quantification with advanced CT, MRI, and ultrasound techniques: prospective comparison with MR spectroscopy. *AJR Am J Roentgenol* 208(1):92–100
- Labranche R, Gilbert G, Cerny M et al (2018) Liver iron quantification with MR imaging: a primer for radiologists. *Radiographics* 38(2):392–412
- Leighton DM, de Campo JF, Matthews R, Sephton RG (1988) Dual energy CT estimation of liver iron content in thalassaemic children. *Australas Radiol* 32(2):214–219
- Luo XF, Xie XQ, Cheng S et al (2015) Dual-energy CT for patients suspected of having liver iron overload: can virtual iron content imaging accurately quantify liver iron content? *Radiology* 277(1):95–103
- Ma J, Song ZQ, Yan FH (2014) Separation of hepatic iron and fat by dual-source dual-energy computed tomography based on material decomposition: an animal study. *PLoS One* 9(10):e110964
- Ma Q, Hu J, Yang W, Hou Y (2020) Dual-layer detector spectral CT versus magnetic resonance imaging for the assessment of iron overload in myelodysplastic syndromes and aplastic anemia. *Jpn J Radiol* 38(4):374–381
- Marx JJ (2000) Primary and secondary haemochromatosis. *Transfus Sci* 23(3):183–184
- Mendonca PR, Lamb P, Kriston A et al (2013) Contrast-independent liver-fat quantification from spectral CT exams. *Med Image Comput Comput Assist Interv* 16(Pt 1):324–331
- Meunier L, Larrey D (2020) Chemotherapy-associated steatohepatitis. *Ann Hepatol* 19(6):597–601
- Nielsen P, Engelhardt R, Fischer R et al (1992) Noninvasive liver-iron quantification by computed tomography in iron-overloaded rats. *Investig Radiol* 27(4):312–317
- Oelckers S, Graeff W (1996) In situ measurement of iron overload in liver tissue by dual-energy methods. *Phys Med Biol* 41(7):1149–1165
- Raptopoulos V, Karellas A, Bernstein J et al (1991) Value of dual-energy CT in differentiating focal fatty infiltration of the liver from low-density masses. *AJR Am J Roentgenol* 157(4):721–725
- Reeder SB, Sirlin CB (2010) Quantification of liver fat with magnetic resonance imaging. *Magn Reson Imaging Clin N Am* 18(3):337–357. ix
- Sun T, Lin X, Chen K (2014) Evaluation of hepatic steatosis using dual-energy CT with MR comparison. *Front Biosci (Landmark Ed)* 19:1377–1385
- Tapper EB, Lok AS (2017) Use of liver imaging and biopsy in clinical practice. *N Engl J Med* 377(8):756–768
- Wang B, Gao Z, Zou Q, Li L (2003) Quantitative diagnosis of fatty liver with dual-energy CT. An experimental study in rabbits. *Acta Radiol* 44(1):92–97
- Werner S, Krauss B, Haberland U et al (2019) Dual-energy CT for liver iron quantification in patients with haematological disorders. *Eur Radiol* 29(6):2868–2877
- Xie T, Li Y, He G et al (2019) The influence of liver fat deposition on the quantification of the liver-iron fraction using fast-kilovolt-peak switching dual-energy CT imaging and material decomposition technique: an in vitro experimental study. *Quant Imaging Med Surg* 9(4):654–661



Bowel Imaging

Markus M. Obmann

Contents

1	Clinical Background	246
2	Physical Background	246
3	Scan Protocol Considerations	247
4	Postprocessing	248
5	Diagnostic Evaluation and Scientific Evidence	249
5.1	Chronic Inflammatory Conditions	249
5.2	Acute Infectious Conditions	249
5.3	Vascular Bowel Conditions	249
5.4	CT Colonography	250
5.5	Contrast Materials	252
6	Conclusion	252
	References	252

Abstract

In the past dual-energy CT of the bowel has played a lesser role compared to solid abdominal organs. However, several applications for bowel imaging have emerged in which dual-energy CT provides additional value. Virtual non-contrast images can distinguish hyperdense intraluminal bowel contents as contrast enhancing such as tumors or acute bleeding

from intrinsically dense feces. In infectious and inflammatory conditions monoenergetic images can be used to improve the visualization of inflammation associated contrast media uptake. In the same way vascular contrast can be enhanced in acute or chronic bowel ischemia using dual-energy CT. Dual-energy reconstructions may be used to reduce the influence of peristalsis artifacts. Initial studies show increased sensitivity for polyp detection in dual-energy CT colonography and it may be used to improve suboptimal fecal tagging.

M. M. Obmann (✉)
Clinic for Radiology and Nuclear Medicine,
University Hospital Basel, Basel, Switzerland
e-mail: markus.obmann@usb.ch

1 Clinical Background

Historically the diagnostic assessment of the luminal gastrointestinal tract has been challenging. Due to its ready availability cross-sectional imaging has become the modality of choice for the initial evaluation of gastrointestinal symptoms with abdominal CT being the workhorse in the acute setting. So far dual-energy CT has played a lesser role in the evaluation of the luminal gastrointestinal tract compared to the solid abdominal organs. This may be because of specific challenges the bowel poses to CT imaging, such as bowel wall peristalsis in combination with gas–tissue interfaces. While these need to be kept in mind when evaluating images, dual-energy CT offers several unique advantages which benefit bowel imaging (Yeh et al. 2018). Clinical conditions of the bowel can broadly be categorized into inflammatory, infectious, vascular, or neoplastic.

Chronic inflammatory conditions such as ulcerative colitis or Crohn's disease are a source of lifelong morbidity and acute episodes may be complicated by abscess formation or fistulas (Torres et al. 2017). Assessment of disease severity is important for acute and long-term treatment decisions and imaging plays a key role in disease monitoring (Deepak et al. 2017; Baker et al. 2018). The most common acute infectious condition in the abdomen that requires surgery is appendicitis. Appendicitis itself is usually confidently diagnosed with conventional CT, as are major complications such as perforation or abscess formation (Tsuboi et al. 2008). However, gangrenous appendicitis which is harder to identify on conventional CT may rapidly develop complications and a more severe clinical course (Romano et al. 2014).

Acute bowel ischemia is a life-threatening disease characterized by high morbidity and mortality. In conventional CT multiphasic CT is employed to assess the vasculature and bowel wall enhancement (Aschoff et al. 2009). Dual-energy CT can be used to increase vascular contrast for mesenteric vessel evaluation, improve the evaluation of bowel wall enhancement as well as generate virtual non-contrast images to exclude

bowel wall hemorrhage. In cases of chronic ischemic colitis dual-energy CT may aid the detection of decreased bowel wall enhancement. In the same way dual-energy can increase the conspicuity of duodenal or gastric ulcers. Gastrointestinal bleeding is common in the emergency setting and dual-energy CT offers ways to either reduce radiation dose or improve the readers confidence in making the correct diagnosis.

Colorectal carcinoma is the second most common cancer in the western world (Siegel et al. 2018). Several screening methods are currently in use, with CT colonography being increasingly used due to improved cost-effectiveness and lower complication rates (van der Meulen et al. 2018).

Another type of bowel cancer is gastrointestinal stromal tumors (GIST). Quantitative biomarkers for treatment response are desired especially as targeted therapies are used and dual-energy provides quantitative iodine metrics, which have been shown to correlate with tumor response (Schramm et al. 2011; Meyer et al. 2013). While not necessarily of gastrointestinal origin, peritoneal metastases can affect the bowel and lead to bowel obstruction. However, in the early stages peritoneal implants may be hard to detect and dual-energy CT may aid the detection of these metastases (Darras et al. 2019).

While in the past oral contrast was often given for CT evaluation of abdominal problems, this practice has been changing, and currently oral contrast is used to a lesser extent (Kielar et al. 2016; Kessner et al. 2017). However, there may be a renaissance of oral contrast media for two reasons. Photon-counting CT is able to more precisely differentiate currently available oral and intravenous contrasts, i.e. gadolinium, iodine, bismuth. Furthermore, new dual-energy CT specific contrast materials are being developed.

2 Physical Background

Most clinical questions for bowel imaging relate to the uptake of intravenous contrast media in CT. Iodine has the favorable property of a higher k-edge (33.2 keV) compared to soft tissues

(0.01–0.53 keV), which can be leveraged using dual-energy CT as there is a significantly higher differential absorption by the lower energetic photons due to the photoelectric effect (Murray et al. 2019).

Reconstructing low energy virtual monoenergetic images, the iodine-based contrast can be increased, allowing for better vessel assessment in portal venous phase images, and possibly skipping an additional arterial phase, saving radiation dose (Hickethier et al. 2018; Shaqdan et al. 2018). Furthermore, not only the intravascular contrast is increased, but also the bowel wall contrast.

On conventional CT, the HU value of a voxel reflects the total attenuation disregarding how photons interact with the material in the voxel. Therefore, voxels with completely different materials may show identical HU values, due to different relative densities of the materials. With dual-energy CT radio-dense structures, such as active bleeding versus dense intraluminal contents may be further characterized using material decomposition images.

Intraluminal fecal material is a special challenge in CT colonography. The current gold standard in CT colonography preparation comprises fecal tagging, where iodine or barium containing oral contrast and cathartic medication is ingested by the patient in the days prior to the scan, to remove as much fecal material as possible before the exam. Not only can polyps be distinguished from the contrast tagged residual fecal material, but also the contrast coats hard to spot flat lesions aiding their detection (Kim et al. 2014, 2016). However, to enable virtual endoscopic views the tagged material needs to be removed using electronic cleansing (Bräuer et al. 2018). While in conventional CT electronic cleansing was purely based on HU thresholds, dual-energy CT offers the opportunity to use spectral cleansing, identifying iodine with a higher precision compared to a pure HU-threshold base approach (Eliahou et al. 2010; Cai et al. 2012, 2013; Tachibana et al. 2015).

Other specific challenges to the luminal gastrointestinal tract are bowel peristalsis in combination with gas–tissue interfaces. Depending on the technical solution of dual-energy CT used

associated artifacts may be reduced or exaggerated due to spatial and temporal differences between the high- and low energy datasets.

3 Scan Protocol Considerations

When acquiring dual-energy CT scans of the bowel the complete abdomen is imaged from the diaphragm to the pelvic symphysis. To reduce respiratory motion artifacts, patients should be instructed to hold their breath, as all current dual-energy CT scanners allow for acquisition of the whole abdomen in one breath hold.

For specific clinical questions acquisition of a non-contrast series may be of interest (Geffroy et al. 2014) and for vessel evaluation an arterial contrast injection phase series is desirable. There is mounting evidence that with dual-energy CT both of these can be replaced using virtual non-contrast images and low keV virtual monoenergetic images (Obmann et al. 2021a; Lennartz et al. 2021).

Hence, for bowel imaging acquisition of a single portal venous phase series is recommended.

Two main challenges need to be kept in mind when imaging bowel with CT, bowel peristalsis and gas–tissue interfaces. As bowel peristalsis is involuntary it cannot be changed by patient instructions as compared to breathing artifacts. While glucagon or other peristalsis reducing agents are in use for MRI imaging (Froehlich et al. 2009), they are not regularly used in CT bowel imaging, as artifacts are less severe in conventional CT acquisitions. As peristalsis artifacts can for some scanners be pronounced in dual-energy reconstructions (Obmann et al. 2021b), gantry rotation time should be kept low to reduce potential artifacts (Shah et al. 2018). As the bowel lumen often contains gas, gas–tissue artifacts are commonly seen in the form of windmill artifacts due to the high HU difference between gas and tissue (Fleischmann and Boas 2011; Boas and Fleischmann 2012). To limit these artifacts pitch should be kept at 1 or lower.

In terms of radiation dose, multiple studies have shown the feasibility of dose neutral dual-

Table 1 Scan parameters for regular dual-energy CT bowel imaging

Scanner	Dual-layer	Rapid-kVp-switching	Dual-source	Split-filter
CTDIvol [mGy]	15	15	15	15
Tube voltage [kVp]	120	80/140	A:100 B:140	120
Additional filtration	–	–	Sn for B	Au and Sn
Tube current [mA]	511	606	A:609 B:471	617
Exposure time [s]	0.325	0.250	0.285	0.285
Collimation [mm]	64 × 0.625	80 × 0.625	128 × 0.6	64 × 0.6
Pitch	1.015	0.992	0.8	0.25
Rotation time [s]	0.33	0.5	0.28	0.28

energy CT acquisition compared to conventional CT (Euler et al. 2016; Uhrig et al. 2016; Grajo and Sahani 2018). Therefore, a radiation dose of around 15 mGy may serve as a target value and be adapted to the institution's standards and patient population. Exemplary acquisition settings for several different dual-energy CT scanners for bowel imaging are provided in Table 1.

For low-dose CT colonography examinations radiation dose levels are usually lower at around 4 mGy (Berrington de Gonzalez et al. 2010), and the same low-dose levels from conventional CT colonography should be aimed for when using dual-energy CT.

4 Postprocessing

For initial clinical review of images, a 120 kVp-equivalent reconstruction is used. This may be either be a linear blend of the high- and low energy dataset (dual-source and split-filter dual-energy CT scanners), a virtual monoenergetic image between 60 and 70 keV (rapid-kVp-switching dual-energy CT scanners), or a true 120 kVp acquisition (detector based dual-energy CT scanners). Evaluation of vascular structures is preferably done on low keV virtual monoenergetic image reconstructions between 40 and 50 keV depending on the scanner type and its noise characteristics. As iodine contrast is

enhanced in the low keV images, inflammatory changes are also accentuated. This can also be leveraged to improve suboptimal fecal tagging in dual-energy CT colonography studies. In the same way subtle bowel wall enhancement differences due to ischemic changes can be depicted. However, to analyze bowel wall enhancement or the lack thereof is more commonly done using iodine maps. These can either be viewed as a separate image series or a colored fusion overlay on top of their corresponding material decomposition pair, i.e. virtual unenhanced images or water images. Either way, iodine images should always be analyzed together with the corresponding material decomposition pair to be able to identify densities on iodine maps as true iodine. Other materials such as calcium or bismuth also appear dense on iodine maps and might therefore be mistaken for iodine. This is solved using the virtual unenhanced images, on which they appear equally dense. This is of special importance when evaluating for bowel wall ischemia and intramural hemorrhage, where the intrinsic density of the mural hemorrhage may appear isodense to normally enhancing bowel on venous phase images. The combination of virtual unenhanced and iodine images is able to identify the hemorrhage, dense on virtual unenhanced images, versus contrast enhancement of the bowel wall, dense on iodine images.

5 Diagnostic Evaluation and Scientific Evidence

5.1 Chronic Inflammatory Conditions

While in chronic inflammatory bowel disease studies have shown the improved contrast-to-noise characteristics using low keV virtual monoenergetic images (Lee et al. 2018), quantitative metrics such as iodine concentration or effective atomic number (Z) have been investigated as potential biomarkers for disease burden and therapy response (Villanueva Campos et al. 2018; Taguchi et al. 2018b; De Kock et al. 2019), with quantitative iodine concentration emerging as a reliable biomarker correlating to the clinically widely used Crohn's Disease activity index score (Van Hees et al. 1980; Kim et al. 2017). All currently clinical available dual-energy platforms enable the quantification of mural iodine uptake (Fig. 1).

5.2 Acute Infectious Conditions

Increased signal-to-noise ratio of low keV virtual monoenergetic images can help identify active inflammatory processes of the bowel, not only is

attenuation of iodine containing structures increased but also density of fat containing tissues is decreased. This is especially useful in the abdomen where mesenteric fat stranding can be the most obvious feature of disease (Fig. 2). For acute appendicitis it has been shown that both low keV virtual monoenergetic images and iodine overlay images may facilitate the differentiation between acute uncomplicated and gangrenous appendicitis (Elbanna et al. 2018). The lack of appendiceal mural iodine uptake is indicative of gangrenous appendicitis (Fig. 3).

5.3 Vascular Bowel Conditions

When evaluating for acute bowel ischemia the mesenteric vasculature needs to be assessed. Dual-energy CT improves visualization of abdominal vessels using low keV virtual monoenergetic images (Shaqdan et al. 2018). This can either be used to reduce the amount of intravenous contrast used or to skip a dedicated arterial phase acquisition (Rajiah et al. 2018; Hicketier et al. 2018; Lourenco et al. 2018). Evaluating the bowel wall is simplified using iodine (fusion overlay) images (Fulwadhva et al. 2016), where perfusion deficits are easily identified. In the same way low keV images can be used to accen-

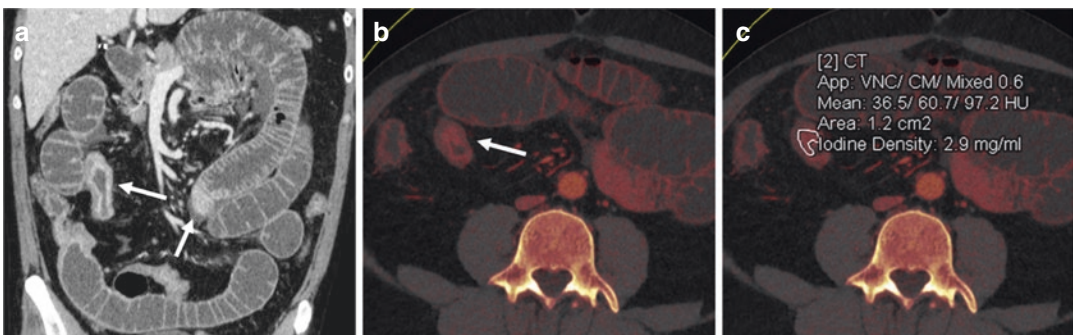


Fig. 1 Dual-source dual-energy CT in portal venous phase of a patient with acute exacerbation of known Crohn's disease. (a) 120 kVp-equivalent mixed image shows multiple stenoses with increased inflammatory iodine uptake of the bowel wall (arrows). (b) The lesion

with the highest iodine uptake (arrow) is visualized in axial plane on the iodine fusion overlay image. (c) Freehand region-of-interest measurement of the quantitative iodine uptake of the inflamed bowel segment



Fig. 2 Dual-source dual-energy CT in portal venous phase of a patient with acute uncomplicated, phlegmonous appendicitis. (a) The 120-kVp-equivalent blended image shows a wall thickened vermiform appendix with surrounding fat stranding (arrow). (b) The low keV

(50 keV) virtual monoenergetic image increases the iodine-based attenuation while lowering the attenuation of fatty structures, accentuating the inflammation process. (c) Iodine fusion overlay images show preserved iodine uptake of the appendiceal wall

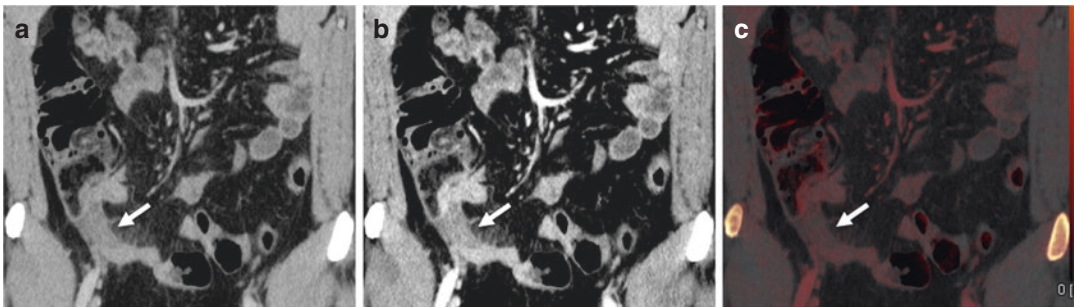


Fig. 3 Dual-source dual-energy CT in portal venous phase of a patient with pathology proven acute gangrenous appendicitis. (a) 120-kVp-equivalent blended image shows a wall-thickened vermiform appendix with surrounding fat stranding (arrow). (b) The low keV (50 keV)

virtual monoenergetic image shows a decreased attenuation of the appendiceal wall. (c) Iodine fusion overlay images show a lack of iodine uptake of the appendiceal wall, confirmative of gangrenous appendicitis, compare also to Fig. 2c

tuate subtle differences in bowel wall enhancement (Potretzke et al. 2014). A pitfall for conventional arterial and venous phase CT imaging is bowel wall hemorrhage, which due to its high attenuation might be misconstrued as mural enhancement (Rondenet et al. 2018). With the combination of VNC images and iodine images of dual-energy CT, true non-contrast images can be simulated and a confident diagnose of bowel wall hemorrhage indicative of transmural necrosis can be made (Fig. 4).

Patients with ischemic colitis usually present with a less acute course of disease. In the majority of cases the underlying cause is non-occlusive mesenteric ischemia (NOMI) (Taourel et al. 2008). The main imaging finding is bowel wall thickening and the differential diagnosis of infec-

tious colitis may be hard to distinguish. Dual-energy CT can reveal the true diagnosis by showing the decreased vascular supply to the affected segments (Fig. 5).

Gastrointestinal bleeding can be detected with dual-energy without the need for an additional non-contrast phase scan, as virtual non-contrast images have been able to perform comparably (Sun et al. 2015; Trabzonlu et al. 2020).

5.4 CT Colonography

Dual-energy CT has been shown to benefit intravenous contrast enhanced CT colonography studies, differentiating impacted stool from polyps (Karcaaltincaba et al. 2009; Taguchi et al. 2017).

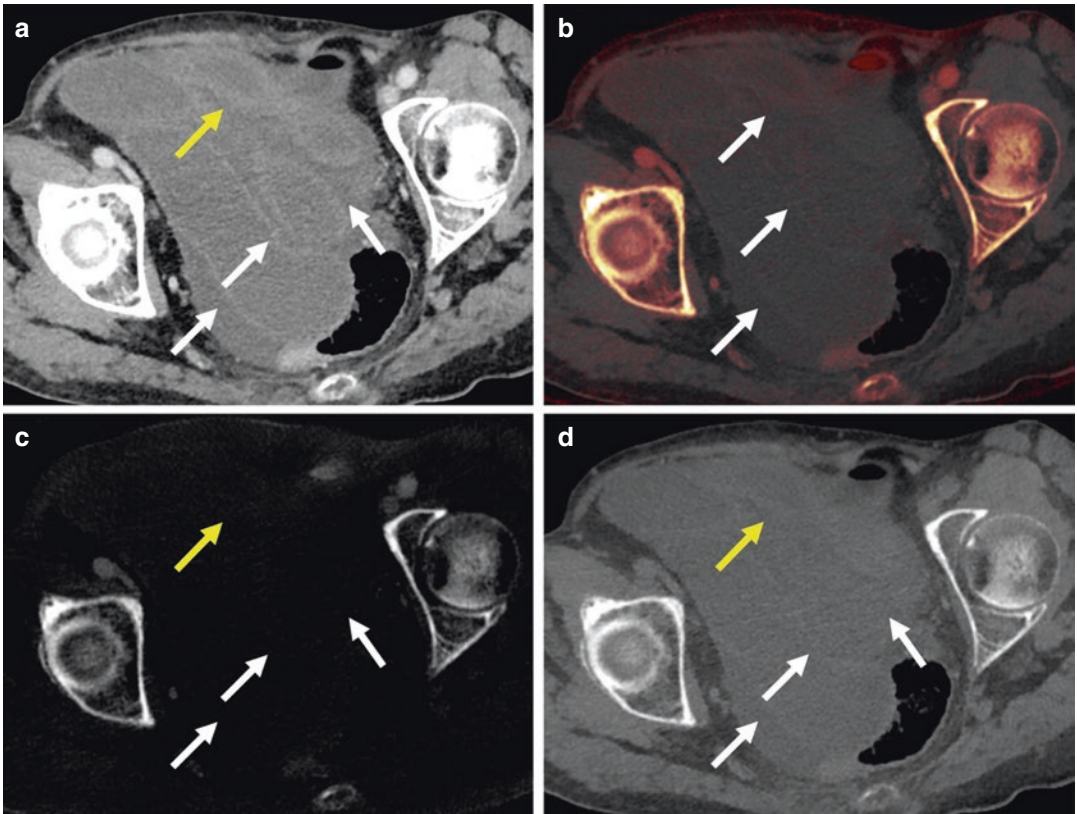


Fig. 4 Split-filter dual-energy CT in portal venous phase of a patient with a closed-loop small bowel obstruction. (a) 120-kVp-equivalent mixed images show dilated small bowel loops with reduced mural enhancement (white arrows) and partially thickened bowel wall (yellow arrow). (c) Iodine images show complete lack of iodine uptake in

both the thickened and the non-thickened bowel segments. (d) Virtual non-contrast images confirm the absence of iodine uptake, as the density of the bowel wall seen in (a) is mapped to the virtual non-contrast image, indicative of bowel wall hemorrhage rather than iodine perfusion. (b) Iodine fusion overlay shows the same findings

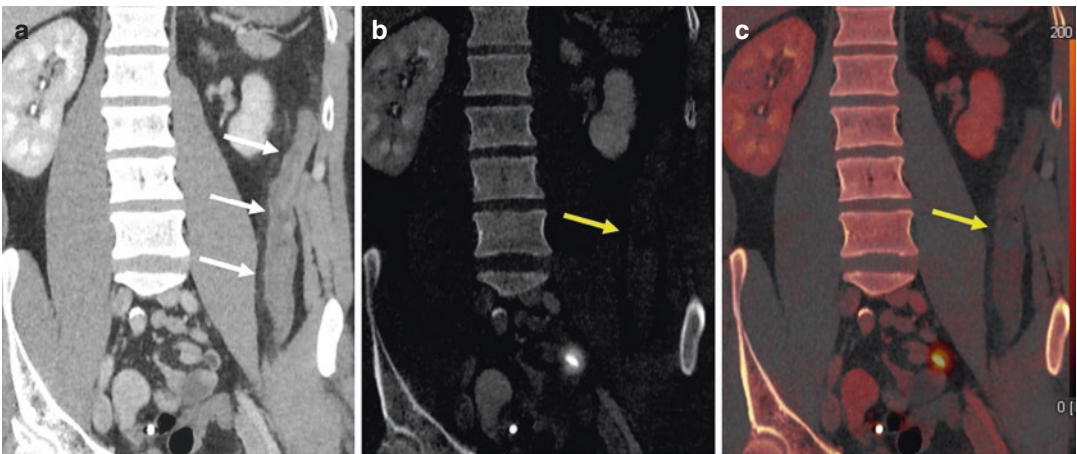


Fig. 5 Dual-source dual-energy CT in portal venous phase of a patient with ischemic colitis. (a) 120kVp-equivalent images show wall thickening of the descending colon (white arrows). (b) Iodine maps show reduced and

focal absent bowel wall enhancement, in keeping with ischemic colitis. (c) Same is visualized on the iodine fusion overlay images

Furthermore multiple studies have shown that low keV virtual monoenergetic images can improve contrast of fecal tagging CT colonography studies (Taguchi et al. 2018a; Obmann et al. 2020).

5.5 Contrast Materials

Current contrast agents (i.e. iodine, barium and gadolinium) are hard to differentiate using dual-energy CT due to the proximity of their k-edges. However, experimental studies have shown the potential of multi-bin photon-counting CT to separate k-edges of multiple currently available contrast agents, either for CT colonography to further differentiation between fecal tagged material and polyps (Muenzel et al. 2017) or to differentiate oral from intravenous contrast material (Ren et al. 2020). In the past it has been suggested that other than the currently available contrast materials, high Z-elements may be used for novel CT contrast agents (FitzGerald et al. 2016). Because of their distinctly different spectral properties compared to current iodinated contrast materials dual-contrast exams in a single dual-energy CT scan may become possible in the future (Mongan et al. 2012, 2013; Rathnayake et al. 2016).

6 Conclusion

So far, the gastrointestinal tract has lagged behind in dual-energy CT application compared to other abdominal organs. However, due the improvements in dual-energy CT scanners with faster acquisitions and thus lower artifacts bowel imaging is becoming more and more mainstream. Similar to other organs most dual-energy CT applications in bowel imaging revolve around iodinated contrast material. Yet, as novel developments such as dual-energy CT colonography or dual-energy specific contrast agents are on the horizon the importance of dual-energy for bowel imaging will increase.

Compliance with Ethical Standards

Disclosure of Interests The manuscript has not been submitted or published elsewhere. None of the paper's contents have been previously published in any form or language (partial or complete). The presented data, text and theories are solely of the author.

There are no financial or other author disclosures.

References

- Aschoff AJ, Stuber G, Becker BW et al (2009) Evaluation of acute mesenteric ischemia: accuracy of biphasic mesenteric multi-detector CT angiography. *Abdom Imaging* 34:345–357. <https://doi.org/10.1007/s00261-008-9392-8>
- Baker ME, Fletcher JG, Al-Hawary M, Bruining D (2018) Interdisciplinary updates in Crohn's disease reporting nomenclature, and cross-sectional disease monitoring. *Radiol Clin N Am* 56:691–707
- Berrington de Gonzalez A, Kim KP, Yee J (2010) CT colonography: perforation rates and potential radiation risks. *Gastrointest Endosc Clin N Am* 20:279–291
- Boas FE, Fleischmann D (2012) CT artifacts: causes and reduction techniques. *Imaging Med* 4:1–19. <https://doi.org/10.2217/iim.12.13>
- Bräuer C, Lefere P, Gryspeerdt S et al (2018) CT colonography: size reduction of submerged colorectal polyps due to electronic cleansing and CT-window settings. *Eur Radiol* 1–9. <https://doi.org/10.1007/s00330-018-5416-0>
- Cai W, Kim SH, Lee JG, Yoshida H (2012) Virtual colon tagging for electronic cleansing in dual-energy fecal-tagging CT colonography. In: Proceedings of the annual international conference of the IEEE Engineering in Medicine and Biology Society, EMBS. IEEE, pp 3736–3739
- Cai W, Kim SH, Lee J-G, Yoshida H (2013) Informatics in radiology: dual-energy electronic cleansing for fecal-tagging CT colonography. *Radiographics* 33:891–912. <https://doi.org/10.1148/rg.333125039>
- Darras KE, Clark SJ, Kang H et al (2019) Virtual monoenergetic reconstruction of contrast-enhanced CT scans of the abdomen and pelvis at 40 keV improves the detection of peritoneal metastatic deposits. *Abdom Radiol* 44:422–428. <https://doi.org/10.1007/s00261-018-1733-7>
- De Kock I, Delrue L, Lecluyse C et al (2019) Feasibility study using iodine quantification on dual-energy CT enterography to distinguish normal small bowel from active inflammatory Crohn's disease. *Acta Radiol* 60:679–686. <https://doi.org/10.1177/0284185118799508>
- Deepak P, Park SH, Ehman EC et al (2017) Crohn's disease diagnosis, treatment approach, and management

- paradigm: what the radiologist needs to know. *Abdom Radiol* 42:1068–1086. <https://doi.org/10.1007/s00261-017-1068-9>
- Elbanna KY, Mohammed MF, Chahal T et al (2018) Dual-energy CT in differentiating nonperforated gangrenous appendicitis from uncomplicated appendicitis. *Am J Roentgenol* 1–7. <https://doi.org/10.2214/AJR.17.19274>
- Eliahou R, Azraq Y, Carmi R et al (2010) Dual-energy based spectral electronic cleansing in non-cathartic computed tomography colonography: an emerging novel technique. *Semin Ultrasound, CT MRI* 31:309–314. <https://doi.org/10.1053/j.sult.2010.05.005>
- Euler A, Obmann MM, Szucs-Farkas Z et al (2016) Comparison of single-source split-filter dual-energy abdominal CT with single-energy abdominal CT using automatic tube voltage modulation: assessment of image quality and radiation dose. In: *Radiological Society of North America 2016 scientific assembly and annual meeting*, Chicago
- FitzGerald PF, Colborn RE, Edic PM et al (2016) CT image contrast of high-Z elements: phantom imaging studies and clinical implications. *Radiology* 278:723–733. <https://doi.org/10.1148/radiol.2015150577>
- Fleischmann D, Boas FE (2011) Computed tomography – old ideas and new technology. *Eur Radiol* 21:510–517. <https://doi.org/10.1007/s00330-011-2056-z>
- Froehlich JM, Daenzer M, von Weymarn C et al (2009) Aperistaltic effect of hyoscine N-butylbromide versus glucagon on the small bowel assessed by magnetic resonance imaging. *Eur Radiol* 19:1387–1393. <https://doi.org/10.1007/s00330-008-1293-2>
- Fulwadhva UP, Wortman JR, Sodickson AD (2016) Use of dual-energy CT and iodine maps in evaluation of bowel disease. *Radiographics* 36:393–406. <https://doi.org/10.1148/rg.2016150151>
- Geffroy Y, Boulay-Coletta I, Jullès M-C, et al (2014) Increased unenhanced bowel-wall attenuation at multidetector CT is highly specific of ischemia complicating small-bowel obstruction. *Radiol* 270:159–167. <https://doi.org/10.1148/radiol.13122654>
- Grajo JR, Sahani DV (2018) Dual-energy CT of the abdomen and pelvis: radiation dose considerations. *J Am Coll Radiol* 15:1128–1132. <https://doi.org/10.1016/j.jacr.2017.08.012>
- Hickethier T, Byrtus J, Hauger M et al (2018) Utilization of virtual mono-energetic images (MonoE) derived from a dual-layer spectral detector CT (SDCT) for the assessment of abdominal arteries in venous contrast phase scans. *Eur J Radiol* 99:28–33. <https://doi.org/10.1016/j.ejrad.2017.12.007>
- Karacaaltincaba M, Karaosmanoglu D, Akata D et al (2009) Dual energy virtual ct colonoscopy with dual source computed tomography: initial experience. *RoFo Fortschritte auf dem Gebiet der Rontgenstrahlen und der Bildgeb Verfahren* 181:859–862. <https://doi.org/10.1055/s-0028-1109569>
- Kessner R, Barnes S, Halpern P et al (2017) CT for acute nontraumatic abdominal pain-is oral contrast really required? *Acad Radiol* 24:840–845. <https://doi.org/10.1016/j.acra.2017.01.013>
- Kielar AZ, Patlas MN, Katz DS (2016) Oral contrast for CT in patients with acute non-traumatic abdominal and pelvic pain: what should be its current role? *Emerg Radiol* 23:477–481. <https://doi.org/10.1007/s10140-016-1403-4>
- Kim DH, Hinshaw JL, Lubner MG et al (2014) Contrast coating for the surface of flat polyps at CT colonography: a marker for detection. *Eur Radiol* 24:940–946. <https://doi.org/10.1007/s00330-014-3095-z>
- Kim DH, Matkowskyj KA, Lubner MG et al (2016) Serrated polyps at CT colonography: prevalence and characteristics of the serrated polyp spectrum. *Radiology* 280:455–463. <https://doi.org/10.1148/radiol.2016151608>
- Kim YS, Kim SH, Ryu H, Han JK (2017) Iodine quantification on spectral detector-based dual-energy CT enterography: correlation with Crohn's disease activity index. In: *RSNA*
- Lennartz S, Laukamp KR, Tandon Y, et al (2021) Abdominal vessel depiction on virtual triphasic spectral detector CT: initial clinical experience. *Abdom Radiol (New York)* 46:3501. <https://doi.org/10.1007/S00261-021-03001-2>
- Lee SM, Kim SH, Ahn SJ et al (2018) Virtual monoenergetic dual-layer, dual-energy CT enterography: optimization of KeV settings and its added value for crohn's disease. *Eur Radiol* 28:2525–2534. <https://doi.org/10.1007/s00330-017-5215-z>
- Lourenco PDM, Rawski R, Mohammed MF et al (2018) Dual-energy CT iodine mapping and 40-keV monoenergetic applications in the diagnosis of acute bowel ischemia. *Am J Roentgenol* 211:564–570. <https://doi.org/10.2214/AJR.18.19554>
- Meyer M, Hohenberger P, Apfaltrer P et al (2013) CT-based response assessment of advanced gastrointestinal stromal tumor: dual energy CT provides a more predictive imaging biomarker of clinical benefit than RECIST or Choi criteria. *Eur J Radiol* 82:923–928. <https://doi.org/10.1016/j.ejrad.2013.01.006>
- Mongan J, Rathnayake S, Fu Y et al (2012) In vivo differentiation of complementary contrast media at dual-energy CT. *Radiology* 265:267–272. <https://doi.org/10.1148/radiol.12120692>
- Mongan J, Rathnayake S, Fu Y et al (2013) Extravasated contrast material in penetrating abdominopelvic trauma: dual-contrast dual-energy CT for improved diagnosis – preliminary results in an animal model. *Radiology* 268:738–742. <https://doi.org/10.1148/radiol.13121267>
- Muenzel D, Bar-Ness D, Roessl E et al (2017) Spectral photon-counting CT: initial experience with dual-contrast agent K-edge colonography. *Radiology* 283:723–728. <https://doi.org/10.1148/radiol.2016160890>
- Murray N, Darras KE, Walstra FE et al (2019) Dual-energy CT in evaluation of the acute abdomen. *Radiographics* 39:264–286. <https://doi.org/10.1148/rg.2019180087>
- Obmann MM, An C, Schaefer A et al (2020) Improved sensitivity and reader confidence in CT colonography using dual-layer spectral CT: a phantom study. *Radiology* 297:99–107. <https://doi.org/10.1148/radiol.2020200032>

- Obmann MM, Punjabi G, Obmann VC, et al (2021a) Dual-energy CT of acute bowel ischemia. *Abdom Radiol*. <https://doi.org/10.1007/s00261-021-03188-4>
- Obmann MM, Sun Y, An C, et al (2021b) Bowel peristalsis artifact on dual-energy CT: In-Vitro study of the influence of different dual-energy CT platforms and enteric contrast agents. *Am J Roentgenol*. <https://doi.org/10.2214/ajr.21.26345>
- Potretzke TA, Brace CL, Lubner MG et al (2014) Early small-bowel ischemia: dual-energy CT improves conspicuity compared with conventional CT in a swine model. *Radiology* 275:119–126. <https://doi.org/10.1148/radiol.14140875>
- Rajiah P, Rong R, Martinez-Rios C et al (2018) Benefit and clinical significance of retrospectively obtained spectral data with a novel detector-based spectral computed tomography – initial experiences and results. *Clin Imaging* 49:65–72. <https://doi.org/10.1016/j.clinimag.2017.10.019>
- Rathnayake S, Mongan J, Torres AS et al (2016) In vivo comparison of tantalum, tungsten, and bismuth enteric contrast agents to complement intravenous iodine for double-contrast dual-energy CT of the bowel: enteric contrast comparison for dual-energy CT of the bowel. *Contrast Media Mol Imaging* 11:254–261. <https://doi.org/10.1002/cmmi.1687>
- Ren L, Rajendran K, Fletcher JG et al (2020) Simultaneous dual-contrast imaging of small bowel with iodine and bismuth using photon-counting-detector computed tomography: a feasibility animal study. *Investig Radiol* 55:688–694. <https://doi.org/10.1097/RLI.0000000000000687>
- Romano A, Parikh P, Byers P, Namias N (2014) Simple acute appendicitis versus non-perforated gangrenous appendicitis: is there a difference in the rate of post-operative infectious complications? *Surg Infect* 15:517–520. <https://doi.org/10.1089/sur.2013.106>
- Rondenot C, Millet I, Corno L et al (2018) Increased unenhanced bowel-wall attenuation: a specific sign of bowel necrosis in closed-loop small-bowel obstruction. *Eur Radiol* 28:4225–4233. <https://doi.org/10.1007/s00330-018-5402-6>
- Schramm N, Schlemmer M, Enghart E et al (2011) Dual energy CT for monitoring targeted therapies in patients with advanced gastrointestinal stromal tumor: initial results. *Curr Pharm Biotechnol* 12:547–557. <https://doi.org/10.2174/138920111795164066>
- Shah R, Khoram R, Lambert JW et al (2018) Effect of gantry rotation speed and scan mode on peristalsis motion artifact frequency and severity at abdominal CT. *Abdom Radiol* 43:2239–2245. <https://doi.org/10.1007/s00261-018-1497-0>
- Shaqdan KW, Parakh A, Kambadakone AR, Sahani DV (2018) Role of dual energy CT to improve diagnosis of non-traumatic abdominal vascular emergencies. *Abdom Radiol* 1–16. <https://doi.org/10.1007/s00261-018-1741-7>
- Siegel RL, Miller KD, Jemal A (2018) Cancer statistics, 2018. *CA Cancer J Clin* 68:7–30. <https://doi.org/10.3322/caac.21442>
- Sun H, Hou XY, Xue HD et al (2015) Dual-source dual-energy CT angiography with virtual non-enhanced images and iodine map for active gastrointestinal bleeding: image quality, radiation dose and diagnostic performance. *Eur J Radiol* 84:884–891. <https://doi.org/10.1016/j.ejrad.2015.01.013>
- Tachibana R, Näppi JJ, Kim SH, Yoshida H (2015) Electronic cleansing for dual-energy CT colonography based on material decomposition and virtual monochromatic imaging. In: Hadjiiski LM, Tourassi GD (eds) *Proceedings of SPIE – the International Society for Optical Engineering*, p 94140Q
- Taguchi N, Oda S, Imuta M et al (2017) Dual-energy CT colonography using dual-layer spectral detector computed tomography: feasibility of virtual monochromatic imaging for electronic cleansing. In: *RSNA, Chicago*
- Taguchi N, Oda S, Imuta M et al (2018a) Dual-energy computed tomography colonography using dual-layer spectral detector computed tomography: utility of virtual monochromatic imaging for electronic cleansing. *Eur J Radiol* 108:7–12. <https://doi.org/10.1016/j.EJRAD.2018.09.011>
- Taguchi N, Oda S, Kobayashi T et al (2018b) Advanced parametric imaging for evaluation of Crohn's disease using dual-energy computed tomography enterography. *Radiol Case Reports* 13:709–712. <https://doi.org/10.1016/j.radcr.2018.04.002>
- Taourel P, Aouf S, Merigeaud S et al (2008) Imaging of ischemic colitis. *Radiol Clin N Am* 46:909–924. <https://doi.org/10.1016/j.rcl.2008.06.003>
- Torres J, Mehndru S, Colombel JF, Peyrin-Biroulet L (2017) Crohn's disease. *Lancet* 389:1741–1755
- Trabzonlu TA, Mozaffary A, Kim D, Yaghmai V (2020) Dual-energy CT evaluation of gastrointestinal bleeding. *Abdom Radiol* 45. <https://doi.org/10.1007/s00261-019-02226-6>
- Tsuboi M, Takase K, Kaneda I et al (2008) Perforated and nonperforated appendicitis: defect in enhancing appendiceal wall – depiction with multi-detector row CT. *Radiology* 246:142–147. <https://doi.org/10.1148/radiol.2461051760>
- Uhrig M, Simons D, Kachelrieß M et al (2016) Advanced abdominal imaging with dual energy CT is feasible without increasing radiation dose. *Cancer Imaging* 16:15. <https://doi.org/10.1186/s40644-016-0073-5>
- van der Meulen MP, Lansdorp-Vogelaar I, Goede SL et al (2018) Colorectal cancer: cost-effectiveness of colonoscopy versus CT colonography screening with participation rates and costs. *Radiology* 162359. <https://doi.org/10.1148/radiol.2017162359>
- Van Hees PAM, Van Elteren P, Van Lier HJJ, Van Tongeren JHM (1980) An index of inflammatory activity in patients with Crohn's disease. *Gut* 21:279–286. <https://doi.org/10.1136/gut.21.4.279>
- Villanueva Campos AM, Tardáguila de la Fuente G, Utrera Pérez E et al (2018) Value of dual-energy CT enterography in the analysis of pathological bowel segments in patients with Crohn's disease. *Radiologia* 60:223–229. <https://doi.org/10.1016/j.rx.2018.01.004>
- Yeh BM, Obmann MM, Westphalen AC et al (2018) Dual energy computed tomography scans of the bowel: benefits, pitfalls, and future directions. *Radiol Clin N Am* 56:805–819



Role of Dual-Energy Computed Tomography (DECT) in Acute Abdomen

Saira Hamid, Muhammad Umer Nasir,
Aneta Kecler-Pietrzyk, Adnan Sheikh,
Nicolas Murray, Faisal Khosa, and Savvas Nicolaou

Contents

1	Introduction	257
2	Role of DECT in Non-traumatic Acute Abdomen	257
3	Bowel Ischemia	257
4	Bowel Perforation	258
5	Diverticulitis	258
6	Ruptured Abdominal Aortic Aneurysm	260
7	Gastrointestinal (GI) Hemorrhage	260
8	Gangrenous Cholecystitis	261
9	Gangrenous Appendicitis	262
10	Pancreatitis	264
11	Urinary Tract Calculi	265
12	Ovarian Torsion	266
13	DECT in the Acute Traumatic Abdomen	266
13.1	Blunt Abdominal Trauma	266
13.2	Pneumoperitoneum	267
13.3	Hemoperitoneum	267
14	Active Extravasation on DECT	267
15	Visceral Injuries on DECT	268
16	Splenic Injuries	268
17	Hepatic Injuries	268
18	Pancreatic Injuries	269

S. Hamid (✉) · M. U. Nasir · A. Kecler-Pietrzyk ·
A. Sheikh · N. Murray · F. Khosa · S. Nicolaou
Vancouver General Hospital, University of British
Columbia, Vancouver, BC, Canada
e-mail: Saira.hamid@vch.ca

19	Urinary Tract Injuries	269
20	Diaphragmatic Injuries	270
21	Bowel and Mesenteric Injuries	271
22	Vascular Injuries	272
23	Bone Injuries	272
24	Penetrating Abdominal Trauma	272
25	Conclusions	273
	References	273

Abstract

Acute abdominal and pelvic pain can have a wide range of etiologies, from self-limiting conditions to acute pathologies requiring emergent surgery. Emergency radiology plays a pivotal role in the routine diagnosis and outcomes of patients with these disorders. Computed tomography (CT) with evolved protocols and technological advancements in particular with advent of dual-energy CT remains the first diagnostic modality of choice in patients with non-traumatic surgical abdomen, including appendicitis, cholecystitis, bowel ischemia, bowel obstruction, visceral perforation, bowel hemorrhage, and abdominal aortic aneurysm rupture. Renal calculi are also frequently encountered non-surgical causes of acute abdominal pain.

Conversely of the spectrum, abdominal trauma is one of the leading causes of death and morbidity. Mechanism of injury classifies abdominal trauma into blunt and penetrating. Blunt abdominal trauma usually results from falls from heights, motor vehicle collisions (MVC), and assaults. Penetrating abdominal trauma arises from stab wounds and gunshot wounds. In both blunt and abdominal trauma, imaging should exclude life-threatening injuries after careful examination and primary survey. Ultrasound is rapid and portable imaging modality making it a good option for abdominal trauma screening. However, fast scan is limited to look for hemoperitoneum, and evaluation of intra-abdominal organ injuries is

dependent on MDCT. The hemodynamically stable patient should receive a multidetector computed tomography (MDCT) scan with IV contrast in the assessment of visceral and vascular injuries. DECT can increase the conspicuity of traumatic solid organ and hollow visceral damage by utilizing its post-processing applications like selective iodine imaging, virtual monoenergetic imaging.

Abbreviations

CT	Computed tomography
DECT	Dual-energy computed tomography
ED	Emergency department
GI	Gastrointestinal
IV	Intravenous
MDCT	Multidetector computed tomography
MVC	Motor vehicle collisions
VNC	Virtual non-contrast

Learning Objectives

- To emphasize the role of dual-energy computed tomography (DECT) in the non-traumatic and traumatic emergencies of the abdomen.
- To highlight the significance of an optimized DECT protocol imperative for an accurate and prompt diagnosis.
- To demonstrate the spectrum of the imaging findings in acute traumatic and non-traumatic disorders of the abdomen.

1 Introduction

Acute abdominal pain is one of the most common presentations in the emergency department (ED) and comprises approximately 15% of all emergent cases (Kamin et al. 2003). Acute onset of severe abdominal pain raises the concern for intra-abdominal emergencies, such as perforated solid viscera, bowel ischemia/bleeding, or acute visceral inflammation. Therefore, based on the imaging findings and diagnosis, patients may require immediate intervention or follow-up. Evaluation of abdominal pain in the ED requires a thorough approach, based on patient's history, physical examination, laboratory tests and imaging studies. Despite extensive evaluation, mostly half of these patients still remain undiagnosed, however with latest imaging advancements this number has decreased significantly. Abdominal radiographs have limited diagnostic value. However, because of the easy availability, they can be used as a first line of investigation to guide the treatment and further investigations.

Prompt diagnosis and characterization of abdominal injuries are essential in polytraumatic patients to avoid mortality. The most commonly injured intra-abdominal organ is the spleen, followed by the liver and the genitourinary tract (Soto and Anderson 2012). Computed tomography (CT) helps distinguish injuries that require immediate surgical or angiographic management. DECT for abdominal and pelvic trauma is an emerging application (Jeremy et al. 2018). DECT allows us to acquire images at different Kev and improve the detection and assessment of organ lacerations and decreased organ perfusion by obtaining low Kev images. Moreover, creating virtual non-contrast (VNC) images by subtracting the iodine and iodine overlay images helps to look for active bleeding, and many studies have shown the accuracy of iodine maps and VNC images with solid organs (Glazer et al. 2014; Ascenti et al. 2013; Wortman et al. 2016). In this review article, we will discuss the spectrum of abdominal injuries in a motor vehicle collision with emphasis on the CT protocols, imaging findings, and illustrations.

2 Role of DECT in Non-traumatic Acute Abdomen

Dual-energy CT has emerged as a promising tool in imaging the patients presenting with nontraumatic causes of acute abdomen and has multiple potential clinical applications. Use of the dual-energy CT acquisition allows characterization of various materials depending on their differential attenuation and thus helps to identify the material composition (Grajo et al. 2016). Hence, selective identification of the iodine content can provide information about the visceral enhancement, including decreased or no enhancement in case of vascular compromise or hyperenhancement in inflammation. Besides identifying iodine, its quantitative analysis can help differentiate between the inflammatory and neoplastic pathologies. Virtual nonenhanced images can lower the patient dose by eliminating the need of performing a non-contrast phase. DECT with VNC images can help differentiate hemorrhage from tissue enhancement or mineralization. Furthermore, the ability of dual-energy CT to substantially reduce metallic prosthesis related artifact is an added advantage to unmask the underlying anatomical and pathological details.

3 Bowel Ischemia

Bowel ischemic can be seen as a consequence of arterial embolism, venous thrombosis, hypoperfusion, vasculitis and small bowel obstruction, particularly a closed-loop obstruction (Fig. 1). Hypoenhancement or lack of bowel wall enhancement is considered a direct sign of bowel ischemia (Wallace et al. 2016; Potretzke et al. 2015a). Other cross-sectional imaging findings include direct visualization of the thrombus in the mesenteric arterial or venous circulation. Non-specific imaging findings may include bowel distension, bowel wall edema, hyperenhancement of the mucosa, circumferential mural thickening, and surrounding fat stranding. In advanced cases, pneumatosis, portal/mesenteric venous gas, peritonitis/ascites, and free gas can be found. Iodine

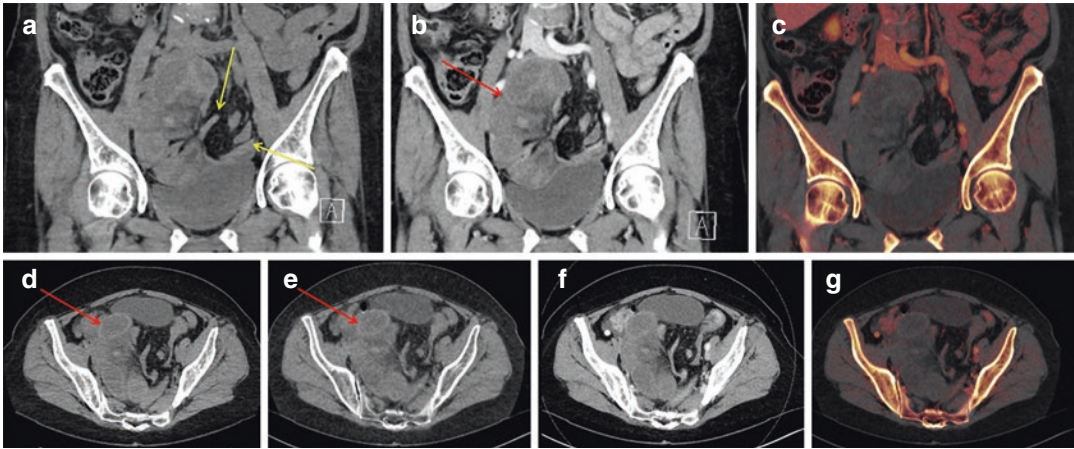


Fig. 1 An 82-year-old female with acute onset of abdominal pain and elevated lactate. (a, d) Unenhanced axial and coronal CT images show multiple mildly dilated small bowel loops in the right lower quadrant with two transition points (yellow arrow) signifying closed loop obstruction. Mural hyper-attenuation (red arrow) on the unenhanced images can be accurately seen on the virtual

non-contrast image (e), this appearance is consistent with mural hemorrhage. (b, f) Post-contrast coronal and axial CT images show no attenuation difference or enhancement on the venous phase on comparison to the VNC or unenhanced images. This feature is seen as no iodine uptake on iodine overlay coronal and axial images (c, g)

overlay imaging and virtual monoenergetic imaging at lower energy levels can detect and differentiate mural hypoperfusion from normally perfused bowel wall (Wallace et al. 2016; Potretzke et al. 2015a). Early detection of the bowel ischemia is crucial to prevent development of the gangrenous bowel and can significantly impact the patient outcome (Fig. 2).

4 Bowel Perforation

Abdominal pain in hollow viscus perforation is usually very severe and diffuse rather than localized to one quadrant. Other associated symptoms include fever, nausea, vomiting, dizziness, and shortness of breath. Bowel perforation can be secondary to myriads of pathologies including appendicitis, diverticulitis, stomach ulcers, inflammatory bowel disease, ischemia, ingestion of foreign body, or long-standing bowel tumor (Fig. 3). Iatrogenic causes may include post colonoscopy or endoscopy bowel perforation (<https://radiopaedia.org/articles/bowel-perforation-summary>). Bowel perforation is an acute surgical emergency and CT scan with intravenous (IV)

contrast is the investigation of choice. The direct evidence of bowel perforation on CT is demonstration of free air and fluid within peritoneal cavity or concealed extraluminal collection (<https://radiopaedia.org/articles/bowel-perforation-summary>). Dual-energy CT is helpful in identifying underlying causes like bowel ischemia, bowel related tumors, perforated diverticulitis (Fig. 4), gangrenous appendicitis, and cholecystitis. Treatment is dependent on the identification of underlying cause followed by surgical intervention.

5 Diverticulitis

Diverticulosis is the herniation of the mucosa and the submucosa through the muscular layer of the bowel, which if develops inflammation results in diverticulitis. The abdominal pain is usually localized to the respective abdominal quadrant, mostly left lower quadrant. Apart from the abdominal pain, other symptoms include nausea, vomiting, fever, and localized tenderness. If left untreated, the complications of diverticular disease include focal colitis, lower gastrointestinal

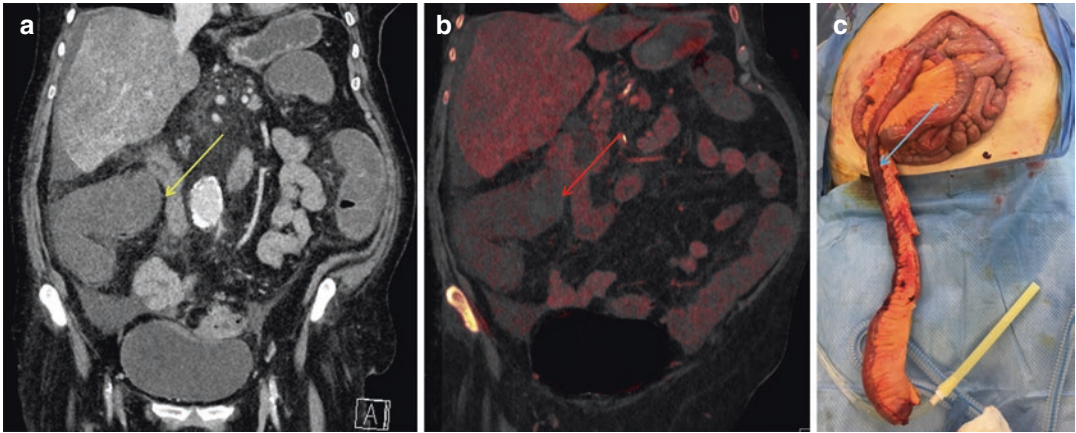


Fig. 2 A 75-year-old female with end stage COPD who presented with abdominal pain (a). Coronal post-contrast CT image shows fluid filled ascending colon with questionable mural enhancement (yellow arrow). (b) Coronal iodine overlay image confirms the lack of iodine uptake

signifying ischemia (red arrow). (c) Perioperative picture shows the blackish discoloration (blue arrow) of the ascending colon signifying ischemic insult leading to hemicolectomy

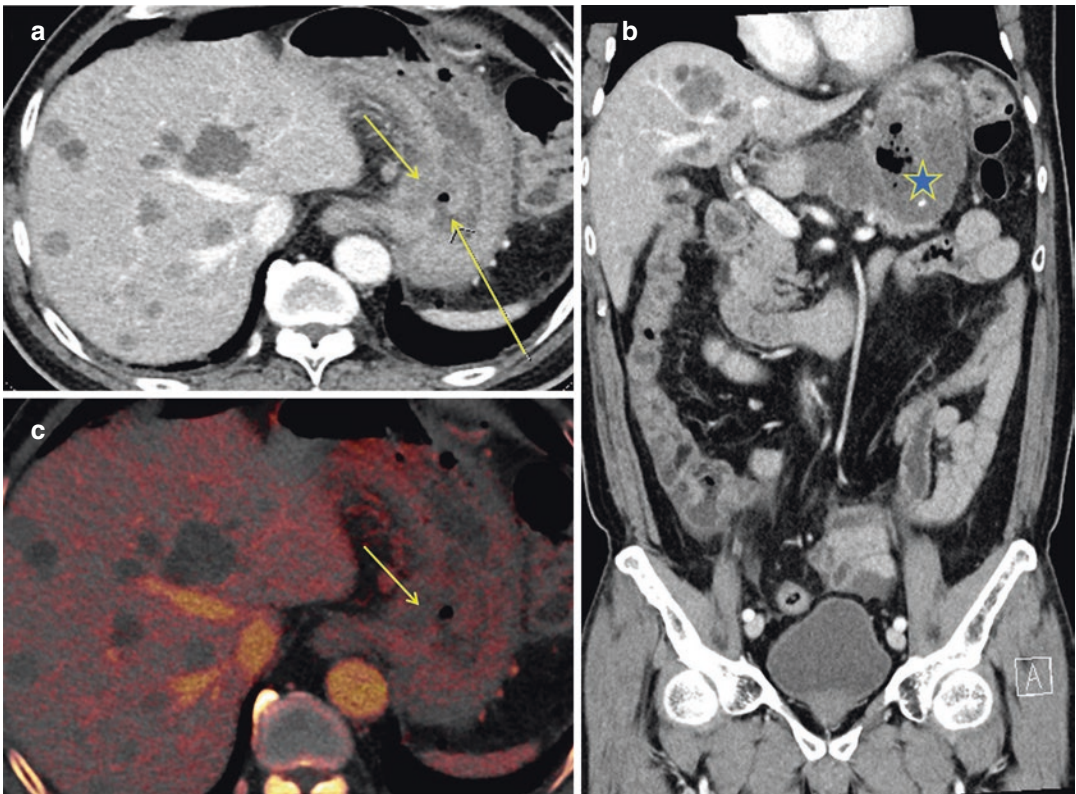


Fig. 3 A 63-year-old male with known history of GIST presented with marked epigastric pain. (a) DECT post-IV contrast in portal venous phase shows 1 cm focal defect along the lesser curvature of the stomach with small gas

locule adjacent to it (yellow arrow), confirmed on iodine map (b). (c) Coronal reformates demonstrate heterogeneous partially calcified lesion involving the lesser curvature of the stomach (asterisk)

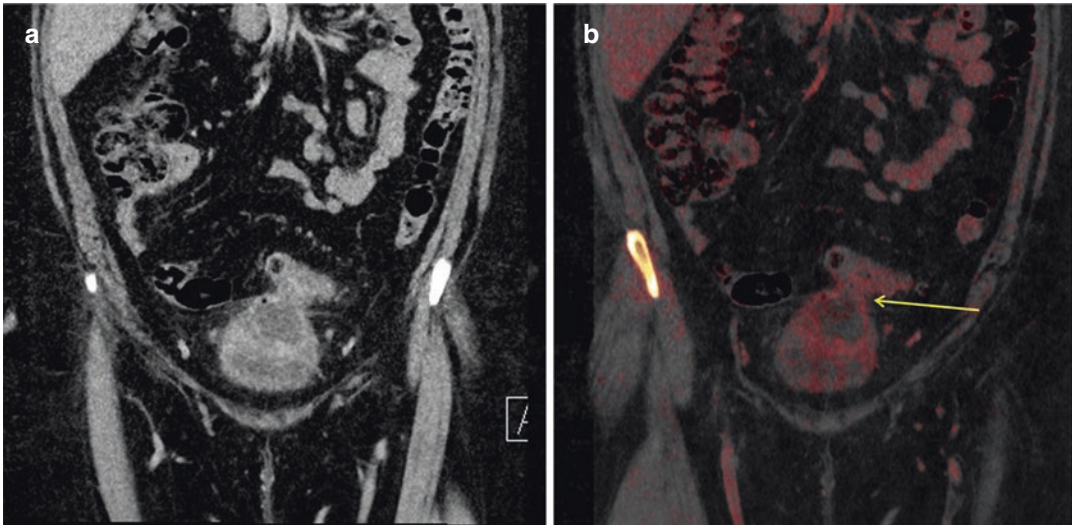


Fig. 4 A 44-year-old female with suprapubic pain and elevated inflammatory markers. (a) Coronal image showing communication between the sigmoid colon and supra-

vesical collection on the background of acute diverticulitis. (b) Sinus tract (yellow arrow) is highlighted with peripheral iodine uptake on the overlay maps

bleeding, infection, abscess, perforation, peritonitis, fistula formation, and obstruction. CT with IV contrast is the imaging modality of choice for both acute complicated and uncomplicated diverticulitis. Colonoscopy is advised in older patients and patients with long-standing history of diverticulitis, after resolution of the symptom to exclude any underlying pathology. Common findings on CT scan include segmental bowel wall thickening, peri-colonic fat stranding, localized fluid, and air (Fig. 4). In complicated diverticulitis, CT scan findings include localized bowel perforation with abscess formation, fistulous tracts, with extravasation of gas and fluid in the peritoneal cavity in cases of perforation. Acute complicated diverticulitis with bowel perforation is a surgical emergency because of the associated risk of peritonitis (Suzanne Albrecht 2010).

6 Ruptured Abdominal Aortic Aneurysm

Abdominal aortic aneurysms can have an indolent course with slow rate of progression in size and no obvious symptoms. Acutely enlarging

abdominal aneurysm can present with diffuse abdominal discomfort, back pain, or in advanced cases with pulsatile abdominal mass, especially in thin lean patients. Rupture of the abdominal aneurysm can cause life-threatening hemorrhage and in these patients a sudden drop of blood pressure should be considered a red flag. CT can have typical signs of impending rupture such as aortic wall edema, presence of gas, interrupted peripheral calcifications, aorto-enteric fistulas, and in cases of ruptured aneurysm signs like retroperitoneal hematoma and visualization of direct defect in wall can be seen (Rakita et al. 2007).

7 Gastrointestinal (GI) Hemorrhage

A common presentation for the patients with suspected gastrointestinal hemorrhage is diffuse severe abdominal pain and hematemesis. Though it is imperative to obtain a careful history and physical examination, a well-coordinated approach between the referring physician and the emergency radiologist prior to the CT scan is crucial for the optimized protocol mandatory to diagnose the GI hemorrhage. The oral contrast

should not be used in these patients, as the high attenuation intraluminal contrast can obscure identification of the GI hemorrhage.

Dual-energy CT can be valuable in the setting of the GI hemorrhage, resulting in improved diagnostic accuracy (Sun et al. 2013). The ability to generate the virtual non-contrast (VNC) images from the post-contrast dual-energy CT can effectively reduce the radiation dose by eliminating the need to perform non-contrast images (Fig. 1). Dual-energy CT can help to distinguish high attenuation enteric contents from intraluminal iodinated contrast extravasation using the VNC reconstructions. The iodine overlay color map can easily detect and increase the diagnostic confidence to detect the presence of intraluminal iodine (Fig. 5).

8 Gangrenous Cholecystitis

Cholecystitis is one of the most common causes of pain in the right upper quadrant. Usually, ultrasound is the first investigation of choice. Typical ultrasound findings in the acute cholecystitis include gallstones, pericholecystic fluid, gallbladder wall thickening, and positive Murphy’s sign. However, it is noteworthy that the ultrasound cannot accurately differentiate between the gangrenous and simple cholecystitis, which is decisive in the management of the patient (Ratanaprasatporn et al. 2018). CT scan can further demonstrate cholecystitis related complications like perforation/abscess formation, hemorrhage, gas, stone lodged in the gallbladder neck or cystic duct, and gallbladder wall gan-

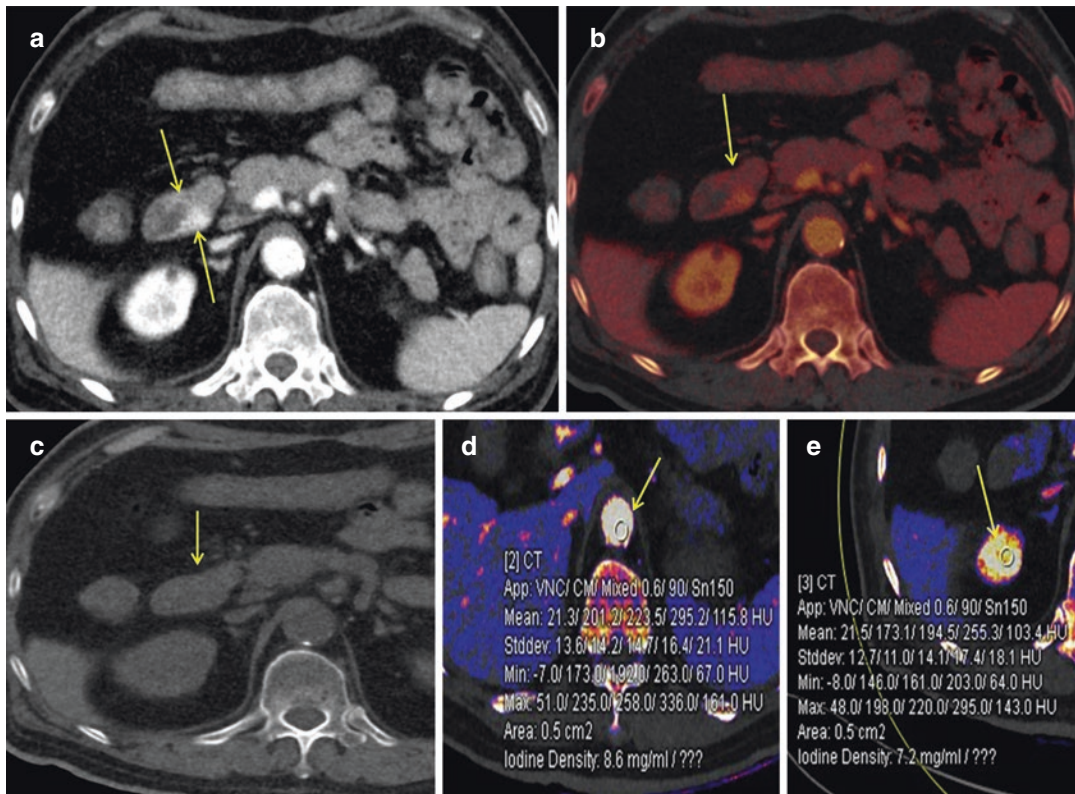


Fig. 5 A 64-year-old male presented with symptoms of intestinal obstruction and hematemesis. (a) Axial sequence of DECT abdomen with intravenous contrast demonstrates high density material in second part of the duodenum in the dependant part (yellow arrow). (b) On DECT color iodine map, iodine uptake is seen. (c) On vir-

tual non-contrast subtraction images complete subtraction is noted suggestive of active bleed rather than calcification (yellow arrow). (d, e) show iodine quantification with approximately similar iodine density in second part of duodenum and aorta

grene (Kim et al. 2012; Murray et al. 2019). Moreover, dual-energy CT can demonstrate the areas of absent wall enhancement consistent with gangrenous cholecystitis, more conspicuously as compared to the conventional CT (Fig. 6). These findings can alter the surgical approach with a need for an open rather than a laparoscopic cholecystectomy. Dual-energy CT can be helpful in identifying the gallstones which are isodense to the bile (Sulu et al. 2010). Prior studies have shown that gallstones are better visualized on monochromatic low KeV (Fig. 7). Moreover, impacted stone in cystic duct resulting in Mirizzi syndrome and gallstone in small bowel causing the gallstone ileus can be easily identified by using the dual-energy gallstone application (Figs. 8 and 9).

9 Gangrenous Appendicitis

Acute appendicitis is one of the most common causes of acute right lower abdominal pain leading to surgery. In North America, incidence of appendicitis ranges between 75 and 83 cases per 1000,000 population (Sulu et al. 2010). Diagnostic modalities including ultrasound, CT, and MRI in selective patient population (young females of childbearing age or pregnancy) have an important role in the diagnosis of acute appendicitis and its related complications.

Long-standing, progressive transmural inflammation causes ischemia and necrosis of the appendix, thus resulting in gangrenous appendicitis which is prone to complications such as perforation, abscess formation, and sepsis. It is important

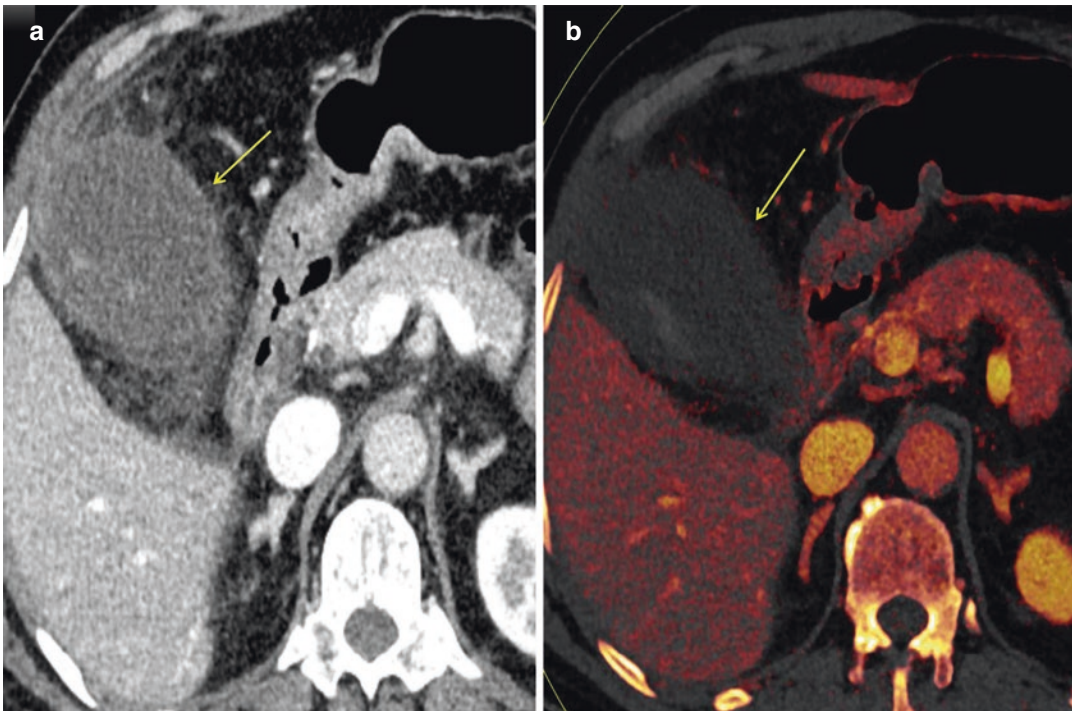


Fig. 6 A 73-year-old male presented with abdominal pain, jaundice, weight loss. **(a)** Axial CT abdomen shows markedly dilated gallbladder with hyperdense content, extensive pericholecystic fluid, mild sloughing of the gall-

bladder wall, and a few areas of decreased wall enhancement are concerning for gangrenous cholecystitis (yellow arrow). **(b)** Color coded iodine map shows absent wall enhancement suggestive of gangrenous (yellow arrow)

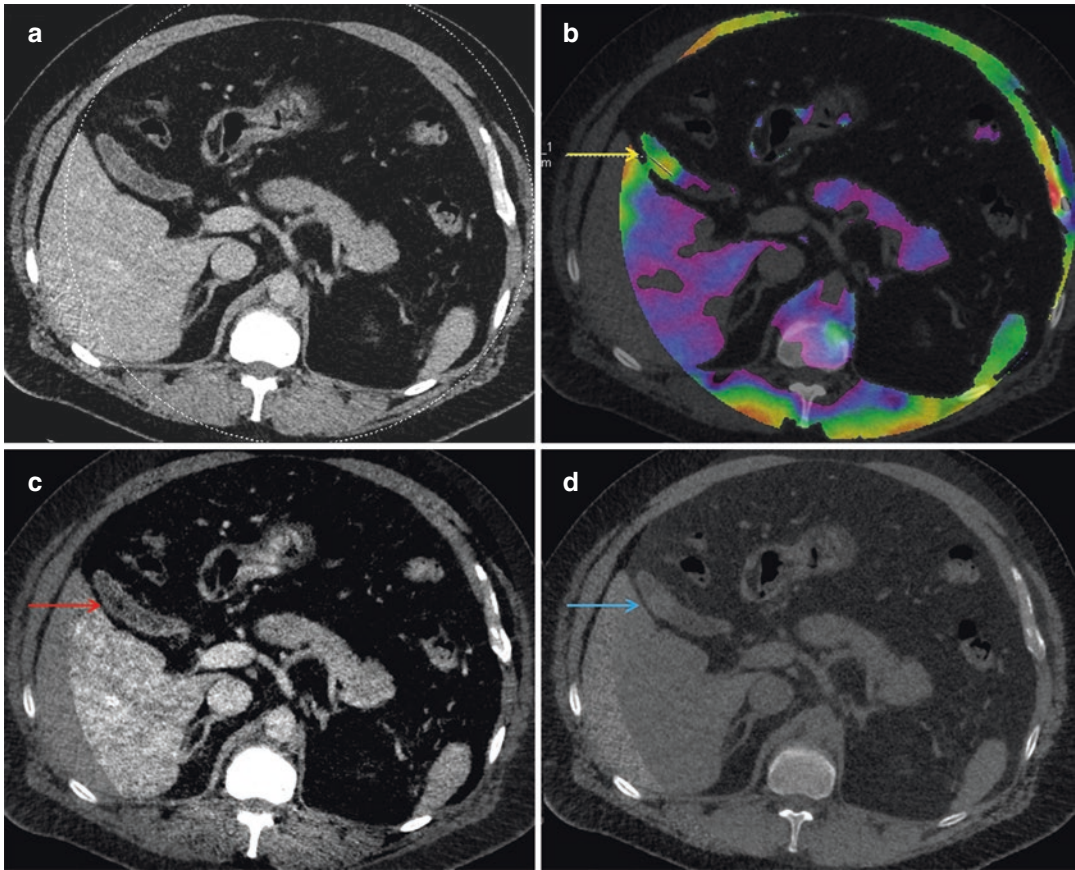


Fig. 7 A 43-year-old male patient presented with abdominal discomfort to emergency department. **(a)** 120 keV axial CT image shows decompressed gall bladder with questionable intraluminal high density. **(b)** Dual-energy color coded overlay image shows the presence of 2 cm calculus in the gall bladder. **(c)** 40 KeV virtual monoenergetic axial image reconstruction shows the correlative low

attenuation of the calculus (red arrow) signifying lipid rich content of the calculus. **(d)** 190 KeV axial monoenergetic image shows relative hyperattenuation of the calculus (blue arrow)

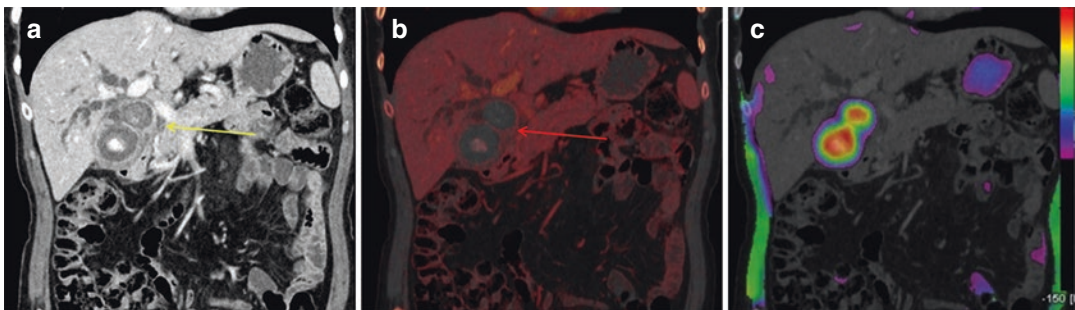


Fig. 8 A 65-year-old female with fever and elevated LFTs. Multiple large gallbladder stones. **(a)** Coronal reformatted image of CT shows gallbladder cauli associated with circumferential gallbladder thickening with trace of pericholecystic fluid and fat stranding (yellow arrow). These findings are associated with intrahepatic

biliary dilatation consistent with Mirizzi syndrome. **(b)** Iodine overlay map shows iodine uptake of the gall bladder wall consistent with inflammation (red arrow). **(c)** Dual-energy color coded overlay image shows variable composition of the calculi with red, yellow, and green colors

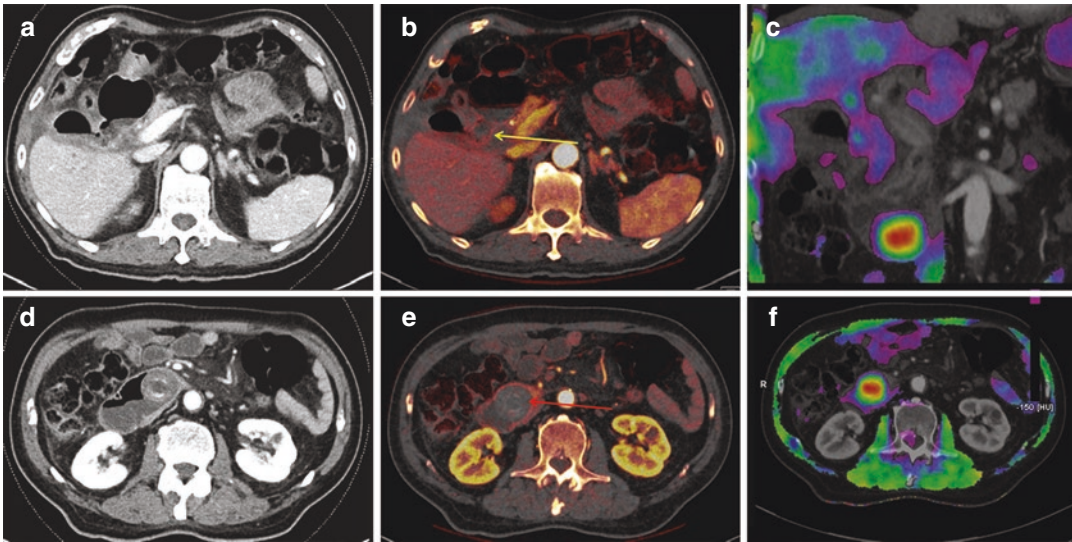


Fig. 9 An 80-year-old male with severe abdominal pain and deranged LFTs. (a, d) Contrast enhanced axial CT images show fistula extending from the gallbladder neck to the first part of duodenum. Large laminated impacted gallstone in the proximal 3rd part of duodenum with upstream

duodenal dilatation. (b, e) Iodine overlay map highlights the fistulous communication (yellow arrow). (c, f) Dual-energy color coded overlay images confirm the gallstone within the 3rd part of duodenum (red arrow)

to identify gangrenous appendicitis prior to surgery as the rate of postoperative complications is relatively higher than uncomplicated appendicitis. Thick-walled, dilated, fluid-filled appendix along with hyperenhancement of the mucosa and edematous wall are the most common CT findings to diagnose acute appendicitis. Dual-energy CT can detect the presence of transmural necrosis of the wall of the appendix on the iodine overlay images and on low 40-KeV virtual monoenergetic images. The difference between a subtle non enhancing gangrenous segment of the appendix with low iodine uptake from a normal enhancing mucosa of the appendix is crucial to identify because if left untreated, it can lead to perforation (Fig. 10). The ability of the dual-energy CT to distinctly differentiate the gangrenous mucosa from the normal enhancing mucosa clearly adds value in patient management (Elbanna et al. 2018).

10 Pancreatitis

Acute pancreatitis is a common abdominal emergency and has a broad spectrum of presentations and outcomes. Although acute pancreatitis is a clinical

diagnosis, however, it can be difficult to differentiate it from other causes of upper abdominal pain, especially if the serum amylase and lipase levels are non-contributory. Pancreatitis can be frequently seen as a complication of long-standing gallstones or alcohol abuse. Other etiologies include trauma, interventional pancreato-biliary procedures, drugs, tumors, and hereditary pancreatitis.

A standard venous phase CT abdomen is used in cases with low clinical suspicion; however, a dedicated multiphase pancreatic protocol should be used in cases with high clinical suspicion and for the follow-up of known pancreatitis. Usually, no oral contrast is required and only IV contrast administration is preferred. CT findings range from a normal or nearly normal pancreas, mild focal, or diffuse peripancreatic inflammation to marked pancreatic edema and associated necrosis. While diagnosing pancreatitis, careful attention should be given to the related complications such as necrosis, fluid collections, erosions, thrombosis of SMV or splenic artery pseudoaneurysms. In the initial few days, CT findings do not necessarily correlate with the patient outcome, but later in the disease course, the CT findings have greater prognostic significance.

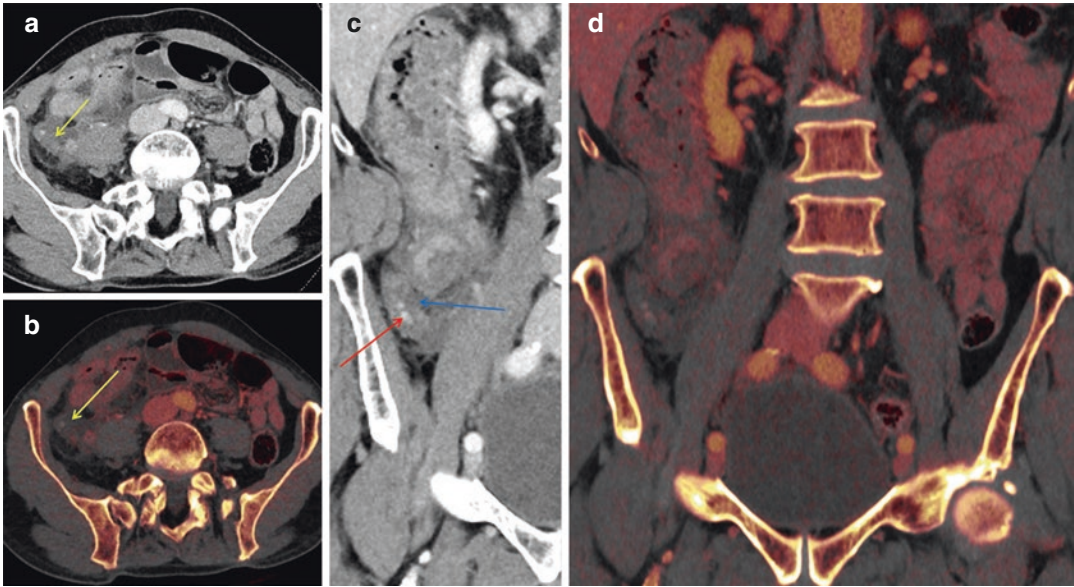


Fig. 10 An 81-year-old male with acute onset of right abdominal pain overnight. (a, b) Axial and coronal post-contrast images show thickening of the appendix (yellow arrow) with surrounding fat stranding and free fluid which is in keeping with appendicitis. Central high-density foci

represent appendicolith (red arrow). There is a segment of poor mucosal enhancement seen as discontinuous iodine uptake on the iodine overlay maps (c, d) in the anterosuperior wall suggesting gangrenous changes (blue arrow)

There are two main types of acute pancreatitis: interstitial edematous versus necrotizing. CT scoring systems are frequently used to characterize acute pancreatitis and provide prognostic information. Scoring is dependent on the number of collections, pseudocyst formation, necrosis, and associated complications (White et al. 1986). CT-guided aspiration is very useful when indicated, to distinguish sterile from infected necrosis/fluid collections. Dual-energy CT helps to identify necrosis of the pancreatic tissue by detecting the iodine content.

11 Urinary Tract Calculi

Patients presenting with acute flank pain is usually suspected to have urinary tract calculi and CT KUB (Kidney, ureter, and bladder) is requested. Administration of IV contrast is usually not indicated in the routine cases, and it is reserved for those cases in which there is a high clinical suspicion of pyelonephritis. CT KUB has the highest sensitivity and specificity for the

identification of urinary tract calculi, size of calculi, overall calculus burden, associated complications while accurately identifying an alternate diagnosis as well.

The majority of renal calculi are radiopaque with a few exemptions such as medication induced calculi (Indinavir, sulfonamide, ciprofloxacin, etc.). Dual-energy CT can identify the specific composition of the calculus and especially can differentiate non-uric acid from the uric acid calculi (Hidas et al. 2010). Moreover, other related findings like hydronephrosis, periureteric/perinephric fat stranding, and ureteric wall enhancement can be seen (Fig. 11). The presence of phleboliths in the pelvis can sometimes make it difficult to diagnose the distal ureteric calculi. The provision of multiplanar sagittal and coronal reconstructions and identification of a peripheral rim of soft tissue created by the ureteral wall around the calculus can help in differentiating the ureteral calculi from the phleboliths. CT can demonstrate a wide variety of alternative diagnoses in patients presenting with renal colic without urinary tract calculus.

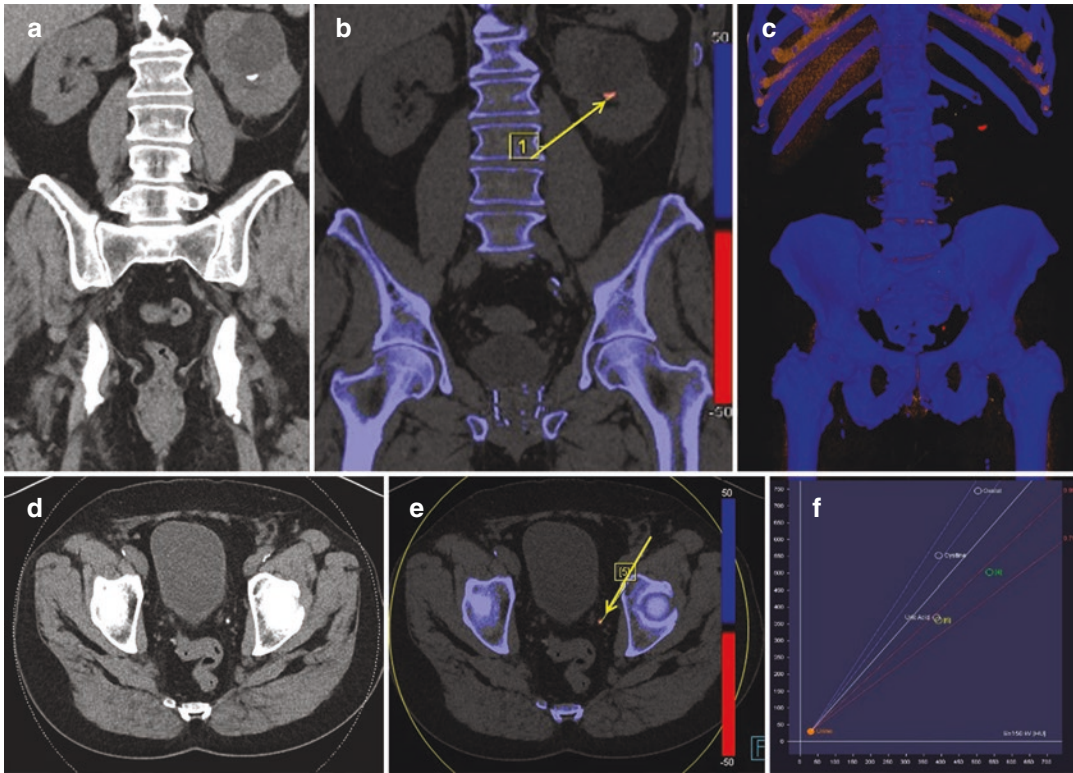


Fig. 11 A 68-year-old male with left flank pain. (a, d) Noncontrast coronal and axial images show high density calculi in the interpolar region of the left kidney and distal ure-

ter. (b, c, e) Coronal and axial DECT images show red color coding of the calculi (yellow arrows in b and e). (f) Graphic representation of the uric acid composition of the calculi

12 Ovarian Torsion

Ovarian torsion occurs when the ovary twists around its ligamentous attachments. It can occur at any age but is most commonly seen in women of childbearing age. It is mostly associated with benign and malignant tumors. Direct CT findings include thickening of the fallopian tube, the twisted structure of the adnexa and on dual-energy iodine maps, reduced iodine uptake can be seen suggestive of disruption in the blood flow secondary to the torsion. However, CT findings are mostly non-specific and presence of the indirect findings including edematous swollen ovary, free fluid, and dilated fallopian tube usually support the diagnosis (Iraha et al. 2017) (Fig. 12).

13 DECT in the Acute Traumatic Abdomen

13.1 Blunt Abdominal Trauma

Blunt abdominal trauma is the main cause of mortality among all age groups. CT has become the primary imaging examination for evaluating blunt abdominal trauma. Fast scan plays a vital role in the detection of hemoperitoneum in hemodynamically unstable patients. Identifying severe abdominal injuries is often challenging, and many injuries may not become visible during the initial period. The presence of a seat belt protects the chest and head but increases the chances of abdominal injuries.

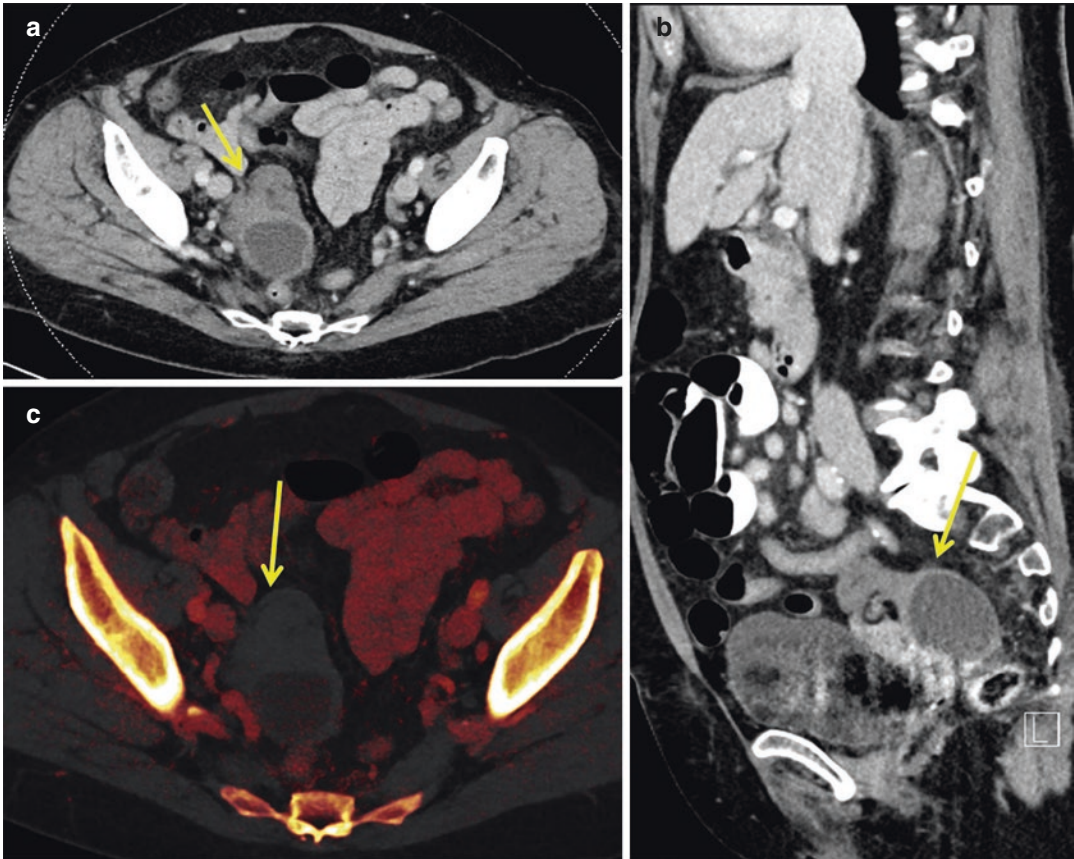


Fig. 12 A 74-year-old female presented with severe right lower quadrant pain. (a) On axial CT post-contrast portal venous phase images, septated cystic structure in the right adnexa (yellow arrow). (b) Sagittal reformates shows

swirl sign (yellow arrow). (c) On dual-energy analysis, no iodine uptake is noted in adnexa suggestive of absent perfusion (yellow arrow)

13.2 Pneumoperitoneum

On MDCT, pneumoperitoneum is described as the presence of free air under the diaphragm or small gas locules trapped between the layers of the mesentery, and using lung window settings can help identify small amounts of intraperitoneal gas. In the background of trauma, pneumoperitoneum raises concerns for bowel perforation, and any area of localized gas locules adjacent to abnormal-looking bowel may indicate the site of injury.

13.3 Hemoperitoneum

In trauma patients, the presence of free fluid in the peritoneal cavity likely represents blood called hemoperitoneum having an average atten-

uation of 30–45 HU, and potential causes are injury to the liver, spleen, bowel, or mesentery. Dot signs can be seen adjacent to the source of hemorrhage, which can help identify the site of bleeding.

14 Active Extravasation on DECT

The importance of active extravasation of contrast has been demonstrated in multiple studies, and usually, its presence indicated urgent surgical intervention. For example, in cases of active extravasation of contrast along with splenic injury, the preferred treatment is splenectomy (Dreizin and Munera 2012; Federle et al. 1998). Similarly, in patients with bowel and mesenteric

injuries, open laparotomy is indicated when active extravasation of contrast is present. Moreover, studies done on pelvic trauma suggest embolization and laparotomy in patients with active extravasation of contrast and pelvic fractures (Federle et al. 1998).

In hemoperitoneum cases, 5–10 min of delayed scans are usually performed to look for active extravasation of contrast. If the attenuation or size of the hemoperitoneum increases on delayed scans, it is consistent with active extravasation (Marmery et al. 2007). DECT can help in better evaluation of the active extravasation of contrast. There is no CT evidence of active extravasation of contrast if high attenuation material seen on VNC images does not correspond with iodine density images. Moreover, in patients with pelvic fractures, it is difficult to differentiate between high attenuation material and fracture fragments. DECT VNC images help to differentiate between the two (Fig. 11).

15 Visceral Injuries on DECT

The surgical injury grading scale for each organ was created by the American Association for the Surgery of Trauma (AAST) (Dreizin and Munera 2012). However, in AAST guidelines, CT findings in acute trauma like active extravasation and vascular injury were not considered (Federle et al. 1998). Therefore, various CT grading systems have been designed by incorporating and modifying the AAST guidelines to predict better which patients will not respond to conservative treatment and will require surgery (Marmery et al. 2007; Shanmuganathan et al. 2017).

For both types of trauma, traumatic solid organ injuries manifest as geographic areas of parenchyma that are relatively hypoattenuating, with organ lacerations generally hypoattenuating linear or branching in appearance. A contusion is a vague, poorly defined hypodense area in a solid organ. DECT improves the detection of laceration on low Kev images as the contrast between the hypovascular laceration and organ parenchyma increases. This concept is taken from the fact that at low Kiloelectron volt images, there is

improve sensitivity for detection of hypovascular lesions (Yamada et al. 2012; Sudarski et al. 2014; Robinson et al. 2010). Iodine quantification in the injured and uninjured parenchyma can be done using iodine-selective images. Another significant advantage of iodine-selective imaging of solid-organ injury is its ability to allow parenchymal hematomas to be distinguished from organ lacerations. Hematomas are hyperdense on non-enhanced images, and subcapsular hematoma is a well-defined collection of blood “high attenuation” that appears as an indentation over an organ. DECT virtual non-contrast images can help identify hyperattenuating blood products in patients with hematoma.

16 Splenic Injuries

The splenic injuries in the majority of cases are managed conservatively. Early identification of injuries that requires surgical or angiographic intervention is of critical importance. The AAST grading system is dependent on the size of the splenic laceration, active extravasation, pseudoaneurysm, and involvement of vascular pedicle. Surgical therapy is required for higher-grade injuries (generally AAST grade III and higher). The delayed phase image acquisition is useful for the definitive characterization of splenic vascular injury as active hemorrhage or contained vascular injury as contrast washes out in the latter.

CT features of splenic trauma including the parenchymal hypoattenuation, presence of active hemorrhage, a pseudoaneurysm, or an arteriovenous (AV) fistula. Pseudoaneurysms often can be managed conservatively, whereas arteriovenous fistulas generally require embolization (Federle et al. 1998; Marmery et al. 2007).

17 Hepatic Injuries

The AAST liver injury scale is commonly used to assess the severity of hepatic injuries. The liver injury grading scale is based on the location, size of liver lacerations, hematomas, or devascularization in higher-grade injuries.

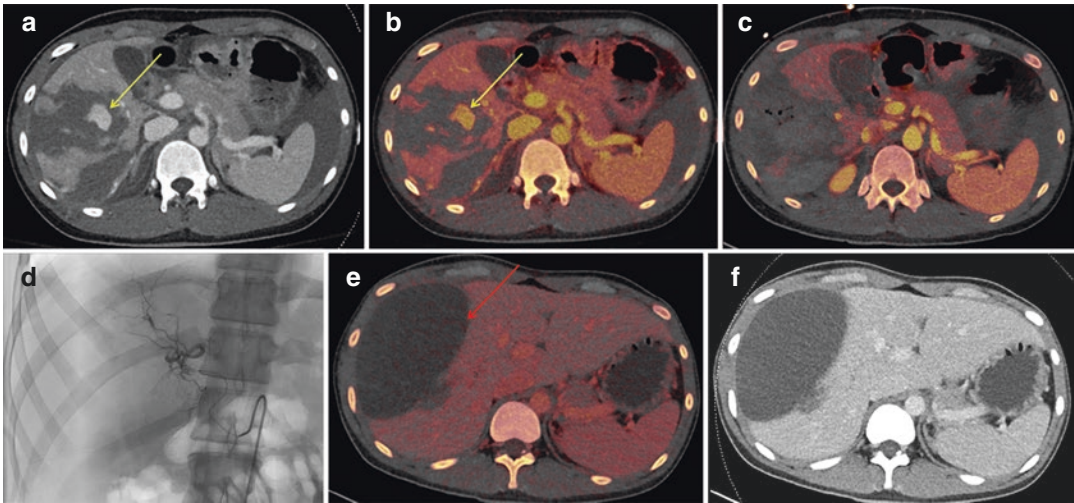


Fig. 13 A 23-year-old male with blunt abdominal injury after crashing into a fence while skating. (a) Axial post-contrast CT image shows central high density material within a large hepatic laceration (yellow arrow). (b) Iodine map shows accumulation of iodinated material within this high density focus signifying active hemorrhage, orange color coding (yellow arrow). (d)

Conventional angiography image post-gel foam embolization of distal right hepatic artery. (c) Follow-up axial iodine overlay CT image after embolization shows no pooling of iodinated material. (e, f) Follow-up CT after 4 weeks shows low attenuation collection in the right hepatic lobe likely suggesting biloma

CT findings include hypoattenuating lacerations, subcapsular or intraparenchymal hematomas, the involvement of intrahepatic ducts and vessels, active extravasation, and the presence of large volume hemoperitoneum. DECT is helpful to better characterize lacerations and hypoperfused segments (Fig. 13) (Yamada et al. 2012; Sudarski et al. 2014; Robinson et al. 2010).

Major hepatic vein injury requires surgery, whereas active extravasation can usually be treated with endovascular intervention. Delayed complications are the formation of pseudoaneurysms, hepatic abscess, and bilomas.

18 Pancreatic Injuries

Pancreatic trauma has higher mortality than other solid-organ injuries (Venkatesh and Wan 2008) – the most common site of pancreatic injuries in the neck and body. Direct signs of pancreatic injury on CT scan include contusions and laceration, appearing as focal areas of hypoattenuation or linear low attenuation defects. Pancreatic duct

injuries are difficult to characterize; however, they become more conspicuous on peak enhancement of the pancreatic tissue (Patel et al. 2013). Lacerations that involve more than 50% of the pancreatic thickness usually cause pancreatic ductal injury (Figs. 14 and 15). Pancreatic injuries can be subtle and difficult to identify in the early posttraumatic period; therefore, particular attention should be given to peripancreatic fluid or fat stranding. DECT low KEV images can better delineate pancreatic duct (Rekhi et al. 2010). DECT has shown improve visualization of hypovascular pancreatic lesions and, therefore, can be differentiated with lacerations (Rekhi et al. 2010; Macari et al. 2010; Marin et al. 2010; Patel et al. 2013; McNamara et al. 2015). Pancreatic injuries may progress to pancreatitis.

19 Urinary Tract Injuries

The severity of renal trauma is based on the size and location of renal laceration according to the AAST grading system. Isolated renal injury

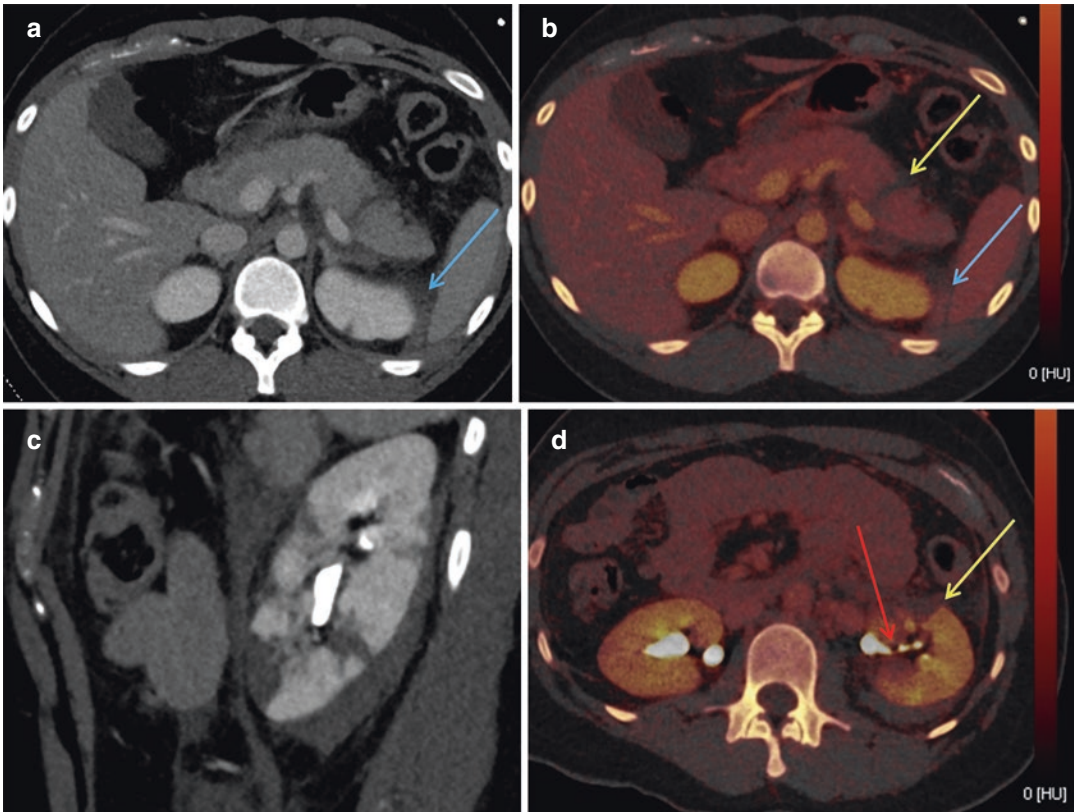


Fig. 14 A 25-year-old female with blunt abdominal trauma secondary to mountain biking accident. (a) Axial CT image shows linear hypoattenuation through the pancreatic tail and high density hematoma in left perinephric location (blue arrow). (b) Axial image with iodine overlay shows the laceration conspicuously confirming complete transection of the pancreatic tail (yellow arrow). High

attenuation hematoma in left superior perinephric location shows iodine uptake suggesting active hemorrhage (blue arrow). (c) Coronal CT image shows complex laceration of the left kidney. (d) Iodine overlay map shows devascularization of a small fragment of the anterior inferior pole (yellow arrow) and filling defect in the renal pelvis (red arrow), showing clot

results in contained hemorrhage within the Gerota fascia and perirenal fascia. Delayed excretory CT imaging is necessary to assess the collecting system and search for leaks, usually approximately 5 min after contrast material administration. Retrograde urethrography or voiding cystourethrography can be performed to evaluate urethral injuries, whereas, for bladder injuries, CT cystography can be done.

CT findings, including avulsion of the pedicle or absent enhancement of the kidney, are a high risk of renal devascularization and usually require surgical treatment (Fig. 14) (McGuire et al.

2011). DECT is specifically helpful to look for active renal extravasation and arteriovenous fistulas requiring embolization (Dinkel et al. 2002).

20 Diaphragmatic Injuries

In blunt abdominal trauma, the sudden increase in intra-abdominal pressure can result in diaphragmatic injury. CT findings include discontinuity of diaphragm, herniation, and constriction of abdominal viscera into the thorax, and dependent position of the herniated viscera along the

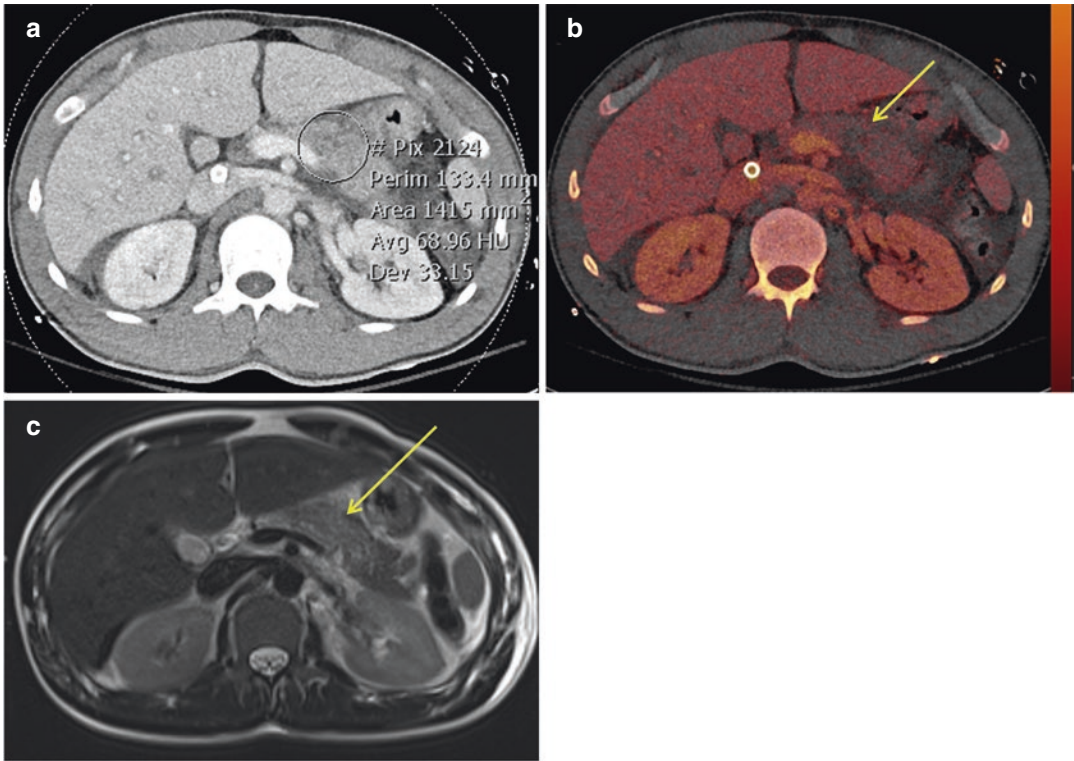


Fig. 15 A 29-year-old male patient with blunt abdominal trauma. (a) Axial post-contrast CT image shows low attenuation in the pancreatic body which is consistent with laceration in settings of trauma. (b) Axial image of iodine overlay map shows the lack of iodine uptake in the

full thickness of pancreatic parenchyma (yellow arrow). (c) T2 weighted MRI image confirms the full thickness laceration (yellow arrow) with absence of surrounding pancreatic fluid collection favoring an intact main pancreatic duct

posterior chest wall (dependent viscera sign) (Iochum et al. 2002). DECT can be helpful in identifying focal defects and reduced enhancement of the constricted viscera.

21 Bowel and Mesenteric Injuries

Injuries to the hollow viscera and mesentery occur in approximately 5% of patients with blunt abdominal trauma. CT findings of bowel injuries are subtle, and it is the most frequently missed diagnosis. The most commonly involved bowel segments are the proximal jejunum and the distal ileum. Specific signs of bowel injury include

hematoma, peritoneal extravasation of intravenous contrast-enhanced blood, focal discontinuity of the bowel wall (transection), focal wall thickening, abnormal bowel wall enhancement, and intramural hematoma (Brofman et al. 2006). DECT can detect the change in bowel wall enhancement and thus extremely helpful in suspected bowel injury. Iodine map images can increase the visibility of iodine content in the bowel wall, and VNC images can improve the visualization of intramural hemorrhage (Hamilton et al. 2008).

In some cases, diffuse bowel wall thickening usually may not be secondary to trauma but may be related to the hypoperfusion complex. Other CT features of the hypoperfusion complex

include a collapse of the inferior vena cava, small aortic diameter, peripancreatic fluid, splenic hyperenhancement, and liver heterogeneity (Joseph et al. 2013; Landry et al. 2016; Sivit et al. 1994; Potretzke et al. 2015b; Mirvis et al. 1994). DECT can detect intramural hemorrhage, mucosal bowel wall hyperenhancement and differentiate ingested high attenuating material from blood products in these patients. Complications of bowel injuries include fistulous formations.

22 Vascular Injuries

Retroperitoneal injuries, including major vascular injuries, are challenging to identify without performing CT.

In hepatic lacerations, it is important to determine the extent of laceration and involvement of hepatic veins or inferior vena cava. Patients with vascular involvement have a higher likelihood of hemodynamic instability. Similarly, in cases of splenic and renal trauma, the presence of vascular injury/avulsion of the pedicle increases the grading scale and usually requires intervention (Uyeda et al. 2014; Hamid et al. 2020).

Abdominal aortic injuries are uncommon but highly lethal. Common CT finding includes active extravasation, intramural, and retroperitoneal hematoma. Specific signs on DECT are large hematoma or active extravasation of contrast-enhanced blood, whereas non-specific signs include small pseudoaneurysms, intimal flaps, or even thrombosis (Vlahos et al. 2012).

Low-kiloelectron volt monoenergetic images can improve vascular contrast-to-noise ratios in the abdomen and pelvis (Vlahos et al. 2012). Therefore, vascular injuries in patients with abdominal trauma can be evaluated using low-kilo electron volt virtual monoenergetic images. In patients with severe atherosclerotic disease, the calcium subtraction technique can help

evaluate the lumen (Hamid et al. 2020; Korn et al. 2011).

23 Bone Injuries

Fractures are associated with both blunt and penetrating trauma. DECT has an added advantage in assessing the age and extent of the fracture, especially in older patients and in cases with subtle findings. Bone marrow edema is a biomarker of acute occult fracture (Wang et al. 2013). In patients with abdominal and pelvic trauma, virtual noncalcium images can be used to differentiate chronic fractures from acute (Fig. 16) and non-displaced occult fractures.

24 Penetrating Abdominal Trauma

Penetrating injuries such as blast injuries and gunshot wounds are much more complex injuries and are difficult to evaluate clinically. Trauma from blast injuries can result in retained material in the soft tissues or solid organs. Moreover, gunshot wounds may have entry and exit wounds. CT is helpful in recognizing the path of the bullet and identifying solid and hollow organ injuries. Solid-organ injuries are staged using the AAST criteria. CT is not sensitive in detecting bowel injuries. However, some of the indirect signs include free air and free fluid (Navsaria et al. 2009).

Management of stab wounds depends on the location and depth of penetration. In an anterior stab wound, if it penetrates through the deep layers of the abdominal wall, laparotomy is indicated by the higher likelihood of bowel injury. Posterior stab wounds confined to the paraspinal musculature with no extension into the peritoneum may not require surgical exploration. CT can identify the tract of the wound through gas locules dissecting through the muscles and the presence of the hemoperitoneum.

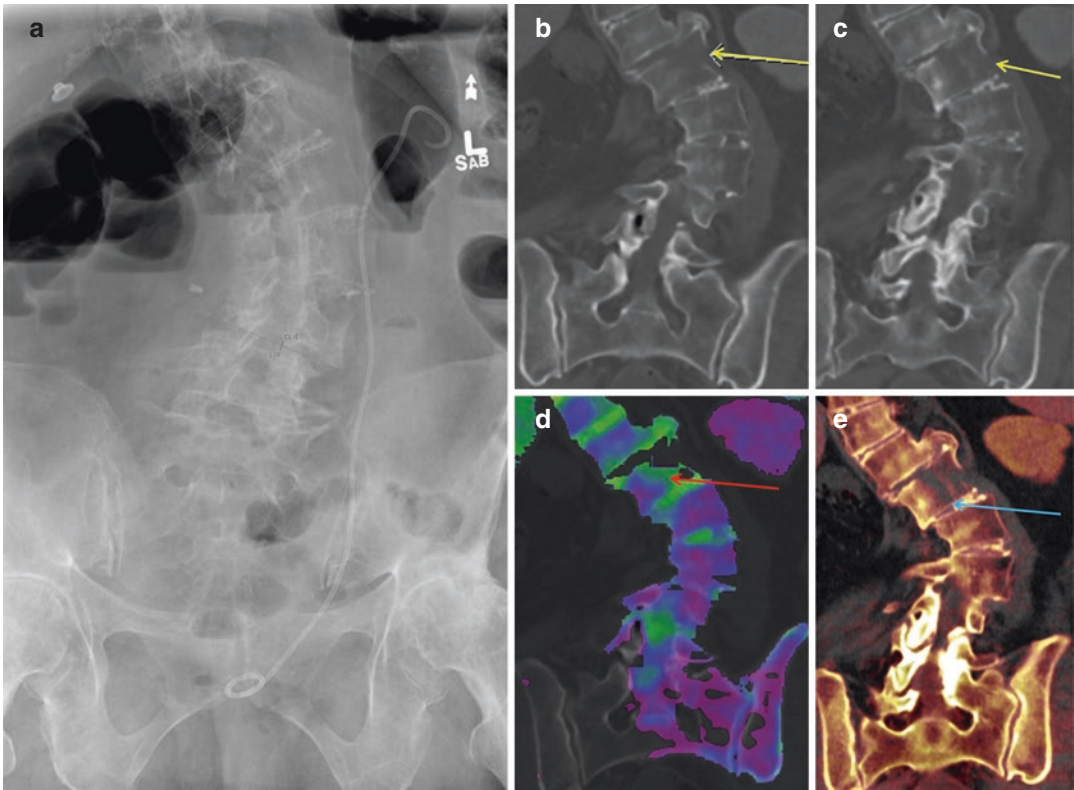


Fig. 16 A 72 female with backpain. (a) Frontal radiograph shows S-shaped thoracolumbar scoliosis with the caudal convex left lumbar curve having a Cobb angle of 62 degrees. No obvious fracture noted. (b, c) Coronal reformatted CT images of the lumbar spine show L1 frac-

ture (yellow arrow). (d, e) Coronal reformatted color coded DECT images demonstrate associated marrow edema, color coded as green (red arrow), and extension of the fracture into the end plates (blue arrow)

25 Conclusions

Dual-energy CT, with its unique ability to identify the material composition, qualitative and quantitative assessment of the iodine content, and the provision of virtual non-contrast imaging, is a game-changer in diagnosing the patients presenting with acute abdomen in emergency settings. It increases diagnostic confidence by accentuating the difference in iodine uptake between pathological and normal tissues.

Compliance with Ethical Standards

Funding No funding was required for the study.

Disclosure of Interests All authors declare they have no conflict of interest.

Ethical Approval This article does not contain any studies with human participants performed by any of the authors.

References

- Ascenti G, Mileto A, Krauss B et al (2013) Distinguishing enhancing from nonenhancing renal masses with dual-source dual-energy CT: iodine quantification versus standard enhancement measurements. *Eur Radiol* 23(8):2288–2295
- Brofman N, Atri M, Hanson JM, Grinblat L, Chughtai T, Brenneman F (2006) Evaluation of bowel

- and mesenteric blunt trauma with multidetector CT. *Radiographics* 26(4):1119–1131
- Dinkel HP, Dansuer H, Triller J (2002) Blunt renal trauma: minimally invasive management with microcatheter embolization – experience in nine patients. *Radiology* 223(3):723–730
- Dreizin D, Munera F (2012) Blunt polytrauma: evaluation with 64-section whole-body CT angiography. *Radiographics* 32(3):609–631
- Elbanna KY, Mohammed MF, Chahal T, Khosa F, Ali IT, Berger FH, Nicolaou S (2018) Dual-energy CT in differentiating nonperforated gangrenous appendicitis from uncomplicated appendicitis. *Am J Radiol* 211:776–782
- Federle MP, Courcoulas AP, Powell M, Ferris JV, Peitzman AB (1998) Blunt splenic injury in adults: clinical and CT criteria for management, with emphasis on active extravasation. *Radiology* 206(1):137–142
- Glazer DI, Maturen KE, Kaza RK et al (2014) Adrenal incidentaloma triage with single-source (fast-kilovoltage switch) dual-energy CT. *AJR Am J Roentgenol* 203(2):329–335
- Grajo JR, Patino M, Prochowski A, Sahani DV (2016) Dual energy CT in practice: basic principles and applications. *Appl Radiol* 2:6–12
- Hamid S, Nicolaou S, Khosa F, Andrews G, Murray N, Abdellatif W, Qamar SR (2020) Dual-energy CT: a paradigm shift in acute traumatic abdomen. *Can Assoc Radiol J* 71(3):371–387. <https://doi.org/10.1177/0846537120905301>. Epub 2020 Mar 11. PMID: 32157893
- Hamilton JD, Kumaravel M, Censullo ML, Cohen AM, Kievlan DS, West OC (2008) Multidetector CT evaluation of active extravasation in blunt abdominal and pelvic trauma patients. *Radiographics* 28(6):1603–1616
- Hidas G, Eliahou R, Duvdevani M, Coulon P, Lemaitre L, Gofrit ON, Pode D, Sosna J (2010) Determination of renal stone composition with dual-energy CT: in vivo analysis and comparison with X-ray diffraction. *Radiology* 257(2):394–401
- <https://radiopaedia.org/articles/bowel-perforation-summary>
- Iochum S, Ludig T, Walter F d'r, Sebbag H, Grosdidier G, Blum AG (2002) Imaging of diaphragmatic injury: a diagnostic challenge? *Radiographics* 22(1):S103–S118
- Iraha Y, Okada M, Iraha R, Azama K, Yamashiro T, Tsubakimoto M, Aoki Y, Murayama S (2017) CT and MR imaging of gynecologic emergencies. *Radiographics* 37:1569–1586
- Jeremy R, Wortman JWU, Fulwadhva UP, Sodickson AD (2018) Dual-energy CT for abdominal and pelvic trauma. *Radiographics* 38(2):586–602
- Joseph DK, Kunac A, Kinler RL et al (2013) Diagnosing blunt hollow viscus injury: is computed tomography the answer? *Am J Surg* 205(4):414–418
- Kamin RA, Nowicki TA, Courtney DS, Powers RD (2003) Pearls and pitfalls in the emergency department evaluation of abdominal pain. *Emerg Med Clin North Am* 21:61–72
- Kim JE, Lee JM, Baek JH, Han JK (2012) Initial assessment of dual-energy CT in patients with gallstones or bile duct stones: can virtual nonenhanced images replace true nonenhanced images? *Am J Roentgenol* 198(198):817–824. <https://doi.org/10.2214/AJR.11.6972>
- Korn A, Bender B, Thomas C et al (2011) Dual energy CTA of the carotid bifurcation: advantage of plaque subtraction for assessment of grade of the stenosis and morphology. *Eur J Radiol* 80(2):e120–e1e5
- Landry BA, Patlas MN, Faidi S et al (2016) Are we missing traumatic bowel and mesenteric injuries? *Can Assoc Radiol J* 67(4):420–425
- Macari M, Spieler B, Kim D et al (2010) Dual-source dualenergy MDCT of pancreatic adenocarcinoma: initial observations with data generated at 80 kVp and at simulated weighted-average 120 kVp. *AJR Am J Roentgenol* 194(1):W27–W32
- Marin D, Nelson RC, Barnhart H et al (2010) Detection of pancreatic tumors, image quality, and radiation dose during the pancreatic parenchymal phase: effect of a low-tube-voltage, high-tube-current CT technique – preliminary results. *Radiology* 256(2):450–459
- Marmery H, Shanmuganathan K, Alexander MT, Mirvis SE (2007) Optimization of selection for nonoperative management of blunt splenic injury: comparison of MDCT grading systems. *AJR Am J Roentgenol* 189(6):1421–1427
- McGuire J, Bultitude MF, Davis P, Koukounaras J, Royce PL, Corcoran NM (2011) Predictors of outcome for blunt high grade renal injury treated with conservative intent. *J Urol* 185(1):187–191
- McNamara MM, Little MD, Alexander LF, Carroll LV, Beasley TM, Morgan DE (2015) Multireader evaluation of lesion conspicuity in small pancreatic adenocarcinomas: complimentary value of iodine material density and low keV simulated monoenergetic images using multiphasic rapid kVp-switching dual energy CT. *Abdom Imaging* 40(5):1230–1240
- Mirvis SE, Shanmuganathan K, Erb R (1994) Diffuse small-bowel ischemia in hypotensive adults after blunt trauma (shock bowel): CT findings and clinical significance. *AJR Am J Roentgenol* 163(6):1375–1379
- Murray N, Darras KE, Walstra FE, Mohammed MF, McLaughlin PD, Nicolaou S (2019) Dual-energy CT in evaluation of the acute abdomen. *Radiographics* 39:264–286
- Navsaria PH, Nicol AJ, Krige JE et al (2009) Selective nonoperative management of liver gunshot injuries. *Ann Surg* 249(4):653–656
- Patel BN, Thomas JV, Lockhart ME, Berland LL, Morgan DE (2013) Single-source dual-energy spectral multidetector CT of pancreatic adenocarcinoma: optimization of energy level viewing significantly increases lesion contrast. *Clin Radiol* 68(2):148–154
- Potretzke TA, Brace CL, Lubner MG, Sampson LA, Willey BJ, Lee FT Jr (2015a) Early small-bowel isch-

- emia: dual-energy CT improves conspicuity compared with conventional CT in a swine model. *Radiology* 275:119–126
- Potretzke TA, Brace CL, Lubner MG, Sampson LA, Willey BJ, Lee FT Jr (2015b) Early small-bowel ischemia: dual-energy CT improves conspicuity compared with conventional CT in a swine model. *Radiology* 25(1):119–126
- Rakita D, Newatia A, Hines JJ, Siegel DN, Friedman B (2007) Spectrum of Ct findings in rupture and impending rupture of abdominal aortic aneurysms, impending rupture of abdominal aortic aneurysms. *Radiographics* 27:497–507
- Ratanaprasatporn L, Uyeda JW, Wortman JR, Richardson I, Sodickson AD (2018) Multimodality imaging, including dual-energy CT in the evaluation of gallbladder disease. *Radiographics* 38:75–89
- Rekhi S, Anderson SW, Rhea JT, Soto JA (2010) Imaging of blunt pancreatic trauma. *Emerg Radiol* 17(1):13–19
- Robinson E, Babb J, Chandarana H, Macari M (2010) Dual source dual energy MDCT: comparison of 80 kVp and weighted average 120 kVp data for conspicuity of hypo-vascular liver metastases. *Investig Radiol* 45(7):413–418
- Shanmuganathan K, Mirvis SE, Boyd-Kranis R, Takada T, Scalea TM (2017) Nonsurgical management of blunt splenic injury: use of CT criteria to select patients for splenic arteriography and potential endovascular therapy. *Radiology* 1:75–82
- Sivit CJ, Eichelberger MR, Taylor GA (1994) CT in children with rupture of the bowel caused by blunt trauma: diagnostic efficacy and comparison with hypoperfusion complex. *AJR Am J Roentgenol* 163(5):1195–1198
- Soto JA, Anderson SW (2012) Multidetector CT of blunt abdominal trauma. *Radiology* 265(3):678–693
- Sudarski S, Apfaltrer P, Nance JW Jr et al (2014) Objective and subjective image quality of liver parenchyma and hepatic metastases with virtual monoenergetic dual-source dual-energy CT reconstructions: an analysis in patients with gastrointestinal stromal tumor. *Acad Radiol* 21(4):514–522
- Sulu B, Günerhan Y, Palanci Y, Isler B, Caglayan K (2010) Epidemiological and demographic features of appendicitis and influences of several environment factors. *Ulus Travma Acil Cerrahi Derg* 16:38–42
- Sun H, Xue H-D, Wang Y-N, Qian J-M, Yu J-C, Zhu F, Zhu H-D, Jin Z-Y, Li X-G (2013) Dual-source dual-energy computed tomography angiography for active gastrointestinal bleeding: a preliminary study. *Clin Radiol* 68(2):139–147
- Suzanne Albrecht P (2010) Management of diverticular disease. *Gastroenterology* 35:12
- Uyeda JW, LeBedis CA, Penn DR et al (2014) Active hemorrhage and vascular injuries in splenic trauma: utility of the arterial phase in multidetector CT. *Radiology* 270(1):99–106
- Venkatesh SK, Wan JM (2008) CT of blunt pancreatic trauma: a pictorial essay. *Eur J Radiol* 67(2):311–320
- Vlahos I, Chung R, Nair A, Morgan R (2012) Dual-energy CT: vascular applications. *AJR Am J Roentgenol* 199:s87–s97
- Wallace AB, Raptis CA, Mellnick VM (2016) Imaging of bowel ischemis. *Curr Radiol Rep* 4:29
- Wang CK, Tsai JM, Chuang MT, Wang MT, Huang KY, Lin RM (2013) Bone marrow edema in vertebral compression fractures: detection with dual-energy CT. *Radiology* 269(2):525–533
- White EM, Simeone JF, Mueller PR, Simeone JF, Butch RJ, Warshaw AL, Neff CC, Nardi GL, Ferrucci JT Jr (1986) Pancreatic necrosis: CT manifestations. *Radiology* 158(2):343
- Wortman JR, Bunch PM, Fulwadhva UP, Bonci GA, Sodickson AD (2016) Dual-energy CT of incidental findings in the abdomen: can we reduce the need for follow-up imaging? *AJR Am J Roentgenol* 6:W1–W11
- Yamada Y, Jinzaki M, Tanami Y, Abe T, Kuribayashi S (2012) Virtual monochromatic spectral imaging for the evaluation of hypovascular hepatic metastases: the optimal monochromatic level with fast kilovoltage switching dual-energy computed tomography. *Investig Radiol* 47(5):292–298



Spectral Computed Tomography Imaging of the Adrenal Glands

Matthias Benndorf, August Sigle,
and Fabian Bamberg

Contents

1	Introduction	277
2	Lipid-Rich Adenoma and Virtual Non-contrast Imaging	278
3	Lipid-Poor Adenoma, Washout Analysis, and Chemical Shift MRI	281
4	Quantification of Iodine	281
5	Summary	283
	References	283

Abstract

Spectral computed tomography offers additional diagnostic information for the evaluation of adrenal lesions in contrast enhanced examinations. Virtual non-contrast (VNC-CT) images can be used as a substitute for true unenhanced images to confidently diagnose lipid-rich adenoma with a threshold of ≤ 10 HU, making additional unenhanced scans or work-up unnecessary in these cases. However, sensitivity for

lipid-rich adenoma is lower compared to unenhanced scans, since VNC-CT images tend to systematically overestimate HU of lipid-rich adenomas. The American College of Radiology's white paper on the management of incidental adrenal lesions explicitly mentions dual-energy CT and the potential usage of VNC-CT with a threshold of ≤ 10 HU for diagnosis. In this chapter, we provide an overview and comparison of the diagnostic accuracy of unenhanced CT, VNC-CT, CT washout calculations, and chemical shift MRI for the diagnosis of adrenal adenoma versus non-adenoma.

M. Benndorf (✉) · F. Bamberg
Department of Radiology, Medical Center -
University of Freiburg, Faculty of Medicine,
University of Freiburg, Freiburg, Germany
e-mail: matthias.benndorf@uniklinik-freiburg.de;
fabian.bamberg@uniklinik-freiburg.de

A. Sigle
Department of Urology, Medical Center - University
of Freiburg, Faculty of Medicine, University of
Freiburg, Freiburg, Germany
e-mail: august.sigle@uniklinik-freiburg.de

1 Introduction

With the increasing use of computed tomography (CT) as a widely available imaging modality in emergency diagnosis and diagnostic body imaging for benign and malignant diseases, the detec-

tion of incidental findings has increased substantially in the last decades. On the one hand, the adrenal glands are a common site for incidentally detected lesions. Estimates of the percentage of patients with incidentally detected adrenal lesions range between 3% and 8% (Barrett et al. 2009; Bovio et al. 2006; Mansmann et al. 2004; Mayo-Smith et al. 2017). For example, Barrett et al. report that incidental adrenal lesions are detected in 3.8% of patients who undergo CT for diagnosis in trauma (Barrett et al. 2009). The majority of incidental lesions of the adrenal glands proves to be hormonally inactive adenoma (Mansmann et al. 2004). On the other hand, the adrenal glands are also a site that is predisposed to harbor metastasis in a variety of malignancies. In 9% of living patients with non-small cell lung cancer adrenal metastases are evident, with numbers rising to 25–39% in autopsy series (Bazhenova et al. 2014).

Because lesions of the adrenal glands are common, accurate differentiation of benign and malignant lesions is crucial. Different imaging modalities can be employed to classify adrenal lesions—with dedicated conventional CT offering a reliable diagnostic tool with unenhanced images and washout calculation in contrast enhanced images (Johnson et al. 2009a). In this chapter, we provide an overview of the diagnostic accuracy of spectral CT compared with conventional dedicated CT and MRI for the diagnosis of adrenal lesions (mainly, to distinguish adenomas from metastases). We highlight the possibility to avoid further work-up of incidental adrenal lesions in a proportion of cases when spectral imaging is implemented as standard of care in diagnostic, contrast enhanced CT examinations.

2 Lipid-Rich Adenoma and Virtual Non-contrast Imaging

Adenomas originate from the cortex of the adrenal gland. The cells of adrenal adenomas often contain a considerable amount of intracytoplasmatic fat (Korobkin et al. 1996). The higher the amount of intracytoplasmatic fat, the lower the

corresponding Hounsfield units (HU) of the lesion measured in unenhanced CT (Korobkin et al. 1996). This observation has led to the classification of adrenal adenomas as either lipid-rich (defined in unenhanced CT as having mean $HU \leq 10$) or lipid-poor (mean $HU > 10$). Around 70% of adrenal adenomas are of the lipid-rich type (Boland et al. 1998).

The diagnosis of an (lipid-rich) adenoma can be made with 71% sensitivity and 98% specificity by using a HU threshold of ≤ 10 to indicate adenoma, measured in unenhanced CT (Boland et al. 1998). The high specificity means that only rarely the diagnosis adenoma based on this HU threshold is wrong. With virtual non-contrast images derived from contrast enhanced spectral CT acquisitions (VNC-CT), there is the opportunity to reliably classify a proportion of otherwise indeterminate adrenal lesions as (lipid-rich) adenomas.

In a systematic review and meta-analysis of the diagnostic accuracy of VNC-CT for adrenal adenoma, Connolly et al. report a pooled sensitivity of 54% for (lipid-rich) adenoma (Connolly et al. 2017). They do not derive a pooled estimate for specificity, since no false positive findings occur in the included five studies (Ho et al. 2012; Kim et al. 2013; Botsikas et al. 2014; Gnannt et al. 2012; Helck et al. 2014), all of which use a dual-source dual-energy technique for image acquisition of spectral CT. Notably, Connolly et al. report a pooled sensitivity of 57% for unenhanced CT (Connolly et al. 2017), being lower than the oftentimes quoted 71% (Boland et al. 1998). Connolly et al. reason that selection bias might be responsible for this deviation (Connolly et al. 2017). All of the included studies employ a threshold of 10 HU on VNC-CT for the diagnosis of adenoma. Figure 1 provides an example for the potential of VNC-CT to diagnose lipid-rich adenomas.

VNC-CT HU measurements of adrenal lesions tend to systematically result in higher HU values compared to measurements in unenhanced CT (Kim et al. 2013; Botsikas et al. 2014; Nagayama et al. 2020). Kim et al. report an average of 11.7 HU of lipid-rich adenomas when measured in VNC-CT derived from early phase contrast

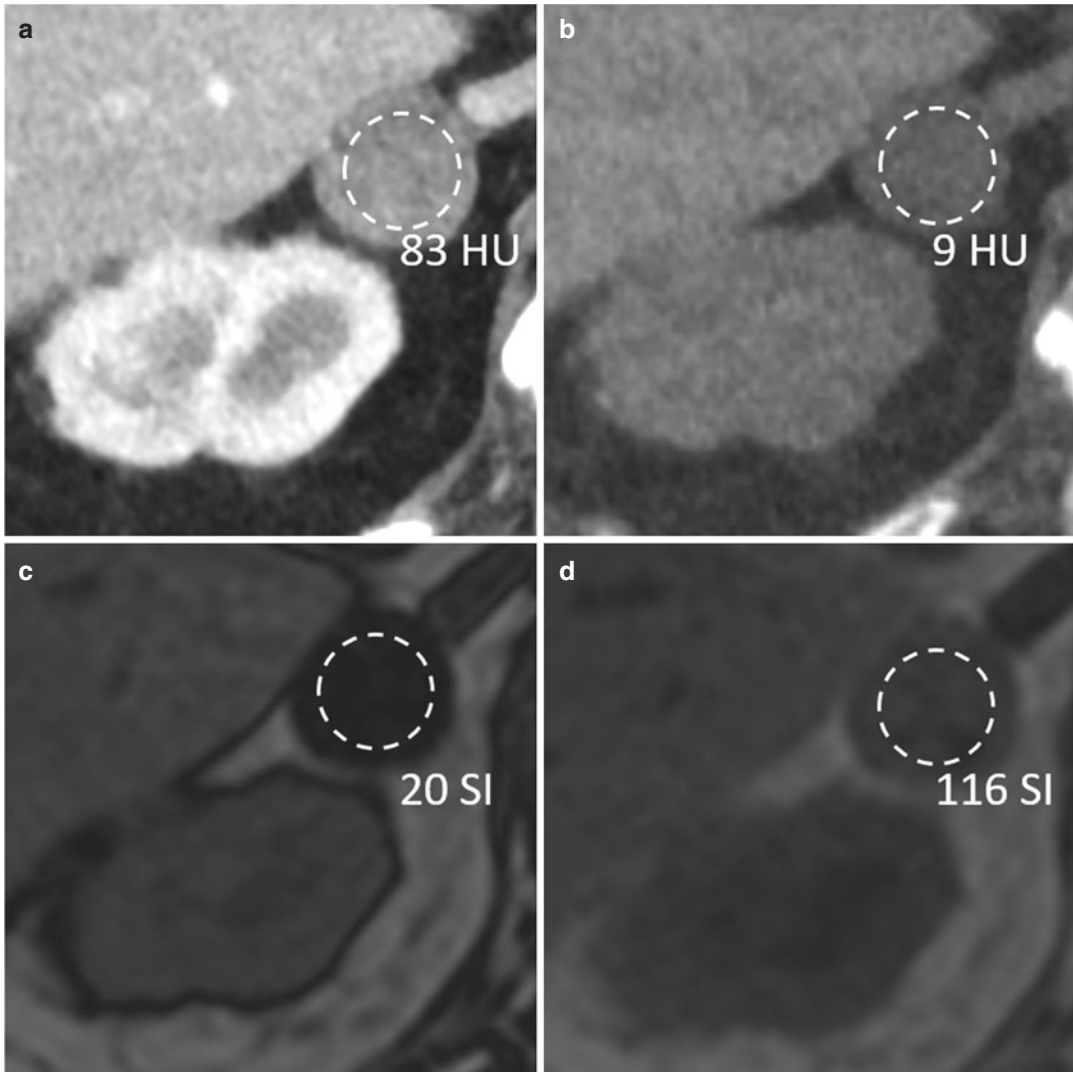


Fig. 1 An 80-year-old female patient with left buccal Merkel-cell carcinoma is referred for staging CT. In the dual-energy, portal venous phase scan of the abdomen, a 2 cm lesion is observed in the right adrenal gland (**a**), with mean HU of 83. In the derived VNC-CT the lesion demonstrates $\text{HU} \leq 10$, prompting the diagnosis of a lipid-rich

adenoma (**b**). One month later, liver MRI is performed for evaluation of an unclear focal liver lesion (not shown). In this examination, chemical shift MRI demonstrates a marked signal drop in opposed-phase images (**c**) compared to in-phase images (**d**), confirming the VNC-CT diagnosis of a lipid-rich adenoma

enhanced images, compared to 0.7 HU in unenhanced CT (Kim et al. 2013). Botsikas et al. report a mean difference of 4 HU for all lesions analyzed (Botsikas et al. 2014). Small, statistically non-significant differences in HU measurement are reported by Ho et al. and Gnannt et al. (difference of 1.8 HU and 1.1 HU, respectively) (Ho et al. 2012; Gnannt et al. 2012). There is a trend towards smaller differences when delayed

contrast phases are taken for VNC-CT calculation compared to earlier contrast phases (Kim et al. 2013; Botsikas et al. 2014). By using a dual-layer CT detector for acquisition of spectral CT, Nagayama et al. report a mean difference of 11 HU between measurements of lipid-rich adenomas in VNC-CT and unenhanced CT (Nagayama et al. 2020). This phenomenon is not restricted to the adrenal glands, but pertains to a variety of

abdominal organs (Durieux et al. 2018). Notably, the same systematic difference of HU values between measurements in VNC-CT and unenhanced CT does not automatically extend to adrenal metastases (Nagayama et al. 2020). Figure 2 provides an example of different HU obtained in VNC-CT and unenhanced CT.

For these reasons (systematic difference between VNC-CT and unenhanced CT of adeno-

mas and this difference not necessarily extending to metastases) there is no generally agreed upon adapted HU threshold for measurements in VNC-CT at which to consider a lesion a lipid-rich adenoma. With the threshold of ≤ 10 HU in VNC-CT, a smaller proportion of cases can be classified as lipid-poor adenoma compared to assessment with unenhanced CT. Given that the HU difference is generally positive between

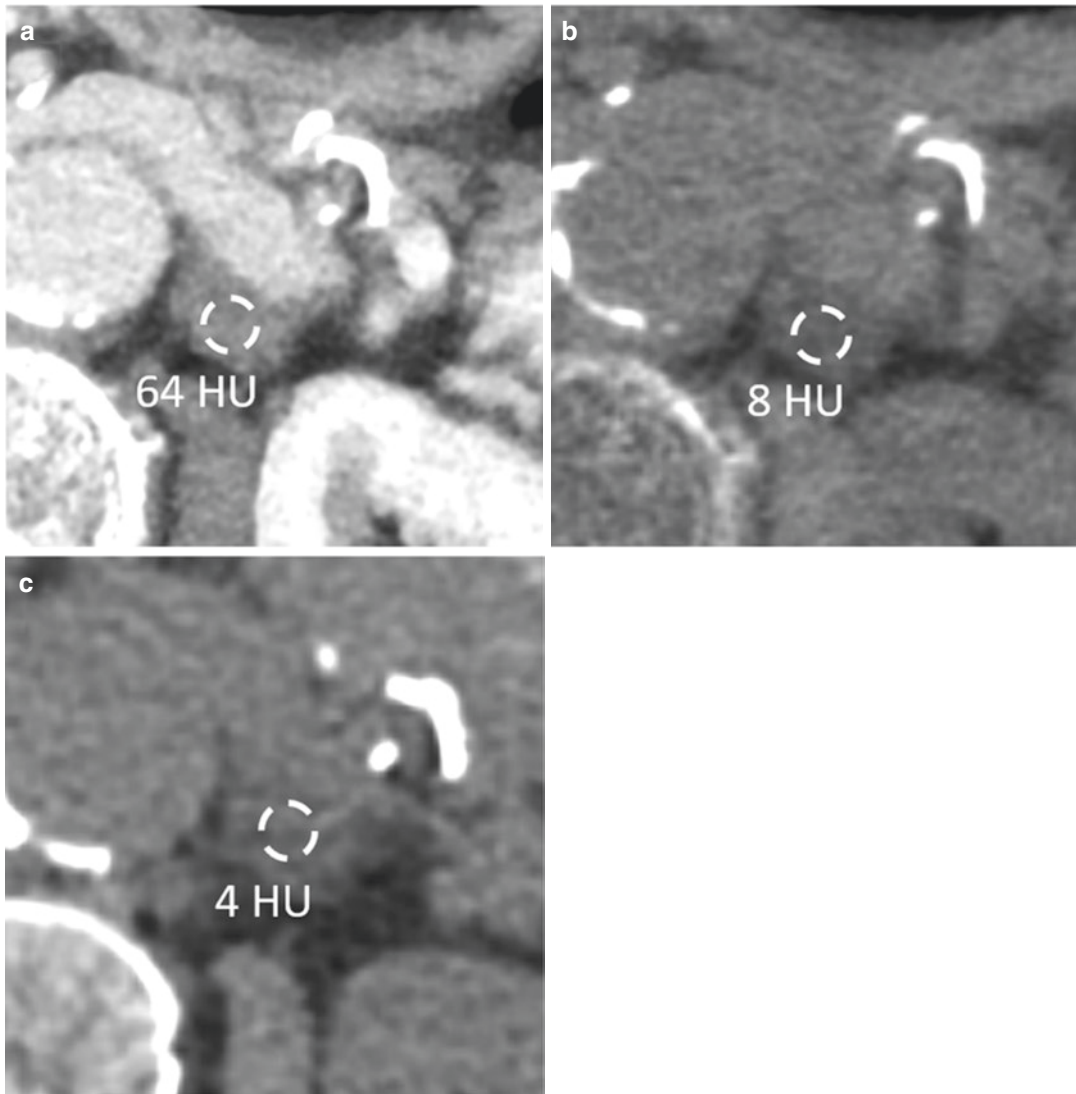


Fig. 2 A 70-year-old male patient with non-small cell lung cancer referred for staging. An adrenal lesion of 1.9×1.2 cm is observed in the left adrenal gland, with 64 HU in the dual-energy, portal venous phase scan (a). In the derived VNC-CT, the lesion is measured with an aver-

age of 8 HU (b). In a true unenhanced CT acquired earlier the lesion measures 4 HU (c). In this lipid-rich adenoma, the tendency of spectral CT to overestimate HU of lipid-rich adenoma in VNC-CT is demonstrated

VNC-CT and unenhanced CT, specificity should not be impaired, and the common ≤ 10 HU threshold for diagnosis of adenoma can be applied to VNC-CT (Mayo-Smith et al. 2017).

3 Lipid-Poor Adenoma, Washout Analysis, and Chemical Shift MRI

Around 30% of adenomas belong to the lipid-poor type (compare for above). This means they cannot reliably be diagnosed with unenhanced, or VNC, CT (HU in unenhanced CT > 10). There are two commonly employed imaging techniques that can further classify this type of lesions.

Firstly, chemical shift MRI (csMRI) is able to quantify the amount of intracytoplasmic fat (Adam et al. 2016). There is a characteristic drop in signal intensity in opposed-phase images compared to in-phase images (Adam et al. 2016) in a large proportion of adrenal adenomas, compare to Fig. 1, c and d. Several metrics can quantify the degree of signal loss: the Adrenal Signal Intensity Index (ASII) uses signal intensities from in-phase and opposed-phase images only, whereas other metrics normalize the signal drop to the signal of liver, spleen, and skeletal muscle (Ream et al. 2015). csMRI is highly sensitive and specific for the diagnosis for adrenal adenoma—a systematic review and meta-analysis report a pooled sensitivity of 94% and a specificity of 95% (Platzek et al. 2019). However, there is evidence that the higher the HU of the lesion in unenhanced CT, the worse the sensitivity of csMRI (Haider et al. 2004). Therefore, csMRI cannot be generally recommended as a work-up test in lesions >30 HU in unenhanced CT (Adam et al. 2016; Haider et al. 2004).

Secondly, contrast enhanced CT with washout calculation is routinely performed to further classify indeterminate adrenal lesions. For washout evaluation, an unenhanced, an early phase (60–90s) and a delayed phase (10 min or 15 min) scan are acquired. The absolute washout percentage is derived from all three phases, whereas for relative washout percentage early phase and delayed phase images suffice (Johnson et al. 2009b).

Diagnostic accuracy of washout analysis for the diagnosis of adenoma is generally very good (Johnson et al. 2009b); in a summary by Johnson et al. 6/7 studies report a sensitivity between 96% and 100% and 6/7 studies report a specificity between 95% and 100% (Johnson et al. 2009b). The technique is considered the gold standard method of evaluation for adrenal lesions by some authors (Albano et al. 2019)—since higher HU values of adenomas on unenhanced scans do not affect the high sensitivity of washout analysis as compared to csMRI (Seo et al. 2014; Warda et al. 2016).

A possible application of spectral CT in this setting is the replacement of the unenhanced scan by VNC-CT for absolute percent washout calculation. Kim et al. study the performance of absolute washout percentage using VNC-CT as unenhanced scan and report a sensitivity of 100% and a specificity of 87.5% (Kim et al. 2013). Washout analysis that employs the unenhanced scan has a reported sensitivity of 100% and a specificity of 93.8% in this study (Kim et al. 2013). Botsikas et al. report that washout calculated with VNC-CT is higher when VNC-CT is derived from early (portal venous) scans compared to VNC-CT derived from delayed scans (Botsikas et al. 2014). At this stage, additional studies seem warranted to investigate this approach.

4 Quantification of Iodine

Adrenal adenomas typically enhance avidly in early (60–90s) phases after intravenous contrast agent injection, and there is evidence that absolute contrast enhancement (defined as difference in HU between enhanced and unenhanced scans) is higher in early phases in adenomas than in non-adenomas (Korobkin et al. 1996; Szolar and Kammerhuber 1998; Peña et al. 2000; Foti et al. 2010). However, the absolute HU value in enhanced early phases is not a meaningful diagnostic variable, since here HU values are quite similar for adenomas and non-adenomas (Korobkin et al. 1996; Szolar and Kammerhuber 1998; Peña et al. 2000; Foti et al. 2010). Spectral

CT offers the possibility of material decomposition (Patino et al. 2016) and thus to directly measure the high absolute contrast enhancement of adenomas in early phase images by quantifying the corresponding iodine concentration.

For iodine-density (concentration, given in mg/ml), Nagayama et al. report a sensitivity of 78% and a specificity of 71% for adrenal ade-

noma (Nagayama et al. 2020)—being inferior to the performance of the unenhanced scan. This is improved to 95% sensitivity and 95% specificity when normalization to VNC-CT HU is performed (iodine-density to VNC ratio) (Nagayama et al. 2020), compare to Fig. 3. Confirmatory studies of this promising finding are pending. In accordance with the presented literature that adrenal adeno-

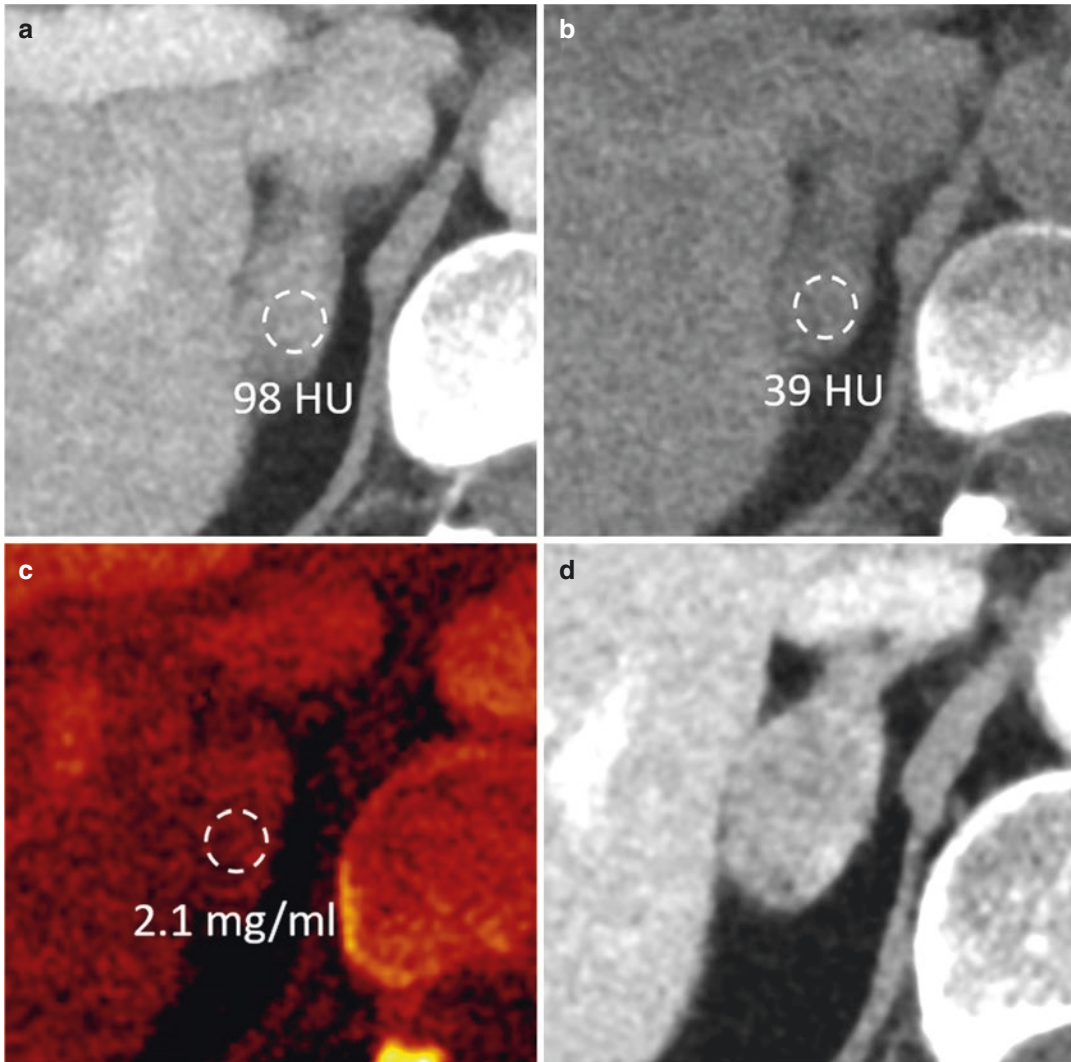


Fig. 3 A 59-year-old female patient with non-small cell lung cancer is referred for staging CT. A lesion of 2.2×1.3 cm is observed in the right adrenal gland. The lesion measures 98 HU in the portal venous dual-energy CT (a) and 39 in the derived VNC image (b). The iodine-density of the lesion is 2.1 mg/ml (c), resulting in an

iodine-density to VNC ratio of 5.4. This is suggestive of a metastasis, according to the article by Nagayama et al. (2020). The lesion demonstrates rapid growth in a follow-up examination performed three months later and therefore is considered a metastasis (d)

mas show higher absolute contrast enhancement compared to metastases in early phase images (Korobkin et al. 1996; Szolar and Kammerhuber 1998; Peña et al. 2000; Foti et al. 2010), adenomas tend to have higher iodine-density in this study (Nagayama et al. 2020). The opposite relationship is reported by Martin et al. and Mileto et al., here adenomas demonstrate significantly lower iodine-density compared to non-adenomas (Martin et al. 2018; Mileto et al. 2014). At the moment, there is not enough evidence to recommend a diagnostic threshold of iodine-density to accurately classify adrenal lesions as adenoma or non-adenoma in clinical routine.

5 Summary

Spectral (contrast enhanced) CT offers additional diagnostic information for the evaluation of adrenal lesions. VNC-CT images can be used as a substitute for unenhanced images to confidently diagnose lipid-rich adenoma with a threshold of ≤ 10 HU, making additional unenhanced scans or workup unnecessary in these cases. However, sensitivity for lipid-rich adenoma is lower compared to unenhanced scans, since VNC-CT images tend to systematically overestimate HU of lipid-rich adenomas. The American College of Radiology's white paper on the management of incidental adrenal lesions explicitly mentions dual-energy CT and the potential usage of VNC-CT with a threshold of ≤ 10 HU (Mayo-Smith et al. 2017) for diagnosis. Replacement of the true unenhanced scan for washout calculation with VNC-CT and iodine-density is not explicitly mentioned.

Compliance with Ethical Standards

Ethical Approval: For this chapter no studies on humans or animals were performed.

References

- Adam SZ, Nikolaidis P, Horowitz JM, Gabriel H, Hammond NA, Patel T, Yaghamai V, Miller FH (2016) Chemical shift MR imaging of the adrenal gland: principles, pitfalls, and applications. *RadioGraphics* 36:414–432. <https://doi.org/10.1148/rg.2016150139>
- Albano D, Agnello F, Midiri F, Pecoraro G, Bruno A, Alongi P, Toia P, Di Buono G, Agrusa A, Sconfienza LM, Pardo S, La Grutta L, Midiri M, Galia M (2019) Imaging features of adrenal masses. *Insights Imaging* 10:1. <https://doi.org/10.1186/s13244-019-0688-8>
- Barrett TW, Schierling M, Zhou C, Colfax JD, Russ S, Conatser P, Lancaster P, Wrenn K (2009) Prevalence of incidental findings in trauma patients detected by computed tomography imaging. *Am J Emerg Med* 27:428–435. <https://doi.org/10.1016/j.ajem.2008.03.025>
- Bazhenova L, Newton P, Mason J, Bethel K, Nieva J, Kuhn P (2014) Adrenal metastases in lung cancer: clinical implications of a mathematical model. *J Thorac Oncol* 9:442–446. <https://doi.org/10.1097/JTO.0000000000000133>
- Boland GW, Lee MJ, Gazelle GS, Halpern EF, McNicholas MM, Mueller PR (1998) Characterization of adrenal masses using unenhanced CT: an analysis of the CT literature. *AJR Am J Roentgenol* 171:201–204. <https://doi.org/10.2214/ajr.171.1.9648789>
- Botsikas D, Triponez F, Boudabbous S, Hansen C, Becker CD, Montet X (2014) Incidental adrenal lesions detected on enhanced abdominal dual-energy CT: can the diagnostic workup be shortened by the implementation of virtual unenhanced images? *Eur J Radiol* 83:1746–1751. <https://doi.org/10.1016/j.ejrad.2014.06.017>
- Bovio S, Cataldi A, Reimondo G, Sperone P, Novello S, Berruti A, Borasio P, Fava C, Dogliotti L, Scagliotti GV, Angeli A, Terzolo M (2006) Prevalence of adrenal incidentaloma in a contemporary computerized tomography series. *J Endocrinol Investig* 29:298–302. <https://doi.org/10.1007/BF03344099>
- Connolly MJ, McInnes MDF, El-Khodary M, McGrath TA, Schieda N (2017) Diagnostic accuracy of virtual non-contrast enhanced dual-energy CT for diagnosis of adrenal adenoma: a systematic review and meta-analysis. *Eur Radiol* 27:4324–4335. <https://doi.org/10.1007/s00330-017-4785-0>
- Durieux P, Gevenois PA, Muylem AV, Howarth N, Keyzer C (2018) Abdominal attenuation values on virtual and true unenhanced images obtained with third-generation dual-source dual-energy CT. *AJR Am J Roentgenol* 210:1042–1058. <https://doi.org/10.2214/AJR.17.18248>
- Foti G, Faccioli N, Manfredi R, Mantovani W, Mucelli RP (2010) Evaluation of relative wash-in ratio of adrenal lesions at early biphasic CT. *Am J Roentgenol* 194:1484–1491. <https://doi.org/10.2214/AJR.09.3636>
- Gnannt R, Fischer M, Goetti R, Karlo C, Leschka S, Alkadhi H (2012) Dual-energy CT for characterization of the incidental adrenal mass: preliminary observations. *AJR Am J Roentgenol* 198:138–144. <https://doi.org/10.2214/AJR.11.6957>
- Haider MA, Ghai S, Jhaveri K, Lockwood G (2004) Chemical shift MR imaging of hyperattenuating (>10 HU) adrenal masses: does it still have a role?

- Radiology 231:711–716. <https://doi.org/10.1148/radiol.2313030676>
- Helck A, Hummel N, Meinel FG, Johnson T, Nikolaou K, Graser A (2014) Can single-phase dual-energy CT reliably identify adrenal adenomas? *Eur Radiol* 24:1636–1642. <https://doi.org/10.1007/s00330-014-3192-z>
- Ho LM, Marin D, Neville AM, Barnhart HX, Gupta RT, Paulson EK, Boll DT (2012) Characterization of adrenal nodules with dual-energy CT: can virtual unenhanced attenuation values replace true unenhanced attenuation values? *AJR Am J Roentgenol* 198:840–845. <https://doi.org/10.2214/AJR.11.7316>
- Johnson PT, Horton KM, Fishman EK (2009a) Adrenal mass imaging with multidetector CT: pathologic conditions, pearls, and pitfalls. *RadioGraphics* 29:1333–1351. <https://doi.org/10.1148/rg.295095027>
- Johnson PT, Horton KM, Fishman EK (2009b) Adrenal imaging with multidetector CT: evidence-based protocol optimization and interpretative practice. *RadioGraphics* 29:1319–1331. <https://doi.org/10.1148/rg.295095026>
- Kim YK, Park BK, Kim CK, Park SY (2013) Adenoma characterization: adrenal protocol with dual-energy CT. *Radiology* 267:155–163. <https://doi.org/10.1148/radiol.12112735>
- Korobkin M, Giordano TJ, Brodeur FJ, Francis IR, Siegelman ES, Quint LE, Dunnick NR, Heiken JP, Wang HH (1996) Adrenal adenomas: relationship between histologic lipid and CT and MR findings. *Radiology* 200:743–747. <https://doi.org/10.1148/radiology.200.3.8756925>
- Mansmann G, Lau J, Balk E, Rothberg M, Miyachi Y, Bornstein SR (2004) The clinically inapparent adrenal mass: update in diagnosis and management. *Endocr Rev* 25:309–340. <https://doi.org/10.1210/er.2002-0031>
- Martin SS, Weidinger S, Czwikla R, Kaltenbach B, Albrecht MH, Lenga L, Vogl TJ, Wichmann JL (2018) Iodine and fat quantification for differentiation of adrenal gland adenomas from metastases using third-generation dual-source dual-energy computed tomography. *Investig Radiol* 53:173–178. <https://doi.org/10.1097/RLL.0000000000000425>
- Mayo-Smith WW, Song JH, Boland GL, Francis IR, Israel GM, Mazzaglia PJ, Berland LL, Pandharipande PV (2017) Management of incidental adrenal masses: a white paper of the ACR Incidental Findings Committee. *J Am Coll Radiol* 14:1038–1044. <https://doi.org/10.1016/j.jacr.2017.05.001>
- Mileto A, Nelson RC, Marin D, Roy Choudhury K, Ho LM (2014) Dual-energy multidetector CT for the characterization of incidental adrenal nodules: diagnostic performance of contrast-enhanced material density analysis. *Radiology* 274:445–454. <https://doi.org/10.1148/radiol.14140876>
- Nagayama Y, Inoue T, Oda S, Tanoue S, Nakaura T, Ikeda O, Yamashita Y (2020) Adrenal adenomas versus metastases: diagnostic performance of dual-energy spectral CT virtual noncontrast imaging and iodine maps. *Radiology*. <https://doi.org/10.1148/radiol.2020192227>
- Patino M, Prochowski A, Agrawal MD, Simeone FJ, Gupta R, Hahn PF, Sahani DV (2016) Material separation using dual-energy CT: current and emerging applications. *RadioGraphics* 36:1087–1105. <https://doi.org/10.1148/rg.2016150220>
- Peña CS, Boland GW, Hahn PF, Lee MJ, Mueller PR (2000) Characterization of indeterminate (lipid-poor) adrenal masses: use of washout characteristics at contrast-enhanced CT. *Radiology* 217:798–802. <https://doi.org/10.1148/radiology.217.3.r00dc29798>
- Platzek I, Sieron D, Plodeck V, Borkowetz A, Laniado M, Hoffmann R-T (2019) Chemical shift imaging for evaluation of adrenal masses: a systematic review and meta-analysis. *Eur Radiol* 29:806–817. <https://doi.org/10.1007/s00330-018-5626-5>
- Ream JM, Gaing B, Mussi TC, Rosenkrantz AB (2015) Characterization of adrenal lesions at chemical-shift MRI: a direct intraindividual comparison of in- and opposed-phase imaging at 1.5 T and 3 T. *AJR Am J Roentgenol* 204:536–541. <https://doi.org/10.2214/AJR.14.12941>
- Seo JM, Park BK, Park SY, Kim CK (2014) Characterization of lipid-poor adrenal adenoma: chemical-shift MRI and washout CT. *AJR Am J Roentgenol* 202:1043–1050. <https://doi.org/10.2214/AJR.13.11389>
- Szolar DH, Kammerhuber FH (1998) Adrenal adenomas and nonadenomas: assessment of washout at delayed contrast-enhanced CT. *Radiology* 207:369–375. <https://doi.org/10.1148/radiology.207.2.9577483>
- Warda MHA, Shehata SM, Zaiton F (2016) Chemical-shift MRI versus washout CT for characterizing adrenal incidentalomas. *Clin Imaging* 40:780–787. <https://doi.org/10.1016/j.clinimag.2016.02.006>



Urogenital Imaging: Kidneys (Lesion Characterization)

Ali Pourvaziri, Anushri Parakh,
Avinash Kambadakone, and Dushyant Sahani

Contents

1	Virtual Monoenergetic/Monochromatic Imaging (VMI)	286
2	Material Specific Imaging	287
3	Virtual Unenhanced Imaging (VUE)	287
4	Iodine Imaging	288
5	Radiation Dose Consideration	290
6	Conclusion	291
	References	291

Renal lesion detection and characterization is an evolving conundrum with significant economic and healthcare ramifications. Up to 40% of patients have at least one incidental renal lesion discovered on imaging done for another reason (Carrim and Murchison 2003). More than 60% of renal cell carcinomas (RCC) are now incidentally discovered in asymptomatic individuals (Carrim and Murchison 2003; Jayson and Sanders 1998; Pandharipande et al. 2010). The incidence of renal lesions has been rising continuously over

the past decade (Chow et al. 1999). Continuous increase in renal lesion incidence can be explained, at least partially, by growth of cross-imaging utilization and higher accuracy of modalities (Brenner 2010, 2009; Brenner and Hall 2007). Technological improvement, such as multidetector imaging and dose modulation, has steadily increased the clinical application of CT imaging (Brenner and Hall 2007; Frush and Applegate 2004).

In most centers, a multiphasic contrast-enhanced CT scan is the preferred next step in characterizing incidentally found renal lesions. Conventional renal lesion assessment requires at least two phases (non-contrast and contrast scan) for evaluation of any underlying enhancement, which is fundamental for classification methods such as the Bosniak system. However, conventional CT imaging is not without limitations; (a)

A. Pourvaziri · A. Parakh · A. Kambadakone
Department of Radiology, Massachusetts General
Hospital, Harvard Medical School,
Boston, MA, USA

D. Sahani (✉)
Department of Radiology, University of Washington
School of Medicine, Seattle, WA, USA
e-mail: dsahani@uw.edu

The Hounsfield value measurements are subjected to variation based on kV utilization (Afifi et al. 2020). (b) The inherent motion artifact that stems from breathing may lead to difficulty in assessing the pixel by pixel-wise comparison of unenhanced and contrast-enhanced images. This is significantly more cumbersome in small foci of enhancement or lesions. (c) Additionally, pseudoenhancement is an artifact described when measuring the density of small renal lesions—usually less than 1–2 cm. Pseudoenhancement leads to a spuriously increased estimation of density. This artifact is more encountered in the setting of prominent renal parenchymal enhancement and is proposed to be due to beam hardening and partial volume averaging artifacts (Birnbaum et al. 2002; Coulam et al. 2000; Tappouni et al. 2012). These shortcomings have led radiologists to explore solutions that characterize renal lesions in more accurate and efficient ways. In this chapter, we discuss how dual-energy CT scan implementation in clinical practice can address some of these shortcomings and expand on the utility of various images generated from dual-energy scans.

Since the introduction of dual-energy CT scan (DECT) into routine clinical practice more than a decade ago (Acharya et al. 2015), significant hardware and image processing developments have enabled a myriad of clinically useful applications in genitourinary imaging. DECT provides virtual monoenergetic imaging (VMI) and material-specific information that is unobtainable using conventional single energy CT imaging. Additionally, in DECT, two imaging datasets from two different energy is generated near-simultaneously, which considerably improves the prospect of a pixel by pixel-wise comparison with virtual unenhanced images (VUE) (Heye et al. 2012; Heye 2012).

1 Virtual Monoenergetic/ Monochromatic Imaging (VMI)

Depending on the DECT system utilized, VMI is acquired in the data or image domain. Data domain is used in rapid kVp switching DECT

platforms (rsDECT), and image domain is implemented in dual-layer (dIDECT) and dual-source DECT (dsDECT) platforms. VMI reconstructions, as the name implies, are gray-scale images that resemble the appearance of what would be otherwise acquired using single energy photons. VMI acquisition is more thoroughly discussed in other chapters. However, it is worth noting that by definition, monoenergetic imaging is unaffected by beam hardening artifacts (Albrecht et al. 2019). Predictably, VMI utilization has been shown to decrease pseudoenhancement artifact in small renal cysts without the need for generation of a true unenhanced acquisition (Jung et al. 2012; Mileto et al. 2014a).

There is a high reproducibility of attenuation measurements (Hounsfield Unit, HU) with only minor inconsistencies across different DECT technologies of VMI (Sellerer et al. 2018; Jacobsen et al. 2017; Silva et al. 2011). The superiority of image quality of VMIs in comparison to conventional 120-kVp images have been demonstrated in several studies (Yu et al. 2011, 2012; Matsumoto et al. 2011). The energy range of 60–70 keV corresponds to a midpoint between the mean energies of 80 kVp and 140 kVp. Data suggest that as a general rule, range of 60–70 keV provides an optimal contrast-to-noise ratio (CNR) with the lowest amount of noise (Yu et al. 2011, 2012; Matsumoto et al. 2011). However, in evaluating renal cell carcinoma in genitourinary imaging, 60 keV may provide better image quality for nephrographic phase and 50 keV for corticomedullary phase (Martin et al. 2017).

Lesion specific attenuation curve can be generated using ranges of VMIs. The keV range is from 40 to 140 keV in rapid switching (rsDECT), 40–190 keV in dual-source (dsDECT), and 40–200 keV in dual-layer platforms (dIDECT). Enhancing lesions can be differentiated from cysts on a single-phase nephrographic images. Iodine attenuation significantly increases at lower keV range, whereas cyst levels remain relatively similar and demonstrate a relatively flat curve (Fig. 1). Additionally, there is potential for distinguishing malignant from benign lesions using quantitative spectral analysis of these curves (Table 1) (Patel et al. 2017).

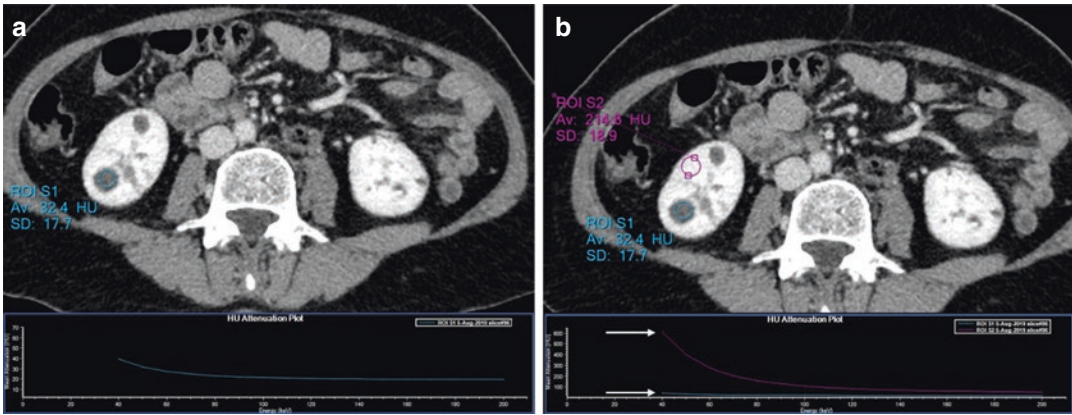


Fig. 1 (a) Axial post-contrast portal phase images in a dual-layer DECT (dIDECT) platform demonstrates a hypodense lesion in the left kidney measuring 32.4 HU. The spectral curve indicates a minimal increase in

attenuation in lower keVs level, reflecting a non-enhanced cyst. (b) Adjacent normal parenchyma enhances brightly measuring 214 HU. Note the up-pick of the HU attenuation plot in lower keVs (arrows) in comparison to the cyst

Table 1 Virtual monoenergetic imaging utility in renal lesion characterization

VM imaging in renal lesion characterization
High reproducibility of HU measurement
Higher image quality
Decrease pseudoenhancement artifact
Optimal CNR and lower noise
Generation and analysis of attenuation curves
<ul style="list-style-type: none"> Differentiation of enhancing lesions from cysts in one phase Potential to distinguish malignant from a benign lesion

CNR contrast to noise ratio, VM virtual monoenergetic

2 Material Specific Imaging

DECT generated data can be used to determine the voxel compositions. Each voxel is analyzed on the basis of two-material decomposition principle for data domain technique and three-material decomposition principle for image domain techniques. In three-material decomposition approach, absorption characteristics of three materials, such as fat, iodine, and soft tissue at two energy levels are idealized and used to create specific material image series. The iodine can be extracted to create virtual unenhanced images. On the other hand, iodine can be overlaid in different ratios to create iodine overlay images or purely used to create iodine maps (Fornaro et al.

2011; Hartman et al. 2012; Kaza et al. 2017a, 2012). A similar technique is used in two material decomposition techniques. However, two material decomposition techniques with two markedly different atomic number or mass-attenuation coefficient is used to generate two sets of images; material density images such as iodine or water images (virtual unenhanced images) (Fornaro et al. 2011; Hartman et al. 2012; Kaza et al. 2017a, 2012, 2011).

3 Virtual Unenhanced Imaging (VUE)

Virtual unenhanced or water-density images can provide information similar to true non-contrast images and may be used as a surrogate for true non-contrast images. Data generated from virtual unenhanced images has been shown to provide a reliable assessment of non-enhanced characteristics of renal lesions such as the presence of fat, hyperdense material or calcification (Fig. 3b, e) (Ascenti et al. 2012). Attenuation measurement is readily available in the latest generation of rapid kVp switching DECT (rsDECT) technology in addition to dual-source (dsDECT) and dual-layer systems (dIDECT). Most studies point to excellent correlation between HU measurement of virtual non-enhanced images and true non-contrast

Table 2 Virtual unenhanced imaging in renal lesion

Virtual unenhanced imaging in renal lesion characterization
Provide information similar to true non-contrast
Reliable assessment for the presence of fat, hyperdense material or calcification
Excellent correlation of HU measurement with true non-contrast exam
Limitations
<ul style="list-style-type: none"> • More than 10 HU variability in measurement of some lesions. • Possible suppression of signal of punctate renal stones (less than 3 mm). • Lack of HU measurement capability in an older generation of rapid switching.

images (Slebocki et al. 2017; Meyer et al. 2019; Kaza et al. 2017b; Borhani et al. 2017). However, HU measurement on virtual unenhanced imaging cannot reliably be used for follow-up CT, if there are two different dual-energy CT platforms used (Obmann et al. 2019).

There are limitations to the usage of virtual non-enhanced images. First, more than 10 HU of variation in attenuation compared to a true non-contrast exam has been reported (Kaza et al. 2017b; Borhani et al. 2017; Çamlıdağ 2020). Further development of post-processing algorithms might be needed for the complete replacement of true non-enhanced images with VUE images. Second, due to excessive iodine suppression, signal of small stones with usually less than 3 mm, could be suppressed in virtual non-enhanced images, and these stones could be missed on these images (Table 2) (Takahashi et al. 2010; Vernuccio et al. 2018).

4 Iodine Imaging

Dual-energy CT data allows for qualitative and quantitative assessment of iodine uptake of tissues.

In the qualitative assessment of iodine imaging, renal cysts and avascular lesions are promptly diagnosed with lack of intralésional signal, whereas iodine signal within lesions could potentially be interpreted as an intralésional enhancement. Thus, iodine qualitative assessment can

readily detect lesions enhancement in one nephrographic phase (Fig. 2). In fact, studies have shown qualitative assessment of iodine allows more confident and faster characterizations of smaller lesions (Pourvaziri et al. 2019). It enables a decrease in readers' interpretation time and simplifies the workflow of renal CT protocols (Kaza et al. 2011; Ascenti et al. 2012; Pourvaziri et al. 2019; Mileto et al. 2014b, 2015; Marin et al. 2014; Graser et al. 2010). This particularly is useful in evaluating multiple lesions, such as in patients with polycystic kidney disease, where it increases readers' confidence and decreases readers' time (Glomski et al. 2018; Arndt et al. 2012).

Quantitative assessment of iodine concentration (IC) is measured based on calculation of the iodine concentration in milligrams per millimeter (mg/mL) (Coursey et al. 2010). Quantitative assessment of iodine provides accurate and rapid determination of enhancement without the need for HU measurement on both unenhanced and contrast-enhanced measurement. In evaluating renal lesions with homogenous attenuation, placement of only one ROI in each phase is sufficient for adequate HU measurement. However, in lesions with cystic, necrotic, or complex structures, multiple matching ROIs placed in both nonenhanced and contrast phase are required. This approach could potentially be biased by inclusion of small areas of necrosis or cystic change. Whereas, measurement of iodine concentration is the sum of all the enhancing areas only, and is less likely affected by the inclusion of cystic or necrotic areas within the ROIs placement (Ascenti et al. 2012, 2013; Mileto et al. 2014c). Iodine concentration of more than 0.5 mg/ml on dual-source DECT (dsDECT) and 1 mg/ml on rapid switching platforms (rsDET) has been show to optimal threshold for depiction of internal enhancement (Pourvaziri et al. 2019; Leng et al. 2015; Mileto et al. 2014d; Chandarana et al. 2011). Iodine quantification not only provides means to quantify enhancement without the need for true non-contrast exam, it also provides higher accuracy than HU measurement (Pourvaziri et al. 2019; Ascenti et al. 2013).

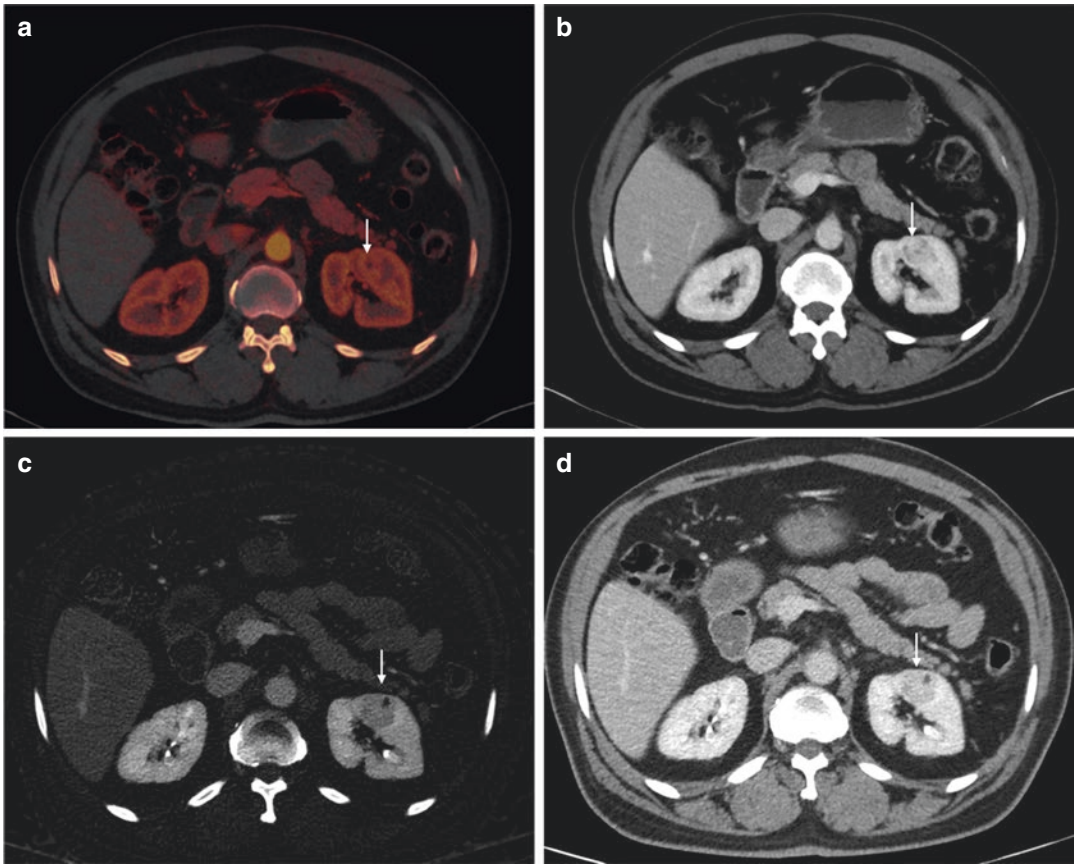


Fig. 2 59-year-old male with incidental enhancing lesions 5 months apart. **(a, b)** Axial post-contrast nephrographic phase on dual-source platform (dsDECT) demonstrates an enhancing lesion in the left kidney. **(c, d)** Axial

post-contrast nephrographic phase on dual-layer platform 5 months later shows an interval increase in the size of previously noted enhancing lesion. Note that enhancing lesion is better demonstrated on Iodine imaging **(a, c)**

Another exciting feature of iodine quantification is the potential of differentiating clear cell carcinoma from other enhancing lesions (Pourvaziri et al. 2019; Mileto et al. 2014d). In dual-source (dsDECT) approach, an iodine concentration threshold of 0.9 mg/ml has been shown to distinguish papillary from clear cell renal cell carcinoma with sensitivity and specificity of 98% and 86%, respectively (Mileto et al. 2014d). In rapid switching platforms (rsDECT), a threshold of 2.1 mg/ml distinguished clear cell from other enhancing lesions with a sensitivity of 92% (Pourvaziri et al. 2019).

Another utility of iodine images is assessing tumor response and predicting tumor progression after ablative therapy. Ablation zones are wedge shape and lack any iodine content (Tan et al.

2004; Vandenbroucke et al. 2015). Iodine content in ablations zones can be assessed both qualitatively and quantitatively on iodine imaging. Regions of intermediate enhancement surrounding the ablation zones could be noted and are better appreciated on iodine imaging (Vandenbroucke et al. 2015). However, ring enhancement, such as seen in hepatic lesions, is not common in post-ablation of renal lesions (Vandenbroucke et al. 2015). Iodine quantification has been able to differentiate reactive tissue from residual tumor after post-radiofrequency ablative treatment (Fig. 3) (Li et al. 2013). Dual-energy iodine and virtual non-enhanced images have been able to predict renal tumors' progression after ablation with 100% sensitivity and 91.5% specificity (Park et al. 2014).

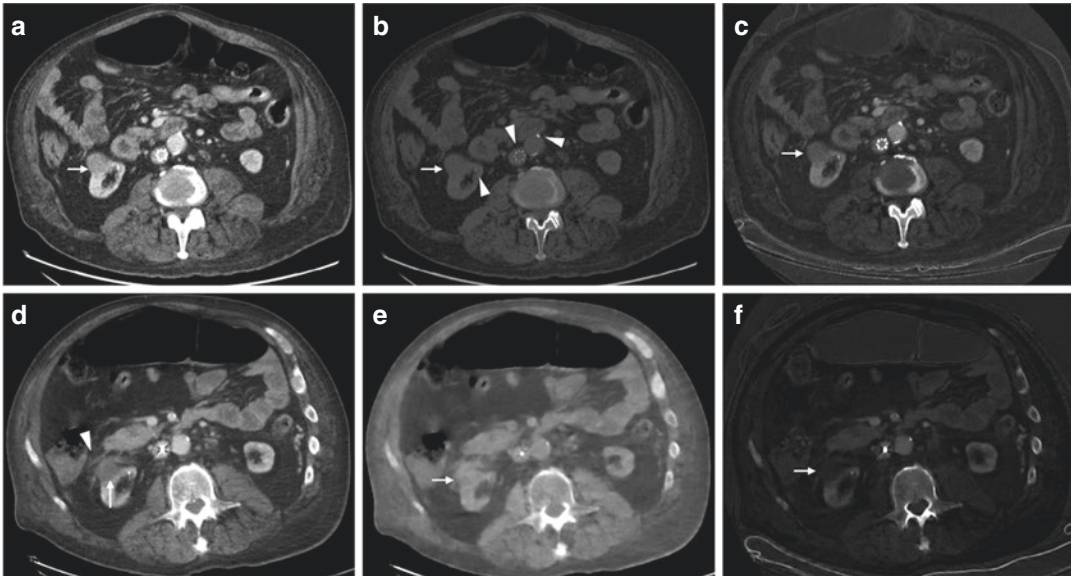


Fig. 3 69-year-old male with chronic kidney disease on hemodialysis was found to have an enhancing 2.6 cm lesion (white arrow in all images) in the lower pole of the right kidney. Renal CT protocol with rapid switching DECT; (a) Axial post-contrast 65 keV monochromatic images demonstrated an enhancing lesion measuring 86 HU. (b) Axial virtual unenhanced images revealed an isodense lesion measuring 30 HU in density. Note the hyperdense structures IVC filter, calcified plaque in the adjacent aorta, and small punctate stone in the right kidney (triangles) (c) Axial material-density iodine images; iodine concentration measured 1.9 mgr/ml consistent with enhancing lesion. The patient underwent interval micro-

wave ablative therapy. The lower set of images is 1-month post-ablation and 5 months after images in the upper row. Renal CT protocol with rapid switching DECT demonstrates. (d) Axial post-contrast 65 keV monochromatic images shows a mixed-density 2.5 cm with surrounding postprocedural stranding (triangle). (e) Axial material-density water image shows hyperdense material in the region of the previously described tumor, consistent with hemorrhage. (f) Material-density iodine image demonstrates a lack of internal iodine signal. Iodine concentration measured 0.08 mgr/ml, consistent with lack of enhancement and no residual tumor

Quantitative assessment of iodine concentration has been used in assessing response to treatment in metastatic renal cell carcinomas. Iodine concentration is significantly more sensitive and reproducible in determining response to anti-angiogenic therapy (Hellbach et al. 2017). Anti-angiogenic treatments decrease tumor angiogenic activity and perfusion without considerable volumetric changes. In assessing the response to treatment in metastatic RCC, criteria that use changes in attenuation and morphology rather than commonly used response evaluation criteria in solid tumors or Choi criteria have been shown to be more accurate and reproducible (Smith et al. 2010). After a successful treatment of metastatic RCC, there is a significant reduction in the enhancement of lesions. However, iodine con-

centration measurement shows significantly more relative reduction than measuring the Hounsfield unit alone (49.8% vs. 29.5%) (Table 3) (Hellbach et al. 2017).

5 Radiation Dose Consideration

Historically, one of the hurdles of dual-energy CT scan utilization was the concern for a hypothetical increase in radiation dose burden to patients. This perpetual increase stems from generating two datasets, instead of one, from two separate tubes with different voltages. First and foremost, in comparing two CT protocols, it is imperative to take into account a potential vari-

Table 3 Iodine imaging utility in renal lesion characterization

Iodine imaging in renal lesion characterization
Qualitative assessment
<ul style="list-style-type: none"> • Internal enhancement evaluation in single phase • Faster interpretation time • Higher readers confidence
Quantitative assessment
<ul style="list-style-type: none"> • Fast measurement of internal enhancement in a single phase • More accurate than HU measurement • Possible differentiation of clear cell RCCs from other enhancing lesions
Possible better prediction of tumor response and progression after ablative therapy
More sensitive and reproducible assessment of response to anti-angiogenic therapy

ability of radiation dose measurement, which can even vary in the same patient. It has been demonstrated that the mean coefficient for variance for size-specific dose estimates for CTs of the abdomen and pelvis may vary with 10.26-mGy (Mileto et al. 2017). Second, mounted bodies of evidence have disapproved of such concerns (Takeuchi et al. 2012; Grajo and Sahani 2018; Shuman et al. 2014; Lin et al. 2012; Dubourg et al. 2014). Optimization of DECT protocols and advancement in radiation dose Modulation have decreased radiation dosage to the level that is comparable or even lower than that of SECT protocols (Takeuchi et al. 2012; Grajo and Sahani 2018; Shuman et al. 2014; Lin et al. 2012; Dubourg et al. 2014). Currently, many institutions perform renal protocol dual-energy CT scan with radiation dose range at the level or below of 16 mGy, which is the achievable dose recommended by American College of Radiology (ACR) (Ascenti et al. 2012; Takeuchi et al. 2012; Grajo and Sahani 2018; Kanal et al. 2017; Jepperson et al. 2015). Dose neutrality offers the opportunity to perform all genitourinary imaging with dual-energy CT (Vernuccio et al. 2018).

Dual-energy CT scan provides several prospects of reducing radiation dosage. Virtual unenhanced imaging might obviate the need for a true non-enhanced phase and decrease in radiation dose up to 50% (Graser et al. 2010, 2009). Iterative reconstruction technique has cut radiation dose up to 30% in abdominal CT scan per-

formed on single energy CT scan. Although Iterative reconstruction techniques have been implemented successfully to reduce dose reduction in dual-energy CT scans (Ohana et al. 2015; Zhao et al. 2017), more studies are needed to further explore iterative reconstruction techniques in this regard. The latest generation of reconstruction techniques implements deep learning technology (Jensen et al. 2020; Kim et al. 2021). Implementation of deep learning-based image reconstruction has been shown to provide higher CNR and lower noise in abdominal CT scans (Jensen et al. 2020). Although more studies are needed, deep learning reconstructions technology offers new horizons for further dose reduction (Greffier et al. 2020; Racine et al. 2020).

6 Conclusion

In this chapter, we discussed how dual-energy CT scan for genitourinary imaging addresses many shortcomings of conventional CT imaging. We discussed the utility of various dual-energy reconstructions in a vendor-neutral fashion, how they compared with conventional imaging. In summary, dual-energy imaging in the assessment of renal lesions provides a faster, more confident, more accurate, and more reproducible evaluation of renal lesions without an increase in radiation exposure.

Compliance with Ethical Standards

Disclosure of Interests None.

Ethical Approval This article does not contain any studies with human participants performed by any of the authors. This article does not contain any studies with animals performed by any of the authors.

References

- Acharya S, Goyal A, Bhalla AS, Sharma R, Seth A, Gupta AK (2015) In vivo characterization of urinary calculi on dual-energy CT: going a step ahead with sub-differentiation of calcium stones. *Acta Radiol* 56(7):881–889. <https://doi.org/10.1177/0284185114538251>
- Afifi MB, Abdelrazek A, Deiab NA, El-Hafez AIA, El-Farrash AH (2020) The effects of CT X-ray tube

- voltage and current variations on the relative electron density (RED) and CT number conversion curves. *J Radiat Res Appl Sci* 13(1):1–11. <https://doi.org/10.1080/16878507.2019.1693176>
- Albrecht MH, Vogl TJ, Martin SS et al (2019) Review of clinical applications for virtual monoenergetic dual-energy CT. *Radiology* 293(2):260–271. <https://doi.org/10.1148/radiol.2019182297>
- Arndt N, Staehler M, Siegert S, Reiser MF, Graser A (2012) Dual energy CT in patients with polycystic kidney disease. *Eur Radiol* 22(10):2125–2129. <https://doi.org/10.1007/s00330-012-2481-7>
- Ascenti G, Mazziotti S, Mileto A et al (2012) Dual-source dual-energy CT evaluation of complex cystic renal masses. *Am J Roentgenol* 199(5):1026–1034. <https://doi.org/10.2214/AJR.11.7711>
- Ascenti G, Mileto A, Krauss B et al (2013) Distinguishing enhancing from nonenhancing renal masses with dual-source dual-energy CT: iodine quantification versus standard enhancement measurements. *Eur Radiol* 23(8):2288–2295. <https://doi.org/10.1007/s00330-013-2811-4>
- Birnbaum BA, Maki DD, Chakraborty DP, Jacobs JE, Babb JS (2002) Renal cyst pseudoenhancement: evaluation with an anthropomorphic body CT phantom. *Radiology* 225(1):83–90. <https://doi.org/10.1148/radiol.2251010930>
- Borhani AA, Kulzer M, Iranpour N et al (2017) Comparison of true unenhanced and virtual unenhanced (VUE) attenuation values in abdominopelvic single-source rapid kilovoltage-switching spectral CT. *Abdom Radiol* 42(3):710–717. <https://doi.org/10.1007/s00261-016-0991-5>
- Brenner DJ (2009) Slowing the increase in the collective dose resulting from CT scans. In: Dössel O, Schlegel WC (eds) *World congress on medical physics and biomedical engineering*. Springer, Berlin, pp 533–535. https://doi.org/10.1007/978-3-642-03902-7_152
- Brenner DJ (2010) Should we be concerned about the rapid increase in CT usage? *Rev Environ Health* 25(1):63. <https://doi.org/10.1515/REVEH.2010.25.1.63>
- Brenner DJ, Hall EJ (2007) Computed tomography – an increasing source of radiation exposure. *N Engl J Med* 357(22):2277–2284. <https://doi.org/10.1056/NEJMr072149>
- Çamlıdağ İ (2020) Compatibility of true and virtual unenhanced attenuation in rapid kV-switching dual energy CT. *Diagn Interv Radiol* 26(2):95–100. <https://doi.org/10.5152/dir.2019.19345>
- Carrim ZI, Murchison JT (2003) The prevalence of simple renal and hepatic cysts detected by spiral computed tomography. *Clin Radiol* 58(8):626–629
- Chandarana H, Megibow AJ, Cohen BA et al (2011) Iodine quantification with dual-energy CT: phantom study and preliminary experience with renal masses. *Am J Roentgenol* 196(6):693–700. <https://doi.org/10.2214/AJR.10.5541>
- Chow W-H, Devesa SS, Warren JL, Joseph F, Fraumeni J (1999) Rising incidence of renal cell cancer in the United States. *JAMA* 281(17):1628–1631. <https://doi.org/10.1001/jama.281.17.1628>
- Coulam CH, Sheafor DH, Leder RA, Paulson EK, DeLong DM, Nelson RC (2000) Evaluation of pseudoenhancement of renal cysts during contrast-enhanced CT. *Am J Roentgenol* 174(2):493–498. <https://doi.org/10.2214/ajr.174.2.1740493>
- Coursey CA, Nelson RC, Boll DT et al (2010) Dual-energy multidetector CT: how does it work, what can it tell us, and when can we use it in abdominopelvic imaging? *RadioGraphics* 30(4):1037–1055. <https://doi.org/10.1148/rg.304095175>
- Dubourg B, Caudron J, Lestrat J-P et al (2014) Single-source dual-energy CT angiography with reduced iodine load in patients referred for aortoiliacofemoral evaluation before transcatheter aortic valve implantation: impact on image quality and radiation dose. *Eur Radiol* 24(11):2659–2668. <https://doi.org/10.1007/s00330-014-3263-1>
- Fornaro J, Leschka S, Hibbeln D et al (2011) Dual- and multi-energy CT: approach to functional imaging. *Insights Imaging* 2(2):149–159. <https://doi.org/10.1007/s13244-010-0057-0>
- Frush DP, Applegate K (2004) Computed tomography and radiation: understanding the issues. *J Am Coll Radiol* 1(2):113–119. <https://doi.org/10.1016/j.jacr.2003.11.012>
- Glomski SA, Wortman JR, Uyeda JW, Sodickson AD (2018) Dual energy CT for evaluation of polycystic kidneys: a multi reader study of interpretation time and diagnostic confidence. *Abdom Radiol* 43(12):3418–3424. <https://doi.org/10.1007/s00261-018-1674-1>
- Grajo JR, Sahani DV (2018) Dual-energy CT of the abdomen and pelvis: radiation dose considerations. *J Am Coll Radiol* 15(8):1128–1132. <https://doi.org/10.1016/j.jacr.2017.08.012>
- Graser A, Johnson TRC, Hecht EM et al (2009) Dual-energy CT in patients suspected of having renal masses: can virtual nonenhanced images replace true nonenhanced images? *Radiology* 252(2):433–440. <https://doi.org/10.1148/radiol.2522080557>
- Graser A, Becker CR, Staehler M et al (2010) Single-phase dual-energy CT allows for characterization of renal masses as benign or malignant. *Investig Radiol* 45(7):399. <https://doi.org/10.1097/RLI.0b013e3181e33189>
- Greffier J, Hamard A, Pereira F et al (2020) Image quality and dose reduction opportunity of deep learning image reconstruction algorithm for CT: a phantom study. *Eur Radiol* 30(7):3951–3959. <https://doi.org/10.1007/s00330-020-06724-w>
- Hartman R, Kawashima A, Takahashi N et al (2012) Applications of dual-energy CT in urologic imaging: an update. *Radiol Clin N Am* 50(2):191–205. <https://doi.org/10.1016/j.rcl.2012.02.007>
- Hellbach K, Sterzik A, Sommer W et al (2017) Dual energy CT allows for improved characterization of response to antiangiogenic treatment in patients with metastatic renal cell cancer. *Eur Radiol* 27(6):2532–2537. <https://doi.org/10.1007/s00330-016-4597-7>
- Heye T (2012) Dual-energy CT applications in the abdomen. *Am J Roentgenol* 199(5):9196
- Heye T, Nelson RC, Ho LM, Marin D, Boll DT (2012) Dual-energy CT applications in the abdomen. *Am J*

- Roentgenol 199(5):64–70. <https://doi.org/10.2214/AJR.12.9196>
- Jacobsen MC, Schellingerhout D, Wood CA et al (2017) Intermanufacturer comparison of dual-energy CT iodine quantification and monochromatic attenuation: a phantom study. *Radiology* 287(1):224–234. <https://doi.org/10.1148/radiol.2017170896>
- Jayson M, Sanders H (1998) Increased incidence of serendipitously discovered renal cell carcinoma. *Urology* 51(2):203–205. [https://doi.org/10.1016/S0090-4295\(97\)00506-2](https://doi.org/10.1016/S0090-4295(97)00506-2)
- Jensen CT, Liu X, Tamm EP et al (2020) Image quality assessment of abdominal CT by use of new deep learning image reconstruction: initial experience. *Am J Roentgenol* 215(1):50–57. <https://doi.org/10.2214/AJR.19.22332>
- Jeperson MA, Cernigliaro JG, Ibrahim E-SH, Morin RL, Haley WE, Thiel DD (2015) In vivo comparison of radiation exposure of dual-energy CT versus low-dose CT versus standard CT for imaging urinary calculi. *J Endourol* 29(2):141–146. <https://doi.org/10.1089/end.2014.0026>
- Jung DC, Oh YT, Kim MD, Park M (2012) Usefulness of the virtual monochromatic image in dual-energy spectral CT for decreasing renal cyst pseudoenhancement: a phantom study. *Am J Roentgenol* 199(6):1316–1319. <https://doi.org/10.2214/AJR.12.8660>
- Kanal KM, Butler PF, Sengupta D, Bhargavan-Chatfield M, Coombs LP, Morin RL (2017) U.S. diagnostic reference levels and achievable doses for 10 adult CT examinations. *Radiology* 284(1):120–133. <https://doi.org/10.1148/radiol.2017161911>
- Kaza RK, Caoili EM, Cohan RH, Platt JF (2011) Distinguishing enhancing from nonenhancing renal lesions with fast kilovoltage-switching dual-energy CT. *Am J Roentgenol* 197(6):1375–1381. <https://doi.org/10.2214/AJR.11.6812>
- Kaza RK, Platt JF, Cohan RH, Caoili EM, Al-Hawary MM, Wasnik A (2012) Dual-energy CT with single- and dual-source scanners: current applications in evaluating the genitourinary tract. *RadioGraphics* 32(2):353–369. <https://doi.org/10.1148/rg.322115065>
- Kaza RK, Ananthakrishnan L, Kambadakone A, Platt JF (2017a) Update of dual-energy CT applications in the genitourinary tract. *Am J Roentgenol* 208(6):1185–1192. <https://doi.org/10.2214/AJR.16.17742>
- Kaza RK, Raff EA, Davenport MS, Khalatbari S (2017b) Variability of CT attenuation measurements in virtual unenhanced images generated using multimaterial decomposition from fast kilovoltage-switching dual-energy CT. *Acad Radiol* 24(3):365–372. <https://doi.org/10.1016/j.acra.2016.09.002>
- Kim JH, Yoon HJ, Lee E, Kim I, Cha YK, Bak SH (2021) Validation of deep-learning image reconstruction for low-dose chest computed tomography scan: emphasis on image quality and noise. *Korean J Radiol* 22(1):131–138. <https://doi.org/10.3348/kjr.2020.0116>
- Leng S, Yu L, Fletcher JG, McCollough CH (2015) Maximizing iodine contrast-to-noise ratios in abdominal CT imaging through use of energy domain noise reduction and virtual monoenergetic dual-energy CT. *Radiology* 276(2):562–570. <https://doi.org/10.1148/radiol.2015140857>
- Li Y, Shi G, Wang S, Wang S, Wu R (2013) Iodine quantification with dual-energy CT: phantom study and preliminary experience with VX2 residual tumour in rabbits after radiofrequency ablation. *BJR* 86(1029):20130143. <https://doi.org/10.1259/bjr.20130143>
- Lin XZ, Wu ZY, Tao R et al (2012) Dual energy spectral CT imaging of insulinoma—value in preoperative diagnosis compared with conventional multi-detector CT. *Eur J Radiol* 81(10):2487–2494. <https://doi.org/10.1016/j.ejrad.2011.10.028>
- Marin D, Boll DT, Mileto A, Nelson RC (2014) State of the art: dual-energy CT of the abdomen. *Radiology* 271(2):327–342. <https://doi.org/10.1148/radiol.14131480>
- Martin SS, Wichmann JL, Pfeifer S et al (2017) Impact of noise-optimized virtual monoenergetic dual-energy computed tomography on image quality in patients with renal cell carcinoma. *Eur J Radiol* 97:1–7. <https://doi.org/10.1016/j.ejrad.2017.10.008>
- Matsumoto K, Jinzaki M, Tanami Y, Ueno A, Yamada M, Kuribayashi S (2011) Virtual monochromatic spectral imaging with fast kilovoltage switching: improved image quality as compared with that obtained with conventional 120-kVp CT. *Radiology* 259(1):257–262. <https://doi.org/10.1148/radiol.11100978>
- Meyer M, Nelson RC, Vernuccio F et al (2019) Virtual unenhanced images at dual-energy CT: Influence on renal lesion characterization. *Radiology* 291(2):381–390. <https://doi.org/10.1148/radiol.2019181100>
- Mileto A, Nelson RC, Samei E et al (2014a) Impact of dual-energy multi-detector row CT with virtual monochromatic imaging on renal cyst pseudoenhancement: in vitro and in vivo study. *Radiology* 272(3):767–776. <https://doi.org/10.1148/radiol.14132856>
- Mileto A, Marin D, Ramirez-Giraldo JC et al (2014b) Accuracy of contrast-enhanced dual-energy MDCT for the assessment of iodine uptake in renal lesions. *Am J Roentgenol* 202(5):466–474. <https://doi.org/10.2214/AJR.13.11450>
- Mileto A, Marin D, Nelson RC, Ascenti G, Boll DT (2014c) Dual energy MDCT assessment of renal lesions: an overview. *Eur Radiol* 24(2):353–362. <https://doi.org/10.1007/s00330-013-3030-8>
- Mileto A, Marin D, Alfaro-Cordoba M et al (2014d) Iodine quantification to distinguish clear cell from papillary renal cell carcinoma at dual-energy multidetector CT: a multireader diagnostic performance study. *Radiology* 273(3):813–820. <https://doi.org/10.1148/radiol.14140171>
- Mileto A, Nelson RC, Paulson EK, Marin D (2015) Dual-energy MDCT for imaging the renal mass. *Am J Roentgenol* 204(6):640–647. <https://doi.org/10.2214/AJR.14.14094>
- Mileto A, Nelson RC, Larson DG et al (2017) Variability in radiation dose from repeat identical CT examinations: longitudinal analysis of 2851 patients undergoing 12,635 thoracoabdominal CT scans in an academic

- health system. *Am J Roentgenol* 208(6):1285–1296. <https://doi.org/10.2214/AJR.16.17070>
- Obmann MM, Kelsch V, Cosentino A, Hofmann V, Boll DT, Benz MR (2019) Interscanner and intrascanner comparison of virtual unenhanced attenuation values derived from twin beam dual-energy and dual-source, dual-energy computed tomography. *Investig Radiol* 54(1):1. <https://doi.org/10.1097/RLI.0000000000000501>
- Ohana M, Labani A, Jeung MY, Ghannudi SE, Gaertner S, Roy C (2015) Iterative reconstruction in single source dual-energy CT pulmonary angiography: is it sufficient to achieve a radiation dose as low as state-of-the-art single-energy CTPA? *Eur J Radiol* 84(11):2314–2320. <https://doi.org/10.1016/j.ejrad.2015.07.010>
- Pandharipande PV, Gervais DA, Hartman RI et al (2010) Renal mass biopsy to guide treatment decisions for small incidental renal tumors: a cost-effectiveness analysis. *Radiology* 256(3):836–846. <https://doi.org/10.1148/radiol.10092013>
- Park SY, Kim CK, Park BK (2014) Dual-energy CT in assessing therapeutic response to radiofrequency ablation of renal cell carcinomas. *Eur J Radiol* 83(2):73–79. <https://doi.org/10.1016/j.ejrad.2013.11.022>
- Patel BN, Bibbey A, Choudhury KR, Leder RA, Nelson RC, Marin D (2017) Characterization of small (< 4 cm) focal renal lesions: diagnostic accuracy of spectral analysis using single-phase contrast-enhanced dual-energy CT. *Am J Roentgenol* 209(4):815–825. <https://doi.org/10.2214/AJR.17.17824>
- Pourvaziri A, Parakh A, Mojtahed A, Kambadakone A, Sahani DV (2019) Diagnostic performance of dual-energy CT and subtraction CT for renal lesion detection and characterization. *Eur Radiol*. <https://doi.org/10.1007/s00330-019-06224-6>
- Racine D, Becce F, Viry A et al (2020) Task-based characterization of a deep learning image reconstruction and comparison with filtered back-projection and a partial model-based iterative reconstruction in abdominal CT: a phantom study. *Phys Med* 76:28–37. <https://doi.org/10.1016/j.ejmp.2020.06.004>
- Sellerer T, Noël PB, Patino M et al (2018) Dual-energy CT: a phantom comparison of different platforms for abdominal imaging. *Eur Radiol* 28(7):2745–2755. <https://doi.org/10.1007/s00330-017-5238-5>
- Shuman WP, Green DE, Busey JM et al (2014) Dual-energy liver CT: effect of monochromatic imaging on lesion detection, conspicuity, and contrast-to-noise ratio of hypervascular lesions on late arterial phase. *Am J Roentgenol* 203(3):601–606. <https://doi.org/10.2214/AJR.13.11337>
- Silva AC, Morse BG, Hara AK, Paden RG, Hongo N, Pavlicek W (2011) Dual-energy (spectral) CT: applications in abdominal imaging. *Radiographics* 31(4):1031–1046. <https://doi.org/10.1148/rg.314105159>
- Slebocki K, Kraus B, Chang D-H, Hellmich M, Maintz D, Bangard C (2017) Incidental findings in abdominal dual-energy computed tomography: correlation between true noncontrast and virtual noncontrast images considering renal and liver cysts and adrenal masses. *J Comput Assist Tomogr* 41(2):294–297. <https://doi.org/10.1097/RCT.0000000000000503>
- Smith AD, Shah SN, Rini BI, Lieber ML, Remer EM (2010) Morphology, attenuation, size, and structure (MASS) criteria: assessing response and predicting clinical outcome in metastatic renal cell carcinoma on antiangiogenic targeted therapy. *Am J Roentgenol* 194(6):1470–1478. <https://doi.org/10.2214/AJR.09.3456>
- Takahashi N, Vrtiska TJ, Kawashima A et al (2010) Detectability of urinary stones on virtual nonenhanced images generated at pyelographic-phase dual-energy CT. *Radiology* 256(1):184–190. <https://doi.org/10.1148/radiol.10091411>
- Takeuchi M, Kawai T, Ito M et al (2012) Split-bolus CT-urography using dual-energy CT: feasibility, image quality and dose reduction. *Eur J Radiol* 81(11):3160–3165. <https://doi.org/10.1016/j.ejrad.2012.05.005>
- Tan BJ, El-Hakim A, Morgenstern N, Semerdzhiev Y, Smith A, Lee BR (2004) Comparison of laparoscopic saline infused to dry radio frequency ablation of renal tissue: evolution of histological infarct in the porcine model. *J Urol* 172(5):2007–2012. <https://doi.org/10.1097/01.ju.0000138083.84066.98>
- Tappouni R, Kissane J, Sarwani N, Lehman EB (2012) Pseudoenhancement of renal cysts: influence of lesion size, lesion location, slice thickness, and number of MDCT detectors. *Am J Roentgenol* 198(1):133–137. <https://doi.org/10.2214/AJR.10.6057>
- Vandenbroucke F, Van Hedent S, Van Gompel G et al (2015) Dual-energy CT after radiofrequency ablation of liver, kidney, and lung lesions: a review of features. *Insights Imaging* 6(3):363–379. <https://doi.org/10.1007/s13244-015-0408-y>
- Vernuccio F, Meyer M, Mileto A, Marin D (2018) Use of dual-energy computed tomography for evaluation of genitourinary diseases. *Urol Clin North Am* 45(3):297–310. <https://doi.org/10.1016/j.ucl.2018.03.012>
- Yu L, Christner JA, Leng S, Wang J, Fletcher JG, McCollough CH (2011) Virtual monochromatic imaging in dual-source dual-energy CT: radiation dose and image quality. *Med Phys* 38(12):6371–6379. <https://doi.org/10.1118/1.3658568>
- Yu L, Leng S, McCollough CH (2012) Dual-energy CT-based monochromatic imaging. *Am J Roentgenol* 199(5):9–15. <https://doi.org/10.2214/AJR.12.9121>
- Zhao Y, Wu Y, Zuo Z, Suo H, Zhao S, Zhang H (2017) CT pulmonary angiography using different noise index values with an iterative reconstruction algorithm and dual energy CT imaging using different body mass indices: image quality and radiation dose. *J Xray Sci Technol* 25(1):79–91. <https://doi.org/10.3233/XST-160608>



Urogenital Imaging: Kidneys: Urinary Stones

Nils Große Hokamp

Contents

1	Introduction: Clinical Workup in Suspected Urolithiasis	295
2	Dual-Energy CT in Suspected Urolithiasis: Protocol Decisions	296
2.1	Protocol Recommendations	296
3	DECT-Concepts to Determine Stone Composition	297
3.1	In Vitro Capabilities for Stone Composition	297
3.2	In Vivo Capabilities for Stone Composition	297
4	Advanced Concepts	299
4.1	Stone Composition	299
4.2	Other Applications	299
4.3	Future Developments	299
5	Conclusion	300
	References	300

Abstract

Urolithiasis is a common disease in the developed world with an incidence as high as 15%; furthermore, the risk for a recurrent episode of kidney stone disease is as high as 50%. CT has become the standard diagnostic tool to detect and locate kidney stones. Dual-energy CT might increase the role in diagnostic work up of suspected kidney stone disease as it can provide guidance with regards to the type of stone detected. While uric acid stones can be reliably

identified using modern DECT scanners and software, evidence for characterization beyond uric acid varies. Depending on the scanner type used to acquire images different protocol and imaging strategies have been suggested. In future, the advent of >3-material decomposition enabled by photon-counting CT might further improve in vivo stone characterization.

N. Große Hokamp (✉)
Institute for Diagnostic and Interventional Radiology,
University Hospital Cologne, Cologne, Germany
e-mail: nils.grosse-hokamp@uk-koeln.de

1 Introduction: Clinical Workup in Suspected Urolithiasis

Flank pain and hematuria are the most common symptoms in patients with kidney stone disease.

In the emergency setting, besides history and physical examination, ultrasonography is frequently performed as first diagnostic testing in suspected urolithiasis. Ultrasonography is particularly helpful in identifying obstructive stones as indicated by pyeloureteral dilatation. However, a computed tomography scan of the abdomen and pelvis represents the diagnostic modality of choice in adults with suspected kidney stones disease (Brisbane et al. 2016; Curhan et al. 2014).

Computed tomography has an excellent sensitivity and specificity in for detection of ureteral calculi (>0.95 for both) even when using low-dose imaging protocols (Brisbane et al. 2016). Such low dose protocols do not impair diagnostic accuracy in non-obese patients, while in patients with a body-mass-index <30 kg/m², smaller stones might be missed (Franken et al. 2018). However, the limit of detection has been challenged by modern image reconstruction algorithms and furthermore, the clinical relevance of very small stones may be questioned (Chang et al. 2019). Therefore, in clinical routine a low dose computed tomography scan is conducted even in (moderately) obese patients.

2 Dual-Energy CT in Suspected Urolithiasis: Protocol Decisions

As elucidated above, scans in suspected urolithiasis are preferably conducted using low dose protocols. According to common understanding in this context, this refers to protocols with a computed tomography dose index (CTDI) up to 5 mGy (Brisbane et al. 2016; Scott Kriegshauser et al. 2015). This reference needs to be considered when considering DECT to improve stone characterization depending on the system used: In sequential scanning, the radiation dose is significantly higher as compared to standard acquisition. In kVp-switching DECT, low dose examinations can be carried out while dose modulation may or may not be used depending on generation of systems in use; this possibly limits the extent of dose reduction. In dual source DECT, low dose scanning is possible; however, as standard images are

obtained by fusion of low and high energy tube information in the image domain, some noise is introduced. A study by Franken et al. demonstrated that in this setting some (particularly small) stones (12%) were missed (Franken et al. 2018). In spectral detector DECT no prospective decision toward acquisition of DECT data has to be made as information is gathered in every scan; however, dual-energy information is available in scans conducted with 120 kVp tube voltage, only, possibly inappropriate for small patients.

To overcome dose and/or noise restrictions in emission-base DECT, different strategies are available: Advances in image reconstruction led to a relevant noise reduction in blended images obtained from dual source DECT. Yet, a proof of concept to which extent this allows for improved detection of calculi has not been conducted. In this context, it needs to be restated, that the relevance of small stones can be clinically questioned according to many guidelines; however, in symptomatic patients, the diagnosis of small calculi might be of diagnostic value to end the search for differential diagnoses. These observations account for blended images (representing conventional images), only, and can certainly be overcome by not-enabling dual-energy mode.

To combine availability of low dose protocols and improved stone characterization by means of dual-energy CT, a hybrid approach has been suggested: Here, a standard CT scan without DE-mode enabled is conducted first and interpreted for presence of stone. In case, that a kidney stone is present, a second DECT scan (with *higher* dose) is conducted in position of the calculi, only. Using this strategy, a reasonable radiation dose can be well achieved (Manglaviti et al. 2011; Nestler et al. 2019). It needs to be considered, that this approach might be disruptive to standardized workflows and possibly prone to errors if the initial reading is faulty.

2.1 Protocol Recommendations

Emission-based DECT: Low dose standard CT from upper pole of the kidneys to pelvis (axial, thin slices, and coronal 3 mm reconstructions). If stone

present additional higher dose DECT acquisition over stone (axial, thin slices, further processing pending on the vendor provided software solution). *Detector-based DECT*: Low dose from upper pole of the kidneys to pelvis (axial, thin slices, and coronal 3 mm reconstructions and further processing pending on the vendor provided software solution).

3 DECT-Concepts to Determine Stone Composition

The vast majority of stones encountered in vivo consist of either calcium-oxalate mono- or dihydrate (sometimes referred to as whewellite and weddelite, 70–85%). Followed by uric acid (10–15%) and struvite (sometimes referred to as infect-stones, 5–10%). Cystine, calcium-phosphate (brushite), and xanthine are considered rare (each <5%) (Große Hokamp et al. 2018).

Standard CT allow for differentiation between calcific and non-calcific stones. The vast majority of the latter are uric acid calculi which (as rule of thumb) exhibit attenuation between 200 and 400 HU, while calcific stones usually exhibit attenuation >600 HU. However, there is a significant overlap between the HU of different stone types which impairs the ability to securely diagnose stone composition based on attenuation characteristics in conventional CT.

Stone composition analysis can be improved by means of DECT, where attenuation of low and high energy photons is separately registered. The slope between attenuation of low and high energy photons can be understood as a simplified approximation of the material-specific attenuation coefficient. Hence, this DECT-slope or its inverse (DECT ratio) can be used to characterize a kidney stone's main component. Other mathematical operations have been suggested including the so-called dual-energy index or the spectral coefficient. Despite being calculated differently, they relate to the very same concept (Graser et al. 2008; Große Hokamp et al. 2018). In this context, the attenuation characteristics of uric acid need to be highlighted as they are quite unique: Here, attenuation of low and high energy photons occurs to a similar extent rendering this material well identifiable with all available DECT techniques (Fig. 1).

3.1 In Vitro Capabilities for Stone Composition

Several groups explored the benefits from DECT in assessing kidney stone composition in vitro. Again, most groups used the DECT ratio or -index concept to assess stone composition. The majority of studies used kidney stones harvested from patients undergoing infrared spectroscopy or radiograph diffraction analysis to determine the standard of reference (Nestler et al. 2019).

One of the earliest studies by Boll et al. investigated differentiation between a wider variety of stones (i.e. calcific, uric acid, cystine, struvite, and mixed) using their DECT ratio. They report an excellent differentiation between these types using a dual source DECT; however, images were acquired with a CTDI of 22.4 mGy which appears unrealistic for a clinical scan (Boll and Patil 2009). Similarly, our group more recently investigated the capability for stone differentiation using dual layer DECT comparing low and normal dose protocols. Here, we reported that using a normal dose protocol (CTDI 10 mGy), calcific, cystine, struvite, uric acid, and xanthine stones can be reliably identified based on their DECT ratio. Using, low dose this discrimination was rendered unfeasible for calcific and cystine stones, while the other stone types remained identifiable (Große Hokamp et al. 2018).

3.2 In Vivo Capabilities for Stone Composition

Most in vivo validation in this regard has been carried out for uric acid as its DECT ratio is close to 1 and therefore clearly different from other materials encountered in kidney stone imaging. Several groups investigated uric acid versus other stones and report excellent results for both, in and ex vivo (Franken et al. 2018; Nestler et al. 2018; Große Hokamp et al. 2020). For example, Graser et al. reported that the dual-energy index can be applied both in and ex vivo to differentiate between uric acid and non-uric acid stones; however, they found an overlap between mixed UA and calcified stones (Graser et al. 2008). In line, Eiber et al. reported excellent performance of the

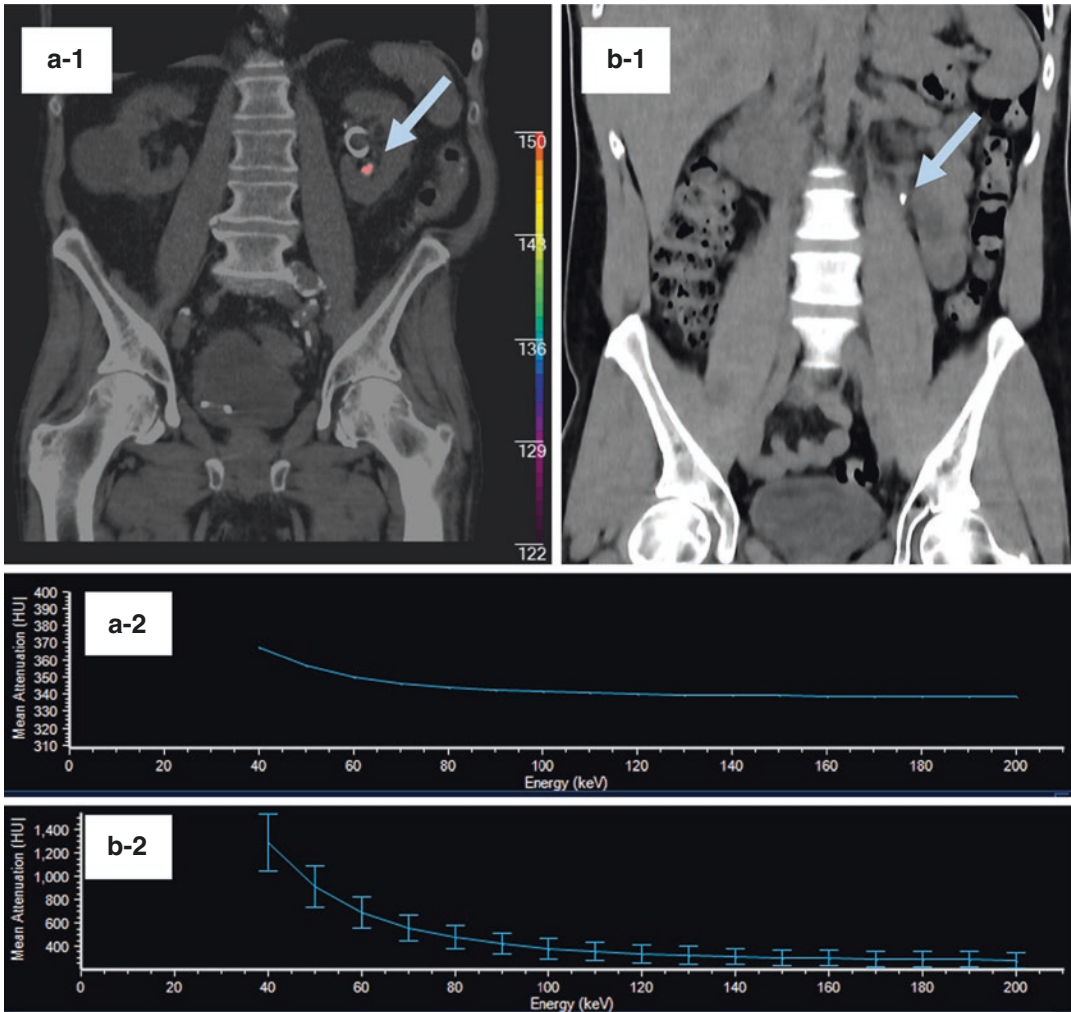


Fig. 1 Two coronal images of two patients with a uric acid stone (a-1) and a calcific, likely calcium-oxalate stone (b-1). Attenuation characteristics of low and high energy attenuation are illustrated for both stones in the lower part (a-2 and b-2) as approximated by virtual

monoenergetic images of 40–200 keV. Note that uric acid shows nearly equivalent attenuation in both low and high keV (a-2). Images acquired on a dual layer DECT. Image courtesy of Robert P. Reimer, University Hospital Cologne

dual-energy index for differentiating between uric acid and non-uric acid stones using dual energy index-based assessment on a dual source scanner while minor misclassifications occurred in mixed UA stones (Eiber et al. 2012). As a matter of fact, most vendors now provide the so-called uric acid maps as a standard reconstruction from DECT data which illustrate structures containing uric acid. Commonly, these maps are illustrated color-coded and superimposed to the conventional gray-scale CT image (Fig. 2).

Beyond this binary differentiation fewer reports are available. Mangliaviti et al. reported that using a dual source DECT, they were able to differentiate Calcium-oxalate, cystine, and uric acid stones with 100% accuracy; however, only stones >5 mm in diameter were included in their analysis.

Differences between in vitro and in vivo accuracy for stone composition assessment likely result from increase in cross scatter and a relative dose reduction due to inhomogeneity of the human body compared to homogeneous phantoms.

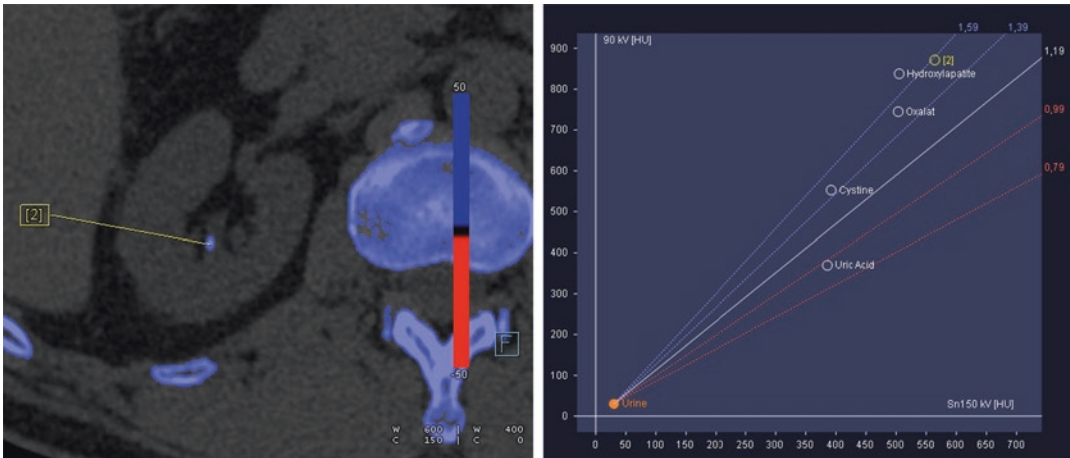


Fig. 2 Small calculi in the right kidney including plotting of the DECT ratio as provided by the vendor analysis tool (Dual Source DECT). The software deemed this stone to

be likely made of brushite. Image courtesy of Matthias Frank Frölich, University Hospital Mannheim

4 Advanced Concepts

4.1 Stone Composition

As in any field related to imaging, the advent of artificial intelligence holds promise to improve stone composition analysis as well. In a recent study by De Perrot et al. it was reported that radiomics and machine learning can help to differentiate phleboliths from small kidney stones which represents a frequent challenge in image interpretation. The authors used radiomics features to train a machine learning-based classifier which allows for accurate differentiation in 85% of cases (De Perrot et al. 2019). Our group attempted to use a shallow neural network to allow for reliable prediction of the main component even in mixed stones. We found that this is feasible in an ex vivo setting; however, translation to in vivo studies has not been demonstrated to date (Große Hokamp et al. 2020).

4.2 Other Applications

Composition analysis is not the only possible application of DECT in assessment of urolithiasis. Lazar et al., for example, investigated if calculi can be assessed in contrast enhanced examinations by means of virtual non-contrast images. They report that the removal of contrast

media is feasible in up to 600 HU contrast-associated attenuation and that the resulting virtual non-contrast images allow for detection of renal calculi with a sensitivity >99% (Lazar et al. 2020). This might hold benefit in the setting of unclear hematuria. In this setting, conducting a multiphase CT examination represents the standard of care. To rule out kidney stone disease as a common reason for hematuria, an unenhanced acquisition is generally included in the diagnostic workup; however, as suggested by their results, this might be overcome due to the high sensitivity of virtual non-contrast images if the examination is conducted on a DECT resulting in a significant radiation dose reduction.

4.3 Future Developments

Photon-counting CT has just become clinically available. This technology will likely impact kidney stone imaging from two angles: (1) Higher spatial resolution might allow for a more precise assessment of stone size. This is of importance as treatment decision as of now is solely based on stone size and location. Composition, on the other hand does not play a leading role in treatment decision as of today, despite specific treatment options are available for certain stone types (e.g. uric acid or struvite). (2) Photon-counting CT will likely improve material decomposition and there-

fore possibly improve stone characterization. With a reliable means for in vivo composition analysis becoming available, targeted therapies may gain importance in kidney stone disease.

5 Conclusion

Dual-Energy CT is helpful in assessment of kidney stone disease. It allows for reliable differentiation of uric acid and non-uric acid stones based on vendor provided reconstructions. Furthermore, a differentiation between different types of non-uric acid stones (e.g. struvite, xanthine) appears feasible according to recent literature. When conducting a CT scan with question of kidney stones on an emission-based DECT, carrying out a low dose conventional scan (DECT-mode disabled) followed by a targeted DECT scan on the kidney stone in question appears appropriate to reduce radiation dose. Future applications include a more detailed stone composition analyses using artificial intelligence and photon-counting CT as well as reliable stone identification on virtual non-contrast images.

Compliance with Ethical Standards

Funding None.

Disclosure of Interests Nils Große Hokamp receives speaker's fees and research support from Philips Healthcare. Nils Große Hokamp is consultant for Bristol-Myers Squibb. Nils Große Hokamp is on the editorial board of *European Radiology*.

Studies involving human

Ethical Approval This chapter does not contain any studies with human participants performed by any of the authors.

References

- Boll DT, Patil NA, Paulson EK et al (2009) Renal stone assessment with dual-energy multidetector CT and advanced postprocessing techniques: improved characterization of renal stone composition--pilot study. *Radiology* 250(3):813–820
- Brisbane W, Bailey MR, Sorensen MD (2016) An overview of kidney stone imaging techniques. *Nat Rev Urol* 13(11):654–662
- Chang D, Slebocki K, Khristenko E et al (2019) Low-dose computed tomography of urolithiasis in obese patients: a feasibility study to evaluate image reconstruction algorithms. *Diabetes Metab Syndr Obes Targets Ther* 12:439–445
- Curhan G, Denu-ciocca CJ, Matlaga BR et al (2014) American Urological Association (AUA) guideline medical management of kidney stones: American urological association medical management of kidney stones. *AUA Clin Guidel*:1–26
- De Perrot T, Hofmeister J, Burgermeister S et al (2019) Differentiating kidney stones from phleboliths in unenhanced low-dose computed tomography using radiomics and machine learning. *Eur Radiol* 29(9):4776–4782
- Eiber M, Holzapfel K, Frimberger M et al (2012) Targeted dual-energy single-source CT for characterisation of urinary calculi: experimental and clinical experience. *Eur Radiol* 22(1):251–258
- Franken A, Gevenois PA, Van Muylem A et al (2018) In vivo differentiation of uric acid versus non-uric acid urinary calculi with third-generation dual-source dual-energy CT at reduced radiation dose. *AJR Am J Roentgenol* 210(2):358–363
- Graser A, Johnson TRC, Bader M et al (2008) Dual energy CT characterization of urinary calculi: initial in vitro and clinical experience. *Investig Radiol* 43(2):112–119
- Große Hokamp N, Salem J, Hesse A et al (2018) Low-dose characterization of kidney stones using spectral detector computed tomography: an ex vivo study. *Investig Radiol* 53(8):457–462
- Große Hokamp N, Lennartz S, Salem J et al (2020) Dose independent characterization of renal stones by means of dual energy computed tomography and machine learning: an ex-vivo study. *Eur Radiol* 30(3):1397–1404
- Lazar M, Ringl H, Baltzer P et al (2020) Protocol analysis of dual-energy CT for optimization of kidney stone detection in virtual non-contrast reconstructions. *Eur Radiol* 30(8):4295–4305
- Manglaviti G, Tresoldi S, Guerrer CS et al (2011) In vivo evaluation of the chemical composition of urinary stones using dual-energy CT. *Am J Roentgenol* 197(1):76–83
- Nestler T, Nestler K, Neisius A et al (2018) Diagnostic accuracy of third-generation dual-source dual-energy CT: a prospective trial and protocol for clinical implementation. *World J Urol*
- Nestler T, Nestler K, Neisius A, Isbarn H, Netsch C, Waldeck S, Schmelz HU, Ruf C. Diagnostic accuracy of third-generation dual-source dual-energy CT: a prospective trial and protocol for clinical implementation. *World J Urol*. 2019;37(4):735–741. <https://doi.org/10.1007/s00345-018-2430-4>. Epub 2018 Aug 3. PMID: 30076456.
- Scott Kriegshauser J, Naidu SG, Paden RG et al (2015) Feasibility of ultra-low radiation dose reduction for renal stone CT using model-based iterative reconstruction: prospective pilot study. *Clin Imaging* 39(1):99–103



Skeletal Imaging: Bones

Christian Booz, Julian L. Wichmann,
and Tommaso D'Angelo

Contents

1	Metal Artifact Reduction Techniques	302
1.1	Introduction	302
1.2	Technical Background	302
1.3	Literature Overview	303
2	Bone Marrow Assessment	304
2.1	Introduction	304
2.2	Technical Background	304
2.3	Applications in Clinical Routine	305
3	Bone Mineral Density Analysis	307
3.1	Introduction	307
3.2	Technical Background	308
3.3	Initial Experience in Literature	308
4	Future Innovations	310
5	Conclusion	310
	References	311

Abstract

Since the advent of dual-energy CT, improvements have been achieved in CT imaging of the skeleton. Through reconstruction of a virtual monochromatic energy spectrum and cor-

responding virtual monoenergetic images, significant metal artifact reduction can be achieved compared to conventional CT, allowing for a more detailed assessment of metal implants and surrounding tissue. Furthermore, visualization of bone marrow pathologies is achieved by creation of virtual non-calcium images which enable subtraction of calcium from cancellous bone based on three-material decomposition. In addition, phantomless bone mineral density measurements of trabecular bone can be performed with dual-energy CT, allowing for opportunistic osteoporosis screening in context of routine CT scans,

C. Booz (✉) · J. L. Wichmann
Department of Diagnostic and Interventional
Radiology, University Hospital Frankfurt,
Frankfurt, Hessa, Germany

T. D'Angelo
Department of Diagnostic and Interventional
Radiology, University Hospital Messina,
Messina, Sicily, Italy

potentially resulting in avoidance of further examinations and—particularly for patients undergoing regular follow-up CT examinations—significant radiation exposure reduction. With introduction of photon-counting CT, advances regarding all mentioned applications are expected due to its technical advances compared to dual-energy CT. In addition, photon-counting CT may also further facilitate visualization of complex and thin skeletal structures by providing highest spatial resolution imaging, as well as bone tumor identification and characterization due to improved material decomposition compared to dual-energy CT.

Abbreviations

BMD	Bone mineral density
BME	Bone marrow edema
DERatio	Dual-energy ratio
DXA	Dual x-ray absorptiometry
HU	Hounsfield unit
MARS	Metal artifact reduction system
ROI	Region of interest
VMI	Virtual monoenergetic image
VNCa	Virtual non-calcium
VOI	Volume of interest

1 Metal Artifact Reduction Techniques

1.1 Introduction

Radiologists are frequently faced with the task of analyzing metallic prostheses for periprosthetic fractures, metallic failure and fracture, liner wear, aseptic loosening, infection, particle disease, and recurrent tumors after surgery in clinical routine. Radiographs are commonly obtained after such surgeries, although low sensitivity and specificity have been reported (Viano et al. 2000; Lüdeke et al. 1985). MRI is advocated for its superior soft tissue detail and sensitivity for bone marrow edema (BME), however, distortion due to metal artifact remains a significant problem (Suh et al.

1998). In this context, invasive joint aspiration is the definitive test in the setting of suspected infection potentially causing complications such as joint inoculation in the presence of overlying cellulitis (White et al. 2000).

CT has suffered from image degradation because of excessive beam attenuation of metal implants, that leads to photon starvation, radiation scatter, beam hardening artifact, excessive quantum noise, and scatter edge effects (Nicolaou et al. 2012; Mallinson et al. 2016). There are specific methods that can reduce the degree of artifact found on conventional polychromatic CT images including optimizing patient position, extending attenuation scales, iterative reconstruction utilization, use of soft tissue filters, and increasing the tube voltage or current. These approaches can significantly decrease photon starvation and beam hardening artifact but can come at the expense of increased dose, decreased soft tissue definition, and diminished spatial resolution (Lee et al. 2007). Hardware and software requirements also limit availability and can hinder widespread utility.

Dual-energy CT provides new possibilities for metal artifact reduction through implementation of energy-specific postprocessing by allowing for reconstruction of a virtual monochromatic energy spectrum and corresponding virtual monoenergetic image (VMI) series. In this context, the higher energy beam (typically set to 140 kV) undergoes less attenuation and therefore less beam hardening, while the lower energy beam (80–100 kV) provides superior soft tissue contrast.

1.2 Technical Background

Images created from a dual-energy CT dataset can simulate those acquired with a monochromatic beam set between 40 and 190 keV. This exceeds the physical range of the beams but is achieved by adjusting the weighting value between the two datasets when blending the data creating the image. The basic principle for metal artifact reduction is that monochromatic images are created from projection space data, which demonstrate a lower susceptibility to beam hard-

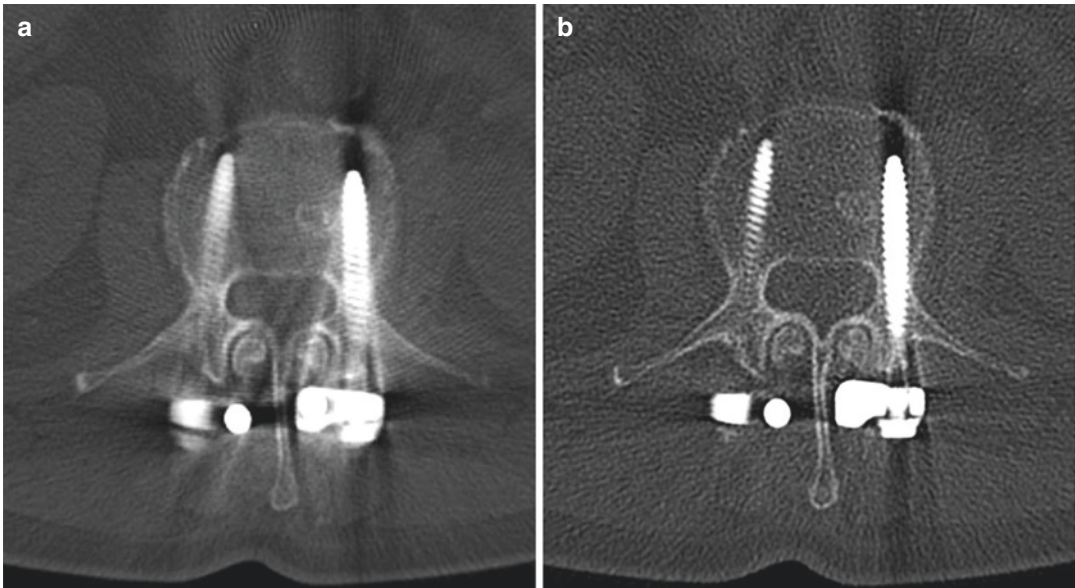


Fig. 1 Metal artifact reduction in dual-energy CT. Case of a 67-year-old woman with dorsal spondylosis in the lumbar spine undergoing regular dual-energy CT imaging. Through creation of high keV virtual monoenergetic

image (VMI) series (**b**, 130 keV in this case) significant metal artifact reduction can be achieved compared to standard linearly-blended images (**a**), allowing for better assessment of the foreign material and surrounding tissue

ening artifacts (Nicolaou et al. 2012; Mallinson et al. 2016; Yu et al. 2009). In this context, VMI allows for reconstruction of dual-energy CT datasets at a chosen hypothetical energy level that would result from an acquisition with a true monoenergetic X-ray beam (Fig. 1).

In clinical routine, these images are readily to reconstruct once the data have been processed. It is performed by the application of a simple sliding tool on the dual-energy CT workstation that allows for the image energy level to be customized continuously, comparable to window/width level adjustment. This helps the reader to optimize the balance between soft tissue detail and artifact reduction.

In case of metal implants, VMI keV levels between 110 and 146 keV have been demonstrated to provide best image quality for assessing foreign material and surrounding tissue, depending on implant size and type (Nicolaou et al. 2012; Mallinson et al. 2016; Meinel et al. 2012; Bamberg et al. 2011; Zhou et al. 2011). Finally, the monochromatic spectrum can also be used to minimize noise at the optimal tube voltage energy.

1.3 Literature Overview

There have been several studies evaluating the potential of dual-energy CT to reduce metal artifacts by application of VMI in the last decade. Guggenberger et al. analyzed spine fusion devices in phantoms by using single-energy 120-kV CT imaging and 140/100-kV dual-energy CT imaging and demonstrated that dual-energy CT provided both improved image quality and reduced metal artifacts (Guggenberger et al. 2012). In this context, the optimal dual-energy CT energy range was found to be between 124 and 146 keV.

Bamberg et al. compared reconstructed high-energy VMI series derived from dual-source dual-energy CT images with conventional CT spectra in a group of 31 patients with various metallic skeletal implants (Bamberg et al. 2011). Subjectively, superior image quality was found in 29 of 31 patients and superior diagnostic quality was demonstrated in 27. Objectively, artifact attenuation decreased from 2882 to 2341 Hounsfield units (HU). Importantly, several lesions were discernable only on high-energy VMI series.

Meinel et al. investigated the optimal settings for dual-source dual-energy CT evaluation of hip prostheses both in phantoms and in 22 patients (Meinel et al. 2012). They concluded that the optimum tube voltage settings were 140/100-kV with extrapolated energies between 105 and 120 keV, providing high image quality in all types of metal implants. Moreover, the optimized reconstructions demonstrated additional findings unseen on conventional CT images, including disk protraction, and osteonecrosis and hardware malposition.

Zhou et al. investigated 47 patients with orthopedic devices in the context of fractures by using a dual-source CT system and found that an extrapolated tube voltage of 130 keV provided optimal and superior images with significantly reduced metal artifact compared with conventional 120 kV datasets (Zhou et al. 2011).

Lee et al. analyzed both phantoms and 26 patients demonstrating that rapid kilovoltage switching dual-energy CT in combination with metal artifact reduction software (MARS) reduced metal artifacts and improved prosthetic/periprosthetic assessment/visualization (Lee et al. 2007). However, this study advised caution in case of titanium implants, as the image quality was found to be slightly poorer compared with other prosthetic compositions.

In conclusion, there have been several both in vitro and in vivo studies demonstrating that dual-energy CT can significantly reduce metal artifacts, improve image quality, and increase diagnostic yield when compared with conventional CT imaging. The extrapolated recommended keV levels for VMI series vary between 110 and 146 keV. In this context, the optimal VMI keV level is likely to depend on the specific dual-energy CT system, hardware size and composition, the pathologic condition being evaluated, and preferences of the radiologist.

2 Bone Marrow Assessment

2.1 Introduction

With the advent of spectral imaging based on dual-energy CT, numerous and noteworthy advantages over conventional CT have been dem-

onstrated such as improved material decomposition. In this context, virtual non-calcium (VNCa) imaging has become an increasingly used post-processing application that allows for subtraction of calcium from anatomical structures, enabling color-coded visualization of bone marrow pathologies such as BME (Fig. 2) (Pache et al. 2010; Booz et al. 2019a, 2020a, b; Frellesen et al. 2018; Koch et al. 2021).

Bone marrow pathologies are usually associated with a reduction of fat component in the trabecular bone, replaced by water, hemorrhage or cancer tissue depending on the underlying pathology. While bone marrow assessment on conventional CT is impeded by the presence of calcium, MRI represents the current gold standard technique for assessing bone marrow disorders including traumatic BME but also oncologic and inflammatory bone marrow disorders. However, due to its limitations in clinical routine such as contraindications or limited availability, dual-energy CT may be considered a potentially cheaper, faster, and more available imaging alternative for bone marrow assessment through creation of VNCa reconstructions. In this context, a large body of evidence has demonstrated the potential of VNCa imaging to serve as a viable imaging alternative to MRI for bone marrow assessment in case of MRI contraindications or limited availability, particularly in emergency setting for traumatized patients.

2.2 Technical Background

Based on three-material decomposition, the amount of calcium on dual-energy CT datasets is estimated and subtracted from images to highlight the anatomical structures that can be covered with bone mineral or gross calcifications in VNCa reconstructions. In this context, a baseline is made connecting CT values of yellow and red marrow (Johnson 2012). Target voxels are projected to the baseline using the characteristic slope of the DE_{ratio} of calcium. As the baseline passes close to the CT value of water (0 HU for both 100 kV and Sn140 kV), the differences among voxels on the baseline reflect mainly the water content in the bone, with calcium removed. These differences

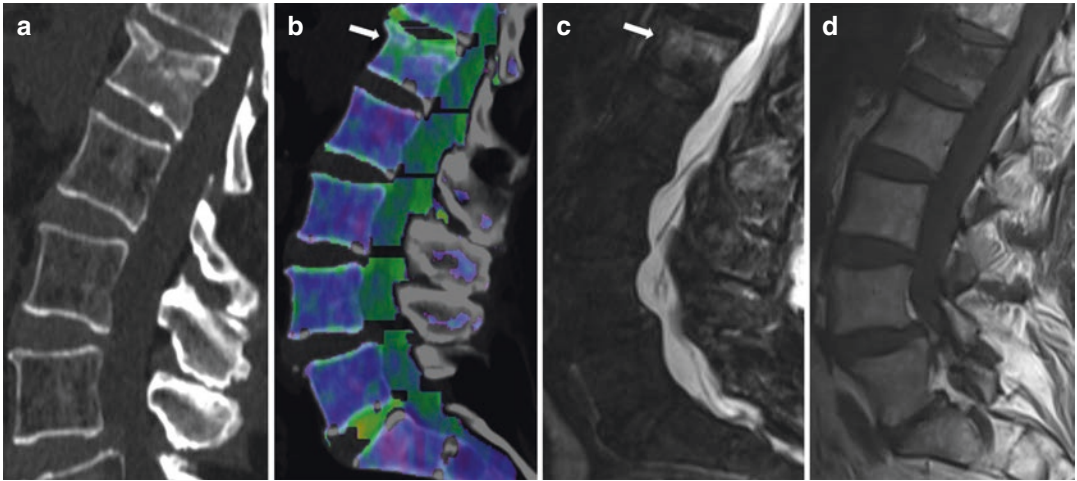


Fig. 2 Bone marrow assessment in dual-energy CT. Case of a 62-year-old man with known impression fracture of L1 but recently increasing lumbar pain undergoing dual-energy CT of the spine. On sagittal conventional grayscale CT series (**a**), the L1 fracture was assessed as being completely old. Creation of colored sagittal virtual non-calcium (VNCa) reconstructions (**b**) showed signs of bone

marrow edema (BME) (*arrow*, green colored area) in L1, indicating acute fracture components. Additionally, performed sagittal MRI sequences (**c** STIR, **d** T1w) confirmed the finding of acute fracture components within the fracture resulting in associated traumatic vertebral BME (*arrow* in **c**)

can be visually interpreted, using color-coded maps, or quantitatively assessed by means of region of interest (ROI) measurements (Booz et al. 2020b; Johnson 2012).

Image quality on VNCa datasets is influenced by dual-energy CT scanning parameters. Best results have been obtained with a DE_{ratio} of 70/150 kV. However, when wide DE_{ratio} are not recommended because of increase of image noise, such as abdomen and pelvis, higher radiation doses help providing optimal image quality (Wang et al. 2013). Pitch and rotation time do not considerably affect image quality, although spiral artifacts can appear when pitch is too low. Color-coded VNCa datasets are usually automatically processed from raw-data of most of modern dual-energy CT platforms, with processing time lasting few minutes, showing the potential to be time-efficiently used in routine clinical practice (Kelcz et al. 1979; Primak et al. 2009). Slice thickness of 1–2 mm and smoother reconstruction kernels are recommended and datasets should be reformatted along two anatomical planes for optimal qualitative evaluation (Booz et al. 2020a; Müller et al. 2019).

Technical limitations of VNCa imaging should also be taken into account. It has been demonstrated the inability to accurately visualize minor bone marrow alterations directly adjacent to cortical bone due to incomplete masking of the cortex and to spatial averaging. Incomplete subtraction of cortical or cancellous bone might also occur in case of arthrosis, and in the presence of gas or severe osteosclerosis, which can cause beam hardening artifacts that may limit bone marrow assessment. For this reason, any user of VNCa imaging should be aware of its potential pitfalls (Booz et al. 2019a, b; Kaup et al. 2016).

2.3 Applications in Clinical Routine

2.3.1 Spine

MRI and CT are currently considered the diagnostic imaging modalities of choice to evaluate spine disorders. While CT imaging is indicated in trauma setting to detect fracture lines due to its excellent spatial resolution, MRI represents the

gold standard technique for evaluation of disks, nerves, musculotendinous structures, and bone marrow disorders. Moreover, MRI is particularly useful to diagnose BME secondary to trauma, which allows to assess the chronicity of a fracture by the presence of interstitial fluid or potential instability. However, MRI access can be limited in routinely trauma setting due to its high costs and long acquisition times, which require prolonged and potentially painful patient positioning as previously stated.

Several studies have been carried out to evaluate the diagnostic performance of VNCA reconstructions to detect acute vertebral fractures (Wang et al. 2013; Kaup et al. 2016; Petritsch et al. 2017). Traumatic BME detection has been qualitatively assessed by using color-coded images, and quantitatively based on ROI measurements of bone marrow attenuation. When vertebral microfractures are present within cancellous bone, bone marrow attenuation increases since its fatty content is replaced by edema and microhemorrhage. Color-coded VNCA reconstructions show good to excellent results for qualitative assessment of vertebral BME, either in terms of sensitivity (range: 72–96%), specificity (range: 70–100%), and accuracy (range: 90–99%) (Wang et al. 2013; Kaup et al. 2016; Petritsch et al. 2017; Diekhoff et al. 2017). In addition, quantitative analysis of vertebral BME on VNCA datasets has also demonstrated excellent sensitivity, specificity, and accuracy, ranging, respectively, between 85% and 96%, 82% and 90%, and 85% and 91%, with a threshold ranging between –80 and 0 HU in these studies.

Promising results have also been carried out for diagnosis of sacral insufficiency fracture-associated BME, showing high sensitivity and specificity (93% and 95%, respectively) for qualitative assessment, and values of 85% and 95% for quantitative assessment using a cut-off value of -43HU (Booz et al. 2020b). This may allow DECT to act as a promising technique to avoid misinterpretation of sacral insufficiency fractures and their related complications, particularly in patients suffering from osteoporosis or diffuse bone disease.

The spine represents the most common site of bone metastases. Only breast, prostate, and lung cancers are together responsible for more than 80% of cases of metastatic bone disease. Contrast-enhanced CT scan is regularly performed in oncologic patients. However, the assessment of bone marrow lesions on standard CT remains challenging. Therefore, patients with high suspicion for bone metastasis frequently need to undergo additional imaging, such as MRI, scintigraphy, or positron emission tomography. The efficacy of VNCA reconstructions to detect metastatic spine lesions has been recently assessed in several studies using different calcium suppression indices. In particular, the use of low- and medium-suppression indices resulted in an increase of about 85% concerning the sensitivity compared to conventional CT, associated with a good inter-reader agreement at subjective image analysis (Abdullayev et al. 2019). In a study from Abdullayev et al. quantitative analysis using low- and medium-suppression indices showed promising results to discriminate between normal and metastatic bone, using thresholds of -143HU and -31 HU, respectively (Abdullayev et al. 2019).

High diagnostic accuracy of VNCA reconstructions has also been demonstrated for assessing infiltrative oncologic disease of vertebral bone marrow such as multiple myeloma. In this context, studies have shown high accuracy of VNCA imaging (ranging between 93% and 99%) in depicting bone marrow alterations based on threshold values ranging between -45HU and -36 HU in objective analyses compared to MRI (Kosmala et al. 2017; Wang et al. 2017).

2.3.2 Appendicular Skeleton

VNCA imaging has been shown to be particularly helpful to detect subtle, non-displaced hip fractures that might be missed on conventional radiographs or conventional CT, especially in patients affected by diffuse skeletal disorders such as osteoporosis or Paget's disease. Different authors focused on diagnostic performance of VNCA reconstructions to detect pelvic fractures, using clinical follow-up as reference standard. In these studies, dual-energy CT performed superior

compared to standard CT, showing an improvement of sensitivity (>5%) when color-coded VNCA images were evaluated (Suh et al. 2018; Burke et al. 2019). Moreover, quantitative analysis with a threshold of -55.3 HU yielded a sensitivity and specificity of 100% and 94%, respectively (Jang et al. 2019).

Different rheumatological disorders such as axial spondylarthritis and sacroiliitis usually require patients to undergo spine and pelvic MRI for assessing bone marrow pathologies caused by inflammation. In this context, studies have shown high diagnostic accuracy of VNCA reconstructions for assessing inflammatory changes of pelvic bone marrow (Wu et al. 2019; Chen et al. 2020; Foti et al. 2020). Authors concluded that dual-energy CT may serve as an appropriate imaging alternative in case of MRI contraindication or limited availability.

Dual-energy CT can complement the information provided by conventional CT imaging and enhance the diagnostic capabilities of VNCA for evaluation of acute knee fractures. In a study by Booz et al., qualitative assessment of knee fractures by color-coded VNCA images yielded sensitivity and specificity of 95%, while at quantitative analysis these values were 96% and 97%, respectively, using a threshold of -51 HU (Booz et al. 2020a). Similar results have been shown by Wang et al., who proposed a cut-off of -67 HU, yielding a sensitivity and specificity of 81% and 99%, respectively (Wang et al. 2019). Compared with conventional CT, dual-energy CT has demonstrated an increase of up to 20% regarding sensitivity to detect fractures, especially for less experienced radiologists (Yang et al. 2020).

Several authors have investigated the performance of VNCA reconstructions to detect traumatic BME in small bones of distal joints such as scaphoid and calcaneus (Booz et al. 2019a; Koch et al. 2021; Müller et al. 2019). In these studies, dual-energy CT was able to highlight traumatic BME with high sensitivity and specificity compared to MRI, both for qualitative and quantitative analysis. Additionally, it has been demonstrated VNCA imaging also allows for high diagnostic accuracy in depicting inflammatory bone marrow alterations related to rheumatoid

arthritis, either in large and small joints, showing good qualitative assessment and excellent agreement with MRI (Jans et al. 2018).

3 Bone Mineral Density Analysis

3.1 Introduction

Osteoporosis is a common bone disease affecting older patient populations, and as such, a great deal of work has been done to find noninvasive, cost-efficient, safe, and expedient methods for the diagnosis. As per current World Health Organization guidelines, the reference standard for osteoporosis assessment and diagnosis is the utilization of dual X-ray absorptiometry (DXA) to clinically assess bone mineral density (BMD) in conjunction with an evaluation of relevant patient risk factors to determine a 10-year fracture risk (Kanis et al. 2008). The accessibility, ease of use and interpretation, short acquisition time, high image resolution, stable instrument calibration, reliability, and very low radiation doses associated with DXA have led to its widespread implementation within this clinical setting.

Despite the extensive use of DXA among clinicians globally, there have been several studies describing the various shortcomings of this diagnostic tool (Bolotin and Sievänen 2001; Bolotin 2007). DXA is particularly susceptible to image distortions secondary to overlying structures, and more importantly, distortions secondary to osteodegenerative changes of the spine (Bolotin and Sievänen 2001; Bolotin 2007; Antonacci et al. 1996). Given that the prevalence of osteoporosis is highest among older patients in whom degenerative change is more common, DXA image distortions could limit its sensitivity and specificity. Moreover, DXA is a two-dimensional imaging modality that averages densities throughout the entire vertebral body. Given the varying metabolic activity among trabecular and cortical bone within the vertebral body, a 3D imaging modality confined to areas of high metabolic activity may provide more accurate assessment. It has also

been proposed that fat content within trabecular bone can significantly modify attenuation values, creating a source of error when utilizing DXA (Genant and Boyd 1977).

Despite these concerns, quantitative CT imaging was initially proposed as a viable modality to provide a true volumetric density calculation; however, due to reliance on individual phantom calibrations preventing opportunistic BMD assessment derived from routine CT scans and a high effective radiation dose (1–3 mSv), there have been concerns which have significantly limited its widespread utilization (Engelke et al. 2008).

In this context, dual-energy CT has been proposed as a viable phantomless alternative for 3D volumetric opportunistic BMD assessment based on its improved material decomposition compared to conventional CT. Additionally, dual-energy CT can image patients with decreased radiation doses when compared with conventional CT, potentially leading to reduced radiation exposure for patients in clinical routine.

3.2 Technical Background

Phantomless dual-energy CT-based volumetric BMD assessment requires prior delineation of the trabecular volume of interest (VOI) for each vertebra, which is either manually or automatic determined using specific software depending on the approach. For phantomless volumetric BMD assessment based on dual-source CT—which currently represents the most frequently applied dual-energy CT BMD approach in clinical routine—the data obtained from VOI and the two dual-energy CT kV series are used for volumetric software-based BMD assessment on the basis of material decomposition for each voxel, as initially described by Nickoloff et al. and applied by Wesarg and Wichmann et al. (Fig. 3) (Nickoloff et al. 1988; Wichmann et al. 2014; Wesarg et al. 2012). This algorithm for material decomposition is based on a biophysical model accounting for the five major substances of trabecular bone (bone minerals, collagen matrix, water, red marrow, and adipose tissue). The following two

equations are derived by using this model (for illustrative purposes we used commonly applied 80 and 140 keV levels):

$$\chi_{\text{HU}}^{80} = (\mu^{80} - \gamma^{80} g) \cdot V_{\text{TB}} + (\beta^{80} t - \gamma^{80} g) \cdot V_F + \gamma^{80} g + \delta \quad (1)$$

$$\chi_{\text{HU}}^{140} = (\mu^{140} - \gamma^{140} g) \cdot V_{\text{TB}} + (\beta^{140} t - \gamma^{140} g) \cdot V_F + \gamma^{140} g + \delta \quad (2)$$

These equations link the intensities X_{HU}^{80} and X_{HU}^{140} in the two CT series obtained at tube energies of 80 and 140 kV to the fraction of the volume occupied by the matrix material (bone mineral + collagen) V_{TB} and the volume of adipose tissue V_F . The values for t and g are 0.92 and 1.02, respectively, whereas the other variables are energy related constants. By calculating the mean intensity for the trabecular bone in both CT data sets, values for V_{TB} and V_F can be attained. Finally, from V_{TB} the BMD value ρ_{BM} (given in g/cm^3) can be calculated by application of the material constants $l = 3.06 \text{ g}/\text{cm}^3$ and $\lambda = 2.11$:

$$\rho_{\text{BM}} = \frac{1 \cdot V_{\text{TB}}}{1 + \lambda} \quad (3)$$

For assessment of spatial BMD distribution, a specific BMD value for each voxel is finally obtained.

Despite dual-source CT-based BMD assessment, similar approaches that allow for phantomless volumetric BMD assessment based on other dual-energy CT techniques such as dual-layer CT and fast kVp switching have been also described recently (Li et al. 2020; van Hamersvelt et al. 2017).

3.3 Initial Experience in Literature

Although earliest literature describing the possibility of dual-energy CT for BMD assessment was published in the late 1970s and throughout the 1980s, only few studies have evaluated the potential of phantomless dual-energy CT-derived BMD assessment (Mallinson et al. 2016; Nickoloff et al. 1988). In 2012, Wesarg et al. initially reported promising results using third-

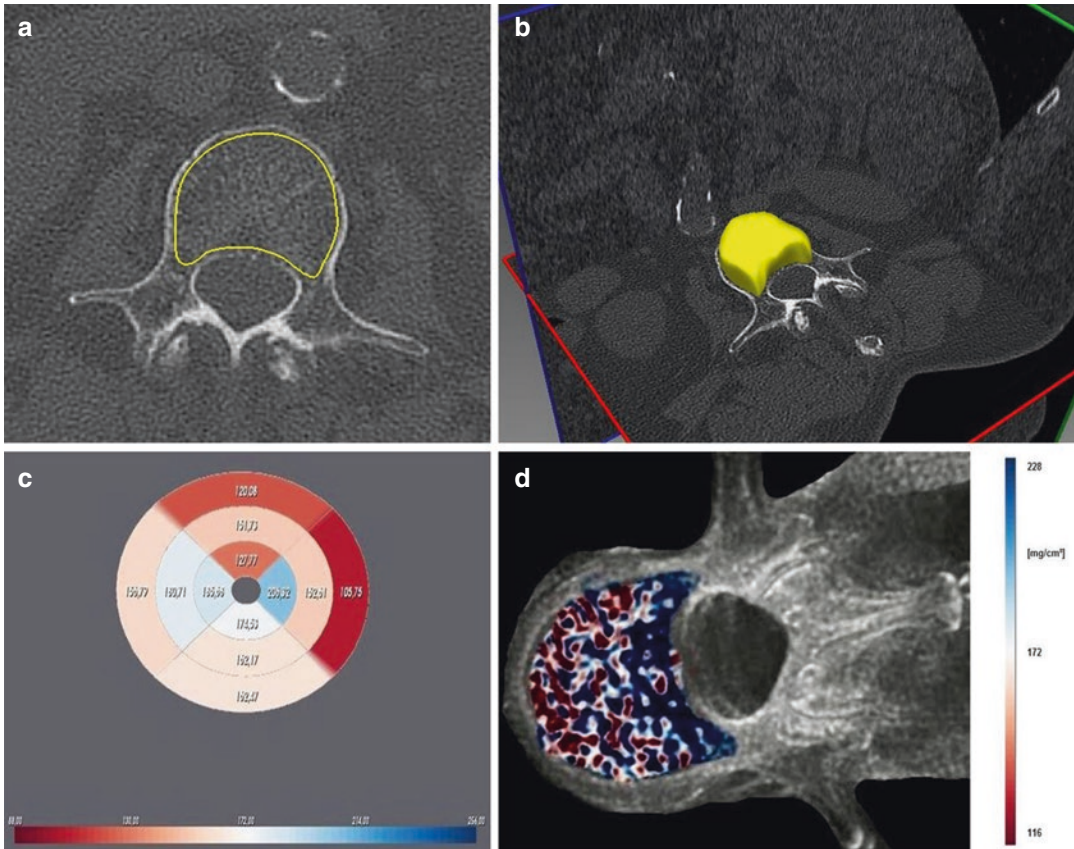


Fig. 3 Phantomless volumetric bone mineral density (BMD) assessment using dual-energy CT. Phantomless dual-energy CT-based volumetric BMD assessment requires prior delineation of the trabecular volume of interest (VOI) for each vertebra, which is commonly manually determined using specific software depending on the approach (**a**, **b**). For phantomless volumetric BMD assessment based on dual-source CT the data obtained from VOI and the two dual-energy CT kV series are used for volumetric software-based BMD assessment on the basis of

material decomposition for each voxel, as initially described by Nickoloff et al. and applied by Wesarg and Wichmann et al. (Nickoloff et al. 1988; Wichmann et al. 2014; Wesarg et al. 2012). After software-based BMD assessment, the results can be color-codedly visualized (osteoporotic BMD, red; normal BMD, blue) for 12 zones in each vertebra (**c**) with corresponding volumetric BMD values. Additionally, freely rotatable colored 3D visualization of the trabecular BMD distribution is feasible further facilitating the analysis (**d**)

generation dual-source CT for phantomless volumetric BMD assessment, however, this study was limited to exclusively *in vitro* vertebral body analysis (Wesarg et al. 2012). In 2014, Wichmann et al. conducted an *in vivo* analysis of 160 lumbar vertebrae and confirmed that 3D visualization of trabecular bone could be obtained from routinely performed third-generation dual-source CT scans (Wichmann et al. 2014). In another study, Wichmann et al. further evaluated cancellous BMD assessment of thoracic and lumbar pedicles in a cadaver study and showed high correlation

between BMD values and pull-out forces (Wichmann et al. 2015). In addition, Booz et al. have shown that phantomless volumetric BMD assessment based on dual-source CT yields superior diagnostic accuracy for the detection of osteoporosis compared to simple HU measurements (sensitivity 96% vs. 65%) (Booz et al. 2020c).

Zhou et al. showed strong correlations between dual-energy CT- and quantitative CT-derived BMD at both the participant level and the vertebral level (adjusted $R^2 = 0.983\text{--}0.987$) using rapid kVp switching (Zhou et al. 2021). Li

et al. demonstrated in a phantom study that BMD can be accurately measured either by using rapid kVp switching dual-energy CT or quantitative CT with even smaller bias using dual-energy CT (Li et al. 2020). Hamersvelt et al. evaluated the possibility of accurate BMD quantification using dual-layer spectral CT and showed strong linear correlations ($R^2 \geq 0.970$, $P < 0.001$) to DXA (van Hamersvelt et al. 2017). Additionally, Roski et al. found high correlations between BMD values derived from dual-layer spectral CT and those from quantitative CT by analyzing 174 vertebrae in 33 patients (Roski et al. 2019).

However, no data have been published that directly evaluate the potential of this technique for fracture prediction and identification of patients at risk. In addition, cost-effectiveness studies are missing to date. Nevertheless, dual-energy CT and its phantom BMD application represent a promising advance in the assessment of osteoporosis.

4 Future Innovations

With the advent of photon-counting CT, it has been demonstrated that this new technique allows for improved spatial resolution, higher contrast-to-noise ratio and substantial radiation dose reductions compared to conventional and dual-energy CT (Willeminck et al. 2018).

High-spatial resolution is essential for imaging of thin or complex skeletal structures such as the temporal bone. Small structures such as the auditory ossicles are inadequately depicted on low resolution images. Leng et al. applied a research full-body photon-counting CT system to scan the cadaveric temporal bone of a swine at a high-spatial resolution (Leng et al. 2016). Photon-counting CT allowed for clear visualization of crucial anatomic structures, such as the stapes superstructure, while reducing the radiation dose compared with high-spatial resolution conventional CT, which uses a removable comb that blocks up to three-quarters of the incident photons. Additionally, visualization of complex fractures of small bones (e.g. of the wrist) can potentially be further improved by using high-

spatial resolution photon-counting CT compared to conventional CT systems.

Moreover, it has been shown that photon-counting CT enables improved material decomposition even compared with dual-energy CT (Willeminck et al. 2018). In this context, photon-counting CT may be used to reconstruct sharper and more detailed VNCa images, potentially allowing for more accurate evaluation of BME without the need for MRI. In addition, improved material decomposition may also further improve volumetric BMD assessment as well as provide new opportunities for bone tumor identification, visualization and characterization.

Finally, photon-counting CT potentially allows for improved evaluation of metal implants and associated prosthesis loosening due to reduced beam hardening artifacts, lack of electronic noise, and higher spatial resolution. In this context, metal artifact reduction algorithms that rely on the multiple energy bins of photon-counting CT have been already proposed showing promising initial results (Nasirudin et al. 2015).

5 Conclusion

In the last 10 years, dual-energy CT has been shown to provide additional clinically relevant information compared to conventional CT in several musculoskeletal applications. Greatest experience exists in bone marrow assessment using VNCa imaging to date, particularly for trauma, but also for inflammatory and oncologic bone marrow pathologies. In addition, dual-energy CT can significantly improve assessment of metal implants through reduction of artifacts using VMI at high keV levels. Furthermore, phantomless opportunistic volumetric BMD assessment is provided, potentially resulting in avoidance of further examinations in context of routine CT scans and significant radiation exposure reduction, particularly for young patients undergoing regular follow-up CT examinations. With the advent of photon-counting CT, advances regarding all mentioned applications are expected due to its technical advances compared to dual-energy

CT. In addition, photon-counting CT may also further facilitate visualization of complex and thin skeletal structures by providing high-spatial resolution imaging as well as bone tumor identification and characterization due to improved material decomposition.

Compliance with Ethical Standards

Disclosure of Interests Authors declare that there are no conflicts of interest present regarding this book chapter.

References

- Abdullayev N, Hokamp NG, Lennartz S, Holz J, Romman Z, Pahn G et al (2019) Improvements of diagnostic accuracy and visualization of vertebral metastasis using multi-level virtual non-calcium reconstructions from dual-layer spectral detector computed tomography. *Eur Radiol* 29(11):5941–5949
- Antonacci MD, Hanson DS, Heggenes MH (1996) Pitfalls in the measurement of bone mineral density by dual energy x-ray absorptiometry. *Spine* 21(1):87–90
- Bamberg F, Dierks A, Nikolaou K, Reiser MF, Becker CR, Johnson TR (2011) Metal artifact reduction by dual energy computed tomography using monoenergetic extrapolation. *Eur Radiol* 21(7):1424–1429
- Bolotin H (2007) DXA in vivo BMD methodology: an erroneous and misleading research and clinical gauge of bone mineral status, bone fragility, and bone remodelling. *Bone* 41(1):138–154
- Bolotin H, Sievänen H (2001) Inaccuracies inherent in dual-energy X-ray absorptiometry in vivo bone mineral density can seriously mislead diagnostic/prognostic interpretations of patient-specific bone fragility. *J Bone Miner Res* 16(5):799–805
- Booz C, Nöske J, Albrecht MH, Lenga L, Martin SS, Wichmann JL et al (2019a) Traumatic bone marrow edema of the calcaneus: evaluation of color-coded virtual non-calcium dual-energy CT in a multi-reader diagnostic accuracy study. *Eur J Radiol* 118:207–214
- Booz C, Nöske J, Martin SS, Albrecht MH, Yel I, Lenga L et al (2019b) Virtual noncalcium dual-energy CT: detection of lumbar disk herniation in comparison with standard grayscale CT. *Radiology* 290(2):446–455
- Booz C, Nöske J, Lenga L, Martin SS, Yel I, Eichler K et al (2020a) Color-coded virtual non-calcium dual-energy CT for the depiction of bone marrow edema in patients with acute knee trauma: a multireader diagnostic accuracy study. *Eur Radiol* 30(1):141–150
- Booz C, Nöske J, Albrecht MH, Lenga L, Martin SS, Bucher AM et al (2020b) Diagnostic accuracy of color-coded virtual noncalcium dual-energy CT for the assessment of bone marrow edema in sacral insufficiency fracture in comparison to MRI. *Eur J Radiol* 129:109046
- Booz C, Noeske J, Albrecht MH, Lenga L, Martin SS, Yel I et al (2020c) Diagnostic accuracy of quantitative dual-energy CT-based bone mineral density assessment in comparison to Hounsfield unit measurements using dual x-ray absorptiometry as standard of reference. *Eur J Radiol* 132:109321
- Burke MC, Garg A, Youngner JM, Deshmukh SD, Omar IM (2019) Initial experience with dual-energy computed tomography-guided bone biopsies of bone lesions that are occult on monoenergetic CT. *Skeletal Radiol* 48(4):605–613
- Chen M, Herregods N, Jaremko JL, Carron P, Elewaut D, Van den Bosch F et al (2020) Bone marrow edema in sacroiliitis: detection with dual-energy CT. *Eur Radiol* 30:3393–3400
- Diekhoff T, Hermann K, Pumberger M, Hamm B, Putzier M, Fuchs M (2017) Dual-energy CT virtual non-calcium technique for detection of bone marrow edema in patients with vertebral fractures: a prospective feasibility study on a single-source volume CT scanner. *Eur J Radiol* 87:59–65
- Engelke K, Adams JE, Armbrecht G, Augat P, Bogado CE, Bouxsein ML et al (2008) Clinical use of quantitative computed tomography and peripheral quantitative computed tomography in the management of osteoporosis in adults: the 2007 ISCD Official Positions. *J Clin Densitom* 11(1):123–162
- Foti G, Faccioli N, Silva R, Oliboni E, Zorzi C, Carbognin G (2020) Bone marrow edema around the hip in non-traumatic pain: dual-energy CT vs MRI. *Eur Radiol* 30(7):4098–4106
- Frellesen C, Azadegan M, Martin SS, Otani K, D’Angelo T, Booz C et al (2018) Dual-energy computed tomography-based display of bone marrow edema in incidental vertebral compression fractures: diagnostic accuracy and characterization in oncological patients undergoing routine staging computed tomography. *Investig Radiol* 53(7):409–416
- Genant HK, Boyd D (1977) Quantitative bone mineral analysis using dual energy computed tomography. *Investig Radiol* 12(6):545–551
- Guggenberger R, Winkhofer S, Osterhoff G, Wanner G, Fortunati M, Andreisek G et al (2012) Metallic artefact reduction with monoenergetic dual-energy CT: systematic ex vivo evaluation of posterior spinal fusion implants from various vendors and different spine levels. *Eur Radiol* 22(11):2357–2364
- Jang SW, Chung BM, Kim WT, Gil JR (2019) Nondisplaced fractures on hip CT: added value of dual-energy CT virtual non-calcium imaging for detection of bone marrow edema using visual and quantitative analyses. *Acta Radiol* 60(11):1465–1473
- Jans L, De Kock I, Herregods N, Verstraete K, Van den Bosch F, Carron P et al (2018) Dual-energy CT: a new imaging modality for bone marrow oedema in rheumatoid arthritis. *Ann Rheum Dis* 77(6):958–960
- Johnson TR (2012) Dual-energy CT: general principles. *Am J Roentgenol* 199(5_suppl):S3–S8

- Kanis J, Johnell O, Odén A, Johansson H, McCloskey E (2008) FRAX™ and the assessment of fracture probability in men and women from the UK. *Osteoporos Int* 19(4):385–397
- Kaup M, Wichmann JL, Scholtz J-E, Beeres M, Kromen W, Albrecht MH et al (2016) Dual-energy CT–based display of bone marrow edema in osteoporotic vertebral compression fractures: impact on diagnostic accuracy of radiologists with varying levels of experience in correlation to MR imaging. *Radiology* 280(2):510–519
- Kelcz F, Joseph PM, Hilal SK (1979) Noise considerations in dual energy CT scanning. *Med Phys* 6(5):418–425
- Koch V, Müller FC, Gosvig K, Albrecht MH, Yel I, Lenga L et al (2021) Incremental diagnostic value of color-coded virtual non-calcium dual-energy CT for the assessment of traumatic bone marrow edema of the scaphoid. *Eur Radiol* 31(7):4428–4437
- Kosmala A, Weng AM, Heidemeier A, Krauss B, Knop S, Bley TA et al (2017) Multiple myeloma and dual-energy CT: diagnostic accuracy of virtual noncalcium technique for detection of bone marrow infiltration of the spine and pelvis. *Radiology* 286(1):205–213
- Lee M-J, Kim S, Lee S-A, Song H-T, Huh Y-M, Kim D-H et al (2007) Overcoming artifacts from metallic orthopedic implants at high-field-strength MR imaging and multi-detector CT. *Radiographics* 27(3):791–803
- Leng S, Yu Z, Halaweish A, Kappler S, Hahn K, Henning A et al (2016) A high-resolution imaging technique using a whole-body, research photon counting detector CT system. In: *Medical imaging 2016: physics of medical imaging: international society for optics and photonics*, p 978311
- Li X, Li J, Jiao X, Jia X, Zhang X, Fan G et al (2020) The accuracy of bone mineral density measurement using dual-energy spectral CT and quantitative CT: a comparative phantom study. *Clin Radiol* 75(4):320.e9–320.e15
- Lüdeke K, Röschmann P, Tischler R (1985) Susceptibility artefacts in NMR imaging. *Magn Reson Imaging* 3(4):329–343
- Mallinson PI, Coupal TM, McLaughlin PD, Nicolaou S, Munk PL, Ouellette HA (2016) Dual-energy CT for the musculoskeletal system. *Radiology* 281(3):690–707
- Meinel FG, Bischoff B, Zhang Q, Bamberg F, Reiser MF, Johnson TR (2012) Metal artifact reduction by dual-energy computed tomography using energetic extrapolation: a systematically optimized protocol. *Investig Radiol* 47(7):406–414
- Müller FC, Børgesen H, Gosvig K, Rodell A, Booz C, Schmidt B et al (2019) Optimising dual-energy CT scan parameters for virtual non-calcium imaging of the bone marrow: a phantom study. *Eur Radiol Exp* 3(1):1–8
- Nasirudin RA, Mei K, Panchev P, Fehringer A, Pfeiffer F, Rummeny EJ et al (2015) Reduction of metal artifact in single photon-counting computed tomography by spectral-driven iterative reconstruction technique. *PLoS One* 10(5):e0124831
- Nickoloff E, Feldman F, Atherton J (1988) Bone mineral assessment: new dual-energy CT approach. *Radiology* 168(1):223–228
- Nicolaou S, Liang T, Murphy DT, Korzan JR, Ouellette H, Munk P (2012) Dual-energy CT: a promising new technique for assessment of the musculoskeletal system. *Am J Roentgenol* 199(5_Suppl):S78–S86
- Pache G, Krauss B, Strohm P, Saueressig U, Blanke P, Bulla S et al (2010) Dual-energy CT virtual noncalcium technique: detecting posttraumatic bone marrow lesions—feasibility study. *Radiology* 256(2):617–624
- Petrtsch B, Kosmala A, Weng AM, Krauss B, Heidemeier A, Wagner R et al (2017) Vertebral compression fractures: third-generation dual-energy CT for detection of bone marrow edema at visual and quantitative analyses. *Radiology* 284(1):161–168
- Primak A, Ramirez Giraldo J, Liu X, Yu L, McCollough CH (2009) Improved dual-energy material discrimination for dual-source CT by means of additional spectral filtration. *Med Phys* 36(4):1359–1369
- Roski F, Hammel J, Mei K, Baum T, Kirschke JS, Laugerette A et al (2019) Bone mineral density measurements derived from dual-layer spectral CT enable opportunistic screening for osteoporosis. *Eur Radiol* 29(11):6355–6363
- Suh J-S, Jeong E-K, Shin K-H, Cho JH, Na JB, Kim DH et al (1998) Minimizing artifacts caused by metallic implants at MR imaging: experimental and clinical studies. *AJR Am J Roentgenol* 171(5):1207–1213
- Suh CH, Yun SJ, Jin W, Lee SH, Park SY, Ryu C-W (2018) Diagnostic performance of dual-energy CT for the detection of bone marrow oedema: a systematic review and meta-analysis. *Eur Radiol* 28(10):4182–4194
- van Hamersvelt RW, Schilham AM, Engelke K, den Harder AM, de Keizer B, Verhaar HJ et al (2017) Accuracy of bone mineral density quantification using dual-layer spectral detector CT: a phantom study. *Eur Radiol* 27(10):4351–4359
- Viano AM, Gronemeyer SA, Haliloglu M, Hoffer FA (2000) Improved MR imaging for patients with metallic implants☆. *Magn Reson Imaging* 18(3):287–295
- Wang C-K, Tsai J-M, Chuang M-T, Wang M-T, Huang K-Y, Lin R-M (2013) Bone marrow edema in vertebral compression fractures: detection with dual-energy CT. *Radiology* 269(2):525–533
- Wang Q, Sun Z, Li S, Zhang H, Li J, Zhang L et al (2017) Bone marrow imaging by third-generation dual-source dual-energy CT using virtual noncalcium technique for assessment of diffuse infiltrative lesions of multiple myeloma. *Acta Acade Med Sin* 39(1):114–119
- Wang M-Y, Zhang X-Y, Xu L, Feng Y, Xu Y-C, Qi L et al (2019) Detection of bone marrow oedema in knee joints using a dual-energy CT virtual non-calcium technique. *Clin Radiol* 74(10):815.e1–815.e7
- Wesarg S, Kirschner M, Becker M, Erdt M, Kafchitsas K, Khan M (2012) Dual-energy CT-based assessment of the trabecular bone in vertebrae. *Methods Inf Med* 51(5):398

- White LM, Kim JK, Mehta M, Merchant N, Schweitzer ME, Morrison WB et al (2000) Complications of total hip arthroplasty: MR imaging—initial experience. *Radiology* 215(1):254–262
- Wichmann JL, Booz C, Wesarg S, Kafchitsas K, Bauer RW, Kerl JM et al (2014) Dual-energy cT–based phantomless in vivo three-dimensional bone mineral density assessment of the lumbar spine. *Radiology* 271(3):778–784
- Wichmann JL, Booz C, Wesarg S, Bauer RW, Kerl JM, Fischer S et al (2015) Quantitative dual-energy CT for phantomless evaluation of cancellous bone mineral density of the vertebral pedicle: correlation with pedicle screw pull-out strength. *Eur Radiol* 25(6):1714–1720
- Willemink MJ, Persson M, Pourmorteza A, Pelc NJ, Fleischmann D (2018) Photon-counting CT: technical principles and clinical prospects. *Radiology* 289(2):293–312
- Wu H, Zhang G, Shi L, Li X, Chen M, Huang X et al (2019) Axial spondyloarthritis: dual-energy virtual noncalcium CT in the detection of bone marrow edema in the sacroiliac joints. *Radiology* 290(1):157–164
- Yang SJ, Jeon JY, Lee S-W, Jeong YM (2020) Added value of color-coded virtual non-calcium dual-energy CT in the detection of acute knee fractures in non-radiology inexpert readers. *Eur J Radiol* 129:109112
- Yu L, Li H, Mueller J, Kofler JM, Liu X, Primak AN et al (2009) Metal artifact reduction from reformatted projections for hip prostheses in multislice helical computed tomography: techniques and initial clinical results. *Investig Radiol* 44(11):691
- Zhou C, Zhao YE, Luo S, Shi H, Zheng L, Zhang LJ et al (2011) Monoenergetic imaging of dual-energy CT reduces artifacts from implanted metal orthopedic devices in patients with fractures. *Acad Radiol* 18(10):1252–1257
- Zhou S, Zhu L, You T, Li P, Shen H, He Y et al (2021) In vivo quantification of bone mineral density of lumbar vertebrae using fast kVp switching dual-energy CT: correlation with quantitative computed tomography. *Quant Imaging Med Surg* 11(1):341



Gout

Torsten Diekhoff

Contents

1	Pathogenesis and Clinical Presentation	316
2	Diagnostic Options	316
3	Dual-Energy CT	317
3.1	Physics: Two-Material Decomposition	317
3.2	Clinical Indications for DECT	318
3.3	Scan Protocols	319
3.4	Contrast Media	320
3.5	Image Reconstruction	321
3.6	Image Interpretation	322
3.7	Report: What Information to Include	322
3.8	Issues Regarding Tophus Density and Radiation Exposure	323
3.9	DECT for Follow-Up	323
4	Case Discussions	324
4.1	Case 1: Patient with Acute Wrist Arthritis	324
4.2	Case 2: Chronic Pain of the Feet	325
4.3	Case 3: Pain of the First MTP Joint	325
4.4	Case 4: Patient with Knee Pain	326
4.5	Case 5: Patient with Rheumatoid Arthritis	328
5	Summary	329
	References	329

Abstract

Imaging of gouty arthritis was one of the first clinical indications for dual-energy computed tomography (DECT). The course of this auto-inflammatory disease is characterized by the

development of soft tissue tophi of uric acid, which can specifically be detected by DECT. The highly innovative imaging modality is in continuous competition with established tests like arthrocentesis or ultrasonography for advanced, atypical cases of gout. Here, DECT benefits from its highly standardized scanning and evaluation process and at the same time provides additional information from conventional CT and virtual non-

T. Diekhoff (✉)
Department of Radiology, Charité -
Universitätsmedizin Berlin, Berlin, Germany
e-mail: torsten.diekhoff@charite.de

calcium images. While it is less sensitive for very early gouty arthritis, it has gained an important role in the diagnostic process and also has a unique ability to assess the disease burden and therapy response. This chapter summarizes the pathogenesis of gouty arthritis and the clinical indications, protocols, and image interpretation of DECT in these patients and provides clinical examples to illustrate its different applications.

1 Pathogenesis and Clinical Presentation

- or: why birds suffer from gout but not dolphins.

Uric acid is the end product of purine metabolic pathways in the human body and usually eliminated by the kidneys. However, its solubility limit is far lower than that of its precursors, hypoxanthine and xanthine (Schett et al. 2015). Species like birds or humans that cannot process uric acid to the more soluble allantoin are at risk of uric acid crystal precipitation within joints and soft tissues. Interestingly, also early ancestors of birds shared this condition, and some fossilized *Tyrannosaurus* bones show typical gouty erosions (Rothschild et al. 1997).

Gout is the most common inflammatory joint disease in the western world with a prevalence of 1–4% (Kuo et al. 2015) and has been increasing over recent years (Zhu et al. 2011). Men are more often affected than women. However, postmenopausal women may sometimes develop gout and then suffer even more severely. A genetic predisposition, cultural habits, and kidney function play a role in the development of the disease as well as purine-rich food, alcohol, and diet sodas (Choi et al. 2004a, b; Choi and Curhan 2008). All of these aspects should be taken into account when treating gouty arthritis. Gout is a systemic disease with several metabolic and cardiovascular comorbidities (Zhu et al. 2012). Therefore, early detection of its musculoskeletal manifestations is crucial for a swift treatment initiation.

Unlike autoimmune diseases such as rheumatoid arthritis, gout is a so-called autoinflammation with a typical immune response (Ziegeler et al. 2020b). Patients experience sudden attacks of pain with redness, swelling, and stiffness that decline within 7–10 days. Changing attack locations with asymptomatic intervals are common, while later stages are characterized by polyarticular manifestations without complete symptom relief between acute episodes (Parathithasan et al. 2016). Gouty tophi can manifest in several locations in the joint capsule, surrounding soft tissues and regions with increased mechanical stress such as entheses, ligaments, bursae or ear helix (Wright and Pinto 2003). Most commonly affected are the joints of the lower extremities, especially the first metatarsophalangeal joint.

2 Diagnostic Options

In the vast majority of cases, no advanced diagnostic testing is necessary. When a patient presents with typical clinical signs and symptoms (podagra), at most a laboratory test for determination of uric acid in serum is indicated (Underwood 2006). However, as gouty arthritis is so common, many patients have uncharacteristic clinical presentations. In such cases of suspected but unproven gout, arthrocentesis is the standard of reference for diagnosis. Here, polarization microscopy depicts the birefringent crystals in the joint fluid (see Fig. 1) (Phelps and McCarty Jr. 1966). However, in clinical practice, the sensitivity of this test is reduced in symptom-free intervals, and rheumatologists use aspiration cautiously, fearing its complications (Neogi et al. 2015; Taylor et al. 2016). For this reason, imaging plays an essential role in the diagnosis of atypical forms.

Imaging in gouty arthritis has three aims: to establish the diagnosis by demonstrating typical bone changes or uric acid depositions and to exclude differential diagnoses, to assess the joint for subsequent arthrocentesis, and to monitor the response to treatment. To ascertain the diagnosis, usually, a high-resolution cross-sectional imaging method, namely arthrosonography or dual-

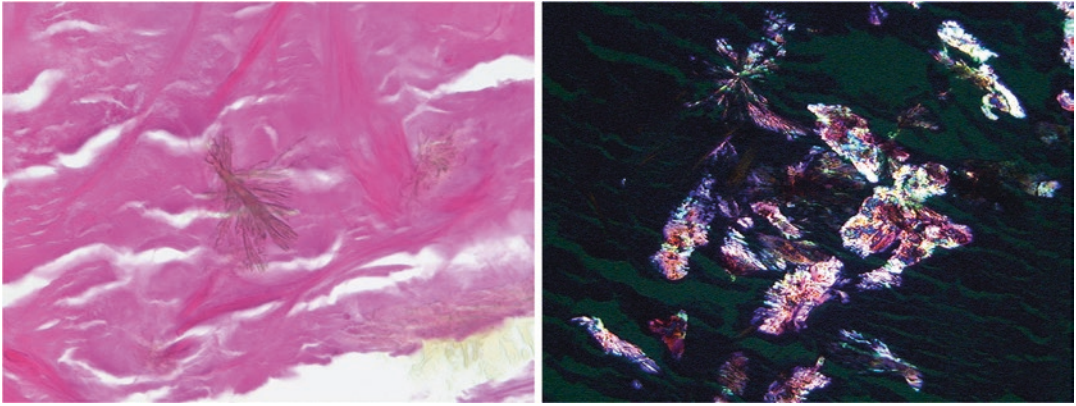


Fig. 1 Microscopic views of uric acid crystals. The needle-shaped crystals in conventional microscopy (left) are negatively birefringent in polarization microscopy (right). The material was obtained by surgical tophus excision

energy computed tomography (DECT), is needed. Only advanced stages show typical “punched-out” erosions, sometimes more distant from the joint, and periosteal reactions and faint gouty tophi in radiography (Buckley 1996). However, radiography can depict differential diagnoses such as osteoarthritis or calcium pyrophosphate deposition disease. It is also a readily available tool for follow-up examinations.

Arthrosonography is well-suited to detect earlier stages of gouty arthritis by directly demonstrating uric acid crystals in the joint fluid (so-called double-contour sign) or tophi (Thiele and Schlesinger 2007). It can also be used for planning a joint aspiration or to guide the needle during this intervention (Grassi et al. 2001). Finally, arthrosonography can also demonstrate acute arthritic inflammation, which, however, is not specific to gouty arthritis (Chowalloor and Keen 2013).

Magnetic resonance imaging (MRI) can also demonstrate active inflammation in the course of gouty arthritis. Nevertheless, these changes do not help in distinguishing gout from other inflammatory joint diseases (Cimmino et al. 2011). As conventional MR sequences cannot depict the bony surface directly, it is less well suited to assess erosions and their morphology than ultrasound and CT (Ulas, Diekhoff et al. 2019). It also fails to demonstrate uric acid depositions and can only detect large tophi. Therefore, it is inferior to DECT when it comes to establishing the diagnosis (Schumacher et al. 2006).

3 Dual-Energy CT

CT vendors have developed several methods to perform dual-energy or spectral imaging that can be used to image gouty arthritis patients. The direct demonstration of uric acid tophi with high sensitivity and specificity and the excellent reproducibility with standardized protocols favor DECT over other imaging methods in gout and earned it the first indication in clinical guidelines (Neogi et al. 2015). While the detection of tophi with a two-material decomposition algorithm is at the core of DECT imaging in gout, it provides further information about bone destruction and even active inflammation, when applied correctly.

3.1 Physics: Two-Material Decomposition

DECT allows the differentiation of two objects with similar X-ray attenuation (e.g., calcium phosphate and uric acid) when their effective atomic number Z_{eff} is sufficiently different. To accomplish this, information about the attenuation of high and low energy X-rays is needed. Thus, most CT machines apply two different X-ray spectra (tube voltages) and compare the attenuation. While materials with high Z_{eff} (e.g., calcium or iodine) exhibit greater attenuation at low energy compared to high energy scans, this

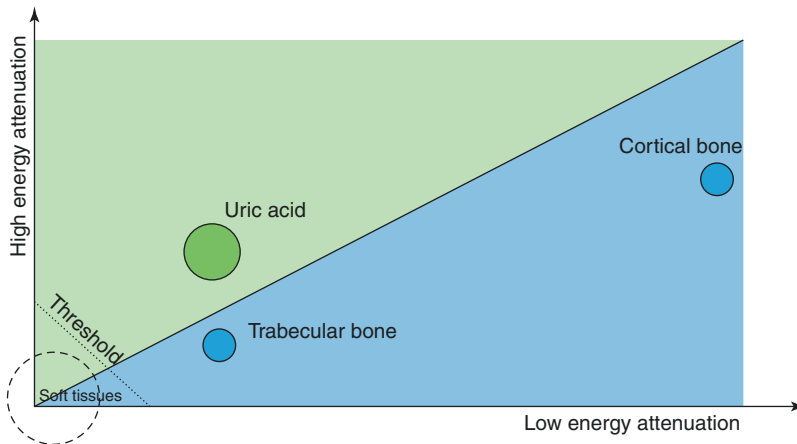


Fig. 2 Principles of two-material decomposition. The software distinguishes two materials, e.g., bone and uric acid, according to their dual-energy index by applying a detection threshold. Every voxel above the threshold and

above the line is characterized as uric acid tophus. At the same time, the software tool takes other parameters such as proximity to bone into account

effect becomes less pronounced with decreasing Z_{eff} and is reversed for molecules with very small atoms, such as hydrogen and carbon. This behavior is measured by the dual-energy index or gradient, which is relatively specific for a certain material and, thus, allows its distinction from others, even if they have the same attenuation in conventional CT (Diekhoff et al. 2015).

DECT in gout utilizes the relatively low Z_{eff} of uric acid together with its relatively high CT density when present in sufficiently high concentration to specifically detect tophi. Figure 2 illustrates the postprocessing algorithm graphically. However, as soft tissues such as muscles and ligaments show similar Z_{eff} but lower density, a threshold must be established to eliminate false-positive detection. Nonetheless, this threshold decreases the sensitivity for early tophi with low uric acid concentrations (see Fig. 3).

3.2 Clinical Indications for DECT

Whenever atypical gouty arthritis is suspected in a patient, choosing the proper diagnostic test is key to establish the diagnosis. The measurement of serum uric acid can point in the right direction

but is controversial as some patients with elevated levels will never develop gout and it can be normal even during an acute attack (Campion et al. 1987; Rymal and Rizzolo 2014). While arthrocentesis is the diagnostic gold standard, it is often not performed in clinical practice.

DECT is reported to show high sensitivity and specificity in the search for gouty arthritis. It also provides all information of a conventional CT scan such as erosions or other soft tissue calcifications and is, therefore, well-suited for differential diagnoses. However, DECT has limited sensitivity in early stages of the disease as it relies on the presence of tophi (Bongartz et al. 2015). On the other hand, tophi have been reported in patients with asymptomatic hyperuricemia (Wang et al. 2018), pointing out that earlier stages of gouty arthritis (beginning with hyperuricemia and acute arthritis in contrast to established tophaceous disease) might not reflect the clinical reality, and a new system is warranted (Dalbeth and Stamp 2014).

Studies show that joint aspiration can prove gout in DECT-negative patients but might also be negative, for several reasons, when DECT demonstrates tophi (Notzel et al. 2018). Therefore, when available, the less invasive test should be

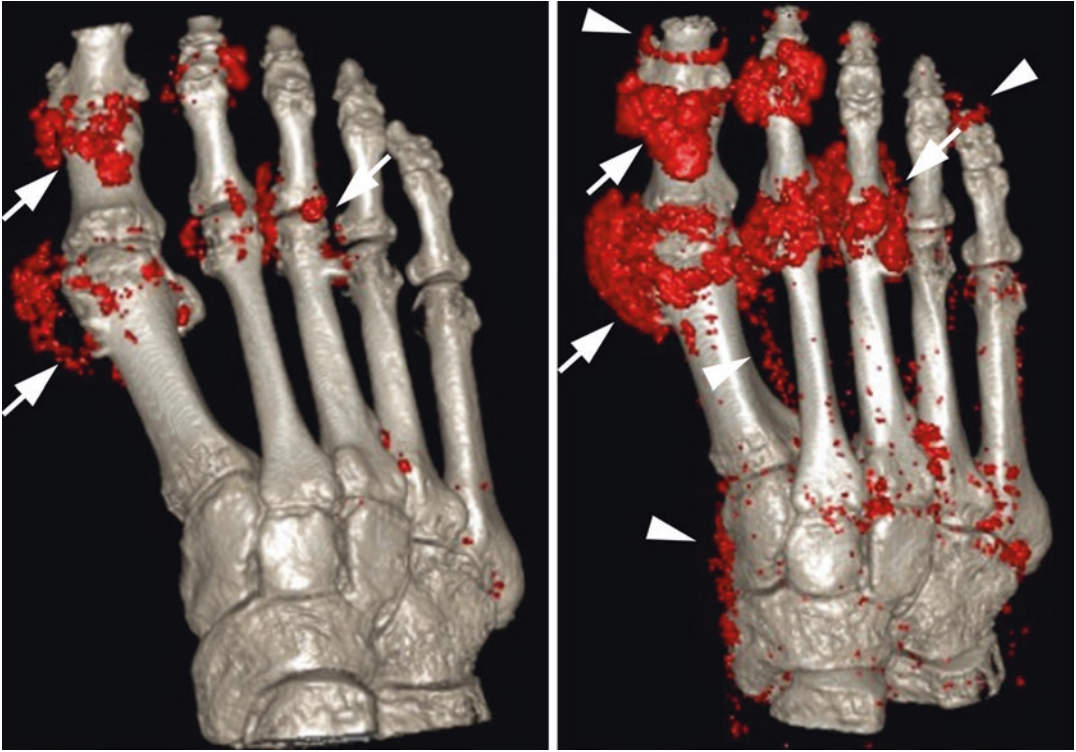


Fig. 3 Threshold adjustment. A patient with tophaceous gouty arthritis underwent DECT of the right foot. The same scan was reconstructed applying a conventional threshold (left) and a lowered threshold (right). While

more and larger tophi are depicted (arrows), there are also more artifacts, leading to false-positive detection in toe nails and tendons (arrowheads)

performed first and, if negative, followed by joint aspiration if the diagnosis is still suspected. While its diagnostic accuracy is similar to that of arthrosonography, DECT might be less sensitive in early disease (Shang et al. 2020). Ultrasound, on the other hand, can capture some findings (e.g., double-contour sign or synovitis) that are hidden from DECT but is hard to standardize and, therefore, less suited for follow-up examinations. To date, ultrasonography and DECT can be regarded as equivalent for the diagnosis and should be used according to their availability and the experience of the interpreter (Ramon et al. 2018). While arthrosonography and DECT are still regarded as second-line imaging after radiography, both are gaining in importance and can establish the diagnosis also in earlier disease.

3.3 Scan Protocols

Details of the DECT protocol depend on the vendor, the patient and the joint. Modern machines support automated tube current settings and modulation during the scan to optimize image quality and radiation exposure. For systems that allow individual adjustment of tube currents in high and low energy scans, a similar image quality of both datasets is desirable—usually the ratio of mAs between high and low energy spectra is best between 1:2 and 1:4 for gout imaging. The tin filter, which is available for some systems, optimizes the X-ray spectrum and should be applied whenever possible.

It is well known that in patients with gouty arthritis joints can be painful and swollen but

exhibit no proof of tophi in imaging whereas asymptomatic joints show definite positive findings. Therefore, the regions to be scanned need careful consideration. In clinical practice, a protocol has become established that covers the currently painful joints and both feet and ankles, as they are most commonly affected (Huppertz et al. 2014). This approach offers the highest chance of finding tophi.

The lower extremities can be scanned in supine position. The knees can easily be imaged in extension or light ($10\text{--}20^\circ$) flexion. Both ankles and forefeet are usually imaged in one scan in firm plantar flexion to minimize artifacts. To accomplish this, flexion of the knee, supported by a bolster, can be helpful so that the patient can rest his or her soles on the table. Positioning is less complex with the patient prone and the arches of the feet resting on the table. For all scans, it is useful to place the legs as close as possible together and in the middle of the gantry to ensure high resolution through a small field of view and to reduce possible artifacts. In some cases, it can be appropriate to image only one foot. Then, the other leg should be placed outside the beam path, e.g., by bending the knee as much as possible.

For the upper extremities, the patient is usually in prone position with the arms elevated over the head. Both hands and wrists can be scanned simultaneously or separately. Note that a simultaneous scan in a larger field of view will decrease the spatial resolution, which is not of advantage in the small structures of the wrist and finger joints. With some machines, it is possible to image one hand/wrist comfortably with the patient standing beside the table or behind the gantry. If this maneuver includes a table movement, a secure rest of the arm on the table is desirable and can be achieved by using a sandbag or straps. The elbow is sometimes harder to image. Machines with enough z-axis coverage allow the scanning without table movement and a patient standing behind the gantry and reaching into the scanner. For other systems, prone positioning of the patient with

the arm elevated and sideways flexion of the head might be an alternative. Under no circumstances should hands or elbows be scanned resting on the abdomen or besides the patient, as this will result in unnecessarily high radiation exposure and a severe loss of image quality. Furthermore, it is crucial never to place the joint in a way that the whole forearm is in the beam path.

There are only a few reports on gout imaging of the axial skeleton (Gibney and Murray 2020). Here, the protocol should use a sufficiently large amount of radiation to ensure optimal image quality. Especially the low energy scan is critical as increased image noise might lead to more false-positive detections. As DECT cannot use conventional methods to cope with obese patients (e.g., use of higher tube voltage), an optimal image quality can only be achieved with an increase in tube current and rotation time.

3.4 Contrast Media

In most patients with gouty arthritis, imaging can be performed without administration of contrast medium. However, recent studies suggest that contrast-enhanced CT (Diekhoff, Ulas et al. 2019) or DECT (Fukuda et al. 2017) depicts acute soft tissue inflammation and, therefore, enhances the diagnostic capability of a DECT scan (see Fig. 4). Nonetheless, it is unclear whether tophus enhancement might distort the effective Z of a voxel sufficiently to interfere with two-material decomposition. Therefore, contrast medium should be used with caution.

In the search for active soft tissue inflammation like synovitis or enthesitis, the iodinated contrast medium should be administered at a volume of 1 ml/kg of body weight followed by a sufficient amount of saline solution. Three minutes after contrast medium injection, inflammatory soft tissue already shows enhancement while contrast medium diffusion into joint effusion is still minimal. Therefore, this is the best timepoint for imaging.

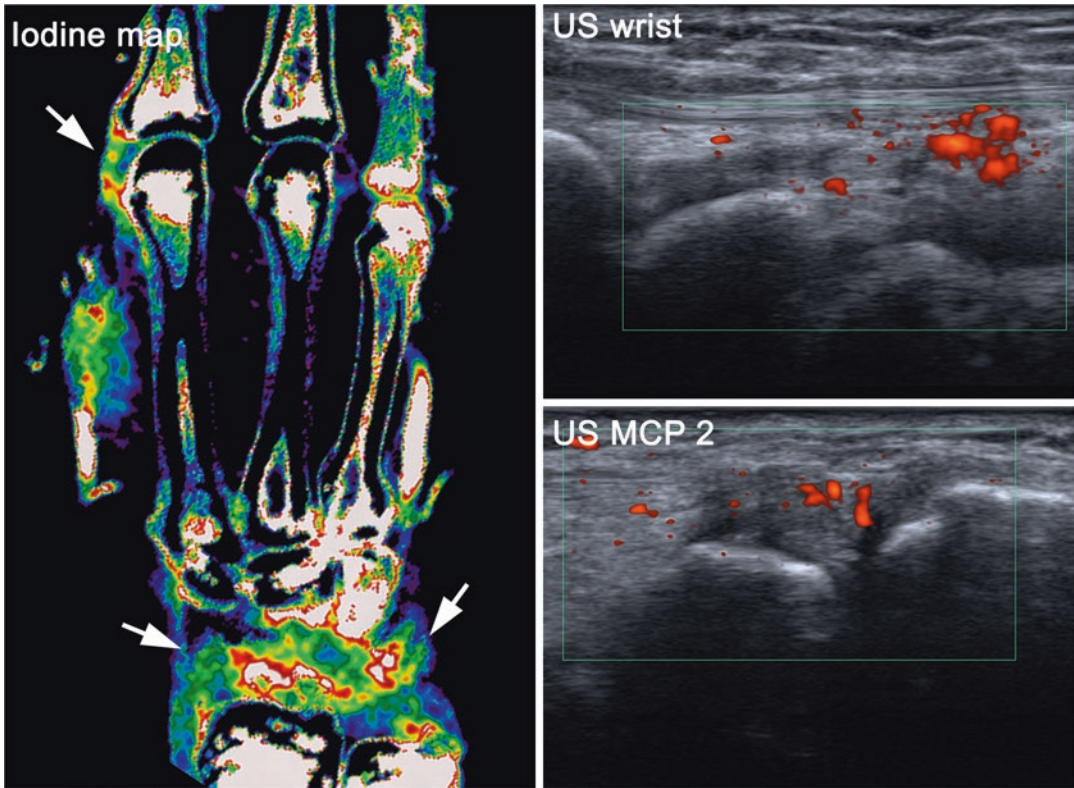


Fig. 4 Synovitis in DECT iodine maps after contrast medium injection. The iodine map (left) demonstrates contrast enhancement at the wrist and the second metacarpophalangeal (MCP) joint, indicating acute soft tissue

inflammation. Synovitis is confirmed by arthrosonography (right), which shows hypoechoic soft tissue swelling and increased perfusion in the power Doppler mode. The patient was later diagnosed with rheumatoid arthritis

3.5 Image Reconstruction

It is recommended to reconstruct standard, conventional CT images in a sharp bone kernel and medium soft tissue kernel and to generate appropriate multiplanar reformations. Either 70–75 keV monochromatic or 120 kV-equivalent weighted average images come closest to a standard CT. When no automated reconstruction of these images is possible, reconstruction of the base scans is also fine. Using the high energy scan for soft tissue reconstructions results in better visualization of gouty tophi (as uric acid attenuates slightly more in high energy scans) and low image noise. Bone kernel reconstructions can be done from either the low energy scan (which will result in better contrast at the expense of image noise) or the high energy scan. The latter might be preferable for the axial skeleton.

Depending on the particular settings of the CT machine, secondary reconstruction of the gout images using two-material decomposition and virtual non-calcium (VNCa) images using three-material decomposition is done automatically, on the CT console, a stand-alone workstation or a cloud-based software. Examples are given in Fig. 5. For gout images, some software applications have an option to eliminate certain artifacts, e.g., from beam hardening or toe nails, directly during the reconstruction process. This is especially important when measuring and reporting the total tophus volume. Whenever possible, iterative reconstruction or artificial intelligence reconstruction that reduces the image noise should be applied (Diekhoff et al. 2018).

When DECT is performed with contrast medium administration additional iodine maps will depict regions of soft tissue enhancement.

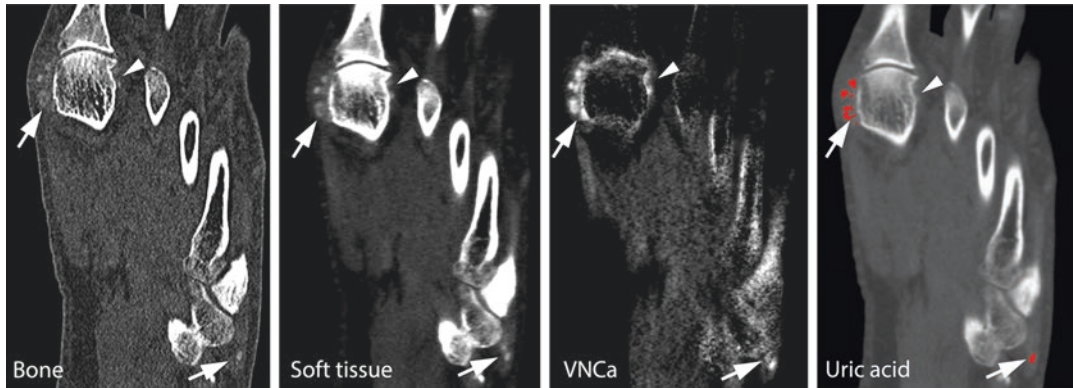


Fig. 5 Reconstructions from DECT. Bone kernel reconstruction depicts erosions and other bone pathologies. Soft tissue kernel reconstruction shows gouty tophi. VNCA reconstructions are used to search for bone marrow lesions and two-material decomposition uric acid images are used to identify gouty tophi. Note that tophi are less

well depicted in bone kernel reconstructions (arrow) compared to the other images. Tophi are not subtracted in VNCA images, occasionally resulting in their superior visualization compared to soft tissue or uric acid images (arrowheads)

3.6 Image Interpretation

The interpretation of color-coded images generated with the two-material decomposition algorithm, highlighting gouty tophi in green or red, is fairly straightforward (Huppertz et al. 2014). The unequivocal presence of tophi in a typical location confirms the diagnosis with high specificity (Choi et al. 2009). Nevertheless, especially small tophi should be confirmed in standard CT images and typical artifacts should be considered. Artifacts include physiological soft tissues with high density, e.g., toe nails or calluses at the heel, atherosclerotic plaques, or tiny calcifications (Choi et al. 2012; Christiansen et al. 2020). Beam hardening on the bone surface can also lead to false-positive detection. However, those are easy to identify and there are some robust software solutions for this problem. Very tiny tophi of only a few voxels in size within ligaments or menisci should not be overestimated.

Conventional CT reconstructions require careful attention. They contain the most information and are assessed for erosions and soft tissue depositions. Depending on the concentration of uric acid, gouty tophi can be visible in conventional CT images while they are not highlighted in gout images due to their low uric acid concen-

tration or secondary calcification (see Fig. 6) (Lee et al. 2019). Furthermore, morphology of the tophi is important and careful consideration can help to prevent false-positive findings (Ziegeler et al. 2020a). Especially in gout-negative cases, CT can confirm or rule out differential diagnoses such as osteoarthritis, calcium pyrophosphate deposition disease or septic arthritis.

VNCA images provide useful additional information. In case of severe inflammation, they delineate the underlying osteitis (Jans et al. 2018). When gout cannot be proven with DECT, the presence of bone marrow lesions can identify joints for further diagnostic examination such as arthrocentesis or ultrasonography. Notably, VNCA reconstructions do not subtract the gouty tophi so that they become even more conspicuous compared to standard CT images (see Fig. 5).

3.7 Report: What Information to Include

It is not easy to make recommendations on what a radiology report should contain as findings and structure have to consider the needs of the radiologist and referring physicians. However, there

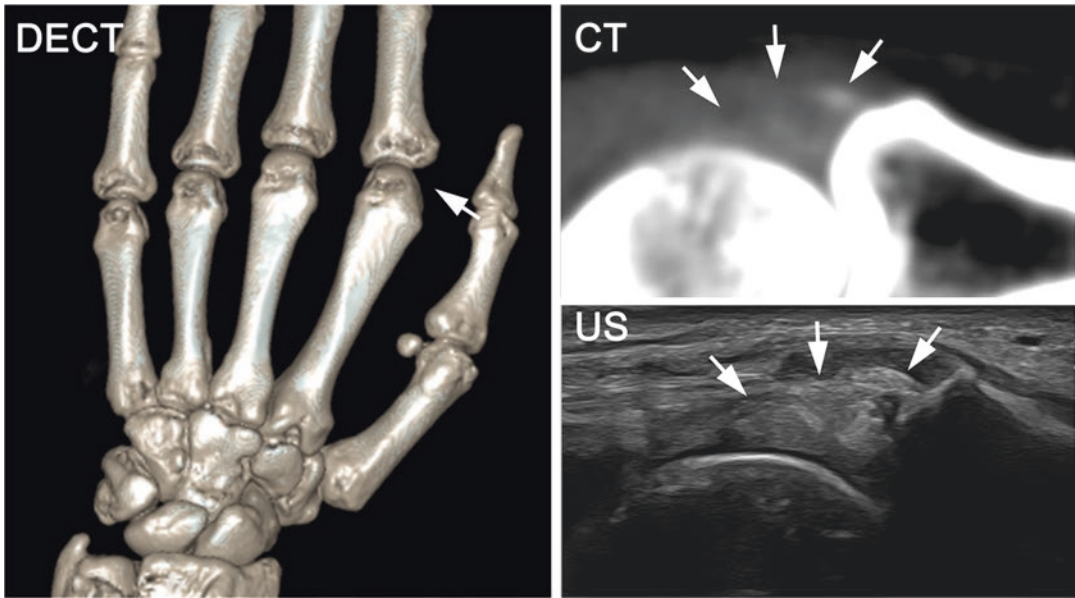


Fig. 6 False-negative tophus. A patient with suspected gouty arthritis shows no tophus after two-material decomposition in DECT. The conventional CT image (here

135 kVp source data) depicts faint uric acid depositions (arrows) that are confirmed by ultrasonography

is a certain minimum of information that should be provided. The report should state concisely and clearly whether the scan confirmed the suspected diagnosis of gouty arthritis by unequivocal depiction of uric acid depositions, is compatible with gout (i.e., changes are suggestive but tophus is not definitely confirmed), is normal or a differential diagnosis is more likely. The tophus volume is an important marker for the disease and the confidence of findings and should be included. Also worth mentioning are erosions and other arthritis findings as well as active inflammatory bone marrow lesions detected in VNCA reconstructions.

3.8 Issues Regarding Tophus Density and Radiation Exposure

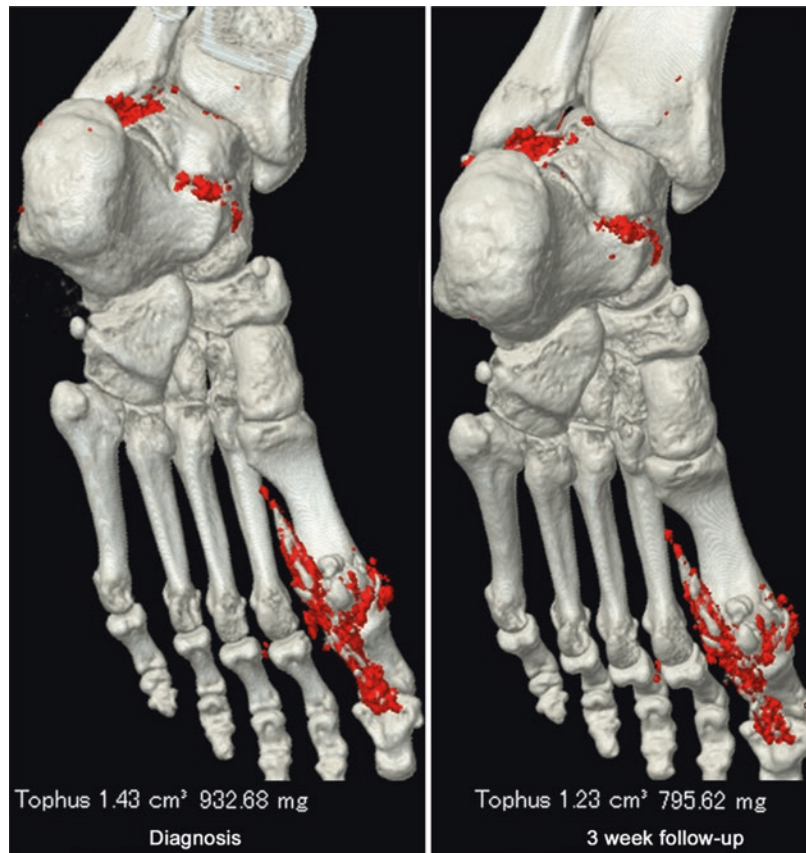
The analysis threshold selected for the two-material decomposition algorithm depends on the density of the soft tissues that might cause false-positive detections (e.g., tendons) and image noise. Therefore, the sensitivity of DECT for the

detection of gouty tophi and their volume will improve with increasing radiation exposure and the use of noise-reducing software and reconstructions. The lower the threshold, the lower the detectable concentrations of uric acid (see Fig. 3). With established DECT protocols currently in use, uric acid concentrations between 30% and 40% can be detected (Diekhoff et al. 2018).

3.9 DECT for Follow-Up

DECT offers the unique option to quantify tophus volume and, thus, the disease burden of a patient. This is not only helpful in assessing the severity of gout in an interindividual comparison but also allows intraindividual follow-up after initiation of dietary measures or treatment (see Fig. 7) (Sun et al. 2015). Interestingly, the development of tophi and recurrence under therapy is not well understood. For example, it has been reported that, while treatment induces tophus resorption, new tophi form on different joints or in different sites (Zhang et al. 2017). Also, measurement of uric acid volume might not fully capture the dis-

Fig. 7 Follow-up of a patient with gouty arthritis. A patient with gouty tophi underwent DECT for primary diagnosis before starting treatment. Three weeks later, he presented with worsening of pain and treatment failure was suspected. Whereas the three-dimensional reconstructions of the two scans do not show an unequivocal tophus reduction, the volume measurements and mass calculations confirm a treatment response. Treatment was continued and additional analgesics administered



ease burden as tophi might vary in uric acid concentration (Kotlyarov et al. 2020). Therefore, further advances in software development and clinical studies are needed before DECT can be recommended for regular follow-up in gout patients.

4 Case Discussions

4.1 Case 1: Patient with Acute Wrist Arthritis

A 70-year-old male patient presented to the emergency department with acute onset of severe wrist pain, redness, and swelling. MRI showed severe inflammation with synovitis, peritendonitis, and tenosynovitis of the wrist. In addition, some hypointense structures at the

triangular fibrocartilage complex were seen. Clinically, septic arthritis, acute pseudogout, and gout were possible differential diagnoses. DECT confirmed the presence of uric acid tophi, and a corresponding treatment was started. However, after 6 weeks, there was only mild resolution of symptoms. A follow-up DECT scan demonstrated an increase in uric acid depositions and a switch in medical treatment was indicated. The images are presented in Fig. 8.

Conclusion MRI often fails to demonstrate gouty tophi and cannot differentiate between uric acid and calcium pyrophosphate depositions. DECT is a noninvasive tool to establish the diagnosis and its quantitative measurements can be used for follow-up and monitoring the response to treatment.

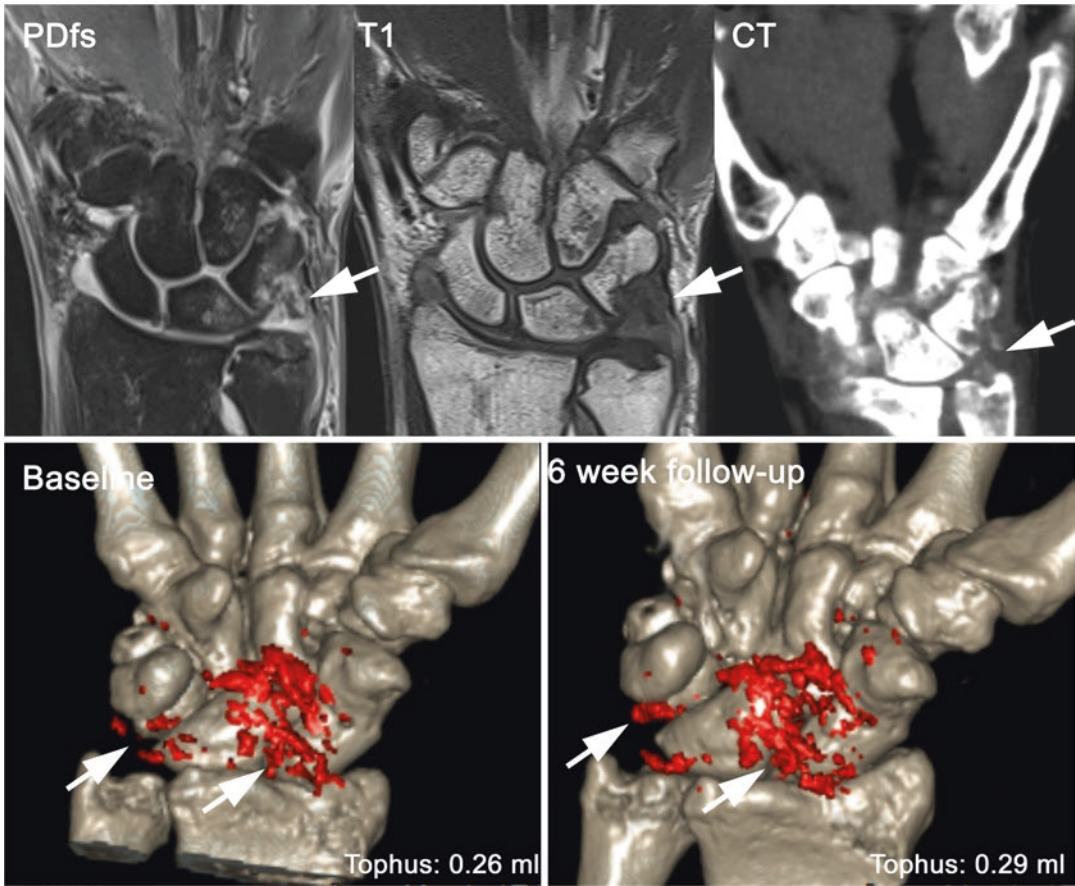


Fig. 8 70-year-old patient with wrist arthritis. MRI shows severe inflammation with synovitis of the wrist but misses the uric acid tophi (arrow). CT confirms the soft tissue depositions that are characterized as gout by two-

material decomposition (arrows). Follow-up demonstrates progression of the depositions (arrows) that was quantified by volumetric measurements. Also, other joints such as knee and ankles showed a progress of tophi

4.2 Case 2: Chronic Pain of the Feet

An 82-year-old female patient suffered from occasional pain at the hands and feet that had persisted for several years. Her family physician suspected gouty arthritis and treated correspondingly. As she still suffered several episodes of mild to moderate pain every year despite drug treatment and diet, she presented to a rheumatologist. The DECT scan shows no uric acid depositions besides a typical toe nail artifact. However, the standard CT reconstructions prove erosions on the first metatarsal head with sclerotic rims and overhanging edges, typical of gouty arthritis. Images are shown in Fig. 9.

Conclusion Standard CT images are important to establish the diagnosis in the absence of uric acid depositions. They display structural lesions and gouty tophi that do not reach the threshold in two-material decomposition.

4.3 Case 3: Pain of the First MTP Joint

A 41-year-old male patient presents in the outpatient rheumatology clinic with redness and swelling of the first metatarsophalangeal joint on the left side. He reports a one-year history with several episodes of mild to moderate pain with exacerbation a few days before presentation. He had



Fig. 9 Gouty arthritis without tophi. In this chronic case of gouty arthritis, standard CT reconstructions in bone kernel show typical erosions (arrow) at the first metatarsal

head. However, two-material decomposition fails to demonstrate tophi. A false-positive toe nail artifact is present (arrowhead)

no history of joint disease and was otherwise healthy as well.

Radiography was already performed by the referring physician and fairly unremarkable. The rheumatologist suspected gouty arthritis; however, the diagnostic criteria were not fulfilled and further proof was needed to establish the diagnosis. Therefore, a DECT scan was ordered.

DECT did not show any tophus formation, and the CT source images were unremarkable. However, VNCA images showed acute bone marrow lesions (osteitis) of the first metatarsophalangeal joint, indicating severe inflammation. Hence, an additional arthrosonography was performed, which confirmed synovitis and gouty arthritis by showing a double-contour sign. The images are presented in Fig. 10.

Conclusion DECT may fail to demonstrate uric acid depositions in very early gouty arthritis. However, it provides crucial information on active inflammation, even when performed without contrast medium. Therefore, it can pave the way to further diagnostic tests or suggest other possible differential diagnoses.

4.4 Case 4: Patient with Knee Pain

A 52-year-old construction worker was referred to undergo an MRI examination for severe knee pain. He had complaints for several years but was not able to schedule an appointment because he was traveling to construction sites. MRI showed inflammatory arthritis with soft tissue depositions, highly suggestive of severe gouty arthritis. A DECT scan



Fig. 10 41-year-old patient with pain. DECT and CT do not show any uric acid deposition. VNCa reconstructions from the DECT scan, however, reveal active inflammation on the first MTP joint (arrows) when compared to the con-

tralateral side. The diagnosis of gouty arthritis was later confirmed by ultrasonography (US) with demonstration of active synovitis (arrowheads) and a double-contour sign (arrow)

was obtained and demonstrated gouty tophi at knees, feet, ankles, and elbows (see Fig. 11). The DECT scan was completed in less than 15 minutes with a total radiation exposure of less than 1 mSv and gave an easy overview of the disease burden.

Conclusion In severe cases, DECT is not needed to establish the diagnosis. However, it confirms uric acid tophi with high specificity, gives an excellent overview of the disease burden, and is faster than other imaging methods.

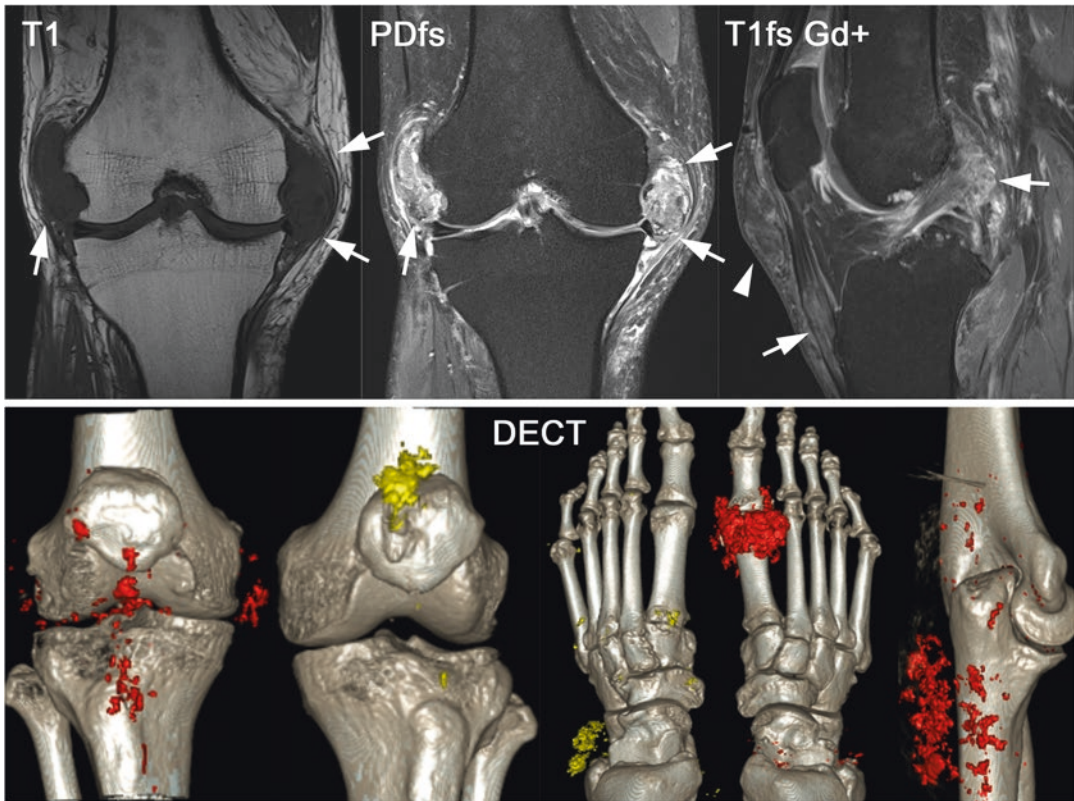


Fig. 11 Severe gouty arthritis. MRI already shows soft tissue depositions, consistent with advanced gouty arthritis. While DECT was not needed to establish the diagnosis

in this patient, it provided an excellent overview of the total disease burden. Here, the software color-codes left and right side differently

4.5 Case 5: Patient with Rheumatoid Arthritis

A 52-year-old physician treated himself for several years for rheumatoid arthritis. For some time, he sensed several rheumatic nodes on both elbows that worsened over the last months. A rheumatologist to whom he finally presented ordered a DECT scan. While several joints

showed unequivocal tophi, the bursa olecrani was filled with calcified and uric-acid-positive structures (see Fig. 12). Surgery confirmed the presence of severe gouty arthritis.

Conclusion Calcified tophi might be misclassified by DECT. In those cases, DECT can be false-negative and underestimate the total amount of uric acid.

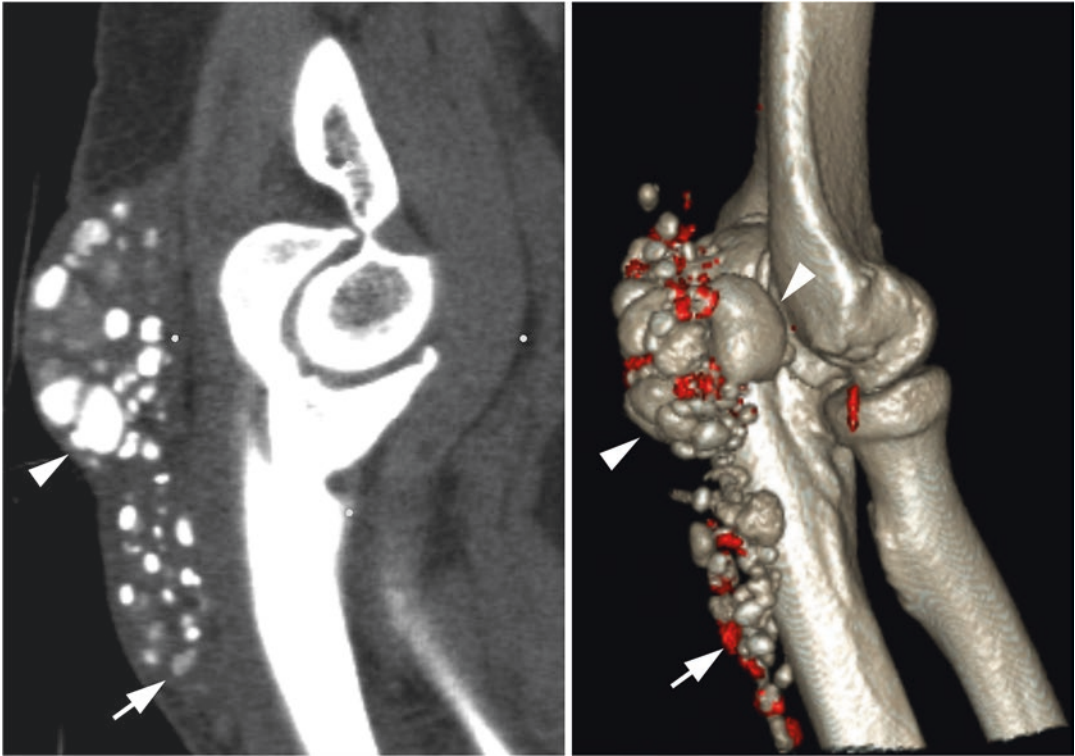


Fig. 12 Calcified gouty tophi within a bursa. Only the faint characteristic tophi (arrows) are correctly characterized. The more dense, calcified tophi are false-negative (arrowheads)

5 Summary

DECT is a robust, sensitive, and specific tool to assess gouty arthritis and its differential diagnoses. When used correctly and with consideration of artifacts and possible false-positive and false-negative findings, it can establish the diagnosis, elucidate differential diagnoses, and monitor treatment. The field of DECT in gouty arthritis has undergone some changes during the last years. While previously only color-coded uric acid tophi were considered to be relevant, more recently, grayscale conventional CT images and VNCA reconstructions have found their way into clinical practice. Furthermore, the benefit of contrast medium administration is currently being investigated and may be useful in identifying soft tissue inflammation. Providing a multiparametric overview in patients with suspected gouty arthri-

tis, DECT has earned its prominent place in current rheumatology guidelines.

Compliance with Ethical Standards

Funding not applicable.

Disclosure of Interests The author has received a speaker honorarium from Canon Medical Systems, Novartis and MSD. The author's institution received research grants from Canon Medical Systems.

References

- Bongartz T, Glazebrook KN, Kavros SJ, Murthy NS, Merry SP, Franz WB 3rd, Michet CJ, Veetil BM, Davis JM 3rd, Mason TG 2nd, Warrington KJ, Ytterberg SR, Matteson EL, Crowson CS, Leng S, McCollough CH (2015) Dual-energy CT for the diagnosis of gout: an accuracy and diagnostic yield study. *Ann Rheum Dis* 74(6):1072–1077

- Buckley TJ (1996) Radiologic features of gout. *Am Fam Physician* 54(4):1232–1238
- Campion EW, Glynn RJ, DeLabry LO (1987) Asymptomatic hyperuricemia. Risks and consequences in the Normative Aging Study. *Am J Med* 82(3):421–426
- Choi HK, Curhan G (2008) Soft drinks, fructose consumption, and the risk of gout in men: prospective cohort study. *BMJ* 336(7639):309–312
- Choi HK, Atkinson K, Karlson EW, Willett W, Curhan G (2004a) Alcohol intake and risk of incident gout in men: a prospective study. *Lancet* 363(9417):1277–1281
- Choi HK, Atkinson K, Karlson EW, Willett W, Curhan G (2004b) Purine-rich foods, dairy and protein intake, and the risk of gout in men. *N Engl J Med* 350(11):1093–1103
- Choi HK, Al-Arfaj AM, Eftekhari A, Munk PL, Shojania K, Reid G, Nicolaou S (2009) Dual energy computed tomography in tophaceous gout. *Ann Rheum Dis* 68(10):1609–1612
- Choi HK, Burns LC, Shojania K, Koenig N, Reid G, Abufayyah M, Law G, Kydd AS, Ouellette H, Nicolaou S (2012) Dual energy CT in gout: a prospective validation study. *Ann Rheum Dis* 71(9):1466–1471
- Chowalloor PV, Keen HI (2013) A systematic review of ultrasonography in gout and asymptomatic hyperuricaemia. *Ann Rheum Dis* 72(5):638–645
- Christiansen SN, Müller FC, Østergaard M, Slot O, Møller JM, Børgesen HF, Gosvig KK, Terslev L (2020) Dual-energy CT in gout patients: do all colour-coded lesions actually represent monosodium urate crystals? *Arthritis Res Ther* 22(1):212
- Cimmino MA, Zampogna G, Parodi M, Andracco R, Barbieri F, Paparo F, Ferrero G, Garlaschi G (2011) MRI synovitis and bone lesions are common in acute gouty arthritis of the wrist even during the first attack. *Ann Rheum Dis* 70(12):2238–2239
- Dalbeth N, Stamp L (2014) Hyperuricaemia and gout: time for a new staging system? *Ann Rheum Dis* 73(9):1598–1600
- Diekhoff T, Kiefer T, Stroux A, Pilhofer I, Juran R, Mews J, Blobel J, Tsuyuki M, Ackermann B, Hamm B, Hermann KG (2015) Detection and characterization of crystal suspensions using single-source dual-energy computed tomography: a phantom model of crystal arthropathies. *Investig Radiol* 50(4):255–260
- Diekhoff T, Kotlyarov M, Mews J, Hamm B, Hermann KGA (2018) Iterative reconstruction may improve diagnosis of gout: an ex vivo (bio)phantom dual-energy computed tomography study. *Investig Radiol* 53(1):6–12
- Diekhoff T, Ulas ST, Poddubnyy D, Schneider U, Hermann S, Biesen R, Burmester GR, Hamm B, Hermann KG (2019) Ultra-low-dose CT detects synovitis in patients with suspected rheumatoid arthritis. *Ann Rheum Dis* 78(1):31–35
- Fukuda T, Umezawa Y, Asahina A, Nakagawa H, Furuya K, Fukuda K (2017) Dual energy CT iodine map for delineating inflammation of inflammatory arthritis. *Eur Radiol* 27(12):5034–5040
- Gibney B, Murray N (2020) Dual-energy CT of spinal tophaceous gout. *Radiology* 296(2):276
- Grassi W, Farina A, Filippucci E, Cervini C (2001) Sonographically guided procedures in rheumatology. *Semin Arthritis Rheum* 30(5):347–353
- Huppertz A, Hermann KG, Diekhoff T, Wagner M, Hamm B, Schmidt WA (2014) Systemic staging for urate crystal deposits with dual-energy CT and ultrasound in patients with suspected gout. *Rheumatol Int* 34(6):763–771
- Jans L, De Kock I, Herregods N, Verstraete K, Van den Bosch F, Carron P, Oei EH, Elewaut D, Jacques P (2018) Dual-energy CT: a new imaging modality for bone marrow oedema in rheumatoid arthritis. *Ann Rheum Dis* 77(6):958–960
- Kotlyarov M, Hermann KGA, Mews J, Hamm B, Diekhoff T (2020) Development and validation of a quantitative method for estimation of the urate burden in patients with gouty arthritis using dual-energy computed tomography. *Eur Radiol* 30(1):404–412
- Kuo CF, Grainge MJ, Zhang W, Doherty M (2015) Global epidemiology of gout: prevalence, incidence and risk factors. *Nat Rev Rheumatol* 11(11):649–662
- Lee SK, Jung JY, Jee WH, Lee JJ, Park SH (2019) Combining non-contrast and dual-energy CT improves diagnosis of early gout. *Eur Radiol* 29(3):1267–1275
- Neogi T, Jansen TL, Dalbeth N, Fransen J, Schumacher HR, Berendsen D, Brown M, Choi H, Edwards NL, Janssens HJ, Liote F, Naden RP, Nuki G, Ogdie A, Perez-Ruiz F, Saag K, Singh JA, Sundy JS, Tausche AK, Vaquez-Mellado J, Yarows SA, Taylor WJ (2015) 2015 Gout classification criteria: an American College of Rheumatology/European League Against Rheumatism collaborative initiative. *Ann Rheum Dis* 74(10):1789–1798
- Notzel A, Hermann KG, Feist E, Kedor C, Ziegeler K, Stroux A, Mews J, Schnorfeil M, Hamm B, Diekhoff T (2018) Diagnostic accuracy of dual-energy computed tomography and joint aspiration: a prospective study in patients with suspected gouty arthritis. *Clin Exp Rheumatol* 36(6):1061–1067
- Parathithasan N, Lee WK, Pianta M, Oon S, Perera W (2016) Gouty arthropathy: review of clinicopathologic and imaging features. *J Med Imaging Radiat Oncol* 60(1):9–20
- Phelps P, McCarty DJ Jr (1966) Crystal-induced inflammation in canine joints. II. Importance of polymorphonuclear leukocytes. *J Exp Med* 124(1):115–126
- Ramon A, Bohm-Sigand A, Pottecher P, Richette P, Maillefert JF, Devilliers H, Ornetti P (2018) Role of dual-energy CT in the diagnosis and follow-up of gout: systematic analysis of the literature. *Clin Rheumatol* 37(3):587–595
- Rothschild BM, Tanke D, Carpenter K (1997) Tyrannosaurs suffered from gout. *Nature* 387(6631):357–357
- Rymal E, Rizzolo D (2014) Gout: a comprehensive review. *Jaapa* 27(9):26–31

- Schett G, Schauer C, Hoffmann M, Herrmann M (2015) Why does the gout attack stop? A roadmap for the immune pathogenesis of gout. *RMD Open* 1(Suppl 1):e000046
- Schumacher HR Jr, Becker MA, Edwards NL, Palmer WE, MacDonald PA, Palo W, Joseph-Ridge N (2006) Magnetic resonance imaging in the quantitative assessment of gouty tophi. *Int J Clin Pract* 60(4):408–414
- Shang J, Zhou LP, Wang H, Liu B (2020) Diagnostic performance of dual-energy CT versus ultrasonography in gout: a meta-analysis. *Acad Radiol* 29(1):56–68
- Sun Y, Chen H, Zhang Z, Ma L, Zhou J, Zhou Y, Ding Y, Jin X, Jiang L (2015) Dual-energy computed tomography for monitoring the effect of urate-lowering therapy in gouty arthritis. *Int J Rheum Dis* 18(8):880–885
- Taylor WJ, Fransen J, Dalbeth N, Neogi T, Ralph Schumacher H, Brown M, Louthrenoo W, Vazquez-Mellado J, Eliseev M, McCarthy G, Stamp LK, Perez-Ruiz F, Sivera F, Ea HK, Gerritsen M, Scire CA, Cavagna L, Lin C, Chou YY, Tausche AK, da Rocha Castelar-Pinheiro G, Janssen M, Chen JH, Slot O, Cimmino M, Uhlig T, Jansen TL (2016) Diagnostic arthrocentesis for suspicion of gout is safe and well tolerated. *J Rheumatol* 43(1):150–153
- Thiele RG, Schlesinger N (2007) Diagnosis of gout by ultrasound. *Rheumatology (Oxford)* 46(7):1116–1121
- Ulas ST, Diekhoff T, Hermann KGA, Poddubnyy D, Hamm B, Makowski MR (2019) Susceptibility-weighted MR imaging to improve the specificity of erosion detection: a prospective feasibility study in hand arthritis. *Skelet Radiol* 48(5):721–728
- Underwood M (2006) Diagnosis and management of gout. *BMJ* 332(7553):1315–1319
- Wang P, Smith SE, Garg R, Lu F, Wohlfahrt A, Campos A, Vanni K, Yu Z, Solomon DH, Kim SC (2018) Identification of monosodium urate crystal deposits in patients with asymptomatic hyperuricemia using dual-energy CT. *RMD Open* 4(1):e000593
- Wright JD, Pinto AB (2003) Clinical manifestations and treatment of gout. *Prim Care Update OB/GYNS* 10:19–23
- Zhang Z, Zhang X, Sun Y, Chen H, Kong X, Zhou J, Zhou Y, Ma L, Jiang L (2017) New urate depositions on dual-energy computed tomography in gouty arthritis during urate-lowering therapy. *Rheumatol Int* 37(8):1365–1372
- Zhu Y, Pandya BJ, Choi HK (2011) Prevalence of gout and hyperuricemia in the US general population: the National Health and Nutrition Examination Survey 2007–2008. *Arthritis Rheum* 63(10):3136–3141
- Zhu Y, Pandya BJ, Choi HK (2012) Comorbidities of gout and hyperuricemia in the US general population: NHANES 2007–2008. *Am J Med* 125(7):679–687.e1
- Ziegeler K, Hermann S, Hermann KGA, Hamm B, Diekhoff T (2020a) Dual-energy CT in the differentiation of crystal depositions of the wrist: does it have added value? *Skelet Radiol* 49(5):707–713
- Ziegeler K, Eshed I, Diekhoff T, Hermann KG (2020b) Imaging of joints and bones in autoinflammation. *J Clin Med* 9(12):4074



Dual-Energy CT in Radiation Oncology

Christian Richter and Patrick Wohlfahrt

Contents

1	Introduction: Dual-Energy CT in Radiotherapy: From First Idea to Clinical Application	334
2	Dual-Energy CT Techniques in Radiation Oncology	335
2.1	Spectral Separation	335
2.2	Temporal Coherence	336
2.3	Spatio-Temporal Resolution	336
2.4	Cross-Scattering	337
2.5	Imaging Dose	337
2.6	Field of View	337
2.7	Respiratory	337
3	Tumor and Organ Segmentation	337
4	Treatment Planning and Dose Calculation	338
4.1	Photon Therapy	341
4.2	Proton Therapy	341
5	Potential of Photon-Counting CT in Radiation Oncology	343
6	Conclusion	345
	References	345

C. Richter (✉)

OncoRay – National Center for Radiation Research in Oncology, Faculty of Medicine and University Hospital Carl Gustav Carus, Technische Universität Dresden, Helmholtz-Zentrum Dresden - Rossendorf, Dresden, Germany

Helmholtz-Zentrum Dresden - Rossendorf, Institute of Radiooncology - OncoRay, Dresden, Germany

Department of Radiotherapy and Radiation Oncology, Faculty of Medicine and University Hospital Carl Gustav Carus, Technische Universität Dresden, Dresden, Germany
e-mail: christian.richter@oncoray.de

P. Wohlfahrt

OncoRay – National Center for Radiation Research in Oncology, Faculty of Medicine and University Hospital Carl Gustav Carus, Technische Universität Dresden, Helmholtz-Zentrum Dresden - Rossendorf, Dresden, Germany

Massachusetts General Hospital and Harvard Medical School, Department of Radiation Oncology, Boston, MA, USA

Now with Siemens Healthineers, Forchheim, Germany

Abstract

In radiation oncology, CT imaging is of crucial importance for consistent and accurate delineation of target and organ-at-risk structures as well as for highly precise treatment planning and prediction of the deposited dose. Even though the potential benefit of dual-energy CT for those purposes was identified early, its implementation in clinical practice is still in an early stage. Here, we want to give an overview of current and potential future applications of dual-energy CT in the field of radiation oncology. Since the next generation of X-ray computed tomography with a photon-counting detector technology is rising at the horizon, we also want to give an outlook on radiotherapeutic applications that will benefit or even become possible for the first time with this technological evolution.

1 Introduction: Dual-Energy CT in Radiotherapy: From First Idea to Clinical Application

Nowadays, radiotherapy is an important treatment technique in oncology, being applied either alone or together with surgery or chemotherapy in about every second cancer patient (Borras et al. 2015). In most cases, high-energy external photon beams of several Megavolt (MV) are used to locally maximize the dose deposition to the target while at the same time minimizing the damage of the surrounding normal tissue (Baumann et al. 2016). Alternatively, beams of high-energetic particles, mostly protons but also carbon ions, are used. In general, particle beams lead to a better dose sparing of normal tissue due their well-defined maximum of dose deposition shortly before stopping in the patient. In contrast to photons, they possess no or negligible dose deposition “behind” the tumor target.

In both photon and proton therapy, an accurate prediction of interactions of the therapeutic beam with patients’ tissue and thereby precisely planning

of the dose deposition in the target and normal tissue is crucial. For this purpose, X-ray computed tomography (CT) is the common imaging technique in external beam radiotherapy. However, CT is not only used for predicting the physical dose deposition but is needed for several tasks in the radiotherapeutic treatment chain. The clinical workflow in radiation oncology (RO) relies on a well-coordinated interaction of a multitude of processes guided by imaging: Therapy decision before and adaptation during the course of treatment, organ and tumor segmentation, treatment planning, and dose calculation as well as patient immobilization and motion handling. Dual- or multi-energy CT offers potential benefits compared to classical single-energy CT (SECT) in general but also specifically for the individual tasks which have different requirements on CT imaging.

The idea of the application of dual-energy CT in radiotherapy is anything but new. In his epoch-breaking publication introducing the first clinical X-ray CT scanner in 1973 (Hounsfield 1973), Godfrey Hounsfield not only introduced the basic idea of dual-energy CT (DECT) by using two CT scans with different tube voltages, but he also mentioned its potential use for improved tissue characterization, especially the effective atomic number. Only 4 years later, Michael Goitein, a Boston-based pioneer of the translation of proton therapy in clinical application saw its potential for improved treatment planning in proton therapy (Goitein 1977).

Due to the different relative contributions of photoelectric effect and incoherent/coherent scattering, the two CT scans contain partly complementary attenuation information of tissues. The basic idea is that two different quantities can be obtained from two CT scans with different ratio of the two main interaction processes of kilovoltage (kV) X-rays. Such tissue parameters are typically the relative electron density (RED) and effective atomic number (EAN), which characterize the photoelectric effect and incoherent/coherent scattering. Especially in proton or particle therapy, exact knowledge of tissue parameters is crucial to accurately predict the particles stopping behavior and thereby the dose deposition. As the stopping behavior and dose deposition are extremely sensi-

tive to the traversed tissue, the application of DECT in particle therapy seems utmost promising already since the very beginning of CT imaging. Despite these clear conceptual benefits, it took until 2015 as DECT was first used for clinical treatment planning in proton therapy (Wohlfahrt et al. 2017) probably due to the lack of practical hardware and software solutions in the decades before and challenges in data processing, e.g. its increased noise level.

Although the main motivation for deploying DECT in radiation oncology is currently the improvement of proton treatment planning (Paganetti et al. 2020; Wohlfahrt and Richter 2020), several other potential use cases are discussed and investigated including (van Elmpt et al. 2016):

- Improvements in tumor and organ segmentation;
- Direct calculation of relative electron density for photon treatment planning;
- Tissue classification, e.g. as input for Monte Carlo transport calculations;
- Improvement of image quality including metal artifact reduction and variable image contrast;
- Virtual subtraction of contrast agent information to generate a virtual non-contrast and contrast-enhanced dataset from only one single DECT scan;
- Functional imaging.

In the following, we want to give an overview on these different applications in radiation oncology and also evaluate the different DECT techniques for RO-specific applications. Furthermore, the potential benefit of RO applications from photon-counting CT technology will be illuminated.

2 Dual-Energy CT Techniques in Radiation Oncology

The various clinically available DECT acquisition techniques enabled by single-source CT scanners:

- consecutive (dual-spiral mode) (Chap. 3),
- split-beam filter in scan direction (twin-beam mode) (Chap. 3),
- dual-layer detector (dual-layer mode) (Chap. 4),
- fast tube-voltage switching (fast-kVp mode) (Chap. 5),
- slow tube-voltage switching (slow-kVp mode) (Chap. 6).

and dual-source CT scanners (Chap. 3) open up new possibilities to reduce uncertainties in the overall radiotherapeutic chain. However, they also add a new layer of complexity in the decision process which CT equipment might be best suited for the type and range of clinical applications used preferably in the respective radiotherapy institution. Hence, an individual optimization of CT scan and reconstruction settings together with a careful weighing of technical benefits and limitations of each method are essential. To reliably obtain accurate and precise quantitative measures from DECT, the overall image quality is an important prerequisite for material decomposition, because even small differences between CT numbers in the low- and high-energy CT dataset can be amplified in the highly sensitive post-processing algorithms. The following technical criteria are distinctive features of the various DECT acquisition techniques, which considerably influence the DECT image quality and thus affecting the performance of clinical tasks from delineation to treatment planning and adaptive dose delivery.

2.1 Spectral Separation

The overlap of the low- and high-energy X-ray spectrum characterizes the gain of independent attenuation information for material differentiation. No spectral overlap would be ideal, because fully disjunct material attenuation properties are gathered. In general, a high spectral separation facilitates accurate and precise material decomposition and can better tolerate image noise. It also defines the capability to reliably classify two materials with only a slightly

different spectral attenuation behavior, e.g. low iodine concentrations in contrast-enhanced DECT scans.

DECT acquisition techniques with independent adjustment of their X-ray tube configurations (dual-source, dual-spiral, slow-kVp) achieve a high spectral separation by selecting the lowest and highest available tube voltage. The spectral overlap can be further decreased by adding an extra filter material for the high-energy CT scan (dual-source, dual-spiral). Since a perfect voltage modulation following a rectangular function is technically challenging in fast-kVp mode, the original X-ray spectra are partly mixed in the transition period resulting in a reduced spectral separation. The use of a single tube voltage with two different filters in scan direction (twin-beam) or an energy discrimination at detector level (dual-layer) also show an inferior spectral separation (McCullough et al. 2020).

A quantitative determination of material parameters required for dose calculation (electron density and stopping power) or tumor delineation in low-contrast regions (concentration contrast agent) benefit from an increase in spectral separation. The assessment whether a spectral separation is sufficient depends on the purpose of the respective clinical task as well as the targeted accuracy and precision.

2.2 Temporal Coherence

A short or ideally no time interval between acquisitions of low- and high-energy X-ray attenuations ensures a temporal coherence of the DECT data collection. It reduces the impact of motion-induced anatomical changes or varying concentrations and tissue distributions of contrast agents over time. This is a crucial prerequisite to enable projection-based algorithms for material decomposition and advanced physical corrections, e.g. of beam hardening, based on spectral X-ray information.

DECT in dual-layer mode has an almost perfect temporal coherence. A high temporal coherence is also guaranteed by fast voltage alteration within 0.5 ms (fast-kVp) or simulta-

neous acquisition of DECT projections with 90° offset (dual-source), however, resulting in a temporal shift of at least 66 ms (quarter of rotation time). The time offset in twin-beam and slow-kVp mode is at least one rotation time. Due to an additional time delay for tube adjustments in slow-kVp mode, the temporal coherence is further reduced. The lowest temporal coherence is present in dual-spiral mode, because the consecutive high-energy CT scan is delayed by the scan time as well as additional time lags for tube adjustment and potential couch movements. Despite that deformable image registration can reduce the impact of anatomical changes, the dual-spiral mode is currently recommended for static tumors only. Contrast-enhanced dual-spiral DECT scans are restricted to late phase with an almost stable distribution of contrast agent.

A high temporal coherence ensures accurate DECT-based material differentiation in non-static imaging situations. A stable patient immobilization or breath-hold techniques can further help to mitigate body motion.

2.3 Spatio-Temporal Resolution

The temporal resolution is characterized by half of the rotation time and thus depends on the respective CT scanner capabilities in general.

The spatial resolution is mainly influenced by focal spot size, slice collimation, and number of X-ray projections. All DECT modes except for fast-kVp can exploit the full CT scanner capabilities. In fast-kVp mode, a large focal spot is used and the projections per rotation need to be divided in a ratio of 65:35 to increase exposure times for low-energy projections, because the tube current cannot be changed so fast. Due to the reduced number of projections per energy, the spatial resolution is deteriorated.

A high spatio-temporal resolution is intended at tissue transitions with high density gradients to prevent edge blurring, which can lead to a potential loss of attenuation information and thus deviations in quantitative results relevant for dose calculation.

2.4 Cross-Scattering

An impact of cross-scatter radiation on the detector signal is present in dual-source and dual-layer mode and can be partly mitigated in post-processing algorithms. An insufficient correction could result in a systematic bias in the assessment of material parameters.

2.5 Imaging Dose

DECT can be performed with the same total dose as required for SECT while enabling more post-scan flexibility without compromising image quality (Wohlfahrt et al. 2017). Standard CT dose reduction techniques, such as tube current modulation, can be also applied in all DECT modes except for fast-kVp due to limitations in current tube technology. In dual-layer mode, the noise ratio between low- and high-energy CT data directly follows from the design of the two detector layers and is thus optimized for specific scan conditions.

Imaging dose becomes even more important in an adaptive radiotherapy workflow relying on continuous quantitative CT imaging during the course of treatment for an early detection of anatomical changes and tumor response assessment. With the use of iterative image reconstruction, the image noise can be clearly reduced to still guarantee a good performance of material characterization at lower CT doses.

2.6 Field of View

All DECT modes except for dual-source acquire DECT information in a scan field of view of at least 500 mm. The DECT field of view in dual-source mode is restricted to maximal 350 mm due to limitations in detector space within the CT gantry. This currently hampers the use for treatment planning in the thoracic, abdominal, or pelvic region and a proper coverage of immobilization devices.

2.7 Respiratory

A time-resolved (4D) respiratory acquisition is not yet available in clinical routine for the recent DECT techniques. Only stable respiratory phases realized by a breath-hold approach can be considered. In first proof-of-concept studies, the clinical feasibility of 4D DECT has been demonstrated (Ohira et al. 2018; Wohlfahrt et al. 2018), however, confirmation for a broad variety of motion amplitudes and frequencies is desired.

The image quality of DECT acquisitions depends on a multitude of technical parameters and needs to be optimized for the various processes in the complex radiotherapeutic workflow. Clinical applications in radiation oncology desire

- a highly accurate and precise calculation of quantitative material parameters for dose calculation enabled by a good spectral separation,
- a large scan field of view to cover the entire patient and all necessary immobilization devices,
- a time-resolved respiratory CT acquisition for moving targets to estimate tumor motion as well as optimize the treatment plan and dose delivery,
- lowering the dose for CT acquisitions during the course of treatment to still ensure an image quality for a reliable assessment of material parameters.

However, since none of the recent techniques can fully satisfy all requirements, more exploratory clinical studies are needed to generate evidence under clinical conditions and balance pros and cons of the respective techniques.

3 Tumor and Organ Segmentation

The main aim of segmentation in radiation oncology is a reliable delineation of the clinical target volume, encompassing the tumor region with an

additional clinical safety margin covering microscopic tumor spread and tumor motility, as well as surrounding organs at risk as input for the patient-specific treatment planning process.

The benefits of DECT associated with an improved tissue differentiation are commonly employed in diagnostic oncological imaging to increase diagnostic efficiency and efficacy (Agrawal et al. 2014). Typically, various datasets with different image contrasts are generated from DECT after acquisition and then jointly used to improve tumor visibility and thus detectability (Forghani and Mukherji 2018). Depending on the selected energy of DECT-derived virtual monoenergetic image (VMI) datasets, the soft tissue contrast and tissue enhancement of contrast agents (low energy from 40 to 60 keV) can be increased or metal artifacts (high energy from 120 to 200 keV) can be reduced (Fig. 1). The distribution and tissue enrichment of contrast medium obtained by a DECT-based material decomposition is an additional indicator to differentiate between tumor invasion and ossification. A reliable quantification of contrast medium in anatomical structures and tumors could potentially even serve as biomarker for an early assessment of therapy response (Fukukura et al. 2020).

Based on the clinical experience and evidence gathered in diagnostic radiology within the last two decades and the gradual implementation of DECT in radiation oncology, the above-mentioned DECT applications also seem to be promising for radiotherapeutic purposes. Their integration in the radiotherapeutic workflow enables an individual assessment of the optimal usage and potential benefit for tumor and organ segmentation. The number of clinical studies in radiation oncology is still scarce, which demonstrate that an increased tissue contrast or a combination of image representations of different tissue characteristics can translate into an improved delineation accuracy and reduced intra- and inter-observer variability (Wohlfahrt et al. 2018; Wohlfahrt et al. 2019). A multitude of exploratory studies are needed in future to comprehensively evaluate the clinical usability for different tumor entities and tumor stages as well as elaborate on potential improvements for radiation

oncology. Joint efforts in collaborative trials between diagnostic radiology and radiation oncology could be worth aspiring to generate evidence in patient cohorts monitored in a standardized approach covering diagnosis, therapy preparation, course of treatment, and follow-up. This can contribute to encourage a more widespread routine use of DECT for tumor and organ segmentation in radiation oncology.

In addition to an anatomical representation of the patient, functional information of organs can be considered as an important input for treatment planning and foster its individualization by incorporating information on the patient's condition. In active and well-functioning regions within organs, the dose could be proactively reduced. Such areas with the potential of dose sparing cannot only be identified with magnetic resonance imaging (MRI) or positron-emission tomography (PET), but also with the help of DECT. For example, the distribution of active bone marrow can be derived from a native DECT scan (McGuire et al. 2011) and the lung function can be obtained from the iodine distribution of a contrast-enhanced DECT scan (Bahig et al. 2017).

4 Treatment Planning and Dose Calculation

With the input of tumor and normal tissue segmentation, as well as case-specific dose prescriptions to the target and organ-specific tolerance doses for healthy tissues according to clinical guidelines, the dose distribution is optimized in a multi-step process to achieve a homogeneous distribution of the prescribed dose in the target volume while minimizing the dose to critical healthy anatomical structures. This optimization process aims at reaching a high tumor control while at the same time minimizing radiation-induced toxicities in healthy tissues. The calculation of the physical dose deposition based on the individual anatomy and tissue properties as well as the setup of the radiation beam is a core element in this process. For this purpose, the voxelwise image information from CT and in some cases

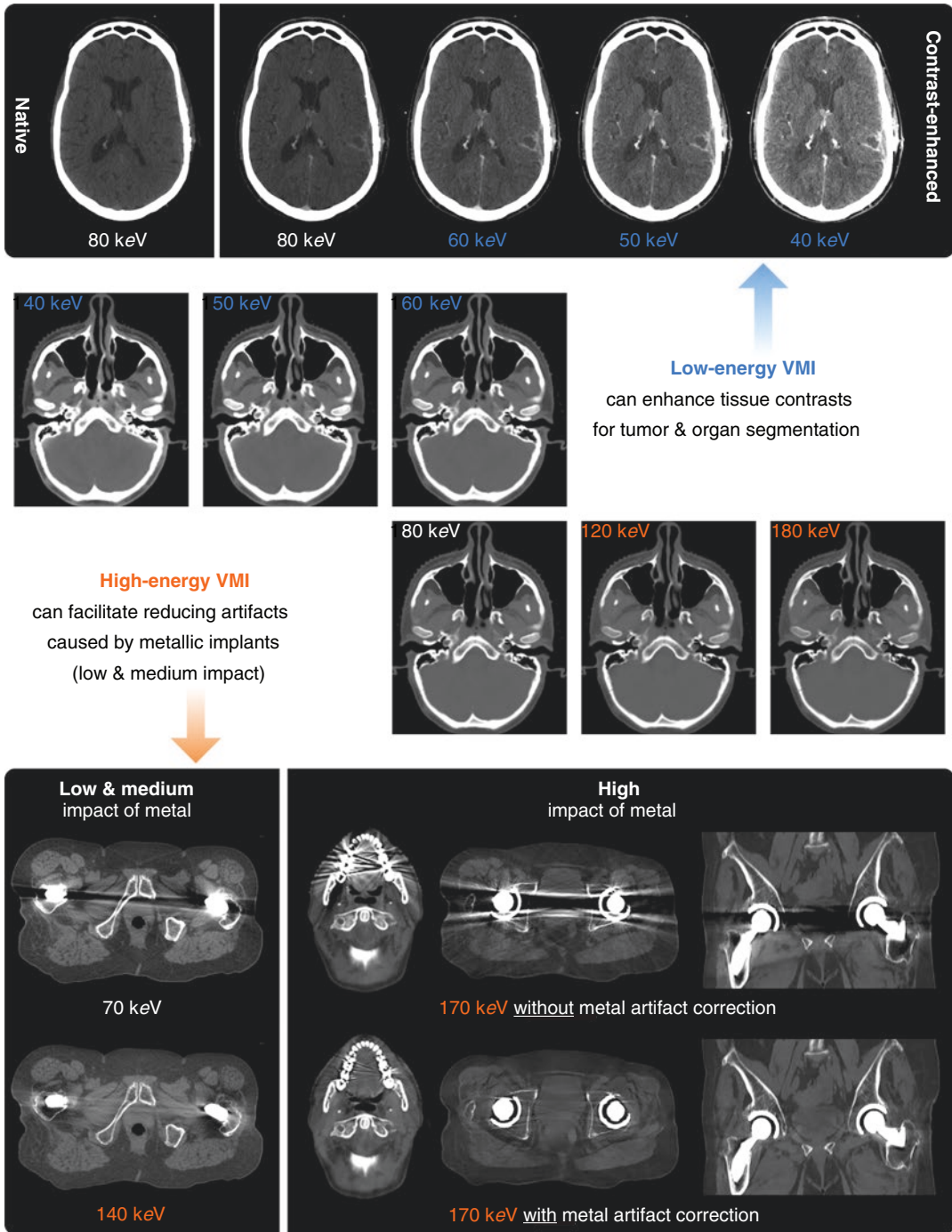
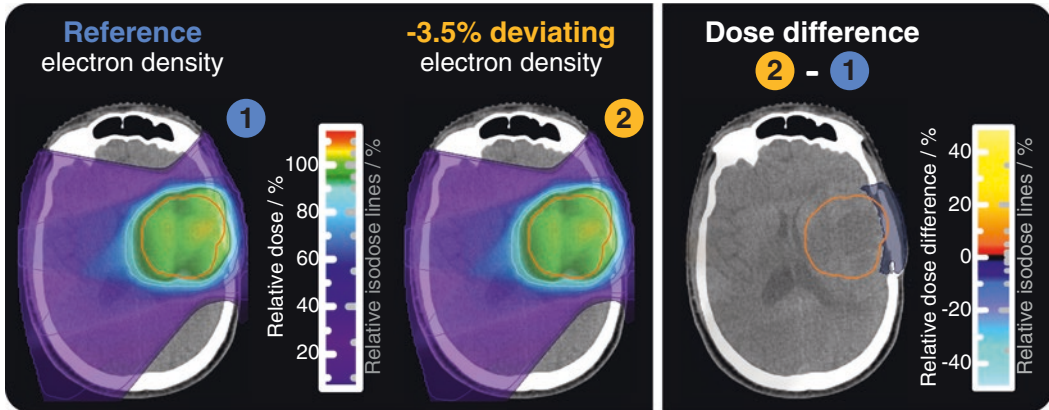


Fig. 1 The reconstruction of virtual monoenergetic image (VMI) datasets with different energies from dual-energy CT can contribute to enhance the tissue contrast for tumor and organ segmentation (low energies) or partly mitigate image artifacts caused by metallic implants (high

energies). For severe metal artifacts, the application of a dedicated metal artifact reduction technique can be beneficial to improve the visual image impression. Adapted from (Wohlfahrt 2018)

a Photon therapy: Impact of uncertainty in electron-density prediction on dose



b Proton therapy: Impact of uncertainty in stopping-power prediction on dose

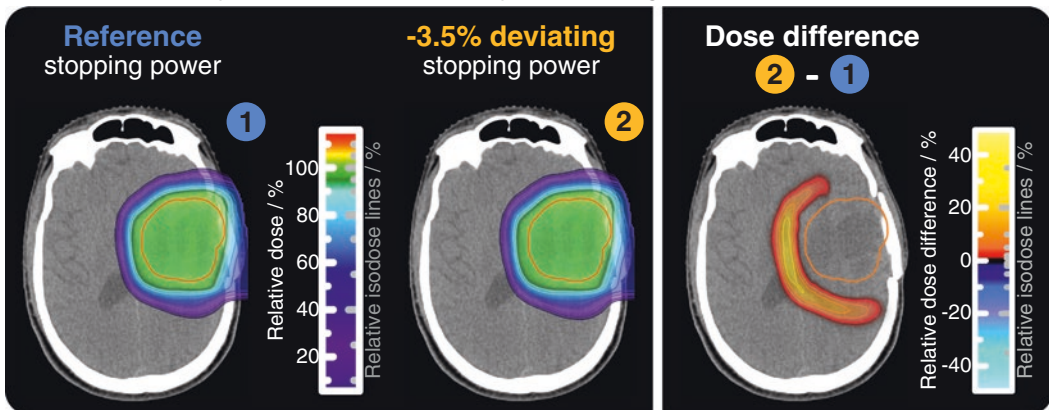


Fig. 2 Impact of a 3.5% deviation in electron-density (photon therapy, **a**) and stopping-power (proton therapy, **b**) prediction on the clinical dose distribution of an exemplary brain-tumor patient case. Severe dose differences

distal to the target region are visible in proton therapy, whereas only a small change in the proximal dose distribution is noticeable for photon therapy

from MRI, have to be converted in physical quantities needed for dose calculation of the treatment beam, namely RED for photon therapy and proton stopping-power ratio (SPR) for proton therapy.

An uncertainty in the CT-based prediction of the respective material parameter has a direct impact on the accuracy of the dose calculation. This effect is particularly pronounced in proton therapy (Fig. 2), since protons stop at a certain depth in the patient and deposit their maximal energy shortly before within the so-called Bragg peak, followed by a steep distal dose fall-off to zero dose deposition behind the stopping posi-

tion. A slight change in the predicted stopping behavior of the traversed tissue will result in a change of the proton's stopping position causing severe changes in the local dose deposition. In contrast, in photon therapy, the variation of dose deposition over the beam's penetration depth is much smaller, resulting in a much smaller dependency on the predicted tissue parameter.

The standard procedure for the voxelwise conversion of CT information (CT number, CTN) into a parameter required for treatment planning (RED, SPR) is the use of a heuristic stepwise linear correlation function, a so-called Hounsfield look-up table (HLUT). The HLUT can be derived

from CT scans of tissue-equivalent materials with known RED/SPR properties (experimental HLUT calibration) or from the elemental composition of tabulated human tissues (Woodard and White 1986) combined with a theoretical prediction of the scanner-specific CT numbers of those non-available tissue samples (stoichiometric HLUT calibration).

Despite its broad use in photon and proton therapy, the HLUT approach has several general limitations (Wohlfahrt and Richter 2020). Tissues with similar CTN but different RED or SPR cannot be distinguished. Since non-tissue materials, e.g. implants, are often not covered by the HLUT due to different elemental composition, severe deviations can occur for them. Moreover, a HLUT is per definition not patient-specific and thus cannot consider the intra- and inter-patient variability in the conversion from CTN to RED or SPR, which can arise from variations in tissue composition (e.g. different calcium content in bones).

In the following, the benefit of DECT for dose calculation is discussed for photon and proton therapy consecutively.

4.1 Photon Therapy

The physical dose deposition of high-energetic MeV photons in tissue is dominated by incoherent scattering, which depends only on the relative electron density of tissue. The most obvious benefit of DECT is that the only quantity needed for MV photon dose calculation, the electron density, can be directly derived from the two scans with very high accuracy. This is possible, because the influence of the photoelectric effect, that also depends on EAN, can be eliminated by a specific weighted superimposition of the DECT scans. In this case, it is a weighted subtraction of the low-energy CT image, possessing a higher influence of photoelectric effect, from the high-energy CT image. This results in an image contrast characterized by incoherent scattering, which only depends on RED. Several DECT-based implementations of RED determination have been introduced and their methodological uncertainty

has been confirmed to be far below 1% (Möhler et al. 2017). Interestingly, some of those algorithms are even mathematically equivalent (Möhler et al. 2018). Ultimately, by implementing such a DECT-based direct RED determination in photon treatment planning, the HLUT approach would be completely discarded together with the associated disadvantages. This leads to reduced dose calculation uncertainties and a better consideration of non-tissue materials. However, this has not yet become broad clinical practice, probably due to a rather small sensitivity of the photon dose calculation to RED uncertainties and practical limitations of DECT techniques (limited field of view or the challenges in the presence of motion).

Another application of DECT with an even higher clinical impact is the ability to virtually remove the influence of the injected contrast agent in tissue from CT images. This allows for the generation of quasi-native CT datasets from contrast-enhanced DECT acquisitions, the so-called virtual non-contrast (VNC) datasets. Hence, instead of acquiring a contrast-enhanced CT scan to support tumor delineation and a native CT scan required for dose calculation, only the contrast-enhanced DECT scan is needed with the VNC approach. This reduces the imaging dose by 50%, eliminates potential registration inaccuracies between native and contrast-enhanced CT images, and also reduces the time of the patient on the CT couch. First investigations showed that VNC-based dose calculation does not lead to clinically relevant dose differences compared to dose calculation on native CT scans (Noid et al. 2021). However, a decrease of the CTN in bones has been noticed, indicating the need for further optimization of the VNC approach towards better differentiation between dense bone and iodine contrast.

4.2 Proton Therapy

For proton therapy, the dose deposition is characterized by the so-called stopping-power ratio (SPR) of the tissue, which mainly depends on RED but also on the mean excitation potential

(MEP) of the tissue. The SPR, which is the stopping power of the material divided by the stopping power of water, can be described as product of RED and a term called relative stopping number (RSN), which includes the MEP as exclusive tissue parameter.

As already described in the previous section, RED can be directly derived from DECT with very high accuracy. Even though DECT imaging allows for determining two tissue parameters, MEP cannot be directly obtained from DECT, because it does not directly affect the photon interactions in CT imaging. Hence, a heuristic conversion from EAN, which is a common second tissue quantity determined from DECT, towards MEP or RSN is needed. Even though this step is associated with all disadvantages of a heuristic conversion as discussed for the HLU approach, its influence on the overall SPR prediction is very limited: The variability of RSN in human tissues only contributes to roughly 5% of the overall SPR variability in those tissues (Möhler et al. 2016), whereas the remaining 95% are caused by RED variations. Consequently, the impact of the remaining uncertainty in the EAN-to-RSN or EAN-to-MEP conversion on the SPR uncertainty is highly suppressed.

In the past decade, about two dozen of algorithms have been proposed to realize a direct DECT-based SPR prediction (DirectSPR) (Wohlfahrt and Richter 2020). Most of them are image-based and use the analytical SPR calculation as described above, but also machine learning approaches or completely empirical parametrizations as well as projection-based SPR calculation have been proposed. Even though a correct and robust algorithmic parametrization is important, other factors in the implementation of a DirectSPR approach are also crucial to fulfill the high requirements on accuracy and precision and need to be considered as well:

- The optimization of the CTN constancy for different scanning conditions by appropriate beam hardening correction;
- The comprehensive calibration of the approach also including different beam hardening conditions or even introducing an object-size dependent calibration;

- The application of sophisticated noise reduction approaches, as especially EAN datasets can introduce a high noise level in the RSN/MEP and subsequent SPR images.

Those characteristics of a DirectSPR implementation ultimately define the accuracy of SPR prediction in a real-world clinical scenario. In general, the accuracy of RED and EAN datasets generated in applications designed for diagnostic purposes do not necessarily satisfy the requirements needed for SPR prediction in proton therapy. Hence, certain CT manufacturer start to provide dedicated PT implementations for SPR prediction with optimized image post-processing. This includes a sophisticated noise-suppression algorithm over the full image post-processing chain, which reduces the noise in SPR datasets by roughly a factor of 2 with respect to the classic convolution of the high- and low-energy CT scan. The selection of a size-dependent calibration for each individual axial CT slice is another benefit for an SPR calculation directly integrated in the CT software. Such an integration can be seen as a paradigm shift, as so far the CTN-to-SPR conversion has been calibrated by each proton center individually and then applied within the treatment planning system. In 2019, the first clinical implementation of DirectSPR for proton treatment planning has been realized (Wohlfahrt and Richter 2020) and medical products have recently become available for the whole workflow from generating SPR datasets to TPS import and processing. Still, the method is far away from broad clinical application despite the great interest in the PT community (Taasti et al. 2018). Nevertheless, it has been shown that the accuracy of range prediction in treatment planning can be improved from 3.5% of the absolute range to 2% or even less in specific geometries (1.7% for brain-tumor treatments) (Peters et al. 2022). This results in a reduction of the safety margin by 35% and thus a relevantly decreased integral dose as well as dose to organs at risk, as shown in Fig. 3 for a representative patient case.

For both treatment modalities, Monte Carlo dose calculation is becoming more and more popular as their calculation speed has improved. Since those algorithms require the elemental

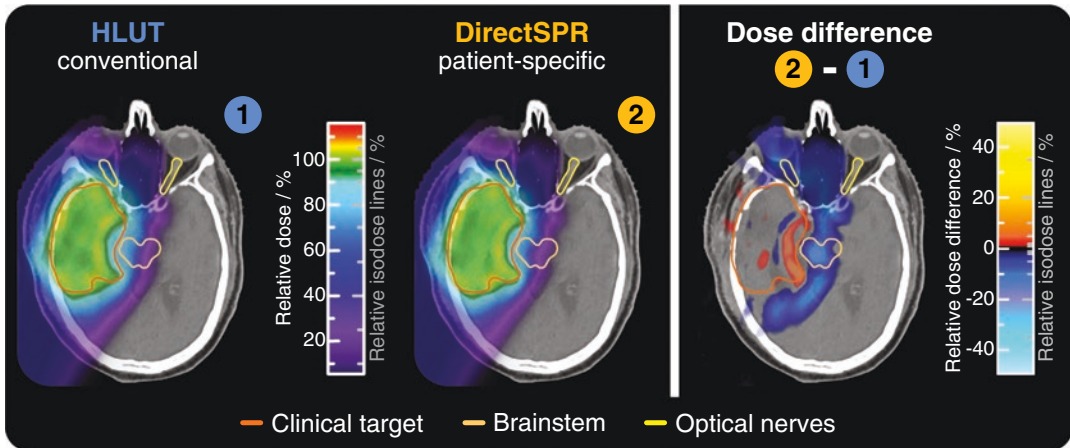


Fig. 3 Exemplary differences in clinical proton dose distribution using the conventional Hounsfield look-up table (HLUT) with a relative range uncertainty of 3.5% of total proton range and a direct stopping-power prediction (DirectSPR) from dual-energy CT with a reduced range

uncertainty of 1.7%. Critical anatomical structures such as the brainstem can be spared more effectively while increasing the tumor coverage close to the brainstem. The clinical patient case was kindly provided by Nils Peters (OncoRay, Dresden)

material composition for each CT voxel, DECT can also be used for an improved material assignment. The implementation of direct RED and SPR prediction is also fully compatible with highly accurate particle transport calculations of Monte Carlo algorithms (Permatasari et al. 2020).

5 Potential of Photon-Counting CT in Radiation Oncology

Within the last two decades, substantial progress in research and development of a new CT detector technology has been made to potentially overcome limitations in current CT imaging by translating from common energy-integrating solid-state scintillation detectors to photon-counting semiconductor detectors in future (Chap. 7). Photon-counting CT always allows for spectrally resolved multi-energy CT acquisitions in the full scan field of view with a high spectral separation, perfect temporal coherence, and high spatio-temporal resolution. Due to a threshold-based signal read-out of photon-counting detectors, electronic noise can be suppressed and thus a lower image noise or a further dose reduction as well as a higher CT number stability can be

achieved. In combination with an almost constant detector sensitivity, even for low-energy X-rays, the soft tissue contrast as well as the contrast enhancement after contrast agent administration can be further improved (Flohr et al. 2020). The selection of more than two energy bins for CT reconstruction even enables multi-material decompositions and differentiation of multiple contrast agents with different attenuation characteristics (k-edge imaging) (Chap. 8). Since the energy discrimination is realized on detector level, the spectral information is perfectly aligned, not hampered by motion-induced anatomical changes, and can thus be used for projection-based material decomposition and physics-based artifact correction, e.g. beam hardening.

These advantages of a photon-counting CT system also tackle current restrictions of the various dual-energy CT techniques as described above (Table 1). With photon-counting CT, a high spectral separation, good quantitative performance in low-dose scenarios, no limitation in field of view and time-resolved respiratory spectral CT acquisition are feasible. The technical advances might then also potentially translate into clinical benefits in the radiotherapeutic chain:

Table 1 Comparison of spectral CT imaging enabled by various dual-energy CT techniques and photon-counting CT concerning technical specifications and specific applications in radiation oncology (RO)

Technical specification	Dual-source CT with EID	Single-source CT with EID				Photon-counting CT
		dual-spiral	slow-kVp	fast-kVp	dual-layer twin-beam	
Spectral separation	Very high	Very high	High	Medium	Low	High
Temporal coherence	High	Low	Medium	High	Perfect	Perfect
Spatio-temporal resolution	Full capabilities	Full capabilities	Full capabilities	Limited capability	Full capabilities	Full capabilities
Cross scatter	Yes	No	No	No	Yes	No
Imaging dose	Individual tube current modulation	Individual tube current modulation	No tube current modulation	No tube current modulation	Tube current modulation	Tube current modulation
Field of view	Limited up to 350 mm	Full	Full	Full	Full	Full
Time-resolved respiratory imaging	Feasible with phase matching in post-processing	Feasible with phase matching in post-processing	Feasible with phase matching in post-processing	No limitation	No limitation	No limitation
Contrast-enhanced imaging	Multi-phase (arterial & venous)	Limited to late or delayed phase	Multi-phase (arterial & venous)	Multi-phase (arterial & venous)	Limited to late or delayed phase	Multi-phase (arterial & venous)
Tissue segmentation	Improved compared to SECT	Improved compared to SECT	Improved compared to SECT	Improved compared to SECT	Improved compared to SECT	Superior spatial resolution, contrast and noise
Projection-based material decomposition	No	No	Yes	Yes	No	Yes

superior spatial resolution

less noise at same dose

multiple contrast agents

- Improved tumor and organ segmentation due to a higher spatial resolution, less noise, and increased image contrast,
- Reduction of uncertainties in treatment planning and dose calculation with a further improved quantitative prediction of material parameters by projection-based material decomposition and physics-based corrections,
- More frequent quantitative image guidance during the course of treatment enabled by dose reduction to better support the patient-specific adaptive workflow with continuous therapy response and toxicity assessment,
- Increased flexibility in contrast agent administration and CT acquisition of different contrast phases.

In summary, photon-counting CT could facilitate the widespread clinical implementation of spectral CT in radiation oncology potentially leading to relevant improvements in the field of radiation oncology imaging.

6 Conclusion

For CT industry, radiation oncology is definitely only a niche market. As the vast majority of CT scanners are used for diagnostic radiology, the development of CT innovations initially focuses on use cases in radiology, just as it was the case for dual-energy CT and is the case for photon-counting CT. Still, radiation oncology can greatly benefit from those technologies, if explored and tailored to the specific needs of RO applications. Improved accuracy of proton therapy by DECT-based treatment planning is probably the most prominent example along this line. Without any doubt, the further exploration of dual- and multi-energy CT for improved tumor and organ segmentation, dose reduction and its expansion towards time-resolved imaging has high potential to relevantly contribute to an advanced radiation therapy of tomorrow.

Compliance with Ethical Standards

Disclosure of Interests The authors received individual funding as lecturer from Siemens Healthineers (2018), which was not related to this study. OncoRay had an

institutional research agreement with Siemens Healthineers in the field of dual-energy CT for particle therapy as well as an institutional agreement as reference center for dual-energy CT in radiotherapy and a software evaluation contract. The authors received no financial support for the present contribution.

References

- Agrawal MD, Pinho DF, Kulkarni NM, Hahn PF, Guimaraes AR, Sahani DV (2014) Oncologic applications of dual-energy CT in the abdomen. *Radiographics* 34:589–612. <https://doi.org/10.1148/rg.343135041>
- Bahig H, Campeau M-P, Lapointe A, Bedwani S, Roberge D, de Guise J, Blais D, Vu T, Lambert L, Chartrand-Lefebvre C, Lord M, Filion E (2017) Phase 1-2 study of dual-energy computed tomography for assessment of pulmonary function in radiation therapy planning. *Int J Radiat Oncol Biol Phys* 99:334–343. <https://doi.org/10.1016/j.ijrobp.2017.05.051>
- Baumann M, Krause M, Overgaard J, Debus J, Bentzen SM, Daartz J, Richter C, Zips D, Bortfeld T (2016) Radiation oncology in the era of precision medicine. *Nat Rev Cancer* 16:234–249. <https://doi.org/10.1038/nrc.2016.18>
- Borras JM, Lievens Y, Dunscombe P, Coffey M, Malicki J, Corral J, Gasparotto C, Defourny N, Barton M, Verhoeven R, van Eycken L, Primic-Zakelj M, Trojanowski M, Strojjan P, Grau C (2015) The optimal utilization proportion of external beam radiotherapy in European countries: an ESTRO-HERO analysis. *Radiother Oncol* 116:38–44. <https://doi.org/10.1016/j.radonc.2015.04.018>
- Flohr T, Petersilka M, Henning A, Ulzheimer S, Ferda J, Schmidt B (2020) Photon-counting CT review. *Phys Med* 79:126–136. <https://doi.org/10.1016/j.ejmp.2020.10.030>
- Forghani R, Mukherji SK (2018) Advanced dual-energy CT applications for the evaluation of the soft tissues of the neck. *Clin Radiol* 73:70–80. <https://doi.org/10.1016/j.crad.2017.04.002>
- Fukukura Y, Kumagai Y, Higashi R, Hakamada H, Nagano H, Hidaka S, Kamimura K, Maemura K, Arima S, Yoshiura T (2020) Visual enhancement pattern during the delayed phase of enhanced CT as an independent prognostic factor in stage IV pancreatic ductal adenocarcinoma. *Pancreatol* 20:1155–1163. <https://doi.org/10.1016/j.pan.2020.07.009>
- Goitein M (1977) The measurement of tissue heterogeneity to guide charged particle radiotherapy. *Int J Rad Oncol Biol Phys* 3:27–33. [https://doi.org/10.1016/0360-3016\(77\)90223-1](https://doi.org/10.1016/0360-3016(77)90223-1)
- Hounsfield GN (1973) Computerized transverse axial scanning (tomography). 1. Description of system. *Br J Radiol* 46:1016–1022. <https://doi.org/10.1259/0007-1285-46-552-1016>
- McCollough CH, Boedeker K, Cody D, Duan X, Flohr T, Halliburton SS, Hsieh J, Layman RR, Pelc NJ (2020)

- Principles and applications of multienergy CT: report of AAPM task group 291. *Med Phys* 47:e881–e912. <https://doi.org/10.1002/mp.14157>
- McGuire SM, Menda Y, Ponto LLB, Gross B, Juweid M, Bayouth JE (2011) A methodology for incorporating functional bone marrow sparing in IMRT planning for pelvic radiation therapy. *Radiother Oncol* 99:49–54. <https://doi.org/10.1016/j.radonc.2011.01.025>
- Möhler C, Wohlfahrt P, Richter C, Greilich S (2016) Range prediction for tissue mixtures based on dual-energy CT. *Phys Med Biol* 61:N268–N275. <https://doi.org/10.1088/0031-9155/61/11/N268>
- Möhler C, Wohlfahrt P, Richter C, Greilich S (2017) Methodological accuracy of image-based electron density assessment using dual-energy computed tomography. *Med Phys* 44:2429–2437. <https://doi.org/10.1002/mp.12265>
- Möhler C, Wohlfahrt P, Richter C, Greilich S (2018) On the equivalence of image-based dual-energy CT methods for the determination of electron density and effective atomic number in radiotherapy. *Phys Imag Rad Oncol* 5:108–110. <https://doi.org/10.1016/j.phro.2018.03.003>
- Noid G, Schott D, Paulson E, Zhu J, Shah J, Li XA (2021) Technical note: using virtual noncontrast images from dual-energy CT to eliminate the need of precontrast CT for x-ray radiation treatment planning of abdominal tumors†. *Med Phys* 48:1365–1371. <https://doi.org/10.1002/mp.14702>
- Ohira S, Wada K, Hirata T, Kanayama N, Ikawa T, Karino T, Nitta Y, Isono M, Ueda Y, Miyazaki M, Koizumi M, Teshima T (2018) Clinical implementation of contrast-enhanced four-dimensional dual-energy computed tomography for target delineation of pancreatic cancer. *Radiother Oncol* 129:105–111. <https://doi.org/10.1016/j.radonc.2018.01.012>
- Paganetti H, Beltran CJ, Both S, Dong L, Flanz JB, Furutani KM, Grassberger C, Grosshans DR, Knopf A-C, Langendijk JA, Nyström H, Parodi K, Raaymakers BW, Richter C, Sawakuchi GO, Schippers JM, Shaitelman SF, Teo K, Unkelbach J, Wohlfahrt P, Lomax AJ (2020) Roadmap: proton therapy physics and biology. *Phys Med Biol*. <https://doi.org/10.1088/1361-6560/abcd16>
- Permatasari FF, Eulitz J, Richter C, Wohlfahrt P, Lühr A (2020) Material assignment for proton range prediction in Monte Carlo patient simulations using stopping-power datasets. *Phys Med Biol* 65:185004. <https://doi.org/10.1088/1361-6560/ab9702>
- Peters et al. 2022, *Radiother Oncol* 166, <https://doi.org/10.1016/j.radonc.2021.11.002>
- Taasti VT, Bäumer C, Dahlgren CV, Deisher AJ, Ellerbrock M, Free J, Gora J, Kozera A, Lomax AJ, de Marzi L, Molinelli S, Kevin Teo B-K, Wohlfahrt P, Petersen JBB, Muren LP, Hansen DC, Richter C (2018) Inter-Centre variability of CT-based stopping-power prediction in particle therapy: survey-based evaluation. *Phys Imag Rad Oncol* 6:25–30. <https://doi.org/10.1016/j.phro.2018.04.006>
- van Elmpt W, Landry G, Das M, Verhaegen F (2016) Dual energy CT in radiotherapy: current applications and future outlook. *Radiother Oncol* 119:137–144. <https://doi.org/10.1016/j.radonc.2016.02.026>
- Wohlfahrt P (2018) Dual-energy computed tomography for accurate stopping-power prediction in proton treatment planning. Technische Universität Dresden. Available from: <https://nbn-resolving.org/urn:nbn:de:bsz:14-qucosa2-317554>
- Wohlfahrt P, Richter C (2020) Status and innovations in pre-treatment CT imaging for proton therapy. *Br J Radiol* 93:20190590. <https://doi.org/10.1259/bjr.20190590>
- Wohlfahrt P, Möhler C, Hietschold V, Menkel S, Greilich S, Krause M, Baumann M, Enghardt W, Richter C (2017) Clinical implementation of dual-energy CT for proton treatment planning on pseudo-monoenergetic CT scans. *Int J Radiat Oncol Biol Phys* 97:427–434. <https://doi.org/10.1016/j.ijrobp.2016.10.022>
- Wohlfahrt P, Troost EGC, Hofmann C, Richter C, Jakobi A (2018) Clinical feasibility of single-source dual-spiral 4D dual-energy CT for proton treatment planning within the thoracic region. *Int J Radiat Oncol Biol Phys* 102:830–840. <https://doi.org/10.1016/j.ijrobp.2018.06.044>
- Wohlfahrt P, Agolli L, Krause M, Pilz K, Richter C, Troost E (2019) PO-1012 dual-energy computed tomography for improved delineation in postoperative brain-tumor patients. *Radiother Oncol* 133:S559–S560. [https://doi.org/10.1016/S0167-8140\(19\)31432-X](https://doi.org/10.1016/S0167-8140(19)31432-X)
- Woodard HQ, White DR (1986) The composition of body tissues. *Br J Radiol* 59:1209–1218. <https://doi.org/10.1259/0007-1285-59-708-1209>



The Future of Spectral CT: Radiomics and Beyond

Bettina Baessler and Davide Cester

Contents

1	Introduction	348
2	Future Advancements in Scanning Techniques and Image Reconstruction	348
2.1	Automated Voltage and Current Optimization Techniques	349
2.2	Automated Patient Positioning and Scan Length Optimization	349
2.3	A Novel Image Quality Metric: The Detectability Index	350
2.4	Advancements in Contrast Media Applications	350
2.5	Reconstruction Techniques	351
3	The Hidden Potential of Underutilized Data	352
3.1	Radiomics	353
3.2	Machine Learning for Diagnosis	354
3.3	Opportunistic Screening	355
3.4	Distributed Learning	355
4	Limitations of Radiomics and Artificial Intelligence	356
5	Outlook	356
	References	357

Abstract

The spectral sensitivity of spectral detectors is adding a whole new dimension to the data and this will soon lead to images obtained with lower radiation dose, in shorter times, and bearing greater diagnostic significance. Image quality is just one aspect of the rapid evolution enabled by modern technologies: through

automation, the clinical histories of the patients and their individual characteristics are going to become even more relevant in the determination of the investigation parameters, while the automated algorithms based on techniques from the field of artificial intelligence will increasingly benefit from the knowledge embedded in billions of archived images. Advancements in the fields of image analysis and radiomics will soon be able to supply the radiologists with a growing number of robust and standardized indicators, seamlessly integrated into clinical devices and information

B. Baessler (✉) · D. Cester
University Hospital Würzburg, Department of
Diagnostic and Interventional Radiology,
Würzburg, Germany
e-mail: baessler_b@ukw.de

systems. This chapter summarizes four of the main current research areas: the improvement of the scan conditions, the optimization of the applications of contrast media, new methods for image reconstruction and quality assessment, and the increasing use of “hidden data” and quantitative imaging biomarkers, including radiomics, machine learning, and artificial/augmented intelligence.

also at reducing the scan time or the dose absorbed by the patient.

We present here an overview of four of these research areas (Fig. 1): the improvement of the scan conditions, the optimization of the applications of contrast media, new methods for image reconstruction and quality assessment, and the increasing use of “hidden data” and quantitative imaging biomarkers, including radiomics, machine learning (ML), and artificial/augmented intelligence (AI).

1 Introduction

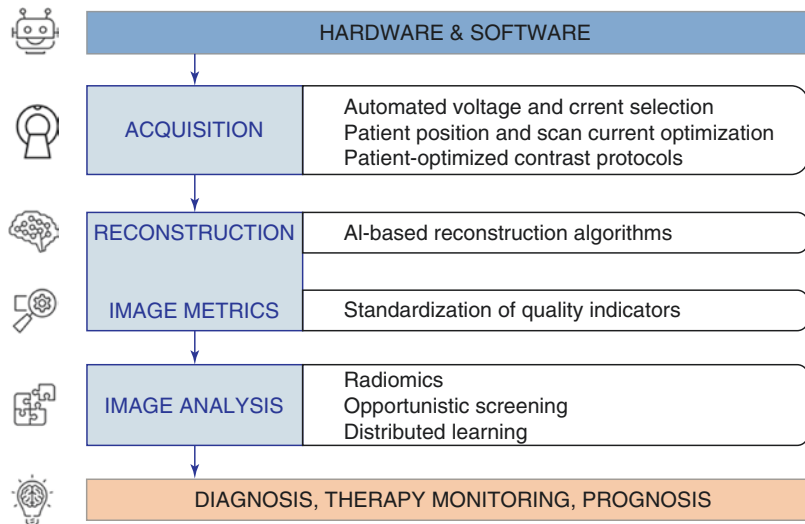
Despite being firstly demonstrated in the 1970s, CT is still an evolving technology with a lot of potential for improvement on the hardware (as demonstrated by the recent introduction of PCCT (see Chap.20)), software, and post-processing side. Generation after generation, CT scanners haven been able to provide more and better images. At the same time, the continuous progress of computer science has enabled an incredible research effort in the field of software-based image analysis, aiming to provide more information that can be used in the diagnostic process.

In addition to the hardware and image analysis domains, there are other areas where innovation can have a significant impact on the efficiency of the diagnostic process, not necessarily aimed at improving the quality of the resulting images, but

2 Future Advancements in Scanning Techniques and Image Reconstruction

Compared to the years when CT was introduced, there is nowadays much more awareness from the public regarding the biological effects of radiation. While the use of CT in the last decades has emerged to become standard practice, a growing proportion of the research effort has been dedicated to dose optimization. However, despite the introduction of dose registers and dedicated initiatives, dose levels used in modern radiology are still hugely different across countries and institutions. A recent multinational study based on two million CT scans found a four-fold range of effective dose for a standard abdominal CT with a 17-fold range for high-dose CT (Smith-

Fig. 1 Summary of the different levels of a CT investigation and the relative topics discussed in the chapter



Bindman et al. 2019). After adjusting for patient characteristics, the major source of dose variation was attributed to institutional choices regarding scan parameters. These findings strongly suggest that the measured differences do not originate from limitations of CT technology, but rather from the lack of consistent and shared standards regarding its applications.

The most promising way to achieve the necessary homogenization is by means of automated procedure optimization and automated evaluation metrics. Standardized algorithms could soon enable a complete customization of the scan parameters in order to minimize the absorbed dose depending on the device and patient characteristics. At the same time, novel and standardized metrics will provide an objective evaluation of the image quality in terms of the actual effectiveness of the diagnostic process.

2.1 Automated Voltage and Current Optimization Techniques

Several techniques have been successfully established in order to limit dose levels in CT imaging by taking into account patient characteristics in a standardized fashion, the most common ones being automatic tube current modulation (ATCM) and automatic tube voltage selection (ATVS). The underlying concept is based on the acquisition of low-dose images of the patient, called scout images, which enable the calculation of the actual size of the patient and the approximated attenuation profiles. The extracted data and the user settings are then used to optimize the scanner parameters in order to minimize the patient dose while reaching the required imaging performance.

ATCM works by modulating the current along all three axes depending on the inhomogeneities in the attenuation; in particular, the current will be lower than the average settings along directions where the scout images showed a stronger attenuation, allowing to achieve dose reduction factors up to 68%. ATVS, on the other hand, combines the estimation of the attenuation profile along the

z-axis with a user-provided parameter representing the desired contrast-to-noise value (CNR). The software then determines the tube voltage which minimizes the radiation dose while reaching the requested CNR (Winklehner et al. 2011). The dose reduction potential of this technique has been reported to be between 13% and 77% (Niemann et al. 2013; Papadakis and Damilakis 2019; Winklehner et al. 2011; Yu et al. 2013).

The dose reduction potential of voltage and current optimization could be further boosted by the introduction of AI algorithms. As an example, AI models could be trained on large datasets of patients, and the acquisition of scout images could be replaced by an automated selection of voltage and current based on simpler patient characteristics and the type of examination.

2.2 Automated Patient Positioning and Scan Length Optimization

Within the process of homogenization of scan procedures, a fundamental factor which should be taken into account is patient positioning. Not only can patient off-centering directly impact image quality and radiation dose (Euler et al. 2019; Filev et al. 2016; Kaasalainen et al. 2019; Li et al. 2007; Schmidt et al. 2020; Toth et al. 2007; Habibzadeh et al. 2012; Toth et al. 2007) but it can also affect other aspects of the scan procedure; as an example, both ATCM and ATVS suffer from patient malpositioning (Euler et al. 2019; Filev et al. 2016; Gudjonsdottir et al. 2009; Kaasalainen et al. 2019; Marsh and Silosky 2017; Matsubara et al. 2009; Saltybaeva and Alkadhi 2017; Schmidt et al. 2020; Winslow et al. 2018) because off-centering leads to magnification effects of the scout images.

Even when the patient is perfectly placed on the table, further optimization of radiation dose can be achieved by automated planning of the scan range. An excessive scan range in up to 80% of thoracoabdominal CT scans was recently observed by Zanca et al. (2012), a finding that varied substantially among institutions (Schwartz et al. 2018).

The use of three-dimensional cameras based on infrared light, in combination with dedicated AI algorithms, has been investigated to address both these issues. The optimization of the patient positioning can be achieved by measuring the body contour of the patient in order to create a virtual representation, which then can be used to calculate the optimal table height. This method proved to significantly improve patient centering for CT of the chest and abdomen compared with manual positioning using the built-in laser system (Booij et al. 2019; Saltybaeva et al. 2018). By using a similar setup of infrared lights and 3D cameras in combination with AI algorithms, it was also possible to estimate the appropriate scan ranges in order to minimize unnecessary radiation dose (Coley et al. 2019). In a few more years, the task of correctly positioning the patient could be completely automated and performed by the CT device itself instead of being manually encoded into the protocol parameters.

2.3 A Novel Image Quality Metric: The Detectability Index

A successful diagnosis is undoubtedly the true goal of a CT scan, and in principle, any potential improvement resulting from a change in the scan parameters should be measured against its real impact on the effectiveness in the diagnostic process. This is unfortunately not completely possible, given the fundamental role played by the human factor, and researchers have reverted to use simpler but more measurable and reproducible indicators like image contrast.

The administered dose level, or more specifically its reduction, has become one of the most used metrics in the field, given its fundamental importance in terms of patient safety. The radiation dose alone, however, does not guarantee the quality of a CT scan. On the contrary, the continuous search for lower radiation dose carries the risk of worsening the actual detectability of lesions, and therefore negatively impact the patient outcome. It is clear that the effort to reduce the dose of the administered radiation has to be balanced by the need to maintain the diag-

nostic accuracy. Currently, the quality assessment of CT images still relies heavily on direct evaluation by radiologists, preventing a complete and reproducible standardization of the process.

The answer to this issue can be found, when radiation dose and other acquisition parameters can be formally linked with image quality and diagnostic accuracy. This approach is called task-based image quality assessment and represents a paradigm shift in the evaluation of CT image quality. Images are assessed based on their performance with respect to a specific diagnostic task and not the quality perceived by a human observer (Samei et al. 2019). The detectability index d' has been recently proposed and validated in clinical studies as a promising task-based image quality metric (Smith et al. 2017; Solomon et al. 2015). One study has shown that d' can reflect lesion detection and image quality perception for clinical CT scans with hepatic metastases (Cheng et al. 2020). When considering the recent developments of Spectral CT, a standardized metric like d' constitutes a highly interesting tool to perform studies aimed at investigating the energy dependence of both new and existing techniques.

Further work will be needed before these indicators can be officially integrated into dose management workflows. Nevertheless, d' and comparable metrics represent the first steps of a necessary patient outcome-centric approach to the standardized benchmark of radiation dose.

2.4 Advancements in Contrast Media Applications

2.4.1 Patient-Optimized Contrast Media Protocols

The K-absorption edge of iodine is 33.2 keV, a value approximately located at the lower boundary of the X-ray energy range used in CT. In proximity of the K-edge, the energy absorption due to photoelectric effect increases abruptly; for this reason, lowering the tube voltage results in higher attenuation by iodinated contrast media and produces stronger features in the images. The main consequence in CT angiography is the pos-

sibility to administer lower volumes of contrast media while preserving the usual image quality (Lell et al. 2017; Martens et al. 2019; Schindera et al. 2009; Winklehner et al. 2011). When combined with ATVS, this technique allows to minimize the radiation dose received by the patient.

The use of ATVS provides another possibility to reduce the contrast media by increasing the tube current (Hendriks et al. 2018; Higashigaito et al. 2016). While in this case the dose reduction potential of ATVS is not fully exploited, the quantity of contrast agent can be personalized for each individual patient (Higashigaito et al. 2016) which can be of particular importance when dealing with patients with reduced kidney functionality (Nijssen et al. 2019).

Further possibilities to reduce the amount of contrast media and the radiation dose may come from future studies exploring the energy dimension of the scan parameters enabled by modern DECT and PCCT technology, for example, by investigating the impact of dual-energy scanners and Virtual Monoenergetic Images (VMI) (Grant et al. 2014; Husarik et al. 2015; Skawran et al. 2020).

2.4.2 Patient-Optimized Contrast Media Timing

As usual in the CT domain, when performing a contrasted CT angiography, the scan duration should be reduced to the necessary minimum. However, this task is made more difficult by the simultaneous effort of minimizing the quantity of contrast agent, as discussed before. Optimizing the scan timing is therefore an essential technique to reduce radiation dose without compromising image quality or the quantity of contrast agent.

To reduce the overall scan duration, two main methods are commonly employed in CT angiography. The most common technique is bolus tracking, in which the scan initiates when the contrast enhancement on a predefined vessel reaches a predefined threshold value. An alternative is the test bolus technique; in this method, a small test bolus of contrast medium (10–20 ml) is used to assess the cardiovascular circulation of the specific patient before the main scan is performed (Mahnken et al. 2007). Due to the addi-

tional test bolus injection, bolus tracking technique is usually preferred as it needs less contrast media and a simpler, shorter scan procedure (Bae 2010). It is not immune from drawbacks, though: bolus tracking uses a fixed trigger delay to start a scan after the attenuation threshold is reached, and optimizing this delay for each patient and examination would add considerable complexity to the procedure.

Efforts to introduce automation in this area have already been made. A contrast enhancement prediction (CEP) algorithm was recently presented (Korporaal et al. 2015). This algorithm incorporates population-averaged blood circulation characteristics and could be used for real-time prediction of the scan delay with performance comparable with the traditional approach. The introduction of AI algorithms in the field of CT angiography will help to further tailor the scan parameters to each specific patient, leading to further reduction of absorbed radiation dose.

2.5 Reconstruction Techniques

The traditional filtered back projection is still regarded as the reference technique for CT image reconstruction. However, in recent years, several vendors have introduced different hybrid and model-based iterative reconstruction (IR) algorithms. Many of these IRs are optimized for a specific application and each of them features its own advantages and trade-offs in terms of image quality (principally SNR), reconstruction speed and dose reduction. Radiation dose reductions up to 76% have been reported, depending on the body region and the reference dose (Willemink et al. 2013). Chest CT and CT angiography have been found to particularly benefit from IR (Den Harder et al. 2015a, b), while in the case of low-contrast tasks in abdominal CT the benefits are reported to be lower (Jensen et al. 2018; Schindera et al. 2013) and there could even be a worsening of the examination yield when IR is used to achieve high-dose reductions (Schindera et al. 2013).

AI-driven image reconstruction techniques, often called deep learning reconstruction or res-

toration (DLR), have recently showed great potential. A DLR is constituted by a DL model which is trained using the physics of the CT scanner and the scanned object (i.e., the patient), as well as a large sample of clinical CT images. Depending on the training, the model can then be used for image denoising or to predict missing information. Convolutional neural networks (CNNs) trained on low-dose CT images have been shown to have the potential to generate full-dose CT images (Wolterink et al. 2017) and early clinical studies have reported improved image quality compared with IR for abdominal CT (Akagi et al. 2019) and coronary CT angiography (Liu et al. 2020; Tatsugami et al. 2019). In situations when sparse-sampling CT techniques must be employed and fewer projections are purposely acquired, DLR can be used to generate this missing information, with the potential net effect of reducing radiation dose while limiting the loss in image quality (Dong et al. 2019; Racine et al. 2020). Based on the same principle of predicting missing information, DLR can also be used to decrease streaking artifacts from metal implants (Gjesteby et al. 2019; Liang et al. 2019). Another study has shown the potential for DL to generate high-resolution images from low-resolution images in chest CT (Umehara et al. 2018). Another phantom study reported superior image noise, spatial resolution, and task-based detectability of DLR compared with IR (Higaki et al. 2020). Finally, DLR has been successfully applied to improve X-ray scatter estimation, which is essential to improve image quality (Jiang et al. 2019; Maier et al. 2019).

One of the most important features introduced by spectral CT is the possibility to use the energy information to separate different materials; however, this new aspect of image reconstruction requires sophisticated algorithms and a precise physical model. CNNs have the potential to circumvent this complexity, and they have already been applied to Multimaterial Decomposition (MMD) (Chen and Li 2019) and K-edge imaging (Zimmerman et al. 2020).

All these findings indicate great potential for deep learning techniques to provide substantial improvements in terms of dose reduction, image

quality, and reconstruction time. However, CNNs are still considered “black boxes” with the power to alter the image data in an unpredictable way. The absence of an a priori analytical model for the predictions typical of DL techniques implies a certain degree of risk that algorithms based on unsupervised learning might add or subtract structures and lesions from images, leading to wrong diagnoses with potentially severe consequences for the patients. The quantity and variety of training data play by definition a major role in the process of determining this prediction model; the current practice is to train CNNs on small and properly sampled image data, commensurate to the level of complexity encountered in the clinical routine clinical. Further effort will be needed to address all the safety concerns and to enable a successful implementation of DLRs in the clinical practice.

3 The Hidden Potential of Underutilized Data

Due to its advantages and the continued improvements of the underlying technology, CT has enjoyed an emerging popularity in the clinical workflow. Not only the use of CT has continuously increased since its introduction, but the tendency has even accelerated during the last decades (Bly et al. 2015; Le Coultre et al. 2016; Mettler et al. 2009; Pola et al. 2018). Several billions of images are generated every year, covering a vast variety of diseases and population characteristics. Most of the datasets represent a complete 3D reconstruction for a specific organ or an entire body region and potentially constitutes valuable data for countless studies; however, the extraction of useful data by trained human experts represents a huge bottleneck and just a minority of the available information is actually extracted and used during the clinical diagnostic process. Moreover, data is usually locally stored in the so-called data silos: data from each institution can hardly be shared outside the boundaries of the local IT infrastructure, mainly due to ethical, regulatory, and privacy concerns. These restrictions severely limit the

amount of data available to each AI research project, and ultimately limit the exploitation of its potential. The recent evolution of AI applications to medical imaging aims to address both issues.

3.1 Radiomics

One emerging variant of using underutilized data is radiomics. Radiomics represents a quantitative approach to medical imaging, which aims at enhancing the existing clinical data by means of advanced mathematical and/or statistical analysis. The concept of radiomics, which has most broadly been applied in the field of oncology, is based on the assumption that biomedical images contain information of disease-specific processes that are imperceptible by the human eye (Mannil et al. 2018) and thus not accessible through traditional visual inspection of an image (and, as a consequence, are underutilized). Through mathematical extraction of the spatial distribution of signal-intensities and pixel-interrelationships, radiomics quantifies this textural information (Castellano et al. 2004; Tourassi 1999) (also known as texture analysis). Hence, differences in image intensity, shape or texture can be quantified by means of radiomics, thus overcoming the subjective nature of image interpretation. An exemplary radiomics workflow for spectral CT data is shown in Fig. 2.

Since radiomics represents “big data,” analysis methods from the field of AI such as ML are usually used to generate knowledge out of these data. As a consequence, radiomics is of high interest in order to enhance existing diagnostic processes with additional, quantitative data. In addition, radiomics—combined with advanced modeling - might be a valuable tool in providing prognostic information in various diseases.

Radiomic analysis in general can be performed on medical images from all available modalities. When it comes to spectral CT, however, the potential additive diagnostic and prognostic value of spectral CT data with their additional quantitative information on the energy-dependent attenuation changes in various tissues (Al Ajmi et al. 2018) is of high interest in order to improve predictive models in radiomics studies.

While the number of publications on radiomics in CT imaging has risen exponentially over the last few years, only very few proof-of-concept studies applying radiomic analyses on spectral CT datasets have been published so far. However, it is to be expected that more and more studies exploring the additive diagnostic potential of the spectral information and radiomics will appear.

Already in 2013, the first application of texture analysis on spectral CT data has been reported by Depeursinge et al. (Depeursinge et al. 2013). They had noticed that the wealth of

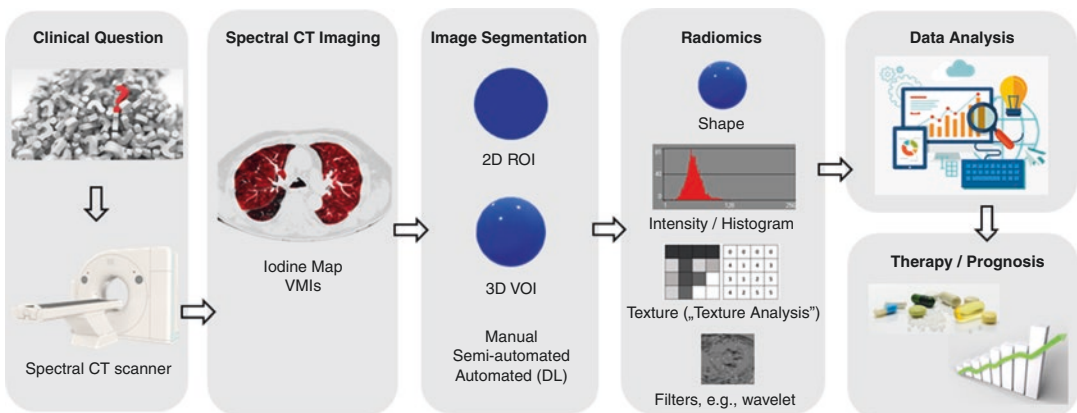


Fig. 2 Exemplary radiomics workflow for Spectral CT. Schematic illustration of the entire patient journey including image acquisition, two- or three-dimensional

image segmentation, radiomic feature extraction, and data-driven patient-specific diagnostic or prognostic assessment

the recently introduced spectral CT 4D data (i.e., the 3D image series obtained for every X-ray energy level between 40 and 140 keV) was mostly discarded by clinicians in clinical routine and that clinicians used only the single-energy images at 70 keV during diagnostic workup. The group proposed a self-developed computerized multiscale rotation-covariant texture analysis of spectral CT data for local pulmonary perfusion assessment in patients with acute pulmonary embolism. This rotation covariant texture analysis was aimed at allowing subtle characterization of directional vascular morphological changes associated with acute pulmonary embolism. In their small proof-of-concept study in 19 patients with acute pulmonary embolism and 8 controls, they demonstrated the feasibility of their approach and an improved diagnostic accuracy of the multiscale texture analysis model over the standard 70 keV approach (area under the curve [AUC] in receiver operating curve [ROC] analysis 0.85 vs. 0.77, respectively).

Further studies reporting the application of radiomics in spectral CT imaging have been published over the last 3 years. The time gap from 2013 to 2018 might be due to the now increasing availability of easily applicable and—at least to some extent—commercially available radiomics software, whereas previous approaches had been self-developed and self-programmed.

Radiomics has been applied in several different settings, such as to classify histopathology of benign parotid tumors (Al Ajmi et al. 2018), to predict lymph node metastasis in head and neck squamous cell cancer (Forghani et al. 2019), papillary thyroid cancer (Zhou et al. 2020), and gastric cancer (Li et al. 2020a, b), to predict microsatellite instability in colorectal carcinoma (Wu et al. 2019), for differentiating benign and malignant liver lesions (Homayounieh et al. 2020), to classify renal clear cell carcinoma (Han et al. 2021), and to assess biopsy-proven liver fibrosis (Choi et al. 2020). Four of these studies (two from the same group) additionally investigated the additive potential of the spectral information (i.e., multi-energy virtual monoenergetic reconstructions) as compared to the clinically

often used single-energy datasets (in this case 65 keV) (Al Ajmi et al. 2018; Forghani et al. 2019; Han et al. 2021; Li et al. 2020a, b). In the example of classifying the histopathology of benign parotid tumors, classification accuracy increased from 75% using the 65 keV monoenergetic dataset to 92% when multi-energy datasets were used (Al Ajmi et al. 2018). It has to be noted, that in general, patient populations in these studies were relatively small, ranging from 42 (Al Ajmi et al. 2018) to 204 (Li et al. 2020a, b).

Although there has not been published any study so far on the prognostic value of combining the spectral information with radiomics, the potential of radiomics combined with the information on the energy-dependent attenuation changes in the tissue for assessment of treatment response, outcome prediction, and risk assessment is huge. It is to be expected, that first studies will become available in this field within the next months and years.

3.2 Machine Learning for Diagnosis

Besides the traditional, “hand-crafted” radiomics approach, where individual features are extracted from a drawn region or volume of interest in an image and then fed into some sort of ML algorithm for the respective classification task or predictive modeling, techniques from the ML spectrum also can be directly applied on the images. While such computer vision tasks have been applied broadly on standard CT images, a deep learning algorithm based on spectral CT images has been reported only for the task of body composition analysis (Zopfs et al. 2020), as further discussed in the section “opportunistic screening.” The diagnostic potential of these approaches is yet to be determined and is expected to be an important research topic for the following years.

Interesting applications recently have been reported for ML techniques in combination with low and high keV virtual monoenergetic images (without the use of radiomics or computer vision

tasks). Große Hokamp and colleagues used ML and spectral CT images to facilitate renal stone characterization (Große Hokamp et al. 2020) in a recently published *ex vivo* study. They showed that even in compound stones the main component could be reliably determined using spectral datasets combined with an ML approach. The identification of the main stone components thereby was independent of the dose protocol used for image acquisition.

ML-based CAD systems for a) determination of preoperative invasion depth of gastric cancer (Li et al. 2015) and b) for distinguishing pancreatic mucinous cystic neoplasms from serous oligocystic adenomas (Li et al. 2016).

3.3 Opportunistic Screening

By enabling a greater extent of the available data to be processed in a fully automated way (either using radiomics or techniques from the field of ML, DL, and computer vision), AI can bypass the current bottleneck in the extraction of relevant information from images. Several different analyses of CT images could be conducted in background, while at the same time, the radiologist continues to focus on the investigation which originally motivated the scan. The additional information could be immediately accessed to help the diagnostic process or just be stored for later use. This strategy goes under the name of opportunistic screening.

One key feature potentially provided by AI algorithms is the automated quantification of different human tissues, also called body composition analysis. The ability to quantitatively discriminate the different tissues could enable cost-effective opportunistic screening and risk stratification, thus maximizing the effectiveness of CT scanning performed for other indications. Early studies have shown promising results for cardiovascular risk stratification with automated assessment of coronary artery stenosis (Hong et al. 2019), automated Agatston score calculation (Cano-Espinosa et al. 2018), and epicardial

fat quantification (Commandeur et al. 2018). In addition, the assessment of skeletal muscle mass, visceral adipose tissue, and bone mineral density may provide prognostic information for the general population as well as for patients with comorbidities (Burns et al. 2020; Cano-Espinosa et al. 2018; Dabiri et al. 2019; Lee et al. 2017; Wang et al. 2017; Weston et al. 2019). Very recently, the first deep learning algorithm based on spectral CT images has been reported for the task of body composition analysis (Zopfs et al. 2020).

Another AI field under rapid development is segmentation. Automated segmentation of organ size and volume may allow to determine population-specific size percentiles with greater precision. The combination of AI-automated analysis with access to data from multiple geographically-distributed datacenters would provide a unique opportunity to correlate disease and patient outcome with body composition on a regional or even global scale.

3.4 Distributed Learning

In order to fully exploit the potential of opportunistic automated image analysis, advancements to individual AI algorithms must be complemented by improvements in the way data is stored and accessed between different data centers, with special attention to the topics of data governance and privacy issues. Federated learning (FL), also called distributed learning, has recently emerged as an effective paradigm to balance data access with protection of sensible information (Li et al. 2020a, b; Rieke et al. 2020). With FL the patient data is actually never transferred outside of the original institution; instead, the analysis process occurs locally, and only the resulting model characteristics are shared. For many AI algorithms, the possibility to access data from multiple institutions could finally provide sufficient data to enable the transition from research to clinical practice.

4 Limitations of Radiomics and Artificial Intelligence

Although radiomics, ML, DL, and all abovementioned techniques have been shown to exhibit a huge potential for diagnostic, prognostic, and predictive purposes, the field is facing several challenges. One of the most important limitations in the field of radiomics is the often poor reproducibility of radiomic studies due to lack of standardization, insufficient reporting or limited open source code and data. The lack of proper validation with the subsequent risk of false positive or negative results limits translation to clinical practice (Chalkidou et al. 2015). As detailed above, current radiomics studies in the field of spectral CT represent first and small proof-of-concept studies based on retrospectively collected data, whereas prospective randomized controlled studies are required in the future to confirm the value of radiomics (van Timmeren et al. 2020).

In most radiomic studies, imaging protocols, including acquisition- and reconstruction settings, usually are not controlled or standardized. Various studies have demonstrated the high impact of these technical settings on radiomic features or attempted to minimize their influence by eliminating features that are sensitive to these variabilities. A summary can be found in van Timmeren et al. van Timmeren et al. (2020). While the Image Biomarker Standardization Initiative (IBSI) (Zwanenburg et al. 2020; Zwanenburg et al. 2016) has made some effort to achieve better standardization of radiomics, only sparse information is available when it comes to the robustness of radiomic features computed from spectral CT. Nevertheless, it is crucial, that future radiomics studies in spectral CT adhere to these guidelines (which was not the case in nearly all of the abovementioned studies).

Apart from the variations in scanners and settings, radiomic feature values are also influenced by patient variabilities, e.g. geometry, which impact the levels of noise and presence of artifacts in an image (Mühlberg et al. 2020).

ML and DL techniques are highly “data hungry.” For an ML model to be robust, it may require millions of observations to reach accept-

able performance levels (Halevy et al. 2009). This lies in contrast to the usually small patient cohorts used in diagnostic studies, especially in cases with rare diseases. ML algorithms have a large number of parameters to train, and the training typically involves a lot of randomness. This poses unique challenges to the reproducibility of trained algorithms (Beam et al. 2020; Hutson 2018). As a consequence, the interpretation of a reported model performance should be undertaken with caution, since it may be over-optimistic, especially in the lack of external validation (Liu et al. 2019; Park and Han 2018).

5 Outlook

It is to be expected that an increasing number of studies will come out, underlying the potential of the abovementioned techniques especially from the field of AI and radiomics. The spectral sensitivity of the new detectors is adding a whole new dimension to the data and this will soon lead to images obtained with lower radiation dose, in shorter times, and bearing greater diagnostic significance. Image quality is just one aspect of the rapid evolution enabled by modern technologies: through automation, the clinical histories of the patients and their individual characteristics are going to become even more relevant in the determination of the investigation parameters, while the automated algorithms will increasingly benefit from the knowledge embedded in billions of archived images. Advancements in the fields of image analysis and radiomics will soon be able to supply the radiologists with a growing number of robust and standardized indicators, seamlessly integrated into clinical devices and information systems.

Most of the improvements presented in this chapter are likely to take a few years, if not a decade, to make their way to the clinical workflow; some of them may even be replaced by newer techniques before they reach full maturity. In the meantime, the evolution of detectors and the advancements of Computer Science will continue to provide even more data and new methods to process it, soon followed by applications to X-ray imaging.

The future of Spectral CT is now!

Compliance with Ethical Standards

Disclosure of Interests None.

Ethical Approval This article does not contain any studies with human participants performed by any of the authors.

This article does not contain any studies with animals performed by any of the authors.

Informed Consent Informed consent was not necessary since the article does not contain any studies with human participants.

References

- Akagi M, Nakamura Y, Higaki T, Narita K, Honda Y, Zhou J, Yu Z, Akino N, Awai K (2019) Deep learning reconstruction improves image quality of abdominal ultra-high-resolution CT. *Eur Radiol* 29:6163–6171. <https://doi.org/10.1007/s00330-019-06170-3>
- Al Ajmi E, Forghani B, Reinhold C, Bayat M, Forghani R (2018) Spectral multi-energy CT texture analysis with machine learning for tissue classification: an investigation using classification of benign parotid tumours as a testing paradigm. *Eur Radiol* 28:2604–2611. <https://doi.org/10.1007/s00330-017-5214-0>
- Bae KT (2010) Intravenous contrast medium administration and scan timing at CT: considerations and approaches. *Radiology* 256:32–61. <https://doi.org/10.1148/radiol.10090908>
- Beam AL, Manrai AK, Ghassemi M (2020) Challenges to the reproducibility of machine learning models in health care. *JAMA* 323:305. <https://doi.org/10.1001/jama.2019.20866>
- Bly R, Jähnen A, Järvinen H, Olerud H, Vassileva J, Vogiatzi S (2015) Collective effective dose in Europe from X-ray and nuclear medicine procedures. *Radiat Prot Dosim* 165:129–132. <https://doi.org/10.1093/rpd/ncv094>
- Booij R, Budde RPJ, Dijkshoorn ML, van Straten M (2019) Accuracy of automated patient positioning in CT using a 3D camera for body contour detection. *Eur Radiol* 29:2079–2088. <https://doi.org/10.1007/s00330-018-5745-z>
- Burns JE, Yao J, Chalhoub D, Chen JJ, Summers RM (2020) A machine learning algorithm to estimate sarcopenia on abdominal CT. *Acad Radiol* 27:311–320. <https://doi.org/10.1016/j.acra.2019.03.011>
- Cano-Espinosa C, González G, Washko GR, Cazorla M, Estépar RSJ (2018) Automated Agatston score computation in non-ECG gated CT scans using deep learning. *Proc SPIE Int Soc Opt Eng*:10574. <https://doi.org/10/gjpxxq>
- Castellano G, Bonilha L, Li LM, Cendes F (2004) Texture analysis of medical images. *Clin Radiol* 59:1061–1069. <https://doi.org/10.1016/j.crad.2004.07.008>
- Chalkidou A, O'Doherty MJ, Marsden PK (2015) False discovery rates in PET and CT studies with texture features: a systematic review. *PLoS One* 10:e0124165. <https://doi.org/10.1371/journal.pone.0124165>
- Chen Z, Li L (2019) Robust multimaterial decomposition of spectral CT using convolutional neural networks. *Opt Eng* 58:1. <https://doi.org/10.1117/1.OE.58.1.013104>
- Cheng Y, Smith TB, Jensen CT, Liu X, Samei E (2020) Correlation of algorithmic and visual assessment of lesion detection in clinical images. *Acad Radiol* 27:847–855. <https://doi.org/10.1016/j.acra.2019.07.015>
- Choi B, Choi IY, Cha SH, Yeom SK, Chung HH, Lee SH, Cha J, Lee J-H (2020) Feasibility of computed tomography texture analysis of hepatic fibrosis using dual-energy spectral detector computed tomography. *Jpn J Radiol*. <https://doi.org/10.1007/s11604-020-01020-5>
- Colevray, M., Tatard-Leitman, VM., Gouttard, S., Douek, P., Bussel, L., 2019. Convolutional neural network evaluation of over-scanning in lung computed tomography. *Diagn Interv Imaging* 100, 177–183. doi:<https://doi.org/10.1016/j.diii.2018.11.001>
- Commandeur F, Goeller M, Betancur J, Cadet S, Doris M, Chen X, Berman DS, Slomka PJ, Tamarappoo BK, Dey D (2018) Deep learning for quantification of Epicardial and thoracic adipose tissue from non-contrast CT. *IEEE Trans Med Imaging* 37:1835–1846. <https://doi.org/10/df7b>
- Dabiri S, Popuri K, Cespedes Feliciano EM, Caan BJ, Baracos VE, Beg MF (2019) Muscle segmentation in axial computed tomography (CT) images at the lumbar (L3) and thoracic (T4) levels for body composition analysis. *Comput Med Imaging Graph* 75:47–55. <https://doi.org/10.1016/j.compmedimag.2019.04.007>
- Den Harder AM, Willeminck MJ, De Ruiter QMB, De Jong PA, Schilham AMR, Krestin GP, Leiner T, Budde RPJ (2015a) Dose reduction with iterative reconstruction for coronary CT angiography: a systematic review and meta-analysis. *BJR* 89:20150068. <https://doi.org/10.1259/bjr.20150068>
- Den Harder AM, Willeminck MJ, de Ruiter QMB, Schilham AMR, Krestin GP, Leiner T, de Jong PA, Budde RPJ (2015b) Achievable dose reduction using iterative reconstruction for chest computed tomography: a systematic review. *Eur J Radiol* 84:2307–2313. <https://doi.org/10.1016/j.ejrad.2015.07.011>
- Depeursinge A, Foncubierta-Rodriguez A, Vargas A, Van de Ville D, Platon A, Poletti P-A, Muller H (2013) Rotation-covariant texture analysis of 4D dual-energy CT as an indicator of local pulmonary perfusion. In: 2013 IEEE 10th International Symposium on Biomedical Imaging. Presented at the 2013 IEEE 10th International Symposium on Biomedical Imaging (ISBI 2013). IEEE, San Francisco, CA, pp 145–148. <https://doi.org/10.1109/ISBI.2013.6556433>
- Dong J, Fu J, He Z (2019) A deep learning reconstruction framework for X-ray computed tomography with incomplete data. *PLoS One* 14:e0224426. <https://doi.org/10.1371/journal.pone.0224426>

- Euler A, Saltybaeva N, Alkadhi H (2019) How patient off-centering impacts organ dose and image noise in pediatric head and thoracoabdominal CT. *Eur Radiol* 29:6790–6793. <https://doi.org/10/gjpxxn>
- Filev PD, Mittal PK, Tang X, Duong P-A, Wang X, Small WC, Applegate K, Moreno CC (2016) Increased computed tomography dose due to Miscentering with use of automated tube voltage selection: phantom and patient study. *Curr Probl Diagn Radiol* 45:265–270. <https://doi.org/10.1067/j.cpradiol.2015.11.003>
- Forghani R, Chatterjee A, Reinhold C, Pérez-Lara A, Romero-Sanchez G, Ueno Y, Bayat M, Alexander JWM, Kadi L, Chankowsky J, Seuntjens J, Forghani B (2019) Head and neck squamous cell carcinoma: prediction of cervical lymph node metastasis by dual-energy CT texture analysis with machine learning. *Eur Radiol* 29:6172–6181. <https://doi.org/10.1007/s00330-019-06159-y>
- Gjesteby L, Shan H, Yang Q, Xi Y, Jin Y, Giantsoudi D, Paganetti H, Man BD, Wang G (2019) A dual-stream deep convolutional network for reducing metal streak artifacts in CT images. *Phys Med Biol* 64:235003. <https://doi.org/10.1088/1361-6560/ab4e3e>
- Grant KL, Flohr TG, Krauss B, Sedlmair M, Thomas C, Schmidt B (2014) Assessment of an advanced image-based technique to calculate virtual Monoenergetic computed tomographic images from a dual-energy examination to improve contrast-to-noise ratio in examinations using iodinated contrast media. *Investig Radiol* 49:586–592. <https://doi.org/10.1097/RLI.0000000000000060>
- Große Hokamp N, Lennartz S, Salem J, Pinto dos Santos D, Heidenreich A, Maintz D, Haneder S (2020) Dose independent characterization of renal stones by means of dual energy computed tomography and machine learning: an ex-vivo study. *Eur Radiol* 30:1397–1404. <https://doi.org/10.1007/s00330-019-06455-7>
- Gudjonsdottir J, Svensson JR, Campling S, Brennan PC, Jonsdottir B (2009) Efficient use of automatic exposure control systems in computed tomography requires correct patient positioning. *Acta Radiol*. <https://doi.org/10.3109/02841850903147053>
- Habibzadeh MA, Ay MR, Asl ARK, Ghadiri H, Zaidi H (2012) Impact of miscentering on patient dose and image noise in x-ray CT imaging: phantom and clinical studies. *Phys Med* 28:191–199. <https://doi.org/10.1016/j.ejmp.2011.06.002>
- Halevy A, Norvig P, Pereira F (2009) The unreasonable effectiveness of data. *IEEE Intell Syst* 24:8–12. <https://doi.org/10.1109/MIS.2009.36>
- Han, D., Yu, Y., He, T., Yu, N., Dang, S., Wu, H., Ren, J., Duan, X., 2021. Effect of radiomics from different virtual monochromatic images in dual-energy spectral CT on the WHO/ISUP classification of clear cell renal cell carcinoma. *Clin Radiol* S0009926021002063. <https://doi.org/10/gkjhj5>
- Hendriks BMF, Eijssvoegel NG, Kok M, Martens B, Wildberger JE, Das M (2018) Optimizing pulmonary embolism computed tomography in the age of individualized medicine: a prospective clinical study. *Investig Radiol* 53:306–312. <https://doi.org/10.1097/RLI.0000000000000443>
- Higaki T, Nakamura Y, Zhou J, Yu Z, Nemoto T, Tatsugami F, Awai K (2020) Deep learning reconstruction at CT: phantom study of the image characteristics. *Acad Radiol* 27:82–87. <https://doi.org/10.1016/j.acra.2019.09.008>
- Higashigaito K, Husarik DB, Barthelmes J, Plass AR, Manka R, Maisano F, Alkadhi H (2016) Computed tomography angiography of coronary artery bypass grafts: low contrast media volume protocols adapted to tube voltage. *Investig Radiol* 51:241–248. <https://doi.org/10.1097/RLI.0000000000000233>
- Homayounieh F, Singh R, Nitiwarangkul C, Lades F, Schmidt B, Sedlmair M, Saini S, Kalra MK (2020) Semiautomatic segmentation and Radiomics for dual-energy CT: a pilot study to differentiate benign and malignant hepatic lesions. *Am J Roentgenol* 215:398–405. <https://doi.org/10/gkjhj9>
- Hong Y, Commandeur F, Cadet S, Goeller M, Doris MK, Chen X, Kwiecinski J, Berman DS, Slomka PJ, Chang H-J, Dey D (2019) Deep learning-based stenosis quantification from coronary CT angiography. *Proc SPIE Int Soc Opt Eng* 10949. <https://doi.org/10.1117/12.2512168>
- Husarik DB, Gordic S, Desbiolles L, Krauss B, Leschka S, Wildermuth S, Alkadhi H (2015) Advanced virtual Monoenergetic computed tomography of Hyperattenuating and Hypoattenuating liver lesions: ex-vivo and patient experience in various body sizes. *Investig Radiol* 50:695–702. <https://doi.org/10.1097/RLI.0000000000000171>
- Hutson M (2018) Artificial intelligence faces reproducibility crisis. *Science* 359:725–726. <https://doi.org/10.1126/science.359.6377.725>
- Jensen CT, Wagner-Bartak NA, Vu LN, Liu X, Raval B, Martinez D, Wei W, Cheng Y, Samei E, Gupta S (2018) Detection of colorectal hepatic metastases is superior at standard radiation dose CT versus reduced dose CT. *Radiology* 290:400–409. <https://doi.org/10.1148/radiol.2018181657>
- Jiang Y, Yang C, Yang P, Hu X, Luo C, Xue Y, Xu L, Hu X, Zhang L, Wang J, Sheng K, Niu T (2019) Scatter correction of cone-beam CT using a deep residual convolution neural network (DRCNN). *Phys Med Biol* 64:145003. <https://doi.org/10.1088/1361-6560/ab23a6>
- Kaasalainen T, Mäkelä T, Kortensniemi M (2019) The effect of vertical centering and scout direction on automatic tube voltage selection in chest CT: a preliminary phantom study on two different CT equipments. *Eur J Radiol Open* 6:24–32. <https://doi.org/10.1016/j.ejro.2018.12.001>
- Korporaal JG, Mahnken AH, Ferda J, Hausleiter J, Baxa J, Flohr TG, Schmidt BT (2015) Quantitative evaluation of the performance of a new test BolusYBased computed tomographic angiography contrast-EnhancementYPrediction algorithm. *Investig Radiol* 50:8

- Le Coultre R, Bize J, Champendal M, Wittwer D, Ryckx N, Aroua A, Trueb P, Verdun FR (2016) Exposure of the Swiss population by radiodiagnostics: 2013 review. *Radiat Prot Dosim* 169:221–224. <https://doi.org/10.1093/rpd/ncv462>
- Lee H, Troschel FM, Tajmir S, Fuchs G, Mario J, Fintelmann FJ, Do S (2017) Pixel-level deep segmentation: artificial intelligence quantifies muscle on computed tomography for body morphometric analysis. *J Digit Imaging* 30:487–498. <https://doi.org/10/gjpxxp>
- Lell MM, Fleischmann U, Pietsch H, Korporea JG, Haberland U, Mahnken AH, Flohr TG, Uder M, Jost G (2017) Relationship between low tube voltage (70 kV) and the iodine delivery rate (IDR) in CT angiography: an experimental in-vivo study. *PLoS One* 12:e0173592. <https://doi.org/10.1371/journal.pone.0173592>
- Li C, Lin X, Hui C, Lam KM, Zhang S (2016) Computer-aided diagnosis for distinguishing pancreatic mucinous cystic neoplasms from serous Oligocystic adenomas in spectral CT images. *Technol Cancer Res Treat* 15:44–54. <https://doi.org/10.1177/1533034614563013>
- Li C, Shi C, Zhang H, Hui C, Lam KM, Zhang S (2015) Computer-aided diagnosis for preoperative invasion depth of gastric cancer with dual-energy spectral CT imaging. *Acad Radiol* 22:149–157. <https://doi.org/10.1016/j.acra.2014.08.006>
- Li J, Dong D, Fang M, Wang R, Tian J, Li H, Gao J (2020a) Dual-energy CT-based deep learning radiomics can improve lymph node metastasis risk prediction for gastric cancer. *Eur Radiol* 30:2324–2333. <https://doi.org/10/gkhjgt>
- Li J, Udayasankar UK, Toth TL, Seamans J, Small WC, Kalra MK (2007) Automatic patient centering for MDCT: effect on radiation dose. *Am J Roentgenol* 188:547–552. <https://doi.org/10.2214/AJR.06.0370>
- Li L, Fan Y, Tse M, Lin K-Y (2020b) A review of applications in federated learning. *Comput Ind Eng* 149:106854. <https://doi.org/10.1016/j.cie.2020.106854>
- Liang K, Zhang L, Yang H, Yang Y, Chen Z, Xing Y (2019) Metal artifact reduction for practical dental computed tomography by improving interpolation-based reconstruction with deep learning. *Med Phys* 46:e823–e834. <https://doi.org/10.1002/mp.13644>
- Liu P, Wang M, Wang Y, Yu M, Wang Y, Liu Z, Li Y, Jin Z (2020) Impact of deep learning-based optimization algorithm on image quality of low-dose coronary CT angiography with noise reduction: a prospective study. *Acad Radiol* 27:1241–1248. <https://doi.org/10.1016/j.acra.2019.11.010>
- Liu Y, Chen P-HC, Krause J, Peng L (2019) How to read articles that use machine learning: users' guides to the medical literature. *JAMA* 322:1806. <https://doi.org/10.1001/jama.2019.16489>
- Mahnken AH, Rauscher A, Klotz E, Mühlenbruch G, Das M, Günther RW, Wildberger JE (2007) Quantitative prediction of contrast enhancement from test bolus data in cardiac MSCT. *Eur Radiol* 17:1310–1319. <https://doi.org/10.1007/s00330-006-0486-9>
- Maier J, Eulig E, Vöth T, Knaup M, Kuntz J, Sawall S, Kachelrieß M (2019) Real-time scatter estimation for medical CT using the deep scatter estimation: method and robustness analysis with respect to different anatomies, dose levels, tube voltages, and data truncation. *Med Phys* 46:238–249. <https://doi.org/10.1002/mp.13274>
- Mannil M, von Spiczak J, Manka R, Alkadhi H (2018) Texture analysis and machine learning for detecting myocardial infarction in noncontrast low-dose computed tomography: unveiling the invisible. *Investig Radiol* 53:338–343. <https://doi.org/10.1097/RLI.0000000000000448>
- Marsh RM, Silosky MS (2017) The effects of patient positioning when interpreting CT dose metrics: a phantom study. *Med Phys* 44:1514–1524. <https://doi.org/10/gjpxxm>
- Martens B, Hendriks BMF, Eijvoogel NG, Wildberger JE, Muhl C (2019) Individually body weight-adapted contrast media application in computed tomography imaging of the Liver at 90 kVp. *Investig Radiol* 54:177–182. <https://doi.org/10.1097/RLI.0000000000000525>
- Matsubara K, Koshida K, Ichikawa K, Suzuki M, Takata T, Yamamoto T, Matsui O (2009) Misoperation of CT automatic tube current modulation systems with inappropriate patient centering: phantom studies. *Am J Roentgenol* 192:862–865. <https://doi.org/10.2214/AJR.08.1472>
- Mettler FA, Bhargavan M, Faulkner K, Gilley DB, Gray JE, Ibbott GS, Lipoti JA, Mahesh M, McCrohan JL, Stabin MG, Thomadsen BR, Yoshizumi TT (2009) Radiologic and nuclear medicine studies in the United States and worldwide: frequency, radiation dose, and comparison with other radiation sources—1950–2007. *Radiology* 253:520–531. <https://doi.org/10.1148/radiol.2532082010>
- Mühlberg A, Katzmann A, Heinemann V, Kärger R, Wels M, Taubmann O, Lades F, Huber T, Maurus S, Holch J, Faivre J-B, Stühling M, Nörenberg D, Rémy-Jardin M (2020) The Technome - a predictive internal calibration approach for quantitative imaging biomarker research. *Sci Rep* 10:1103. <https://doi.org/10.1038/s41598-019-57325-7>
- Niemann T, Henry S, Faivre J-B, Yasunaga K, Bendaoud S, Simeone A, Remy J, Duhamel A, Flohr T, Remy-Jardin M (2013) Clinical evaluation of automatic tube voltage selection in chest CT angiography. *Eur Radiol* 23:2643–2651. <https://doi.org/10.1007/s00330-013-2887-x>
- Nijssen EC, Nelemans PJ, Rennenberg RJ, Theunissen RA, van Ommen V, Wildberger JE (2019) Prophylaxis in high-risk patients with eGFR < 30 mL/min/1.73 m². *Investig Radiol* 54(9):580–588
- Papadakis AE, Damilakis J (2019) Automatic tube current modulation and tube voltage selection in pediatric computed tomography: a phantom study on radiation dose and image quality. *Investig Radiol* 54:265–272. <https://doi.org/10.1097/RLI.0000000000000537>
- Park SH, Han K (2018) Methodologic guide for evaluating clinical performance and effect of artificial

- intelligence technology for medical diagnosis and prediction. *Radiology* 286:800–809. <https://doi.org/10.1148/radiol.2017171920>
- Pola A, Corbella D, Righini A, Torresin A, Colombo PE, Vismara L, Trombetta L, Maddalo M, Introini MV, Tinelli D, Strohmenger L, Garattini G, Munari A, Triulzi F (2018) Computed tomography use in a large Italian region: trend analysis 2004–2014 of emergency and outpatient CT examinations in children and adults. *Eur Radiol* 28:2308–2318. <https://doi.org/10.1007/s00330-017-5225-x>
- Racine D, Becce F, Viry A, Monnin P, Thomsen B, Verdun FR, Rotzinger DC (2020) Task-based characterization of a deep learning image reconstruction and comparison with filtered back-projection and a partial model-based iterative reconstruction in abdominal CT: a phantom study. *Phys Med* 76:28–37. <https://doi.org/10.1016/j.ejmp.2020.06.004>
- Rieke N, Hancox J, Li W, Milletari F, Roth HR, Albarqouni S, Bakas S, Galtier MN, Landman BA, Maier-Hein K, Ourselin S, Sheller M, Summers RM, Trask A, Xu D, Baust M, Cardoso MJ (2020) The future of digital health with federated learning. *NPJ Digit Med* 3:119. <https://doi.org/10.1038/s41746-020-00323-1>
- Saltybaeva N, Alkadhi H (2017) Vertical off-centering affects organ dose in chest CT: evidence from Monte Carlo simulations in anthropomorphic phantoms. *Med Phys* 44:5697–5704. <https://doi.org/10/gbhpwdd>
- Saltybaeva N, Schmidt B, Wimmer A, Flohr T, Alkadhi H (2018) Precise and automatic patient positioning in computed tomography: avatar modeling of the patient surface using a 3-dimensional camera. *Investig Radiol* 53:641–646. <https://doi.org/10/ggrmf>
- Samei E, Bakalyar D, Boedeker KL, Brady S, Fan J, Leng S, Myers KJ, Popescu LM, Giraldo JCR, Ranallo F, Solomon J, Vaishnav J, Wang J (2019) Performance evaluation of computed tomography systems: summary of AAPM task group 233. *Med Phys* 46:e735–e756. <https://doi.org/10.1002/mp.13763>
- Schindera ST, Graca P, Patak MA, Abderhalden S, von Allmen G, Vock P, Szucs-Farkas Z (2009) Thoracoabdominal-Aortoiliac multidetector-row CT angiography at 80 and 100 kVp: assessment of image quality and radiation dose. *Investig Radiol* 44:650–655. <https://doi.org/10.1097/RLI.0b013e3181acaf8a>
- Schindera ST, Odedra D, Raza SA, Kim TK, Jang H-J, Szucs-Farkas Z, Rogalla P (2013) Iterative reconstruction algorithm for CT: can radiation dose be decreased while low-contrast detectability is preserved? *Radiology* 269:511–518. <https://doi.org/10.1148/radiol.13122349>
- Schmidt C, Baessler B, Nakhostin D, Das A, Eberhard M, Alkadhi H, Euler A (2020) Dual-energy CT-based iodine quantification in liver tumors—impact of scan-, patient-, and position-related factors. *Acad Radiol* 28(6):783–789. S1076633220302142. <https://doi.org/10.1016/j.acra.2020.04.021>
- Schwartz F, Stieltjes B, Szucs-Farkas Z, Euler A (2018) Over-scanning in chest CT: comparison of practice among six hospitals and its impact on radiation dose. *Eur J Radiol* 102:49–54. <https://doi.org/10.1016/j.ejrad.2018.03.005>
- Skawran S, Angst F, Blüthgen C, Eberhard M, Kälin P, Kobe A, Nagy D, Szucs-Farkas Z, Alkadhi H, Euler A (2020) Dual-energy low-keV or single-energy low-kV CT for Endoleak detection?: a 6-reader study in an aortic aneurysm phantom. *Investig Radiol* 55:45–52. <https://doi.org/10.1097/RLI.0000000000000606>
- Smith TB, Solomon JB, Samei E (2017) Estimating detectability index in vivo: development and validation of an automated methodology. *JMI* 5:031403. <https://doi.org/10.1117/1.JMI.5.3.031403>
- Smith-Bindman R, Wang Y, Chu P, Chung R, Einstein AJ, Balcombe J, Cocker M, Das M, Delman BN, Flynn M, Gould R, Lee RK, Yellen-Nelson T, Schindera S, Seibert A, Starkey J, Suntharalingam S, Wetter A, Wildberger JE, Miglioretti DL (2019) International variation in radiation dose for computed tomography examinations: prospective cohort study. *BMJ* 364. <https://doi.org/10.1136/bmj.k4931>
- Solomon J, Mileto A, Ramirez-Giraldo JC, Samei E (2015) Diagnostic performance of an advanced modeled iterative reconstruction algorithm for low-contrast detectability with a third-generation dual-source multidetector CT scanner: potential for radiation dose reduction in a multireader study. *Radiology* 275:735–745. <https://doi.org/10.1148/radiol.15142005>
- Tatsugami F, Higaki T, Nakamura Y, Yu Z, Zhou J, Lu Y, Fujioka C, Kitagawa T, Kihara Y, Iida M, Awai K (2019) Deep learning-based image restoration algorithm for coronary CT angiography. *Eur Radiol* 29:5322–5329. <https://doi.org/10.1007/s00330-019-06183-y>
- van Timmeren J, Cester D, Tanadini-Lang S, Alkadhi H, Baessler B (2020) Radiomics in medical imaging – “how-to” guide and critical reflection. *Insights Imaging* 11(1):1–16
- Toth T, Ge Z, Daly MP (2007) The influence of patient centering on CT dose and image noise. *Med Phys* 34:3093–3101. <https://doi.org/10.1118/1.2748113>
- Tourassi GD (1999) Journey toward computer-aided diagnosis: role of image texture analysis. *Radiology* 213:317–320. <https://doi.org/10.1148/radiology.213.2.r99nv49317>
- Umehara K, Ota J, Ishida T (2018) Application of super-resolution convolutional neural network for enhancing image resolution in chest CT. *J Digit Imaging* 31:441–450. <https://doi.org/10.1007/s10278-017-0033-z>
- Wang Y, Qiu Y, Thai T, Moore K, Liu H, Zheng B (2017) A two-step convolutional neural network based computer-aided detection scheme for automatically segmenting adipose tissue volume depicting on CT images. *Comput Methods Prog Biomed* 144:97–104. <https://doi.org/10/gbgxvq>
- Weston AD, Korfiatis P, Kline TL, Philbrick KA, Kostandy P, Sakinis T, Sugimoto M, Takahashi N, Erickson BJ (2019) Automated abdominal segmentation of CT scans for body composition analysis using deep learning. *Radiology* 290:669–679. <https://doi.org/10/ggv9fz>

- Willeminck MJ, Leiner T, de Jong PA, de Heer LM, Nivelstein RAJ, Schilham AMR, Budde RPJ (2013) Iterative reconstruction techniques for computed tomography part 2: initial results in dose reduction and image quality. *Eur Radiol* 23:1632–1642. <https://doi.org/10.1007/s00330-012-2764-z>
- Winklehner A, Goetti R, Baumüller S, Karlo C, Schmidt B, Raupach R, Flohr T, Frauenfelder T, Alkadhi H (2011) Automated attenuation-based tube potential selection for Thoracoabdominal computed tomography angiography: improved dose effectiveness. *Investig Radiol* 46:767–773. <https://doi.org/10.1097/RLI.0b013e3182266448>
- Winslow J, Zhang Y, Koweek L, Samei E (2018) Dependency of prescribed CT dose on table height, patient size, and localizer acquisition for one clinical MDCT. *Phys Med* 55:56–60. <https://doi.org/10.1016/j.fqd6h>
- Wolterink JM, Leiner T, Viergever MA, Išgum I (2017) Generative adversarial networks for noise reduction in low-dose CT. *IEEE Trans Med Imaging* 36:2536–2545. <https://doi.org/10.1109/TMI.2017.2708987>
- Wu J, Zhang Q, Zhao Y, Liu Y, Chen A, Li X, Wu T, Li J, Guo Y, Liu A (2019) Radiomics analysis of iodine-based material decomposition images with dual-energy computed tomography imaging for pre-operatively predicting microsatellite instability status in colorectal cancer. *Front Oncol* 9:1250. <https://doi.org/10.3389/fonc.2019.01250>
- Yu L, Fletcher JG, Grant KL, Carter RE, Hough DM, Barlow JM, Vrtiska TJ, Williamson EE, Young PM, Goss BC, Shiung M, Leng S, Raupach R, Schmidt B, Flohr T, McCollough CH (2013) Automatic selection of tube potential for radiation dose reduction in vascular and contrast-enhanced abdominopelvic CT. *Am J Roentgenol* 201:W297–W306. <https://doi.org/10.2214/AJR.12.9610>
- Zanca F, Demeter M, Oyen R, Bosmans H (2012) Excess radiation and organ dose in chest and abdominal CT due to CT acquisition beyond expected anatomical boundaries. *Eur Radiol* 22:779–788. <https://doi.org/10.1007/s00330-011-2332-y>
- Zhou Y, Su G-Y, Hu H, Ge Y-Q, Si Y, Shen M-P, Xu X-Q, Wu F-Y (2020) Radiomics analysis of dual-energy CT-derived iodine maps for diagnosing metastatic cervical lymph nodes in patients with papillary thyroid cancer. *Eur Radiol* 30:6251–6262. <https://doi.org/10/gkhjhh>
- Zimmerman KC, Sharma G, Parchur AK, Joshi A, Schmidt TG (2020) Experimental investigation of neural network estimator and transfer learning techniques for K-edge spectral CT imaging. *Med Phys* 47:541–551. <https://doi.org/10.1002/mp.13946>
- Zopfs D, Bousabarah K, Lennartz S, dos Santos DP, Schlaak M, Theurich S, Reimer RP, Maintz D, Haneder S, Große Hokamp N (2020) Evaluating body composition by combining quantitative spectral detector computed tomography and deep learning-based image segmentation. *Eur J Radiol* 130:109153. <https://doi.org/10.1016/j.ejrad.2020.109153>
- Zwanenburg, A., Leger, S., Vallières, M., Löck, S., 2016. Image biomarker standardisation initiative
- Zwanenburg A, Vallières M, Abdalah MA, Aerts HWJL, Andrearczyk V, Apte A, Ashrafinia S, Bakas S, Beukinga RJ, Boellaard R, Bogowicz M, Boldrini L, Buvat I, Cook GJR, Davatzikos C, Depeursinge A, Desserot M-C, Dinapoli N, Dinh CV, Echegaray S, El Naqa I, Fedorov AY, Gatta R, Gillies RJ, Goh V, Götz M, Guckenberger M, Ha SM, Hatt M, Isensee F, Lambin P, Leger S, Leijenaar RTH, Lenkowicz J, Lippert F, Losnegård A, Maier-Hein KH, Morin O, Müller H, Napel S, Nioche C, Orhac F, Pati S, Pfaehler EAG, Rahmim A, Rao AUK, Scherer J, Siddique MM, Sijtsema NM, Socarras Fernandez J, Spezi E, Steenbakkers RJHM, Tanadini-Lang S, Thorwarth D, Troost EGC, Upadhaya T, Valentini V, van Dijk LV, van Griethuysen J, van Velden FHP, Whybra P, Richter C, Löck S (2020) The image biomarker standardization initiative: standardized quantitative Radiomics for high-throughput image-based phenotyping. *Radiology*:191145. <https://doi.org/10.1148/radiol.2020191145>



Photon-Counting CT: Initial Clinical Experience

Victor Mergen, André Euler, Kai Higashigaito, Matthias Eberhard, and Hatem Alkadhi

Contents

1	Introduction	363
2	Technical Specifications	364
3	Cardiovascular Imaging	365
4	Abdominal Imaging	367
5	Lung Imaging	369
6	Skeletal Imaging	372
7	Conclusions	373
	References	373

1 Introduction

Photon-counting detector computed tomography (PCD-CT) is an emerging technology and represents the next milestone in CT developments. Compared to conventional energy-integrating detectors in which an indirect conversion technology is used to detect incident photons, PCD technology uses semiconductors that directly convert X-ray photons to an electrical signal. This generated signal includes the energy infor-

mation of every individually detected photon enabling intrinsic spectral imaging in every CT scan.

The clinical benefits of PCD-CTs are the elimination of classical electronic noise (Yu et al. 2016; Sartoretti et al. 2020; Sartoretti et al. 2021; Symons et al. 2018; Flohr et al. 2020a; Ferda et al. 2021), a higher spatial resolution (Flohr et al. 2020a; Leng et al. 2016; Pourmorteza et al. 2018; von Spiczak et al. 2018; Mannil et al. 2018), reduction of metal artifacts (Do et al. 2020; Zhou et al. 2019), improved iodine contrast-to-noise ratio (CNR) (Symons et al. 2018; Flohr et al. 2020a; Gutjahr et al. 2016a; Schmidt 2009; Symons et al. 2019), and improved radiation dose efficiency (Symons et al. 2019; Alkadhi and Euler 2020; Leng et al. 2018). Simultaneous multi-energy acquisition at a single

V. Mergen · A. Euler · K. Higashigaito · M. Eberhard
H. Alkadhi (✉)
Institute of Diagnostic and Interventional Radiology,
University Hospital Zurich, Zurich, Switzerland
e-mail: victor.mergen@usz.ch; andre.euler@usz.ch;
kai.higashigaito@usz.ch; matthias.eberhard@usz.ch;
hatem.alkadhi@usz.ch

X-ray tube potential also permits new ways of advanced data processing. The energy of every transmitted photon is allocated between multiple energy thresholds, called bins, leading to energy-based attenuation profiles of tissue. This allows, for example, for the simultaneous detection of one or more k-edge contrast agents. The specific visualization of exogenous contrast agent enables single-scan multiphase imaging demonstrating a new way of functional imaging (Tao et al. 2019; Si-Mohamed et al. 2019; Symons et al. 2017a). In addition, virtual non-contrast reconstructions can be computed obviating the need for additional non-enhanced scans thus substantially reducing the radiation dose of the examination (Alkadhi and Euler 2020; Tao et al. 2019; Symons et al. 2017a; Leng et al. 2019). PCD-CT offers new options for material decomposition and quantification. For example, this novel imaging technique is capable of quantifying bone mineral density from localizer radiographs (Nowak et al. 2021), assessing the macrophage burden in atherosclerotic plaques using gold nanoparticles (Si-Mohamed et al. 2021) and differentiating between blood and iodine (Riederer et al. 2019) or between calcium pyrophosphate and hydroxyapatite deposits (Stamp et al. 2019).

In April 2021, we got the first worldwide PCD-CT system for full clinical use installed in our radiology department. In this chapter, we briefly explain the technical aspects of PCD-CT and present our first experience with this new CT system with benefits highlighted with several clinical case examples. For a detailed description of the underlying physical principles of PCD-CT please refer to Chap. 6.

2 Technical Specifications

Current medical CT systems use energy-integrating detectors (EID) in which the incident photons are converted into an electrical signal during a two-step detection process. The EID consist of a scintillation crystal attached to a photodiode made of semiconducting material. During the detection process, the incident X-rays first strike the scintillation crystal and generate

secondary visible light photons. These are absorbed by the photodiode and are converted into an electrical signal. The intensity of the generated electrical signal depends on the amount of incident photons and is proportional to the total energy deposited during a measurement interval. Based on their detection principle, these detectors are called “energy-integrating detectors” and do not provide energy-resolved signals. The EIDs are separated by thin, optically intransparent collimator blades to prevent optical cross-talk (Flohr et al. 2020a; Alkadhi and Euler 2020; Leng et al. 2019; Willeminck et al. 2018; Flohr et al. 2020b).

Significant progress in the fields of detector materials, electronics and software allowed the development of PCD-CTs during the last few years. In 2021, Siemens Healthineers, Forchheim (Germany), presented the world’s first PCD-CT for full clinical use, the NAEOTOM Alpha, heralding a new era of CT imaging.

The underlying principle in PCD-CT is the use of a semiconductor diode capable of directly converting the incident photons into an electrical signal. Research focused on cadmium telluride (CdTe), cadmium zinc telluride (CdZnTe), and silicon (Si) as semiconductor material. Between the cathode at the top of the thick layer of semiconductor material (1.4–30 mm depending on material) and the pixelated anode at the bottom a strong electric field is applied. During imaging the incident photon is absorbed in the photoconductor and creates an electron-hole pair. The electrons are immediately attracted by the anode and induce short currents of a few nanoseconds (10^{-9} s). The height of the voltage pulse is directly proportional to the amount of absorbed charge and is counted when exceeding a defined energy threshold level. The strong electrical field between the cathode and the pixelated anode obviates the need for collimator blades and increases geometrical dose efficiency. Moreover, current pulses are counted only when exceeding a preset energy threshold level, set above the electronic noise level, but lower than pulses generated by striking photons reducing electronic noise in the generated images. By defining several threshold levels, PCD can assign the incoming photons to precise energy bins, thus

generating energy-based attenuation profiles of tissue (Tao et al. 2019; Leng et al. 2019; Willeminck et al. 2018; Flohr et al. 2020b).

Current challenges with PCD-CT systems are cross-talk and pile-up. Due to physical effects a single incident photon may be erroneously registered in two different detectors referred to as cross-talk. If the photon is absorbed at the border of neighboring PCD charge sharing may occur during which the generated charge is detected by more than one PCD with only part of the original energy registered in each. In addition, secondary photons may be generated during the absorption process in the PCD, or because of Compton scatter or in the form of fluorescent X-rays. These secondary photons diverge randomly and can be registered in neighbored detectors. Cross-talk deteriorates the image’s spatial resolution and contrast-to-noise ratio as well as its energy resolution. During medical imaging, PCD need a fast read-out of the incident photons. If consecutive photons hit the PCD too closely in time, the electrical pulses will superimpose on each other, a phenomenon called pulse pile-up. Pule pile-up impairs image noise and measured signal as less photons contribute to the image and influences energy resolution (Flohr et al. 2020a; Alkadhi and Euler 2020; Tao et al. 2019; Willeminck et al. 2018; Flohr et al. 2020b).

The NAEOTOM Alpha is the world’s first dual-source PCD-CT system for full clinical use and was installed in April 2021 at our Department in the University Hospital Zurich, Switzerland. This system uses cadmium telluride (CdTe) as semiconductor material. The X-ray tubes can be operated at voltages up to 140 kVp, the tube current can be set to values between 10 and 1300 mA and the shortest rotation time of the system is 0.25 s. Further technical specifications of this system can be found in Table 1. The PCD consists of sub-pixels, the so-called S1-pixels, measuring $0.2 \times 0.2 \text{ mm}^2$. Figure 1 depicts the precise detector layout. 2×2 sub-pixels form a “macro-pixel,” the so-called M4-pixel, measuring $0.4 \times 0.4 \text{ mm}^2$. The detector provides two energy thresholds per sub-pixel. The sub-pixels can be combined and read-out with different weightings (Table 2). In standard mode 144 macro-pixels

Table 1 Technical specifications of first-generation dual-source photon-counting CT

Detector type	2 × 6 cm photon-counting detector, equipped with four energy thresholds
Rotation time	0.25 s
Temporal resolution	66 ms
Scan speed	737 mm/s
Tube type	2 × VECTRON tubes
Power	2 × 120 kW
Bore size	82 cm

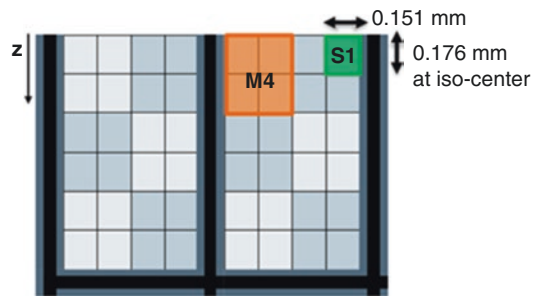


Fig. 1 Photon-counting detector layout of the NAEOTOM Alpha, Siemens Healthineers, Forchheim, Germany

with a z-coverage of 57.6 mm and a spectral image acquisition considering two energy levels is used. Applying the ultra-high-resolution mode, UHR mode, 120 pixels measuring $0.2 \times 0.2 \text{ mm}^2$ with a z-coverage of 24 mm and a spectral image acquisition considering two energy levels are used. A third research mode is available using 96 macro-pixels and differentiating between four energy thresholds.

3 Cardiovascular Imaging

The first-generation dual-source PCD-CT scanner has the advantages of a third-generation dual-source CT with high temporal resolution (gantry rotation time 0.25 s, temporal resolution 66 ms) and fast volume coverage (high pitch with 737 mm/s). In addition, the PCD-CT system offers—through inherent multi-energy capabilities—the possibility of direct reconstruction of virtual monoenergetic images, virtual non-iodine (i.e. non-enhanced) images, iodine maps, and of virtual

Table 2 Acquisition modes of the NAEOTOM Alpha, Siemens Healthineers, Forchheim, Germany

	Detectors	Detector size	z-coverage
Standard mode	1376 M4—pixels	144 × 0.4 mm	57.6 mm
Ultra-high-resolution (UHR) mode	2752 S1—pixels	120 × 0.2 mm	24 mm
Research mode	1376 M4—pixels	96 × 0.4 mm	38.4 mm

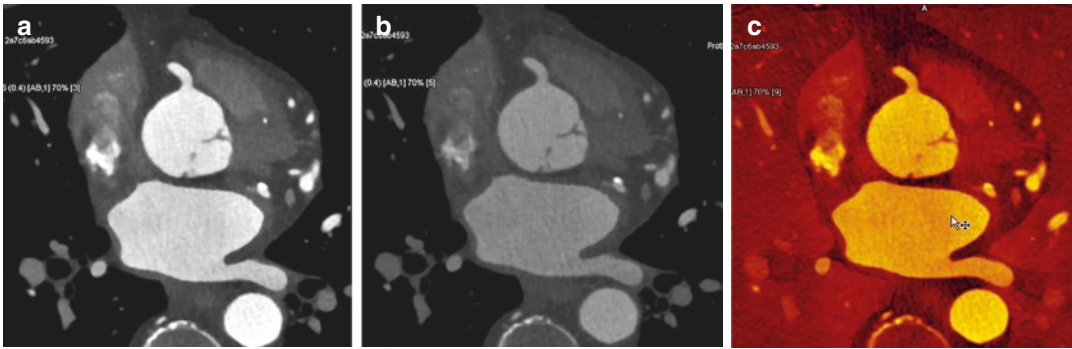


Fig. 2 Cardiac photon-counting detector CT in a 53-year-old male patient with atypical chest pain. (a) Transverse reformation of a virtual monoenergetic image at 45 keV

and (b) at 65 keV. (c) shows corresponding iodine map from material decomposition

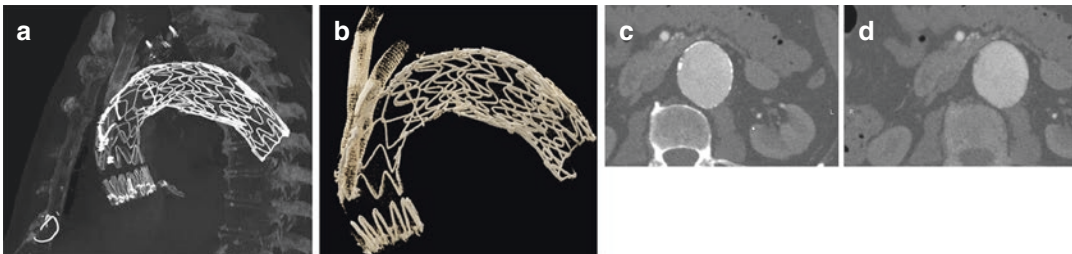


Fig. 3 Photon-counting CT angiography of the chest and abdomen in a 69-year-old male patient after endovascular repair. (a) Maximum intensity projection of virtual monoenergetic images at 190 keV and (b) 3D cinematic rendering of the same dataset show the prosthesis without

artifacts. (c) Transverse axial images at the level of the kidneys showing a partially calcified abdominal aneurysm before and (d) after calcium subtraction (virtual non-calcium image)

non-calcium images from each dataset (Figs. 2 and 3). Also, the multi-energy option opens the door to the potential application of new contrast media in cardiovascular CT imaging (Mergen et al. 2022).

Symons et al. (2019) showed in their study in a calcium phantom, in ex vivo human hearts, and in asymptomatic volunteers the potential of PCD-CT to improve the image quality of coronary artery calcium scoring with the potential to reduce radiation dose at a constant image quality. In another study, Symons et al. (2018) included asymptomatic

subjects for imaging of the major arteries of the head and neck with PCD-CT and found an improved image quality of carotid and intracranial arteries along with fewer artifacts as compared to conventional single-energy CT with energy-integrating detectors. In that study, a head phantom was used to validate iodine concentration measurements in PCD-CT showing an excellent correlation between actual and measured iodine concentrations and in addition a higher CNR in iodine maps compared with non-spectral PCD-CT images.

Sartoretti et al. (2020) investigated the potential of a preclinical prototype PCD-CT scanner with a tungsten-based contrast medium for carotid artery imaging using a human ex vivo specimen with the aim of differentiating between the contrast-enhanced lumen and the calcified vessel wall. Authors could show that PCD-CT employing the multi-energy bin option in combination with tungsten as contrast medium enabled an improved carotid artery imaging with respect to lumen and plaque visualization as well as image noise. In another study, Sartoretti et al. (2021) systematically evaluated the potential of PCD-CT for investigational contrast media for subtraction of calcified plaques in a small vessel phantom. Five contrast media with iodine, bismuth, hafnium, holmium, and tungsten at equal mass concentrations were tested, and authors found that contrast maps with tungsten and, to a lesser extent, with hafnium yielded superior image noise properties and improved vessel lumen visualization including an improved subjective image quality as compared with the reference standard with iodinated contrast media. Si-Mohamed et al. (2021) performed k-edge imaging with a prototype PCD-CT system using both iodinated contrast media and gold nanoparticles to detect and quantify the macrophage burden within the atherosclerotic aortas of rabbits in vivo. Authors found that PCD-CT imaging with gold nanoparticles allowed for the noninvasive evaluation of both molecular and anatomic information of atherosclerotic plaques. Dangelmeier et al. (2018) evaluated in an ex vivo phantom study simulating an abdominal aortic aneurysm a mixture of iodine and gadolinium and could show that PCD-CT was able to differentiate the distributions within different compartments filled with iodine, gadolinium and with calcifications.

The potential of higher spatial resolution of PCD-CT deserves further note. In a phantom study, Mannil et al. (2018) included 18 different coronary stent types, filled with iodinated contrast media, and imaged in different orientations with a prototype PCD-CT scanner. At matched CT scan protocol settings and identical image reconstruction parameters, the PCD system

yielded superior in-stent lumen delineation of stents as compared to conventional scans with energy-integrating detectors. These results could be further improved when using dedicated sharp tissue convolution kernels yielding superior qualitative and quantitative image characteristics of the in-stent lumen (von Spiczak et al. 2018).

Our first study included 40 patients who underwent clinical PCD-CT angiography of the thoraco-abdominal aorta and who had a previous CT angiography on a conventional EID-CT system with automatic tube voltages selection (Euler et al. 2021). Radiation dose at both CT scanners was kept intentionally at the same level. We found that high-pitch PCD-CT angiography of the aorta with reconstruction of virtual monoenergetic images at 40 and 45 keV resulted in a significantly higher contrast-to-noise-ratio, an effect which was pronounced in overweight patients. This indicates the potential for further radiation dose and/or contrast media volume reductions with PCD-CT.

4 Abdominal Imaging

Dual-energy CT has shown beneficial applications in abdominal imaging in the last decades with improvements in, e.g., lesion detection or conspicuity (Shuman et al. 2014; Darras et al. 2019), lesion characterization (Nagayama et al. 2020), tumor treatment response monitoring (Parakh et al. 2018; Jiang et al. 2017; Aoki et al. 2016), evaluation of liver parenchyma (Marri et al. 2021; Elbanna et al. 2020), detection of gallstones (Uyeda et al. 2017), or urinary stone characterization (Zheng et al. 2016; Habashy et al. 2016). However, dual-energy CT exams commonly have to be prospectively ordered and protocolled, particularly on the widely prevalent scanners using fast kVp-switching or dual-source dual-energy CT. The introduction of PCD-CT improves the workflow of CT protocoling because spectral information is available from each image acquisition and can be retrospectively accessed and reconstructed if needed. This saves time and resources for CT protocoling and improves standardization. This holds great potential to improve

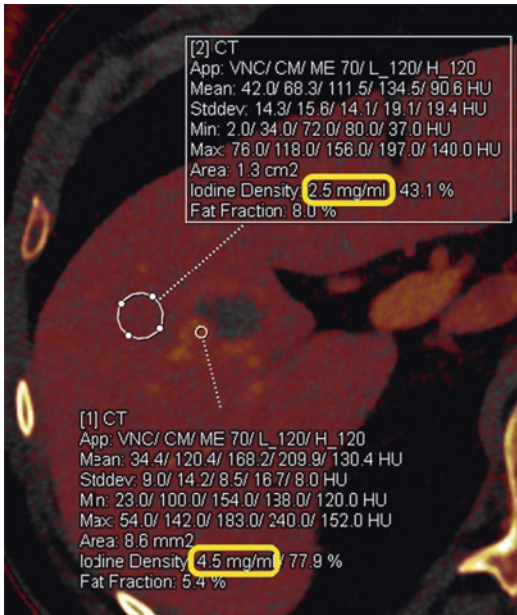


Fig. 4 Iodine map of the right liver lobe showing a hemangioma with increased iodine concentration measured at the lesion's periphery (4.5 mg iodine per mL) as compared to the normal liver parenchyma (2.5 mg iodine per mL). With PCD-CT, the reconstruction of iodine maps has become available from each scan

the characterization of incidental lesions, avoid additional imaging, and decrease patient anxiety. Spectral imaging is automatically available in the standard scan mode, the so-called Quantum Plus mode, with a collimation of 144×0.4 mm and currently utilizing two energy levels.

Classic post-processing options, e.g., virtual non-contrast reconstructions (Sartoretti et al. 2022a), iodine maps (Fig. 4), liver iron or fat fraction estimation as well as characterization of kidney stones or gout are available on PCD-CT and might benefit from the improved spectral separation provided by the novel detector. First preclinical studies have indicated improved characterization of small urinary stones of less than 3 mm as compared to dual-energy EID-CT (Marcus et al. 2018). In addition to these traditional options, the vendor has introduced the routine use of virtual monoenergetic images (VMIs) as the routine diagnostic reading series (Fig. 5).

VMIs-energies (in keV) are optimized based on the desired imaging task and body region (e.g.,

55 keV to improve contrast in vascular imaging and 60 keV to improve CNR in parenchymal imaging). Our first study included 39 patients who underwent clinical abdominal PCD-CT in the portal venous phase who also had a foregoing abdominal CT on a conventional EID-CT system with automatic tube voltages selection (Higashigaito et al. 2021). Radiation dose between systems was intentionally kept constant. Results indicated that PCD-CT with reconstruction of VMI at 50 keV yielded significantly higher contrast-to-noise-ratio in various abdominal organs and vessels as compared to EID-CT. Another recent study showed that image quality of portal-venous phase PCD-CT is further improved by applying the new iterative reconstruction technique of the scanner (i.e., quantum iterative reconstruction) (Sartoretti et al. 2022b).

In addition, the reconstruction of polychromatic images, the so-called T3D images, is available. These images are reconstructed by using the data of the lowest energy threshold at 20 keV in a conventional, non-spectral image reconstruction and aim to emulate the image perception of a conventional polychromatic image at 120 kV. Compared to EID-CT, PCD-CT has the advantage to decrease image noise at low X-ray photon flux by excluding electronic noise (Willeminck et al. 2018). This potentially benefits imaging at very low radiation doses and in large-sized patients.

PCD-CT has the unique capability to discriminate among different contrast agents, e.g., iodine, gadolinium, and bismuth (Tao et al. 2019; Ren et al. 2020). This enables simultaneous multi-contrast agent imaging (Si-Mohamed et al. 2019; Symons et al. 2017a; Willeminck et al. 2018). This in combination with a split-bolus injection and virtual non-contrast imaging could be used to transform traditional three-phase exams on traditional EID-CT (unenhanced, arterial, portal venous phase) to a single-phase acquisition on PCD-CT (Willeminck et al. 2018). To date, however, multi-contrast imaging on PCD-CT has been limited to animal models due to the current off-label use of different contrast agents in CT imaging of humans.

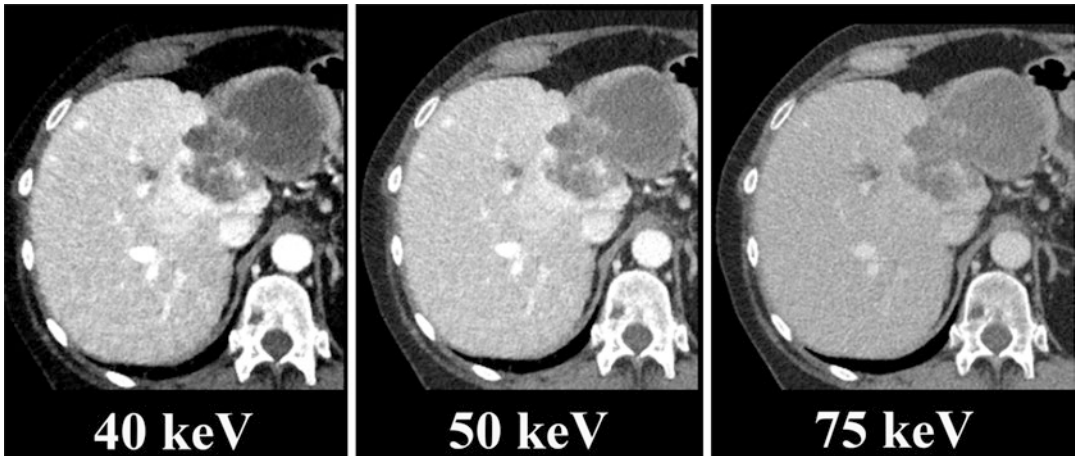


Fig. 5 Axial virtual monoenergetic CT images at different energies of a 55-year-old male patient with an intrahepatic cholangiocarcinoma of the left liver lobe. Note the

substantially increasing CT attenuation of the ring enhancement of the lesion with decreasing keV level

5 Lung Imaging

CT has a fundamental role in noninvasive imaging of the chest. Within a single breath-hold, CT enables the acquisition of isotropic, high-resolution images providing detailed anatomic information about thoracic disease. Inherent opportunities of the PCD-CT, such as availability of spectral data, ultra-high-resolution imaging, and reduction of image noise may further improve this technique (Flohr et al. 2020a; Willeminck et al. 2018).

In the last two decades evolution of scanner technology and iterative image reconstruction have led to an improvement in diagnostic quality of chest CT while being able to reduce radiation dose and noise levels. In contrast to energy-integrating detector CT images, the fraction of lower energy photons contributing to PCD-CT images is higher due to the photon binning process (Farhadi et al. 2021). Moreover, the exclusion of high-energy photons in monoenergetic image reconstruction further improve image contrast and CNR in PCD-CT compared to energy-integrating detector CT (Symons et al. 2019). Cadaver studies (Gutjahr et al. 2016a) as well as first patient experience with a single-source, full field-of-view PCD-CT have shown significantly lower image noise with PCD-CT compared to

energy-integrating detector CT (Ferda et al. 2021). Symons et al. showed in a study with 30 asymptomatic volunteers that PCD-CT chest CT images have an approximately 20% higher CNR of lung nodules compared to conventional energy-integrating detector CT (Symons et al. 2017b). Lower noise levels may facilitate radiation dose reduction with PCD-CT, which may be especially beneficial in lung cancer screening examinations or follow-up chest CT. Comparable to the use of tin filtration on a dual-source chest CT, the application of tin filters may further lower noise levels with the potential for radiation dose reduction (Martini et al. 2015).

As stated above, the photon-counting detector enables the possibility to scan with an ultra-high-resolution mode, with 120 pixels measuring $0.2 \times 0.2 \text{ mm}^2$. In contrast to an energy-integrated detector, there is no need for a mechanical separation of detector cells (Flohr et al. 2020a). Bartlett et al. (2019) as well as Ferda et al. (2021) showed an improved visualization and delineation of third-, fourth- and fifth-order bronchi using ultra high-resolution lung PCD-CT with a 1024 image matrix reconstruction compared to conventional chest EID-CT (Fig. 6). As a drawback, increased spatial resolution is inherently accompanied by increased noise or the need for higher radiation doses to maintain noise levels of

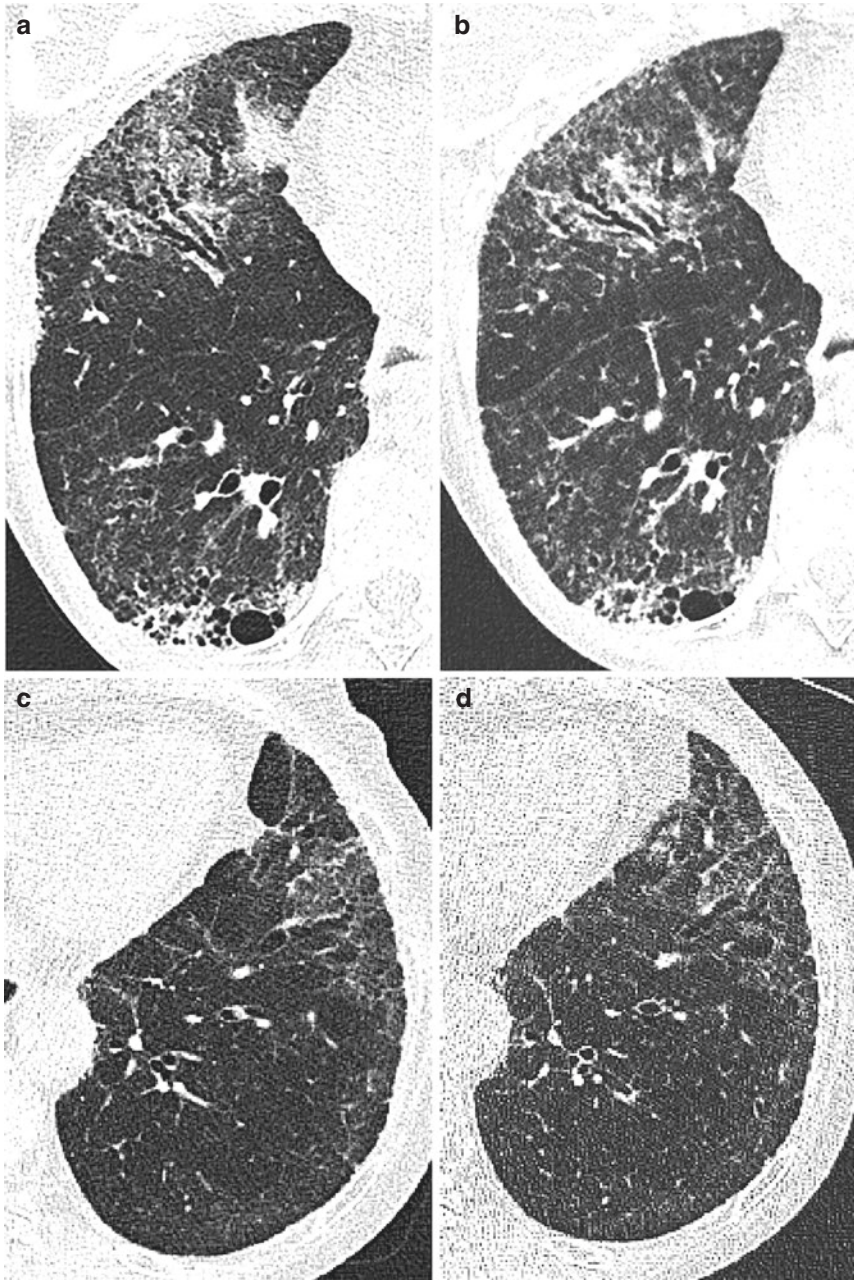


Fig. 6 Comparison of photon-counting detector CT images (PCD-CT; left column) and conventional energy-integrating detector CT images (EID-CT; right column). The upper row shows images of a 46-year-old female patient with mixed connective tissue disease and basal predominant lung fibrosis. The left image (a) was acquired with a dual-source PCD-CT (NAEOTOM Alpha, Siemens); tube voltage, 100 kV with tin filtration; CTDIvol, 0.68 mGy; Kernel, BI64; Matrix 512×512), the right image (b) was acquired with a single-source EID-CT (SOMATOM Edge Plus, Siemens); tube voltage, 100kV;

CTDIvol, 1.25 mGy; Kernel, BI64; Matrix 512×512). The bottom row shows images of an 83-year-old female patient with systemic sclerosis. The left image (c) was acquired with a dual-source PCD-CT (NAEOTOM Alpha, Siemens); tube voltage, 100 kV with tin filtration; CTDIvol, 0.51 mGy; Kernel, BI64; Matrix 512×512), the right image (d) was acquired with a third-generation, dual-source EID-CT (SOMATOM Force, Siemens); tube voltage, 100 kV; CTDIvol, 1.70 mGy; Kernel, BI64; Matrix 512×512). Note the improved spatial resolution of PCD-CT despite of lower radiation doses

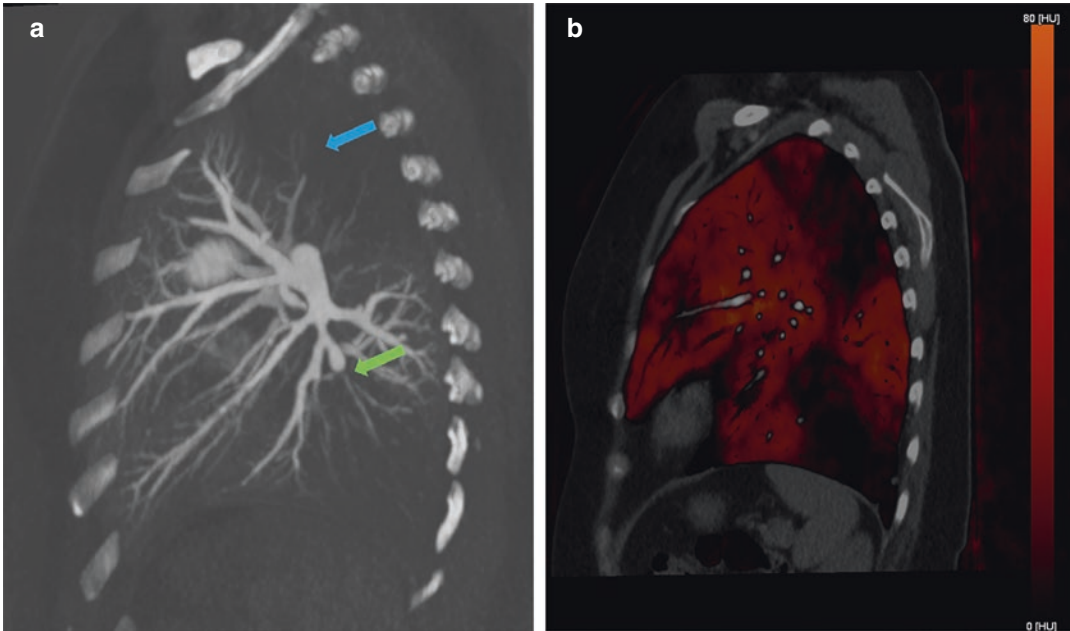


Fig. 7 Images of a 43-year-old female patient with chronic thromboembolic pulmonary hypertension undergoing photon-counting detector CT pulmonary angiography. Maximum intensity reconstruction of iodine-weighted images (a) illustrates the sudden change of caliber of a

subsegmental branch of the posterobasal segmental artery (green arrow) and rarefaction of subsegmental arteries of the apico-posterior segment of the left lung (blue arrow). The iodine map (b) illustrates the corresponding segmental perfusion defects

images with lower spatial resolution. Future research may show whether improved evaluation of the morphology of lung nodules and lung masses may improve differentiation between benign and malignant as well as characterization of lesions and outweigh the potential drawbacks.

In our experimental study using an anthropomorphic chest phantom containing various sized pulmonary nodules we found that image quality of PCD-CT was superior to EID-CT while showing comparably lower image noise (Jungblut et al. 2021).

Directly counting the energy of an incident photon, PCD-CT can be utilized for material decomposition of tissues with equal densities but different elemental composition (Flohr et al. 2020a). Spectral information may help to amplify subtle attenuation differences as well as the distribution of enhancement for detection and characterization of lung nodules and tumors (Chae et al. 2010). In chest imaging, material decomposition is frequently used in the evaluation of pulmonary vessels in patients with suspected acute or chronic

thromboembolism. The calculation of iodine maps may assist in detecting subsegmental perfusion defects (Fig. 7). Masy et al. have shown that dual-energy CT-derived iodine maps for the assessment of lung perfusion show excellent agreement with V/Q scintigraphy in diagnosing chronic thromboembolic pulmonary hypertension with a kappa of 0.8 (Masy et al. 2018). In their study, the combination of CT pulmonary angiography and iodine maps enabled to correctly diagnose all patients with chronic thromboembolic pulmonary hypertension (Masy et al. 2018). Furthermore, spectral information in CT pulmonary angiography may enable the reduction of contrast media by providing low keV monoenergetic images with improved contrast attenuation (Meier et al. 2016). Using dual-energy CT, Meier et al. could show that CT pulmonary angiography is feasible with only 6 g of iodine corresponding to 15 ml of contrast media at a concentration of 400 mg iodine/ml (Meier et al. 2016).

CT pulmonary angiography is especially susceptible to the transient interruption of contrast

inflow from the superior vena cava due to the increase of intrathoracic pressure by patients taking a deep breath before scan initiation. In these cases, advanced monoenergetic reconstructions may help to increase the attenuation of pulmonary arteries compared to single-energy scans and avoid unnecessary repetition of CT studies in patients with suboptimal opacification of pulmonary arteries.

6 Skeletal Imaging

The novel PCD-CT system offers various benefits in musculoskeletal imaging such as the constant availability of spectral information or the higher spatial resolution of bone structures using (UHR) mode.

The main advantage of PCD-CT in musculoskeletal imaging is the constant availability of spectral information. Spectral information from PCD-CT can be used for various advanced imaging processing application similar to dual-energy CT. In musculoskeletal imaging, numerous dual-energy applications are already well established,

such as monosodium urate detection in gout arthropathy, detection of bone marrow edema in fractures or metal artifact reduction using virtual monoenergetic images (Rajiah et al. 2019). In theory, PCD-CT enables perfect spectral separation which would result in superior performance of those applications compared to dual-energy CT. However, in practice, spectral separation of PCD-CT is impaired by various effects such as K-escape, charge sharing or detector polarization (Gutjahr et al. 2016b; Taguchi and Iwanczyk 2013). So far, only limited literature is available about the performance of PCT-CT in musculoskeletal imaging. Stamp et al. were able to detect monosodium urate with PCT-CT using a prototype scanner in a cadaver finger. Recently, Zhou et al. demonstrated the superior metal artifact reduction capability of PCD-CT using tin filter in combination with high-energy threshold compared to EID-CT (Zhou et al. 2019). Our first clinical experience of PCD-CT in musculoskeletal imaging is limited to virtual non-calcium imaging and gout detection. Using virtual non-calcium imaging, we were able to reliably detect bone marrow edema adjacent to fractures (Fig. 8).

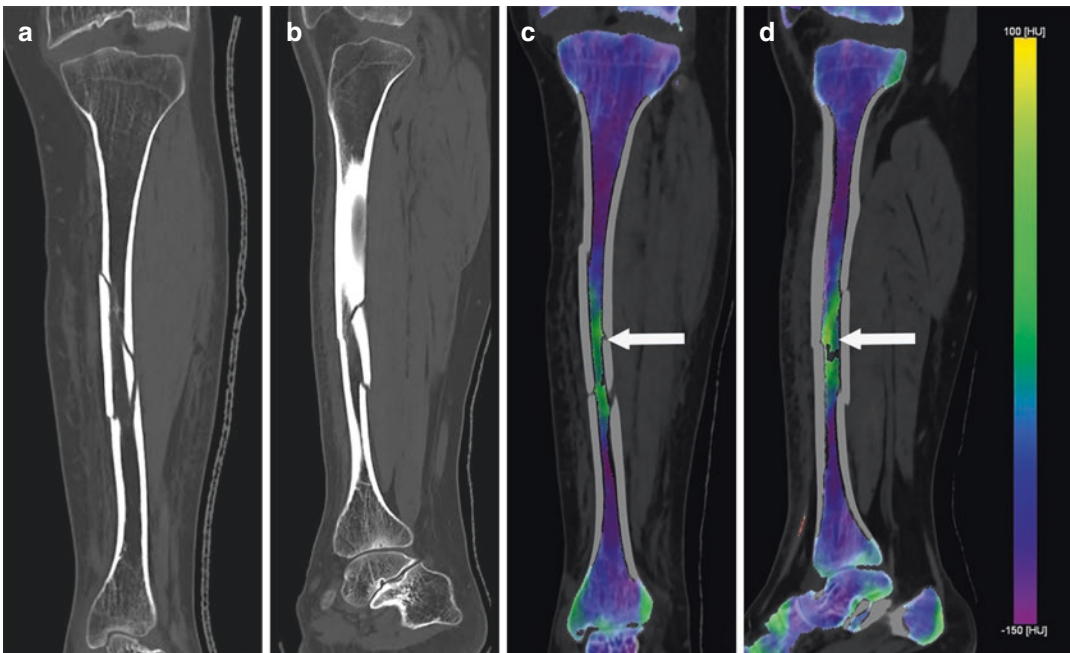


Fig. 8 Photon-counting detector CT of the lower extremity of a 28-year-old male patient in coronal (a) and sagittal plane (b) with corresponding virtual non-calcium images

in coronal (c) and sagittal (d) plane. Note the bone marrow edema (white arrow) adjacent to the fractures

Another promising advantage of PCD-CT is the so-called ultra-high-resolution (UHR) mode. High spatial resolution of CT plays a crucial role in the assessment of delicate osseous structures such as the incudo-malleolar joint in the temporal bone. Spatial resolution in conventional EID-CT is limited due to the larger size of the detector cell and the requirement of septa between each cell. To overcome this limitations, spatial resolution in EID-CT can be improved by using an additional attenuation comb filter in front of the detector which reduces the detector aperture but also decreases dose efficiency of EID (Leng et al. 2015). In contrast, PCD is equipped with smaller detector cells ($0.2 \times 0.2 \text{ mm}^2$) and has no requirement for septa or attenuation comb which results in higher spatial resolution and higher dose efficiency compared to EID. In temporal bone CT, higher spatial resolution and higher dose efficiency of prototype PCD-CT compared to EID-CT has been already demonstrated (Zhou et al. 2018; Rajendran et al. 2020). For example, Zhou et al. demonstrated a substantially better delineation of the anatomy of the temporal bones of ten cadavers scanned on PCD-CT with UHR mode compared to EID-CT using identical radiation dose (Zhou et al. 2018) and Rajendran et al. demonstrated a radiation dose reduction of greater than 80% in temporal bone CT using PCD-CT compared to EID-CT maintaining similar image quality (Rajendran et al. 2020).

7 Conclusions

Our initial experience with the first PCD-CT system for full clinical use shows promising results in several clinical application fields. The low electronic noise and high spatial resolution improve diagnostic accuracy especially in cardiovascular, lung, and musculoskeletal imaging. The superior iodine CNR is particularly valuable in abdominal imaging depicting lesions of parenchymatous organs as well as in cardiovascular imaging increasing vessel attenuation. Large potential of PCD-CT lies in the intrinsic spectral imaging properties in every CT scan enabling

material decomposition and quantification. This feature allows for the identification of contrast media and the computation of virtual non-contrast reconstructions or iodine maps. Moreover, precise material characterization is capable of identifying the composition of, e.g., urinary stones or differentiating between crystal arthropathies. Feasibility of CT imaging simultaneously using different k-edge contrast agents or targeted nanoparticles has already been proved in experimental studies but is yet to be assessed in clinical studies. Undoubtedly, this new imaging approach will reveal previously unseen information and offer a new dimension of functional imaging.

In conclusion, PCD-CT will push the boundaries of future CT imaging and opens new, currently unpredictable areas of application.

Compliance with Ethical Standards

Disclosure of Interests The manuscript has not been submitted to more than one publication simultaneously. The submitted work is original and has not been published elsewhere in any form or language (partial or complete). The authors have followed the rules for obtaining, selecting, and processing image data and have not presented any data or text of other authors as if they were their own.

References

- Alkadhi H, Euler A (2020) The future of computed tomography: personalized, functional, and precise. *Investig Radiol* 55(9):545–555. <https://doi.org/10.1097/RLI.0000000000000668>
- Aoki M, Hirose K, Sato M, Akimoto H, Kawaguchi H, Hatayama Y, Fujioka I, Tanaka M, Ono S, Takai Y (2016) Prognostic impact of average iodine density assessed by dual-energy spectral imaging for predicting lung tumor recurrence after stereotactic body radiotherapy. *J Radiat Res* 57(4):381–386. <https://doi.org/10.1093/jrr/rrv100>
- Bartlett DJ, Koo CW, Bartholmai BJ, Rajendran K, Weaver JM, Halaweish AF, Leng S, McCollough CH, Fletcher JG (2019) High-resolution chest computed tomography imaging of the lungs: impact of 1024 matrix reconstruction and photon-counting detector computed tomography. *Investig Radiol* 54(3):129–137. <https://doi.org/10.1097/RLI.0000000000000524>
- Chae EJ, Song JW, Krauss B, Song KS, Lee CW, Lee HJ, Seo JB (2010) Dual-energy computed tomog-

- raphy characterization of solitary pulmonary nodules. *J Thorac Imaging* 25(4):301–310. <https://doi.org/10.1097/RTI.0b013e3181e16232>
- Dangelmaier J, Bar-Ness D, Daerr H, Muenzel D, Si-Mohamed S, Ehn S, Fingerle AA, Kimm MA, Kopp FK, Boussel L, Roessl E, Pfeiffer F, Rummeny EJ, Proksa R, Douek P, Noël PB (2018) Experimental feasibility of spectral photon-counting computed tomography with two contrast agents for the detection of endoleaks following endovascular aortic repair. *Eur Radiol* 28(8):3318–3325. <https://doi.org/10.1007/s00330-017-5252-7>
- Darras KE, Clark SJ, Kang H, Mohammed MF, Barrett S, Chang SD, Harris AC, Nicolaou S, McLaughlin PD (2019) Virtual monoenergetic reconstruction of contrast-enhanced CT scans of the abdomen and pelvis at 40 keV improves the detection of peritoneal metastatic deposits. *Abdom Radiol (NY)* 44(2):422–428. <https://doi.org/10.1007/s00261-018-1733-7>
- Do T, Sawall S, Heinze S, Reiner T, Ziener C, Stiller W, Schlemmer H, Kachelrieß M, Kauczor H, Skornitzke S (2020) A semi-automated quantitative comparison of metal artifact reduction in photon-counting computed tomography by energy-selective thresholding. *Sci Rep* 10(1):1–10. <https://doi.org/10.1038/s41598-020-77904-3>
- Elbanna KY, Mansoori B, Mileto A, Rogalla P, Guimaraes SL (2020) Dual-energy CT in diffuse liver disease: is there a role? *Abdom Radiol (NY)* 45(11):3413–3424. <https://doi.org/10.1007/s00261-020-02702-4>
- Euler A, Higashigaito K, Mergen V, Sartoretti T, Zanini B, Schmidt B, Flohr TG, Ulzheimer S, Eberhard M, Alkadhi H (2021) High-pitch photon-counting detector computed tomography angiography of the aorta: Intraindividual comparison to energy-integrating detector computed tomography at equal radiation dose. *Investig Radiol*. <https://doi.org/10.1097/rli.0000000000000816>
- Farhadi F, Rajagopal JR, Nikpanah M, Sahbaee P, Malayeri AA, Pritchard WF, Samei E, Jones EC, Chen MY (2021) Review of technical advancements and clinical applications of photon-counting computed tomography in imaging of the thorax. *J Thorac Imaging* 36(2):84–94. <https://doi.org/10.1097/RTI.0000000000000569>
- Ferda J, Vendiš T, Flohr T, Schmidt B, Henning A, Ulzheimer S, Pecen L, Ferdová E, Baxa J, Mírka H (2021) Computed tomography with a full FOV photon-counting detector in a clinical setting, the first experience. *Eur J Radiol* 137:109614. <https://doi.org/10.1016/j.ejrad.2021.109614>
- Flohr T, Petersilka M, Henning A, Ulzheimer S, Ferda J, Schmidt B (2020a) Photon-counting CT review. *Phys Med* 79:126–136. <https://doi.org/10.1016/j.ejmp.2020.10.030>
- Flohr T, Ulzheimer S, Petersilka M, Schmidt B (2020b) Basic principles and clinical potential of photon-counting detector CT. *Chin J Acad Radiol* 3(1):19–34. <https://doi.org/10.1007/s42058-020-00029-z>
- Gutjahr R, Halaweish AF, Yu Z, Leng S, Yu L, Li Z, Jorgensen SM, Ritman EL, Kappler S, McCollough CH (2016a) Human imaging with photon-counting-based CT at clinical dose levels: contrast-to-noise ratio and cadaver studies. *Investig Radiol* 51(7):421. <https://doi.org/10.1097/RLI.0000000000000251>
- Gutjahr R, Halaweish AF, Yu Z, Leng S, Yu L, Li Z, Jorgensen SM, Ritman EL, Kappler S, McCollough CH (2016b) Human imaging with photon counting-based computed tomography at clinical dose levels: contrast-to-noise ratio and cadaver studies. *Investig Radiol* 51(7):421–429. <https://doi.org/10.1097/rli.0000000000000251>
- Habashy D, Xia R, Ridley W, Chan L, Ridley L (2016) Impact of dual energy characterization of urinary calculus on management. *J Med Imaging Radiat Oncol* 60(5):624–631. <https://doi.org/10.1111/1754-9485.12497>
- Higashigaito K, Euler A, Eberhard M, Flohr TG, Schmidt B, Alkadhi H (2021) Contrast-enhanced abdominal CT with clinical photon-counting detector CT: assessment of image quality and comparison with energy-integrating detector CT. *Acad Radiol*. <https://doi.org/10.1016/j.acra.2021.06.018>
- Jiang C, Yang P, Lei J, Li J, Yan K, Li F, Yan R, Xia L (2017) The application of iodine quantitative information obtained by dual-source dual-energy computed tomography on Chemoradiotherapy effect monitoring for cervical cancer: a preliminary study. *J Comput Assist Tomogr* 41(5):737–745. <https://doi.org/10.1097/rct.0000000000000603>
- Jungblut L, Blüthgen C, Polacin M, Messerli M, Schmidt B, Euler A, Alkadhi H, Frauenfelder T, Martini K (2021) First performance evaluation of an artificial intelligence-based computer-aided detection system for pulmonary nodule evaluation in dual-source photon-counting detector CT at different low-dose levels. *Investig Radiol*. <https://doi.org/10.1097/rli.0000000000000814>
- Leng S, Bruesewitz M, Tao S, Rajendran K, Halaweish AF, Campeau NG, Fletcher JG, McCollough CH (2019) Photon-counting detector CT: system design and clinical applications of an emerging technology. *Radiographics* 39(3):729–743. <https://doi.org/10.1148/rg.2019180115>
- Leng S, Diehn FE, Lane JJ, Koeller KK, Witte RJ, Carter RE, McCollough CH (2015) Temporal bone CT: improved image quality and potential for decreased radiation dose using an ultra-high-resolution scan mode with an iterative reconstruction algorithm. *Am J Neuroradiol* 36(9):1599–1603. <https://doi.org/10.3174/ajnr.A4338>
- Leng S, Rajendran K, Gong H, Zhou W, Halaweish AF, Henning A, Kappler S, Baer M, Fletcher JG, McCollough CH (2018) 150- μ m spatial resolution using photon-counting detector computed tomography technology: technical performance and first patient images. *Investig Radiol* 53(11):655–662. <https://doi.org/10.1097/RLI.0000000000000488>
- Leng S, Yu Z, Halaweish A, Kappler S, Hahn K, Henning A, Li Z, Lane J, Levin DL, Jorgensen S (2016) Dose-

- efficient ultrahigh-resolution scan mode using a photon counting detector computed tomography system. *J Med Imag* 3(4):043504. <https://doi.org/10.1117/1.JMI.3.4.043504>
- Mannil M, Hickethier T, von Spiczak J, Baer M, Henning A, Hertel M, Schmidt B, Flohr T, Maintz D, Alkadhi H (2018) Photon-counting CT: high-resolution imaging of coronary stents. *Investig Radiol* 53(3):143–149. <https://doi.org/10.1097/rli.0000000000000420>
- Marcus RP, Fletcher JG, Ferrero A, Leng S, Halaweish AF, Gutjahr R, Vrtiska TJ, Wells ML, Enders FT, McCollough CH (2018) Detection and characterization of renal stones by using photon-counting-based CT. *Radiology* 289(2):436–442. <https://doi.org/10.1148/radiol.2018180126>
- Marri UK, Das P, Shalimar M, Kalavani DNS, Madhusudhan KS (2021) Noninvasive staging of liver fibrosis using 5-minute delayed dual-energy CT: comparison with US Elastography and correlation with histologic findings. *Radiology* 298(3):600–608. <https://doi.org/10.1148/radiol.2021202232>
- Martini K, Higashigaito K, Barth BK, Baumüller S, Alkadhi H, Frauenfelder T (2015) Ultralow-dose CT with tin filtration for detection of solid and sub solid pulmonary nodules: a phantom study. *Br J Radiol* 88(1056):20150389. <https://doi.org/10.1259/bjr.20150389>
- Masy M, Giordano J, Petyt G, Hossein-Foucher C, Duhamel A, Kyheng M, De Groote P, Fertin M, Lamblin N, Bervar JF, Remy J, Remy-Jardin M (2018) Dual-energy CT (DECT) lung perfusion in pulmonary hypertension: concordance rate with V/Q scintigraphy in diagnosing chronic thromboembolic pulmonary hypertension (CTEPH). *Eur Radiol* 28(12):5100–5110. <https://doi.org/10.1007/s00330-018-5467-2>
- Meier A, Higashigaito K, Martini K, Wurnig M, Seifert B, Keller DI, Frauenfelder T, Alkadhi H (2016) Dual energy CT pulmonary angiography with 6g iodine—a propensity score-matched study. *PLoS One* 11(12):e0167214. <https://doi.org/10.1371/journal.pone.0167214>
- Mergen V, Sartoretti T, Klotz E, Schmidt B, Jungblut L, Higashigaito K, Manka R, Euler A, Kasel M, Eberhard M, Alkadhi H (2022) Extracellular volume quantification with cardiac late enhancement scanning using dual-source photon-counting detector CT. *Invest Radiol*. <https://doi.org/10.1097/RLI.0000000000000851>. Epub ahead of print. PMID: 35066531
- Nagayama Y, Inoue T, Oda S, Tanoue S, Nakaura T, Ikeda O, Yamashita Y (2020) Adrenal adenomas versus metastases: diagnostic performance of dual-energy spectral CT virtual noncontrast imaging and iodine maps. *Radiology* 296(2):324–332. <https://doi.org/10.1148/radiol.2020192227>
- Nowak T, Eberhard M, Schmidt B, Frey D, Distler O, Saltybaeva N, Alkadhi H, Euler A (2021) Bone mineral density quantification from localizer radiographs: accuracy and precision of energy-integrating detector CT and photon-counting detector CT. *Radiology* 298(1):147–152. <https://doi.org/10.1148/radiol.2020202767>
- Parakh A, Patino M, Muenzel D, Kambadakone A, Sahani DV (2018) Role of rapid kV-switching dual-energy CT in assessment of post-surgical local recurrence of pancreatic adenocarcinoma. *Abdom Radiol (NY)* 43(2):497–504. <https://doi.org/10.1007/s00261-017-1390-2>
- Pourmorteza A, Symons R, Henning A, Ulzheimer S, Bluemke DA (2018) Dose efficiency of quarter-millimeter photon-counting computed tomography: first-in-human results. *Investig Radiol* 53(6):365–372. <https://doi.org/10.1097/RLI.0000000000000463>
- Rajendran K, Voss BA, Zhou W, Tao S, DeLone DR, Lane JJ, Weaver JM, Carlson ML, Fletcher JG, McCollough CH, Leng S (2020) Dose reduction for sinus and temporal bone imaging using photon-counting detector CT with an additional tin filter. *Investig Radiol* 55(2):91–100. <https://doi.org/10.1097/rli.0000000000000614>
- Rajiah P, Sundaram M, Subhas N (2019) Dual-energy CT in musculoskeletal imaging: what is the role beyond gout? *AJR Am J Roentgenol* 213(3):493–505. <https://doi.org/10.2214/ajr.19.21095>
- Ren L, Rajendran K, Fletcher JG, McCollough CH, Yu L (2020) Simultaneous dual-contrast imaging of small bowel with iodine and bismuth using photon-counting-detector computed tomography: a feasibility animal study. *Investig Radiol* 55(10):688–694. <https://doi.org/10.1097/rli.0000000000000687>
- Riederer I, Si-Mohamed S, Ehn S, Bar-Ness D, Noël PB, Fingerle AA, Pfeiffer F, Rummeny EJ, Douek P, Pfeiffer D (2019) Differentiation between blood and iodine in a bovine brain—initial experience with spectral photon-counting computed tomography (SPCCT). *PLoS One* 14(2):e0212679. <https://doi.org/10.1371/journal.pone.0212679>
- Sartoretti T, Eberhard M, Nowak T, Gutjahr R, Jost G, Pietsch H, Schmidt B, Flohr T, Alkadhi H, Euler A (2021) Photon-counting multienergy computed tomography with spectrally optimized contrast Media for Plaque Removal and Stenosis Assessment. *Investig Radiol*. <https://doi.org/10.1097/rli.0000000000000773>
- Sartoretti T, Eberhard M, Rüschoff JH, Pietsch H, Jost G, Nowak T, Schmidt B, Flohr T, Euler A, Alkadhi H (2020) Photon-counting CT with tungsten as contrast medium: experimental evidence of vessel lumen and plaque visualization. *Atherosclerosis* 310:11–16. <https://doi.org/10.1016/j.atherosclerosis.2020.07.023>
- Sartoretti T, Mergen V, Higashigaito K, Eberhard M, Alkadhi H, Euler A (2022a) Virtual noncontrast imaging of the liver using photon-counting detector computed tomography: a systematic phantom and patient study. *Invest Radiol*. <https://doi.org/10.1097/RLI.0000000000000860>. Epub ahead of print. PMID: 35136003
- Sartoretti T, Landsmann A, Nakhostin D, Eberhard M, Röeren C, Mergen V, Higashigaito K, Raupach R, Alkadhi H, Euler A (2022b) Quantum iterative reconstruction for abdominal photon-counting detector ct improves image quality. *Radiology*.

- <https://doi.org/10.1148/radiol.211931>. Epub ahead of print. PMID: 35103540
- Schmidt TG (2009) Optimal “image-based” weighting for energy-resolved CT. *Med Phys* 36(7):3018–3027. <https://doi.org/10.1118/1.3148535>
- Shuman WP, Green DE, Busey JM, Mitsumori LM, Choi E, Koprowicz KM, Kanal KM (2014) Dual-energy liver CT: effect of monochromatic imaging on lesion detection, conspicuity, and contrast-to-noise ratio of hypervascular lesions on late arterial phase. *AJR Am J Roentgenol* 203(3):601–606. <https://doi.org/10.2214/ajr.13.11337>
- Si-Mohamed S, Tatarad-Leitman V, Laugerette A, Sigovan M, Pfeiffer D, Rummeny EJ, Coulon P, Yagil Y, Douek P, Boussel L (2019) Spectral photon-counting computed tomography (SPCCT): in-vivo single-acquisition multi-phase liver imaging with a dual contrast agent protocol. *Sci Rep* 9(1):1–8. <https://doi.org/10.1038/s41598-019-44821-z>
- Si-Mohamed SA, Sigovan M, Hsu JC, Tatarad-Leitman V, Chalabreyse L, Naha PC, Garrivier T, Dessouky R, Carnaru M, Boussel L, Cormode DP, Douek PC (2021) In vivo molecular K-edge imaging of atherosclerotic plaque using photon-counting CT. *Radiology*:203968. <https://doi.org/10.1148/radiol.2021203968>
- von Spiczak J, Mannil M, Peters B, Hickethier T, Baer M, Henning A, Schmidt B, Flohr T, Manka R, Maintz D, Alkadhi H (2018) Photon counting computed tomography with dedicated sharp convolution kernels: tapping the potential of a new Technology for Stent Imaging. *Investig Radiol* 53(8):486–494. <https://doi.org/10.1097/rli.0000000000000485>
- Stamp LK, Anderson NG, Becce F, Rajeswari M, Polson M, Guyen O, Viry A, Choi C, Kirkbride TE, Raja AY (2019) Clinical utility of multi-energy spectral photon-counting computed tomography in crystal arthritis. *Arthritis Rheumatol* 71(7):1158–1162. <https://doi.org/10.1002/art.40848>
- Symons R, Krauss B, Sahbaee P, Cork TE, Lakshmanan MN, Bluemke DA, Pourmorteza A (2017a) Photon-counting CT for simultaneous imaging of multiple contrast agents in the abdomen: an in vivo study. *Med Phys* 44(10):5120–5127. <https://doi.org/10.1002/mp.12301>
- Symons R, Pourmorteza A, Sandfort V, Ahlman MA, Cropper T, Mallek M, Kappler S, Ulzheimer S, Mahesh M, Jones EC, Malayeri AA, Folio LR, Bluemke DA (2017b) Feasibility of dose-reduced chest CT with photon-counting detectors: initial results in humans. *Radiology* 285(3):980–989. <https://doi.org/10.1148/radiol.2017162587>
- Symons R, Reich DS, Bagheri M, Cork TE, Krauss B, Ulzheimer S, Kappler S, Bluemke DA, Pourmorteza A (2018) Photon-counting computed tomography for vascular imaging of the head and neck: first in vivo human results. *Investig Radiol* 53(3):135–142. <https://doi.org/10.1097/rli.0000000000000418>
- Symons R, Sandfort V, Mallek M, Ulzheimer S, Pourmorteza A (2019) Coronary artery calcium scoring with photon-counting CT: first in vivo human experience. *Int J Cardiovasc Imaging* 35(4):733–739. <https://doi.org/10.1007/s10554-018-1499-6>
- Taguchi K, Iwanczyk JS (2013) Vision 20/20: single photon counting x-ray detectors in medical imaging. *Med Phys* 40(10):100901. <https://doi.org/10.1118/1.4820371>
- Tao S, Rajendran K, McCollough CH, Leng S (2019) Feasibility of multi-contrast imaging on dual-source photon counting detector (PCD) CT: an initial phantom study. *Med Phys* 46(9):4105–4115. <https://doi.org/10.1002/mp.13668>
- Uyeda JW, Richardson IJ, Sodickson AD (2017) Making the invisible visible: improving conspicuity of noncalcified gallstones using dual-energy CT. *Abdom Radiol (NY)* 42(12):2933–2939. <https://doi.org/10.1007/s00261-017-1229-x>
- Willeminck MJ, Persson M, Pourmorteza A, Pelc NJ, Fleischmann D (2018) Photon-counting CT: technical principles and clinical prospects. *Radiology* 289(2):293–312. <https://doi.org/10.1148/radiol.2018172656>
- Yu Z, Leng S, Kappler S, Hahn K, Li Z, Halaweish AF, Henning A, McCollough CH (2016) Noise performance of low-dose CT: comparison between an energy integrating detector and a photon counting detector using a whole-body research photon counting CT scanner. *J Med Imag* 3(4):043503. <https://doi.org/10.1117/1.JMI.3.4.043503>
- Zheng X, Liu Y, Li M, Wang Q, Song B (2016) Dual-energy computed tomography for characterizing urinary calcified calculi and uric acid calculi: a meta-analysis. *Eur J Radiol* 85(10):1843–1848. <https://doi.org/10.1016/j.ejrad.2016.08.013>
- Zhou W, Bartlett DJ, Diehn FE, Glazebrook KN, Kotsenas AL, Carter RE, Fletcher JG, McCollough CH, Leng S (2019) Reduction of metal artifacts and improvement in dose efficiency using photon-counting detector computed tomography and tin filtration. *Investig Radiol* 54(4):204–211. <https://doi.org/10.1097/rli.0000000000000535>
- Zhou W, Lane JI, Carlson ML, Bruesewitz MR, Witte RJ, Koeller KK, Eckel LJ, Carter RE, McCollough CH, Leng S (2018) Comparison of a photon-counting-detector CT with an energy-integrating-detector CT for temporal bone imaging: a cadaveric study. *AJNR Am J Neuroradiol* 39(9):1733–1738. <https://doi.org/10.3174/ajnr.A5768>